A NEW DIRECTION FOR DISTRIBUTED-SCALE SOLAR-THERMAL CO-GENERATION

A Dissertation

by

NATHAN R. KAMPHUIS

Submitted to the Office of Graduate and Professional Studies of
Texas A&M University
in partial fulfillment of the requirements for the degree of

DOCTOR OF PHILOSOPHY

Chair of Committee,	Kaylan Annamalai
Committee Members,	Andrew Duggleby
	Michael Johnson
	Richard J. Malak Jr.
	David Staack
Department Head,	Andreas Polycarpou

August 2018

Major Subject: Mechanical Engineering

ABSTRACT

The goal for a distributed-scale solar-thermal co-generation (DSSTC) design is a realistic solar-thermal heat and electrical generation system for residential, commercial, and industrial applications. A holistic design approach is accomplished by advancing and adapting knowledge from several fields of study. The research includes solar irradiance modeling from the atmospheric science and engineering perspectives, thermal-fluids design of heat engines and the search for working fluids, organic Rankine cycle design, system design optimization. Previous works focus only on one or two of these fields, while neglecting the design requirements of one or more of the others. No work has shown that DSSTC can be cost effective despite functioning designs as early as the late 19th Century. This work evaluates design requirements by synthesizing fundamentals in each field to build a complete analysis. Design methodology and cost effectiveness are fundamentally advanced, while identifying key future research needs. This is achieved by building a complete system simulation that accounts for size, part-load and realistic solar variability, which naturally lead to advances in the fundamental fields. Solar irradiance modeling for solar thermal collector is advanced by evaluating the testing standard and demonstrating the benefit of angular distribution sky radiance modeling. The search for working fluids is extended from the heating, ventilation, and air-conditioning equipment field to organic Rankine cycle heat engines. The cost of DSSTC is compared to Photovoltaic (PV) on an electricity generation and heat production basis. By properly accounting for both the anisotropy of the sky and the collector, solar model prediction is improved. Adapting the fluid search criteria finds few current fluid options that met both thermodynamic as well as health, safety, and environmental requirements. There exists a possibility of finding new working fluids for higher temperature organic Rankine cycle applications. The fluid search process is incomplete and remains future work. System simulation at four levels of detail are completed. Increasing detail lowers predicted energy yield and reveals additional design problems of increasing complexity. DSSTC comparison to PV shows that PV is more cost effective for electricity only production and DSSTC is more cost effective for heat production in the 150–250°C range, which is the N–S XCPC marketed range. It remains unclear which system, if either, can be cost effective for both electrical and thermal energy needs, although PV is making progress by competing in space heating and domestic hot water thermal end uses. Additional simulation is required to evaluate the possible benefit of using DSSTC in a co-generation capacity.

DEDICATION

In loving memory of Betty Rose (DeHaan) Kamphuis; she was a mother of three, daughter of two, and wife of one. Betty was the first child in her family to attend and graduate from college, and dedicated her life to education. She was passionate about life-long learning and demonstrated this through her individual learning, teaching elementary students, raising children, and helping others to learn how to navigate life. She instilled in me at an early age to think for myself and ask the simple yet difficult question "Does this make sense?" She helped me learn to overcome the difficulties of a learning disability in reading, taught me to persevere in the most difficult of situations, and to try new approaches when a problem does not yield. It is the skill of being a life-long learner that I have found most useful and prize above all other traits. Betty instilled in me her fierce nature; which caused me to thrive in the most difficult of environments. This equipped me to meet the challenges I have faced; whether it was Marine Corps service, undergraduate physics at University of California–Berkeley, or researching renewable energy technology at Texas A&M University. Even though mathematics was not Betty's strong suit, it was her creativity, persistence, and work ethic that caused me to succeed in the mathematics-dominated fields of physics, computer programming, and engineering. Her fearless love of learning, instilled in me at a young age, allowed me to push the boundaries of learning through the research of solar-thermal energy technologies. I am forever grateful for all of our birthdays that you gave up in celebration of mine.

ACKNOWLEDGEMENTS

First and foremost, I would like to recognize my Lord and Savior Jesus Christ. His generous grace and mercy have carried me through the worst and best of times. To my dearest wife Tiffany, thank you for all of your support which enabled my continued work. Your constant encouragement, patience, and love motivated me through the tough times. Best of all, I love how much you champion my success.

I would also like to thank the committee members for all the conversations and advice on how to apply their domain expertise and knowledge to the solar thermal power generation field. In particular, I would like to thank Dr. Annamalai for helping me compete this process and for generously giving his time to guide me across the finish line. I would like to thank Dr. Duggleby for continual support and encouragement. Dr. Duggleby has so much integrity in how he as helped me and stood by me. I would also like to thank Dr. Staack for generously stepping in at the last minute, joining the committee, and advice on the two-phase flow issue which has helped guide me to a much better discussion of the problem and presentation of an expectation about the impact of the assumptions. Dr. Malak has been instrumental in advising me on the proper use of decision theory and design optimization. Dr. Johnson kindly help me navigate the bridge between core engineering and the subjective would of cost. I would also like to thank Dr. Mark T. Holtzapple of the Department of Chemical Engineering at Texas A&M for generously editing Chapters 1–17. His suggestions and advice on communication style and technique are invaluable knowledge. Much thanks is also due Dr. Christian (Chris) Gueymard of Solar Consulting Services for his generous advice and expertise in solar modeling.

I would also like to thank the Texas A&M Supercomputing Facility for gener-

ously donating computing time to run some of the more computationally expensive code. Special thanks to Marinus Pennings for his assistance in the process of porting REFPROP to the Unix resources on EOS and ADA. Additionally, I would like to thank the Texas A&M Library, in particular Drs. Zheng Ye (Lan) Yang, and Tatyana Chubaryan, as well as Bruce Neville, for their assistance in finding documents, books, and papers. Without the excellent resources from the University library and expert knowledge of the helpful staff, my research efforts would not have been possible. This is especially true for the research into the origin and geometry of the Isotropic Sky Model which depended heavily on Dr. Chubaryan's kind translation of selected works in Russian. I would also like to thank colleague and dear friend, Dr. Irina Gaynanova for her translation of selected Russian works and statistics advice.

I would like to thank the NIST team who are too many to name them individually. In particular, Piotr Domanski, Eric Lemmon, and Mark McLinden for kindly sharing their knowledge and expertise in the fields of fluid modeling, refrigeration cycles, and the refrigerant creation process. I would also like to thank them for sharing their algorithms with the world. Having access to REFPROP, Evap-Cond, and DB103b are critical to my own research efforts. I would also like to thank the NREL team for sharing the knowledge about solar PV, solar modeling, and for sharing the following algorithm and data SPA, and TMY2/TMY3. Additionally, I would like to thank Sandia National Laboratory, all the researchers who contributed to PVPMC (PV_LIB Toolbox), and specifically, Dr. Joshua Stein. Lastly, thank you to all the researchers who have shared their knowledge. It is through this sharing that we stimulate and accelerate the learning process.

NOMENCLATURE

Abbreviations

ASHRAE	American Society of Heating, Refrigerating, and Air-Conditioning Engineers
ASRC	Atmospheric Sciences Research Center at the State University of New York
ASM	All-Sky Model by Igawa et al.
ATV	All-terrain vehicle
AWM	All-Weather Model by Perez et al.
CEO	Chief Executive Officer
CDRS	Computation of Diffuse Radiation on Slopes by Gueymard
CIE	International Commission on Illumination (Commission Internationale de l'Eclairage)
COP	Coefficient of performance, unitless
CVT	Continuously variable transmission
DB	Database
DHI	Diffuse horizontal irradiance
DHIU	Diffuse horizontal irradiance percent uncertainty
DHW	Domestic hot water
DIPPR	Design Institute for Physical Property Research
DNI	Direct normal irradiance
DNIU	Direct normal irradiance percent uncertainty
DSSTC	Distributed-scale solar-thermal co-generation

EPA	Environmental Protection Agency
ETRN	Extraterrestrial radiation normal to the sun
ETR	Extraterrestrial radiation on a horizontal surface
EU	European Union
FP	Flat-plate STC
FOV	Field of view
FOM	Figure of merit
GHI	Global horizontal irradiance
GHIU	Global horizontal irradiance percent uncertainty
GIS	Geographical Information System
GSI	Global Sloped Irradiance see POAI
GTI	Global Tilted Irradiance see POAI
GUM	Generalized Uncertainty of Measurement (ISO standard)
GWP	Global Warming Potential
HSE	Health, safety, and environment
HVAC-R	Heating, ventilation, air conditioning, and refrigeration industry
HX	Heat exchanger
IAM	Incident angle modifier
IASM	Improved All-Sky Model by Igawa
IHX	Internal heat exchanger
ISM	Isotropic Sky Model
ISO	Organization for Standardization
LCOE	Lifecycle cost of energy or levelized cost of energy
LFOV	Limited field of view
MBE	Mean bias error

MIDC	Measurement and Instrumentation Data Center at NREL
M3DISM	Modified 3D Isotropic Sky Model by Kamphuis
NASA	National Aeronautics and Space Administration
NFPA	National Fire Protection Association
NIST	National Institute of Standards and Technology
NREL	National Renewable Energy Laboratory
NSRDB	National Solar Resource Database
ODP	Ozone Depletion Potential
ORC	Organic Rankine cycle
POA	Plane of array
POAI	Plane of array irradiance
PV	Photovoltaic
PVC	Photovoltaic collector
PVPMC	Photovoltaic Performance Modeling Collaborative
R	Refrigerant as in R-134a
RSME	Root-squared-mean error
SHIP	Solar heat for industrial process
SOF	Surface orientation factor
SOF_s	South-facing surface orientation factor
SPA	Solar Position Algorithm by NREL
SRCC	Solar Rating and Certification Corporation
STC	Solar-thermal collector
SUNY	State University of New York at Albany
TMY	Typical meteorological year
TMY2	Typical meteorological year Version 2 by NREL

TMY3	Typical meteorological year Version 3 by NREL
US	United States of America
USD	United States Dollars
USNO	United States Naval Observatory
UV	Ultraviolet light
VCC	Volumetric cooling capacity (see also Q_{vol})
VHC	Volumetric heating capacity (see also Q_{vol})
VWC	Volumetric work capacity (see also ψ)
XCPC	External compound parabolic collector, by Roland Winston
3DISM	3D Isotropic Sky Model by Badescu

Latin Symbols

A	Area, m^3
C	Solar collector concentration ratio (also known as suns i.e., $C = 2$ is two suns), unitless
C_p	Specific heat capacity at constant pressure, kJ/(kg·K) or J/(kg·K) depending on context
C_p^0	Specific heat capacity at constant pressure given at 300 K, J/(kg·K)
D_h	Hydraulic diameter for internal flow, m or mm
D_T	Diffuse irradiance contribution on a tilted surface, $\mathrm{W/m^2}$ or $\mathrm{kWh/(m^2 \cdot day)}$
E^*	Optimal energy yield, $\mathrm{MWh/(m^2 \cdot yr)}$ or $\mathrm{kWh/(m^2 \cdot yr)}$
E_{shaft}	Shaft energy of a heat engine, $\mathrm{MWh/(m^2 \cdot yr)}$, $\mathrm{kWh/(m^2 \cdot yr)}$, or $\mathrm{Wh/(m^2 \cdot yr)}$

F_{12}	View factor from heat transfer, unitless, or correction factor used in the Perez models, unitless
F_1	Perez 1990 model Circumsolar Brightening Coefficent, unitless
F_2	Perez 1990 model Horizon Brightening Coefficent, unitless
F'	Klucher Clearness index, unitless
G	Irradiance: solar radiosity, or total irradiance, W/m^2 or kWh/(m^2·day)
G_{eff}	Effective irradiance on a solar collector, W/m^2, kWh/(m^2·day), or MWh/(m^2·yr)
G_m	Measured G at stagnation condition in a STC, W/m^2 or kWh/(m^2·day)
G_s	G at specified or reported stagnation condition in a STC, W/m^2 or kWh/(m^2·day)
h	Specific enthalpy, kJ/kg
$\bar{h}$	Average convective heat transfer coefficient, W/(m^2 K)
I	Intensity, W/(m^2·sr)
I_d	Diffuse Intensity, W/(m^2·sr)
$I_{b,n}$	DNI, W/m^2 or kWh/(m^2·day)
$I_{b,n}^0$	ETRN, W/m^2 or kWh/(m^2·day)
$I_{d,h}$	DHI, W/m^2 or kWh/(m^2·day)
$I_{t,h}$	GHI, W/m^2 or kWh/(m^2·day)
$I_{t,h}^0$	Extraterrestrial global horizontal irradiance (ETR), W/m^2 or kWh/(m^2·day)
I_T	Irradiance: solar radiosity, or total irradiance, W/m^2 or kWh/(m^2·day)

k	Cloud ratio, unitless
k	Thermal conductivity, W/(m K)
k_t	Atmospheric clearness index, unitless
K	IAM function for STC, unitless
K_d	Diffuse IAM function for STC, unitless
K_θ	The standard functional form of the IAM function of STC, unitless
$K_{\theta b}$	Beam IAM function of STC for collector, unitless
L	length of the fluid flow path in a heat exchanger, m
lv	Relative sky radiance, unitless
Lv	Absolute sky radiance, W/(m^2·sr)
m	Relative Optical Air Mass, unitless
$\dot{m}$	Mass flow rate, kg/s
Nu	Nusselt number, unitless
P	Pressure, Pa
P_c	Critical Pressure, Pa
P_{shaft}	Shaft power output of a heat engine, W
Q_{vol}	Volumetric capacity, kJ/m^3
$\dot{Q}$	Heat - the flow of thermal energy, kW_th
r	radius, m
$\boldsymbol{R}$	Rotation Matrix, unitless
R	Universal ideal gas constant, 8.31451 J/(mol·K)
R_d	Diffuse transposition factor, unitless
$\overline{R_d}$	Irradiance weighted average diffuse transposition factor, unitless
Re_d	Reynolds number based on internal flow, unitless
R_r	Reflected transposition factor, unitless

R_T	Reflected irradiance contribution on a tilted surface, W/m^2 or kWh/(m^2·day)
s	Entropy, J/(K·kg)
t	Time, s
T	Temperature, °F, °C, K
T_c	Critical temperature, °F, °C, K
T_{amb}	Ambient temperature, °F, °C, K
T_{as}	T_{amb} at specified or reported stagnation condition in a STC, °C, K
T_H	High temperature, °F, °C, K
T_L	Low temperature, °F, °C, K
T_m	Mean fluid temperature in a STC, °C, K
T_m^*	Reduced mean fluid temperature in a STC, (K·m^2)/W
$T_{m\ \mathrm{stag}}^*$	T_m^* at specified or reported stagnation condition in a STC, (K·m^2)/W
T_s	STC absorber tube surface temperature, °C, K
T_{sm}	Measured T_m at stagnation conditions in a STC, °C, K
T_{stag}	T_m at specified or reported stagnation condition in a STC, °C, K
V_{pump}	Inlet chamber size of the pump, m^3
$V_{expander}$	Inlet chamber size of the expander, m^3
$\dot{V}$	Volumetric flow, m^3/s

Greek Symbols

α_{LR}	Angle of acceptance limit for a STC in the left/right direction, rad or °
α_{TB}	Angle of acceptance limit for a STC in the top/bottom direction, rad or °

β	Solar collector mounting angle from horizontal (also tilt or slope), rad or °
β^*	Optimal mounting angle, rad or °
γ	Solar collector mounting angle (azimuth from south as defined in SPA documentation), rad or °
γ^*	Optimal mounting angle in the azimuth direction, rad or °
Γ	Solar azimuth angle (as defined in SPA documentation), rad or °
δ	Solar declination angle at solar noon in the middle of a month, rad or °
Δ	Perez 1990 / AWM Sky Brightness, unitless
ΔT	Temperature difference, °F, °C, K (time difference: Astronomical Almanac, s)
$\Delta UT1$	Observed irregular rotation rate of the earth, s
ϵ	Perez 1990 / AWM Sky Clearness or the emissivity depending on context, unitless
ζ	Solar zenith angle, rad or °
ζ_{se}	Zenith angle of a sky element, rad or °
η	Efficiency as a ratio, unitless
η_{Carnot}	Carnot's efficiency for a cycle, unitless
η_{col}	Collector efficiency as a ratio, unitless
η_{cycle}	Efficiency of a thermodynamic cycle, unitless
η_{sys}	System efficiency, unitless
η_2	Second law efficiency of a thermodynamic cycle, unitless
η_p	Pump efficiency as a ratio, unitless
η_t	Expander efficiency as a ratio, unitless

η^*_{net}	Net efficiency as a ratio, unitless
θ	Polar angle, reference: normal of a STC (unrotated, horizontal mounting, and this also corresponds to the zenith angle of a sky element), rad or °
θ'	Polar angle, reference: normal of a STC (single rotated), rad or °
θ''	Polar angle, reference: normal of a STC (double rotated), rad or °
θ_s	Polar angle, reference: normal of a STC for the location of the sun (unrotated), rad or °
θ''_s	Polar angle, reference: normal of a STC for the location of the sun (double rotated), rad or °
θ_L	Angle of incidence in the solar collector longitudinal direction, rad or °
θ_{LR}	Angle of incidence in the solar collector left-right orientation (see Table 9.2), rad or °
θ_T	Angle of incidence in the solar collector transverse direction, rad or °
θ_{TB}	Angle of incidence in the solar collector top-bottom orientation (see Table 9.2), rad or °
θ_i	Angle of incidence between the collector normal and the sun beam, rad or °
θ_{ses}	Angle of incidence between a sky element and the sun beam, rad or °
θ_{secn}	Angle of incidence between a sky element and the collector normal, rad or °
λ	Wavelength, m
μ	Dynamic viscosity, cP, kg/(m s), or Pa s
ν	specific volume, m^3/kg

ρ	Density, kg/m^3 or albedo, unitless; depending on context
ρ_c	Critical density, kg/m^3
σ	Slope of the saturated vapor entropy line or the Stefan-Boltzmann constant depending on the context
Υ	Expansion ratio based on specific volume or density, unitless
ϕ	Azimuth angle in reference to the normal of a STC (unrotated), rad or °
ϕ'	Azimuth angle in reference to the normal of a STC (single rotated), rad or °
ϕ''	Azimuth angle in reference to the normal of a STC (double rotated), °
ϕ_s	Azimuth angle in reference to the normal of a STC for the location of the sun (unrotated), rad or °
ϕ''_s	Azimuth angle in reference to the normal of a STC for the location of the sun (double rotated), rad or °
Φ	Latitude, rad or °
ψ	Volumetric work capacity, a measure of machine size, kJ/m^3 or J/m^3
Ω	Solid angle of a sphere, sr

TABLE OF CONTENTS

Page

LIST OF FIGURES

FIGURE Page

LIST OF TABLES

PART I. CONTEXTUALIZING THE ENERGY PROBLEM

1. INTRODUCTION

> *"The opportunities and demands of human activity have increased far more rapidly than the exercise of human power, or the application of known principles, or the appropriation of external forces; and man is crippled to-day for lack of auxiliaries... Can we not employ something which will still remain for to-morrow after we have used it to-day? As the flowing stream gives its aid, so may not other natural movements be harnessed into our service?" [3]*
>
> – Charles Henry Pope, 1903

Engineers solve social problems using technical solutions. In the industrialized world, unprecedented energy use has lead to an extremely high quality of life. This colossal amount of energy consumption also has negative impacts—such as environmental degradation, energy insecurity, and price volatility. Energy efficiency and renewable (sustainable) energy sources provide avenues to reduce environmental impact, improve security, and stabilize the price of energy. One renewable energy technology is Distributed-Scale ($\sim$10 kW) Solar-Thermal Co-generation (DSSTC).

1.1 Energy technology comparison

1.1.1 Selected overview of Energy Resources

To better understand DSSTC and how it fits into the overall energy landscape, this section briefly discusses some major types of sustainable energy technologies and then highlights DSSTC.

Figure 1.1 shows the major types of energy resources.

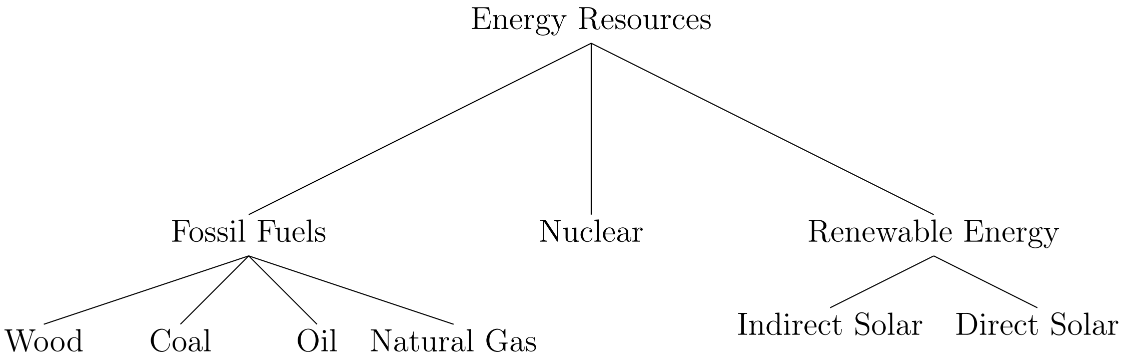

Figure 1.1: Types of energy resources.

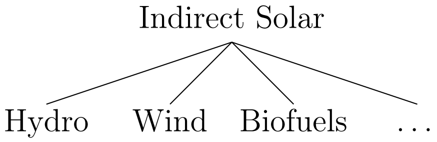

Figure 1.2: Renewable energy source indirectly received from the sun.

1.1.2 Selected types of renewable energy

The many diverse renewable energy technologies can be broadly categorized into direct solar and indirect solar technologies. Examples of indirect solar technology (Figure 1.2) are wind, ocean wave, ocean current, and biofuels. Examples of direct solar technology (Figure 1.3) are photovoltaic solar panels and solar thermal collectors. There are other types of renewable energy that do not fit into these two broad categories, for example, tidal energy (motion driven by gravitational forces from the Moon) and geothermal energy (heat derived from nuclear fission of radioactive material).

Solar thermal collector designs have many forms (Figure 1.4). Typically, trough, dish, and power-tower designs are used at large scale (500+ kW), employ solar tracking (single or dual-axis), and have high concentration ratios of more than 5–10 suns to produce high temperatures for power generation. Flat-plate and evacuated-

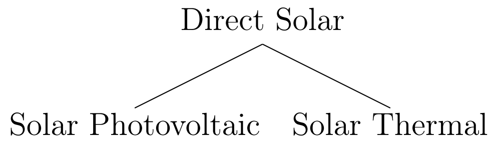

Figure 1.3: Renewable energy source directly received from the sun.

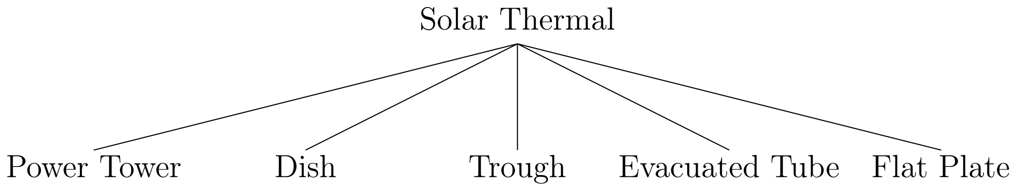

Figure 1.4: Types of solar thermal collectors.

tube designs are typically used for heating single-phase fluids at lower temperatures (e.g., pool heating, domestic hot water, and space heating) in non-tracking/non-concentrating applications (Figure 1.5).

1.2 DSSTC

DSSTC is a seldom-studied area of power generation that operates at small temperature differences (100–250 K) produced with solar thermal collectors. The generated heat can either be used to meet the thermal needs of a facility or converted into electricity, that can be consumed on site, or sold to the grid. The current work primarily focuses on developing the heat-to-electricity conversion equipment and—as a tool—secondarily modeling heat production from solar thermal collectors.

1.3 Research overview

This research explores the technical details needed to evaluate if DSSTC can be economically viable. This is accomplished through a multi-pronged research effort:

1. Improve the modeling methods being employed in the field to provide a better understanding of the true design problem.

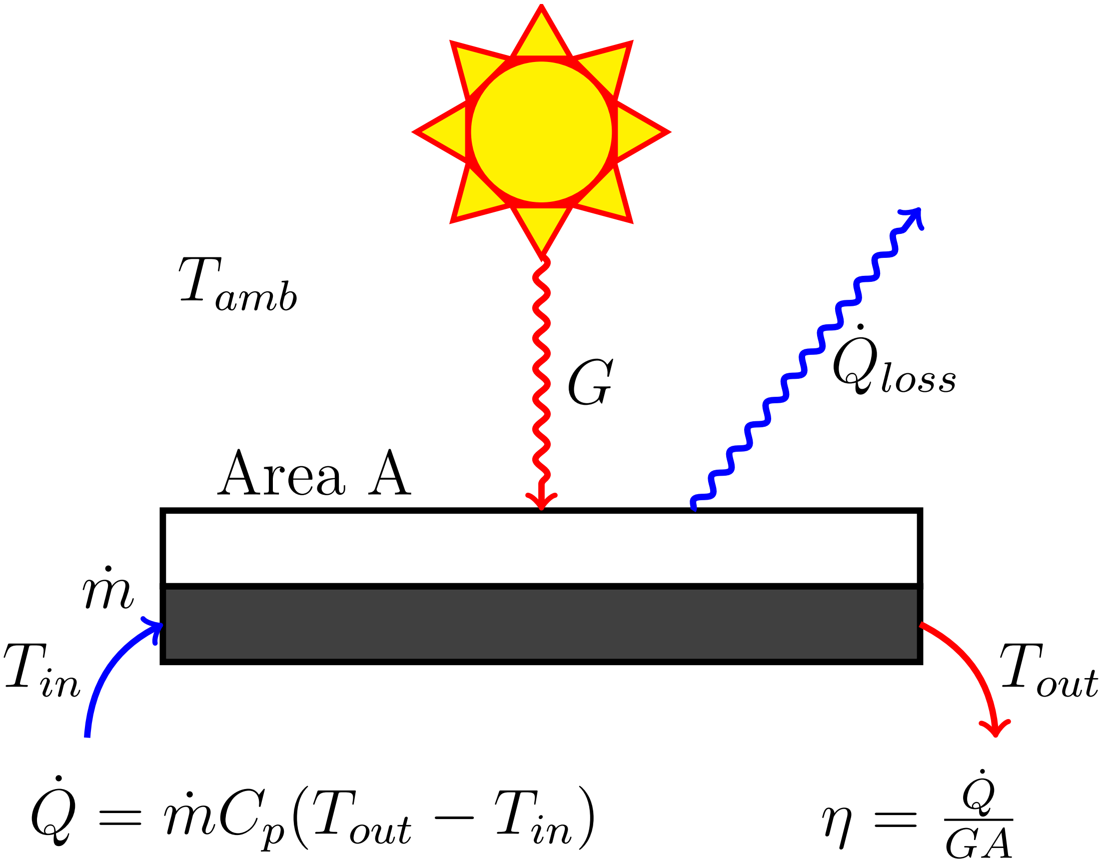

Figure 1.5: Cross-section of solar thermal collector depicting energy flows.

2. Review thermal-fluid design of heat engines to enable improved performance.
3. Apply the latest technology to explore solutions to the design problems identified through the simulation of component-level system models.
4. Contextualize this new knowledge by comparing DSSTC performance to its closest competitor: solar photovoltaic.
5. Propose a technology road map to guide future research in DSSTC.

In short, the journey will start broadly and go into key details with the objective of making the most comprehensive simulation of DSSTC to date. This approach produces key discoveries about the nature of the optimal DSSTC design. Finally, returning to a broad overview, take stock of these new discoveries, and begin anew by charting a revised course for DSSTC technology.

2. ENERGY, SOCIETY, AND THE ENVIRONMENT

> *"The more often we see the things around us—even the beautiful and wonderful things—the more they become invisible to us. That is why we often take for granted the beauty of this world: the flowers, the trees, the birds, the clouds—even those we love. Because we see things so often, we see them less and less."*
>
> – Joseph B. Wirthlin

Energy—the modern world loves the benefits, ignores the costs, and assumes a continuous supply. Society's use of energy and its environmental impact are largely ignored by most humans. The purpose of this chapter is to introduce the basics of energy and resources from a policy perspective, then to use those principles to motivate the current research effort.

Humanity's use of fire has profoundly impacted the quality of human life: heat at night and during cold months, the ability to cook food, dry/cure items such as bricks, metal refinement and fabrication, etc. This has resulted in the progressive use of trees, coal, whale oil, and petroleum to meet humanity's energy needs. In short, this consumption results in many benefits to humanity (some of which were listed above) and also in costs. These costs include the loss of environmental services that provide clean water, air, wild game, and fish. The methods of loss can range from mine waste that poisons streams, rivers, and ground drinking water to coal-fired power plant flue stack emissions polluting the surrounding air.

Given the single planet—Earth—on which humans live, it is in humanity's best interest to properly manage both the benefits derived from the use of natural resources and the environmental costs. This is as natural and self-evident as the need for an individual or family to manage their own financial resources, maximizing the benefit of purchases against the costs of those purchases within the limits of their means. Unfortunately, humanity struggles to manage its natural resources and environment as do many individuals, families, cities, states, and countries struggle to manage their finances.

Hope is not lost. As a society we have the understanding in how to manage well and govern well. Those who have this knowledge have an obligation to share this knowledge and help those who struggle with its application in practice. By working together we will overcome our difficulties.

2.1 History of environmental policy

One family of societal problems is found in the question of how can we mitigate the negative effects of anthropogenic activities on the environment? The history of environmental policy is centered on a natural cycle of events that leads to environmental policy. Scientific curiosity and subsequent assessment identify environmental pollution that results in negative health effects on humans, animals, or plants. When these effects and processes become well documented and scientifically understood, a social and political debate ensues. When consensus is achieved, laws are enacted to avert, stop, and/or encourage change to prevent and/or repair the environmental damage. We have seen this cycle take place in society many times. Typically, the enacted polices ultimately limit or mitigate environmental damage from human activity. The following process helps limit environmental damage:

1. Discover/identify environmental damage

2. Study of the damage and related processes by scientists

3. Educate the public to what is happening

4. Create dialog between scientists, the public, and policy makers
5. Repeat Steps 2–4 until consensus is achieved and legislation is enacted to address/mitigate the environmental damage to a socially acceptable level.

Of course, it is possible that once studied, some environmental damage does not require regulation and attrition is an implicit natural part of the process.

Environmental policy development has occurred for many environmental issues. One such example is the obvious need for sanitation in urban areas, which is met through running water and sewage systems that collect and treat the waste water, then releasing it back into the environment. Here are a few of the key environmental issues in various stages of development:

- Leaded gasoline
- Urban air quality
- Acid rain
- Ozone depletion
- Climate change

In each of the above environmental issues, there are various stages of consensus ranging from scientific acceptance (all listed) to nearly universal social acceptance (leaded gasoline) to partial social acceptance (climate change). It is interesting to note that in many of these cases, some parties in certain industries resisted change by attempting to discredit the scientists studying the environment. First, they claimed there was no issue to address, and then they claimed the problem was small compared to the economic hardship of the solution. Finally, legislation was enacted to mitigate, limit or eliminate the pollution as required by the social consensus achieved at the time.

2.2 Further information on selected cases

Examples from the 19th and 20th centuries include lead pollution from combustion of leaded gasoline. The negative effects of leaded gasoline were first documented by Clair Patterson [4]. F. Herbert Bormann [5] first documented flue stack emissions causing acid rain and smog, which resulted in a variety of environmental damages that harm humans, animals, and plants. Ozone depletion, first identified by a group of British scientist in 1984 [6] later resulted in regulations requiring the refrigeration and foam-blowing industries to search for and transition away from the compounds that caused ozone depletion.

We can learn several things from past cycles of anthropogentically driven environmental change. First, that human activity can and does negatively effect the environment at the local, regional, and global scales. Secondly, that through the application of the scientific method, these effects can be documented and understood, even when the time scales are much longer than societal memory. Third, that society can work effectively together to solve these environmental crises. Fourth, during this process, scientists and engineers develop new understandings and technologies that later society used to mitigate environmental damage. This perspective can be applied to the current crisis of global climate change.

2.3 Climate change basics and potential solutions

Why is climate change a problem? Among the many issues that climate change presents, the central issue is that rising annual average global temperature has resulted in the partial melting of almost all glaciers in the world. The final impact depends on how much temperature rise happens and in turn how much of the glaciers melt. Greenland and Antarctic ice caps are at risk of melting, which would result in 20 and 200 ft of sea level rise, respectively [7]. A large portion of the world population lives in coastal areas at or near sea level. With these facts, one can conclude there is a real risk that unchecked temperature rise will displace a large portion of the world population.

What is the cause of the temperature rise? In short, humanity's rise in quality of life is built largely on harvesting stored energy (biomass) by burning trees and fossil fuels, which releases carbon dioxide into the atmosphere. The rising atmospheric carbon level was first documented by C. David Keeling in 1958 [8]. Increasing greenhouse gas levels in the atmosphere increases heat trapping by the atmosphere, where carbon dioxide is the main contributing greenhouse gas. This results in hotter temperatures in the lower atmosphere and colder temperatures in the upper atmosphere. There is a 95% confidence that the dominant drivers of climate change are human-caused with the top two sources being fossil fuel combustion and change in land use (deforestation) [9]. Figure 2.1 shows a simple box model of the carbon stocks and flows of the atmosphere. To control the stock of carbon in the atmosphere, there are only four general things that can be done: (1) decrease natural carbon emissions, (2) decrease anthropogenic carbon emissions, (3) increase natural carbon uptake, and (4) increase anthropogenic carbon uptake. The top–two human activities that contribute to climate change follow:

1. Fossil fuel consumption – increases anthropogenic emissions

2. Deforestation – increases antrhopogenic emissions and decreases natural uptake

Pacala and Socolow [10] are the first researchers to note that simply cutting out emissions from energy production will not be enough to return the earth to its natural climate. Reducing greenhouse gas emissions by displacing fossil fuel combustion

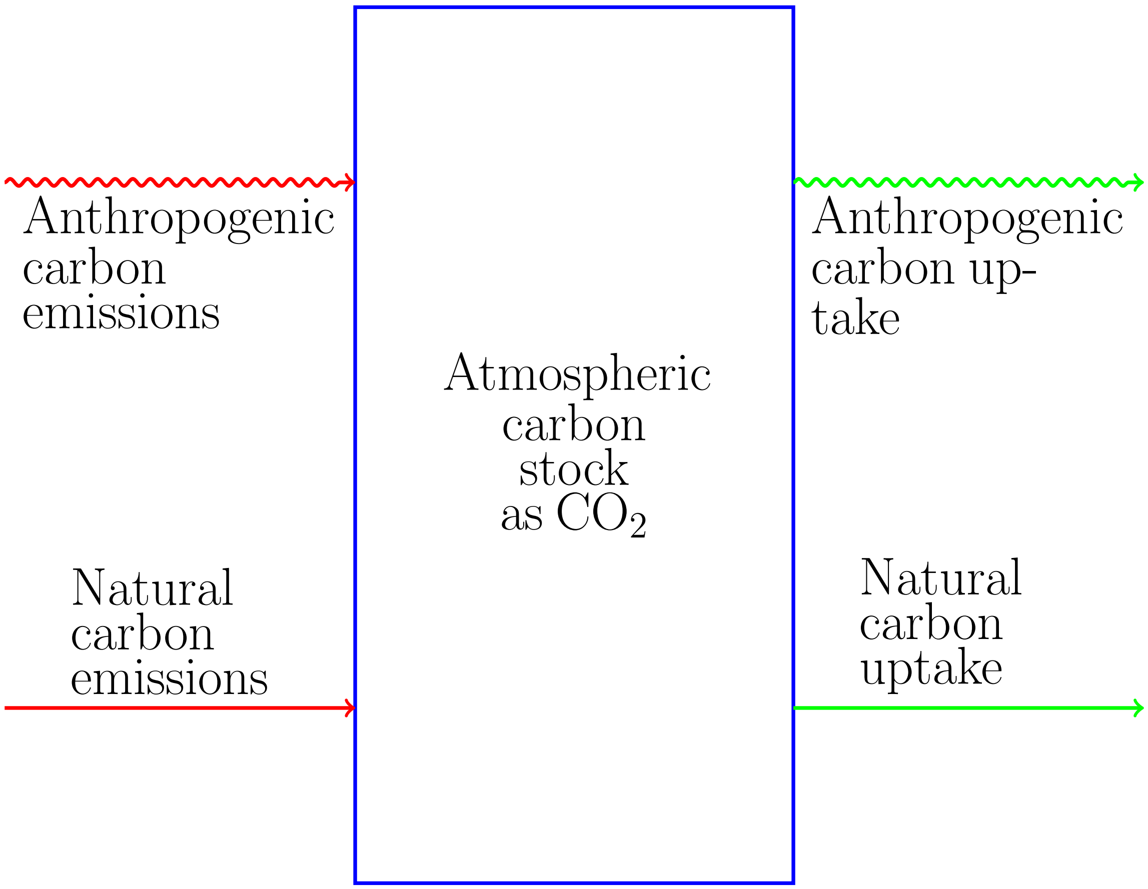

Figure 2.1: Simplifed atmospheric carbon box model.

is one of the goals of renewable energy technology and plays an important partial solution to the anthroprogenic climate crisis. As a society, if the carbon concentration in the atmosphere is to be controlled, a method to stablize the carbon stock in the atmosphere by balancing emissions and uptake must be found. Many solutions are being explored. Two powerful solutions are relevant to the current research effort. First, energy efficiency seeks to reduce anthropogenic carbon emissions by reducing the amount of energy and other natural resources needed to produce a specific human service. Second, renewable energy technologies seek to substantially reduce anthropogenic carbon emissions by transiting to low-carbon energy technologies.

DSSTC is a renewable energy solution with the following benefits:

- Increases end-use energy efficiency
- Substantially reduces energy production emissions
- Increases energy security (can be locally or regionally produced and consumed)
- Improves electricity grid stability and reliability.

As will be described in the next chapter, it is not a question of whether or not the technology works or has benefits. Rather, the question is whether or not DSSTC is overall more resource efficient and if the technology can be advanced enough to economically compete when compared against the next best alternative (opportunity cost from economics). To date, no one has shown DSSTC to be the right choice for any mainstream end-use cases. This work seeks to advance the technology in an effort to increase our knowledge of DSSTC capabilities with the objective that one day a full comparison on a resource and economic basis can be made.

3. BACKGROUND: THE HISTORY OF MEDIUM- TO SMALL-SCALE SOLAR THERMAL POWER GENERATION

> *"The United States used in peace time..., equal if it could be wholly transformed, to a total of seven trillion horse power hours. All this is but trifling compared to the enormous energy of the solar radiation falling each year on the surface of this country. Altogether, if it were possible to convert this solar energy completely, it would represent in power about seven thousand trillion horsepower hours in its rays... It is not surprising, in view of this astonishing comparison, that inventors have busied themselves in the effort to discover a practical means to employ the enormous power and heat resources contained in the sun rays... Yet if all the sunlight necessary for plant growth and for generally diffused heating is reserved, there remains available for power purposes, local heating, and lighting, many thousand times as much solar power as we are using from all other sources combined. Nothing quite satisfactory has been accomplished thus far with it, but the story of the attempts to employ sun rays for power is full of interest." [11]*
>
> – Charles Greeley Abbot, 1943

Harvesting the power of sunlight has a long history that dates back to ancient times. The first modern use was a solar-powered furnace in the 1700's by Frenchman Antoine Lavoisier [12]. The first solar-powered heat engine was developed by Auguste Mouchot in 1860 [13]. Mouchot was a French-Swiss mathematician at Lycee de Tours. After receiving permission to work full time on the invention, Mouchot developed and presented a refined version of the solar-powered heat engine at the Paris Exhibition in 1878, now known as the Third World's Fair. That summer was particularly hot and

Mouchot used the heat collected to drive a chilling process to produce ice, which was served to the audience as Italian ice (shaved ice), making his exhibit quite popular. In the 1880's, the French Ministry of Public Works evaluated the heat engine and found it to be a technical success and a practical failure. One reason for the failure is because the cost of coal had dropped as a result of a new trade relationship with England and improvements in pumping technology that improved coal mining operations. Having lost government funding, Mouchot returned to academics.

During this same time period, Capitan John Ericsson was working on solar assessment and utilization. As some readers may recognize, John Ericsson was a Swedish American engineer who designed and built the Monitor ironside ship that turned the tide of the Naval battles for the Union during the U.S. Civil War. Ericsson is also famous for the Ericsson thermodynamic cycle. He used the profits from his designs to self-fund his research into solar assessment and utilization until his death in 1889.

An American inventor with little formal education, Frank Shuman led a team who designed a solar-thermal irrigation pumping system. The design included a refined parabolic trough collector, although it was very similar to the one by Ericsson in 1876. In 1908, Shuman founded a solar company and built the largest solar conversion system in 1911, at Tocany, Pennsylvania. In 1912, he built an even more efficient system for pumping water from the Nile river at Maadi, Egypt outside Cairo. Shuman successfully faced many technical and business challenges and succeded, although the North African Campaign of World War I quickly ended his solar thermal efforts when the system was destroyed in Maadi [13]. In the end, the materials of the system were recycled for the war effort.

No history of solar energy can be complete without a discussion of Charles Greeley Abbot. He was the fifth director of the Smithsonian and an avid inventor and researcher. Of his many accomplishments, not withstanding his contributions to solar assessment, he designed a solar cooker and solar refrigerator. Contrary to the perception of many that Hottel was the first researcher to quantitatively analyze solar thermal designs, Abbot was the first to apply his knowledge of solar resource assessment to provide quantitative analyses for the performance of various solar utilization devices. This is evidenced in Hottel 1941 [14] who cites Abbot 1934 [15] and Abbot's correction of Hottel's use of his results in Abbot 1943 [11]. The point is further made when one reviews Abbot 1911 [16] and 1929 [17]

Although there are many more scientists and inventors who have contributed to solar-thermal system design (see [3, 11, 15–24] for more information), this discussion shows that contrary to the perception of many, solar-thermal technology is not new and is technologically able to meet our energy needs. These examples also show that the true design challenge is to configure and craft technologies together into a cost-competitive alternative to traditional energy resources. This current research effort seeks to advance solar-thermal technology with that goal in mind.

4. SOLAR-THERMAL CO-GENERATION: THE NEED FOR IMPROVED MODELING AT THE SMALL-TO-MEDIUM SCALE

> *"Good designing, avoiding costly and complicated construction and devices likely to require frequent attention, combined with a fuller knowledge of the properties of materials available, and cleverness in adopting means to promote efficient results,—these if supported by a moderate outlay of money for experimental work may perhaps soon make the utilization of solar energy very extensive." [16]*
>
> – Charles Greeley Abbot, 1911

In following the wise advice of the father of solar energy analysis, in this chapter, the author outlines a plan to improve design methodology, with simplicity, and to further our cleverness by adopting means to promote efficient results. With the many advances in knowledge concerning solar energy analysis, much of it has not been properly applied together on the problem of solar-thermal power generation at the small-to-medium scale.

At the small-to-medium scale, the current state of solar-thermal power generation modeling is to aggregate the irradiance on the collector in a year and to discount the annual energy by the efficiency of collector and by the efficiency of an organic Rankine cycle heat engine. Both the solar collector and the heat engine are assumed to operate at fixed conditions. Then, the annual energy is discounted by an assumed generator efficiency of 90–100%. In several ways, this methodology overestimates the annual energy yield of the system. First, the assumed efficiency of electrical equipment is typical of large-scale power generation equipment, which operates at fixed speeds. In contrast, small-scale systems may not operate at fixed speed. Second, the assumed fixed operating conditions for both the collector and the ORC heat engine significantly overpredict efficiency for both portions of the system. Third, the assumed fixed operating conditions mask the underlying true design requirements. These limitations can be overcome by analyzing the system efficiency at part-load with hourly simulations. This approach will enable a more accurate estimate of equipment performance and improve understanding of the true design problem.

Co-genreation is a term used to describe the process of producing heat, converting some of the heat to electricity, and using some of the heat for thermal energy needs. In traditional large scale fossil-fuel-power generation applications co-generation specifically refers to the process of producing electricity from heat and using the waste heat from that process to meet thermal energy needs such as space heating, domestic hot water, and cooling with absorption chillers. Water is typically the working fluid used in traditional large scale power generation applications. Because of the high normal boiling point for water, water has large machine size when rejecting heat near ambient temperatures. This also results in working fluid pressures below ambient pressure in the condenser. Both of these effects result in savings by rejecting heat at temperatures much higher than ambient. Co-generation allows traditional power generation equipment that reject heat at temperatures much higher than ambient to improve efficiency by using the waste heat for other activities.

4.1 DSSTC overview

Distributed-scale (∼10 kW) solar-thermal power generation is a little-known, seldom-studied area of power generation that operates at small temperature differences (100–250 K) produced with solar-thermal collectors. DSSTC can be applied in residential, commercial, and industrial scales. This work focuses mainly on residential and commercial applications, but could be scaled up to include industrial applications. Of U.S. energy consumption, residential and commercial sectors account for ∼10% and ∼20%, respectively [25]. In reality, there is no DSSTC industry or practical technology yet. Most related work is on organic Rankine cycles (ORC), but is not directly relevant in either the scale, temperature difference, or both [26–29]. Specifically, given solar variability and variation in ambient temperature, the few papers on DSSTC do not properly model part-load performance of components or the system [30–33]. At best, these works are crude estimates of the upper limit of performance for a given design. Furthermore, when one ignores the environmental variability of solar irradiance and ambient temperature—and neglects part-load performance—one can use a simple model of solar-thermal collector performance. For example, the solar collector model could use a constant efficiency (e.g., 50%) and the heat engine model would employ only typical operating condition. To predict annual system performance, this simple approach discounts the total annual irradiance by collector and engine efficiencies, which was done in a group project by Zach Norwood, Nathan Kamphuis, and Dan Soltman [34]. In this context, Norwood made a more complete study of expander performance [33]. This system configuration directly inserts the solar-thermal collector in place of a boiler in an ORC heat engine (direct system, see Figure 4.1(a)), and assumes the benefits of energy storage (variant of an indirect configuration, see Figure 4.1(b)). To accommodate this approach, energy storage needs to be modeled, part-load performance needs to be considered, or both.

Given the DSSTC literature, the central academic complaint is that no works properly handle part-load performance under varying insolation and ambient temperature with scale-appropriate assumptions. However, two notable works come close to achieving the desired results: Delgado-Torres [30] and Twomey [31].

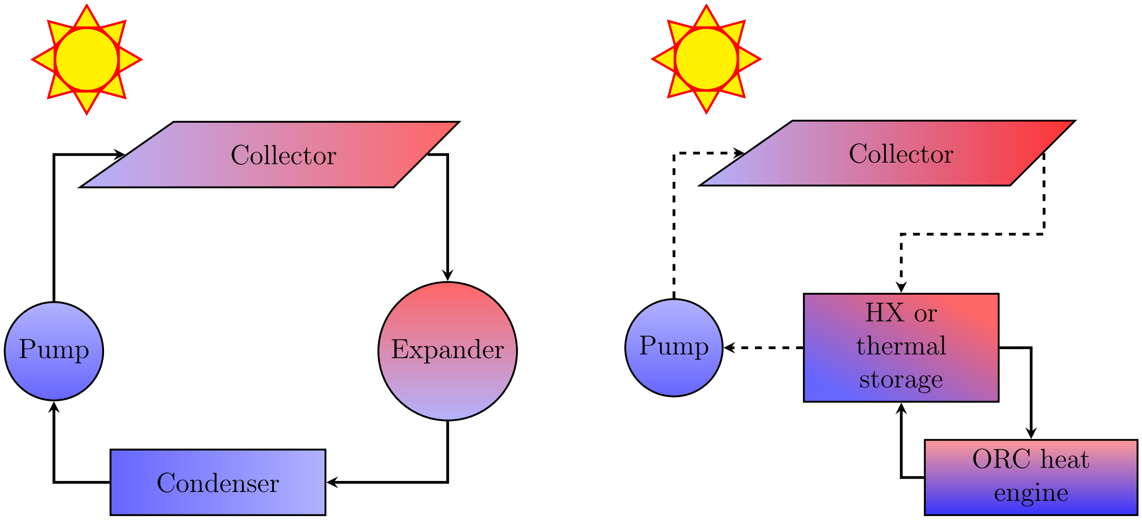

(a) Direct system. (b) Indirect system.

Figure 4.1: Two canonical solar-thermal system configurations.

4.2 The Delgado-Torres contribution

Under fixed irradiance conditions, Delgado-Torres [30] discusses the use of a scroll expander re-purposed from a scroll compressor and models performance of a solar-thermal ORC system purpose-built for desalinization. The authors evaluate 12 refrigerants commonly considered as working fluids in ORC applications, both direct and indirect configurations, and multiple low-temperature solar-thermal collectors. In general, fluids can be categorized as wet or dry based on the expected fluid condition at the exit of an expander (see Figure 4.2(a)). The paper also correctly discusses the slope of the saturated vapor entropy line ($\sigma = \left(\frac{ds^{(\nu)}}{dT}\right)_{\mathrm{sat}}$) in the T-s diagram (see Figure 4.2(b)). In the case of positive slope (dry fluid), an internal-heat exchanger (IHX) (also known as a regenerator) is required (see Figure 4.3). The authors only consider configurations that include an IHX. Delgado-Torres [30] correctly concludes that the direct system configuration requires less collector area than the indirect system, by eliminating losses in thermal grade during the heat exchange process between fluids. Stated in another way, the heat exchanger generates entropy. However, Delgado-Torres [30] does not consider solar variability or part-load performance of the system. He does not search for a new fluid; rather, he attempts to select the best-performing fluids from the list of known, well-studied working fluids.

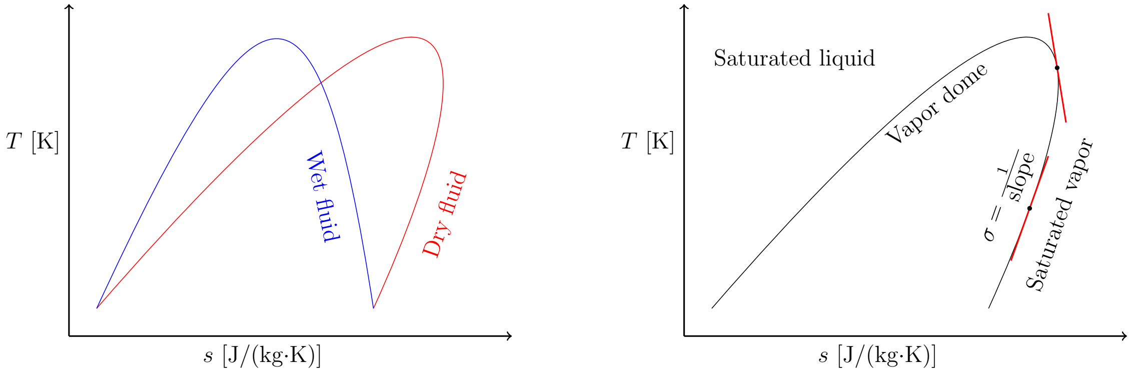

(a) Vapor dome for wet and dry fluids on the T-s diagram.

(b) σ of a dry fluid on the T-s diagram.

Figure 4.2: Fluid categorization method.

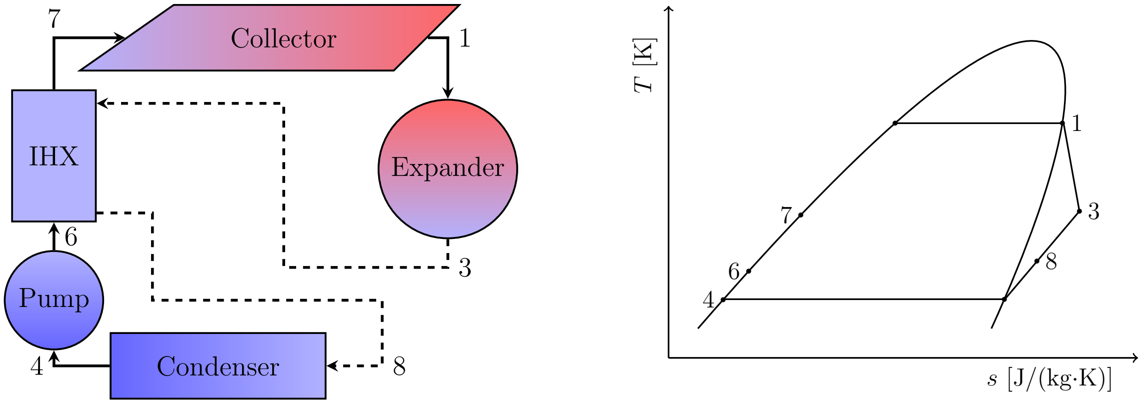

(a) Equipment configuration diagram.

(b) Thermodynamic cycle on the T-s diagram.

Figure 4.3: Direct system with IHX.

4.3 The Twomey contribution

Twomey [31] considered a solar-thermal ORC with R-134a as the working fluid. The indirect configuration was considered with thermal storage functioning as a heat exchanger between the two working fluids. Twomey [31] only considers ORC heat engines without a regenerator. Notably, he considers solar and ambient temperature variability on a monthly basis for Brisbane, Australia. The solar model is a simple sine function normalized to monthly insolation values and temperature is taken as the average daily value for each month. Twomey uses a scroll expander model developed by Lemort [35], which is experimentally validated, and accommodates variable speed and pressure ratio. It is worth noting that the Lemort model is based on R-123 not R-134a. Twomey [31] has taken the beginning steps to meet the need to model part-load performance over solar and thermal variability; however, his work does not do so on a hourly basis with real-world insolation values and ambient temperatures. Additionally, Twomey does not address the direct configuration that Delgado-Torres identified as the most cost effective.

4.4 A note about methods used in the dissertation

The expressed goal of this work is to fill a knowledge gap in the field of solar-thermal co-generation at the distributed scale. Much of the recent work in the field has been to identify an expansion technology to efficiently convert the working fluid energy to shaft power. Quickly during the literature review process, it was realized that the central knowledge gap was not what collector, working fluid, or expansion technology was best. Rather, the central issue was the lack of a system modeling approach that simultaneously accounted for realistic solar variability, part-load performance of components, and component interfaces. Additionally, what efficiency assumptions must be size and application appropriate. In short, building a full system model and simulating it is needed. This is discussed further in Part I. By completing the simulation and making the details readily available, this work will form the foundation from which other works can improve the methods used and extend the analysis to areas not yet completed.

A note on the methods of algorithm validation and verification. In Part II, at several points interim results are checked against publicly available solar data from NREL. Throughout the work, the algorithms are developed and then redeveloped a second and third time. What is meant here is that normally algorithms are developed, checked and then used in published works. In this work, algorithms are developed, left for six months to one year and then overhauled and rewritten. Later this is performed again prior to the completion of this work. This means that each algorithm was carefully reviewed at least three times prior to completing the work. At each step in the process basic checks against experimental data or known results were performed when possible. When possible checks against other algorithms was performed. Additionally, results were checked for functional response and consistency with simpler methods. For example, Chapter 12 uses an oversimplified simulation, Chapter 19 uses the simple simulation and Chapter 20 uses the part-load simulation. Each simulation reduces the annual energy yield by accounting for more physically correct methods. Each simulation forms a basis for comparison to the earlier ones. This revision process was designed to mimic the process of the development of a field of study where many fields have started from a simple back of the envelope calculation and overtime now encompass full texts. This means that one can use the results of the various parts of the dissertation to compare against the other parts as a form of verification. When possible, simple pencil and paper calculations are used to check algorithm results at one data point or operating condition. Because much of this work uses solar methods developed here to account for the anisotropy of both the sky and the collector not experimental data could be used to verify the methods and doing so is left as future work. Part IV is independent of this issue because peak irradiance is assumed rather than calculated from the methods in Part II.

A note on terminology used in decision theory and design optimization fields of study. When possible, this work is written with the goal of clearly using this terminology correctly. Because optimization and decision theory are specific fields, most engineering works do not use the terminology or methods correctly. While this work succeeded in the overall goal, there are several deviations from the correct use of the terminology. For example, in Part III design space exploration is used to identify the best mounting angle of the collector under various conditions and cases. The term optimal is used and this is not pedantically correct. From an engineering perspective 181 angles are considered from 0–90. This means the true optimal angle is bound ±0.5°of the stated optimal angle. In reality, for all practical purposes, this accuracy more than exceeds practical engineering requirements.

4.5 Conclusion

Although the above works have advanced our knowledge and understanding concerning DSSTC design and performance, they do not realistically simulate the designs proposed. Specifically, the following improvements are required and are original contributions of this author:

- Hourly simulation of both temperature and insolation
- Scale- and technology-appropriate efficiency assumptions
- Realistic performance predictions for configurations
    - Part-load performance of equipment
    - Component limitations

  - Component-to-component interface limits

The lack of realistic simulations misses performance constraints for the component models. In turn, missing performance constraints causes the designer to miss key design requirements for DSSTC and limits progress in this field. A simulation platform is needed to correctly predict DSSTC performance. Simulating solar-thermal electricity production is a key portion of the overall simulation and is discussed in the remainder of this work (Figure 4.4). The studies that follow take the initial steps to correct the shortcomings noted above by setting a new direction in DSSTC research.

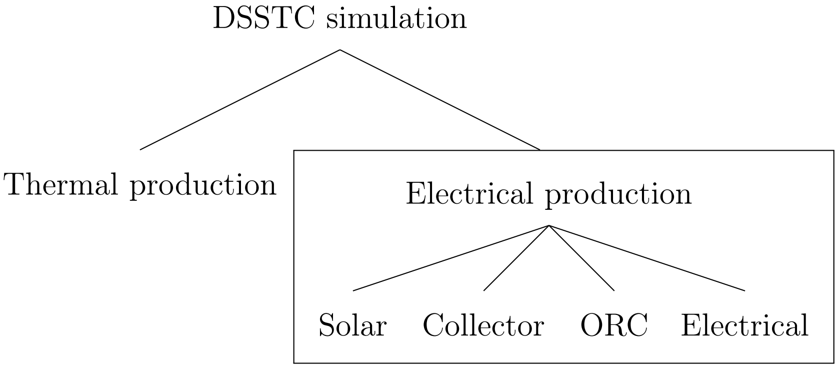

Figure 4.4: Component models needed to perform the electrical portion of a DSSTC simulation.

PART II. DEVELOPMENT OF A CUSTOM SOLAR-THERMAL SIMULATION

5. SOLAR OVERVIEW

> *"A study of the literature on solar energy utilization has convinced me of the existence of an unalterable tradition among speakers and writers on the subject. One must always begin such a discussion by expressing the earth's reception of solar energy in units no one has thought before to use, the more startling the better. In keeping with this tradition, I shall mention a few old figures and add my own... energy at a rate sufficient each year to melt a layer of ice 114 feet thick; on an acre at noon... Having made the conventional beginning, let me add what many of you know; that figures such as these are almost irrelevant to the problem of practical utilization of solar energy. They have attracted uncounted crank inventors who have approached the problem with little more mental equipment than a rosy optimism." [14]*
>
> – Hoyt C. Hottel, 1941

Here the substantial task of learning and using the available/most accurate knowledge about solar energy analysis to build a solar simulation is begun. This effort is undertaken to specifically avoid the dangers of only bringing one's "rosy optimism" to bare on the problem.

A solar simulation with the desired characteristics (previously discussed in Section 4.5) is needed, chiefly hourly meteorological data and part-load performance models. To accomplish the desired level of detail, several options exist and must be evaluated. Of the multiple off-the-shelf codes, none provide the adaptability of in-house code. The in-house constructed code-based simulations can be optimized to determine key design parameters based on current model sophistication and optimization criteria. Chapters 6–9 describe the solar portion of the simulation tool and are the cornerstone upon which the remaining tools and research will be built. The goal of Chapters 6–9 is to build a tool that in a given location will simulate typical weather conditions and model solar-thermal collector (STC) performance from those conditions (see Figure 5.1).

The desired simulation tool requires several sub-models from which the solar-thermal model and simulation can be constructed:

- Meteorological model/data (Chapter 6)
- Solar position model (Chapter 6)
- Sky model (also known as transposition model) (Chapter 7)
- Collector selection and performance model (Chapter 8)
- Combined solar and collector simulation model (Chapter 9)

Within this part of the dissertation, Chapters 6–9 focus on discussing, selecting, adapting the sub-models into a STC performance model that can be simulated over the meteorological data. Where applicable, the sections in these chapters will follow this format:

- Discussion of models available
- Model selection
- Pre-existing validation and limitations
- Model adaption
- Verification

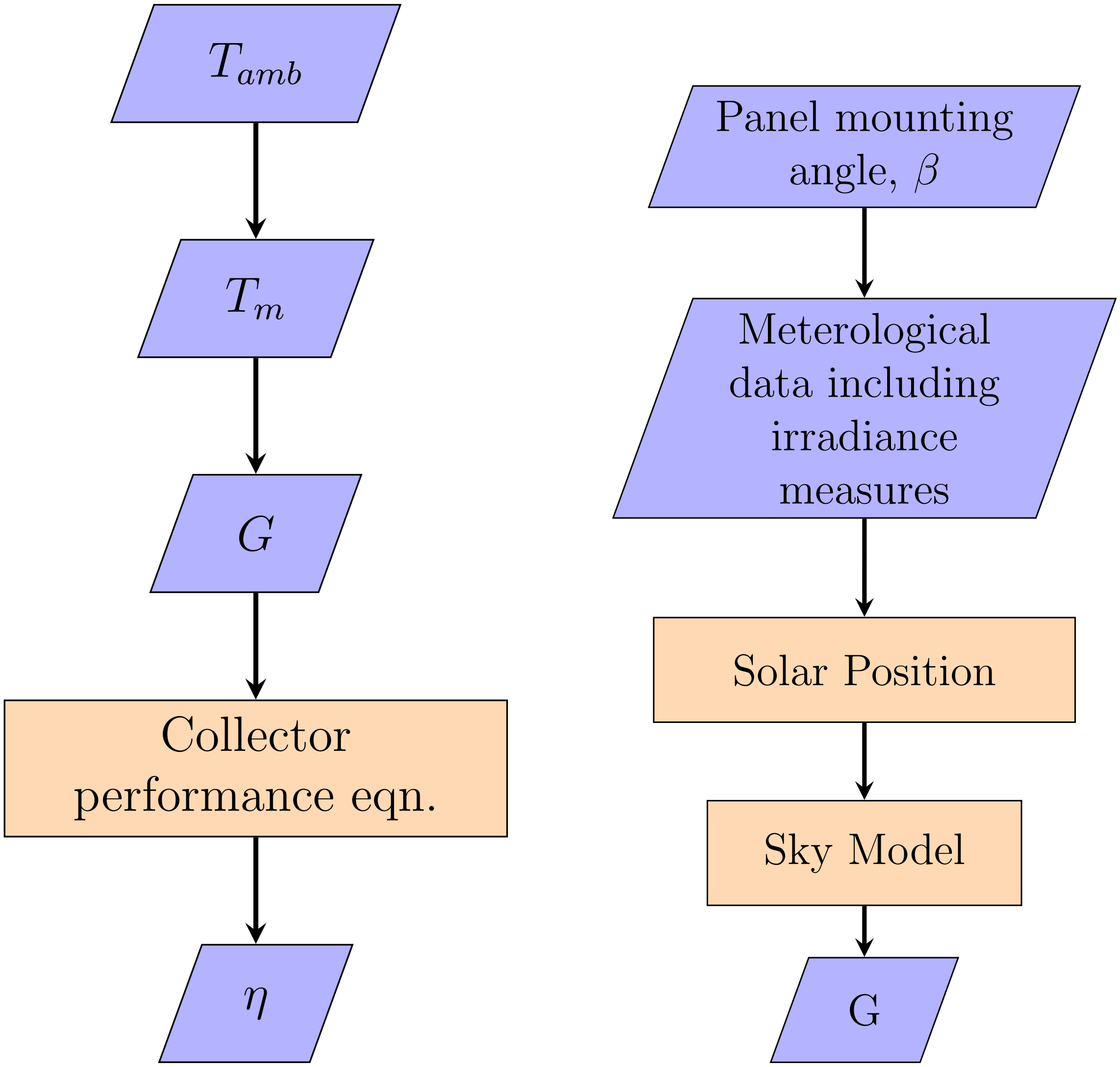

(a) Solar collector model. (b) Irradiance model.

Figure 5.1: Parts of a solar collector performance model.

A clear method for simulating performance is created so that the individual models composing the simulation can be upgraded as needed to improve simulation performance for any particular need. Chapters 6–9 provide a brief background of solar modeling in general and solar-thermal modeling in particular. The reader will become acquainted with some of the prominent sources of information in the field. A reader already knowledgeable in the field will find two unique aspects to the discussion: (1) solar-thermal modeling from the anisotropy perspective and (2) applying sky and collector anisotropy principles to the XCPC collector design for the first time. Although this work is not the first to use angular distribution sky radiance models, it is the first to apply them to the XCPC design.

In Part III, Chapters 10–12 use the simulation tool to study optimal mounting angle for several use cases of the selected solar-thermal collector. More specifically, these chapters explore the optimal mounting angle, as a function of latitude, for several traditional use cases and DSSTC applications. The work will (1) explore the history of optimal mounting angles, (2) describe the proper methodology for determining the optimal mounting angle, (3) compare and contrast the differences between optimizing irradiance G for a sloped surface, effective irradiance G_{eff}, thermal energy output Q, and (4) provide annual-net-energy data for each measure of energy.

6. SOLAR POSITION AND WEATHER DATA

> *"Now an informed pessimism is sometimes the healthiest mood in which to approach an engineering problem; I want to use a little space in an endeavor to put you in that mood. [Given the price of energy, Hottel goes on to estimate the cost per yard a collector system could be]... The result is one so often encountered in engineering projects: indecisive. It may be possible to build a plant for such an amount; much more exact knowledge of the performance and costs is ncessary than was at hand in making the above rough estimate. What I have particluarly wanted to emphasize by this preliminary consideration is perfectly obvious to the engineer, namely, that solar power is not there just for the taking! However, this preview has at least indicated that solar power is not completely outside the realm of economic feasibility. It is worthwhile, then, to examine in more detail the problem which has commanded the attention of engineers for three-quarters of a century." [14]*
>
> – Hoyt C. Hottel, 1941

Hottel's words are as true today as they were when he wrote them roughly 80 years ago. He correctly points out that the activity of collecting solar energy has costs associated. The need for a deeper understanding of solar collector performance and cost remains today. This is particularly true for solar thermal collectors used in power generation applications, especially at the distributed scale. Because capital is required to collect solar energy, given the location and the energy demand, it is important to consider that inefficiently designed equipment leads directly to the need for larger capacity, which result in larger collector area and higher capital costs. This means that it is of paramount importance to optimally design the collector and heat engine system. This task can be accomplished through repeated simulations while varying the design parameters for each simulation.

6.1 Introduction

Simulating solar collector performance has two key steps. First, one must quantify how much light from the sky dome is incident on the collector given the current sky conditions and the mounting of the collector (the subject of this chapter and Chapter 7). Second, one must determine the thermal performance of the collector given the incident light and the operating conditions (the subject of Chapter 8). All this knowledge is then used to build the simulation (Chapter 9). To determine the amount of light on a solar collector, meteorological information is needed such as irradiance, temperature, and pressure (Section 6.2). The apparent location of the sun (Section 6.3) based on observer location, time, and weather information is also needed. The meteorological and solar position information are then supplied to a sky model (also known as a transposition model) (Chapter 7) that determines the amount of light incident on the solar collector of arbitrary mounting.

To discuss meteorological data and solar position, a common system of ideas and terminology must be built. These ideas and terminology also overlap into solar radiation measurement and sky modeling. In scientific terms, light is known as *radiosity* (radiative heat transfer) and radiosity from the sun is known as *radiance*. Radiance recieved on a surface is known as *irradiance*. In the field of physics, light is treated as a particle or as a wave of energy. Light particles are called *photons*. (In the field of lighting (illuminanting engineering), light is known explicitly as only the portion of radiosity that is detected by the average human eye. [36])

Radiance is an intensity and varies with distance from the sun and is proportional to $1/r^2$, where r is the distance. Many readers will be familiar with the concept of the

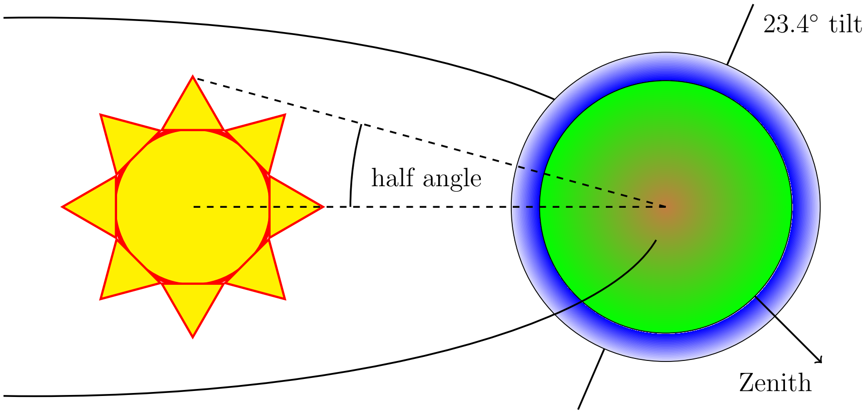

Figure 6.1: Eliptical orbit of the earth around the sun.

solar constant, which is the average solar radiance at the average sun-earth distance and is 1367 W/m^2. Although solar output varies with time because of sun spots and other effects known in helio-physics, the effects are very small and outside the scope of the current discussion. The orbit of the earth is not a perfect circle; in fact, it is an elipse with the sun at one of the foci (Figure 6.1). The sun-earth distance changes with time; therefore, radiance at the top of the atmosphere of earth in the direction of the sun changes with time. Hence, the term solar constant is a misnomer. For the northern hemisphere, the earth is closer to the sun in the winter and further in the summer. See [37–40] for additional information on correcting the solar constant for changing sun-earth distance.

At the top of the earth's atmosphere, the extraterrestrial radiation normal to the sun (ETRN) (solar constant corrected for sun-earth distance) and extraterrestrial radiation on a horizontal surface (ETR) are shown in Figure 6.2. Because ETRN and ETR are above the atmosphere, there are no scattering or absorption losses

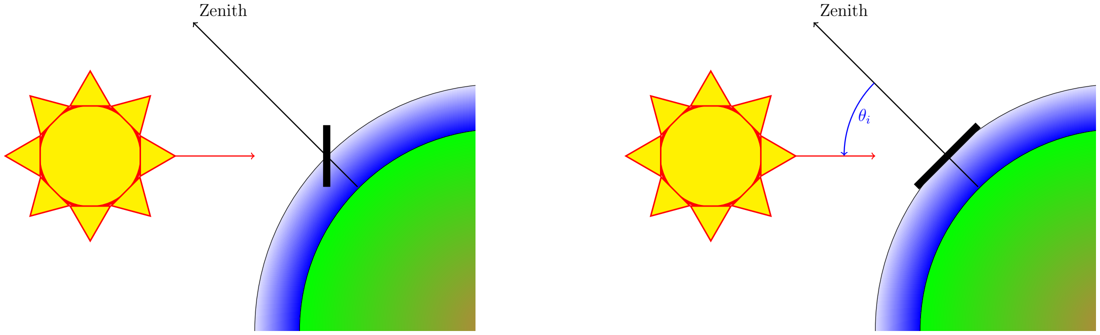

(a) ETRN: normal to the sun.

(b) ETR: on a horizontal surface.

Figure 6.2: Measures of extraterrestrial irradiance.

caused by the atmosphere. ETR is related to ETRN by discounting for the angle of incidence ($\cos \theta_i$). The angle of incidence is the angle between the solar direction and the normal of surface that is being considered. See Solar Energy —Vocabulary, ISO 9488 [41] for more information on many of the terms used in solar energy.

Real sky radiance is complicated by atmospheric scattering of photons by the particles that comprise the atmosphere. As photons travel through the atmosphere, they may not experience scattering, may experience Rayleigh scattering ($r < \lambda$), may experience Mie scattering ($r \sim \lambda$), or experience multiple scattering events of any combination (Figure 6.3). Here, r is the scattering particle radius and λ is the wavelength of light. Atmospheric scattering is dominated by Rayleigh scattering, which does not shift the wavelength of the scattered light. Photons that enter the atmosphere arrive at many locations on the surface of the earth, some are even reflected back into space. To model scattering properly, the real physical processes are complex and require detailed measurements of the atmospheric conditions and properties. This is the subject of atmospheric transmission modeling and is outside the scope of the current discussion.

To avoid the complexities of atmospheric scattering, engineers use *sky models*

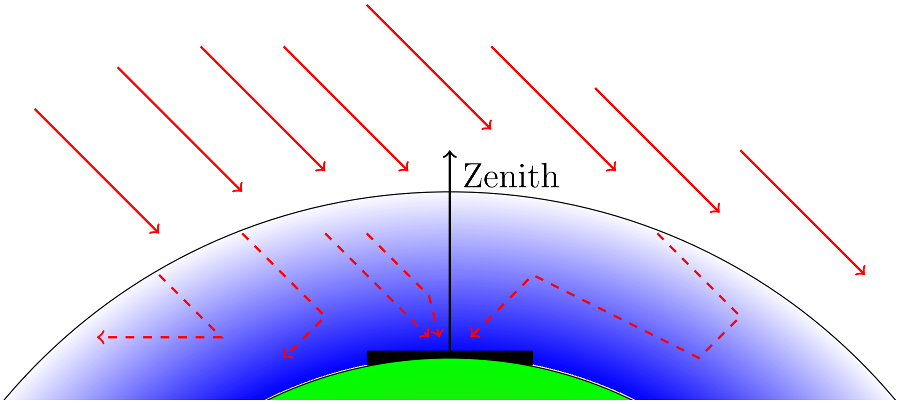

Figure 6.3: Real sky atmospheric scattering of light. From left to right: backscattering out of the atmosphere, scattering of light away from the collector, no scattering, forward scattering, and multiple scattering.

(also known as *transposition models*) to predict the irradiance on an arbitrarily oriented surface. Figure 6.4 shows a simple depiction of a conceptual distribution of the radiance coming directly from the sun and the sky to a horizontally oriented surface. The reader is encouraged to note the differences between Figures 6.3 and 6.4, namely Figure 6.4 only includes the radiance incident to the location of the surface. Figure 6.4 also notes the *circumsolar brightening* that happens because of scattering near the solar direction. It also notes the *horizonatal brightening* that happens near the horizon also because of scattering. See Robinson 1966 [42], for a more detailed discussion of the sky model and atmospheric transmission model approaches.

For completeness, there is a third class of semi-empirical models that attempt to bridge the gap between atmospheric transmission modeling and sky modeling. This class attempts to lift some of the simplifying assumptions and yet still avoid the more challenging complications of atmospheric transmission. When reading the literature,

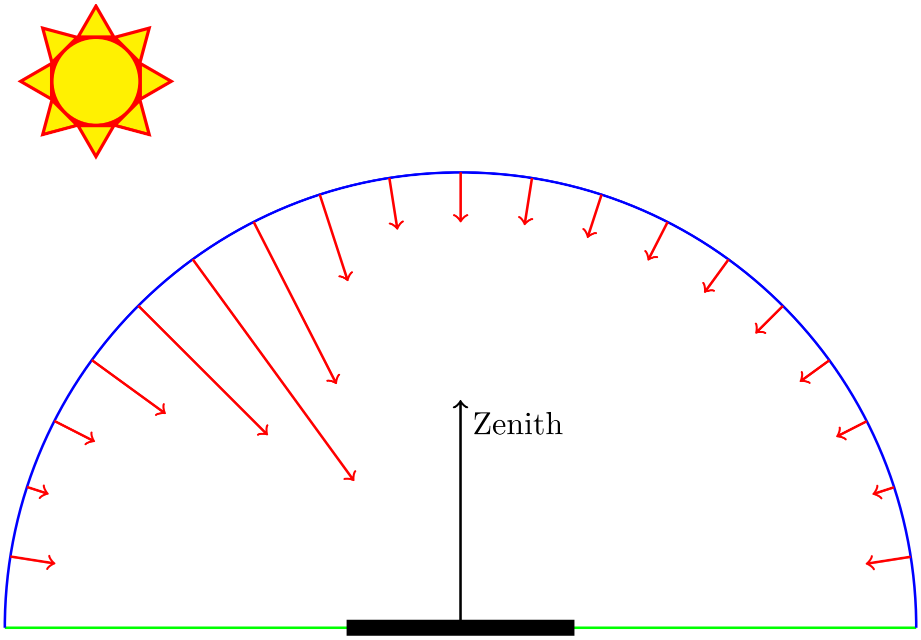

Figure 6.4: Conceptual model of irradiance received at a point on earth.

one should take care to note which class of models is being discussed.

Sky models are known as both “sky models" and as “transposition models" originally, scientists wanted to model the radiance from the sky dome, hence the term “sky model." Later, researchers in the field found it more meaningful to name this class of models based on the mathematical function that the models provided, hence the term “transposition model" (see Chapter 7). In this work, the more intuitive name “sky model" is preferred and will be used hereafter.

Many engineers and scientists use sky models, including those working in solar fields, building energy, and lighting. This results in many names for the same physical quantity and results in much confusion because sometimes the meanings are slightly different. Irradiance on an arbitrarily oriented surface is just such a quantity. Irradiance incident on a surface that is arbitrarily mounted with a slope (also known as tilt) from horizontal and may include azimuthal rotation is defined as *Plane of Array*

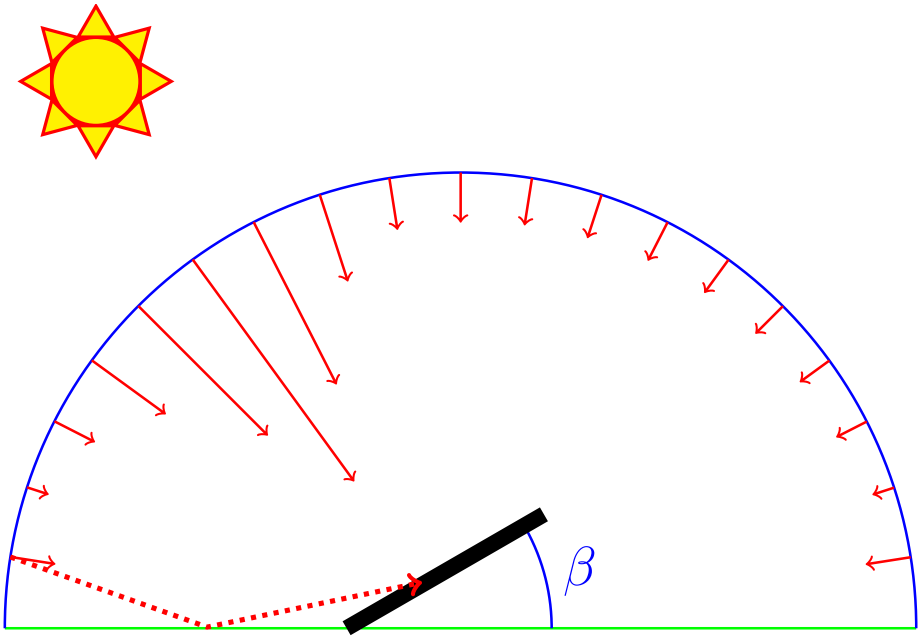

Figure 6.5: POAI: total irradiance on a sloped plane, including direct, diffuse, and reflected components.

Irradiance (POAI, see Figure 6.5). POAI is defined to include the total irradiance incident on the surface from any direction that is within the surface's field of view (FOV). In some of the literature, POAI is also known as Global Sloped Irradiance (GSI) and Global Tilted Irradiance (GTI). POAI will be used hereafter in this work. To avoid confusion and be general, the term Plane of Array (POA) was chosen by several fields. This allows the discussion of radiance or luminance in many fields to be generalized and not limited to solar collectors; however, the term POAI loses some of the intuitiveness that the other terms provide.

The central problem is that it is not cost effective to measure POAI for every location of interest and every slope at each location continuously or discretely with more than a few locations and or slopes at each location. Given an arbitrary collector mounting, sky models were created to address the issue of determining POAI from the three measures of irradiance (discussed in the next paragraph). See Chapter 7

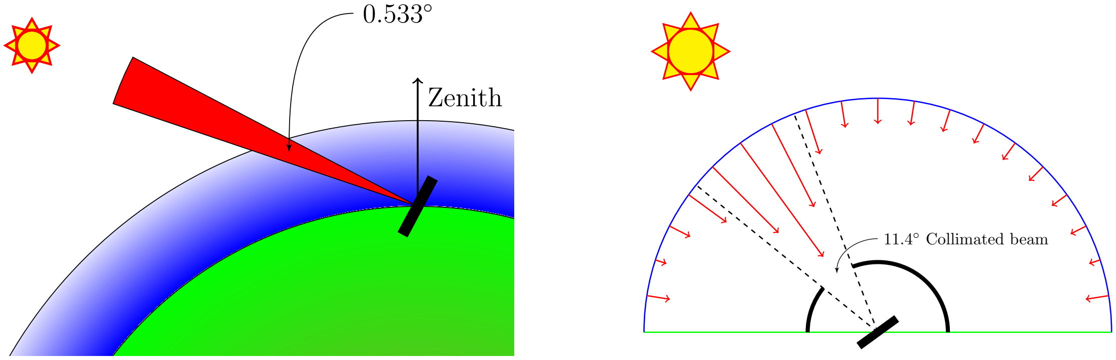

(a) Solar disk 0.266° half angle based on the radius of the sun and the average sun-earth distance.

(b) DNI (5.7° half angle for TMY data).

Figure 6.6: Comparison of the solar disk verses the measurement of the sun beam on the surface of the earth using a pyrheliometer.

for more discussion on the topic of sky models.

On the surface of the earth, there are three measures of irradiance: (1) *direct normal irradiance* (DNI), also known as *beam irradiance*; (2) *diffuse horizontal irradiance* (DHI); and (3) *global horizontal irradiance* (GHI). DNI is the collimated beam from the sun within 6° and includes some forward scattered light (Figure 6.6) and is measured by a pyrheliometer. DHI is scattered in the atmosphere that is incident on a horizontal surface (Figure 6.7(a)) and is measured by a shaded pyranometer. Conceptually, DHI does not include any of the light included in DNI, although in practice one must ensure that the pyrheliometer and pyranometer measuring these quantities are matched correctly for this to be true (or include a correction factor for this). GHI is the combined contributions of the DNI and the DHI (see Figure 6.7(b)) and is measured by an unshaded pyranometer.

An important problem related to the central problem of measuring the POAI is that the common instruments (namely pyranometers) that measure DHI, GHI, and POAI lose the direction information of the sky radiance. Sky models (Chapter 7)

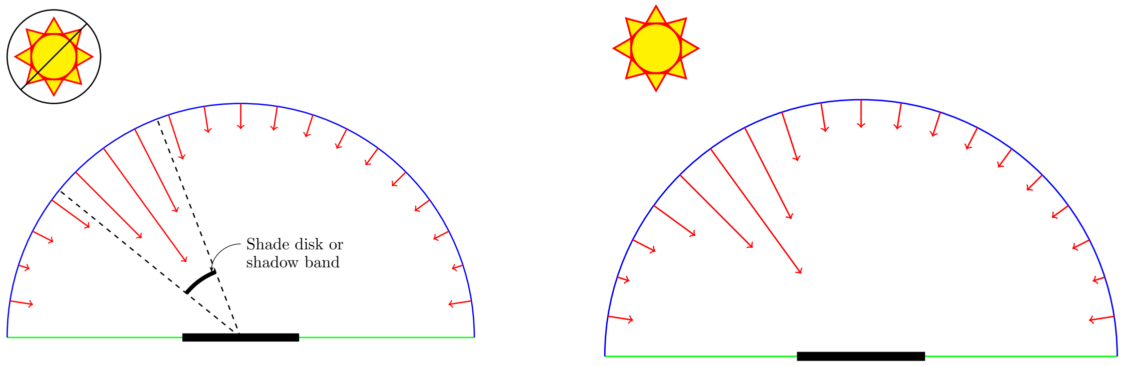

(a) DHI: Horizontal without the sun beam. Measured with a shaded pyranometer.

(b) GHI: Horizontal with the sun beam. Measured with an unshaded pyranometer.

Figure 6.7: Horizontal measures of irradiance on the surface of the earth using a pyranometer.

are used to replace the lost direction information and use the DNI, DHI, and GHI measures to approximate the POAI for an arbitrarily oriented surface for a given location.

Within the sky model framework, one challenge is to properly account for continuously changing sky conditions. The result of this challenge is that sky models are typically accurate in measuring annual energy and typically have higher stastical error for any one measurement. Figure 6.8 depicts several canonical types of sky conditions. There are many good sources for additional information on solar radiation measurement including a 2015 NREL technical report [43], an evaluation by Gueymard and Myers 2009 [44], and a comprehensive book by Vignola et al. 2012 [45]. All of these sources of information are great starting points for readers interested in solar radiance measurement. Lastly, Blanc et al. 2014 [46] has a great discussion on various definitions for DNI, difficulties on ways to measure it, and how that affects how much circumsolar sky radiance is or is not included in DNI.

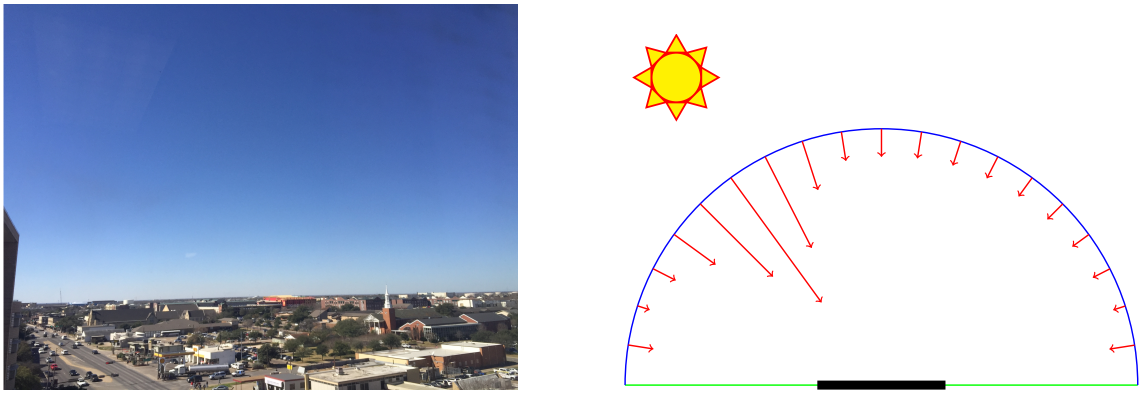

(a) Clear sky. (b) Clear sky irradiance distribution.

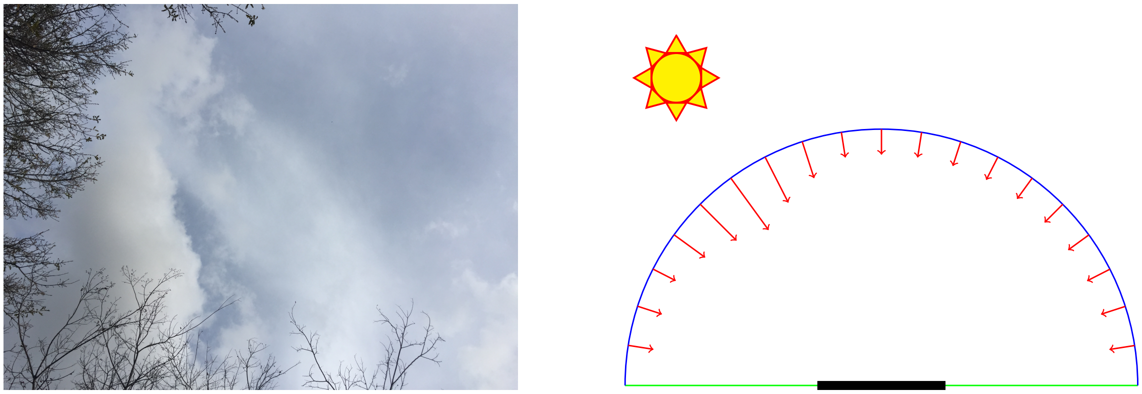

(c) Cloudy sky. (d) Cloudy sky irradiance distribution.

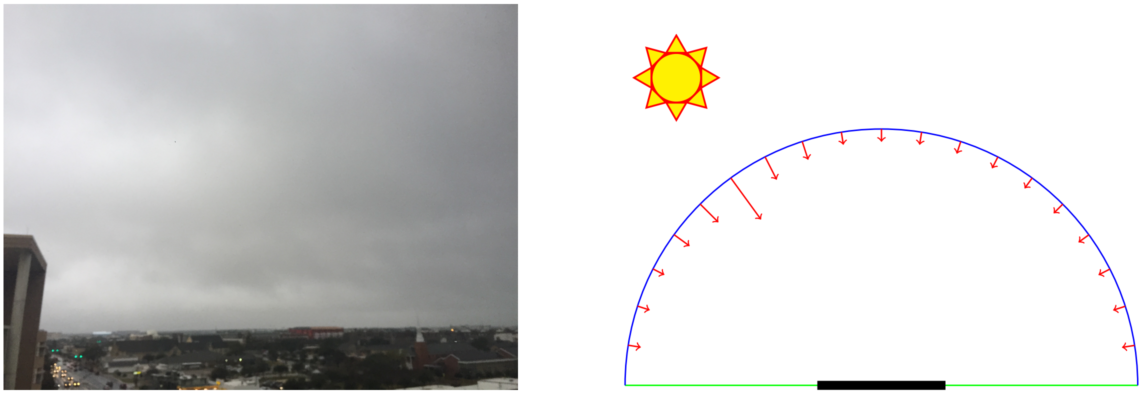

(e) Overcast sky. (f) Overcast sky irradiance distribution.

Figure 6.8: Photos of sky conditions and the corresponding irradiance distributions.

6.2 Meteorological model

There are several sources for the needed meteorological data, including ones for purchase and for free from government agencies or non-profits. Several other authors have produced partial lists of sources [1, 47]. Some of these datasets offer nearly continuous instantaneous data, and others offer averaged data for a one year, month, day, hour, or minute period. Many of the related works discussed in Chapter 4 included annual or monthly meteorological data. Increasing the data resolution to hourly averages will capture the large variance in irradiance, which is caused by the diurnal and annual motions of the earth relative to the sun, and major effects from changing atmospheric conditions. Although a greater resolution than hourly would improve accuracy by better capturing cloud transient effects, sunrise, and sunset, it would also substantially increase computational cost to model roughly half of the 8760 hours in a year (the ones that have daylight). To capture cloud transients, one would need data at sub-minute levels, which would increase the computational load by more than a factor of 3600.

6.2.1 Meteorological model selection

One data source stands out from the rest. The National Renewable Energy Laboratory's (NREL) Typical Meteorological Year 3 (TMY3) dataset [48] provides the needed hourly insolation and meteorological data for 1020 locations in the United States and its territories. This provides several advantages. The dataset is used extensively and its methods have been well documented [48]. At each site, the data are in the same format so that the computer algorithm can be designed to readily read datasets for each site with a generalized method. The TMY3 dataset is the current dataset produced by NREL, provides a large number of locations, and the irradiance values are based on satellite measurements. NREL previously produced the TMY2 dataset [49], which is based on an earlier period, covers about one-quarter the number of sites, and the irradiance values are typically measured by ground-based instruments. This leads to the counter-intuitive result that the irradiance values in the TMY2 dataset have less uncertainty ($\sim 5 - 10+\%$ for TMY2 vs. $\sim 10 - 20+\%$ for TMY3). If researchers require a more detailed assessment, the uncertainty values are given for each irradiance measurement in the two datasets. One issue is that the systematic error and random error components are not separated. All three TMY datasets are based on versions of the National Solar Radiation Data Base (NSRDB). The NSRDB does have a recent updated dataset that shows higher uncertainty [50] and is based on the latest modeling methods which provide 4-km grided data. Although the uncertainty is higher, the methods used to quantify the uncertainty are superior. The latest NSRDB dataset has one key short fall, namely that albedo values are not provided. One may be able to find albedo data from NASA. Processing large geo-spacial datasets to arrive at the very latest data is outside the scope of the original research goals and is left as future work. The current work uses both TMY2 and TMY3 datasets to provide continuity between research results previously completed by others and the current work.

The TMY3 dataset is a powerful tool, but what exactly is it? NREL has taken the meteorological data from 1020 USA weather stations during the period 1976–2005 for many sites including modeled irradiance based on satellite measurements. Then, the data for a given location (e.g., Easterwood Field in College Station, Texas) for a complete month (e.g., January 2005) is selected as most typical. In the TMY3 dataset, data for January 2005 becomes **<u>the</u>** data for January; therefore, the TMY3 dataset covers only one year, a “typical" year. This means real-world hourly averaged meteorological data typical for that location is used for simulation purposes. Here, “typical" is weighted more on irradiance values than other meteorological measures.

TMY data is the keystone for all other calculations.

6.2.2 TMY3 data adaption

The TMY3 dataset has been validated by the NREL staff who produced it, although it comes with certain cautions. The data may contain errors. One such error was discovered during the course of this work; one or more locations in the Caribbean have recorded temperature measurements that are not physically possible. For example, a one-hour time block with an average of –20°C has an average of 16°C in the next time block. This is clearly suspect because typical temperatures in the Caribbean Islands are almost never below 0°C, much less –20°C.

Another data issue was discovered with albeto measurements. Some of the measured values were outside the acceptable range (0–1). These values are replaced with the annual average of acceptable values. Many of the TMY3 measurements are accompanied with uncertainty calculations. Although uncertainty analysis is not typically utilized in solar energy prediction, the uncertainty values for irradiance measurments are included. As previously discussed, another limitation is the data are averaged on an hourly basis. If a more refined interval is needed, it would require significant effort to adapt TMY3 data to reconstruct the needed information. Overall, the TMY3 dataset certainly meet the needs of the currently planned uses of the solar simulation under construction.

The TMY3 dataset contains two general types of data: scalar and vector. Scalar data (e.g., latitude, longitude, and elevation) applies to the overall site. Vector data (e.g., time and irradiance) contain an entry for each hourly time block in the typical year. The TMY3 dataset has a large number of parameters available in vector form, not all of which are needed in the STC model. As a result, vector information (e.g., illuminance and percentage of ground cover by snow) are removed. Also, information

Table 6.1: TMY3 scalar data

Name	Description (Unit)
Time Zone	Hours from Greenwich, negative west
Latitude	(°)
Longitude	(°)
Elevation	(m)
Calculated data	
Avg. pres.	Station pressure (mbar)
Avg. temp.	Dry-bulb temperature (°C)
Non-TMY3 data – collector mounting specifications	
Slope	From horizontal, default set equal to latitude (°)
Azm_Rotation	Azimuth rotation, default zero (°)

(e.g., annual average temperature and pressure) are needed; therefore, they are pre-calculated from the corresponding vector data and stored with the other scalar data. The TMY3 data are provided in a csv-delimited file. To load the csv files for each of the 1020 sites, custom code was written to process the data and store two arrays in a readily loadable .mat MatLab format for use by the simulation. One array stores all the scalar information in a vector and the second array stores all the vector information as columns. Tables 6.1 and 6.2 display the scalar and vector information used in the simulation respectively. Additionally, Table 6.1 has placeholder information specifying the collector mounting. This information has the default values indicated in the table and are intended to be set by the simulation at the beginning of, or during, code execution.

Table 6.2 contains columns of information at each hour block throughout one typical meteorological year (TMY). Not all hour time blocks of information are useful because there is no significant irradiance at night. Hour time blocks (data points) with the value of zero for all three measures of irradiance are removed from the dataset, which eliminates almost half of the 8760 hours in a year. Pre-dawn and post-sunset times do register irradiance. Later in this chapter, solar position is

Table 6.2: TMY3 vector data

Name	Description (Units)
Time data	
Year	Year of the date of the data record
Month	Month of the date of the data record
Day	Day of the date of the data record
Hour	Hour of the Local Standard Time (LST) (no time change)
Irradiance data	
ETR	Extraterrestrial global horizontal irradiance received during the one hour time period (W/m^2)
GHI	Global horizontal irradiance received during the one hour time period (W/m^2)
DNI	Direct normal irradiance received during the one hour time period (W/m^2)
DHI	Diffuse horizontal irradiance received during the one hour time period (W/m^2)
Thermodynamic and optical data	
Dry-bulb temp.	Dry-bulb temperature at the time of the data record (°C)
Station pres.	Station pressure at the time of the data record (mbar)
Albedo	The ratio of reflected solar irradiance to global horizontal irradiance (unitless)
ETRN	Extraterrestrial Normal irradiance received during the one hour time period (W/m^2)
GHIU	Global horizontal irradiance percent uncertainty (%)
DNIU	Direct normal irradiance percent uncertainty (%)
DHIU	Diffuse horizontal irradiance percent uncertainty (%)
zenith	Topocentric zenith angle calculated from SPA (°)
azimuth_astro	Topocentric azimuth angle calculated from SPA (westward from south) (°)

discussed. Data points where the solar position is very near the horizon are also removed (solar zenith angles greater than 90°).

6.2.3 TMY2 data adaption

With a few exceptions, the TMY2 dataset is very similar to the TMY3 dataset. The main difference is that the foreground albedo was not provided and that the irradiance data is typically from ground-based measurements rather than the SUNY satellite model. To overcome the lack of albedo measurements, a small investigation was performed. First, the literature advocates the use of a fixed assumed value for use with TMY2. Albedo can be in the range of 0.1–0.4, typically 0.2. With snow cover, a value of 0.8 is typically used. A value of 0.2 for albedo is used in this work. See Christensen and Barker 2001 [51] for a more detailed discussion. Second, the NREL-provided format for TMY2 is different than TMY3. To account for the format differences, both TMY2 and TMY3 use the same in-house data format as listed in Section 6.2.2.

6.3 Solar position model

To determine the position of the sun and its relative position with respect to collector mounting, there are many sources [39, 52–54]. The central idea is that given the time and location on earth, one can predict the apparent location of the sun relative to that position. This involves converting from terrestrial time to solar time, which requires converting the standard date and time into Julian date and accounting for leap seconds and the observed rotation of the earth. Although these processes are complex, the sources cited above are some of many on how to perform these calculations and algorithms to perform them. The focus here will be to discuss the selection and adaption processes.

6.3.1 Solar position model selection

For a given time, location on earth, and information contained in either TMY dataset, NREL's Solar Position Algorithm (SPA) [39] provides solar location. The SPA has been validated by its creators. The SPA is almost accurate enough to continuously position heliostats for power-tower systems; therefore, it is accurate enough to be used in an hourly data application for a stationary mounted collector. Using the solar position for hourly data means that the solar position will only be calculated in the middle of each hour block. As with either TMY dataset, the SPA has been validated and tested by the creators at NREL and can be reviewed in the SPA user's manual. The algorithm has also been used extensively by NREL and the public. Validation and source code availability are the main reasons why the SPA was chosen over the other models [52–54].

6.3.2 Solar position model adaption

The SPA algorithm was repackaged for direct use by the in-house code. The SPA has as an input, the time difference between the earth rotation time and the terrestrial time (ΔT), which is based only on observation [55]. A second astronomical input is the observed irregular rotation rate of the earth ($-1\text{ s} < \Delta UT1 < 1\text{ s}$) is always less than 1.0 s. For current purposes, the TMY2/TMY3 datasets cover the years 1961–2005, Equation 6.1 shows the interrelationship between the various time values, and the US Naval Observatory provides the leap second information while the Paris Observatory provides the $\Delta UT1$ information,

$$\Delta T = TT - UT1 \tag{6.1}$$

$$\Delta T = 32.184 + \underbrace{(TAI - UTC)}_{\text{Leap seconds}} - \underbrace{(UT1 - UTC)}_{\Delta UT1} \tag{6.2}$$

where TT is terrestrial time, TAI is atomic time, and UTC is uniform time. (Note that the main role of the Paris Observatory is to provide highly accurate measurement data about the irregular rotation rate of the earth ($\Delta UT1$) and the role of the USNO is to project this irregular rotation rate into the future.) Although this explanation is oversimplifed, Appendix A provides the shell script used to download the necessary data and code used to calculate the solar position. Included in the code are plots of data used to verify consistency in the calculations and data filling from historical annual data to current corrections that are nearly continuous. The work to provide $\Delta UT1$ data in Appendix A is original work of this author to adapt knowledge in the Astronomy field and make it readily available in the solar field. Additionally, atmospheric refraction is also fixed to the typical value of 0.5667. This measure affects the prediction of sunrise and sunset as the light is bent around the perceived horizon line. Note: The word “horizon" is used with caution because it has no physical meaning in the context of sunrise and sunset.

The last remaining issue is how to determine a representative solar position. A given data point represents a period of time; therefore, the sun has more than one position during that time period. Blanc and Wald 2016 [56] provide an excellent discussion of the six known methods for determining a single representative sun position for a given time period. Here, a simple and robust method is chosen: simply calculate the sun position at the middle of the hour. Table 6.3 contains a full listing and description of the inputs as adapted for use with the in-house function spa_tmym.c, which provides an interface between the in-house code and the NREL code. These codes are also provided in Appendix A. The solar position algorithm requires several inputs and can return intermediate and final outputs. Table 6.4 lists the values that spa_tmym.c provides.

Table 6.3: SPA input data

Variable name	Description (Units)	Source
Date data		
year	4-digit year	TMY
month	2-digit month	TMY
day	2-digit day	TMY3
SPA: Terrestrial Time (TT), TMY: Local Standard Time (LST)		
hour	Hour	TMY value −1
minute	Minute	Fixed to 30
second	Second	Fixed to 0
Other time information		
$delta\_ut1$	Fractional second difference between UTC and UT (s)	calculated
$delta\_t$	Difference between earth rotation time and terrestrial time (s)	calculated
timezone	Hours from Greenwich (h)	TMY
Location information		
latitude	(°)	TMY
longitude	(°)	TMY
elevation	(m)	TMY
Thermodynamic and optical data		
temperature	Annual average temperature (°C)	TMY
pressure	Annual average pressure (mbar)	TMY
$atmos\_refract$	Atmospheric refraction (°)	Fixed to 0.5667
Collector mounting information		
slope	Slope of the collector from horizontal (°)	Adjustable
$azm\_rotation$	Azimuth rotation of the collector (°)	Adjustable

Table 6.4: SPA output data

Variable name	Description (Units)
Angle information	
incidence	Surface incidence angle (°)
zenith	Topocentric zenith angle (°)
$azimuth\_astro$	Topocentric azimuth angle (westward from south) (°)

6.3.3 SPA verification

In addition to the creator's validation, this author used a prepackaged basecase to ensure the orginal C code was compiled correctly on the local machine. Furthermore, a check was done of the final adapted code, which was discused in the previous section. This check was accomplished by downloading zenith and azimuth angle data from Measurement and Instrumentation Data Center (MIDC) at the NREL website [47]. It is important to note that the MIDC data was originally calculated using the SPA; thus perfect agreement is expected. Using hourly data during the first attempt at verification, the algorithm used 47 s and 0.0 s for ΔT and $\Delta UT1$, respectively, which resulted in differences up to 2.5 and 3.0° for zenith and azimuth angles, respectively. Further investigation found that the NREL-provided solar zenith and azimuth angles were determined for hourly data at the end of the hour. It is important to note that at the time of writing NREL, only provides solar position data for the BMS location.

To correct the discrepancy in the two methods, the following steps were employed: (1) Minutely data were downloaded for solar position values. (2) Astronomical values (ΔT and $\Delta UT1$) were calculated using the method outlined in Section 6.3.2. (3) The mid-point value was confirmed to be a reasonable representation of the time block (Blanc and Wald 2016 [56]. (4) The comparison was performed again.

Figure 6.9 shows the solar position results with substantially reduced differences between the two methods. The two methods differ because of differences in ΔT and $\Delta UT1$; the MIDC data are less precise (see Figure 6.10). The jump in $\Delta UT1$ shows that a leap second was entered several weeks after it actually took place. It is also important to note that the small differences in solar position have no discernible effect on the annual energy yield results presented later in Chapter 7.

It is recommended that NREL staff update the astronomical data used to deter-

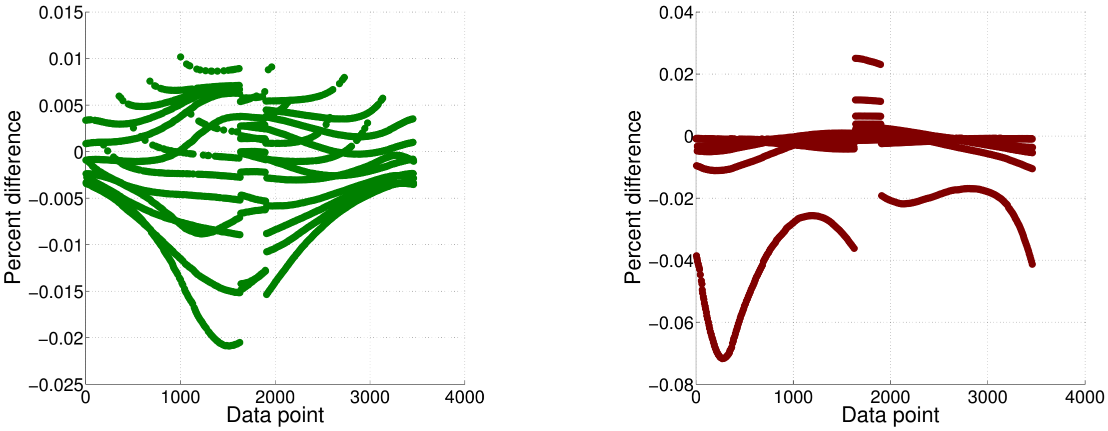

(a) Zenith angle test.

(b) Azimuth angle test.

Figure 6.9: Solar Position Algorithm angle testing: 2015 NREL MIDC data.

mine solar position. Furthermore, they should update methods for determining the effective solar position to the middle of the time period or one of the other more advanced methods described in Blanc and Wald 2016. This verification has shown that the current methods exceed the required accuracy for determining solar position for use in an hourly or minutely simulation. The methods also exceed the accuracy of data provided by NREL.

6.4 Conclusions

In this chapter, basic terminology was defined and explained relating to irradiance measurement. The TMY2 and TMY3 datasets by NREL were chosen for use in the solar simulation. Integrating the latest NSRDB dataset was left as future work because of the lack of albedo data. The SPA by NREL was chosen to determine the solar position, and the in-house calculation of solar position was verified. This verification is the original work of this author and required adapting astronomical knowledge and applying it correctly. This was completed to determine $\Delta UT1$ accurately; therefore, determine the solar position accurately. The next chapter determines the irradiance

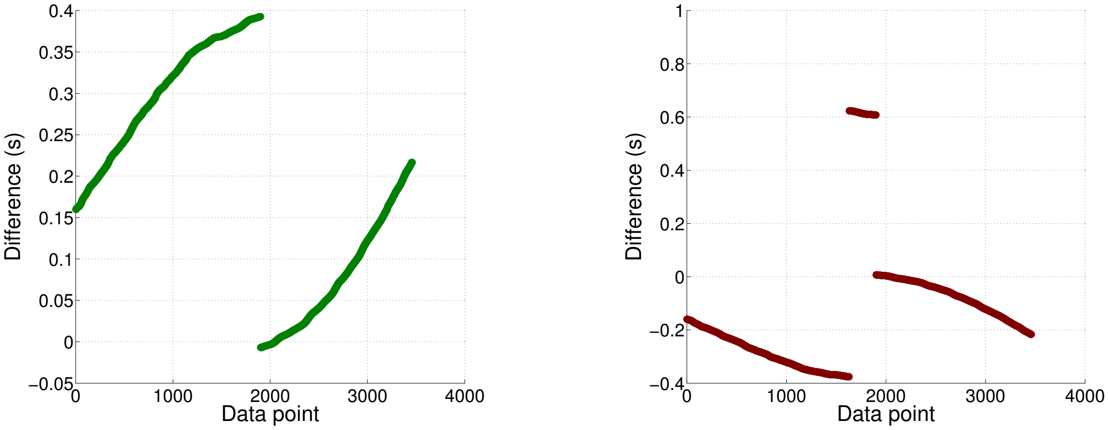

(a) ΔT difference. (b) $\Delta UT1$ difference.

Figure 6.10: Astronomical data comparison.

on a tilted surface of arbitrary orientation given (1) orientation, (2) solar position, and (3) meteorological data.

7. SKY MODELS

> *"At sea level the sky light is a still more considerable portion of the total radiation, but as yet not very exactly measured... Owing to the great extent of the sky, it is not possible, when recieving rays simultaneously from its whole extent, to have them all fall at right angles to the absorbing surface. Hence the sky light is at a disadvantage with respect to sunlight, unless we observe the brightness from every part of the sky by itself and then sum up the results... The percentages [ratio of indirect to direct] depend on the clearness of the sky, increasing with the haziness. If both sun and sky rays are supposed to shine on a horizontal surface, the ratio varies of course greatly from hour to hour." [57]*
>
> – Charles G. Abbot, 1911

This chapter discusses how to account for energy that comes directly from the sun, indirectly from the sky, and indirectly reflected from the ground. The end goal is to predict the amount of solar energy incident on a surface of arbitrary orientation and limited field of view (LFOV). Abbot clearly noted the importance of "sky rays" when determining the total energy from the sun. It is difficult to measure the whole sky; therefore, it is necessary to treat elements of the sky individually. After 105 years of solar radiation measurements, scientists, atmospheric scientists, and solar energy engineers are still struggling to adequately measure the distribution of solar energy across the sky, and to accurately predict the total amount on an arbitrarily tilted surface.

7.1 The general sky model

A sky model provides the interface between the meteorological/solar position models and the collector performance model. Muneer et al. 2004 [58] is an excellent book covering many of the models and methods employed in this chapter. As shown in Figure 7.1, sky models partition the irradiance recieved on a surface into parts: *direct*, *diffuse* (from the sky), and *reflected* (diffuse reflected from the ground). They can be treated mathematically to calculate the total irradiance (POAI or I_T) on a Plane of Array (POA) given the mounting angle β and azimuth rotation γ. Total irradiance incident on the collector is a key datum needed to determine the overall solar-thermal collector performance. For example, direct irradiance affects collector performance very differently than does sky radiance, which is caused by light scattering in the atmosphere. (See Chapter 6 for a review of these terms and concepts.) Reflected irradiance from the surface of the earth onto a tilted panel must be treated differently than either direct or diffuse irradiance. Note that some sources refer generally to both the diffuse and reflected components as diffuse irradiance. This ambiguity can be a point of confusion. Here the two sources of diffuse light will be referred to separately as defined above.

The generalized sky model is shown in Equation 7.1,

$$I_T = \underbrace{I_{b,n} \cos\theta_i}_{\text{Direct}} + \underbrace{I_{d,h} R_d}_{\text{Diffuse}} + \underbrace{\rho I_{t,h} R_r}_{\text{Reflected}} \tag{7.1}$$

where I_T (POAI), $I_{b,n}$ (DNI), $I_{d,h}$ (DHI), and $I_{t,h}$ (GHI) are the total, direct normal, diffuse horizontal, and global horizontal irradiances on the aperture, respectively, θ_i is the angle of incidence between the solar direction and the collector normal, and ρ is the reflectance (albedo) of the foreground [53], where POAI, DNI, DHI, and GHI

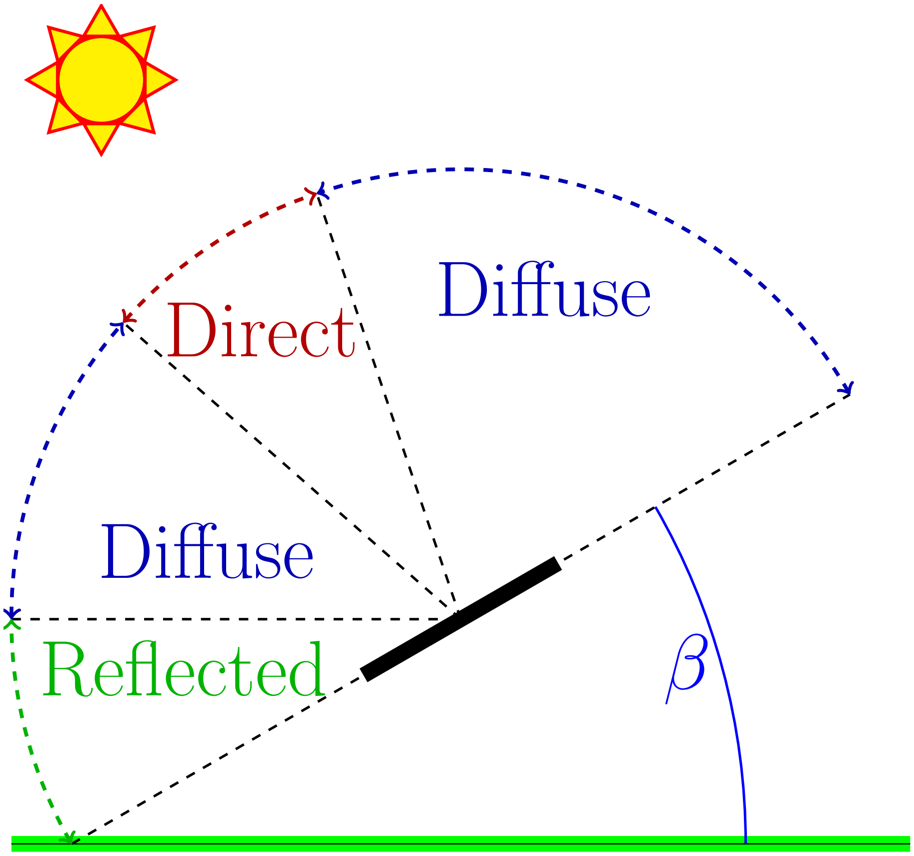

Figure 7.1: Three primary components of a sky model.

are acronyms that are not suitable for use as variables in equations. An excellent book on modeling solar radiation on the surface of the earth was edited by Badescu with contributions from over 30 leaders in various parts of the field [59]. Here the focus is on one key aspect, sky modeling.

Guaymard [1] discusses the generalized terms R_d and R_r, which are the diffuse and reflected transposition factors, respectively. Generally speaking, the transposition factors can be measured or modeled. The direct transposition factor ($\cos\theta_i$) is purely a geometric factor and does not change with sky model. $I_{b,n}$, $I_{d,h}$, and $I_{t,h}$ are related by the Closure Equation 7.2,

$$I_{t,h} = I_{b,n}\cos\zeta + I_{d,h} \tag{7.2}$$

where ζ is the solar zenith angle, which is the angle between the zenith direction and the solar direction at the location of interest.

The direct correction factor is purely geometrical, and is universally used when assuming the sun is a point source. The solar point source assumption is almost always used with the notable acception of models for high-concentration-ratio collectors. The overwhelming majority of sky models use the reflected correction factor R_r from the Isotropic Sky Model (ISM). This is because knowledge about the foreground reflectance is typically measured or assumed to be isotropic. Glass, smooth metal, and ice are examples of things that do not reflect isotropically, yet are difficult to account for in a general method that is not taylored to a specific site. This means that for the majority of sky models, the diffuse correction factor R_d is the only difference [44]. Creators of sky models make different assumptions about how to model the sky radiance from which the diffuse correction factor R_d is determined. Some of these models are discussed in Section 7.2.

The basic models all avoid directly using the angular distribution of sky radiance to determine the diffuse transposition factor R_d; therefore, the computationally expensive process of repeated numerical integration is also avoided. Advanced sky models use the angular distribution of sky radiance directly and require numerical integration after determining the sky condition. There will be more discussion on the details of this in Section 7.3.

7.2 Selected history of basic sky models

Basic sky models range from very simple to complex algorithms. In this section, several models will be discussed to show this progression during the history of sky model development. The discussion is not meant to be a list of the best performing models or to be comprehensive. There is much literature evaluating basic sky models, how to properly compare them, and select them for specific uses. Some of this literature will be referenced in the selection of models to consider for the simulation under construction.

Although the main goal of this section is to give the reader a historical background, it also contains several original contributions to the body of knowledge:

- Review of the history of sky modeling.
- Rediscovery of the oldest known derivation of the Isotropic Sky Model (ISM).
- Explanation of the various geometries used to derive the ISM.
- Investigation into various boundary conditions for integrating portions of the sky to resolve ongoing confusion in the literature and field.

For now, the discussion will begin with the first and simplest basic sky model, the Isotropic Sky Model (ISM). All known references to this model fail to provide a clear first author. Unlike some results that are claimed by many authors, the ISM has no known credible claim of first authorship.

7.2.1 Isotropic Sky Model (ISM) 1942?

The simplest [60] sky model is the Isotropic Sky Model (ISM) shown in Equation 7.3,

$$I_T = \underbrace{I_{b,n} \cos\theta_i}_{\text{Beam}} + \underbrace{I_{d,h}\left(\frac{1+\cos\beta}{2}\right)}_{\text{Diffuse}} + \underbrace{\rho I_{t,h}\left(\frac{1-\cos\beta}{2}\right)}_{\text{Reflected}} \tag{7.3}$$

where β is the mounting angle of the collector measured from horizontal. Note that several authors derived the ISM correction factors as

$$R_d = \cos^2\left(\frac{\beta}{2}\right) \tag{7.4}$$

$$R_r = \left[1 - \cos^2\left(\frac{\beta}{2}\right)\right] = \sin^2\left(\frac{\beta}{2}\right) \tag{7.5}$$

Although these forms have fallen out of use in recent years, they reinforce the fact that together R_d and R_r form the whole hemisphere field of view (FOV) of the receiving surface. The more common form (Equation 7.3) can be quickly obtained using the power reduction trigonometric identities on Equations 7.4 and 7.5.

Isotropy means that a physical quantity is constant in any direction. In the case of sky radiance, this means that the radiosity is constant (or uniform) in all directions in the sky (after accounting for the angle of incidence). The Isotropic Sky Model is known to approach the true sky conditions for the most overcast conditions and underestimates total irradiance during clear-sky conditions. Even the most overcast and clear-sky conditions are isotropic in azimuthal direction and anisotropic in the polar direction defined from zenith. Partly to cloudy sky conditions are anisotropic in both directions and are dynamic.

Researchers misquote and misunderstand several key aspects of the ISM: (1) the origin of the model is often miss attributed [61–65], (2) there is confusion surrounding the geometrical basis for the results of the ISM, (3) tied to the issue of geometry, there is confusion among authors about the appropriate boundary conditions for integrating the sky that is within the view of the surface in question, (4) even in the most overcast sky conditions, sky radiance is known to be non-uniform, yet many authors discuss the uniform overcast sky. For these reasons, a careful review of the history and the various methods of derivation have been sought. This original work, by this author, in researching the history has several goals: (1) to instruct and help bring the field into a clear understanding of the work that has already been completed, (2) to serve as a significant reinterpretation of the fragmented knowledge found in the field, (3) to provide a single location for a continuous discussion related to sky modeling. Ultimately, the goal is to facilitate those who come after to quickly learn the field and build upon the roadway of knowledge.

Lambert 1760 was the first to discuss uniform light from the sky [66–68]. Lambert's work was in the context of luminance from the sky. Luminance is radiance perceived by the human eye; therfore, luminance is a limited portion of the full electro-magnetic spectrum discounted by the optical response of the average human eye. At the time, Lambert discussed the apparent brightness as perceived by the human eye. His work was based on observations of brightness, which he noted is subjective to each observer. Lambert made many contributions to our understanding of *photometry*, light measurement, and *pyrometry*, heat and power measurement. Lambert's work is noted as the first to provide theoretical mathematical analyses in both fields. He also predicted a logical progression that photometry would develop first and then pyrometry upon those results. For some this may be counter-intuitive from a modern perspective given that radiance is the full electro-magnetic spectrum and luminance is a portion of it observable to the human eye. The reason Lambert's developemental perspective makes sense is that the human eye was the first instrument used for brightness measurement from which Lambert built a mathematical and theoretical understanding. Later, this understanding was then used to build measurement instruments. These methods and techniques could then be adapted for pyrometry. From Lamberts works, we can attribute several aspects key to the understanding of the origin of the ISM:

- cosine law of incidence/emission
- uniform surface (isotropic)
- uniform sky assumption for calculation of day-lighting through a window.

From this historical context, it can be readily seen that Lambert provided all of the mathematical theory and necessary framework to derive the ISM, yet no one (to this author's knowledge) has found evidence that he completed such a derivation. One perspective, shared by DiLaura is that the necessary instruments to make accurate measurements of luminance were not developed sufficiently until around the 1920s. This idea that instruments were not developed sufficiently to make accurate measurements can be extended to the radiance field and is supported by the fact that C. G. Abbot (also known as C. G. Abbott) helped develop the silver disk pyrheliometer [69,70], advanced the design of the bolometer created by Langley [71], and created the pyranometer [72,73]. Abbot was one of the first scientists to measure the solar constant with reasonable accuracy and precision [74]. Abbot was one of the central figures in a debate as to whether or not the measurements of the solar constant had accurately accounted for atmospheric effects. He attempted to understand the reasons for the variablity in the measurements after accounting for atmospheric effects as best they could at the time. He was even part of a team that designed an automonus pyrheliometer that was mounted to a group of weather balloons and successfully measured the solar constant above 24/25ths of the atmosphere. Much of this work occurred from around 1900 to 1925 [71]. Later in his life, Abbot became interested in solar energy utilization [75]. Lastly, the work of Abbot et al. on measurement instruments resulted in the ability to measure DNI (pryheliometer), DHI (shaded pryanometer), and GHI (unshaded pyranometer). These instruments are the precursors of the modern pyrheliometer and pyranometer. Abbot's pyranometer came into existence about 30 years before the appearance of the first known-documented derivation of the ISM in the context of illuminance by Moon and Spencer 1942 [76]. It is important to note that Abbot and his collegues were not the only researchers working on pryheliometer and pryanometer instruments. The exact origins and history of these instruments is outside the scope of this research effort.

The developemental perspective presented above are consistent with the notion that results in the radiance field are preceeded by the analogus results in the luminance field. In the context of luminance, Moon and Spencer [76–80] are known for providing one of the first mathematical-based analysis of day-lighting. Moon and Spencer 1942 described the anisotropic overcast sky with a non-uniform function. Near the beginning of the work, the authors state "Despite the extensive literature on day-lighting, however, *all previous work has been based on the assumption of a sky of uniform helios.* But, skies are never uniform". The main focus of their paper was to provide a non-uniform sky assumption for day-lighting of a room through a window by the diffuse sky and a then new graphical method of solution, which was simpler (and faster) than working with the full derivation directly. In their appendix, a derivation was provided for outdoor illumination (unobstructed sky) on a tilted surface. This was performed with both the uniform assumption and a then new non-uniform assumption for the overcast sky. Of interest is that these derivations are based on 3D vector analysis and that is unique from other efforts to derive the ISM. The results of the Moon and Spencer 1942 derivations are two sets of R_d and R_r correction factors. The ones for the uniform sky assumption correspond exactly to the ISM. From this murky history, it is clear that this derivation is the first documented result for the ISM (known to this author) even though it is given in the context of luminance rather than radiance, and is 182 years after Lambert's seminal work.

Returning to the context of radiance, Lambert's predicted order of developement is obsereved (that pyrometry is developed after photometry) and Dilaura's perspective that measurement capablity was developed prior to formal mathematical analysis is also observed. From about the 1880s to about the 1960s, analysis of solar collector performance was limited to comparisons of typical irradiance to measured output. Works in the solar energy field used fixed values at specific times of the day based on clear-sky assumptions and previous measurements [18, 71, 81]. Here, the importance of the Ackermann 1915 paper can not be overstated. During this time period, irradiance measurement started out as daily horizontal totals for a select few locations with typically clear sky and by the 1940s had progressed to hourly values for a given orientation (normal, horizontal, vertical, tilted), where normal to the sun remained most typical.

Hottel and Woertz's 1942 paper is believed by many to be the first analysis of solar-thermal collector performance based on an equation to determine incident irradiance and other heat transfer processes; however, this is simply not the case for a general collector type. It may be true for flat-plate solar-thermal collector. Hottel's works are notable in the field of solar energy with a specific focus on heat transfer [14, 82–84]. He also published extensively on heat transfer in general and specifically in boilers. Some authors [61] cite Hottel and Woertz 1942 as the originators of the ISM, yet when the Hottel and Woertz 1942 work was reviewed, it used $R_d = 1$ and $R_r = 0$ for a tilted flat-plate solar-thermal collector. In Hottel and Woertz's 1942 work, the ISM was not derived, was not provided, and was not used. Hottel did much to advance solar energy analysis, particularly in home heating; however, he was not the first to analyze solar energy.

In reality, Abbot [57] discusses a more in depth perspective of sky radiance (known at the time as sky light) in comparison to direct (beam) radiance. It is clear that several things were understood at that time:

- Sky radiance is an important consideration in determining total energy incident on a surface.
- To determine the sky radiance contribution, one must understand its angular distribution and integrate it over the field of view of the surface.
- Approximating the angular distribution of sky radiance is very challenging.

This is evidenced by the quote and citation at the beginning of this chapter. Measurement of the angular distribution of sky radiance is an ongoing topic of research and has not yet been measured with accuracy and precision; however, quantification of the long-term average distribution for particular sky conditions has been accomplished. Abbot briefly notes that the sky radiance is important to consider in less-than-ideal sky conditions. Although he gives results from combining direct and diffuse radiance, he does not provide the equation with which they are combined. Hottel 1941 does provide such an equation [14].

The simpliest known method to derive the ISM uses a view factor result from Hottel's 1967 book Radiative Heat Transfer [85] and is found in Appendix B. This derivation is based on a portion of an infinitely long half cylinder. Of interest is that Hottel and Moon were both professors at Massachusetts Institute of Technology working in related fields, yet Hottel's work does not seem to reflect the knowledge Moon had concerning the sky and its luminance distribution.

In the same way that knowledge was segmented between two fields of study, knowledge appears to be segmented between cultures as well. In a 1952 journal article in Russian, Aizenshtat gives the oldest known statement of the ISM in the sky radiance context [86]. Note that this is about 40 years after Abbot et al. invented the pyranometer. Aizenshtat 1952 states that the result is well known and can be easily derived, yet does not provide the derivation or cite a source. In 1953, Russians, Kondratyev and Podolskaya [87] cite Aizenshtat 1952 and provided the oldest known (in the radiance context) derivation of the ISM using a 3D spherical coordinate based integration of a lune of a sphere (see Figure 7.2). To determine the polar angle as a function of azimuth angle at the boundary, spherical trigonometry is employed. This process is somewhat involved to both determine the boundary condition and then integrate to obtain the result. Kondratyev does not go on to provide the full solution as presented in modern terms (Equation 7.1); however, it is clear that Kondratyev knew the result. In Kondratyev's 1954 book in Russian [88], he provides the full solution to the problem on pages 406-409. In 1956, Kondratyev published a book on radiation in the atmosphere and expanded it in a 1965 English translation [89, 90]. Kondtratyev and Manolova 1958 evaluate the accuracy of the ISM using experimental data [91]. The work described above is the central basis for the well-known journal article in English, Kondratyev and Manolova 1960 [92]. In the article, they presented some of the results and a brief summary of the knowledge from works on the topic

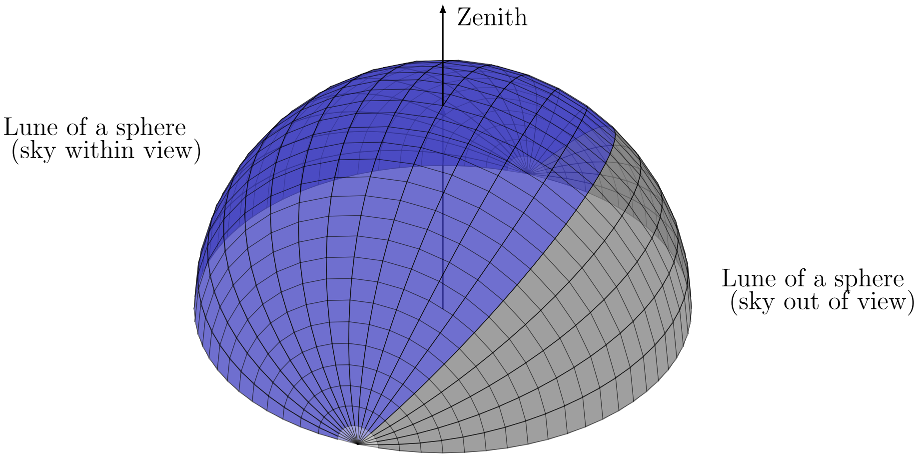

Figure 7.2: Depiction of the sky hemisphere seperated into two parts by a POA (blue shaded lune is the viewable part and the gray shaded lune is the part obscured by the POA). Each band corresponds to 10°of tilt in the POA.

of solar radiation by Kondratyev et al.

Returning to the topic of mis-citations, authors also cite Liu and Jordan 1960, 1961, and 1963 [93–95] as the creators of the ISM despite the fact that the 1960 paper does not contain the derivation or the result. The 1961 paper presents the assumptions, a conceptual setup, and the solution without citation. The 1963 paper presents the results without derivation or citation. In more recent times, the importance of the uniform sky assumption, derivation of the ISM in the Moon and Spencer 1942 appendix, and the Kondratyev works appear to be overlooked. This is surprising because the well-known book on the topic of solar radiation by Robinson 1966 [42] cites Hottel and Woertz 1942 (Feburary), Moon and Spencer 1942 (December), and Kondratyev and Manolova 1960. Robinson 1966 also calls the correction factor R_d for the ISM a law, something that illuminating engineers do not, as it is well known that the sky luminance/radiance has anisotopy in all sky conditions. Because of his untimely death, Robinson 1966 was actually finished by his peers. Chapter 4 contains the cited portion and is known to have been written by W. Schuepp. Schuepp was a contemperary of Linke. The well-known Temps and Coulson 1977 [96] paper on their clear-sky model also cites Kondratyev and Manolova 1960. Hay and Davies 1978 [97] present a more detailed derivation of the ISM in 3D spherical coordinates citing Kondratyev 1969 [98]. These citations show that the western world was very much aware of the Kondratyev works in particular. There is at least one exception to the trend of neglecting the Kondratyev work and it is by Yang 2016 [99].

Confusion continues into the 2000s. In 2002, Badescu [62] presented a 2D derivation of the ISM based on integrating a portion of a semi-circle (Appendix C). Badescu claimed that Liu and Jordan 1963 was one of the first isotropic models and is a 2D model. Badescu goes on to repeat the methods in 3D to form a new version of the ISM, which is given in Equation 7.6. (The full 3D derivation is given in Appendix D.) The derivation is accomplished by integrating portions of a hemisphere. Basescu then went on to verify the 3D result using the Brunger 1993 model for the angular distribution of irradiance. In a 2016 conference paper [65], Xie and Sengupta from NREL numerically validated the original ISM. Xie and Sengupta 2016 found that Badescu's validation work did not match their own. Xie and Sengupta 2016 do not explain the reason for the conflicting results.

$$I_T = \underbrace{I_{b,n} \cos\theta_i}_{\text{Beam}} + \underbrace{I_{d,h}\left(\frac{3+\cos 2\beta}{4}\right)}_{\text{Diffuse}} + \underbrace{\rho I_{t,h}\left(\frac{1-\cos 2\beta}{4}\right)}_{\text{Reflected}} \tag{7.6}$$

In this paragraph, the current author presents his own original explanation using an *almucantar*, a circle drawn on the surface of a sphere parallel to the horizon (Figure 7.3(a)). This meaning is adapted slightly to drop the reference to the horizon and retain the idea that the circle is defined by a constant polar angle for any given coordinate system. The problem with Badescu's method was that a much simpler boundary condition was used where he assumed a constant polar angle for a given

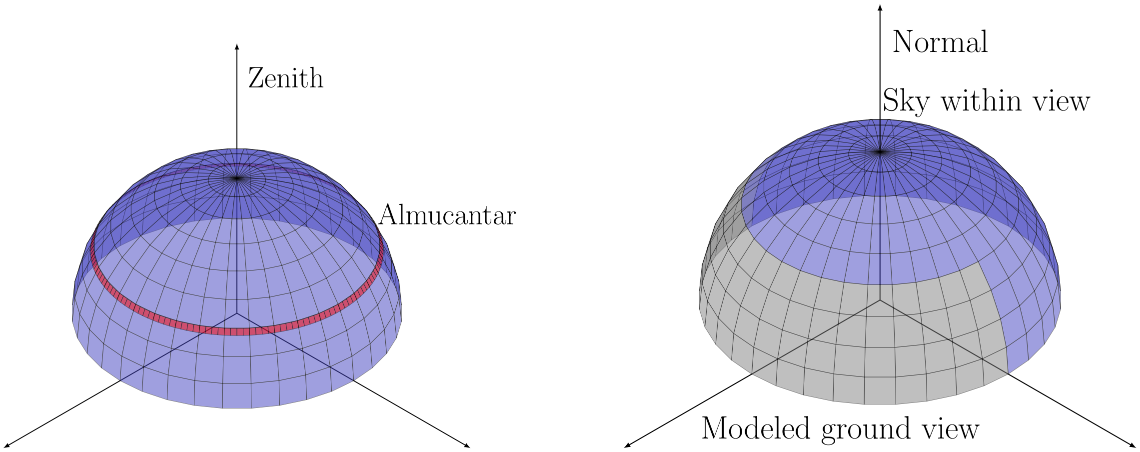

(a) Almucantar defined in the unrotated cordinates.

(b) Hemispherical FOV of the POA defined by the Badescu boundary conditions.

Figure 7.3: Almucantar and resulting Hemispherical FOV using the Badescu 2002 boundary conditions.

range of azimuth angles (i.e, along a segment of an almucantar in the rotated frame defined by the normal of the POA). As depicted in Figure 7.3(b), there is a direct conflict to the shape of a lune of a sphere (planar slice along a great circle), which was used by Kondratyev and Podolskaya 1953 as well as Hay and Davies in 1978. The horizon makes a planar slice of the 2π sr field of view of the Plane of Array (POA), and is the reason why the boundary conditions for a planar slice (lune of a sphere) is preferred to an almucantar (constant polar angle). Extending this discussion from simple POA to solar collector (or any device with optics) leads to two very important questions: (1) What shape does the view take? (2) How much does each element of the view count toward the energy transference process? To a limited extent, these questions are addressed for solar collectors and in particular STC from a modeling perspective in Section 7.3, Chapter 8, and Chapter 9. This is an active research topic.

To numerically integrate, Xie and Sengupta picked a unique coordinate system and method for determining the boundary condition. This author's derivation of Xie and Sengupta's method and a plot confirming Xie and Sengupta's result is found in Appendix E. Notably, the Xie and Sengupta 2016 boundary condition is much simpler than the one used by Kondratyev and Podolskaya 1953 as well as Hay and Davies in 1978. A reveiw of the literature shows that Xie and Sengupta 2016 were not the first to use this method [100–102]. Furthermore, the starting equation (Xie and Sengupta 2016 Equation 2b or Equation E.1 of Appendix E in this work) was known at least as far back as Gordov 1938 [103], who is cited by Aizenshtat 1952. Similarly, Lambert 1760 [104] gives the same mathematical result for the case of a star in twilight. Investigating the history and origin of the starting equation and the method of defining the boundary condition is left to a science historian. To further make the point that the origin of the ISM is misquoted, Xie and Sengupta 2016 cite Liu and Jordan 1961 as the source for the ISM; furthermore, they also claim that Liu and Jordan 1961 analytically solved the 3D integration. There is little-to-no evidence of an actual derivation in Liu and Jordan 1960, 1961, or 1963.

From this history, one can conclude several important things about the origin of the ISM: (1) Aizenshtat 1952 (gives) and Kondratyev and Podolskaya 1953 (derives) the ISM in the context of solar energy (irradiance). (2) Moon and Spencer 1942 is the oldest known work to have produced the result in any context. (3) Lambert 1760 was the first to formalize the mathematical construct and framework needed to create the ISM. (4) Abbot et al. did much to advance measurement instruments for sky radiance that drove the need for such a model. It is left to a science historian to further research the true origins and history of the ISM in detail. From this history, one can also conclude several important things about the nature of the ISM and integrating the sky as a hemisphere: (1) The isotropic sky can be properly modeled as a 3D hemisphere (Spencer and Moon 1942, Kondratyev and Podolskaya 1953, Hay and Davies 1978), 2D half circle (Badescu 2002), or an infinitely long half cylinder (Hottel 1967). This is true because one can cut a hemisphere into a given number of lunes of equal size and each one will carry the same ratio to the whole as an arc from a half circle cut into the same number of equal pieces will. Furthermore, it does not matter the thickness of the 2D pie-shaped pieces. (2) When modeling the sky in 3D, one must take care to properly define the solid angle view of the collector to integrate over. Failing to do this properly will induce errors in the calculation of the amount of sky radiance that the collector can receive (irradiance). Furthermore, those errors will not be apparent if the same integration method is used in the validation process.

Finally, integrating to determine the portion of sky radiance seen by a collector prior to determining the solar conditions is called a *post-integration* method because the sky conditions are determined after the integration was completed. The ISM is a post-integration method. Later, a pre-integration family of methods is discussed.

7.2.2 Temps and Coulson 1977: Clear-sky Model

Now that the seminal sky model and assumptions have been introduced, it should not surprise the reader that there is a plethora of sky models in the literature that attempt to accommodate the anisotropic nature of the sky. In 1977, Temps and Coulson [96] noted that the diffuse sky has anisotropy, especially during clear-sky conditions, which was known to Kondratyev about 30 years earlier and to illumination engineers many years prior to that. Under the ISM, a collector can be tilted the same amount toward or away from the equator and the R_d contribution is the same. The reality is that the sky is anisotropic and the R_d contribution varies in the two cases above. Based on data gathered, Temps and Coulson noted that the anisotropy is because of brightening of several regions of the sky that include circumsolar and horizontal brightening, effects that were also understood many years earlier. Temps and Coulson were not the only researchers to recognize this [52,53]. They introduced two correction factors for the diffuse term, which attempt to properly capture the contributions of horizontal brightening and circumsolar effects. The Temps and Coulson Model works reasonably well for clear-sky conditions, is known to be less accurate for overcast conditions, is also a post-integration method. The Temps and Coulson model is given by Equations 7.7 with $F' = 1$.

7.2.3 Klucher Model 1979

In 1979, Klucher [105] proposed a modification to the Temps and Coulson Model based on his observation that the ISM worked well for overcast conditions, and the Temps and Coulson Model worked well for clear-sky conditions. The Klucher model is given by Equations 7.7,

$$I_T = \underbrace{I_{b,n} \cos \theta_i}_{\text{Beam}} + \underbrace{I_{d,h} \left(\frac{1 + \cos \beta}{2} \right) CF_k}_{\text{Diffuse}} + \underbrace{\rho I_{t,h} \left(\frac{1 - \cos \beta}{2} \right)}_{\text{Reflected}} \tag{7.7a}$$

$$CF_k = \left[1 + F' \sin^3 \left(\frac{\beta}{2} \right) \right] \left[1 + F' \cos^2 \theta_i \sin^3 \zeta \right] \tag{7.7b}$$

$$F' = 1 - \left(\frac{I_{d,h}}{I_{t,h}} \right)^2 \tag{7.7c}$$

where F' is the clearness index, and ζ is the solar zenith angle. Klucher introduced the idea that a shift in sky conditions required a shift in weighting between the two terms for diffuse used by Temps and Coulson. Loutzenhiser [61] provides a concise introduction to several sky models and evaluates them. The Klucher model is also a post-integration method.

7.2.4 Computation of Diffuse Radiation on Slopes (CDRS) Model 1987

In 1987, Gueymard published the CDRS model [106, 107], which is based on a three-dimensional analysis of anisotropic diffuse sky conditions. CDRS is also known as the Gueymard model. CDRS uses a unique approach for determining the diffuse transposition factor (R_d). CDRS is one of the leading models that performs well in most conditions. As with many sky models, the ISM reflected transposition factor is used.

One of the problems of sky models is the lack of universal application. Although some models are most accurate for certain sky conditions (clear, overcast, or turbid), a particular mounting (tilt equal to latitude, vertical, or horizontal), or a select type of tracking (fixed, single-axis, or dual-axis), the CDRS Model is one of the most accurate for a wide range of conditions and applications. Furthermore, Gueymard provides the source code for the CDRS model to anyone who requests it because the algorithm is difficult to implement [108]. The CDRS model is also a post-integration method.

7.2.5 Perez 1990 model for irradiance on a tilted surface

During the late 1980s, Perez et al. published several sky radiance models [36, 109–111]. This progressive work yielded the popular Perez 1990 model [36, 112, 113] for sky irradiance on a tilted surface. Similarly, Yang 2016 [99] referenced Perez 1990 as Perez3. (See Appendix F for model equations and a discussion of the Yang 2016 implementation of the model.) Perez 1990 is built upon measurements at 10 sites in the USA and three sites in Europe. The model has been validated to perform well at other sites that were not part of the training set. This work includes several variations in application: sky luminance angular distribution, diffuse illuminance on a tilted surface, irradiance on a tilted surface, and direct, global, and diffuse daylight

Table 7.1: Selected models from Gueymard evaluation for overall sky conditions [1]

Sky model	MBE %		RSME %	
	Tilt = Lat.	Two-Axis	Tilt = Lat.	Two-Axis
Isotropic [76]	–5.1	–8.1	7.8	9.6
Klucher [105]	–1.4	–6.0	4.6	7.5
Gueymard [106, 108]	–0.8	–1.0	4.3	4.2
Perez 1990 [36]	–2.7	–2.3	6.7	5.8

illuminance. More importantly, the work discussed how various fields interrelate and unify; therefore, only one model is needed for several applications. Perez et al. even evaluates the discrepancy in using the sky luminance angular distribution model to determine sky radiance angular distribution. Again, more will be discussed about angular distribution models in Section 7.3.

7.2.6 Comparison of Isotropic, Klucher, Gueymard, and Perez 1990 sky models

Gueymard [1] evaluated many of the leading sky models with data taken at NREL's Golden, Colorado, facility (typically sunny). Table 7.1 summarizes the mean-bias error (MBE) and root-squared-mean error (RSME) for overall sky conditions with mounting angle equal to latitude and two-axis tracking for four models. Gueymard concludes that his model and the Perez model work best overall.

One can conclude that for sites with clear skies for most of the year, the Gueymard 1987 model may be preferred. Another consideration is the quality of data used as inputs for the models. Gueymard 2008 pointed out that some models handle poor-quality data better than other models. Specifically, the DNI, DHI, and GHI can all be measured with ground-based instruments. For a variety of experimental reasons, these three measures do not always hold for the Closure Equation 7.2. The closer the three measures are in self agreement to the Closure Equation, the better the data.

7.2.7 Basic sky model review and selection

There are many evaluations and verifications of sky models varying from verification at one location of one model to a more comprehensive list of models created todate. A few of the best evaluations have already been referenced in this work [1, 61, 99, 114]. Some evaluations are of little use because they are riddled with errors, whereas others like Demain 2013, provide a good basis for proposing a new model [115]. The sky modeling field is rich with many review papers. A few models repeatedly are shown to work reasonably well for a wide range of uses and locations. The most popular of these is the Perez 1990 tilted surface model.

It is important to point out some limitations of sky models:

1. The goal of any sky model is not to have low error for any one given data point; rather, it is to be correct on average, say over a month or better still a year. This is because the three measures of irradiance (DNI, GHI, and DHI) result in the loss of much of the direction information about the irradiance that is required to reduce the error. In addition to this loss of direction information, radiometry has limited accuracy (2.5% for the best of laboratory conditions and 5–10% in the field) for a variety of measurement challenges.

2. Sky models are typically tested with five mountings (tilt = latitude of the location, vertical pointed in the four cardinal directions). This limits our understanding of model performance outside these mountings. One reprieve from this is that models typically perform the worst for vertical surfaces because only half the sky is seen.

3. Some models such as Perez 1990 have been shown to perform well on an annual basis at many site locations despite the variations in frequency of sky

conditions. To aid in understanding the limits of the above statement, Xie and Sengupta 2016 [65] provide a counter example using short-term data. Average correctness applies best to an annual basis and fails for periods of only a few days. What is the minimum period one must use will likely depend on the location, model and quality of irradiance data. This topic is an active area of research and it is left as future work to further explore. The excellent performance of the Perez model is because his method of sky classification works well. This means that as long as a sufficient number of sky samples are collected for each sky type and the corresponding data used to determine the model coefficients, the error induced by the variability is minimized.

4. Uncertainty of the measured inputs propagates through a sky model in a complex manner; thus determining model uncertainty is challenging because model performance typically varies from location to location. The variance in performance is caused by the variability in the frequency of various sky conditions found during a year at the two sites. This means that uncertainty assessed at one location is unlikely to be the same as that assessed at another location. One method employed is to use empirically derived coefficients for each location of interest to improve model performance. Sometimes uncertainty is given for a particular model based on some form of sky type classification.

5. No one model is known to work best for all locations, all sky conditions, and all possible applications. Some models are known to not work well for vertical surfaces, which is important in building energy applications. Another model may perform well for tilted surfaces that track the sun, which is important to many large-scale solar energy applications. It has also been shown that some models handle poor-quality irradiance data (DNI, DHI, and GHI) better than

others. One of the data quality checks is to determine if the Closure Equation (Equation 7.2 holds for the three measured irradiances (DNI, DHI, and GHI).

There are more concerns in selecting a sky model for POAI determination, yet the above points summarizes many of the key issues. From this list, and the reviews, it is obvious that the Perez 1990 model is one of several great first choices for use with the TMY data. Table 7.2 summarizes the sky models discussed.

7.3 Advanced sky modeling

Now that a general overview of sky model basics has been completed, a detailed discussion is in order. Starting with the fundamental geometry of irradiance—radiosity from the sky to a surface—Equations 12.13–12.14 of *Fundamentals of Heat and Mass Transfer* [116] are given in Equation 7.8

$$I_{t,h} = \iint I(\theta,\phi)\cos\theta d\Omega = \int\limits_{0}^{2\pi}\int\limits_{0}^{\pi/2} I(\theta,\phi)\cos\theta\sin\theta d\theta d\phi \tag{7.8}$$

where θ is the polar angle, ϕ is the azimuth angle, the receiving surface is horizontal, and the intensity (I) includes all sources of emission in the sky dome (see Figure 7.4).

Given the diffuse component only, the previously discussed sky models were concerned with producing overall correction factors R_d to relate the diffuse horizontal irradiance $I_{d,h}$ to that on a tilted surface $I_{d,h}R_d$. The original method was to perform the integration and then apply the resulting R_d correction factor to all possible sky conditions (post-integration). The main reason for this method was the lack of computing power that results in the need for simplicity. In the past, oversimplifying the problem avoided several issues: the lack of knowledge about the distribution of the diffuse sky, limitations preventing detailed measurements (given a direction, the

Table 7.2: Summary of a select list of sky models discussed

Year	Name	Creator	I/A*	$\iint^{\S}$	$\iint^{\#}$	$\$^{\dagger}$	E‡	Notable aspect
1942	Isotropic Sky Model (ISM)	Moon Spencer	I	Yes	Post	L	L	Seminal model, uncertain origin and date
1977	Temps and Coulson Model	Temps Coulson	A	No	Post	ML	ML	Overcast and clear-sky corrections to R_d and R_r
1979	Klucher Model	Klucher	A	No	Post	ML	ML	Linear combination of overcast and clear-sky corrections to R_d and R_r
1987	Computation of Diffuse Radiation on Slopes (CDRS) Model	Gueymard	A	No	Post	H	H	Sky radiance angular distribution only
1990	Perez Model	Perez	A	No	Post	H	H	sky radiance angular distribution only
2002	3D Isotropic Sky Model (misnomer)	Badescu	I	Yes	Post	L	L	Resolves known discrepancy at high slopes and is based on boundary conditions that are known to not match the physical situation, R_d, and R_r

* I and A denote isotropic- and anisotropic-sky assumptions, respectively

§ $\iint$ denotes the diffuse distribution is available as a function that can be integrated over the sky vault

\# $\iint$ denotes the method uses pre- or post-integraiton

† \$ denotes computational cost estimate

‡ E denotes effort to implement the method

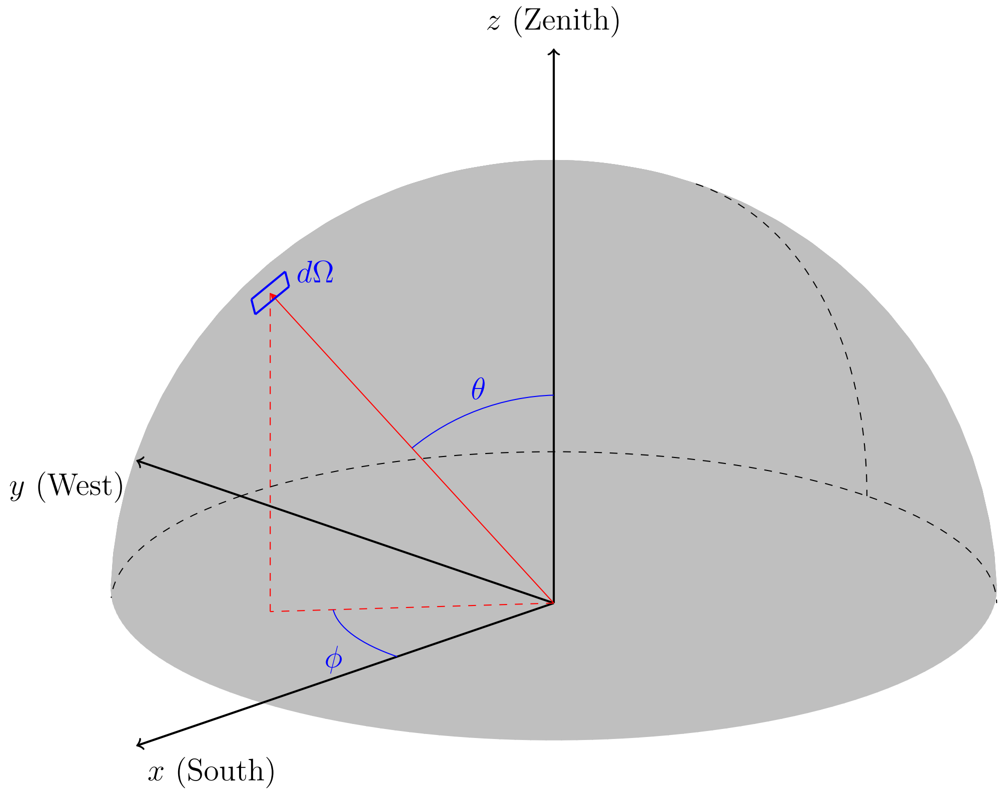

Figure 7.4: Geometry of the sky dome.

spectral intensity) of the diffuse sky, and the massive amount of calculations entailed. Unfortunately, simplification also resulted in limiting accuracy. It is now possible to consider the angular distribution of the sky radiance over the entire sky dome and then perform the integration after the sky condition is determined (e.g., a researcher should consider their current problem and computing resources before selecting a method that uses the simplified (post-integration) or the advanced approach (pre-integration)). Using the pre-integration approach requires that the functional form of the diffuse sky (sky radiance) intensity (I_d (W/(m^2·sr))) to be determined for every possible sky condition over the entire sky dome. In practice, sky radiance distribution I_d models have high RMSE for any given direction within one data point; however, the leading models do afford higher accuracy (low MBE say over a years worth of data). The reason is that the angular distribution models do not include cloud location information when classifying the sky condition. For any given data point, the cloud may or may not be in a specific direction. This results in high RMSE (i.e., the model is wrong in the moment for a given direction). The angular distribution models are more sophisticated; therefore, the quality distribution models tend to have low MBE overall (on a year of data). When designing a model, the goal is not to always be right, but to be right on average as much as possible. This characteristic applies to all sky models and is amplified for angular distribution models.

The sky modeling community has made large advances in improving the ability to accurately approximate irradiance over the three-dimensional surface of the sky dome from three common measures of irradiance (direct normal (DNI), diffuse horizontal (DHI), and global horizontal (GHI)). Up to this point in the discussion of sky models, the goal was to determine the total amount of irradiance incident on a flat surface given the current solar conditions and the mounting of the surface. The discussion has not been concerned with the other surface properties, namely the anisotropy some surfaces have when absorbing (accepting) irradiance. Another advantage of the pre-integration method is that it allows for the proper use of collector Incident Angle Modifier (IAM). IAM account for the optical properties of the collector (both STC and photovoltaic collector) that impact performance. An IAM is unique to each collector design although some researchers use generic IAM for a general type of collector design, for example flat-plate STC. Section 8.4 provides more information about STC IAM and the current methods for determining—and using—diffuse IAM. To improve the accuracy of solar collector modeling, a key step is to account for anisotropy of both the sky dome and solar collector. Another important step is to improve the accuracy of the irradiance data used as inputs, which is outside the scope of the current discussion.

7.3.1 History of sky radiance/luminance angular distribution models

Again, Lambert's developmental perspective is up held in that luminance angular distribution models preceded radiance models. There is a rich selection of luminance distribution models in the literature, which includes models and their evaluations; however, the current focus is on radiance distribution models. The literature is sparse, and even sparser concerning evaluations of said models. One surprising result is that many of the luminance distribution models can be used for radiance and vice versa. This is because both physical quantities have very similar distributions over the sky dome. Even with this redeeming fact, the literature on the subject of sky radiance distribution is very limited [36, 101, 117–125].

7.3.2 ASRC-CIE Model 1990

One of the first anisotropic models for the diffuse intensity I_d (W/(m^2·sr)) is the Perez 1990 Model commonly known as the ASRC-CIE model [36, 117], which was updated in 1992. Perez et al. 1990 is the first work (known to this author) to suggest using the luminance distribution to determine the radiance distribution. Perez et al. 1992 updated the model and verified it against several luminance models.

7.3.3 All-Weather Model (AWM) 1993

The next model of interest is given in Perez et al. 1993 [126, 127] All-Weather Model (AWM). The AWM is an updated work based on past accomplishments and is recommended by Perez as the model of choice (from the Perez works) for sky radiance angular distributions. The AWM classifies the sky conditions by sky clearness and the sky brightness and must be numerically integrated. The All-Weather Model is also a pre-integration method. See Appendix G for more information on the AWM including clarification of its formulation used in this work.

7.3.4 Brunger Model 1993

The Brunger model was also produced in 1993 [121, 128] and came from a series of previous works [118–120]. Many researchers cite Brunger and Hooper 1993 and use the model for evaluating other methods, yet the coefficients given in the works do not cover all possible sky conditions. The sky models are known to be sensitive to the choice in coefficients, which result in difficulties in extrapolation in an effort to obtain the missing coefficients. Perez et al. 1992 provides luminance coefficients for the Brunger model that cover a greater range of sky conditions. See Appendix H for more information on the Brunger model including the lack of coefficients.

7.3.5 All-Sky Model (ASM) 2004

Another angular distribution model is the All-Sky Model (ASM) given in Igawa et al. 2004 [123]. The authors of the ASM provide luminance and radiance coefficients. The ASM is based on a different method of quantifying sky conditions than the AWM.

The most notable difference is that the ASM is based on continuously adjusting the coefficients in the model, whereas the AWM uses the same eight bins as the ASRC-CIE Model; therefore, the AWM has some amount of discretization error and the ASM has interpolation and extrapolation errors (see Fig. 12 of Igawa et al. 2004).

7.3.6 Improved All-Sky Model (IASM) 2014

In Igawa 2014 [125], the ASM model is improved (IASM) and updated with a greater number of measurements from more locations in Japan. The IASM uses the same overall methodology as the ASM with a few adjustments to correlations and additional data. These improvements result in both new sets of radiance and luminance coefficients. What is surprising about the AWM, ASM, and IASM is that the AWM was developed with luminance data and performed almost as well as the IASM and better than the ASM during radiance testing on the datasets used to calibrate the IASM. The IASM lacks external evaluation at the time of writing.

7.3.7 Angular distribution model review and selection

In Garcia et al. 2011 [124], a comparison of four angular distribution models (ASRC-CIE, AWM, Brunger 1993, and ASM) was performed from data collected at four diverse locations. The data were completely independent of the data used in the calibration of any of the models. Not only was the goal of the work to compare four models, it was also to compare several variations on how the calculations were performed with the models. One of the methods is to normalize the sky scan data by measured horizontal irradiance for use as the standard combined with the integral method of calculation (more on this clarification in Appendix G). Garcia et al. 2011 showed that this combination yielded the best results; furthermore, the model that performed best under this variation was the AWM. There has not yet been an evaluation of the IASM using data independent of the training set. It is for these reasons that the AWM is selected as the angular distribution model of choice for the solar simulation under construction. Table 7.3 summarizes the advanced sky models discussed.

7.4 Verification of the proper use of TMY data and the SPA with ISM, Perez 1990 Model, and AWM

Given the previously completed sky model verification work by other authors, a verification of the *simplifed simulation*, the combined parts (TMY, SPA, and sky model) of the simulation to determine POAI is now possible. The goal of the test is to compare the overall performance of the simplified simulation against reported data. Following the methods in this chapter and details outlined in the appendices referenced herein, a simple calculation will determine POAI. This avoids the issues of collector anisotropy and captures the differences caused by using the simplified simulation. Using these differences to determine model error is outside the scope of this work because for this application, no known method has been found to universally determine the error for a sky model that would apply to all locations, climates, weather types, and surface orientations. Model uncertainty assessment is left as possible future work.

NREL provides measured meteorological data for Golden, CO [129], and data for 2015 were used. Using the procedure for a posteriori quality control step described in Yang 2016 [40, 99], the data are reduced. Performing the required calculation for each sky model being considered on the reduced data provides results to analyze, namely POAI measured vs POAI modeled (more on this in Chapter 9). In any numerical integration, a key issue is discretization error (i.e., Did the mesh size choice induce unnecessary errors or was computational cost and accuracy balanced?). In the numerical method a 4:1 ratio of elements was chosen in the azimuth and polar

Table 7.3: Summary of sky models

Year	Name	Creator	I/A*	$\iint^{\S}$	$\iint^{\#}$	$\$^{\dagger}$	E‡	Notable aspect
1990	ARSC-CIE Model	Perez	A	Yes	Pre	H	H	Sky classification by sky clearness index and sky brightness index
1993	All-Weather Model	Perez	A	Yes	Pre	H	H	Sky classification by sky clearness index and sky brightness index
1993	Brunger Model	Brunger	A	Yes	Pre	H	H	Sky condition classification by cloud ratio index k and atmospheric clearness index k_t, R_d only
2004	All-Sky Model (ASM)	Igawa	A	Yes	Pre	H	H	Sky classification by clear sky index K_c and the cloudless index Cle, both independent of solar altitude, R_d only
2014	Improved All-Sky Model (IASM)	Igawa	A	Yes	Pre	H	H	Updated coefficients based on larger experimental dataset

* I and A denote isotropic- and anisotropic-sky assumptions, respectively
§ $\iint$ denotes the diffuse distribution is available as a function that can be integrated over the sky vault
\# $\iint$ denotes the method uses pre- or post-integraiton
† \$ denotes computational cost estimate
‡ E denotes effort to implement the method

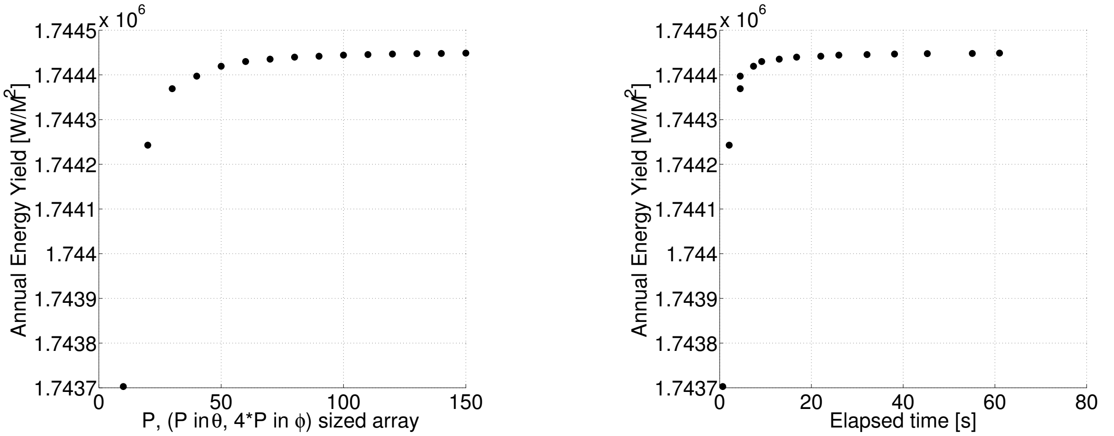

(a) Annual energy yield versus mesh size.

(b) Annual energy yield versus integration time.

Figure 7.5: AWM numerical integration: mesh size convergence.

directions because this ratio naturally exists for a hemisphere (360°:90°). This ratio reduces the mesh size dimensions to one. For more information on how the numerical integration is performed for the simplest case of the ISM, the reader is referred to Appendix I. Figure 7.5 shows the convergence plot for one year of data at College Station, Texas. Note that a mesh size of 50 (in the polar direction) is more than adequate for this particular site. The simulation results for the AWM on the Golden, Colorado, measured data used a mesh number of 90 as an added level of safety.

Following the work of Gueymard and Myers [130], Section 5.2 of said work provides definitions for the mean bias difference (MBD) and root-means-squared difference (RSMD) values. To calculate percent difference, the mean solar irradiance is used as the normalization factor. For the specific case being considered herein, that is the annual mean irradiance of the reduced data. Using the above data and methods gives results for the ISM, the Perez 1990 model, and the AWM, which are found in Table 7.4.

In addition to these traditional measures of performance, percent difference of the

Table 7.4: Sky model verification using the ISM, Perez 1990, and AWM: 2015 NREL Golden, CO, data

Sky model (Tilt = Lat.)	MBD %	RSMD %
ISM [76]	–4.3936	7.2423
Perez 1990 [36]	–0.1085	3.8257
AWM [126]	0.0469	4.1335

hourly data are plotted and histograms are provided for each model to reinforce the idea that the goal is to be correct on a yearly energy yield basis, which is measured by the MBD. Results for each model and are found in Figures 7.6, 7.7, and 7.8. Although all three models perform reasonably well, there is competing performance between the Perez 1990 model and the AWM concerning the MBD and RMSD. The AWM has the lowest MBD, and the Perez 1990 model has the narrowest RMSD for the specific dataset being considered. This means that for locations in the northern hemisphere in the mid-latitudes at high elevation with typically clear skies, similar performance would be expected. Quantitatively, the lack of knowledge limits our ability to assess model performance when changing locations of interest. For many of the popular sky models, enough evaluations have been performed at varying locations that there is a good qualitative understanding of performance.

7.5 Future improvements of sky modeling

In several locations in this chapter, potential improvements have been noted. The goal of this section is to provide a list of potential future work by gathering them into one location and adding a few new ones. Begining with new potential improvements, all sky models discussed herein assume that DNI is a point source. The field of modeling irradiance for high-concentration solar collectors is one notable exception (see [46] for more information). High-concentration collectors typically have an extremely narrow FOV that encompasses the sun and for some designs

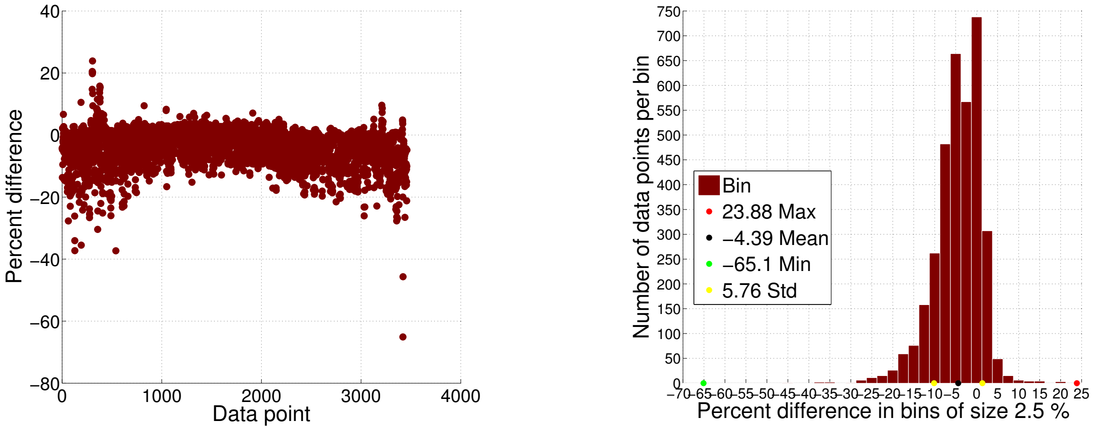

(a) ISM percent difference.

(b) ISM percent difference histogram.

Figure 7.6: POAI: Comparison of NREL measured data at Golden, CO, to the ISM calculated result.

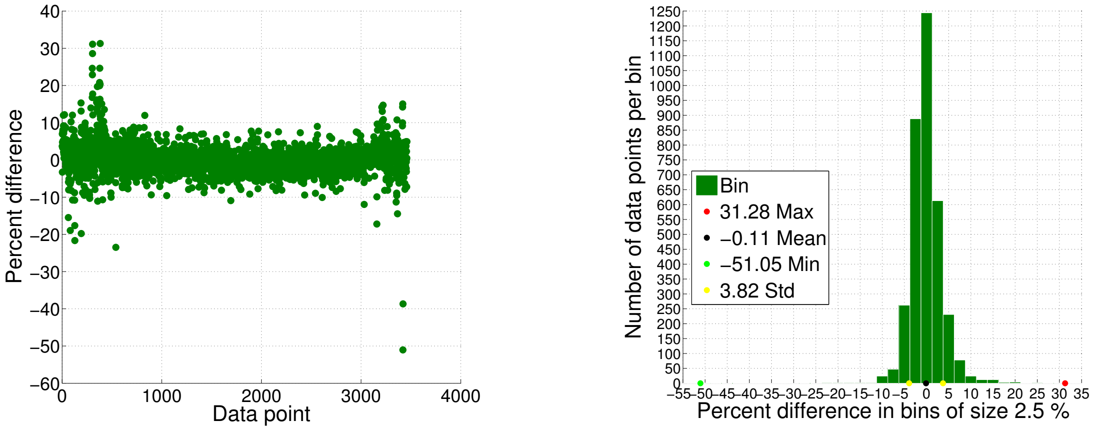

(a) Perez 1990 model: percent difference.

(b) Perez 1900 model: percent difference histogram.

Figure 7.7: POAI: Comparison of NREL measured data at Golden, CO, to the Perez 1990 Model calculated result.

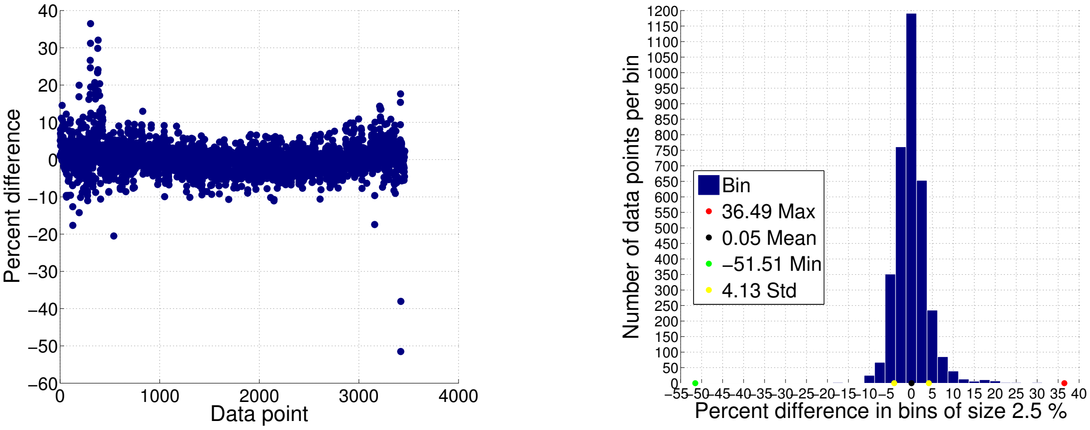

(a) AWM percent difference.

(b) AWM percent difference histogram.

Figure 7.8: POAI: Comparison of NREL measured data at Golden, CO, to the AWM calculated result.

a narrow circumsolar region. Because high-concentration-ratio collectors are only effective in clear-sky conditions, the models determining solar shape (sun shape) and or the circumsolar region around the sun are made for clear-sky conditions only. One future work would be to improve upon the point source assumption for DNI by creating an angular distribution model for DNI similar to the AWM or the ASM ideology for sky radiance.

A second future improvement would be to refine sky radiance angular distribution models to explicitly provide zero sky radiance in the direction covered by DNI as current methods distribute some sky radiance into the region around the sun that are explicitly excluded through shading of the pyranometer.

A third future improvement would be to explore the accuracy of various models under varying periods of time. For example, given the period of time each data point covers (i.e., secondly, minutely, hourly, etc.) determine the model bias error as a function of the period of summation (i.e., weekly, monthly, semi-annualy, annually).

The following list summarizes future improvements noted in this chapter and corresponding appendices:

1. Perform historical research:
    (a) on the origin of the ISM.
    (b) on solar radiation measurement.
2. Improve model uncertainty assessment.
3. Create an improved angular distribution model of DNI in an all-weather or all-sky sense.
4. Prevent sky radiance angular distribution overlap with DNI.
5. Explore the relationship between period of summation and model performance.

7.6 Conclusion

In this chapter, sky modeling was discussed from a post- and pre-integration perspective including the effect on computational cost. This is an original work of this author. The importance of sky radiance anisotropy is highlighted and the impact on model accuracy because of the loss of direction information in both measurement and modeling methods. The Perez 1990 and All-Weather Model (AWM) were chosen in the post- and pre-integration areas, respectively, for the solar-thermal simulation under construction. Both models were verified using 2015 data from NREL and is the original work of this author. During the discussion of the history of sky modeling, several key contributions were made:

- Review of the history of sky modeling, with new contextualization.
- Rediscovery of the oldest known derivation of the Isotropic Sky Model (ISM).

- Explanation of the various geometries used to derive the ISM.
- Investigation into various boundary conditions for integrating portions of the sky, which resolves ongoing confusion in the literature and field.
- Clear mathematical statement for using angular distribution models to determine R_d given in Appendix G.

From this review and reinterpretation of the knowledge about sky modeling, it can be seen that the field is continuing to develop and improve. Additionally, the field is also approaching the limit of how accurate a model can be given the loss in directional information because of measurement limitations. Using weather data, solar position, and a sky model will allow the determination of POAI for an arbitrarily oriented surface. This is the first step in calculating solar collector performance and the topic of the next chapter.

8. TRANSITIONAL SOLAR-THERMAL COLLECTORS: MODELING, PERFORMANCE, AND SELECTION

"These three types [stationary, single-, and dual- axis-tracking collector] are all very intersting on account of the balance of advantages between high efficieny and low cost which they present... [Abbot notes Carnot's Law, temperature limits of metals, and that overall efficiency is composed of both collector and heat engine efficiency.] With these points in mind, it will be appreciated that on account of their high concentration of solar rays, and the resulting high temperatures, the conical reflectors [dual-axis tracking], especially if parabolic, like that of Pifre, give maximum theoretical possiblities of engine efficiency. On the other hand, the hot-box principle of de Saussure [stationary], as used by Willse and Boyle, must necessarily give very low engine efficinecy. The cylindrical-mirror type [single-axis tracking] stands between them in this respect. On the other hand, the cheapness of installation and operation of the heat collectors of the three types runs in the opposite order... The problem of collecting solar heat for power purposes is indeed a very pretty one. It involves knowledge of optics, of mechanism, of the properties of radiation, and of heat engineering. Financial success probably awaits the solver, for with our present outlook it seems likely that within a generation or two power demands will lead to the sun as the most availbable source of supply." [15]

– Charles Greeley Abbot, 1934

Abbot aptly points out the trade-offs in the design choice of collector type. Selecting which collector type to use in a design continues to be hotly debated by engineers in the solar field. Properly selecting the type and design of the solar collectors for a particular application is paramount. Given the current level of understanding, one is forced to make assumptions about which collector type is best for a particular DSTTC application. The next step in building a solar simulation is to properly model collector performance, within the limits of current engineering understanding. Then, a collector can be selected that will perform as effectively as currently possible for the given task.

Previously, Section 1.1.2 described common types of solar-thermal collectors. The main benefit of stationary solar-thermal collectors is that they are much less expensive than the more-sophisticated single- and dual-axis tracking collectors. This benefit is counteracted because stationary collectors have a much lower maximum operating temperature and lower energy yields. To properly quantify the best possible DSSTC performance, a new class of collector is introduced and discussed in reference to current solar-thermal testing standards. Several STC —including some from this new class—will be evaluated and the "best" collector selected for use in the simulation. During the discussion of STC testing standards, several limitations will be noted.

8.1 Transitional solar-thermal collectors

There is a growing number of collectors that seek to fill the gap in operating temperatures between the low-temperature flat-plate and evacuated-tube non-tracking collectors, and the large-scale tracking high-temperature collectors. This group can be called the *transitional class* of solar-thermal collectors. The transitional class includes Fresnel designs that use the Fresnel effect from optics to avoid or minimize tracking, smaller trough versions that provide single-axis tracking, and stationary collectors that use adjustable mirrors to reflect light on the receiver tube. There are also stationary collectors with no moving parts in the transitional class. Many collectors in the transitional group are being developed by start-up companies. Some of these start-up companies have failed, whereas others are newly formed and do not have performance data established. Others simply do not currently offer their product for sale. It is notable that the adjustable-mirror designs seek to challenge the conventional wisdom that tracking and concentration are for large-scale facilities, whereas non-tracking, non-concentrating collectors are for low-to-medium-grade heat applications in residential, commercial, and industrial sectors.

One transitional collector, Roland Winston's XCPC design [131–139], stands apart from the others because it uses no tracking and very low-concentration ratios ($<$ 2 suns) to challenge the conventional wisdom that stationary low-concentration collectors are unable to produce industrial-grade heat. Figure 8.1 compares one of the XCPC versions to the low-temperature collector types. Over many iterations, Dr. Winston and his team at University of California-Merced have refined the XCPC design. The XCPC is stationary with no moving parts, works efficiently at lower to medium temperature difference of 150–250°C, and captures both direct and indirect solar radiation well with low concentration levels [134]. The XCPC design can be used to drive an absorption chiller to provide residential-scale space cooling [134]. The current work seeks to explore the benefits of integrating a transitional collector with a heat engine to provide DSSTC capabilities; therefore, a transitional collector must be selected from among the available options. By reviewing the STC performance standards, quantifying the performance differences between the collectors will enable a sound decision to be made.

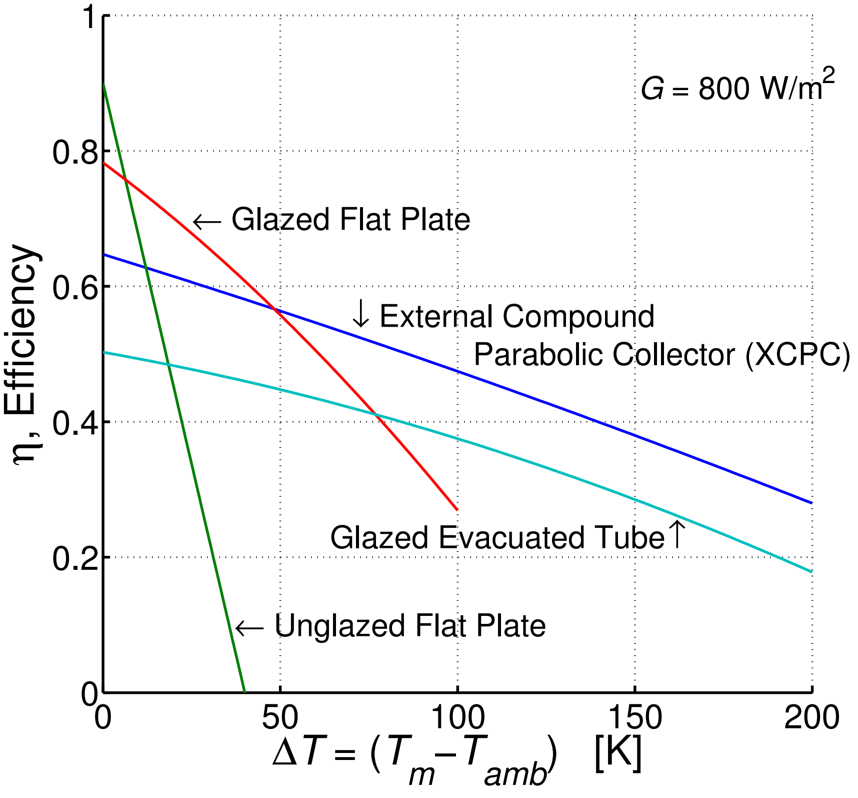

Figure 8.1: XCPC compared to lower temperature collectors.

8.2 Steady-state performance model for STC

The American certification standard by the Solar Rating & Certification Corporation (SRCC) [140] and the European certification standard by Solar Keymark [141] are both based on the International Organization for Standardization: ISO 9806:2013 [142] and other standards relevant to STC performance [143–145]. STC performance is typically modeled by Equations 8.1,

$$\eta = \eta_0 - a_1 T_m^* - a_2 G {T_m^*}^2 \tag{8.1a}$$

$$T_m^* = \frac{T_m - T_{amb}}{G} \tag{8.1b}$$

where η is the collector efficiency, η_0 is the maximum efficiency, a_1 and a_2 are constants, and G is the total irradiance. The coefficients η_0, a_1, a_2 are determined by regressing experimental data. Application of Equation 8.1a is limited in scope and applies to steady-state conditions neglecting the anisotropy of the collector, wind conditons, and other more subtle heat transfer physics. It is important to note that it is quite common to find collector performance curves displayed in a variety of ways to varying degrees of transparency. Figures 8.2–8.4 show three common ways to present collector performance properly. The additional information in the upper-right-hand corner of each plot removes ambiguity. Unfortunately, it is all-to-common to find ambiguous collector performance curves.

It can be readily seen from Figure 8.5 that the *stagnation point*—the point where the efficiency is zero and the temperature difference is maximum—is actually a stagnation curve. Although the stagnation curve can be crudely represented by a vertical line, it is not explicitly vertical or straight. It can also be seen that the performance curve is actually a performance surface. For a given irradiance level, the performance

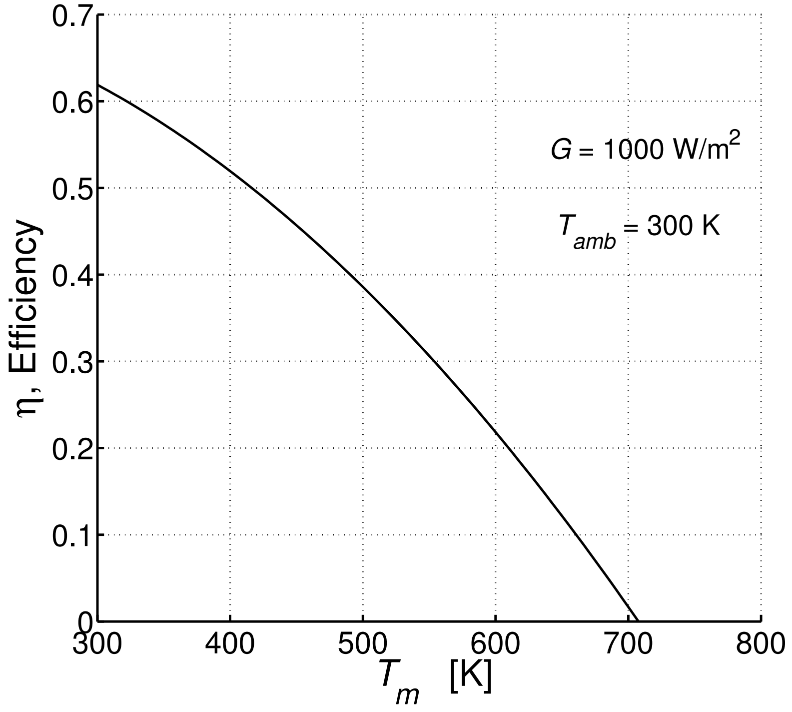

Figure 8.2: STC Performance: Mean fluid temperature method.

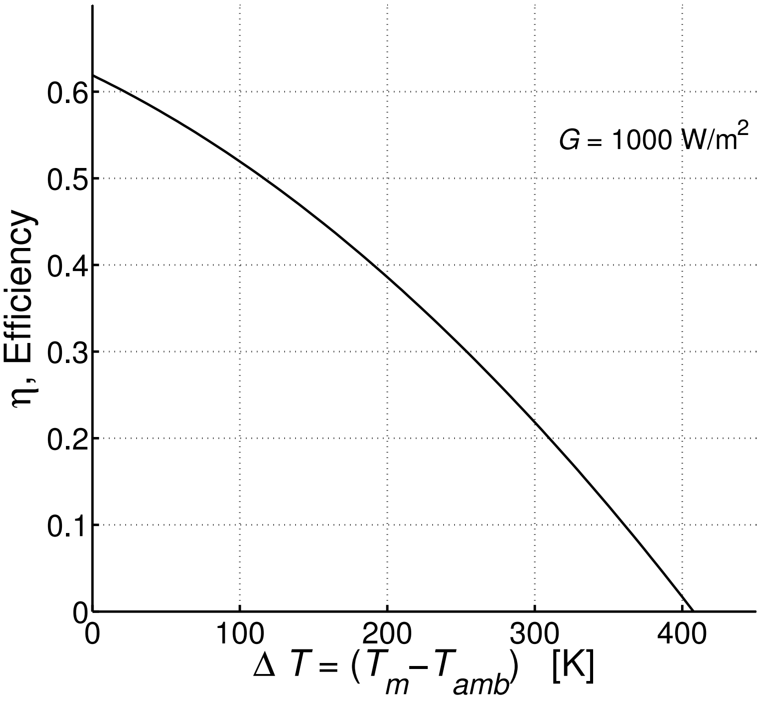

Figure 8.3: STC Performance: Temperature difference method.

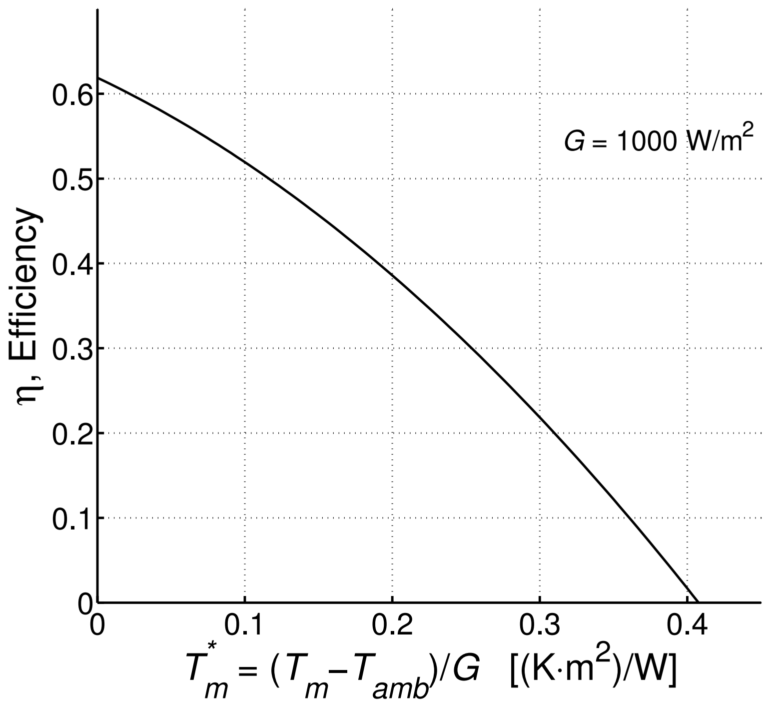

Figure 8.4: STC Performance: Reduced temperature difference method.

surface is sliced and a cross-sectional view of the surface is presented as a curve.

The standard also provides two methods for determining the stagnation point. The first method assumes the stagnation curve is a vertical straight line (constant T_m^*) as shown in Equations 8.2,

$$(T_m^*)_{\text{Stag\_Measured}} = (T_m^*)_{\text{Stag\_Specified}} \tag{8.2a}$$

$$\left(\frac{T_m - T_{amb}}{G}\right)_{\text{Stag\_Measured}} = \left(\frac{T_m - T_{amb}}{G}\right)_{\text{Stag\_Spedified}} \tag{8.2b}$$

$$\left(\frac{T_{sm} - T_{amb}}{G_m}\right) = \left(\frac{T_{stag} - T_{as}}{G_s}\right) \tag{8.2c}$$

$$T_{stag} = T_{as} + G_s\left(\frac{T_{sm} - T_{amb}}{G_m}\right) \tag{8.2d}$$

where T_{stag} is the calculated stagnation temperature. The standard requires the measured irradiance G_m to be within 10% of the reported stagnation irradiance G_s because the founding assumption that the stagnation curve is a vertical line is not true, as shown in Figure 8.5(b).

The second method from ISO 9806:2013 uses Equations 8.1 to extrapolate a stagnation value to reported conditions. This is accomplished by setting Equation 8.1a to zero and solving for T_m as demonstrated in Equations 8.3,

$$\eta = \eta_0 - a_1 T_m^* - a_2 G {T_m^*}^2 \tag{8.3a}$$

$$0 = \eta_0 - a_1 T_m^* - a_2 G {T_m^*}^2, \tag{8.3b}$$

$$T_m^* = \frac{-a_1 + \sqrt{{a_1}^2 + 4a_2 G \eta_0}}{2a_2 G} \tag{8.3c}$$

$$T_{\text{stag}} = T_{as} + \frac{-a_1 + \sqrt{{a_1}^2 + 4a_2 G_s \eta_0}}{2a_2} \tag{8.3d}$$

where the T_m^* data used to determine the constants η_0, a_1 and a_2 are encouraged to

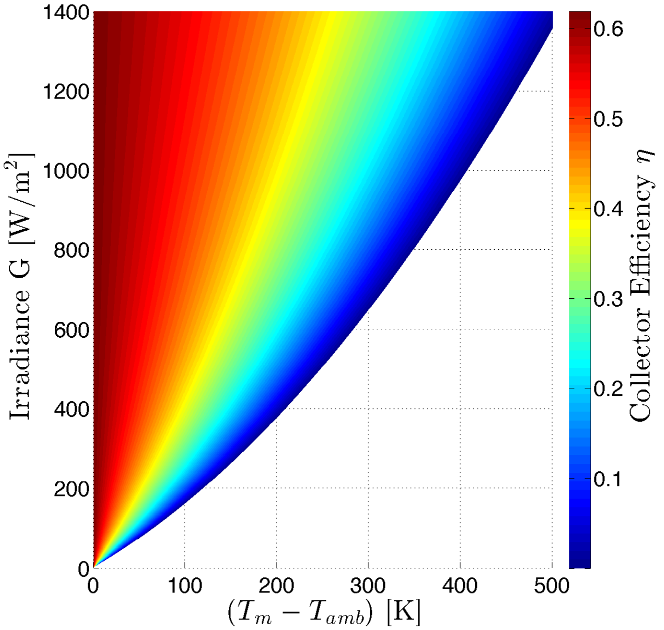

(a) Performance as a function of irradiance and temperature difference.

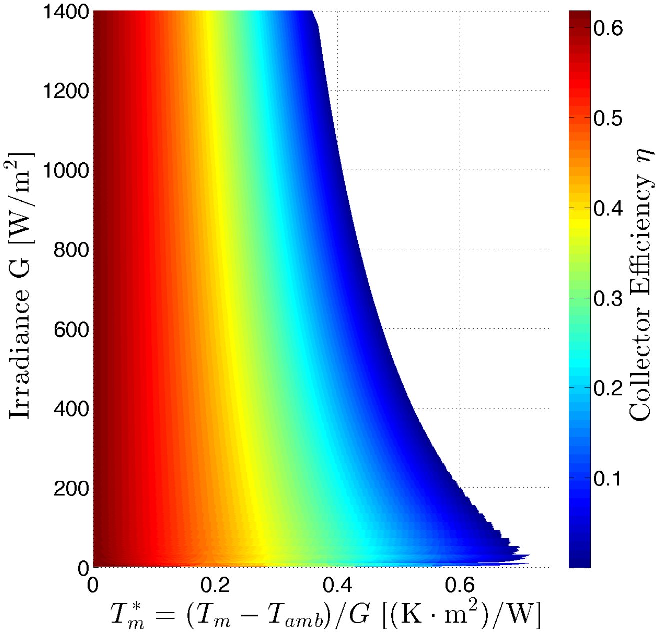

(b) Performance as a function of irradiance and reduced temperature difference.

Figure 8.5: XCPC collector performance as a surface.

cover areas near stagnation; however, the standard requires that at least one data point must be above $\frac{T^*_{m\ stag}}{2}$. This is ambiguous because Figure 8.5(b) shows that stagnation is not a single point, rather a curve of points. The typical irradiance condition is 1000 W/m^2 for reporting stagnation, and the standard allows for other values when reporting the stagnation condition.

Because not all collectors are intended to be used over large areas of the performance surface, the test standard 9806:2013 allows two options for determining a stagnation point; therefore, the test data may not yield model equation constants (see Equation 8.1) that are valid over the whole performance surface. The typically referenced certification annex includes only a summary of test results and provides limited information to determine the valid regions of the performance surface for a particular application. As a consequence, the full test report should be consulted for additional information about the data used to determine the performance surface (i.e., the coefficients η_0, a_1, and a_2), which ensures valid application of the model performance equation. Full test reports are not published by the certifying organizations and collector manufactures have the discretion to share this information or withhold it.

In this section, the primary equation that describes STC performance was presented with a short discussion about the basic limitations, primarily the lack of clarity as to the limits of the collector efficiency equations. Despite the limitations, the model equation is an effective tool to gain information needed to discriminate between various STC for a particular application. An efficiency comparison of this nature should not be the sole means by which a collector is chosen because other aspects should be considered such as cost, expected life, ease of installation, etc.

8.3 Comparison and selection of a transitional solar thermal collector

After reviewing Solar Keymark [141] and SRCC [140] certifications and standards, academic publications, and news releases from start-up companies, only a few collectors have published performance information in the transitional class. The few collectors identified are compared to the XCPC. Of these collectors, one has gone out of business, and one does not offer collectors for sale. It is also worth noting that Arctic Solar, the company marketing the XCPC, is offering, for the first time, the XCPC design for sale in 2015 and is in the process of being certified under the SRCC [146]. Please note that the XCPC sold by Artic Solar is not the exact same design as delineated in Kim et al. 2013 [132], although the performance curves are similar. Table 8.1 compares the few collectors that were found with performance information that could compete in the transitional class. Appendix J discusses the various methods used to determine the performance coefficients in detail.

Winston et al. 2011 [131] performs a similar comparison with an earlier verison of the XCPC. In Winston et al. 2011, Figure 4 and the accompanying discussion did not provide a detailed account of what performance equation values were used or how they were obtained for each collector. There are several differences in the two evaluation methods and in the results. The main difference is that Winston assumed insolation of 800 W/m^2 with 20% diffuse light versus the assumed value of 1000 W/m^2 and no diffuse light that the current work assumes. These differences between the evaluations of the collectors highlight how misleading it is to view only a slice of the performance surface. The Winston choice illuminates the ability of the XCPC design to effectively harvest diffuse light. Appendix J is included to facilitate transparency and allows interested readers to make their own assumptions and evaluations. The goal of the appendix is to outline the methodology used to determine performance

Table 8.1: STC Comparison

MFG	Name	Type	Tracking	Ref.
Viessmann	Vitosol 300-T SP3A	Evacuated tube	Stationary	[141]
TIGI	HC.1	Unique honeycomb	Stationary	[141]
Artic Solar	XCPC	Transitional	Stationary	[132]
Chromasun	MCT	Adjustable Fresnel reflectors	Single axis	[147]
Sopogy	SopoNova	Trough	Single axis	[148]

from literature information, which can, at times, be incomplete. 'Better' initial information tends to yield more accurate results.

There are in fact two XCPC designs discussed in Kim et al. 2013. The N–S XCPC has the absorber tubes orientated in the north–south direction, and the E–W XCPC has the absorber tubes orientated in the east–west direction, which allows for a higher concentration ratio. Both designs have the same functional shape to the reflector. Each has unique choices of reflector height and opening to maximize the ability to collect irradiance for each configuration. Figure 8.6 shows the XCPC performance curves against the other collectors from Table 8.1. Clearly, the SopoNova performs with the highest efficiency, but has a geometric concentration ratio of ∼8.59. This means that only beam and circumsolar irradiance should be considered when determining the energy yield because much of the diffuse light is not 'seen' by the collector, which means a much lower portion of the POAI can be received within the LFOV. The SopoNova design operates in a single-axis tracking mode. It is notable that the SopoNova design seeks to challenge the idea that tracking collectors must be large to be cost effective. The Chromasun MCT uses adjustable Fresnel reflectors within a sealed collector case that track on a single axis. The MCT collector design also challenges conventional thinking about tracking and scale. The tracking reflectors are driven by motors powered by PV cells mounted within the STC. Despite the extra equipment, the MCT does not perform as well as either XCPC design. Like the SopoNova, the MCT is a concentrating collector. The MCT has a reported concentration ratio of 20, which means that most of the diffuse light is unharvestable. The Vitosol 300-T evacuated-tube design was included because it was the 'best' collector from the Delgado-Torres work discussed in Chapter 4. The HC.1 honeycomb flat-plate design, while performing the lowest here, could be considered one of the better performing glazed flat-plate collectors on the market. Next are the XCPC designs, which collect diffuse irradiance well without tracking or any moving parts, making the XCPC inexpensive to manufacture and easy to maintain. These qualities mainly result from the unique reflector/absorber shape, which is illustrated in Figure 8.7. It has excellent thermal performance, low cost, and low maintenance. All these qualities make the XCPC designs the best choices for this study. From Figure 8.6, one may wish to conclude that the E–W XCPC is the better option. At this juncture, concluding which XCPC design is 'better' is premature as will be seen in Section 9.5, where the N–S XCPC is found to have slightly higher annual irradiation received because of the lower concentration ratio. The above limited evaluation is not intended to be an endorsement of any product. The products presented here are for educational purposes only and individual manufacturers should be contacted directly for product information, including thermal performance information. In subsequent chapters—for the purposes of this study—a detailed model of the XCPC designs are developed and used to discover more about optimal DSSTC design.

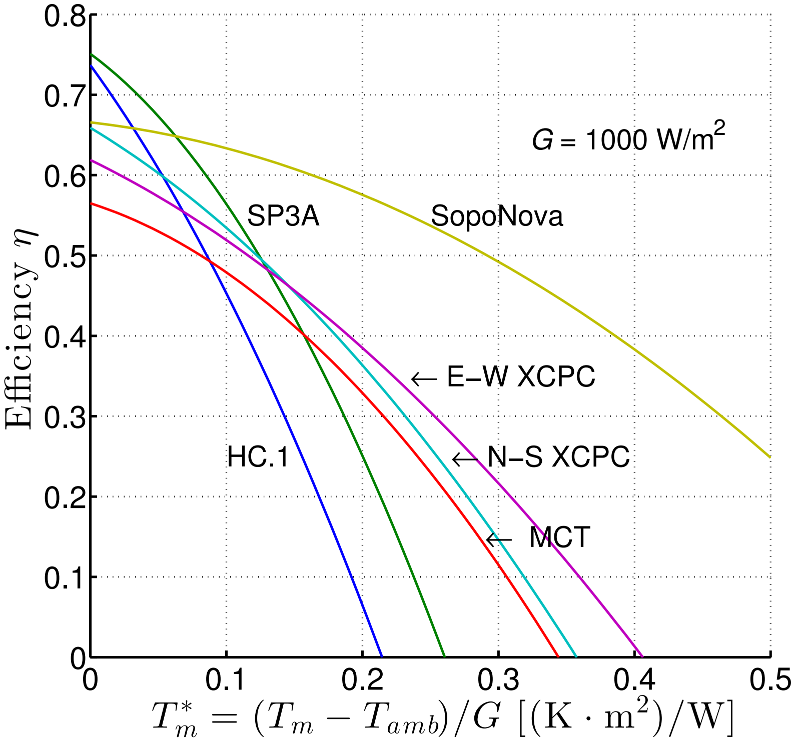

Figure 8.6: XCPC comparison.

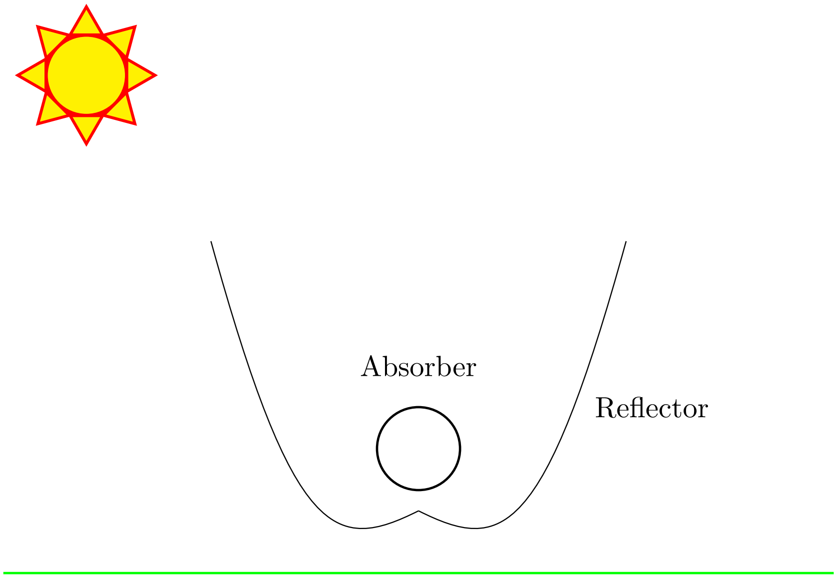

Figure 8.7: Illustration of the unique XCPC shape.

8.4 Full performance model for STC

Now that the steady-state performance model has been reviewed and used to select the XCPC designs for detailed modeling, the full transient performance model will be introduced and discussed. The main focus will be on the heat gain from irradiance terms rather than the heat loss terms. The irradiance contributions in Equation B.1 from ISO 9806:2013 are displayed in Equations 8.4 and 8.5. Neglecting the wind-speed-dependent and transient terms leads to Equation 8.6

$$\begin{aligned}\frac{\dot{Q}}{A} &= \eta_{0,b}K_b(\theta_L,\theta_T)G_b + \eta_{0,b}K_{\theta d}G_d - c_6uG - a_1(T_m - T_{amb}) - a_2(T_m - T_{amb})^2 \\ &\quad - c_3u(T_m - T_{amb}) + c_4(E_L - \sigma T_{amb}^4) - c_5\frac{\mathrm{d}T_m}{\mathrm{d}t} \qquad (8.4)\end{aligned}$$

$$K_\theta = 1 - b_0(\frac{1}{\cos\theta} - 1) \qquad (8.5)$$

$$\frac{\dot{Q}}{A} = \eta_{0,b} K_b(\theta_L, \theta_T) G_b + \eta_{0,b} K_{\theta d} G_d - a_1(T_m - T_{amb}) - a_2(T_m - T_{amb})^2 \tag{8.6}$$

where θ is the angle of incidence between the collector normal and the solar position. The subscripts L and T denote the longitudinal and transverse directions of the collector with respect to the absorber tubes of the collector; hence, θ_L is the component of the angle of incidence in the longitudinal direction.

Note that by assuming: (1) $K_{\theta d} = K_b(\theta_L, \theta_T)$, (2) $G_{eff} = K(\theta_L, \theta_T)G$ (3) $\eta_{0,b} = \eta_0$, and (4) $\dot{Q} = \eta G_{eff} A$, one can recover Equation 8.1, although this shows that it is the effective irradiance (G_{eff}) rather than the irradiance (G or POAI) on a tilted surface that is to be used (see Equation 8.7),

$$\frac{\dot{Q}}{A} = \eta_{0,b} K_b(\theta_L, \theta_T) G_b + \eta_{0,b} K_{\theta d} G_d - a_1(T_m - T_{amb}) - a_2(T_m - T_{amb})^2 \tag{8.7a}$$

$$\frac{\dot{Q}}{A} = \eta_0 \left(G_{eff}\right) - a_1(T_m - T_{amb}) - a_2(T_m - T_{amb})^2 \tag{8.7b}$$

$$\frac{\frac{\dot{Q}}{A}}{G_{eff}} = \eta_0 - a_1 T_m^* - a_2 G_{eff} {T_m^*}^2 \tag{8.7c}$$

$$\eta = \eta_0 - a_1 T_m^* - a_2 G_{eff} {T_m^*}^2 \tag{8.7d}$$

$$T_m^* = \frac{T_m - T_{amb}}{G_{eff}} \tag{8.7e}$$

where K represents the optical performance regardless of the type of irradiance including the cosine effect. This results in defining G_{eff} as the effective irradiance after optics, whereas G is the irradiance on a POA. When defining K in this way, it would require STC testing facilities to measure the angular distribution of the sky radiance using an all-sky camera, which is expensive and not currently possible in a highly accurate way or to make laboratory measurements using a large-area collimated beam to measure differences in performance at different angles. The best available method is to use an all-sky camera and normalize the results by measured

DHI.

Accounting for both directions in the IAM, $K(\theta_L, \theta_T)$ is only required if the collector responds differently in those directions. K_θ (Equation 8.5) denotes the Incident Angle Modifier (IAM) function for both the beam and diffuse components of the irradiance G. If K_θ is required for both direction, then $K(\theta_L, \theta_T)$ is the product of the individual K_θ. The method used in the standard assumes superposition holds and that K is separable into the two directions. In some collectors, particularly those with concentration such as the XCPC, this does not always hold well enough to be an acceptable approximation (see Jiang and Winston 2014 [133]). The diffuse IAM K_d requires an *effective incident angle*, which is the equivalent (psuedo) direction of the diffuse light. Theunissen determined the effective incident angle of various diffuse components [52,149]. More recently, Strobach [150] determined a more general form for the effective incident angle of diffuse light that can be matched with several types of photovolataic collectors. For flate-plate collectors, b_0 defines the function K. For evacuated tube and concentrating collectors, another functional form may be required. ASHRAE 93 [144] provides more detail on the IAM functional form. Additionally there are other other works [151–154] on the topic. The optical efficiency $\eta_{0,b}$ is η_0 from Equation 8.1a. After accounting for the area projection weakening of the irradiance (cosine effect), tests have shown that collector efficiency varies with the angle of incidence. The IAM is a correction introduced to account for this secondary anisotropy of the collector, which is in addition to the primary source of anisotropy, the cosine effect. Although the IAM for the beam is a reasonable physical model, the simple fact is that the above method for determining the usable amount of diffuse light is not based in a descriptive physical model, rather it is a correction factor.

Equation 8.6 combines some aspects of a solar sky model into the solar collector performance equations by splitting the irradiance into separate contributions (diffuse and beam) and then quantifies the anisotropy of a particular STC by characterizing the coefficients that define K. Remember that simple sky models reduce the sky dome by aggregating irradiance and direction information into a few measures of irradiance; therefore, much of the anisotropy information of the sky dome is lost. Combining the loss of anisotropy information of the sky dome with the anisotropy of the collector results in an overall model that performs less than ideally. Pike [155] found the combined error of the sky model and the collector performance model for several collectors. Pike did not delineate or discuss the two errors in the detailed frame work of anisotropy concerning the sky and collector. Hess and Hanby 2014 [100] also pointed out the discrepency between modeled and actual results for STC. Hess and Hanby 2014 introduce the idea to use a radiance angular distribution model to better account for the diffuse sky anisotropy and collector anisotropy. Hess and Hanby 2014 used the Brunger 1993 Model. Performance modeling of the XCPC design would benefit from a more detailed angular distribution model.

It is interesting to note that the E–W XCPC optical efficiency η_0 given in Table 5 of Kim et al. 2013 have two different values corresponding to two different types of insolation conditions. Equation 8.4 provides for two ways the optical efficiency could be adjusted: (1) IAM corrections and (2) an adjustment because of wind speed. ISO 9806:2013 does not provide for an adjustment based on irradiance level or ratio between direct and diffuse. Kim et al. 2013 [132] does not discuss if either corrections in the standard were considered; however, Kim et al. 2013 does admit that diffuse light was present in the value meant to be determined solely from Direct Normal Irradiance (DNI). This means that Kim et al. 2013 has documented an additional limitation in the standard model or not properly measured the optical efficiency at least for the higher irradiance level. The higher optical efficiency values are neglected in modeling the E–W XCPC. This matter should be further investigated experimentally.

Another limitation of STC performance is that ISO 9806:2013 references ASHRAE 93-2010 (RA2014) [144] for detailed collector testing procedures. ASHRAE 93 references ASHRAE 109-1986 (RA2003) and was subsequently withdrawn in 2008. ASHRAE Standard 109 discusses STC with two-phase boiling heat transfer of the heat transfer fluid moving through the collector. Standard 109 does not discuss collectors with heat transfer fluid in the two-phase flow regime (pumped flow through the collector). The original paper by Spears [156] introduced the standard and noted that there were no known collectors under research or use that employed two-phase flow. To the author's knowledge, this has not changed in the last 23 years; however, there is one exception to the previous statement. In 1982, Murphy and May [157] looked at a direct configuration large-scale trough system with flow boiling. A flash valve was used to decrease the amount of liquid water that would need to be removed prior to the expander. There are some indications that large-scale trough manufacturers are now considering a direct configuration similar to what Murphy and May proposed and investigated. Delgado-Torres [30] models the boiling of the heat transfer fluid in the STC with no discussion about the lack of data to support the model. Assuming that the collector efficiency is unchanged with the correct assumption of the mean collector temperature and that Delgado-Torres made these assumptions correctly, the direct configuration with collector boiling is much more efficient than the indirect configuration. Characterizing the boiling/two-phase flow conditions in STC and the effects on performance are vital to determining the true merit of the direct configuration. STC performance under boiling/two-phase flow is greatly needed to experimentally validate any transitional collector design installed in a direct configuration.

8.5 Conclusion

In this chapter, the transitional class of solar thermal collectors was introduced. A discussion of the solar-thermal test standards was discussed and the challenge in obtaining accurate performance information. Particular focus is given to the importance of quantifying the anisotropy of the collector. The goal is to properly account for both the anisotropy of the sky and the collector to improve model accuracy. Several collectors were evaluated and the Winston XCPC designs are selected. While discussing the solar thermal testing standards, the need for several key improvements are discovered and the original work of this author:

1. Discussion of STC performance from a 3D perspective.
2. Communication of the limits where the STC performance equation accurately applies.
3. Superposition of the IAM is not always possible ($K(\theta_L, \theta_T) = K_{\theta_L} * K_{\theta_T}$), which results in the need for non-separable alternatives.
4. Sky model based on accurate quantification of the anisotropy of the sky vault, which will eliminate the need for an effective (pseudo) angle of incidence for the diffuse light.
5. Investigation if $\eta_0 = f(G)$.
6. STC performance under boiling heat transfer conditions.
7. Method to determine the mean temperature under boiling or flow boiling heat transfer.

Once implemented, it is likely that these improvements will lead to revisions of the various standards and/or for the adoption of new standards for STC testing and certification. Also discussed is the need for more information on the performance of the XCPC design and clarification of reported values. In the next chapter, adapting the solar thermal testing standards to properly model XCPC performance is discussed with the goal of eliminating as many limitations as possible without further experimentation.

9. CONSTRUCTION, TESTING, AND VERIFICATION OF A SOLAR-THERMAL SIMULATION FOR THE XCPC

In Chapters 6-8, the meteorological data, solar position, sky modeling, and STC performance were developed. To build an effective solar thermal simulation, adapting the testing standard to properly model the XCPC collector is needed. For the XCPC, several solar collector models will be developed, evaluated, and compared. The option with the "best" accuracy and lowest computational cost will be selected using an informal cost-benefit evaluation. During this process, several attempts were made yielding poor results initially. After perfecting the methods involved, success was achieved using the AWM and a new application of the IAM concept thereby altering the STC testing standards.

One of this author's early attempts to account for the limited view of the XCPC involved the 3DISM by Badescu which was shown in Chapter 7 to use a boundary condition choice that was not physically real. Appendix K contains a new sky model Modified 3DISM (M3DISM) that is analytically integrated including the wrong boundary condition and is evaluated against the Brunger Model, which included the same wrong boundary condition. The implementation of the Brunger Model with the incorrect boundary condition is documented in Appendix L. This includes a discussion on the fit coefficients, which do not cover all possible sky conditions. This limitation prevents applying the Brunger Model to the TMY datasets. Both of these early calculation methods are not recommend for general use because they contain a theoretical oversight and require more refinement.

The importance of making mistakes and learning from them is highlighted by the issue of the boundary conditions. This mistake led directly to researching early derivation methods of the ISM. Conducting this search resulted in many of the rediscoveries in Chapter 7. Another byproduct of this early mistake is a more refined calculation because the method of numerically integrating angular sky radiance distributions was derived twice. This second derivation is much more efficient numerically and conceptually more robust.

The remaining sections in this chapter discuss the refined methodology in its current state. There are a variety of possible improvements that may be undertaken in the future. Returning to the topic of modifying the STC testing standard for use with the XCPC, this will be accomplished in two steps, accounting for the unique IAM of the XCPC and secondly, identifying several sky model options used to determine the effective irradiance for the XCPC. Although this author independently created this methodology, it is in part based on advice received during personal communications with Christian Gueymard. Additionally, evidence was recently found (Hess 2014 [100]) showing support that this is not the first application of angular distribution models to STC to overcome some of the known limitations of the STC testing standard methods. The current work is the first known work to complete this for the XCPC.

9.1 Adapting the STC testing standard for the XCPC: Part 1 beam IAM

Because of the unique XCPC design, there are several complications that must be overcome to properly model the performance:

1. Decompose the angle of incidence into the transverse and longitudinal directions for use with the beam IAMs.
2. Recognize that the beam IAM can be applied to any radiance to determine the irradiance received by the collector, if the angular distribution of the radiance is known or can be reasonably approximated.

3. Identify the beam IAM function for the XCPC in transverse and longitudinal directions.

9.1.1 Decomposition of the angle of incidence

To properly use an IAM function K, the angle of incidence needs to be decomposed into the angle of incidence in the longitudinal and transverse directions of the collector given the collector mounting angles. The SPA documentation defines the solar location as shown in Figure 9.1. The SPA documentation also defines the collector rotation as shown in Figure 9.2. Figure 9.3 depicts the solar position in the collector normal reference frame. Figure 9.4 shows the definitions for the component angles of incidence. Equations 9.1–9.5 specify how the decomposition is performed. Appendix M documents the complete derivation of the equations. It is important to note that the current work is not the first or only work on the topic, for example see McIntire 1983 [152]. Table 9.1 lists the inputs and Table 9.2 lists the outputs of the function acceptanceangle.m used to perform the calculations.

$$x = \cos(\beta)\sin(\zeta)\cos(\Gamma - \gamma) - \sin(\beta)\cos(\zeta) \tag{9.1}$$

$$y = \sin(\zeta)\left[-\sin(\gamma)\sin(\Gamma) + \cos(\gamma)\sin(\Gamma)\right] \tag{9.2}$$

$$z = \sin(\beta)\sin(\zeta)\cos(\Gamma - \gamma) + \cos(\beta)\cos(\zeta) \tag{9.3}$$

$$\theta_{LR} = \arctan(\frac{y}{z}) \tag{9.4}$$

$$\theta_{TB} = \arctan(\frac{x}{z}) \tag{9.5}$$

During the derivation of the component angles of incidence, the angle of incidence equation was recovered and checked against the same equation in the original SPA code, which verifies the derivation methodology. A more complete verification

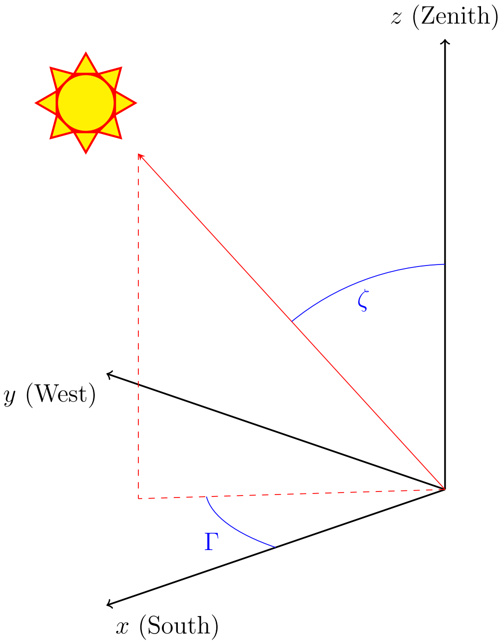

Figure 9.1: Solar direction as defined in the SPA documentation.

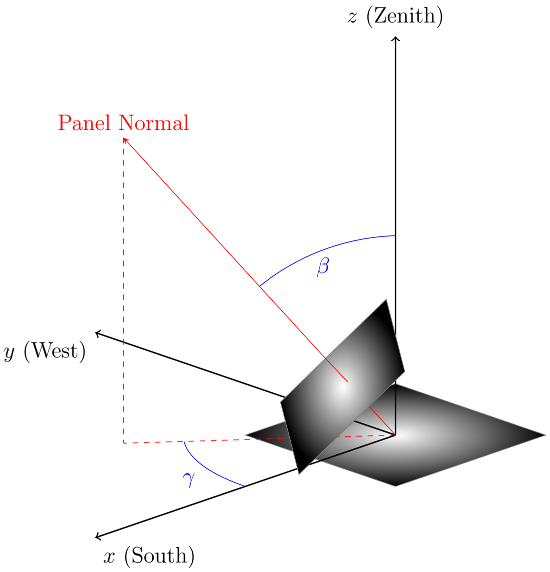

Figure 9.2: Collector mounting as defined in the SPA documentation.

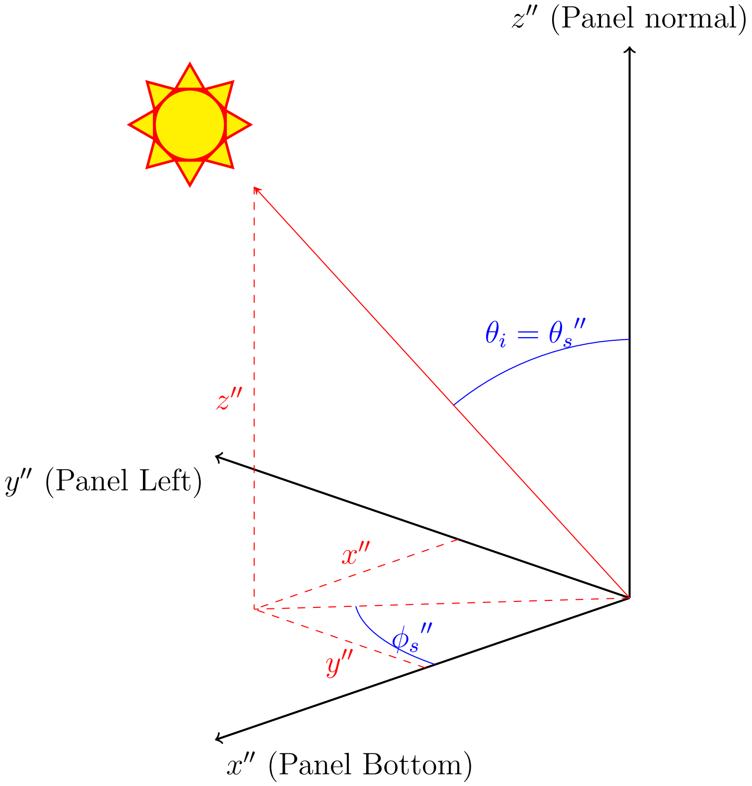

Figure 9.3: The solar direction and the angle of incidence.

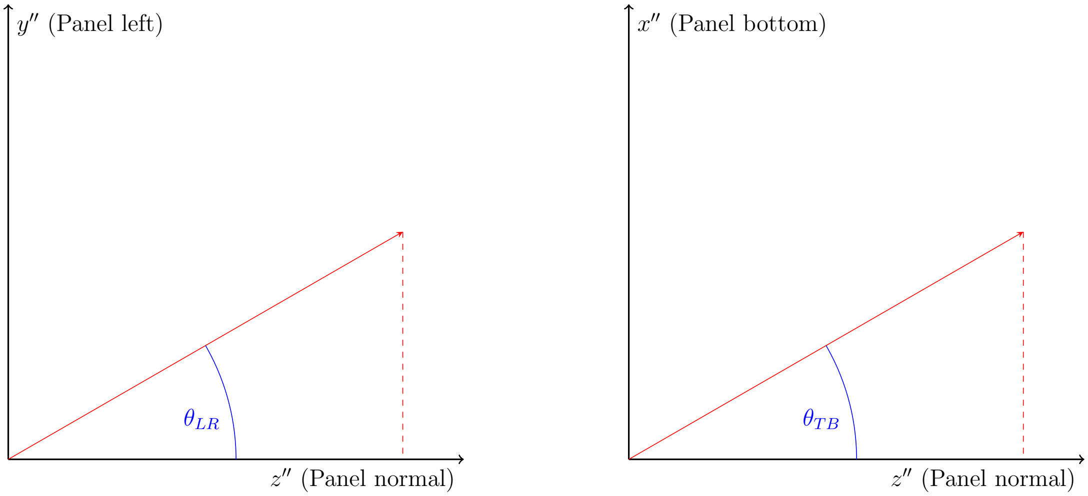

(a) Panel left-right angle of incidence.

(b) Panel top-bottom angle of incidence.

Figure 9.4: Angle of incidence components.

Table 9.1: Acceptance angle input from SPA calculation

Variable	SPA	This work	Description (Units)
Coordinates			
zenith	I	ζ	Topocentric zenith angle (°)
azimuth_astro	Γ	Γ	Topocentric azimuth angle (positive westward from south) (°)
Collector mounting angles			
slope	ω	β	Surface slope of the collector from horizontal (°)
azm_rotation	γ	γ	Surface azimuth rotation of the collector (positive westward from south) (°)

Table 9.2: Accpetance angle output data

Variable	Description (Units)
Sun angle information	
θ_{LR}	Angle of incidence in the panel left–right orientation. In the case of the E–W XCPC, the longitudinal direction. (°)
θ_{TB}	Angle of incidence in the panel top–bottom orientation. In the case of the E–W XCPC, the transverse direction. (°)
"North" is the top edge of the panel and "south" is the bottom edge of the panel in the unrotated coordinates	
Intermediate output values for validation testing.	
x, y, z	Components of the unit vector pointing to the sun from the double-rotated panel location.

method is desired. One could build a physical device that allows a plane to be double rotated to a prescribed mounting, measure the three incidence angles of interest, and check them against the calculated values. Although this option would be quite thorough, it requires resources not available to the author. There are obvious self-consistency checks, such as the magnitude of the x, y, z component vectors must combine to match the hypotenuse of the incidence vector. There is an additional test that can be reasonably performed. By definition, the incidence angle is positive, i.e., $|\theta_x| \leq \theta_i$ for each component. This should be true of all possible angles. Figure 9.5 shows the full results of this validation step using TMY3 data for Eastwood Field, College Station, Texas.

Figure 9.5(a) shows that the test fails for a small potion of results for both of the angle of incidence components. Figure 9.5(b) shows that test results are perfectly correlated (i.e., if the test results are negative for one of the components the results for the other component are also negative). Figure 9.5(c) indicates that the error is happening for $\theta_{LR} \approx \pm 90°$. Figure 9.5(e) shows very similar results for θ_{TB}. Note that $\theta_{TB} \approx -90°$ only. Figure 9.5(d) shows that the error is quite small for θ_{LR}; however, Figure 9.5(f) shows that the error can be rather large for θ_{TB}. This error is likely the result of numerical rounding in conjunction with the use of trigonometric functions, in particular the tangent function. This error never happens for $\theta_i < 90°$, which is the region of interest; therefore, it is not an issue for the current application. Nonetheless, the reader should be warned that additional care in numerical analysis must be taken if use outside this range is desired. The error can further be avoided by limiting results to $\theta_i < 88°$. This is complemented nicely by the fact that the index of refraction for glass causes attenuation problems at angles near 90° for a glass-covered STC. For $\theta_i > 90°$, the sun is pointing at the bottom of the STC or worse yet, below the horizon for some conditions. When avoiding the worst errors

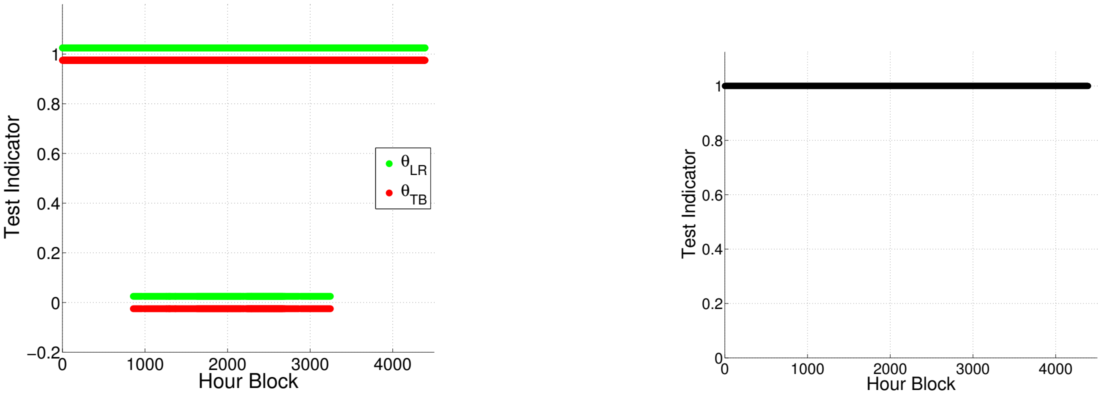

(a) Incidence magnitude test. (Data skewed to avoid overlap)

(b) Correlation of the incidence magnitude test.

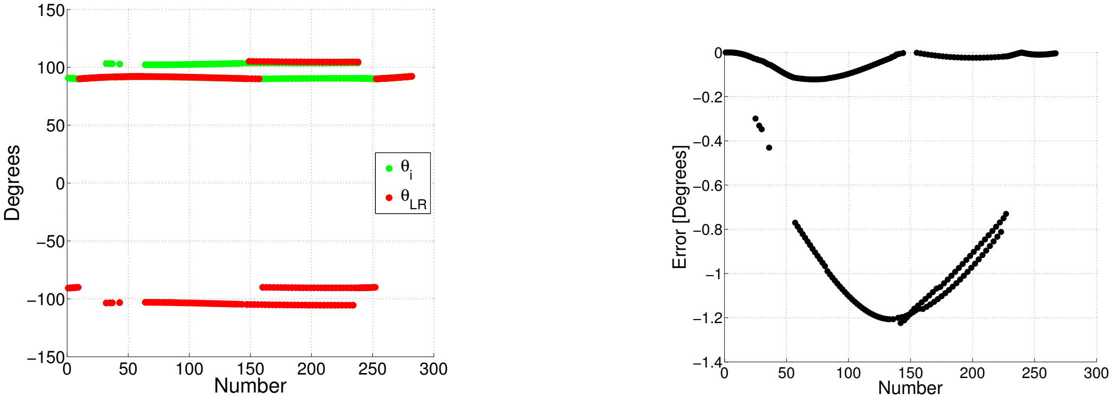

(c) Left–right incidence location of error.

(d) Left–right incidence error.

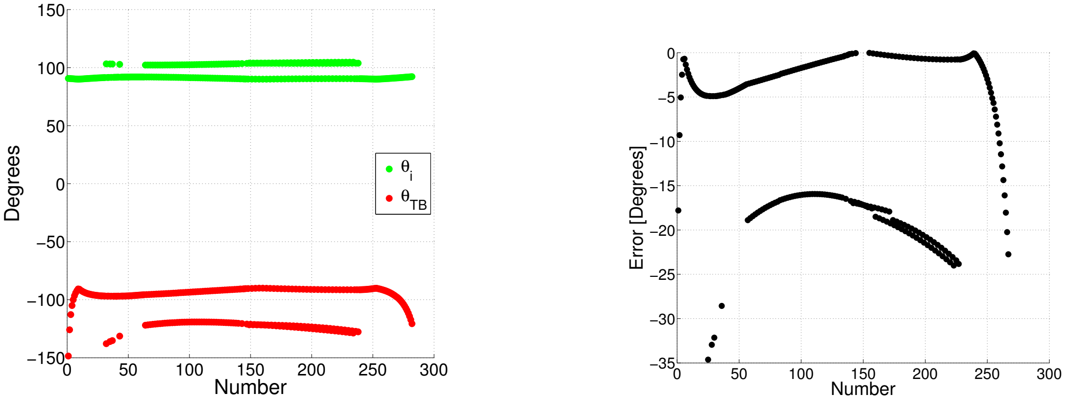

(e) Top–bottom incidence location of error.

(f) Top–bottom incidence error.

Figure 9.5: Angle of incidence decomposition validation.

with θ_{TB}, another favorable aspect is that in the case of the E–W XCPC, the θ_{TB} values of interest are well below 90°; therefore, this error is of little concern.

In this subsection, a method for decomposing the angle of incidence was presented and verified. Although an error in the calculation was found, it is outside the region of interest ($\theta_i < 90°$) for the current solar thermal applications. This method is well suited for the purpose of determining at which sun angles the direct normal irradiance (DNI) should be neglected.

9.1.2 Angle decomposition generalized

In reality, the set of mathematical rotations and angular decomposition described in the previous section can be used in general to determine angles between vectors and the components of those angles. This means that (β, Γ) defines the direction of the surface of interest and (ζ, γ) define the direction of interest as shown in Figure 9.6. The algorithm then determines the angle (and component angles) between them. This methodology can also be used to determine the angle of incidence (and components) of the sky radiance (θ_{secn}) coming from a sky element with respect to the POA i.e., (β, Γ)) and (ζ_{se}, γ_{se}) (see Figure 9.6). This is of great importance when attempting to account for the LFOV of a collector with concentration. This will be discussed more in later sections of this chapter.

9.1.3 IAM function for the XCPC

Now that the component angles of incidence have been successfully determined, an IAM function must be identified. Because the E–W XCPC collector design has a slight concentration ratio (1.82), the standard functional form of the IAM (K_θ) is not appropriate. After reviewing Figure 17 of Kim et al. 2013 [132], a simple step function with a value of 1 between the acceptance angle limits in the transverse direction (±32.5° for E–W and ±55° for N–S Table 5 of Kim et al. 2013) will capture

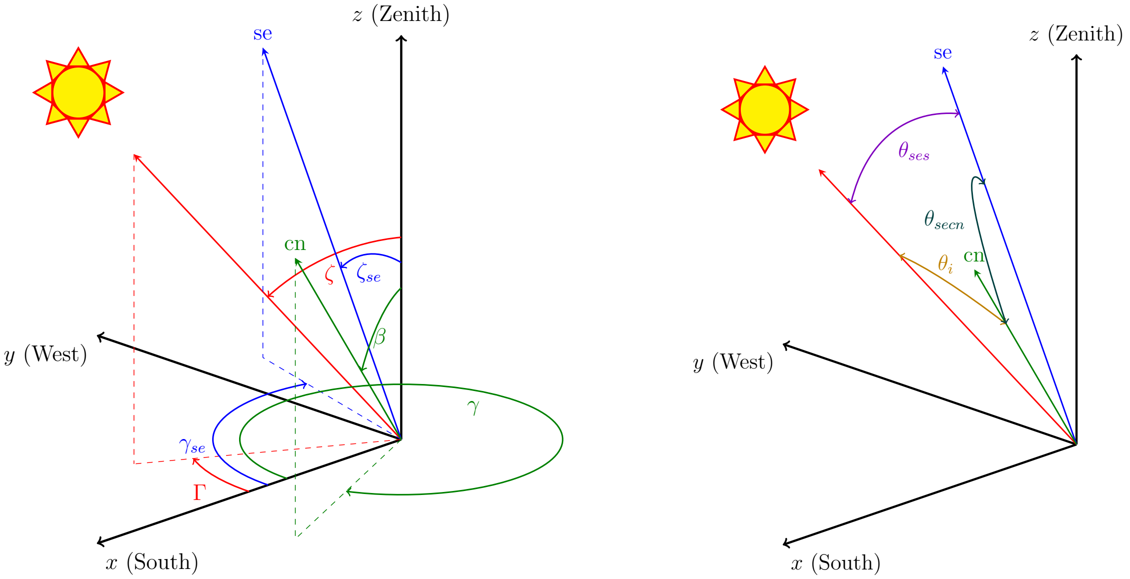

(a) Angles used to define the sun (s), the sky element (se), and the collector normal (cn) directions.

(b) Angles between the sun (s), the sky element (se) and the collector normal (cn) directions.

Figure 9.6: Angles needed in calculation of sky models. Note the choice of coordinate system can vary from work to work.

the functionality of the collector. Limiting the longitudinal direction to ±88° will account for the index of refraction of the glass cover and avoid the region where the angle decomposition calculation fails to be accurate.

There are two important things to note about the glass cover. First, Kim et al. 2013 discusses a cover for the collector and does not specifically mention a glass cover. In Kim et al. 2013, photos of the collector are depicted without the cover present. Secondly, the index of refraction of a glass cover may not be best represented by a step function. The step function assumption is chosen here for convenience. The IAM step function defined here does not include the area projection or cosine of the angle of incidence. This is a direct deviation from the STC testing standard method which includes both the cosine law and the collector response together in the IAM. The differences are a matter of definition and organization because both collector response and cosine law response are include in each method. Figure 9.7 shows the angle of acceptance step functions in both the longitudinal and transverse directions without the cosine. Subfigure 9.7(c) shows the N–S XCPC assumed form and the approximate outer-bound (+) and inner-bound (×) of the data from Kim et al. 2013 for comparison.

The transverse and longitudinal IAM are simplifications of the true collector response. This is a valid choice because the true attenuation is quite steep, making the step function a good approximation. For several reasons, future testing of the XCPC designs should include more testing of the IAM in both the transverse and longitudinal directions. First, the effects of the glass cover have been all but neglected for the longitudinal direction. Second, Figure 17 from Kim et al. 2013 [132] and accompanying discussion show that there is a potential alignment issue with the inner absorber, outer absorber, and the reflector design or an issue with reflector manufacturing precision. The desired outcome would be a smoother, symmetric, and more accurate response. This lack of information was recently reinforced when it was found that the N–S XCPC collector was tested by the SRCC. (Note: This can be found by searching for Artic Solar, Emperor, LH-3-2M which is a N–S XCPC variant in the SRCC directory.) It was found that the diffuse IAM was set to zero and the transverse IAM was neglected only providing the longitudinal IAM. This highlights the following facts:

1. The XCPC performance is not well quantified by the current testing standards.
2. Reinforces the need for the currently proposed changes.
3. The longitudinal IAM for the Emperor collector shows that including the area projection with the step function for the modeled IAM is a good engineering judgment.

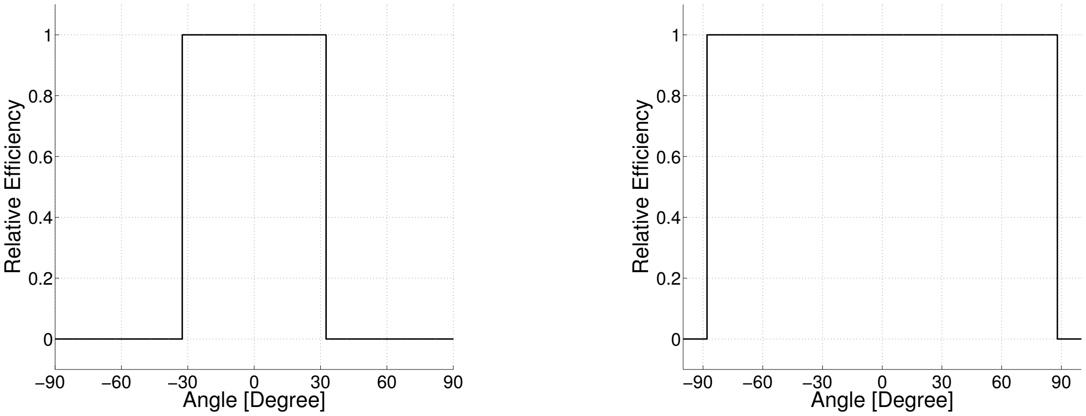

(a) E–W Transverse IAM.

(b) Longitudinal IAM.

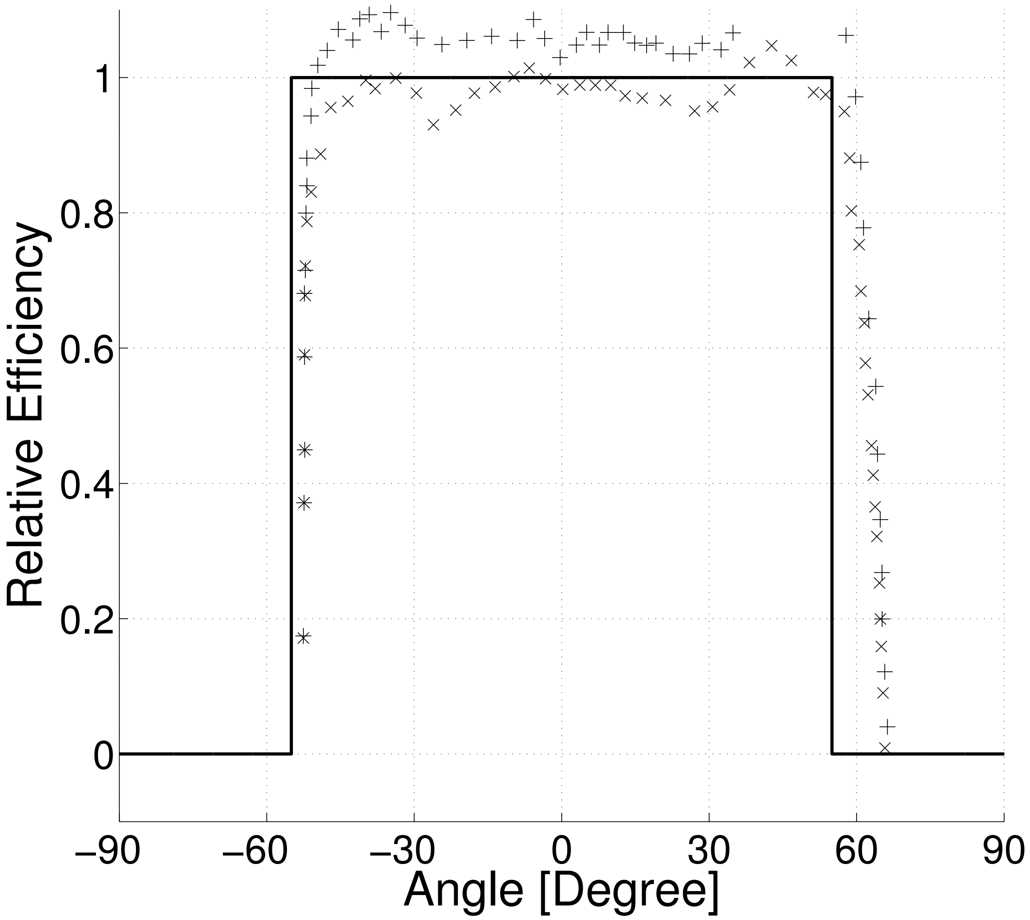

(c) N–S Transverse IAM with data, outer-bound (+) and inner-bound (×).

Figure 9.7: XCPC collector IAM functions.

This 2016 SRCC test of a N–S XCPC variant fails to provide the necessary information to properly model performance. Lun Jiang of the Winston research group noted that a proposed transverse IAM for the Emperor collector was in the process of being published by the group.

Building on the discussion in Chapter 8, the assumption of the IAM function being the superposition of the individual directions has limitations as noted in McIntire 1983 [151]. Specifically, for the XCPC designs, Figure 2 of Jiang and Winston 2014 [133] shows the non-separability. This means that updating the IAM function for the XCPC is of great importance for improving the ability to accurately model XCPC performance, despite being left as future work. Given the limitations of empirically based angular distribution models—namely that they are correct on average (typically annual average)—it is challenging to use angular distribution models to quantify the IAM function. Instead, it is best to use the distribution models to recover angular information only when modeling performance on a monthly – and preferably annual – basis. Other methods should be developed to determine the IAM function, such as the methods used to make angular distribution models (i.e., the all-sky imagery normalized by DHI). Obviously, solving the angular distribution measurement issue is the most comprehensive solution to the problem because it would resolve the accuracy issues with all sky imaging.

9.2 Adapting the STC testing standard for the XCPC: Part 2 sky model general discussion

9.2.1 Possibility of one IAM function

The STC testing standards allow for treatment of the direct, diffuse-sky, and ground-reflected radiance with different IAM functions. In reality, these three components of radiance have some spectral differences. Neglecting these spectral differences, and the angular differences in the spectral response of the STC, allows for the treatment of all three components of radiance with the same IAM function K. To complete this simplification, the angular distribution must be known, approximated, or assumed for each component of radiance. (Note: These components are normally thought to have been received as surface irradiance. This author is specifically choosing to think of them in the modeled sense as coming from certain directions away from the receiving surface while they are still radiance values.)

9.2.2 *Kim et al. 2013 method of concentration ratio adjustment*

Because of the unique XCPC design, one additional complication is that the standard simplified sky model, theoretically speaking, cannot properly treat the diffuse IAM for both the diffuse and reflected components. Equation 14 of Kim et al. 2013 discounts the diffuse irradiance by dividing by the concentration ratio C. Kim et al. 2013 further discusses that this correction is “often appropriate” for collectors with concentration ratios in the range of $1 < C \leq 2$. The discussion of this method comes without citation or any scientific evidence as to the accuracy of this correction method. This means that Kim 2013 is suggesting that $K = \frac{1}{C}$ for the diffuse-sky and ground-reflected components.

9.2.3 *Adapting the sky model used in the STC testing standard*

The STC testing standard sky model is the ISM. Chapter 7 showed that there were many sky models that performed better for a wider range of sky conditions than the ISM. For these reasons, a more general statement of the STC sky model is sought and given in Equations 9.6–9.8:

$$G_{eff} = \underbrace{I_{b,n} R_b(K)}_{\text{Direct}} + \underbrace{I_{d,h} R_d(K)}_{\text{Diffuse}} + \underbrace{\rho I_{t,h} R_r(K(\theta_L, \theta_T))}_{\text{Reflected}} \tag{9.6}$$

$$R_b(K) = \cos\theta_i K(\theta_L, \theta_T) \tag{9.7}$$

$$K(\theta_L, \theta_T) = K_L(\theta_L) K_T(\theta_T) \tag{9.8}$$

where $K_L(\theta_L)$ and $K_T(\theta_T)$ are from Section 9.1.3. $K(\theta_L, \theta_T)$, $R_d(K)$, and $R_r(K)$ will be defined in Section 9.3. $R_d(K)$ and $R_r(K)$ depend on the sky model. The remaining variables are defined the same as in Equation 7.1. Equation 9.6 is a simplified version of Equation 8.6.

9.3 Adapting the STC standard for the XCPC: Part 3 four alternatives and the corrsponding transposition factors

The main goal of this section is to develop and present four options in the following subsections:

1. Isotropic Sky Model with concentration ratio adjustment.
2. Perez 1990 Model with concentration ratio adjustment.
3. ISM with integration limit adjustment.
4. AWM with integration limit adjustment.

These options all fit into a general format given in Equations 9.9–9.12:

$$G_{eff} = \underbrace{I_{b,n} \cos\theta_i K(\theta_L, \theta_T)}_{\text{Beam}} + \underbrace{I_{d,h} R_d(K)}_{\text{Diffuse}} + \underbrace{\rho I_{t,h} R_r(K)}_{\text{Reflected}} \tag{9.9}$$

$$K(\theta_L, \theta_T) = \begin{cases} 1 & \text{if } |\theta_T| \leq 32.5^\circ \wedge |\theta_L| \leq 88^\circ \text{, E–W XCPC} \\ 0 & \text{otherwise} \end{cases} \tag{9.10}$$

$$\eta = \eta_0 - a_1 T_m^* - a_2 G_{eff} {T_m^*}^2 \tag{9.11}$$

$$T_m^* = \frac{T_m - T_{amb}}{G_{eff}} \tag{9.12}$$

The methods to calculate the diffuse ($R_d(K)$) and reflected ($R_r(K)$) transposition factors (correction factors) for the XCPC will be determined in each of the four subsections. The alternatives developed here will be used in the next section to compare their performance, and select the model that “best” fits the current application.

9.3.1 Isotropic Sky Model with concentration ratio adjustment

Given that Kim et al. defined a rule-of-thumb method to account for the concentration/LFOV of the XCPC, the simplest place to start is to apply this method to the given methods in the STC testing standard. The diffuse and reflected transposition factors for this case are given as Equations 9.13–9.16:

$$R_d(K) = \left(\frac{1+\cos\beta}{2}\right) K \tag{9.13}$$

$$R_r(K) = \left(\frac{1-\cos\beta}{2}\right) K \tag{9.14}$$

$$K = \frac{1}{C} \tag{9.15}$$

$$C = 1.82 \text{ for the E–W XCPC} \tag{9.16}$$

9.3.2 Perez 1990 with concentration ratio adjustment

Given that the Perez 1990 model is known to perform quite well, it is natural to combine the Kim et al. 2013 rule of thumb with the Perez 1990 model for comparison purposes. Of course, the tradition of assuming isotropic reflected irradiance is maintained. The diffuse and reflected transposition factors for this case are given as Equations 9.17–9.20:

$$R_d(K) = \left[(1-F_1)\left(\frac{1+\cos\beta}{2}\right) + \left(\frac{a}{b}\right) F_1 + F_2 \sin\beta\right] K\text{, see Appendix F} \tag{9.17}$$

$$R_r(K) = \left(\frac{1-\cos\beta}{2}\right) K \tag{9.18}$$

$$K = \frac{1}{C} \tag{9.19}$$

$$C = 1.82 \text{ for the E–W XCPC} \tag{9.20}$$

9.3.3 ISM with integration limit adjustment

Using the ISM value of $\frac{1}{\pi}$ for I_d and setting up the integration yields the diffuse and reflected transposition factors given in Equations 9.21–9.22:

$$R_d(K) = \int_{\text{Hemisphere of the sky } = \, 2\pi \text{ sr.}} \frac{1}{\pi} K(\theta_{secnL}, \theta_{secnT}) \cos\theta_{secn} d\Omega \tag{9.21}$$

$$R_r(K) = \int_{\text{Ground within hemisphere FOV of POA}} \frac{1}{\pi} K(\theta_{gecn_L}, \theta_{gecn_T}) \cos\theta_{gecn} d\Omega \tag{9.22}$$

9.3.4 AWM with integration limit adjustment

Using the Perez et al. 1993 defined lv which is analogous to I_d for the diffuse transposition factor and the ISM value of I_d for the reflected transposition factor results in the diffuse and reflected transposition factors given as Equations 9.24–9.25:

$$\begin{aligned} lv(\zeta_{se}, \theta_{ses}) = & \left[1 + a \cdot \exp\left(\frac{b}{\cos\zeta_{se}}\right)\right] \\ & \left[1 + c \cdot \exp(d \cdot \theta_{ses}) + e \cdot \cos^2\theta_{ses}\right] \text{, See Appendix G} \end{aligned} \tag{9.23}$$

$$R_d(K) = \left[\frac{\int_{\text{Hemisphere of the sky } = \, 2\pi \text{ sr.}} [lv(\zeta_{se}, \theta_{ses}) K(\theta_{secnL}, \theta_{secnT}) \cos\theta_{secn}] d\Omega}{\int_{\text{Hemisphere of the sky } = \, 2\pi \text{ sr.}} [lv(\zeta_{se}, \theta_{ses}) \cos\zeta_{se}] d\Omega}\right] \tag{9.24}$$

$$R_r(K) = \int_{\text{Ground within hemisphere FOV of POA}} \frac{1}{\pi} K(\theta_{gecn_L}, \theta_{gecn_T}) \cos\theta_{gecn} d\Omega \tag{9.25}$$

9.4 Sky model verification, comparison, and selection within a STC simulation for the XCPC

The main goal of this section is to compare the four alternatives developed in the previous section, and select the model that "best" fits the current application. These steps are accomplished in the following subsections:

1. Simulation overview
2. Transposition factor comparison (R_d and R_r)
3. Effective annual irradiance: flat plate compared to both XCPC designs modeled with alternatives for several locations
4. Effective Annual irradiance: E–W XCPC versus N–S XCPC using the AWM with integration.

Ideally, one would like to directly measure the thermal performance of the XCPC, and the solar conditions during the test. This experimental information would be used to *operationally validate* the predicted performance of the STC simulation; however, operational validation is not possible for two primary reasons: (1) lack of access to the XCPC collector designs from Kim et al. 2013 and (2) lack of research funding to build the necessary equipment and testing facilities. Despite these limitations, all is not lost. There are several self-consistency checks (*algorithm verification*) that can be performed, which will build confidence that the algorithm and conceptual model perform as intended, i.e., to accurately capture the diurnal nature of solar radiation, how it varies during a typical year, and those impacts on collector performance. Performing this algorithm verification for each of the alternatives under consideration will also function as a means to compare their performance and make a selection based on that performance (namely theoretical fidelity and computational cost).

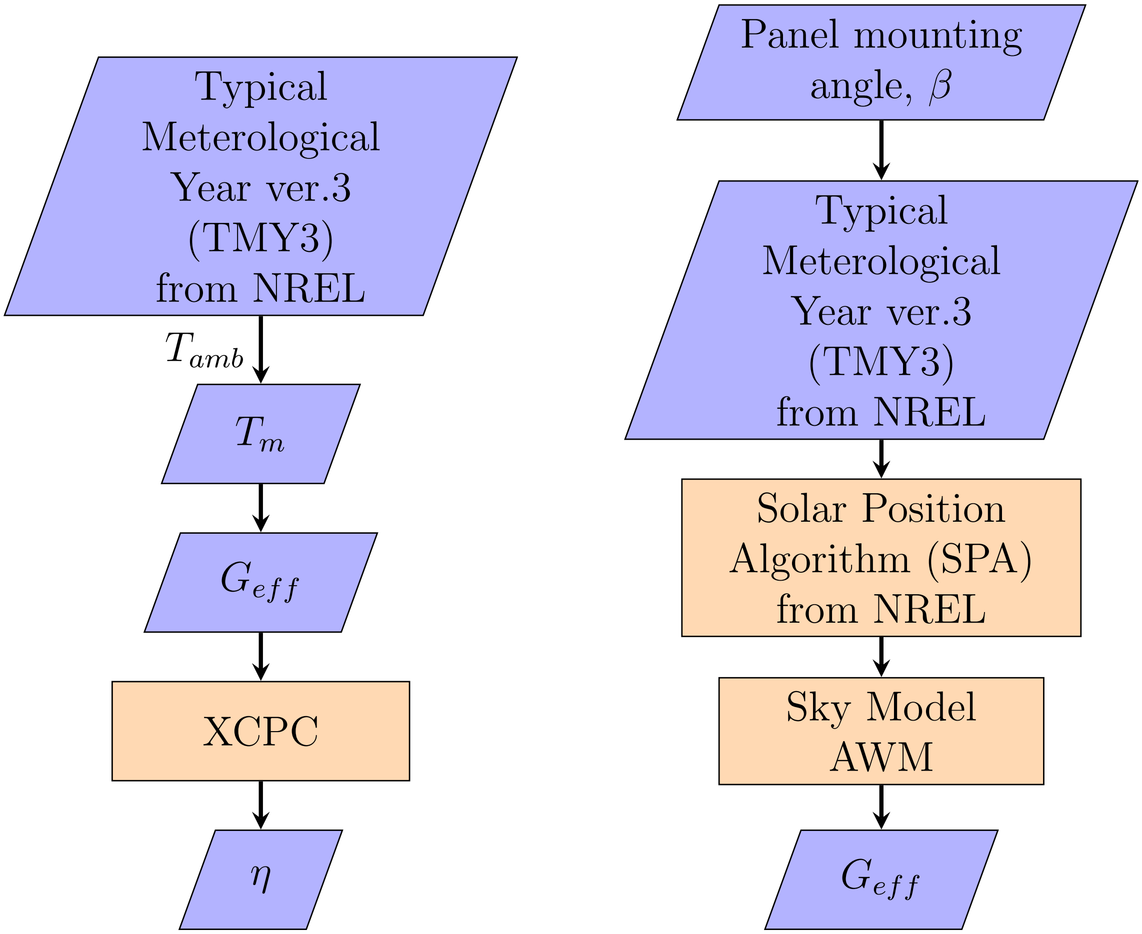

(a) XCPC model.

(b) Irradiance model.

Figure 9.8: Solar model—two major parts.

9.4.1 Simulation overview

The STC performance models and simulation for the XCPC are shown in Figures 9.8 and 9.9. The simulation will enable a greater understanding of XCPC performance for various use conditions.

9.4.2 Transposition factor comparisons

In Section 9.3, several models for the XCPC designs were introduced. In this section they will be compared using the R_d and R_r transposition factors as a basis

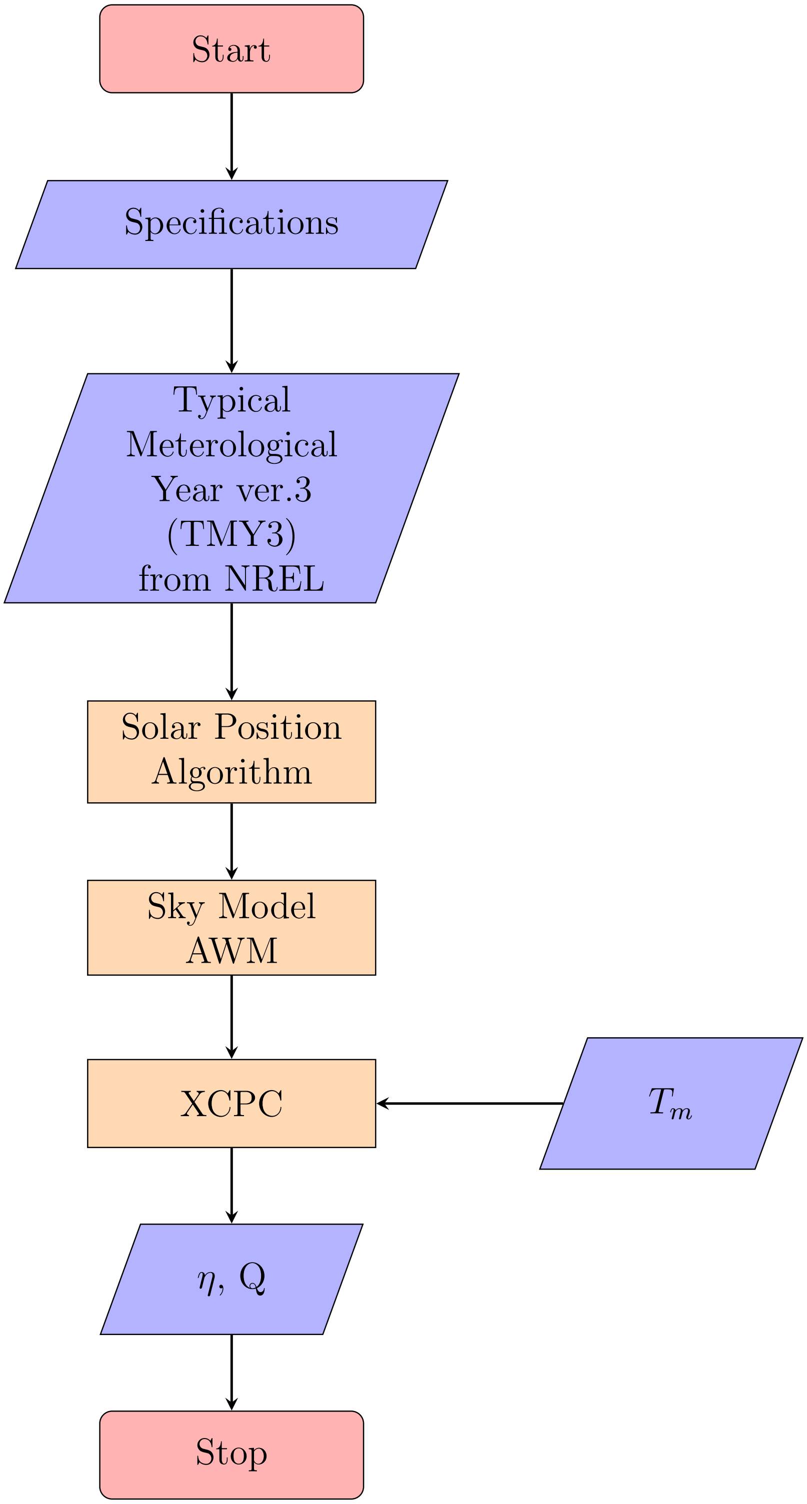

Figure 9.9: Solar model complete.

of comparison.

Starting with the reflected transposition factor R_r, Figures 9.10(a) and 9.10(b), show the results. Four points about the two figures follow:

1. There is only a small difference for the N–S XCPC between $K = \frac{1}{C}$ and the integration method. The E–W XCPC has a higher concentration ratio, which results in a more substantial difference. This is consistent with the fact that the respective concentration ratios are $C = 1.18$ and $C = 1.82$.
2. The N–S XCPC has a half angle of acceptance of 88° meaning the ground comes into view quite quickly when varying the slope, which is why the reflected transposition factor is smoother for the N–S XCPC using the integration method.
3. Using the same logic, this explains why the response for the E–W XCPC is delayed until $57.5^\circ = 90 - 32.5$.
4. Given both figures, it appears that for the reflected transposition factor, the $K = \frac{1}{C}$ method may be a good approximation for slopes very near vertical.

Selecting the isotropic assumption with the integration method provides the 'best' option for several reasons: (1) The isotropic assumption is the best possible one without site specific information. (2) The integration method provides a calculation based in physics. (3) The integration method also provides more conservative results i.e., always has a lower R_r value.

Now the diffuse transposition factor R_d is discussed. Two of the four models yield R_d values for each data point (hourly time block) in the TMY dataset, meaning for those models R_d is dependent on time and location; therefore, an energy-weighted

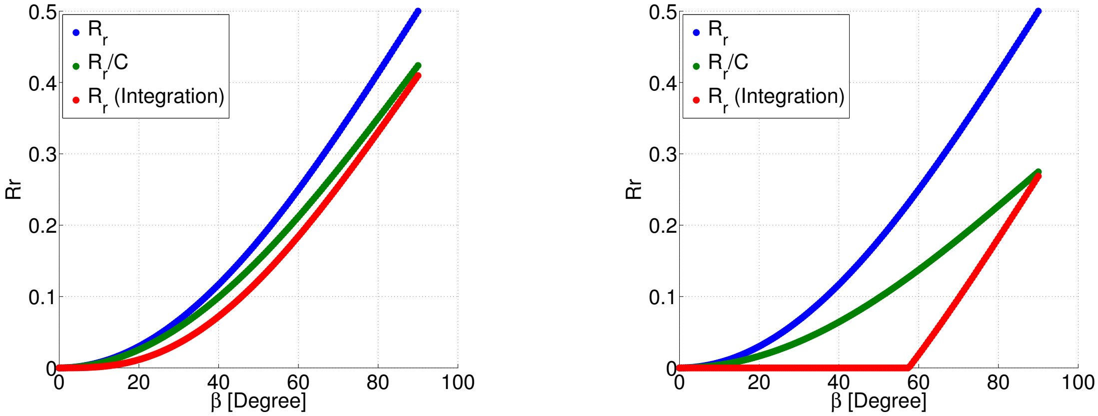

(a) Reflected transposition factor comparison for the N–S XCPC.

(b) Reflected transposition factor comparison for the E–W XCPC.

Figure 9.10: Comparison of reflected transposition factors based on the isotropic assumption.

average R_d ($\overline{R_d}$) is defined in Equation 9.26.

$$\overline{R_d} = \frac{\sum \vec{R_d} \cdot \vec{I_{d,h}}}{\sum \vec{I_{d,h}}} \tag{9.26}$$

The above equation provides a means to compare the R_d of the models. Figures 9.11 and 9.12 display the results for the E–W XCPC and N–S XCPC, respectively. The figures clearly show that the AWM with integration method has a unique functional result that better accounts for the LFOV of the XCPC. This is particularly true for the E–W XCPC collector, which has the most LFOV in the direction of tilt. Although the integration method provides substantially higher computational cost, it provides the best available model based on physics. The Perez/C method provides a close second yielding some accuracy to lower computational cost. This work will proceed using R_d defined by the AWM with integration and only revert to the Perez/C method if computational costs are found to be prohibitive.

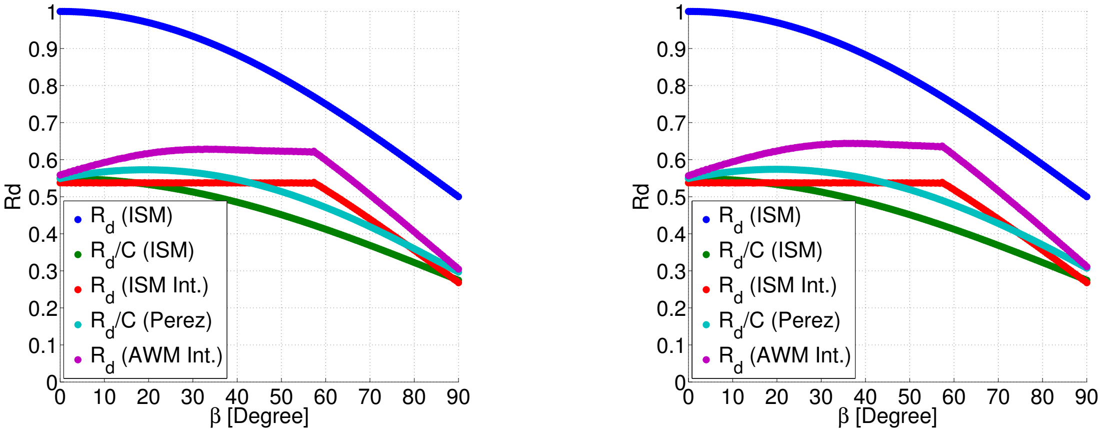

(a) Key West, Florida.

(b) College Station, Texas.

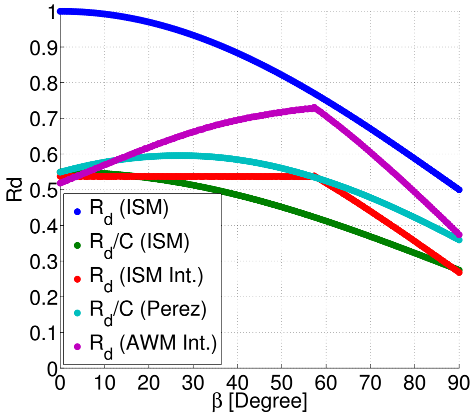

(c) Merced, California.

Figure 9.11: Comparison of R_d: ISM for a flate-plate and E–W XCPC using the ISM/C, Perez/C, ISM integration method, and AWM with integration for three locations in the United States.

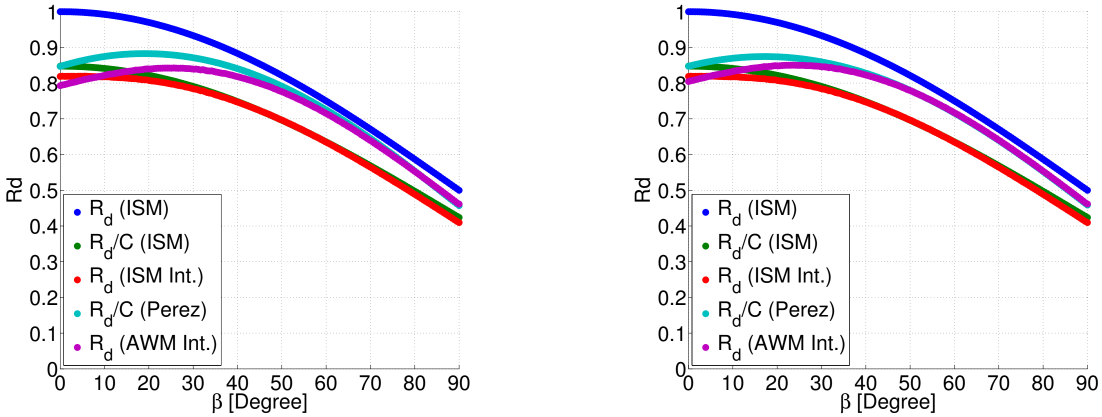

(a) Key West, Florida.

(b) College Station, Texas.

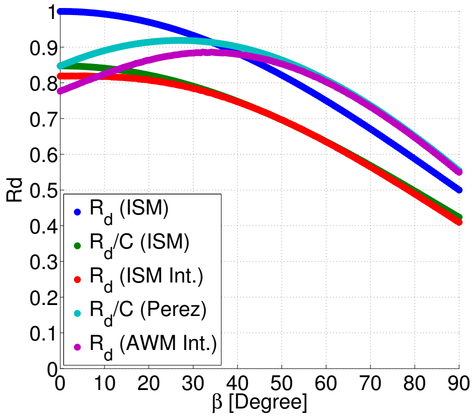

(c) Merced, California.

Figure 9.12: Comparison of R_d: ISM for a flate-plate and N–S XCPC using the ISM/C, Perez/C, ISM integration method, and AWM with integration for three locations in the United States.

9.4.3 Discussion of performance and conformation of final model selection

Now that a detailed look at how the various options for correction factors perform, a review of overall performance is undertaken to confirm that AWM with integration is the best possible choice given the limited information namely, the lack of experimental validation. Figures 9.13–9.15 display the results for both the E–W XCPC and N–S XCPC for Key West, FL, College Station, TX, and Merced, CA. The figures show that the AWM yeilds similar annual energy yield vs. mounting angle results for all three types of climates and both versions of the XCPC. By physical reasoning, the AWM with integration is superior; therefore, it is the preferred choice. Note that Key West and College Station both tend to have more moisture content in the air causing solar conditions to be partly cloudy or overcast more frequently than the Merced location. This results in the over prediction of irradiance when using the Perez/C method during more overcast conditions. This happens because the $1/C$ correction is not angle dependent whereas the AWM with integration method is.

9.5 Comparison of the E–W XCPC and N–S XCPC

Now that a solar simulation has been created for both versions of the XCPC, a more detailed comparison of performance of the two versions is possible. In this section, the goal is to highlight the differences in performance of collector designs with the end goal of making a selection, if possible, when enough performance characteristics have been covered. Figure 9.16 shows the performance data for both designs at the three selected locations using the AWM with integration method only. The fourth location will be discussed shortly. In direct opposition to the thermal results for the two XCPC designs discussed in Section 8.3, the N–S XCPC has better overall acceptance of irradiance on an annual basis for the locations considered. This is a direct result of the concentration ratio of the two designs. Looking deeper at the per-

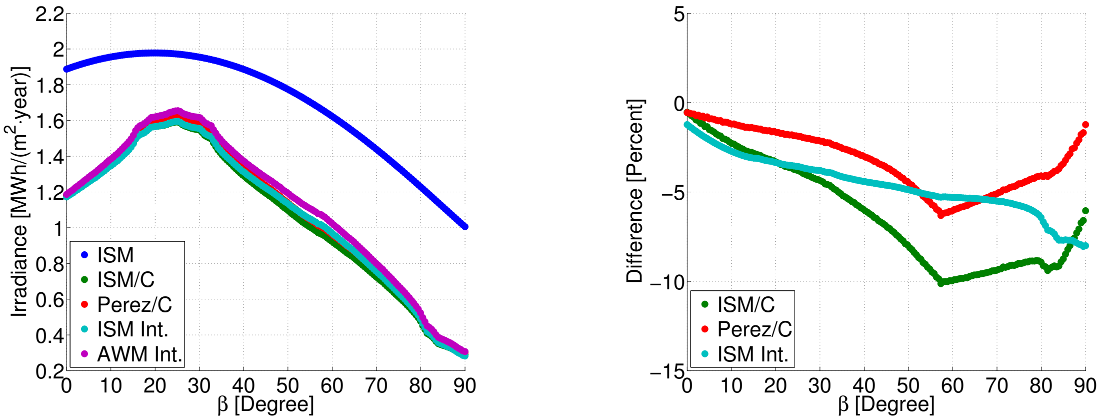

(a) E–W XCPC: Comparison of total annual irradiance: ISM for a flate-plate, ISM/C, Perez/C, ISM integration method, and AWM with integration.

(b) E–W XCPC: Percent Different of ISM/C, Perez/C, and ISM integration method using the AWM with integration as reference.

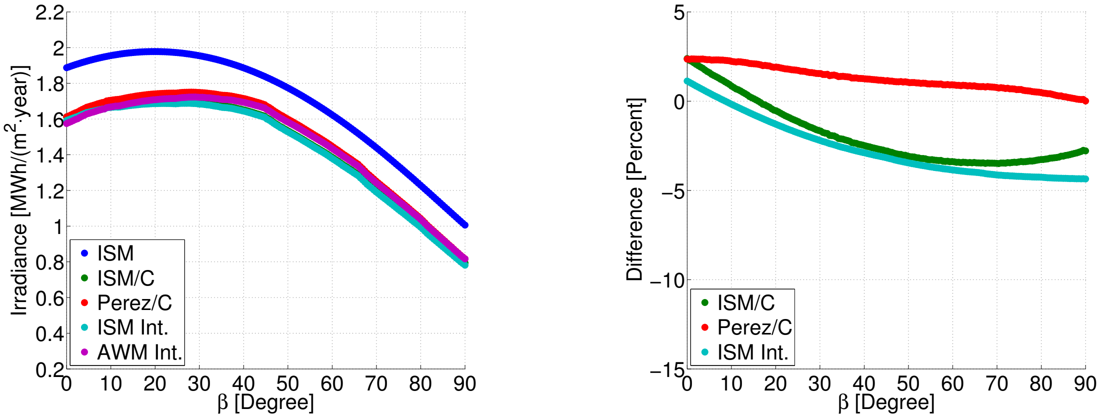

(c) N–S XCPC: Comparison of total annual irradiance: ISM for a flate-plate, ISM/C, Perez/C, ISM integration method, and AWM with integration.

(d) N–S XCPC: Percent Different of ISM/C, Perez/C, and ISM integration method using the AWM with integration as reference.

Figure 9.13: Annual performance at Key West, FL.

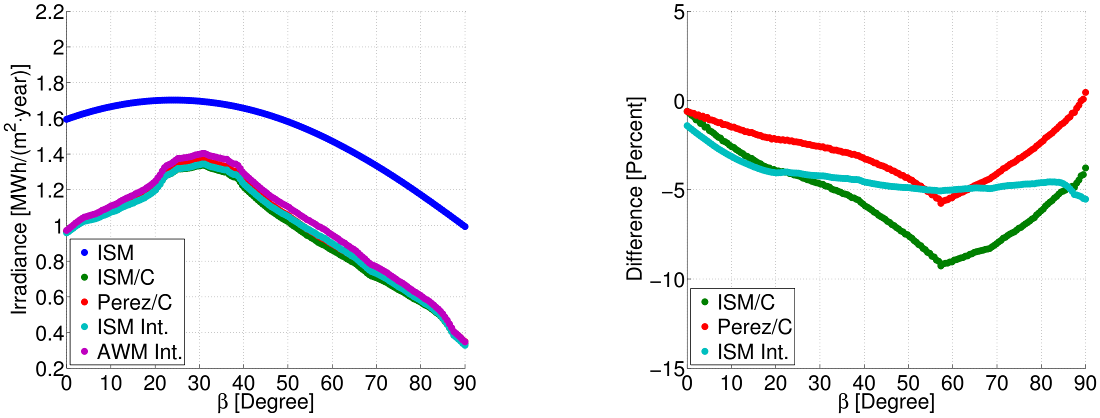

(a) E–W XCPC: Comparison of total annual irradiance: ISM for a flate-plate, ISM/C, Perez/C, ISM integration method, and AWM with integration.

(b) E–W XCPC: Percent Different of ISM/C, Perez/C, and ISM integration method using the AWM with integration as reference.

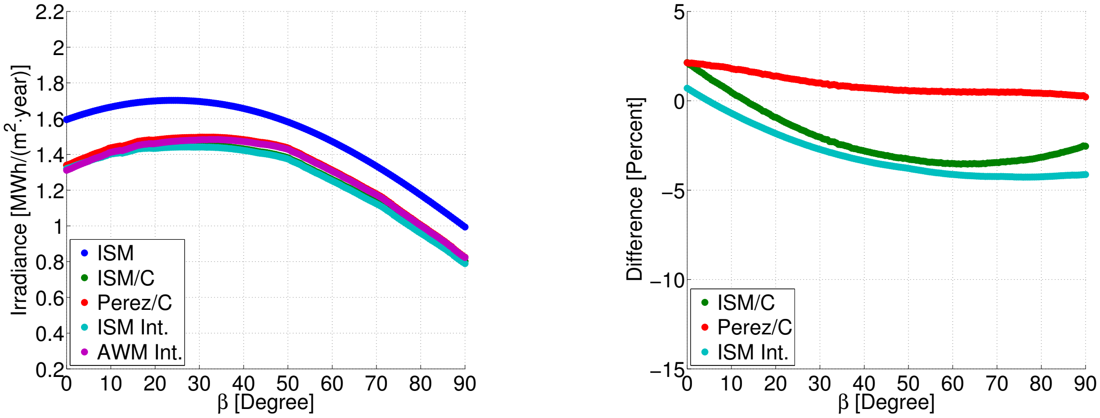

(c) N–S XCPC: Comparison of total annual irradiance: ISM for a flate-plate, ISM/C, Perez/C, ISM integration method, and AWM with integration.

(d) N–S XCPC: Percent Different of ISM/C, Perez/C, and ISM integration method using the AWM with integration as reference.

Figure 9.14: Annual performance at College Station, TX.

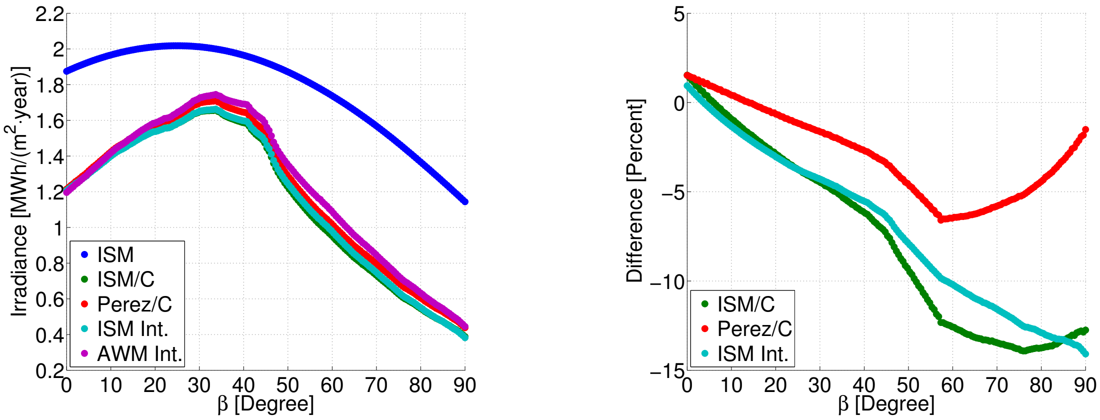

(a) E–W XCPC: Comparison of total annual irradiance: ISM for a flate-plate, ISM/C, Perez/C, ISM integration method, and AWM with integration.

(b) E–W XCPC: Percent Different of ISM/C, Perez/C, and ISM integration method using the AWM with integration as reference.

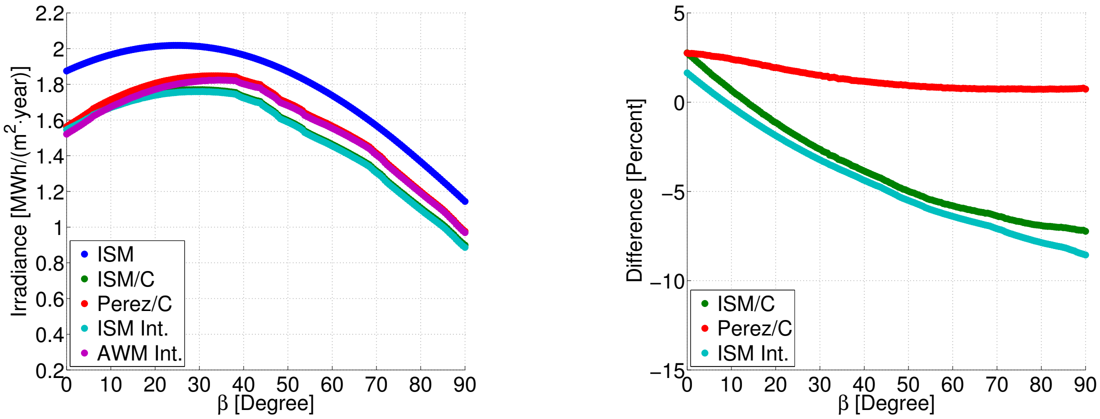

(c) N–S XCPC: Comparison of total annual irradiance: ISM for a flate-plate, ISM/C, Perez/C, ISM integration method, and AWM with integration.

(d) N–S XCPC: Percent Different of ISM/C, Perez/C, and ISM integration method using the AWM with integration as reference.

Figure 9.15: Annual performance at Merced, CA.

formance of the two designs, a plot of a single day of irradiance shown in Figure 9.17 reveals that the N–S XCPC typically has higher energy yields because of the lower concentration ratio, which is consistent with the annual results. The E–W XCPC can have higher energy yields in the early morning or late evening hours because of the orientation of the absorber tubes and the reflectors. This result is possible because the sun is within view of the E–W XCPC and not the N–S XCPC for the hour block ending at 6 pm in the figure.

Figure 2 of Jiang and Winston 2014 [133] shows that the E–W XCPC is better suited for irradiance conditions with higher portions of direct irradiance and the N–S XCPC with higher portions of diffuse light. Given that the three locations were chosen with three different levels of typical moisture content on an annual basis, it was expected that the E–W XCPC would have higher energy yields in Merced and the N–S XCPC would have higher yields in Key West, Florida. Figure 9.16 shows that this is not the case. In an effort to find a location in the USA (lower 48 states) with low irradiation levels that did not have substantial snow fall, the Seattle-Tacoma International Airport location in the TMY3 dataset was reviewed and results are shown in Figure 9.16(d). Even in a location known for a substantial rainy season, there are no data points where the E–W XCPC model yielded more energy than the N–S XCPC model during the hours of 10 am to 4 pm. Although there were 338 data points for which this was true (i.e., near the beginning or end of a day) this is explained by the direct irradiance being blocked by the LFOV as explained above.

Which collector design is ‘best’ remains to be determined because net energy yield is the goal. Because it depends on ambient temperature and operating temperature, it will be evaluated next in Part III.

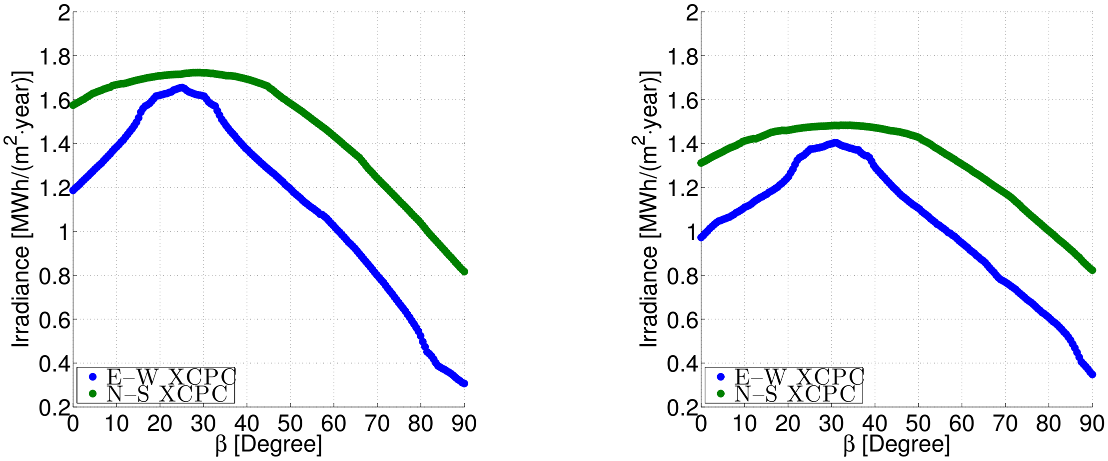

(a) Key West, Florida.

(b) College Station, Texas.

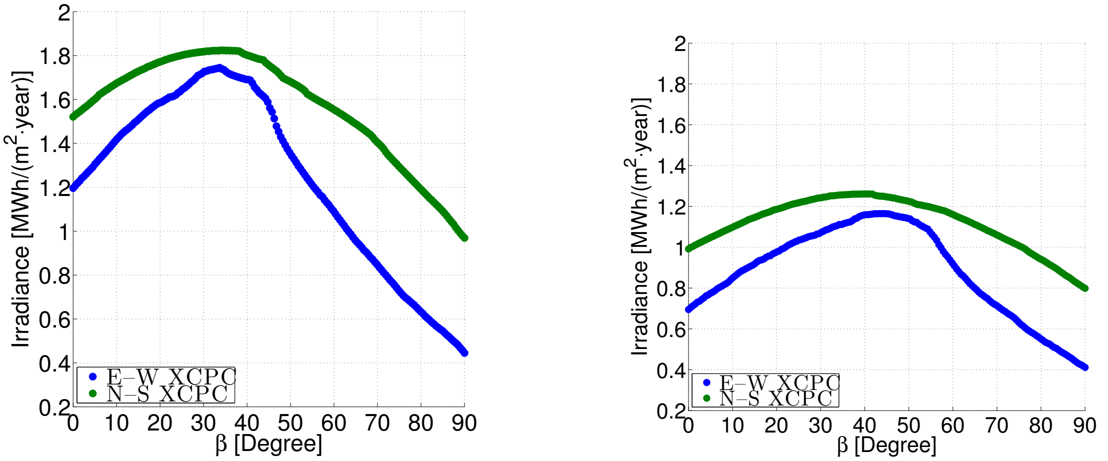

(c) Merced, California.

(d) Seattle-Tacoma, Washington.

Figure 9.16: Irradiance recieved: comparison of E–W XCPC and N–S XCPC performance at four locations, using TMY3 data, and the AWM with integration.

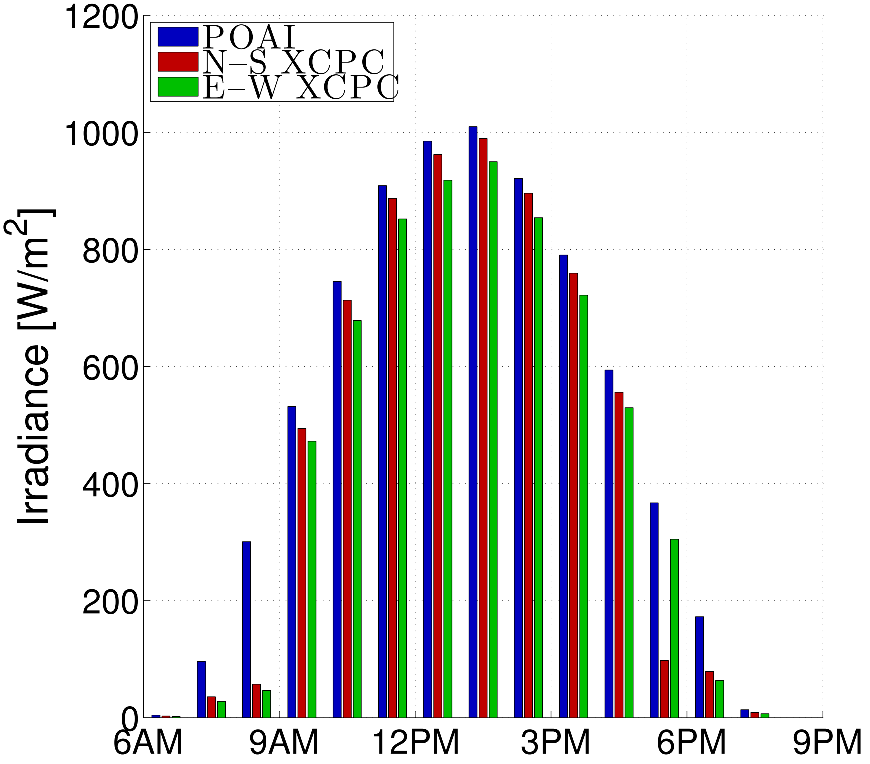

Figure 9.17: Irradiance comparison of POAI, N–S XCPC, and E–W XCPC on August 14th, 2001, Merced, CA using the TMY3 dataset, $\beta = \Phi$ (Lat.), and AWM.

9.6 Conclusions

In this chapter and the previous three, background information was presented and specific models or datasets were selected:

- Meterological data — the TMY datasets by NREL.
- Solar position — the SPA by NREL.
- Sky model — AWM by Perez et al.
- STC — both XCPC versions described by Kim and adapted in this chapter.

These components were grafted into an overall solar-thermal model and simulation. The model and simulation are the original work of this author. The verification of the model and simualion are the original work of this author. While adapting a sky model for use with the XCPC, the need for several key improvements were discovered:

1. Brunger Model — additional data to determine a_i coefficients for more (k, k_t) pairs.
2. Improved information for constructing a more accurate IAM functon for the XCPC designs including experimental IAM response and and non-separable IAM function.
3. Experimental validation of the XCPC performance simulation method created by Kamphuis.

Once implemented, it is likely that these improvements will lead to revisions of the simulation. While building the solar-thermal simulation, several original contributions were made:

- Application of angular distribution model to solar-thermal collector and the most complete known statement of the equations necessary to perform the calculations.
- The first known evaluation of the method for adjusting the diffuse component by the concentration ratio was completed.
- Detailed solar simulation of the XCPC design based on the AWM integration method.

Tailored specifically for the XCPC, a solar-thermal collector model and simulation were developed and verified. This simulation can readily be adapted for other solar collectors or upgraded with improved sub-models. Despite the limitations discussed, the simulation captures the overall functional form of the various physical responses of interest very well. The simulation was verified against known information and found to be more accurate than originally expected. This means that although the STC model and simulation are not expected to exactly match a comprehensive experimental validation, the STC model and simulation will properly represent, in form and functionality, how the XCPC responds to the changing meteorological conditions. This solar thermal simulation will meet the need for performance modeling and enable a more robust design process that can consider the diurnal nature of insolation under real-world meteorological conditions. Next, the simulation will be enlisted to learn more about optimal mounting angles for STC and the expected performance in several typical use cases.

PART III. HARVESTING SUNLIGHT USING SOLAR-THERMAL COLLECTORS

10. EXPLORING THE XCPC SOLAR-THERMAL COLLECTOR PERFORMANCE SPACE: EFFECTIVE IRRADIANCE

In Chapters 6–9, a solar thermal collector performance model and simulation were constructed for the XCPC collector designs in Kim et al. 2013. In this chapter, the simulation will be applied to the TMY2 and TMY3 datasets to accomplish the following:

1. Verification of several principles concerning optimal mounting angle of a solar collector, namely:
    (a) Optimal tilt equal to latitude ($\beta^* = \Phi$) when neglecting atmospheric effects and maximizing annual energy yield for a stationary collector. This relationship is based on solar system geometry at the equator.
    (b) Atmospheric effects and geometry cause a shallowing of the optimal relationship ($\beta^* = \Phi$) at higher latitudes.
    (c) Atmospheric variation (climate) causes further deviations from the relationship and vary by location even at the same latitude.
2. Evaluation of the optimal tilt estimation method by Chrsitensen and Barker 2001 [51] for south-facing collector using the TMY datasets.
3. Determination of optimal mounting angle for the two XCPC designs under consideration using the simulation with the TMY datasets and the AWM because the designers of the XCPC assumed isotropic conditions and $\beta^* = \Phi$ in the design process. This evaluation will provide a preliminary assessment of the validity of those assumptions.

4. Comparison of the optimal mounting angles (β^*) for POAI (G) and the effective irradiance (G_{eff}) for the two XCPC designs as the collector optics alter the distribution of energy yield throughout the year.
5. For the XCPC designs, determination of new fit coefficients of w in the Christensen and Barker 2001 method of calculating the optimal mounting angle (β^*) for a given location.

In Chapters 11 and 12, performance given thermal operating conditions will be considered for both traditional uses and the organic Rankine cycle heat engine use, respectively. One key element will look at how the thermal conditions further change the distribution of energy as a function of mounting angle.

10.1 Introduction

In addition to properly modeling collector optical performance, given a fixed system design, understanding what mounting angle β will maximize energy yield is key to providing clients shorter returns on investment. This perspective must be balanced with the fact that specifically selecting the mounting angle may slightly increase energy yield while increasing installation costs because expensive mounting equipment is required to achieve a mounting angle other than the roof angle. The challenge for any system manufacture is to readily determine these trade offs. The goal of this work is to provide the technical tools to accurately determine collector mounting.

10.2 Background

10.2.1 Overview

There are several relations for flat-plate and photovoltaic (PV) collectors that identify optimal mounting angle β^* (slope or tilt) as a function of latitude Φ ($\beta^* =$

$f(\Phi)$). Some of these works include the effects of azimuth rotation γ, climate, and view obstructions. In the literature, tilt functions are also defined for one location, a region, hemisphere, or globally. Snow and ice cover provides two challenging issues:

1. Snow and ice typically have very high albedo values compared to other types of foreground. Uncertainty in albedo values are known to raise the uncertainty in POAI.
2. On a practical basis, when the ambient temperature is low enough, snow cover on the collector will block the irradiance.

Snow cover represents: (1) an added maintenance cost not typically considered, (2) loss in production, or (3) a combination of both. No relations were found that account for snow covering the collector and that impact on energy yield. It appears that all works reviewed implicitly assume collectors will be kept free of snow cover. Many works even neglected to consider the albedo changes because of snow and ice cover in the foreground of a tilted collector, even though Gueymard 2008 [1] pointed out the negative effect on accuracy of a sky model when albedo is poorly quantified. One work that did consider the albedo effects of snow and ice is Christensen and Barker 2001 [51].

10.2.2 Diverse problem context

In the related works on sky modeling and optimal tilt, there is not a clear best method of evaluation and each analysis utilizes different methods, including how irradiance information is obtained. Studies also differ in the scope of the decision metric. Some studies focus on determining β^* based on the net effective irradiance G_{eff} for a given collector, whereas others complete energy yield calculations and base the decision on heat or electricity yield for a specific use case or condition. Extending the complexity further, some studies consider the time of use of the energy, e.g., the use of solar thermal heating for hot water when the heat demand is higher in the winter months. Another example would be space heating when the demand happens only during the colder months of the year. Considering the time of use or demand for the energy can have large effects on optimal mounting angle. Generalizing this principle results in considering the time value of the energy, where for example in many locations the current cost of electricity is typically higher during the day and higher during the summer. The specific relations for optimal tilt are often contradictory and should not be universally applied. In part, this contradiction is caused by different: (1) simplifying assumptions, (2) modeling choices, and (3) goals. At times, it can also be partially caused by poor methodology.

10.2.3 Optimal tilt relationships

10.2.3.1 Optimal tilt equal to latitude

The simplest of the optimal tilt relations is common knowledge: the optimal mounting angle (β^*) equals latitude (Φ) (Equation 10.1 and Figure 10.1). This method is based on the logical consequences of two simple facts: (1) A south-facing surface in the northern hemisphere with tilt equal latitude has the same angular relationship with direct sunlight as a horizontal plane at the equator. (2) A horizontal surface at the equator will have maximum annual incident solar radiation when there is no seasonal bias in clearness. For the northern hemisphere, Christensen and Barker 2001 [51] explain several possible reasons why this logic fails and results in optimal tilt angles being lower:

1. For lower tilt angles during the summer months, more hours of direct light are inside the view of a planar surface (POA), when compared to higher tilt angles.

2. Lower tilt angles result in larger portions of sky radiance within the POA FOV. Per degree of tilt, sky radiance provides more energy than ground-reflected radiance mainly because of low albedo values of the forground.

3. Atmospheric effects:

    (a) Optical air mass (the amount of the atmosphere direct light travels through, i.e., higher solar zenith angles mean greater optical air mass).

    (b) Weather, i.e., an asymmetry in typical sky clearness with season.

4. As noted in Chapter 6—for the northern hemisphere—the earth is closer to the sun in the winter and further in the summer.

This results in a bias in the opposite direction. These competing effects make it unclear the amount of bias without further analysis. It is important to note that the above logic is based on Christensen and Barker 2001 [51], and is expanded in the current work.

$$\beta^* = \Phi \tag{10.1}$$

10.2.3.2 Optimal tilt equal to latitude minus solar declination

Another common correction is to extend the tilt equal to latitude logic and adjust it on a monthly basis [52], $\beta^* = \Phi - \delta \pm X$, where δ is the solar declination at solar noon in the middle of the month and X represents a constant-value-correction factor specific to a particular study and is determined on a monthly, seasonal, or annual basis. Some references use the ± symbol to cover summer and winter corrections with the same magnitude of X. Depending on the study, X may or may not account for all of the effects previously discussed.

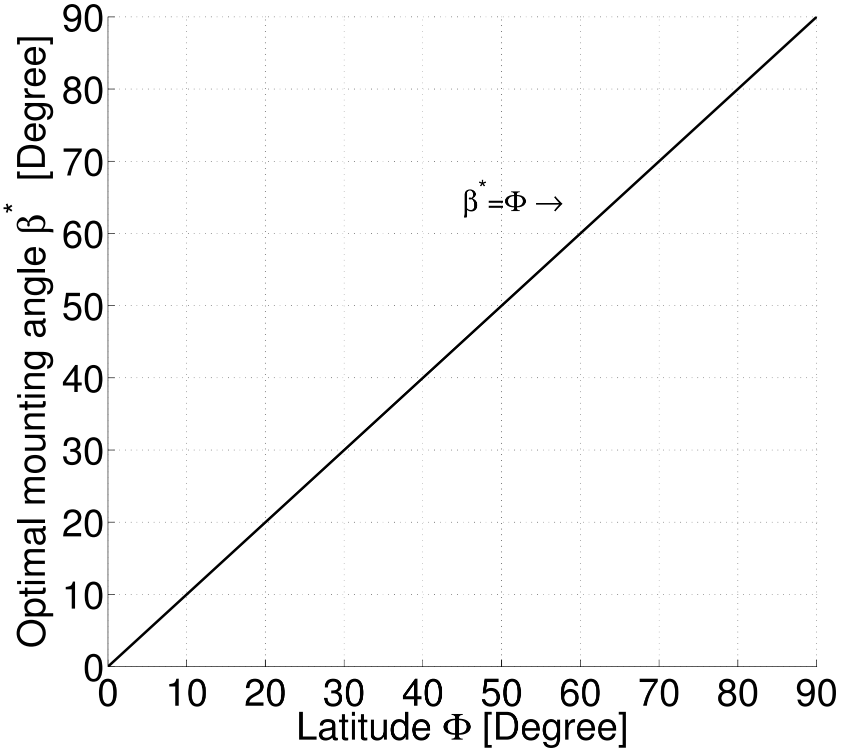

Figure 10.1: Rule of thumb: Optimal mounting angle as a function of latitude.

10.2.3.3 Optimal tilt equal to a linear function of latitude

Similarly, the method to fit the results into a linear function of latitude ($\beta^* = a\Phi + b$) is an other approach. Here b is treated as a constant and the equation is applied across many diverse climates. For the northern hemisphere, a linear relation (see Equation 10.2) by Chang 2009 [63] is shown in Figure 10.2. Chang 2009 does not account for snow cover, and applies the method well into latitudes that have snow coverage nearly year round. More specifically, an albedo of 0.2 is assumed. Additionaly, the work uses modeled radiation values that do not account for climatic effects. The work focused on latitudes along 120° longitude in the northern hemisphere and includes monthly and annual tilt information. The monthly tilt information is typically used for adjustment of systems fitted with manual tracking mechanisms. In contrast, the yearly tilt information is used to select the fixed tilt of an installation without tracking. Chang 2009 modeled the solar irradiance components (DNI, DHI, and GHI) in addition to using the Isotropic Sky Model (ISM) mis-citing Liu and Jordan 1963 [95] as the originators. The research in Chapter 7 found Moon and Spencer 1942 [76] is the oldest known work that derives the ISM, and the true originator remains a mystery. Previously, in Chapter 7 many superior models to the ISM were discussed. Chang 2009 can be improved in the following ways: (1) The use of more accurate modeling of DNI, DHI, and GHI; (2) using a superior sky model that accounts for the anistropy of sky radiance; (3) accounting for climate and other local weather; (4) using more accurate albedo measures instead of assuming the value of 0.2.

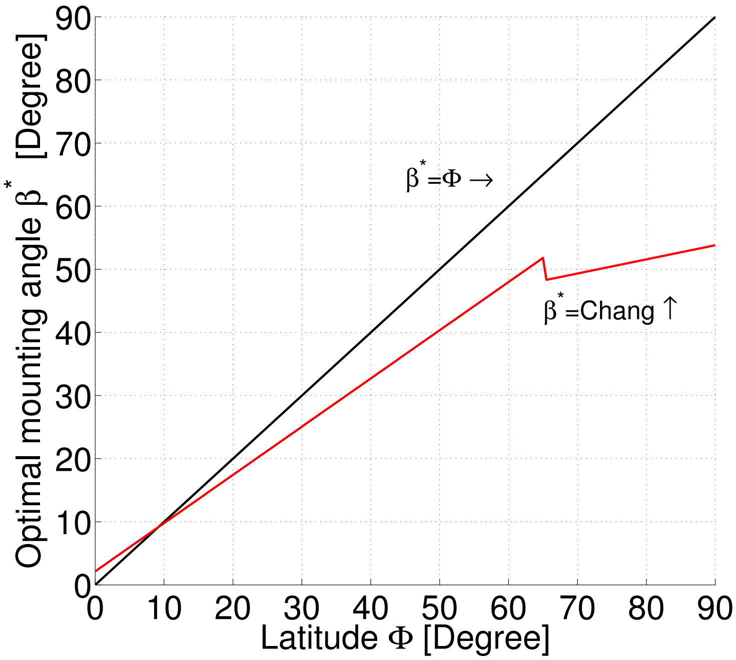

Figure 10.2: Chang 2009 optimal mounting angle. β vs. latitude Φ for the northern hemisphere.

$$\beta^* = \begin{cases} 0.764\Phi + 2.14^\circ & \text{if } \Phi \leq 65^\circ \\ 0.224\Phi + 33.65^\circ & \text{otherwise} \end{cases} \tag{10.2}$$

10.2.3.4 Optimal tilt equal to a non-linear function of latitude

In one study that predates Chang 2009, Christensen and Barker 2001 [51] accomplish the first three needed improvements. The study used the method of $\beta^* = \Phi - w$. Here, w is a function of several clearness measures that account for location-specific climate and is the best-known method for determining optimal tilt for a specific location in the United States short of performing optimization directly (see Equations 10.3).

$$\beta^* = \Phi - w \tag{10.3a}$$

$$w = C_1(1 - \frac{K_{t,\text{ win}}}{K_{t,\text{ sum}}}) + (C_2 - K_{t,\text{ ann}})\Phi \tag{10.3b}$$

$$w = 20.6(1 - \frac{K_{t,\text{ win}}}{K_{t,\text{ sum}}}) + (0.621 - K_{t,\text{ ann}})\Phi \tag{10.3c}$$

$$K_t = \frac{I_{t,h}}{I^0_{t,h}} \tag{10.3d}$$

where w is a non-linear climate correction factor, K_t is the clearness index in which "win" is for winter months (November, December, and January), "sum" is for summer months (May, June, and July), and "ann" is for annual (all months). Lastly, $I_{t,h}$ is the global horizontal irradiance on the surface of the earth, and $I^0_{t,h}$ is the extraterrestrial irradiance on a horizontal surface. Figure 10.3 shows the results for the TMY2 and TMY3 datasets against the other two optimal mounting angle correlations. This shows that the three relations increase in complexity in the order presented and that generally the more complex correlations tend to increase accuracy.

Christensen and Barker 2001 also defined a surface orientation factor for south-facing surfaces (SOF$_s$), which is the ratio of the total annual irradiance given a specific orientation to the orientation that provides the maximum and is defined in Equations 10.4.

$$\text{SOF}_s = \frac{\text{total annual irradiance}}{\text{max total annual irradiance}} \tag{10.4a}$$

$$\text{SOF}_s = 2.0 - [1.0 + C_3(\beta - (\Phi - w))^2]^{\frac{1}{2}} \tag{10.4b}$$

$$\text{SOF}_s = 2.0 - [1.0 + 0.000242(\beta - (\Phi - w))^2]^{\frac{1}{2}} \tag{10.4c}$$

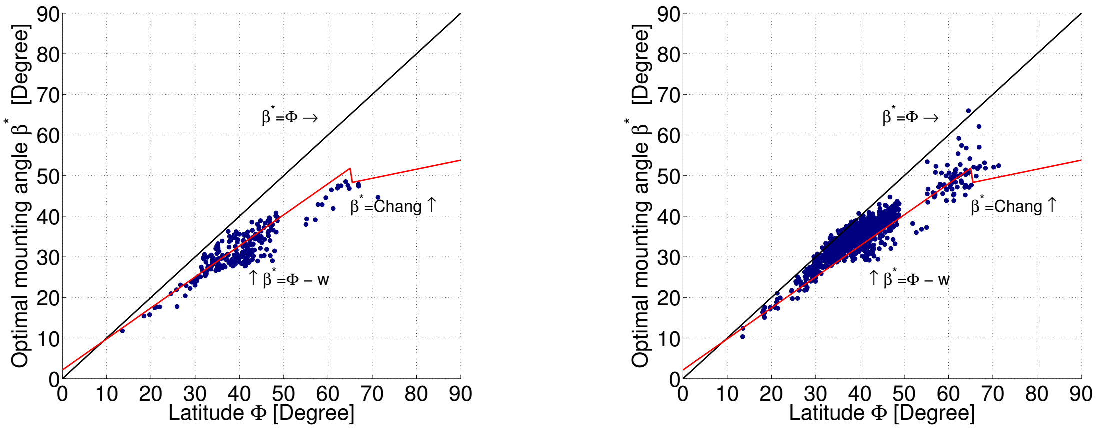

(a) TMY2 dataset.

(b) TMY3 dataset.

Figure 10.3: Christensen and Barker 2001 optimal mounting angle. A function of latitude and climate. Note that the K_t values used to determine w are based on the respective TMY datasets. This means that the Christensen and Barker 2001 correlation is discrete for each location and the other two correlations are continuous. In this unique case, the discrete characteristic does not imply experimentally measured data.

Christensen and Barker 2001 use the the TMY2 dataset and the Perez et al. 1988 [111] model (see also Perez et al. 1987 [110]) to study optimal mounting (tilt and azimuth). As previously noted, they explain the reasons for tilt shallowing at higher latitudes, and provide a simple correction method to determine the optimal tilt angle given the location. The authors also extend this method to provide annual irradiance adjustments for any orientation. The methods developed show that a simple correction to optimal tilt angle based only on latitude will be wrong for some locations and climate must be considered.

There are several pros and cons because the Christensen and Barker 2001 study uses: (1) the Perez et al. 1988 model and (2) the TMY2 dataset. The Perez et al. 1988 model performs well, although the AWM by Perez et al. 1993 has several improvements: (i) anglular distribution of the sky radiance, (ii) optical air mass, and

(iii) the empirical method used to derive the coefficients; therefore the AWM should yield 'better' results. Anecdotally, the AWM is several model generations more refined than the Perez et al. 1988 model. Although these reasons are well founded, one issue is unclear. The Perez et al. 1988 model has two options where one set of coefficients is based on a simplifying assumption of circumsolar radiance being a point source, and the other is not. This results in reduced complexity for a small reduction in accuracy. It could not be determined which version of the model was used in Christensen and Barker 2001 and personal communication with Christensen in March 2017 found that the author was not able to readily determine which model was used because it appears this information is lost to time. The TMY2 dataset has mixed value for the following reasons: (1) TMY2 dataset lacks albedo measurements whereas the TMY3 dataset includes albedo measurements, (2) the TMY2 dataset only covers 239 locations whereas the TMY3 dataset covers 1020 locations, and (3) the TMY3 dataset is based primarily on satellite models. One of the satellite models is an earily version of the SUNY model [158] for irradiance measurement (higher uncertainty) rather the TMY2 dataset. It is based on a higher number of ground-based measurements of irradiance (lower uncertainty). (See Figures 10.4 and 10.5 for more information.) Both datasets are based on very small portions of ground-based measurements. These differences make it unclear which dataset would be 'best' to use during the analysis.

10.2.3.5 General optimal tilt summary

Table 10.1 is a brief overview of the various options used to model solar collector performance and optimal tilt studies.

Table 10.1: Solar tilt study variablity

Solar Simulation	Solar Position	Experimental or modeled
	Meteorological data	Experimental, modeled, or combination
	Sky model	Isotropic assumption, correction factor, or full anisotropic
Location applicability	Latitude (Φ) limit	Equator ($\Phi = 0$)
		tropics ($\Phi = \pm 23.5°$)
		polar circle ($\Phi = \pm 66.5°$)
	Local	Urban area or city
	Regional	Several cities, state, or country
	Hemisphere	Northern or southern
	Global	Planet earth
Mounting angles	Slope β	$0 \leq \beta \leq 90$ (northern hemisphere only)
		$-90 \leq \beta \leq 90$
		$0 \leq \beta \leq 90$ (always toward equator)
	Azimuth rotation ϕ	Variable
		Fixed
Tilt adjustment	Daily	365 times per year
	Monthly	12 times per year
	Bi-seasonally	8 times per year
	Seasonally	4 times per year
	Fixed	No adjustments
Optimization Criteria	Sloped ETR	Extraterrestrial Irradiance on a sloped surface
	POAI	Plane of array irradiance
	G_{eff}	Net effective irradiance on a sloped surface
	Energy yield	Thermal or electric, including the time value of energy
Result form	Linear	$\beta^* = a\Phi + b$
	solar declination (δ)	$\beta^* = \Phi - \delta \pm X$

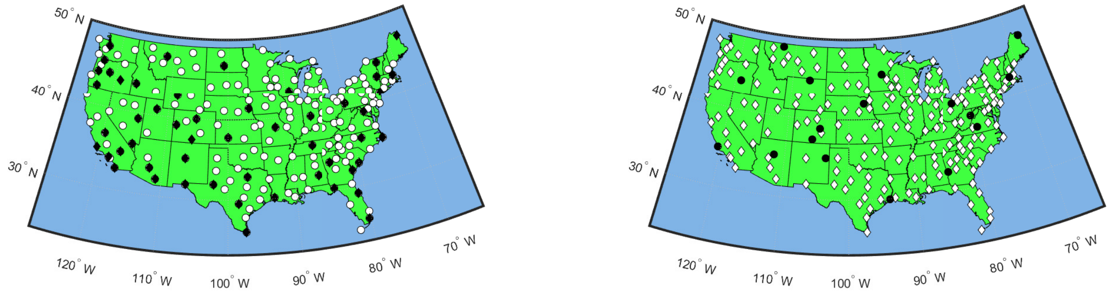

(a) NSRDB classification based on data for a site having: (1) *Primary* (black), any measured irradiance; or (2) *Secondary* (white), satillite based modeled irradiance.

(b) TMY2 classification based on data for a site being: (1) Complete (white), minimum of 15 canidate months with upto 2 consequtive hours of data filling; or (2) Filled (black), requiring more than 2 consequative hours of data filling to achieve 15 canidate months, although less than 47 consequative hours filled.

Figure 10.4: TMY2 site locations. The lower 48 states with two different data quality classifications.

10.2.4 Application to Solar Thermal Collector

There are only a few studies that were performed with Solar Thermal Collector (STC), of which all were flat-plate STC. Christensen and Barker 2001 cover much of the material that was intended for the current research effort. This has enabled the current work to adapt by updating Christensen and Barker 2001 in part and extending the methods to the XCPC designs. What is lacking are evaluations of the optimal mounting angle for both the XCPC designs given their LFOV and an evaluation of the effect of operating conditions on optimal mounting angle. Here, the current work seeks to fill in a knowledge gap concerning optimal mounting angles for the N–S and E–W XCPC. When developing the XCPC versions, the designers assumed a mounting angle set to latitude ($\beta = \Phi$). As described above, both Chang 2009 and Christensen and Barker 2001 emphasize this relationship only approximately applies

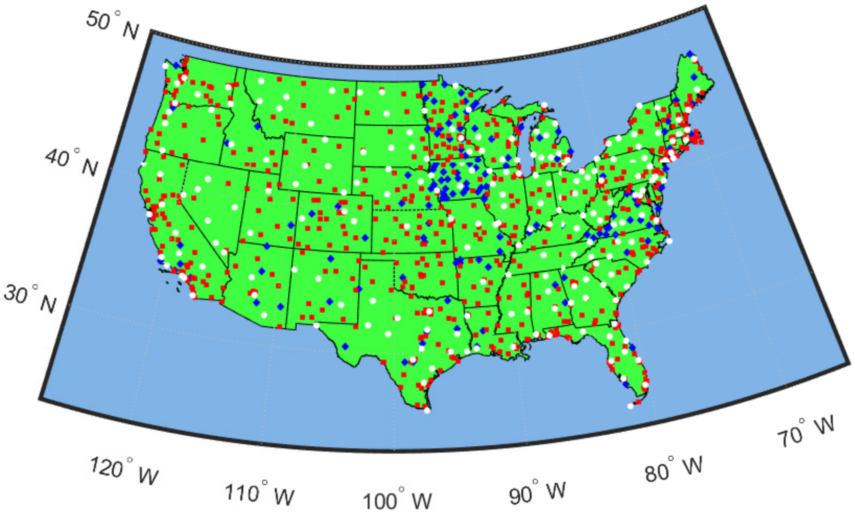

Figure 10.5: TMY3 site locations. Figure based on one data quality classification given by the NSRDB update: (1) *Class I* (white), lowest uncertainty data; (2) *Class II* (red), higher uncertainty data; (3) *Class III* (blue), incomplete record. See the TMY3 and corrisponding NSRDB user manuals for more information.

to lower latitudes with typically clear skies.

10.3 Simulation

In Chapters 6–9, a solar-thermal collector performance model and simulation were constructed for the XCPC collector designs by Kim et al. 2013. This simulation uses the Solar Position Algorithm (SPA) by NREL, the Typical Meteorological Year 2 and 3 (TMY2 and TMY3) datasets by NREL, and a sky model to determine the irradiance on a collector. Which sky model used depends on the collector and its location with respect to the atmosphere.

10.3.1 Extraterrestrial irradiance

At the top of the atmosphere, extraterrestrial irradiance (ET) incident on a POA is given by Equation 10.5,

$$I_T = I_{\text{ETRN}} \cos(\theta_i) \tag{10.5}$$

where I_T is the total irradiance on the surface, I_{ETRN} is the extraterrestrial irradiance normal to the sun, and θ_i is the angle of incidence.

10.3.2 Plane of array irradiance (POAI), N–S XCPC, and E–W XCPC

The POAI is determined using the AWM by Perez et al. 1993 for sky radiance and the Isotropic Sky Model for ground-reflected radiance. The N—S and E–W XCPC use the same methodology except their limited field of view (LFOV) is incorporated as described in Chapters 6–9. Figure 10.6 shows how the simulation is organized.

10.4 Methodology

Rather than approximating the optimal location as was done by Christensen and Barker 2001, a brute-force method is employed here. Using no azimuth rotation

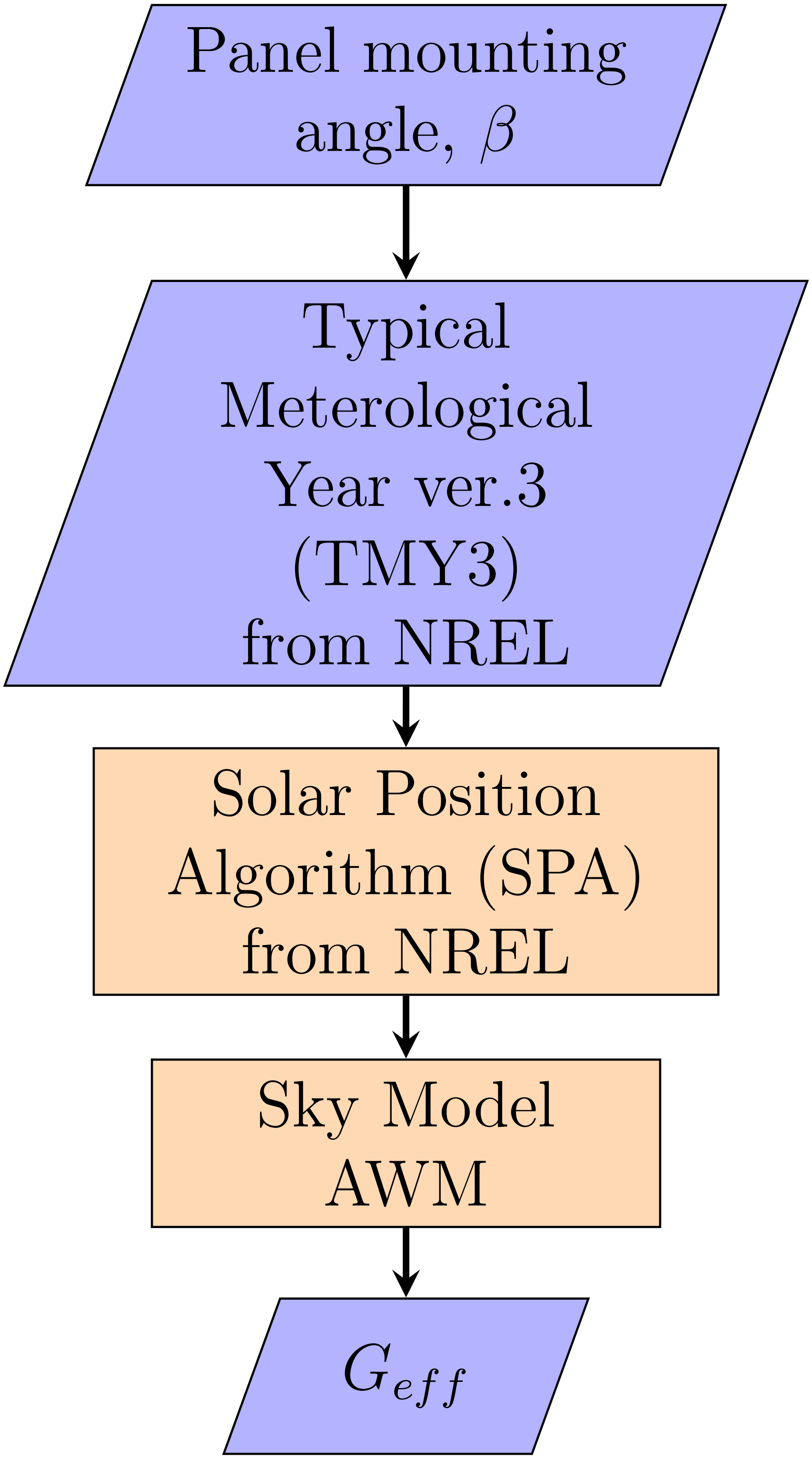

Figure 10.6: Flow chart for the irradiance simulation.

($\gamma = 0$), hourly and annual total irradiance is calculated for each irradiance measure (ET, POAI, N–S XCPC, and E–W XCPC) at every location in both TMY2 and TMY3 datasets for each mounting angle (β) in the range 0–90° using 0.5° increments. The major benefit in this brute-force method is that the results are stored as hourly data and can be used later because there are many optimization methods that would have resulted in greater precision and lower computational costs. If the collector is mounted directly on a residential roof, the roof angle sets the mounting angle β. The 0.5° increment was chosen based on a simple analysis of truss and rafter board uncertainty, and how they impact roof slope. For example, if one orders a 5:12 pitch truss, it could be off at most $\frac{1}{8}$ inch per foot. Rafter boards are commonly accurate to $\frac{1}{4}$ inch per foot. For roofing in the United States, these errors between specification and construction practice result in slopes being 1° or more different than what is specified. Christensen and Barker 2001 also point out the flat/insensitive nature for optimal collector mounting. These results confirm the conclusion that the chosen increment exceeds the needed accuracy. With this methodology, simulating at each location in the TMY2 and TMY3 datasets requires the use of a supercomputer. The ADA cluster at the Texas A&M High Performance Resource Center is used to perform the large number of calculations. Post-processing the results is completed on a local machine.

10.5 Approach

The goals of this work are numerous:

1. Update the models used in Christensen and Barker 2001 using best-available technology.
2. Confirm numerically some of the principles commonly believed in the field.

3. Update or confirm the Christensen and Barker 2001 values for w and SOF_s, which are based on POAI.

4. Provide new values of w and SOF_s for the XCPC designs.

To accomplish these goals, the current work uses the same approach as Christensen and Barker 2001, namely the same equations but with new fitted coefficients. The coefficients are fit using a non-linear least-squares method based on a trust-region-reflective method. It is important to consider the following points:

1. Using the best-available physics-based models is prefered, although they are usually complex and computationally expensive.

2. Using a simplified model sacrifices some accuracy for decreased complexity and computational cost. This was done the Perez et al. All-Weather Model (AWM) and the Perez et al. 1987 model.

3. Using a correlation function (w and SOF_s) greatly simplifies a complex system. This typically reduces complexity and is usually substantially more user friendly, although at the cost of accuracy and universal applicability.

Next these principles will be demonstrated in practice by reviewing and discussing the results.

10.6 Results and discussion

Massive amounts of calculations were required for roughly 4,000 data points of hourly irradiance, each dataset (2), each location (239 and 1020), each type of irradiance (4), and each mounting angle (181). This super-set of data is retained for later use. By doing so, later optimization work will not require recalculation of the hourly irradiance, which is computationally expensive. Summing the hourly data to calculate the annual irradiance yields results that can be more readily visualized for selected locations.

For four locations, Figures 10.7 and 10.8 show the annual energy as a function of mounting angle β and optimal tilt angle β^* for the following: (1) *extraterrestrial* (*ET*) planar surface at the top of the atmosphere, (2) POAI at ground elevation, (3) G_{eff} for the N–S XCPC, and (4) G_{eff} for the E–W XCPC at several locations in the respective datasets.

The optimal points for each curve at each location in each dataset are used later to examine how the optimal mounting angle varies with methodology, dataset, latitude, and irradiance type.

10.6.1 Extraterrestrial irradiance

Starting at the top of the atmosphere with the extraterrestrial irradiance (ET), Figure 10.9 shows that the optimal mounting angle is shallow when compared to tilt-equal-latitude correlation. This is pronounced at increasing latitude, and therefore tilt. During summer months in the northern hemisphere, there are increased times when the sun points to the back of the POA during early-morning and late-evening hours. This result is totally independent of the atmosphere and therefore climate. This also means that optimal tilt equals latitude is never true, even for ET.

As shown in Figure 10.9(b) for the TMY3 dataset, the optimal mounting angle covers a wide range at a given latitude. Sites near each other – or near in latitude and possibly far in longitude – should have the same (or nearly the same) ET value because solar output is nearly constant and sun-earth distance used to adjust the solar constant to determine ETRN does not account for a specific location on earth. At any location for a given UTC, ETRN values should be the same. Another possible source of the discrepancy is the determination of the angle of incidence; however, if

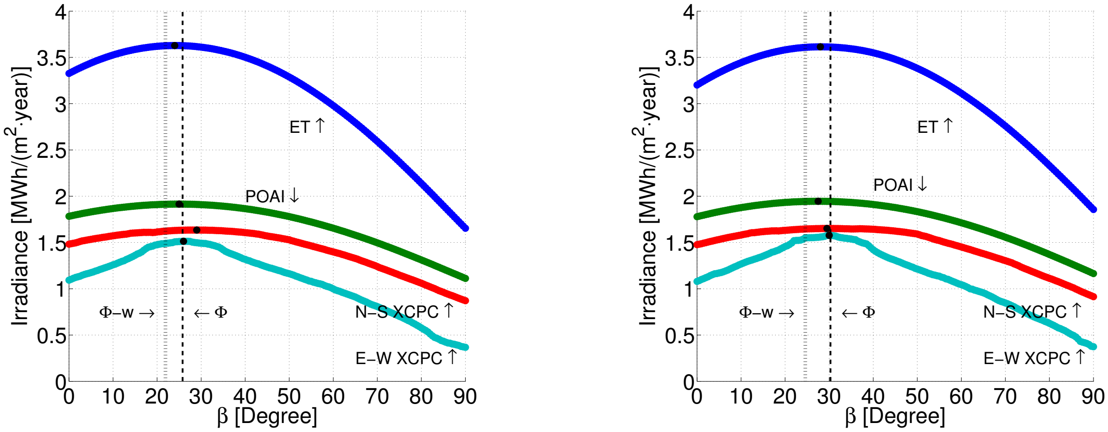

(a) Miami, FL.

(b) Austin, TX.

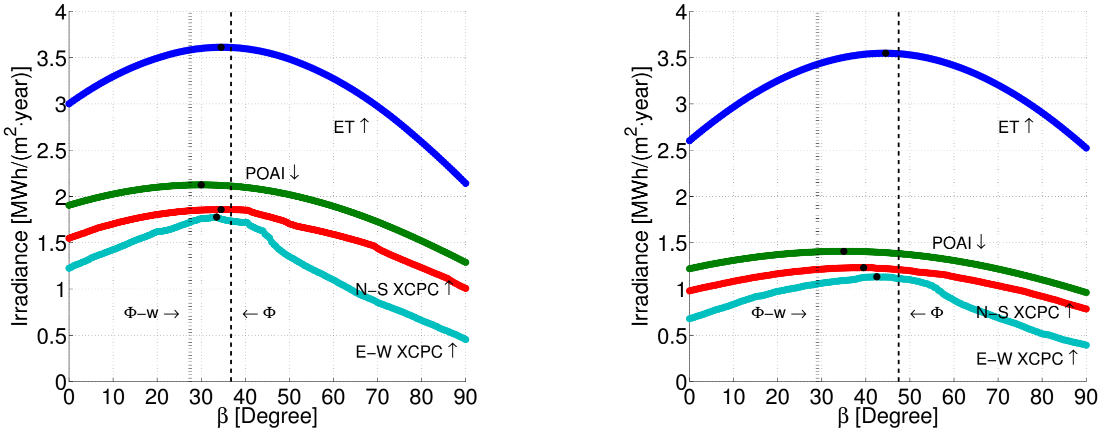

(c) Fresno, CL.

(d) Seattle, WA.

Figure 10.7: Annual energy yield: TMY2. Data as a function of mounting angle for four locations in the TMY2 dataset. ET denotes extraterrestrial POAI at the top of the atmosphere. POAI denotes POAI at the surface of the earth. N–S XCPC and E–W XCPC denote G_{eff} for the repective collector designs. The black dots denote that maximum of each respective function. For $\Phi - w$, w was calculated using the results from Christensen and Barker 2001.

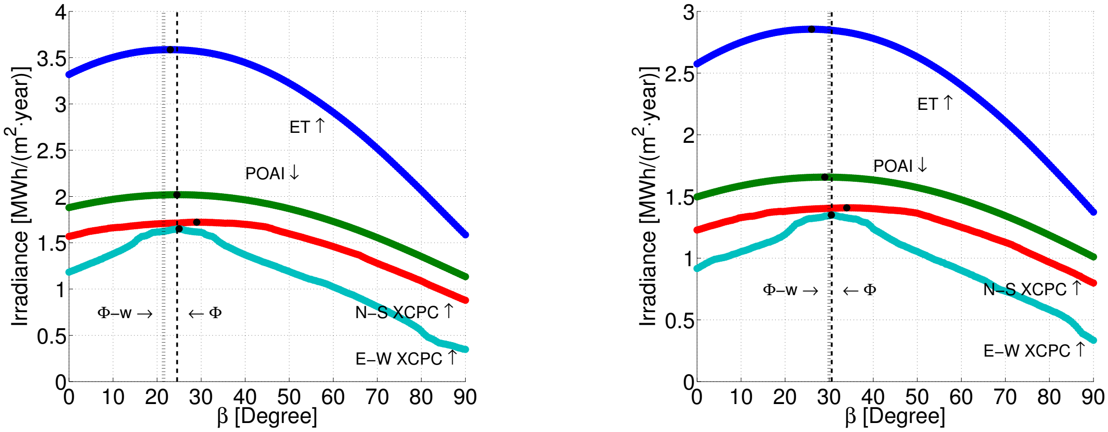

(a) Key West, FL.

(b) College Station, TX.

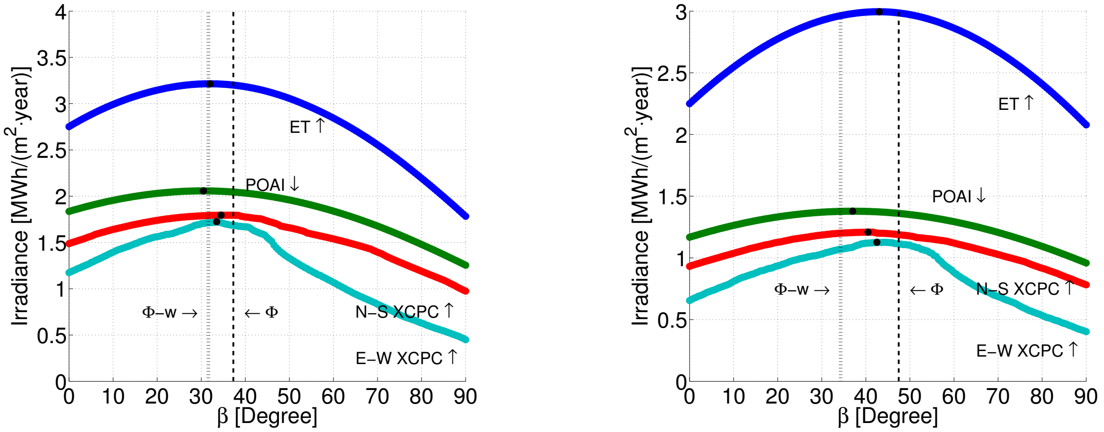

(c) Merced, CA.

(d) Seattle-Tacoma, WA.

Figure 10.8: Annual energy yield: TMY3. Data as a function of mounting angle for four locations in the TMY3 dataset. ET denotes extraterrestrial POAI at the top of the atmosphere. POAI denotes POAI at the surface of the earth. N–S XCPC and E–W XCPC denote G_{eff} for the repective collector designs. For $\Phi - w$, w was calculated using the results from Christensen and Barker 2001.

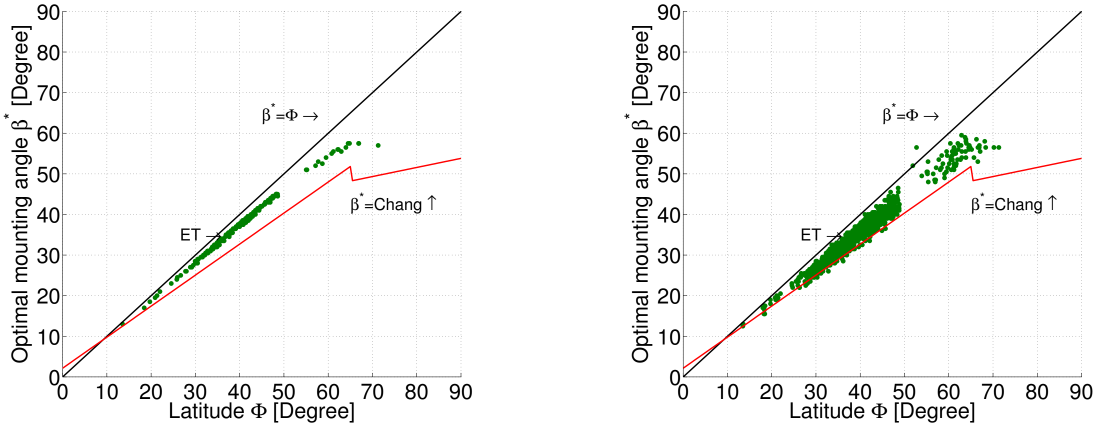

(a) TMY2 dataset.

(b) TMY3 dataset.

Figure 10.9: Extraterrestrial POAI confirms shallowing at higher latitudes.

this were the cause, one would expect the discrepancy to be present in both datasets because the same methods were used on both. It is worth investigating the source of this discrepancy as future work.

10.6.2 POAI

10.6.2.1 Initial review of the data

Ground level includes the effects of the atmosphere and climate; therefore, POAI is considered. The main difference between the current work and Christensen and Barker 2001 is the choice of sky model. The large differences between the predicted optimal mounting angle of Christensen and Barker 2001 and the current work is caused by the sky model choice. Figure 10.10 shows the results for Brownsville, TX, in the TMY2 dataset, which has the largest difference. The flat response of the annual irradiance in the region around the optimum for POAI causes the following: (1) sensitivity in the found optimal mounting angle, and (2) insensitivity in annual energy yield prediction (Figure 10.11). The flat response of the annual irradiance means that uncertainty in the irradiance model and the input data causes uncertainty in the ability to accurately determine the optimum. Uncertainty in irradiance modeling is evidenced by the differing results between the current work and Christensen and Barker 2001 because both did not consider uncertainty and used the same input dataset (TMY2) (Figures 10.11(a) and 10.11(c)). The effect of uncertainty in input data is evident in the difference in the goodness of fit between the TMY2 and TMY3 datasets because the TMY3 has higher uncertainty and more spread in the data. This strong conclusion is weakened by the fact that there is roughly 4 times more data in the TMY3 dataset compared to the TMY2 dataset, which causes one to expect more variability from larger sample size. Figures 10.11(b) and 10.11(d) show that despite the large variability in optimal mounting angle, the annual energy yield is quite steady even for the TMY3 dataset.

10.6.2.2 POAI: Fitting coefficients for w

Table 10.2 shows the many fitting results using various combinations of data inputs. Note that the lower uncertainty sites for the TMY2 dataset are based on the NSRDB primary classification. The fitting results are less than ideal because they seem to show a larger-than-desired variation depending on what dataset is used as input. This may be caused by the different accuracy and precision in each dataset. The differing uncertainty, number of sites, and methods used to create the datasets prevent making strong connections in the fitting results. The results appear to indicate that the uncertainty in the input data masks a good fit. It is also possible that the uncertainty in the selected sky model also contributes to the problem. What is clear is that the use of the w correlation method cannot be applied universally to both datasets with high expectation of accuracy. The various fit coefficients are provided to the reader so that they can select the ‘best’ possible option for use with a specific dataset. Again, here the goal is to predict annual energy yield, which is

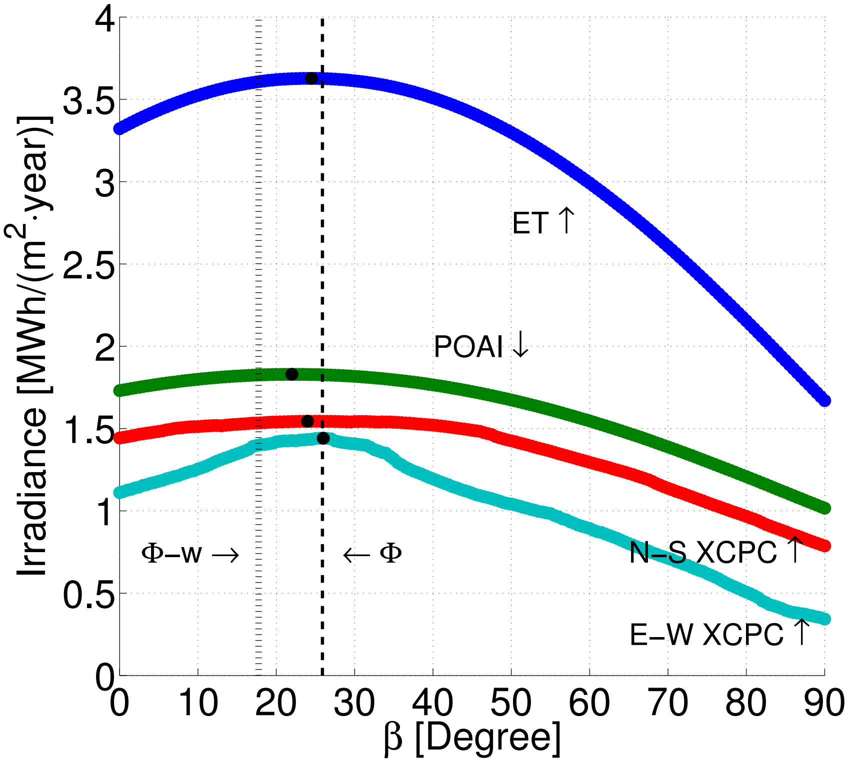

Figure 10.10: Irradiance: Brownsville, TX. The location with the largest difference between the Christensen and Barker 2001 prediction of optimal mounting angle and the current method.

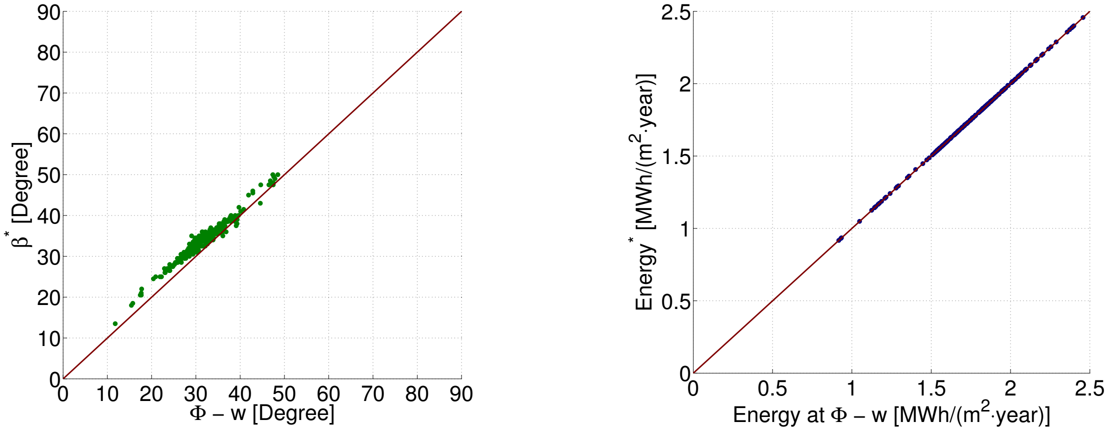

(a) TMY2: differences in predicted optimal mounting angle.

(b) TMY2: corrisponding differences in predicted optimal annual energy yield.

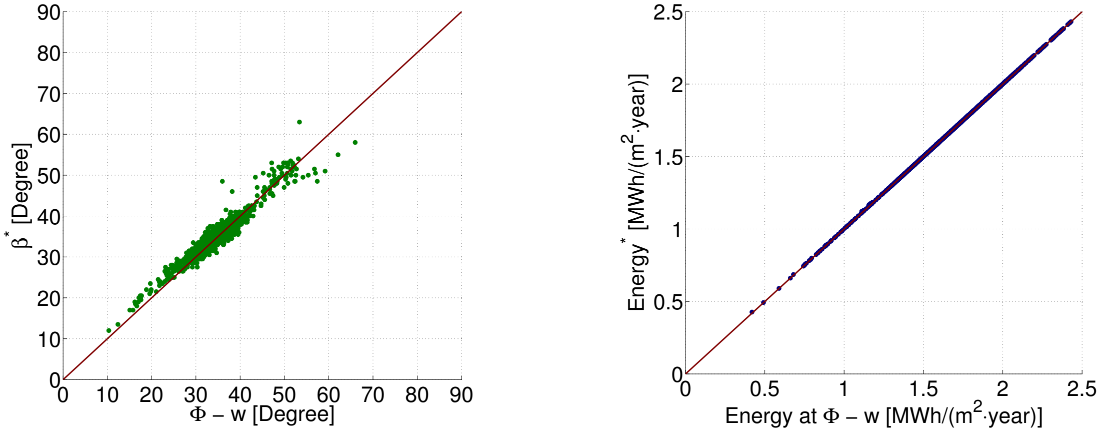

(c) TMY3: Differences in predicted optimal mounting angle.

(d) TMY3: corrisponding differences in predicted optimal annual energy yield.

Figure 10.11: POAI: differences between $\Phi - w$ methods. Differences between Barker and Christensen 2001 and optimal results from current work.

Table 10.2: Fitting data for w with POAI

Dataset		C_1	C_2	R^2
TMY2	Full	15.98	0.5851	0.9347
	Low uncert.	21.31	0.5657	0.9462
TMY3	Full	18.6622	0.6213	0.9143
	Low uncert.	19.27	0.6216	0.8752
Combined	**Full**	**16.0617**	**0.6185**	0.9042
	Low uncert.	16.67	0.6172	0.8655

insensitive to variations in the optimal mounting angle near the optimum.

In Figure 10.12, the coefficients for the combined dataset are used to demonstrate that the exact value of the selected fit coefficients is not critical and that the exact selection of mounting angle is also not critical when attempting to maximize annual energy yield. This supports the earlier statement that annual energy yield is quite insensitive to mounting angle near the optimum.

10.6.2.3 POAI: Fitting coefficients for SOF_s

Table 10.3 shows several fitting options derived again from different portions of the data. The bold-face values are evaluated in this study. Figure 10.13 shows that there is greater variation and the correlation equation is oversimplified. This variation is smaller for the TMY2 dataset and much larger for the TMY3 dataset. Most likely, this variation is caused by the uncertainty in the data, uncertainty in the irradiance model, and the fact that the correlation equation substitutes for the model equation, which also substitutes for the true underlying physics. Given that the TMY2 dataset seems to work reasonably well, this last reason appears to be less important. What is important is that the SOF_s is based on w; therfore, the correlation is based on a correlation, and the discrepancies are compounded. The results are typical of this condition; the SOF_s fit does not perform as well as the w fit.

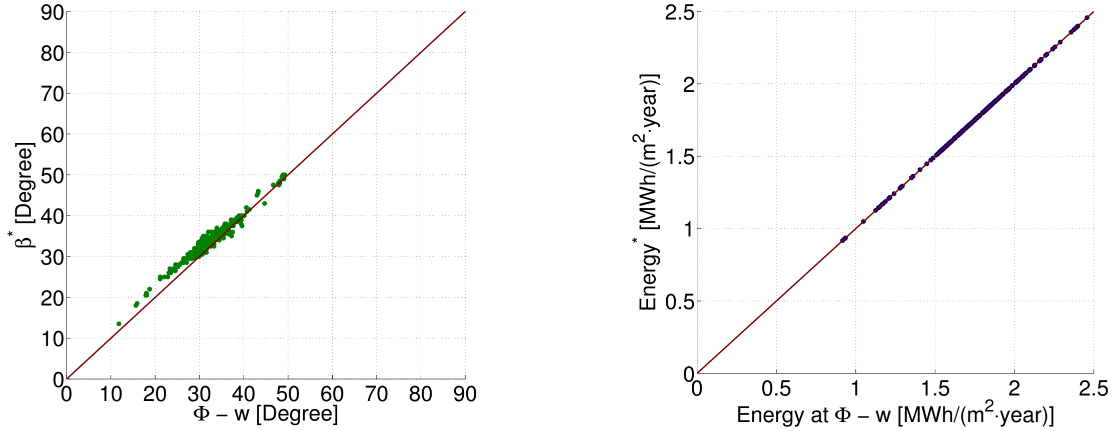

(a) TMY2: differences in predicted optimal mounting angle.

(b) TMY2: corrisponding differences in predicted optimal annual energy yield.

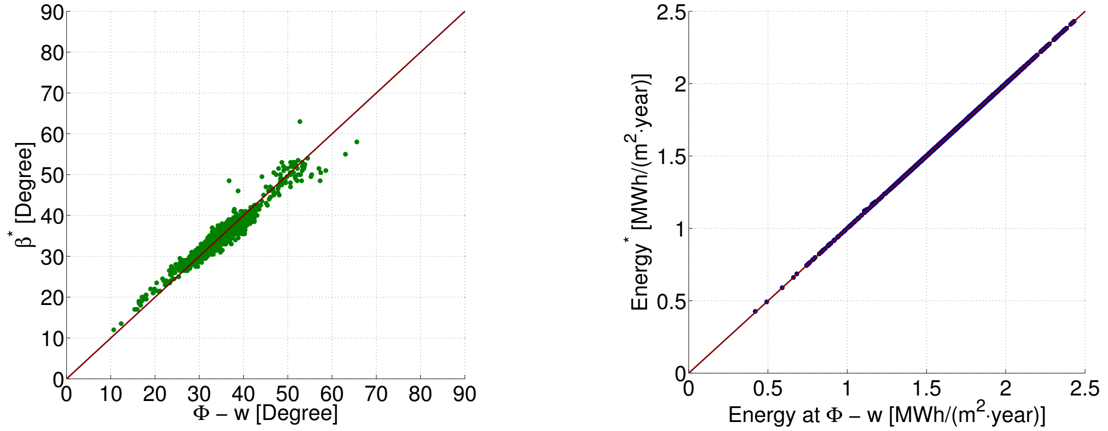

(c) TMY3: Differences in predicted optimal mounting angle.

(d) TMY3: corrisponding differences in predicted optimal annual energy yield.

Figure 10.12: POAI: differences between optimal results and the newly fitted $\Phi - w$ from the current work.

Table 10.3: Fitting data for SOF$_s$ with POAI

Dataset		C_3	R^2
TMY2	Full	2.274e−4	0.9891
	Low uncert.	2.277e−4	0.9888
TMY3	Full	2.475e−4	0.9840
	Low uncert.	2.489e−4	0.9850
Combined	**Full**	**2.432e−4**	0.9831
	Low uncert.	2.440e−4	0.9837

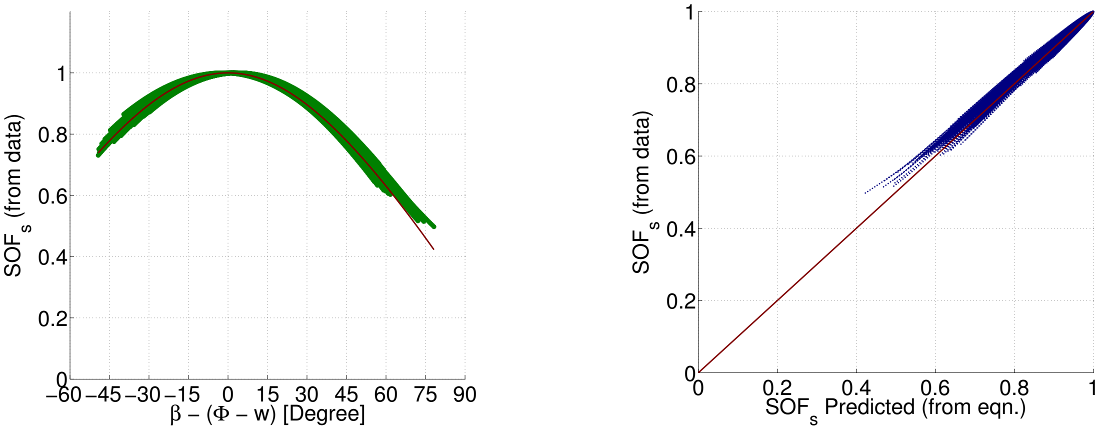

(a) TMY2: SOF$_s$ from data and fit function.

(b) TMY2: Corrisponding differences in data vs fit SOF$_s$.

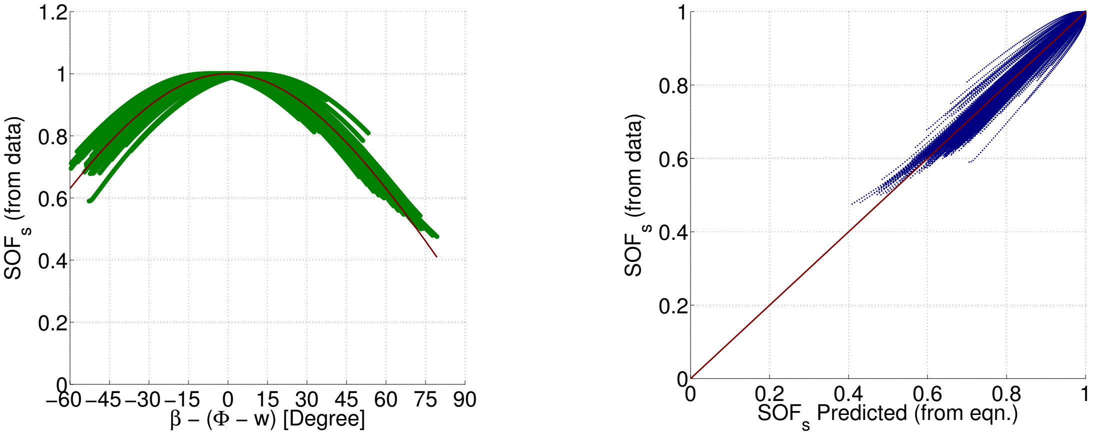

(c) TMY3: SOF$_s$ from data and fit function.

(d) TMY3: Corrisponding differences in data vs fit SOF$_s$.

Figure 10.13: POAI: SOF$_s$ differences between data and newly fitted results. Based on 227,879 data points.

10.6.3 N–S XCPC

10.6.3.1 Initial review of the data

Applying the POAI Christensen and Barker 2001 correlation for w to the G_{eff} values from the N–S XCPC works reasonably well to predict maximum energy yield (Figures 10.14(b) and 10.14(d)). As expected, there were some notable differences in predicted optimal mounting angle (Figures 10.14(a) and 10.14(c)). The small concentration ratio of the collector allows the collector to perform similarly to a POA; however, the differences in field of view (FOV) cause more variability in optimal mounting angle and annual energy yield than for POAI.

10.6.3.2 Fitting coefficients for w

Refitting the w correlation (Table 10.4) re-centers the fit, although it was not possible to notably lower the variability from location to location (Figure 10.15). This inability to lower the variability when fitting the correlation w is likely caused by one or more reasons: (1) uncertainty in the data, (2) uncertainty in the model, and (3) limited degrees of freedom in the correlation function w. Given that the variability is higher for the N–S XCPC than for POAI, it is likely that the correlation w lacks the necessary complexity to properly capture the effects of the limited field of view (LFOV) of the N–S XCPC design. The reader should use caution when using the w correlation for the N–S XCPC. If possible, directly modeling the effective irradiance (G_{eff}) for the location of interest is preferred.

10.6.3.3 Fitting coefficients for SOF_s

The SOF_s correlation (Table 10.5) is to the correlation w, SOF_s has higher variability in the N–S XCPC design as compared to POAI (Figure 10.16). This variability increase is even more pronounced on the TMY3 dataset where the fit for w has the

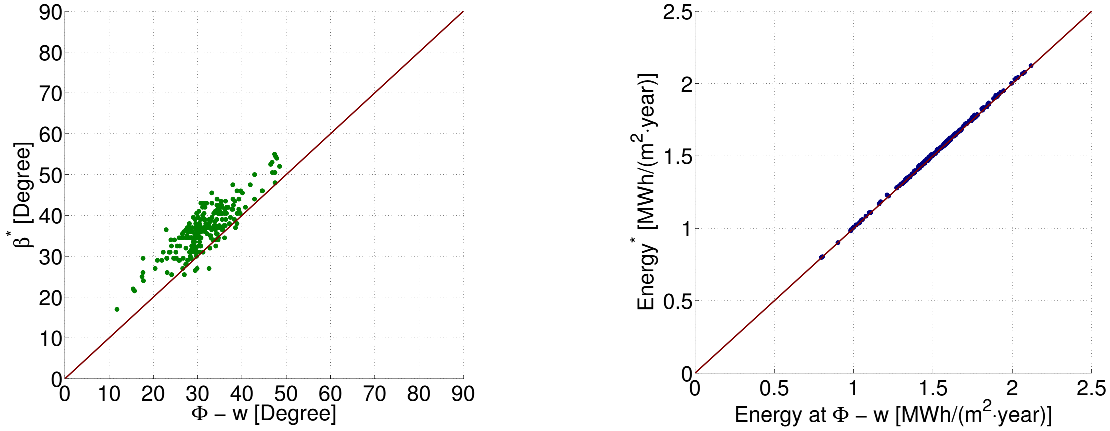

(a) TMY2: differences in predicted optimal mounting angle.

(b) TMY2: corrisponding differences in predicted optimal annual energy yield.

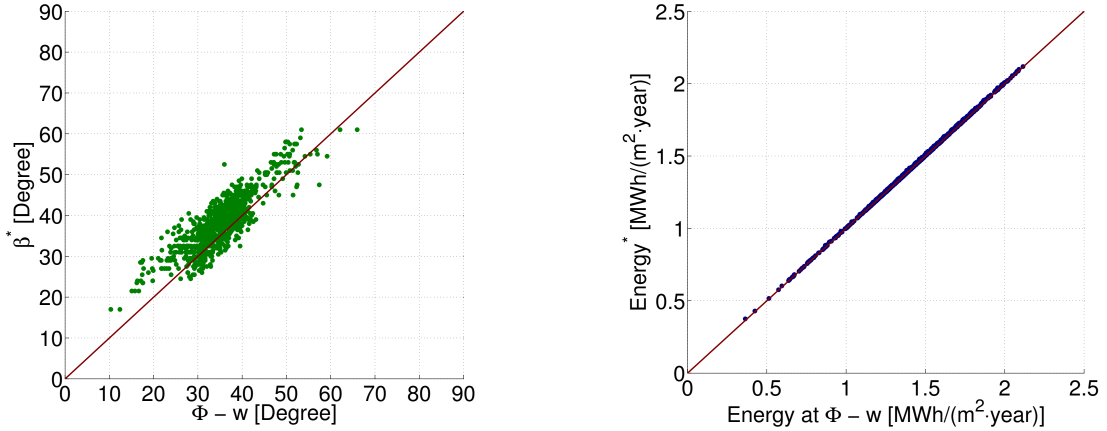

(c) TMY3: Differences in predicted optimal mounting angle.

(d) TMY3: corrisponding differences in predicted optimal annual energy yield.

Figure 10.14: N–S XCPC: differences between $\Phi - w$ from Barker and Christensen 2001 and optimal results from current work.

Table 10.4: Fitting data for w with N–S XCPC

Dataset		C_1	C_2	R^2
TMY2	Full	16.05	0.5176	0.6410
	Low uncert.	28.93	0.4725	0.7256
TMY3	Full	21.86	0.5495	0.6922
	Low uncert.	20.84	0.5545	0.5813
Combined	**Full**	**18.4641**	**0.5474**	0.6720
	Low uncert.	18.84	0.5474	0.5890

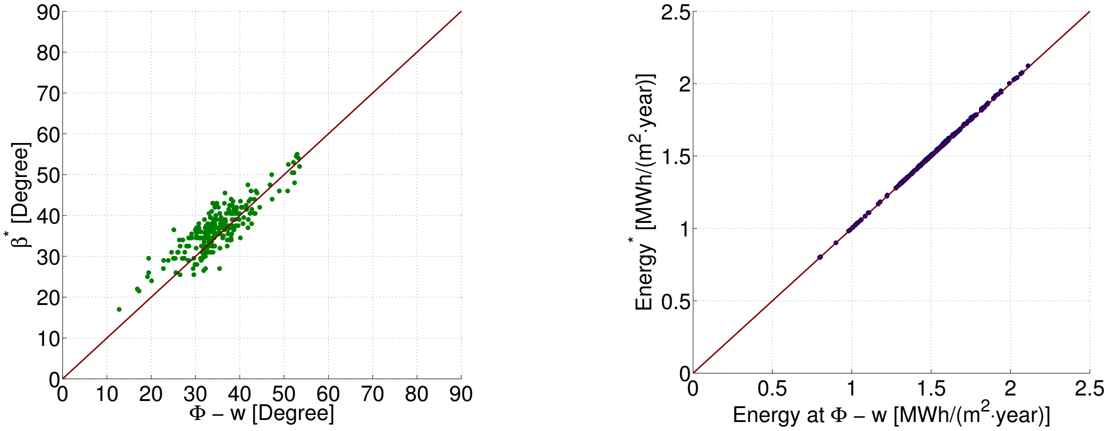

(a) TMY2: differences in predicted optimal mounting angle.

(b) TMY2: corrisponding differences in predicted optimal annual energy yield.

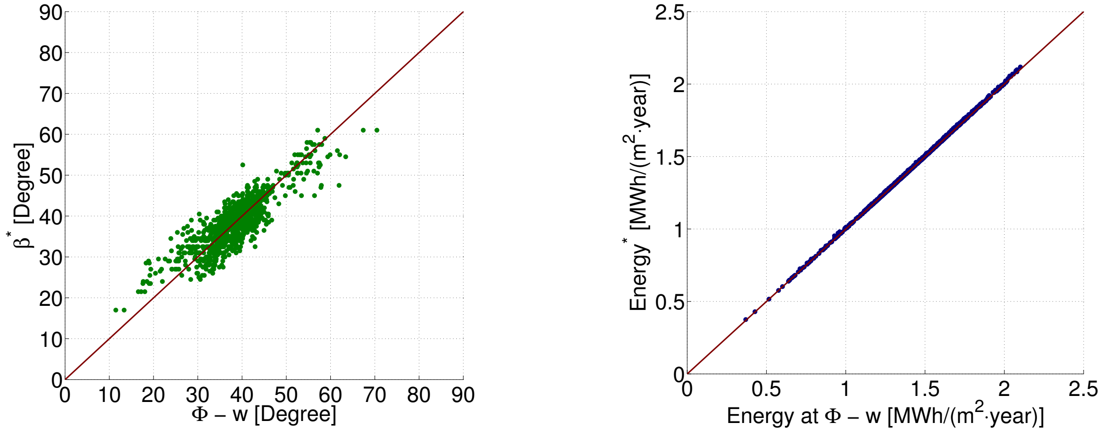

(c) TMY3: Differences in predicted optimal mounting angle.

(d) TMY3: corrisponding differences in predicted optimal annual energy yield.

Figure 10.15: N–S XCPC: differences between optimal results and the newly fitted $\Phi - w$ from the current work.

Table 10.5: Fitting data for SOF_s with N–S XCPC

Dataset		C_3	R^2
TMY2	Full	2.892e−4	0.9734
	Low uncert.	2.901e−4	0.9728
TMY3	Full	3.160e−4	0.9657
	Low uncert.	3.170e−4	0.9670
Combined	**Full**	**3.104e−4**	0.9651
	Low uncert.	3.109e−4	0.9661

greatest deviations from the data. Again, it is recommended to directly model irradiance to determine performance as a function of tilt whenever possible because there are locations and tilts that are poorly represented in the correlation SOF_s.

10.6.4 E–W XCPC

10.6.4.1 Initial review of the data

For the E–W XCPC, the concentration ratio is higher than the N–S XCPC, which results in a substantially more LFOV. The impact on the performance of the Christensen and Barker 2001 correlation for w is notably negative particularly for the annual energy yield (see Figure 10.17).

10.6.4.2 Fitting coefficients for w

Table 10.6 provides updated fit coefficients for w. Figure 10.18 shows again that a new fit can recenter the data, although the variability of the data cannot be reduced using the current form. The E–W XCPC performs the worst of the three irradiance applications.

10.6.4.3 Fitting coefficients for SOF_s

Table 10.7 shows the new fitting coefficients for SOF_s. Despite refitting, both W and SOF_s Figure 10.19 shows an unacceptably wide variation. It is not recommend to use the correlation for energy yield calculations in applications when precision is

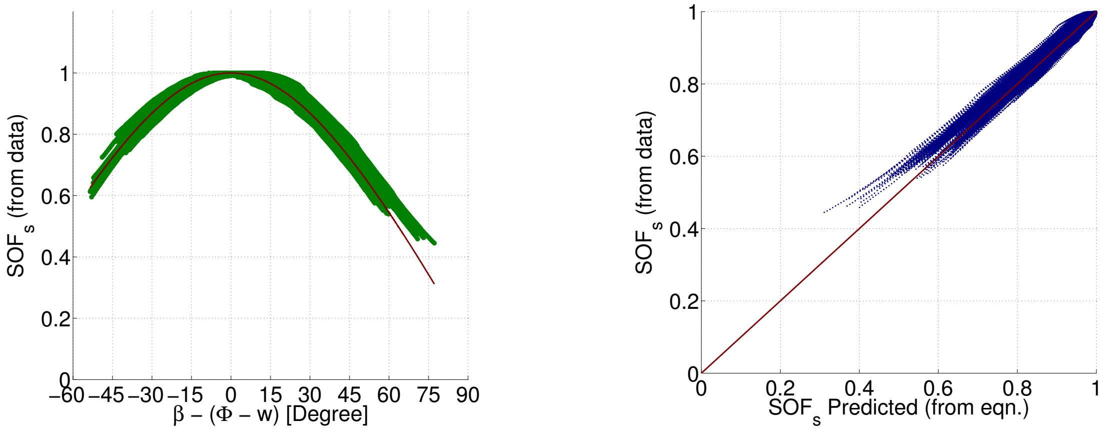

(a) TMY2: SOF$_s$ from data and fit function.

(b) TMY2: Corrisponding differences in data vs fit SOF$_s$.

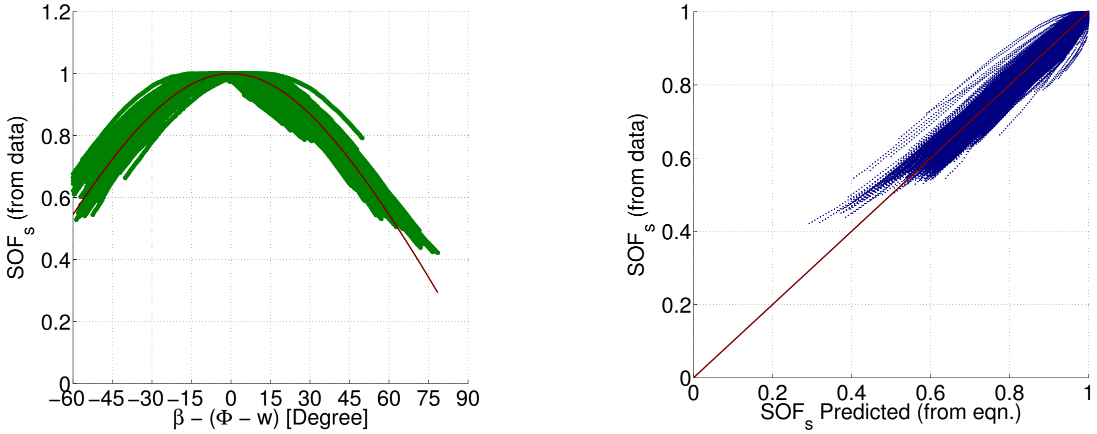

(c) TMY3: SOF$_s$ from data and fit function.

(d) TMY3: Corrisponding differences in data vs fit SOF$_s$.

Figure 10.16: N–S XCPC: SOF$_s$ differences between data and newly fitted results. Based on 227,879 data points.

Table 10.6: Fitting data for w with E–W XCPC

Dataset		C_1	C_2	R^2
TMY2	Full	11.05	0.4912	0.9030
	Low uncert.	13.28	0.4888	0.9168
TMY3	Full	8.4214	0.5601	0.8991
	Low uncert.	7.145	0.5661	0.8489
Combined	**Full**	**5.9599**	**0.5541**	0.8831
	Low uncert.	4.732	0.5595	0.8418

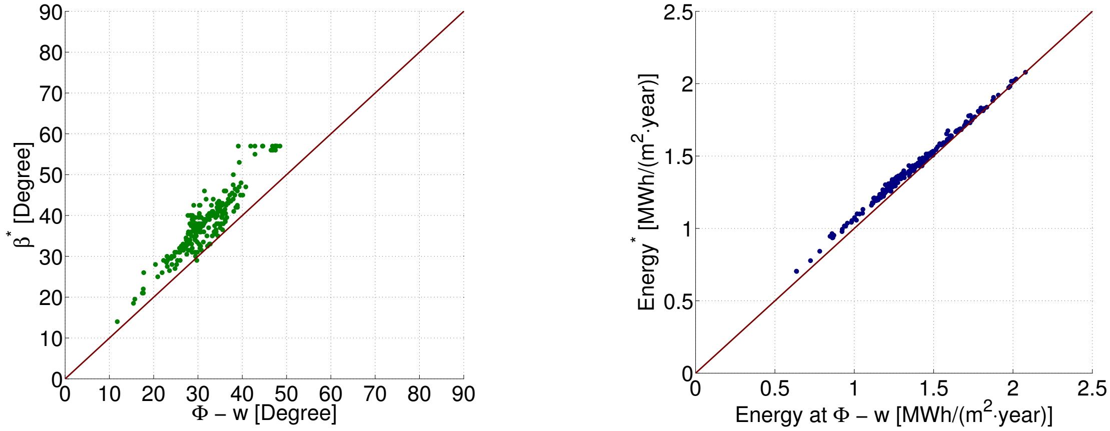

(a) TMY2: differences in predicted optimal mounting angle.

(b) TMY2: corrisponding differences in predicted optimal annual energy yield.

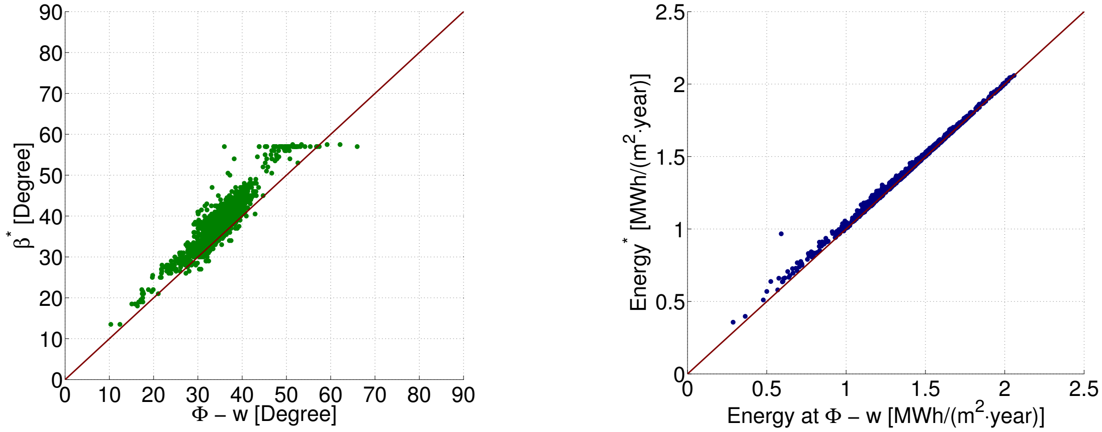

(c) TMY3: Differences in predicted optimal mounting angle.

(d) TMY3: corrisponding differences in predicted optimal annual energy yield.

Figure 10.17: E–W XCPC: differences between $\Phi - w$. Differences between Barker and Christensen 2001 and optimal results from current work.

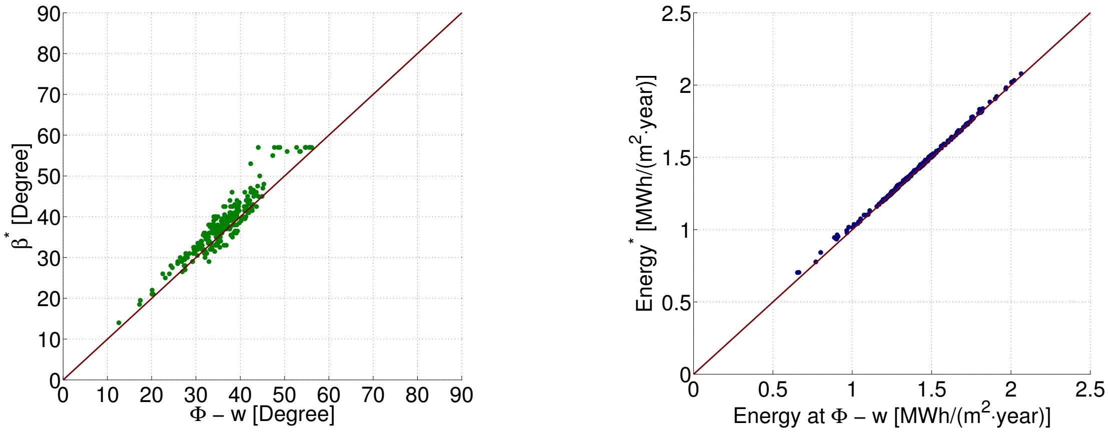

(a) TMY2: differences in predicted optimal mounting angle.

(b) TMY2: corrisponding differences in predicted optimal annual energy yield.

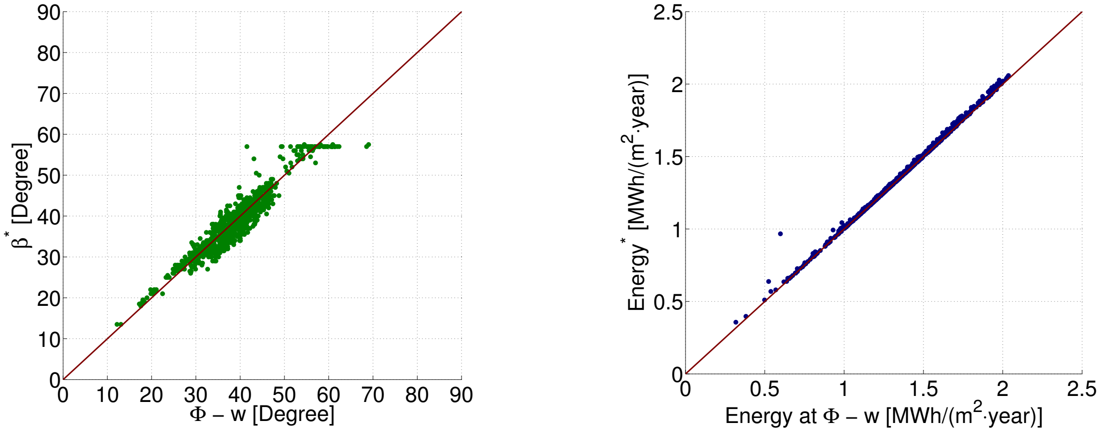

(c) TMY3: Differences in predicted optimal mounting angle.

(d) TMY3: corrisponding differences in predicted optimal annual energy yield.

Figure 10.18: E–W XCPC: differences between optimal results and the newly fitted $\Phi - w$ from the current work.

Table 10.7: Fitting data for SOF_s with E–W XCPC

Dataset		C_3	R^2
TMY2	Full	6.930e−4	0.8738
	Low uncert.	6.906e−4	0.8653
TMY3	Full	7.418e−4	0.8404
	Low uncert.	7.452e−4	0.8343
Combined	**Full**	**7.320e−4**	0.8453
	Low uncert.	7.334e−4	0.8387

required. The concentration and LFOV of the E–W XCPC prevent the correlation functions (w and SOF_s) from providing results with reasonable accuracy. The reader is highly encouraged to use direct modeling methods rather than the correlations.

10.7 Conclusions

Updating the Christensen and Barker 2001 methods and correlation fits confirmed the results of that work, and provided a means to validate the tools used in the current work. The update and validation are original work by this author. During this process, the current work was able to confirm that ET does not follow the $\beta^* = \Phi$ rule of thumb, and it is the original work of this author. The current work also highlighted the effects of uncertainty in data and models on the ability to predict the optimal mounting angle. This effect is magnified by the flat nature of the response. The updated method were also applied for the first time to the N–S XCPC and E–W XCPC designs. Although the correlation method performed reasonably well for POAI, performance was reduced because of the added complexity of concentration and LFOV in the XCPC designs. Applying the correlation methods to the XCPC designs and the determination that the correlations fail for the XCPC designs are both original works of this author.

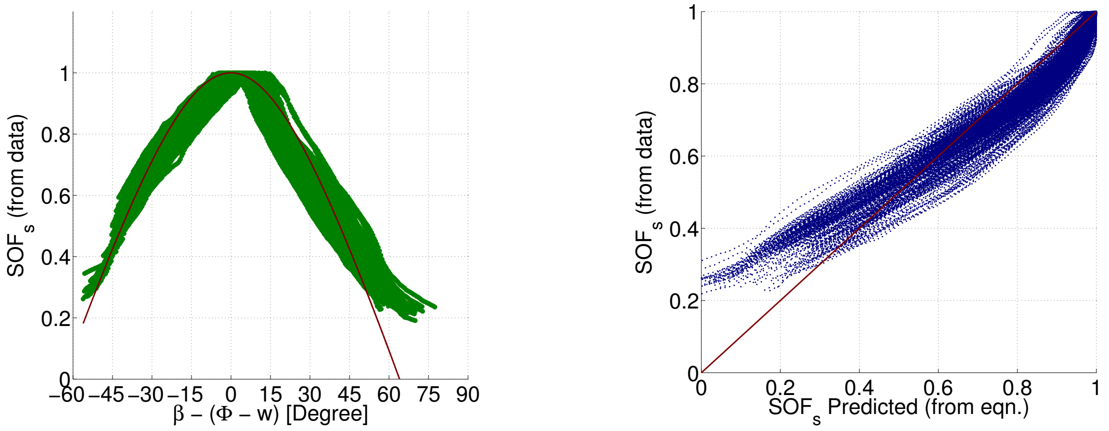

(a) TMY2: SOF$_s$ from data and fit function.

(b) TMY2: Corrisponding differences in data vs fit SOF$_s$.

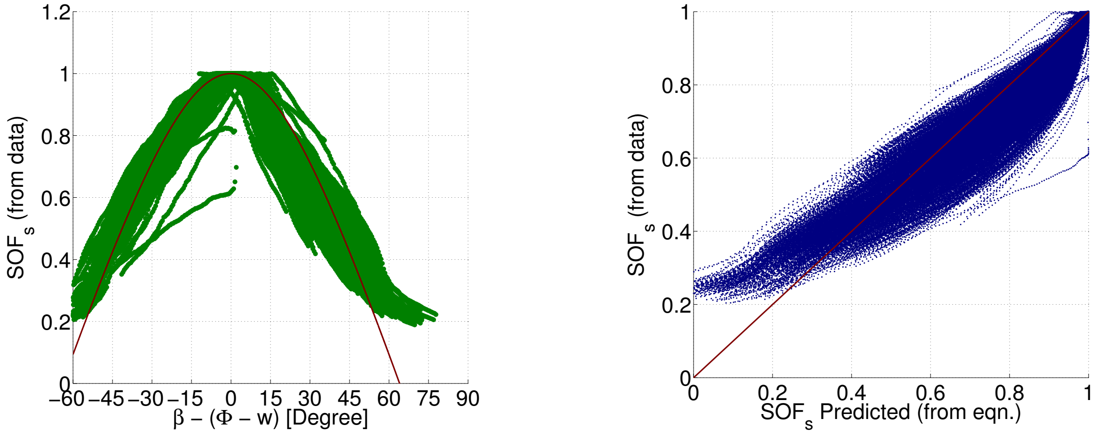

(c) TMY3: SOF$_s$ from data and fit function.

(d) TMY3: Corrisponding differences in data vs fit SOF$_s$.

Figure 10.19: E–W XCPC: SOF$_s$ differences between data and newly fitted results. Based on 227,879 data points.

10.8 Future work

During this work, several opportunities were discovered to advance knowledge:

1. The need to apply a formalized uncertainty analysis to the calculations was realized. NREL advocates the use of the ISO standard on uncertainty (Generalized Uncertainty in Measurement GUM), yet in GUM the analysis of a time series of data is deferred to other sources, yet no justification for treating the time series of irradiance measurements as discrete measurements was found in the literature. This means the methods for uncertainty analysis of irradiance data needs more formalization, but is outside the scope of the current research efforts.
2. Related to the first, there is no formalized method to quantify the uncertainty of irradiance models that are applied to a location outside the validation set.
3. The current work was applied to the new 4-km gridded NSRDB dataset that is under development at NREL.
4. Combining the new dataset and uncertainty methods would yield one of the most complete works on the topic, and may reveal a new-correlation-function form.

11. EXPLORING THE XCPC SOLAR-THERMAL COLLECTOR PERFORMANCE SPACE: TRADITIONAL THERMAL USE CASES

11.1 Background and introduction

In Chapter 10, optimal mounting angle is discussed from the perspective of incident irradiance and effective irradiance. In this chapter, optimal mounting angle will be explored based on thermal energy yield of a solar-thermal collector (STC). The literature has little information on optimal mounting angles for STC based on thermal output. Based on annual total incident or effective irradiance, the optimal mounting angle is the energy-weighted average angle calculated from the optimal angle for each hour. Using this energy-weighted average, the desired design attribute shifts from incident energy to heat yield because changing the energy distribution changes the energy-weighted average optimal mounting angle (Equations 11.1).

$$G = f(\beta) \tag{11.1a}$$

$$Q = fg \tag{11.1b}$$

where G is the irradiance, f is a function that determines incident irradiance, and g is a function that determines energy yield. Here, f and g are arbitrary place holders for the calculations outlined in Chapters 6–9 on solar simulation.

For a given location, the optimal mounting angle for incident irradiance may not be the optimum angle for heat yield of an STC. How much the STC thermal performance changes the optimum depends on (1) collector design, (2) operating conditions, (3) system configuration, and (4) the many location-specific parameters such as weather and climate. This chapter takes a brief look at this issue to illuminate how much the energy weighting changes for a select few traditional use cases of STC. Because the main goal of the dissertation is to review a specific non-traditional use of STC, this chapter is included for completeness and will be brief.

STC are almost exclusively designed for heating single-phase fluids, meaning there is a phase change in the fluid (e.g., boiling). Typically, the fluid is water, a water-antifreeze mixture, or a heat transfer oil. Occasionally, air is used as a working fluid. There are various uses for STC-produced heat: (1) domestic hot water (DHW) heating, (2) space heating, (3) pool heating, (4) space cooling, and (5) commercial/industrial applications. This list is not meant to be exhaustive because there are many niche applications that could be included. This list represents many diverse types of systems, operating conditions, and collector designs. No one item in the list exclusively represents one type of system, operating condition, or collector design. Complicating matters further, a particular collector type and operating conditions may be found in several different system types. For example, flat-plate STC can be used to preheat DHW, heat pool water, or preheat commercial laundry water. This means the list must be processed and re-categorized to treat it in an engineering sense. To that end, several typical *engineering-use cases* are introduced, which are defined in engineering terms rather than the common *social-use cases* listed above.

11.2 Methodology

To define an engineering design space to test how the optimal energy-weighted average mounting angle changes, a selected and brief review of Chapter 8 is provided. This discussion will proceed from the perspective of a system designer who is (1) modeling system and STC performance, and (2) using a STC designed by others; therefore, the STC design is fixed. The reduced mean temperature difference (T_m^*) and the effective irradiance (G_{eff}) are the inputs to the STC efficiency equation

(Equation 11.2). Here, the ambient temperature (T_{amb}) and the effective irradiance (G_{eff}) are determined by location, collector design, and mounting angle. Location and collector design are assumed fixed and mounting angle is not an effective design parameter; although, in Chapter 10 it was found that the collector mounting angle could be selected in the region near the optimum to reduce costs for a small reduction in energy yield. As a result, a designer can only adjust the intermediate variable, i.e., the mean temperature (T_m, Equation 11.2c). Here, the high temperature (T_H, the outlet temperature of the STC) and the low temperature (T_L, the inlet temperature of the STC) provide one degree of freedom in the design parameters. In some cases, the low temperature depends on the system design and can be modeled as a function of ambient temperature, where ΔT is a simple temperature difference. The heat $\dot{Q}$ transferred into the fluid from the STC (Equation 11.2e) must equal the heat gain of the fluid (Equation 11.2f). As a result, the system designer can only adjust two of the three: (1) the low temperature (T_L or ΔT), (2) high temperature (T_H), or (3) mass flow rate ($\dot{m}$). The collector performance is constrained below the stagnation temperature ($0 < T_m^* < T_{mstag}^*$), as shown in Figure 11.1. Equation 11.2e indicates that there is a trade off between the operating temperature and the amount of heat produced. Understanding how this trade-off effects the optimal mounting angle is the focus of this chapter.

Equation 11.2f indicates that if the operating temperatures of the STC (T_H and T_L) are dictated by the system design, then the mass flow rate of the working fluid must be modulated in conjunction with the variability of the effective irradiance (G_{eff}) and the ambient temperature (T_{amb}) because both affect the heat flow into the fluid.

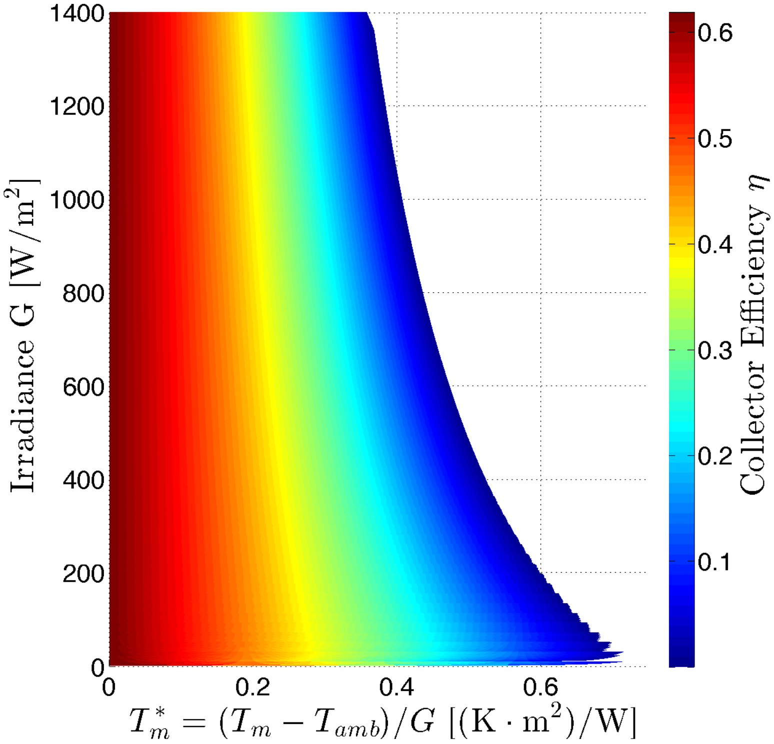

Figure 11.1: XCPC collector performance as a surface.

$$\eta = \eta_0 - a_1 T_m^* - a_2 G_{eff} {T_m^*}^2 \tag{11.2a}$$

$$T_m^* = \frac{T_m - T_{amb}}{G_{eff}} \tag{11.2b}$$

$$T_m = \frac{T_H + T_L}{2} \tag{11.2c}$$

$$T_L = T_{amb} + \Delta T \tag{11.2d}$$

$$\dot{Q} = \eta G_{eff} A \tag{11.2e}$$

$$\dot{Q} = \dot{m} C_p \left(T_H - T_L\right) \tag{11.2f}$$

Simplifying Equation 11.2e results in Equation 11.5,

$$\dot{Q} = \left[\eta_0 G_{eff} - a_1(\frac{T_H + T_L}{2} - T_{amb}) - a_2(\frac{T_H + T_L}{2} - T_{amb})^2\right] A \tag{11.3}$$

$$E = \sum_{\text{annual}} \dot{Q}\Delta t \tag{11.4}$$

$$E = f(\beta, T_H, T_L) \tag{11.5}$$

where G_{eff} is a function of β and Δt is the time duration for each data point. In the case of TMY2 and TMY3 datasets, each data point represents one hour, and E is the annual thermal energy produced by the STC.

It is important to consider that various collector types have niche operating temperatures where they are most efficient (Figure 11.2). Consequently, an XCPC design will not necessarily be the best choice because it depends on operating conditions. Kim et al. 2013 [132] described the XCPC designs that are considered here and form part of the basis for the simulation. Kim et al. note that XCPC designs are targeting the 100–300°C temperature range for T_H. Previously in Chapter 8, several contending STC were compared and XCPC designs were found to be the top-two choices. Jiang and Winston 2014 [133] noted that the N–S XCPC performed better on an irradiance collection basis under a diffuse condition, and the E–W XCPC performed better under clear-sky condition. Reviewing results from Chapter 10, the E–W XCPC design had a greater G_{eff} at optimal mounting angle for 41 locations of the 1020 in the TMY3 dataset, and one location of the 239 in the TMY2 dataset. One possible reason for the conflicting result is that nearly all locations have at least one data point for each type of sky condition; therefore, it is only a matter of the distribution of how many data points there are for each sky condition at each location. Overall, the N–S XCPC design performs better on a G_{eff} basis. Figure 11.3

shows the thermal performance of the XCPC designs. As noted in Chapter 8, the Vitosol 300 SP3A cannot operate in the temperature ranges considered and is shown for comparison. Figure 11.3 indicates that at higher operating temperatures, the E–W XCPC design will perform better on a thermal basis. A main advantage of the XCPC designs is the efficiency at higher temperatures (40% at 200°C) [132]. The goals follow:

1. Compare the two XCPC designs and inspect the region where the E–W XCPC design has greater energy yields, given the above competing characteristics.
2. Evaluate the efficiency under annual operation because the current simulation method calculates G_{eff} differently than Kim et al. 2013. Furthermore, this work defines the net efficiency based on POAI rather than G_{eff} because this is the available energy to collect (Equation 11.6).
3. Clarify the degree to which the optimal mounting angle varies over the operating ranges.

$$\eta_{net} = \frac{\frac{E}{A}}{I_T} \tag{11.6}$$

11.2.1 Mean fluid temperature constant

A simple engineering-use case is to assume that the mean fluid temperature is constant, as shown in Equation 11.7

$$T_m = \frac{T_H + T_L}{2} = C \tag{11.7}$$

Here, the requirement that $T_m \geq \max|T_{amb}|$ is chosen to avoid negative T_m^* values, which are not defined in the STC thermal performance model. The second require-

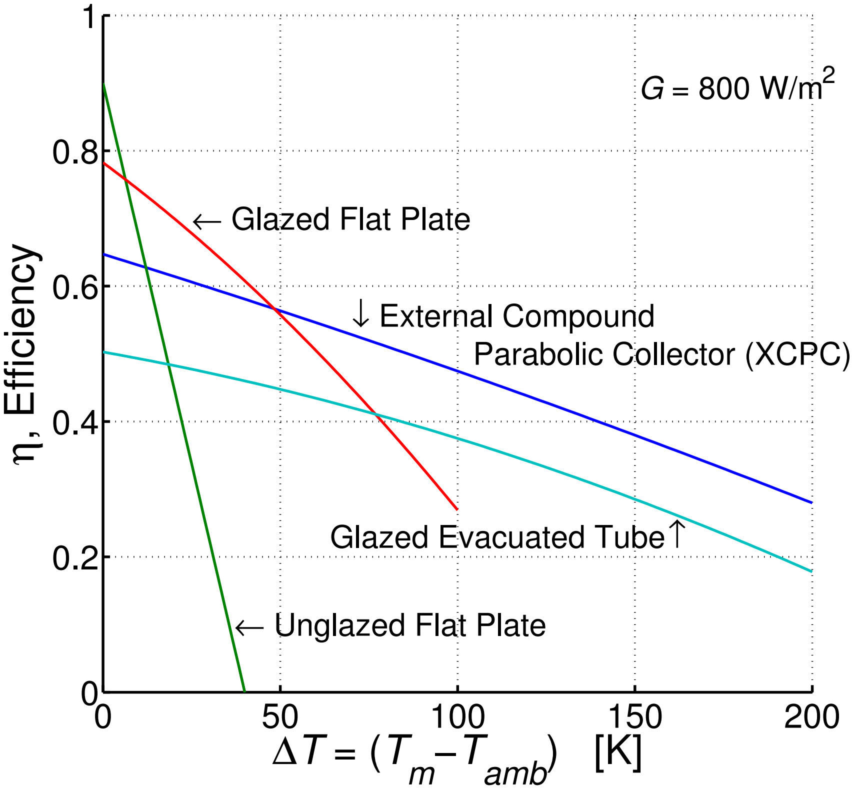

Figure 11.2: XCPC compared to lower temperature collectors.

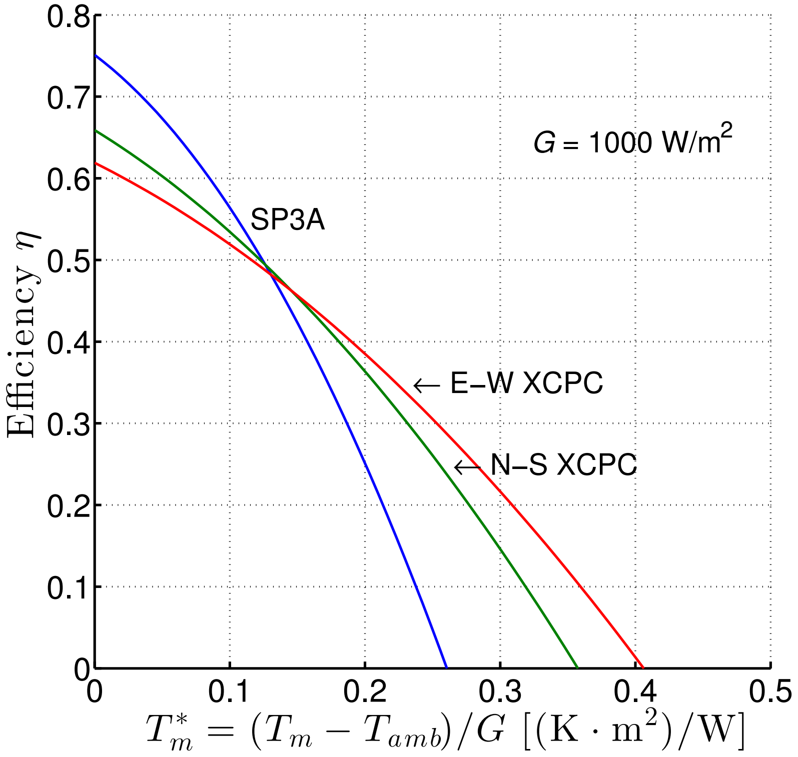

Figure 11.3: Thermal performance of selected STC.

ment is that T_H is in the range of 100–300°C (373–573 K). Assuming that T_L is 2°C (275 K) results in T_m ranging from 325–425 K depending on the assumed T_L. For this engineering case, T_m is tested over the range 325–525 K. This choice was selected to exceed the range given in Kim et al. 2013. This engineering-use case does not necessarily correspond to a specific social-use case, although a social-use case that required a constant high temperature and returned a constant low temperature is a special case of this engineering-use case. The net efficiency is evaluated at $T_m = \frac{500\text{ K}+300\text{ K}}{2} = 400$ K.

11.2.2 High temperature constant

The next engineering-use case is to assume a constant high temperature and allow the low temperature to be a fixed difference from ambient temperature (Equation 11.8). This resembles any case in which the supplied heat is used at a specific temperature and returned through an air-cooled heat exchanger. This engineering-use case could resemble many residential, commercial, and industrial processes. The assumption that T_L has a fixed difference between the ambient temperature is an approximation of reality because how close an air-cooled heat exchanger returns the working fluid to the air temperature depends on the fixed design of the heat exchanger and the instantaneous thermal load. Using a similar methodology as the previous section, the range 375 K $\leq T_H \leq$ 575 K is selected. C_2 is set to an arbitrary value of 10 K, which represents a best-case assumption for average heat exchanger performance. Here, the smaller C_2 is assumed to be, the larger and more expensive the heat exchanger.

$$T_H = C_1 \tag{11.8a}$$

$$T_L = T_{amb} + C_2 \tag{11.8b}$$

$$C_1 \geq \max|T_{amb}| + 10 \text{ K} \tag{11.8c}$$

11.2.3 Temperature difference constant

The next engineering-use case is constant temperature difference (Equations 11.9). This engineering-use case represents several social-use cases, such as a cooling process. It also represents the social-use case when an STC supplies heat to heat engines. Note that applying the equations this way includes a contradiction, namely that T_m has been presented as heating a single-phase fluid. For some of the applications mentioned, heating is often a two-phase flow process. For this work, the contradiction is neglected and resolving it is left as future work. Using a similar methodology as the first engineering-use case, the maximum possible ambient temperature is about 325 K for a location, as a result T_L will be 335 K maximum. Using the maximum of the intended design range of 575 K, this results in C_3 maximum being about 235 K. Selecting a maximum of 300 K is a reasonable choice because some locations will have a lower maximum ambient temperature. For the lower limit of the range of C_3, it is reasonable that one would want to produce at least a 25 K temperature difference; therefore, the range 25 K $\leq C_3 \leq$ 300 K is selected.

$$\Delta T = T_H - T_L = C_3 \tag{11.9a}$$

$$T_L = T_{amb} + C_4 \tag{11.9b}$$

$$T_H = C_3 + C_4 + T_{amb} \tag{11.9c}$$

$$T_H \geq \max|T_{amb}| + 25 + 10 \text{ K} \tag{11.9d}$$

Table 11.1: Selected sites in the TMY2 dataset

Name	ID	Φ [°]	k_t	E^*_{POAI} §
Miami, FL	12839	25.8	0.4901	1.9149
Brownsville, TX	12919	25.9	0.4704	1.8296
Austin, TX	13958	30.3	0.5002	1.9454
Seattle, WA	24233	47.4	0.3988	1.4069
Fresno, CA	93193	36.7	0.5598	2.1249

§ [MWh/(m^2·year)]

Table 11.2: Selected sites in the TMY3 dataset

Name	ID	Φ [°]	k_t	E^*_{POAI} §
Key West Intl Arpt, FL	722010	24.55	0.5219	2.0192
College Station, TX	722445	30.58	0.5430	1.6568
Seattle-Tacoma Intl, WA	727930	47.46	0.4597	1.3783
Merced, CA	724815	37.28	0.6032	2.0573
Shemya AFB, AK	704140	52.71	0.3573	0.4265

§ [MWh/(m^2·year)]

11.3 Results and Discussion

To evaluate the optimal mounting angle based on annual energy yield and exploring the locations and conditions under which the E–W XCPC design produces more energy than the N–W design, five locations in each of the TMY2 and TMY3 datasets were chosen (Tables 11.1 and 11.2). For each of the three engineering-use cases considered, there are two figures for each location; therefore, 20 figures were reviewed for each engineering-use case. Results are also quite consistent from site to site. In the next subsections for each engineering-use case, to be concise and informative, a smaller subset of figures are presented that show the most extreme differences.

11.3.1 Mean fluid temperature constant

Of the 10 locations reviewed, Fresno, CA, has the highest thermal energy yields consistent with POAI, even though it was the location with the second highest annual clearness index k_t (Figure 11.4). There is an overall trend that increases in latitude tended to decrease energy yield and increases in the annual clearness index tended to increase energy yield; however, there are notable exceptions to these trends, Fresno, CA, being one of them. Miami, FL, has the smallest area where the E–W XCPC design produced more thermal energy (Figure 11.5). Figure 11.6 shows Austin, TX, was somewhat typical, although it was the location with the lowest difference between the two optimal mounting angles (based on G_{eff} and thermal energy yield). Figure 11.7 shows Shemya, AK, which has the lowest thermal energy yields, largest difference in optimal mounting angles, and the largest region in which the E–W XCPC performed better on an energy yield basis. The other locations reviewed showed similar results. All locations reviewed showed: (1) minor changes in mounting angle (±5°) resulted in very small changes to energy yield near the optimal mounting angle, (2) considering thermal performance in addition to optical performance had at most minor changes to the optimal mounting angle, (3) the crossover point when the E–W XCPC performs better depends on location, mounting angle, and operating conditions. Tables 11.3 and 11.4 show the net efficiency for the 10 locations under review. Using the new form for G_{eff} and new definition for η_{net} to review the efficiency on an annual basis, shows that one cannot expect instantaneous thermal efficiency to represent average annual net efficiency. Secondly, in practice, the crossover point where a particular collector design has dominant performance shifts to higher operating temperatures. The next subsection where T_H is assumed to be constant provides a more direct comparison to the Kim et al. 2013 results.

11.3.2 High-temperature constant

Selecting the assumed operating condition based on T_H provides results that conceptually consistent with those for the previous subsection where the operating

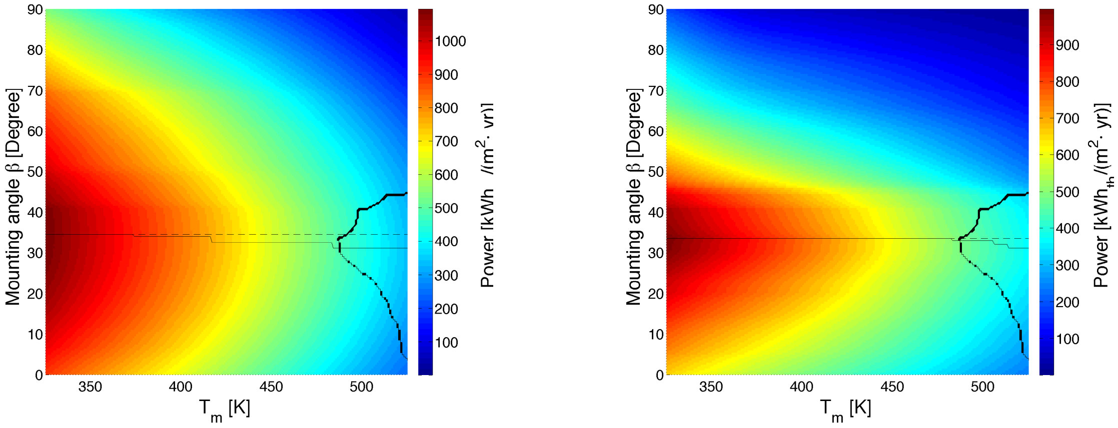

(a) N–S XCPC performance.

(b) E–W XCPC performance.

Figure 11.4: T_m constant, Fresno, CA: Annual energy yield per unit area of collector. Constant dashed line denotes β^* based on G_{eff}, Solid line denotes β^* based on E. If present, region enclosed in black perimeter denotes where the E–W XCPC design yields more energy than the N–S XCPC design.

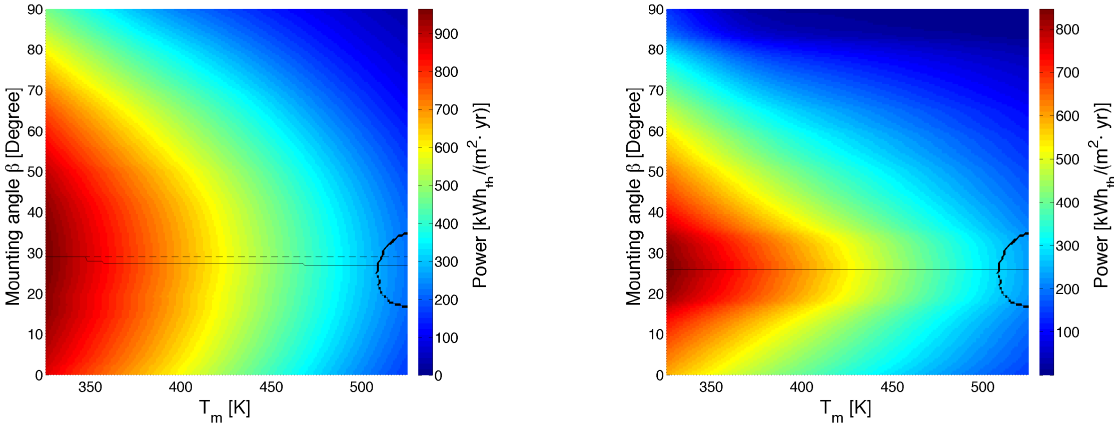

(a) N–S XCPC performance.

(b) E–W XCPC performance.

Figure 11.5: T_m constant, Miami, FL: Annual energy yield per unit area of collector. Constant dashed line denotes β^* based on G_{eff}, Solid line denotes β^* based on E. If present, region enclosed in black perimeter denotes where the E–W XCPC design yields more energy than the N–S XCPC design.

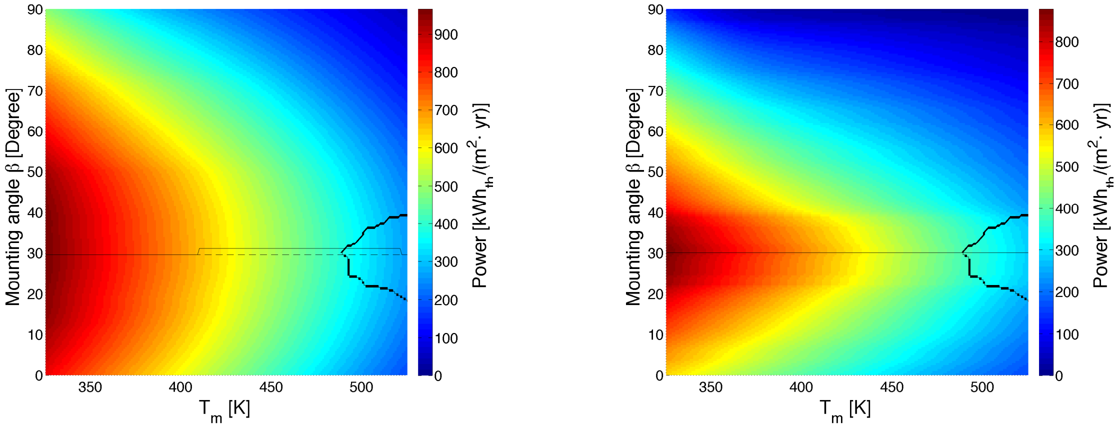

(a) N–S XCPC performance.

(b) E–W XCPC performance.

Figure 11.6: T_m constant, Austin, TX: Annual energy yield per unit area of collector. Constant dashed line denotes β^* based on G_{eff}, Solid line denotes β^* based on E. If present, region enclosed in black perimeter denotes where the E–W XCPC design yields more energy than the N–S XCPC design.

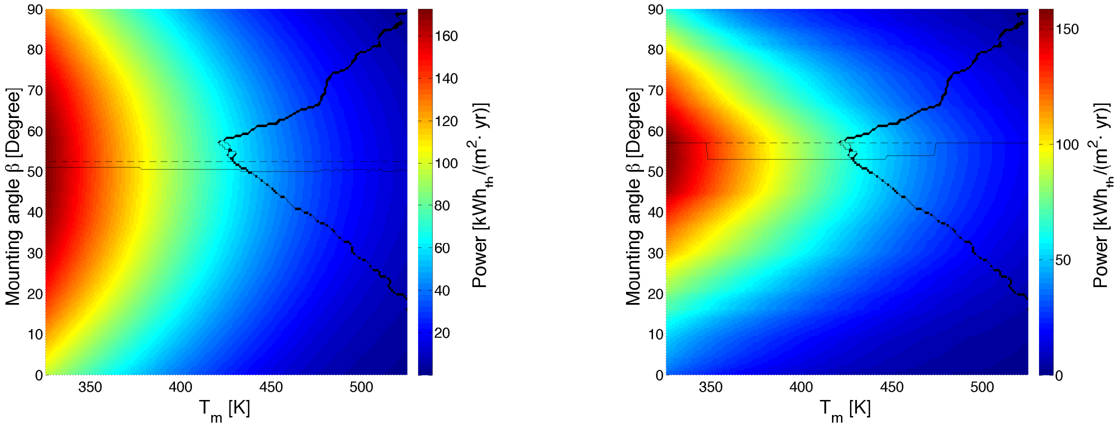

(a) N–S XCPC performance.

(b) E–W XCPC performance.

Figure 11.7: T_m constant, Shemya Air Force Base, AK: Annual energy yield per unit area of collector. Constant dashed line denotes β^* based on G_{eff}, Solid line denotes β^* based on E. If present, region enclosed in black perimeter denotes where the E–W XCPC design yields more energy than the N–S XCPC design.

Table 11.3: Net efficiency (at $T_M = 400$ K and β^*) for selected sites in the TMY2 dataset

Name	ID	Φ [°]	k_t	η_{net} N–S	η_{net} E–W
Miami, FL	12839	25.8	0.4901	35.4	31.6
Brownsville, TX	12919	25.9	0.4704	34.2	30.9
Austin, TX	13958	30.3	0.5002	35.5	33.0
Seattle, WA	24233	47.4	0.3988	31.3	28.6
Fresno, CA	93193	36.7	0.5598	38.8	35.8

Table 11.4: Net efficiency (at $T_M = 400$ K and β^*) for selected sites in the TMY3 dataset

Name	ID	Φ [°]	k_t	η_{net} N–S	η_{net} E–W
Key West Intl Arpt, FL	722010	24.55	0.5219	37.1	33.6
College Station, TX	722445	30.58	0.5430	36.8	33.4
Seattle-Tacoma Intl, WA	727930	47.46	0.4597	32.9	30.2
Merced, CA	724815	37.28	0.6032	39.5	36.6
Shemya AFB, AK	704140	52.71	0.3573	20.4	19.4

condition assumption was T_m constant. Although which site had the larges or smallest characteristic varied a little, the major change is that the domain of tested T_H values was increased to 775 K to observe the crossover where the E–W XCPC producing more energy for all locations under review. For consistency, results for the same four locations are given in Figures 11.8 to 11.11. The net annual efficiency based on POAI for the Fresno, CA, location is shown in Figure 11.12.

Table 11.5: Net efficiency (at $T_H = 500$ K and β^*) for selected sites in the TMY2 dataset

Name	ID	Φ [°]	k_t	η_{net} N–S	η_{net} E–W
Miami, FL	12839	25.8	0.4901	34.6	30.9
Brownsville, TX	12919	25.9	0.4704	33.4	30.3
Austin, TX	13958	30.3	0.5002	35.0	32.5
Seattle, WA	24233	47.4	0.3988	31.5	28.7
Fresno, CA	93193	36.7	0.5598	38.4	35.4

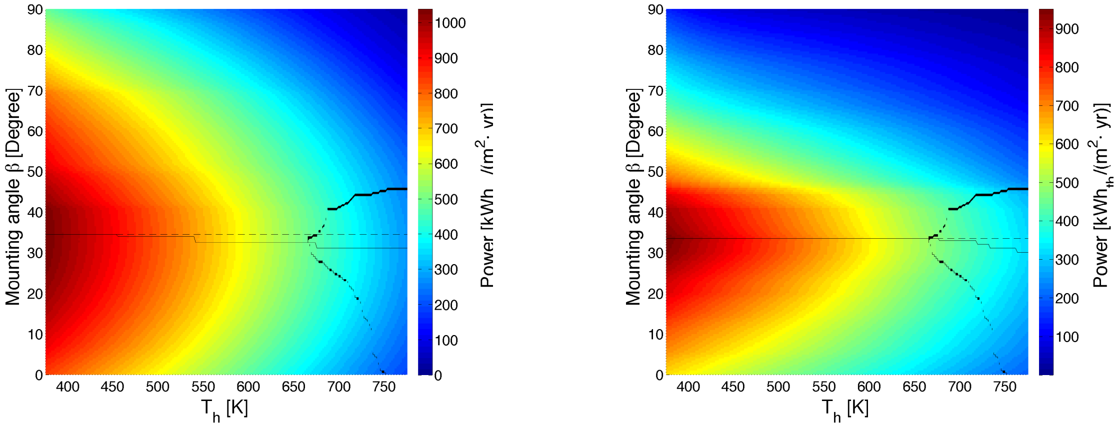

(a) N–S XCPC performance.

(b) E–W XCPC performance.

Figure 11.8: T_H constant, Fresno, CA: Annual energy yield per unit area of collector. Constant dashed line denotes β^* based on G_{eff}, Solid line denotes β^* based on E. If present, region enclosed in black perimeter denotes where the E–W XCPC design yields more energy than the N–S XCPC design.

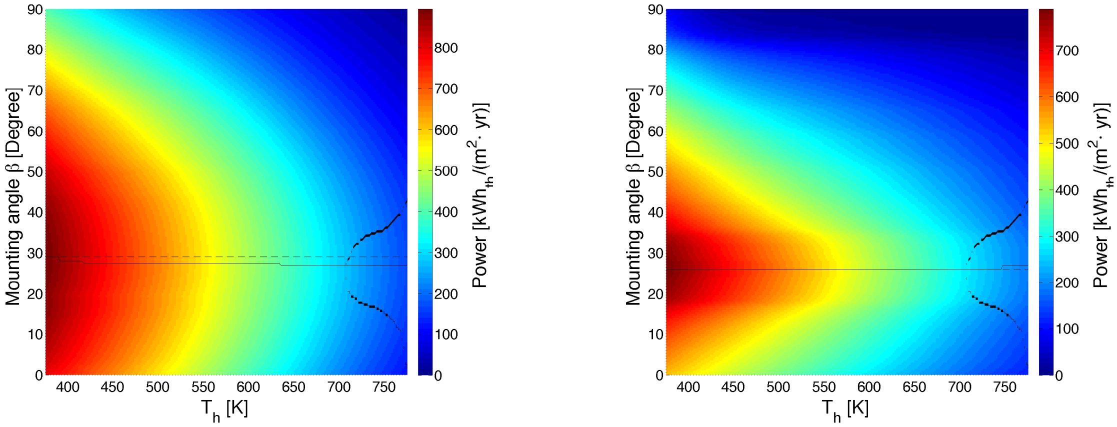

(a) N–S XCPC performance.

(b) E–W XCPC performance.

Figure 11.9: T_H constant, Miami, FL: Annual energy yield per unit area of collector. Constant dashed line denotes β^* based on G_{eff}, Solid line denotes β^* based on E. If present, region enclosed in black perimeter denotes where the E–W XCPC design yields more energy than the N–S XCPC design.

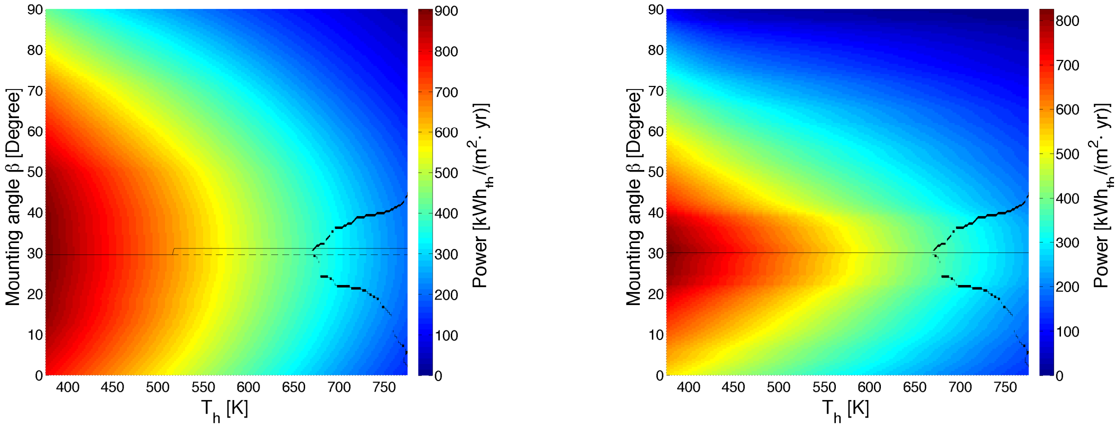

(a) N–S XCPC performance.

(b) E–W XCPC performance.

Figure 11.10: T_H constant, Austin, TX: Annual energy yield per unit area of collector. Constant dashed line denotes β^* based on G_{eff}, Solid line denotes β^* based on E. If present, region enclosed in black perimeter denotes where the E–W XCPC design yields more energy than the N–S XCPC design.

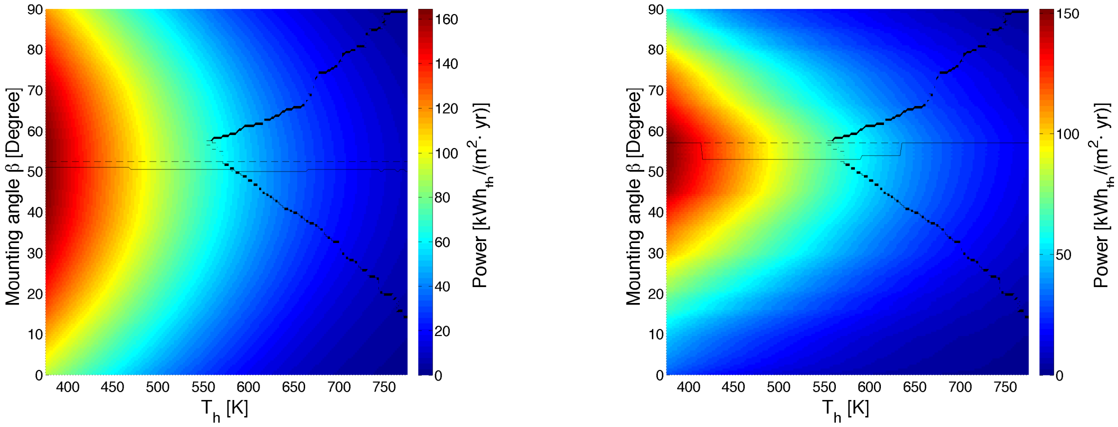

(a) N–S XCPC performance.

(b) E–W XCPC performance.

Figure 11.11: T_H constant, Shemya, AK: Annual energy yield per unit area of collector. Constant dashed line denotes β^* based on G_{eff}, Solid line denotes β^* based on E. If present, region enclosed in black perimeter denotes where the E–W XCPC design yields more energy than the N–S XCPC design.

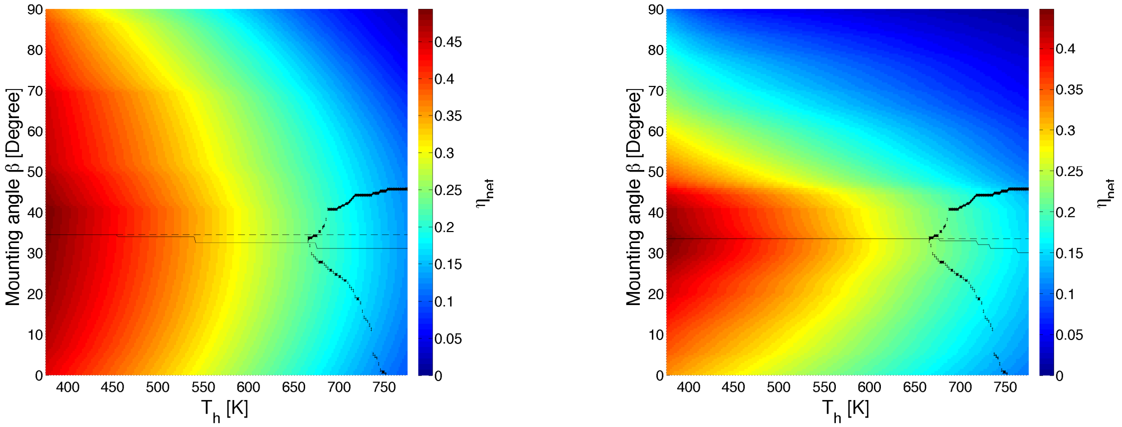

(a) N–S XCPC performance.

(b) E–W XCPC performance.

Figure 11.12: T_H constant, Fresno, CA: Net efficiency. Constant dashed line denotes β^* based on G_{eff}, Solid line denotes β^* based on E. If present, region enclosed in black perimeter denotes where the E–W XCPC design yields more energy than the N–S XCPC design.

Table 11.6: Net efficiency (at $T_H = 500$ K and β^*) for selected sites in the TMY3 dataset

Name	ID	Φ [°]	k_t	η_{net} N–S	η_{net} E–W
Key West Intl Arpt, FL	722010	24.55	0.5219	36.2	32.8
College Station, TX	722445	30.58	0.5430	36.2	33.0
Seattle-Tacoma Intl, WA	727930	47.46	0.4597	33.1	30.4
Merced, CA	724815	37.28	0.6032	39.0	36.2
Shemya AFB, AK	704140	52.71	0.3573	21.9	20.7

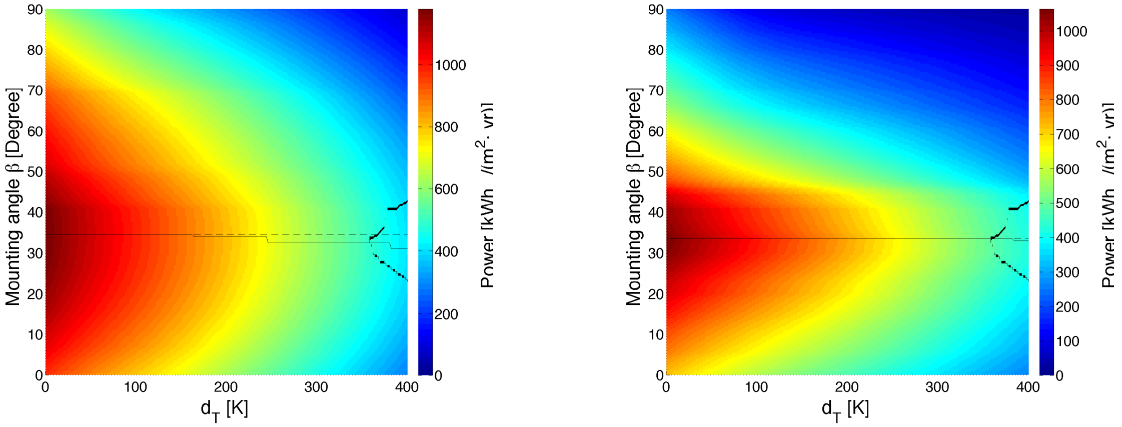

(a) N–S XCPC performance.

(b) E–W XCPC performance.

Figure 11.13: ΔT constant, Fresno, CA: Annual energy yield per unit area of collector. Constant dashed line denotes β^* based on G_{eff}, Solid line denotes β^* based on E. If present, region enclosed in black perimeter denotes where the E–W XCPC design yields more energy than the N–S XCPC design.

11.3.3 Temperature difference constant

Assuming the temperature difference ($\Delta T = T_H - T_L$) is a constant did not materially change collector performance (Figures 11.13 to 11.17). Using the assumption that a 200 K temperature difference approximates a 200°C T_H, efficiency values are given in Tables 11.7 and 11.8.

Table 11.7: Net efficiency (at ΔT = 200 K and β^*) for selected sites in the TMY2 dataset

Name	ID	Φ [°]	k_t	η_{net} N–S	η_{net} E–W
Miami, FL	12839	25.8	0.4901	33.5	30.0
Brownsville, TX	12919	25.9	0.4704	32.3	29.4
Austin, TX	13958	30.3	0.5002	34.2	31.8
Seattle, WA	24233	47.4	0.3988	31.5	28.7
Fresno, CA	93193	36.7	0.5598	37.7	34.9

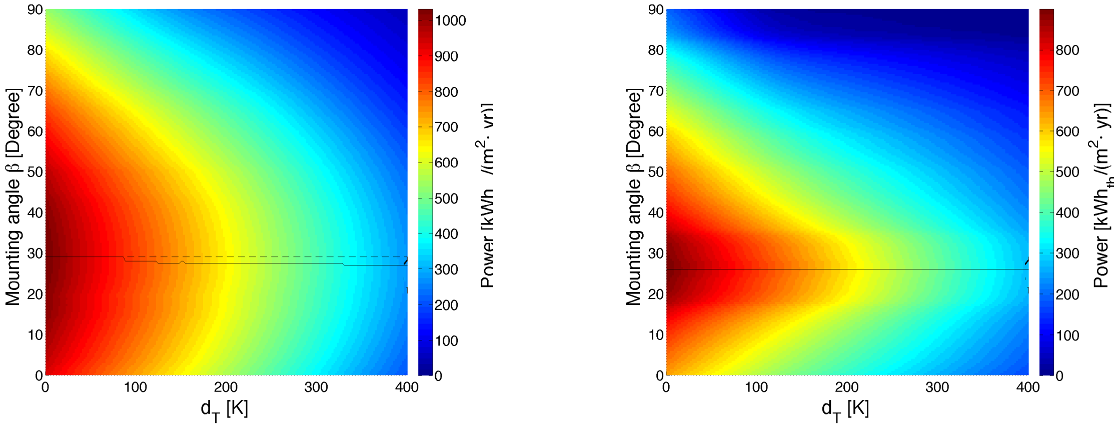

(a) N–S XCPC performance.

(b) E–W XCPC performance.

Figure 11.14: ΔT constant, Miami, FL: Annual energy yield per unit area of collector. Constant dashed line denotes β^* based on G_{eff}, Solid line denotes β^* based on E. If present, region enclosed in black perimeter denotes where the E–W XCPC design yields more energy than the N–S XCPC design.

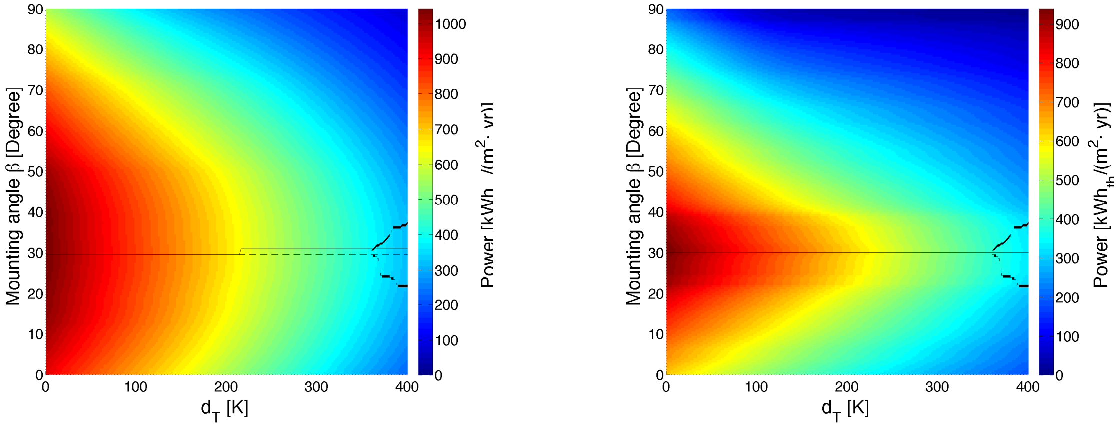

(a) N–S XCPC performance.

(b) E–W XCPC performance.

Figure 11.15: ΔT constant, Austin, TX: Annual energy yield per unit area of collector. Constant dashed line denotes β^* based on G_{eff}, Solid line denotes β^* based on E. If present, region enclosed in black perimeter denotes where the E–W XCPC design yields more energy than the N–S XCPC design.

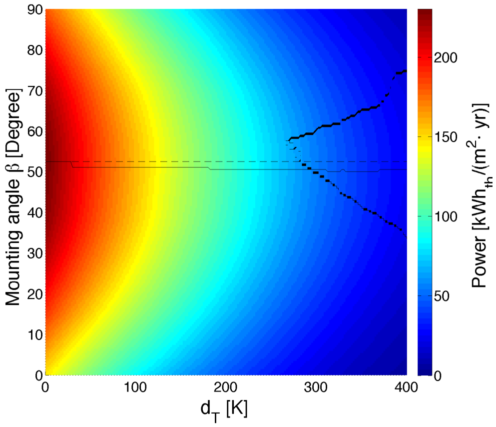

(a) N–S XCPC performance.

(b) E–W XCPC performance.

Figure 11.16: ΔT constant, Shemya, AK: Annual energy yield per unit area of collector. Constant dashed line denotes β^* based on G_{eff}, Solid line denotes β^* based on E. If present, region enclosed in black perimeter denotes where the E–W XCPC design yields more energy than the N–S XCPC design.

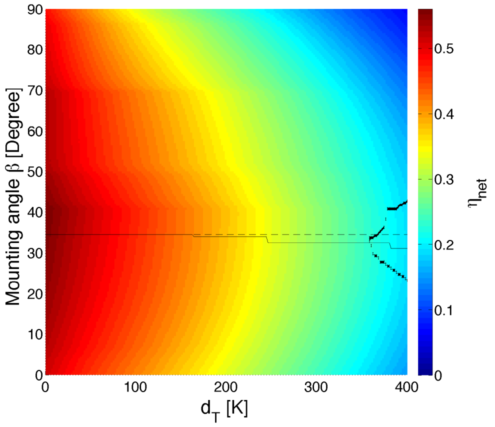

(a) N–S XCPC performance.

(b) E–W XCPC performance.

Figure 11.17: ΔT constant, Fresno, CA: Net efficiency. Constant dashed line denotes β^* based on G_{eff}, Solid line denotes β^* based on E. If present, region enclosed in black perimeter denotes where the E–W XCPC design yields more energy than the N–S XCPC design.

Table 11.8: Net efficiency (at $\Delta T = 200$ K and β^*) for selected sites in the TMY3 dataset

Name	ID	Φ [°]	k_t	η_{net} N–S	η_{net} E–W
Key West Intl Arpt, FL	722010	24.55	0.5219	35.1	32.0
College Station, TX	722445	30.58	0.5430	35.4	32.3
Seattle-Tacoma Intl, WA	727930	47.46	0.4597	33.2	30.4
Merced, CA	724815	37.28	0.6032	38.3	35.6
Shemya AFB, AK	704140	52.71	0.3573	23.3	21.9

11.4 Conclusions and summary

Although the various engineering-use cases have varying performance, the overall results are generally very similar. This means that one can use back-of-the-envelope methods to approximate annual energy yield. Should the system designer require higher accuracy for a specific location, a formal analysis can be completed using the methods demonstrated in this work. The results have clearly shown several key findings:

1. Accounting for both the thermal performance and optical performance is the key to determining energy yield for the XCPC designs.
2. The assertion by Kim et al. 2013 that 165°C is the temperature where the E–W XCPC is more efficient neglects how the concentration ratio reduces G_{eff}. In reality, the temperature where crossover happens varies with location.
3. For the majority of locations in the TMY datasets and the range 100–300°C, the N–S XCPC has higher energy yields and greater η_{net}.
4. For the use cases considered, β^* was observed to have small changes when moving from irradiance to thermal energy yield.
5. Small changes in mounting angle resulted in very small changes in energy yield

near the optimal mounting angle consistent with results based on irradiance from the previous chapter.

The methods used in this work and the resulting findings are the original work of this author.

11.5 Future work

Improving the modeling values that determine XCPC performance and experimentally validating them would improve simulation accuracy. Exploring the possibility of a simple correlation to approximate energy yield from POAI by adjusting for latitude and climate may reduce the costs of design feasibility studies at early stages of project development.

12. EXPLORING THE XCPC SOLAR-THERMAL COLLECTOR PERFORMANCE SPACE: DRIVING A HEAT ENGINE

12.1 Introduction/background

In Chapter 10, optimal mounting angle was discussed from the viewpoint of irradiance. In Chapter 11, thermal performance of the XCPC designs were explored and the impact of considering both the optical and thermal performance on optimal mounting angle. As previously metioned in Chapter 3, there is a long history of using sunlight to drive machinery starting with Auguste Mouchot in 1860 [13]. The Winston research group at the University of California Merced has furthered this history by creating the XCPC designs and used them to drive an absorption chiller to cool an office space [131–139]. The current chapter focuses squarely on exploring XCPC performance when installed as part of a heat engine. As metioned in Norwood et al. 2006 [34], there is a significant benifit to using one set of collectors—as opposed to have both STC and PV collectors—to provide both the various thermal loads of a building and the electrical loads. This allows for more cost-effective use of the collectors on an annual basis. Electricity production using the XCPC designs has not been explored in the literature using an hourly solar simulation or a solar simulation that properly accounts for the angular distribution of the diffuse irradiance. Modeling the performance of a heat engine driven by a STC under real-world conditions has an immense amount of complexity in both the solar model and the heat engine model. It is very rare for a single work to address both areas in detail because two diverse skill sets are required. This task is one of the expressed goals of the dissertation, and it is divided into smaller pieces:

1. In Chapters 6–9 a detailed solar simulation is constructed.

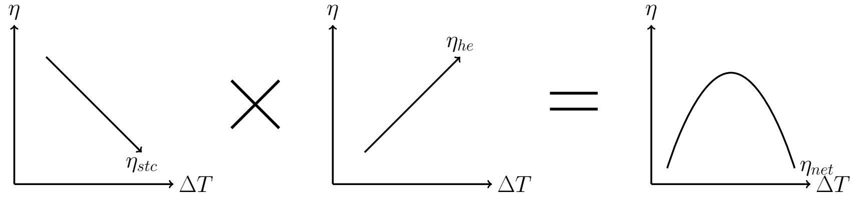

Figure 12.1: Net efficiency of a solar thermal powered heat engine.

2. In this chapter, an oversimplified general performance model will be combined with the solar thermal simulation, which will provide an environment to explore and learn the fundamental principles that govern system performance.
3. In Part IV, a detailed analysis of the thermal-fluid aspects are explored.
4. In Part V, component considerations are evaluated. For now, the discussion will proceed without a specific fluid, thermodynamic cycle, or system components in mind (save the collector).

12.2 Methodology

There is one central principle that informs the basis of the methods used in this chapter. Simply stated, there is a temperature difference that maximizes the performance (annual energy production) of a system consisting of a STC combined with a heat engine. Winters et al. 1991 [159] emphasize this principle for large-scale STC power plants. Here, it is applied to XCPC designs for distributed applications. The logic is simple, tried, and true. A decreasing function (efficiency as a function of temperature i.e., an STC) times an increasing function of similar magnitude (efficiency as a function of temperature i.e., a heat engine) results in an upside-down parabolic that has a maximum efficiency at some temperature (Figure 12.1).

Chapter 8 showed that the efficiency of a STC is not a curve; rather, it is a performance surface depending on the mean temperature difference ($T_m - T_{amb} = \frac{T_H+T_L}{2} - T_{amb}$) and the effective irradiance (G_{eff}) incident on the collector. Another reference frame in which to view temperature difference ($\Delta T = T_H - T_L$) relates to how the heat imparted into the working fluid is calculated. Because of Equation 12.1, it requires a particular mass flow rate ($\dot{m}$). This means that the temperature difference that maximizes system efficiency can be viewed in several ways. It is necessary to be careful in the choice of simplification to reduce the graphical presentation of the design space from six dimensions ($\eta = f(\beta, T_{amb}, T_L, T_H, G_{eff})$) to three dimensions ($\eta = f(\beta, \Delta T)$). Here, it is assumed that $T_L = T_{amb} + 10$ K will naturally reduce one of the dimensions as a simple condenser model. The two other dimensional reductions come from treating T_{amb} and G_{eff} as givens for a location. The root issue is that the temperature difference is the independent variable and the mean temperature is a dependent variable. Using $\Delta T = T_H - T_L$ sets T_H and defines the temperature difference; therefore, setting T_m as a result or the reverse. For simplicity, here T_H will be set as a value above T_L, and T_m is determined as a result of this choice. How and when the temperature difference is determined can vary. Two common methods follow: (1) a fixed temperature difference that does not change with changing environmental conditions for a fixed location, and (2) a variable temperature difference that changes with each data point for a fixed location in the TMY dataset. Both design options will be reviewed in this work.

$$\dot{Q} = \dot{m} C_p (T_H - T_L) \tag{12.1}$$

There are several goals in this study:

1. Observe how the optimal mounting angle changes when accounting for heat engine performance.

2. Explore how the addition of a heat engine impacts energy yield.
3. Approximate the constant operating temperature difference that will maximize system efficiency via design space exploration.
4. Test how energy yield is impacted under varying operating temperature difference while observing the distribution of optimal temperature differences over the typical operating year.
5. Confirm if one XCPC design clearly performs better on an annual energy yield basis.
6. Confirm the operating temperatures are within the operating temperature range of the XCPC designs.

12.2.1 Solar simulation with fixed temperature difference

Equations 12.2 define how the temperature difference (ΔT) is related to thermal operating parameters introduced in previous chapters. Here, the focus in on setting the temperature difference once at the time of design and manufacture. This means that the temperature difference is not adjustable during operation without the penalty of reduced part-load performance of the equipment being operated in an off-design way. Operating the equipment in an off-design way is not considered.

$$\Delta T = T_H - T_L = C_1 \tag{12.2a}$$

$$T_L = T_{amb} + C_2 \tag{12.2b}$$

$$T_H = C_1 + C_2 + T_{amb} \tag{12.2c}$$

$$\Delta T \geq \max |T_{amb}| + 10 \text{ K} \tag{12.2d}$$

12.2.2 Solar simulation with adjustable temperature difference

Equations 12.3 show how the temperature difference can be selected during operation such that energy production is maximized at each data point (hour). Variable temperature difference operations requires an additional constraint because the lowest temperature possible will maximize the heat produced by the STC. The additional constraint is the heat engine performance (Figure 12.1). To achieve variable temperature difference, one would need to design an expander that has variable expansion, which is discussed in more detail in Part IV.

$$T_L = T_{amb} + C \tag{12.3a}$$

$$\Delta T = T_H - T_L = X \tag{12.3b}$$

$$T_H = X + T_{amb} + 10\text{ K} \tag{12.3c}$$

12.2.3 Carnot model of heat engine performance

The simplest possible model of heat engine performance is

$$\eta_{he} = x\left(1 - \frac{T_L}{T_H}\right) \tag{12.4}$$

where x is the assumed second law efficiency typically 0.3–0.5 for large-scale heat engines. Because the goal is to capture the first-order effect of temperature on heat engine performance, x can be treated as constant 1 and later simply multiply the results by a representative assumption for a specific case. Here, by assuming that the STC inlet temperature (T_L) and outlet temperature (T_H) are the heat engine operating temperatures, the system is oversimplified and does not exactly match reality; therefore, the values found in this chapter are an approximation and should not be used in the design of a real-world product. This work is meant as a first look at how performance is affected by adding a heat engine into the solar thermal simulation. Even with the simplest possible heat engine model, the code to perform the calculations for 10 selected sites in the TMY datasets required runs on the ADA cluster at the Texas A&M High Performance Resource Center.

12.2.4 Combined solar and heat engine simulation

Simplify results in Equation 12.7

$$\dot{Q} = \left[\eta_0 G_{eff} - a_1(\frac{T_H + T_L}{2} - T_{amb}) - a_2(\frac{T_H + T_L}{2} - T_{amb})^2\right] A \tag{12.5}$$

$$E = \sum_{\text{annual}} \eta_{he} \dot{Q} \Delta t \tag{12.6}$$

$$E = f(\beta, \Delta T) \tag{12.7}$$

and Equation 12.8

$$\eta_{net} = \frac{\frac{E}{A}}{I_T} \tag{12.8}$$

This oversimplified model of a heat engine driven by a STC does not account for: (1) a real thermodynamic cycle; (2) working fluid; (3) the temperature mismatch between STC and heat engine (i.e., the temperature rise across the pump is neglected); and (4) the possibility of fluid vaporization in the STC, which is outside the scope of the STC performance model. Despite these limitations, this oversimplified model and simulation will illustrate in a simple way several key characteristics and design requirements of a solar-driven heat engine using STC.

12.2.5 Definition of optimization problem for maximizing the annual energy yield with variable temperature difference

Using the oversimplified solar-driven heat engine model from the previous section, one can optimize the temperature difference at each data point (i.e., each hour). Equations 12.9–12.20 define the optimization problem.

$$E^* = \max_{\mathbf{x}} E(\mathbf{x}) \tag{12.9}$$

$$\mathbf{x}^* = \arg\max_{\mathbf{x}} E(\mathbf{x}) \tag{12.10}$$

subject to:

$$0 \leq x_1 \leq 400 \tag{12.11}$$

$$g_1(\mathbf{x}) \leq 0 \tag{12.12}$$

$$g_2(\mathbf{x}) \leq 0 \tag{12.13}$$

where:

$$\mathbf{x} = [x_1]' \tag{12.14}$$

$$E(\mathbf{x}) = f(\beta, \mathbf{x}) \tag{12.15}$$

$$g_1(\mathbf{x}) = -E(\mathbf{x}) \tag{12.16}$$

$$g_2(\mathbf{x}) = -T_m^*(\mathbf{x}) \tag{12.17}$$

$$T_m^*(\mathbf{x}) = \frac{\frac{\Delta T}{2} + 10}{G_{eff}} \tag{12.18}$$

$$x_1 = \Delta T \tag{12.19}$$

$$\beta = [0, 90] \tag{12.20}$$

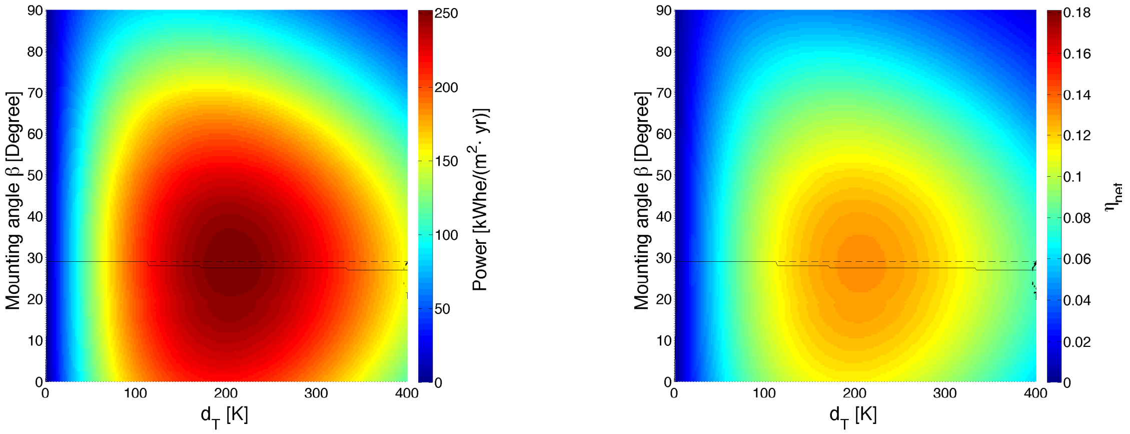

(a) N–S XCPC: annual energy yield per unit area.

(b) N–S XCPC: net efficency based on POAI maximum.

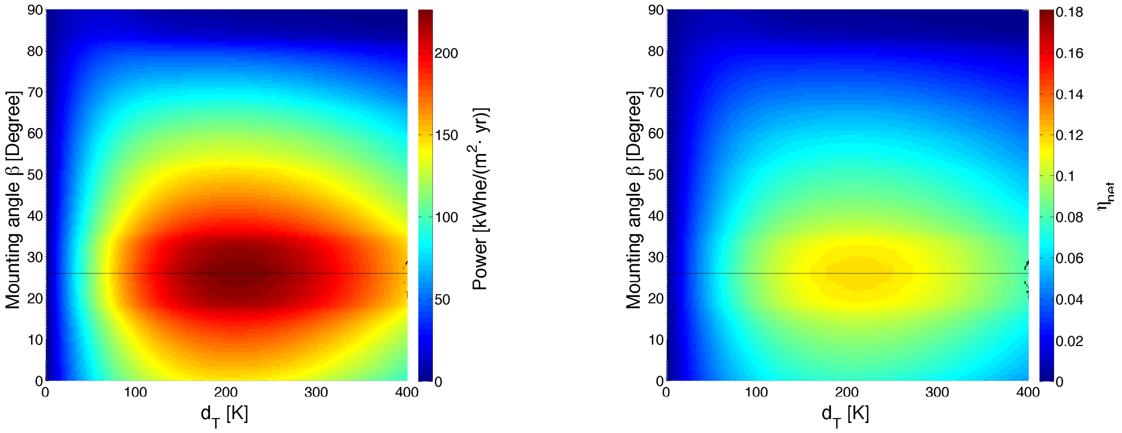

(c) E–W XCPC: annual energy yield per unit area.

(d) E–W XCPC: net efficency based on POAI maximum.

Figure 12.2: Constant temperature difference ORC results for Miami, FL (TMY2). Constant dashed line denotes β^* based on G_{eff}, Solid line denotes β^* based on E. If present, region enclosed in black perimeter denotes where the E–W XCPC design yields more energy than the N–S XCPC design.

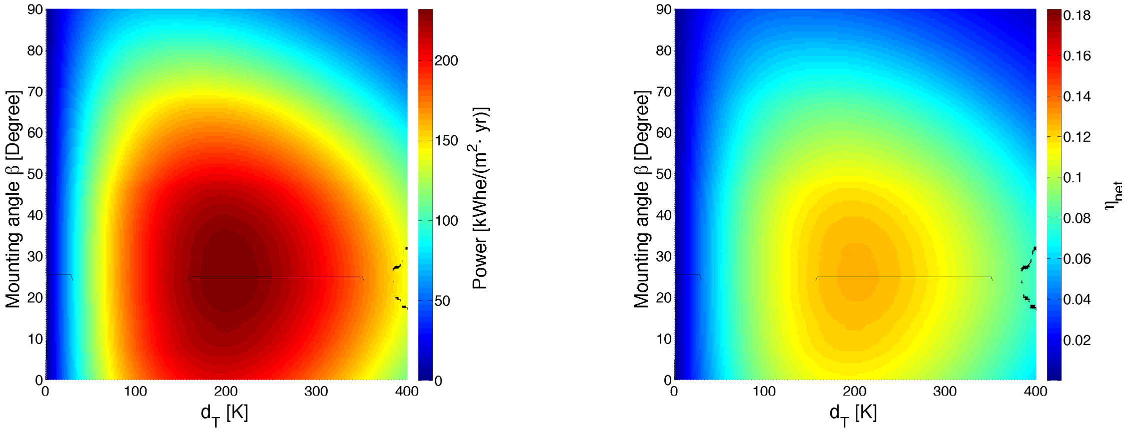

(a) N–S XCPC: annual energy yield per unit area.

(b) N–S XCPC: net efficency based on POAI maximum.

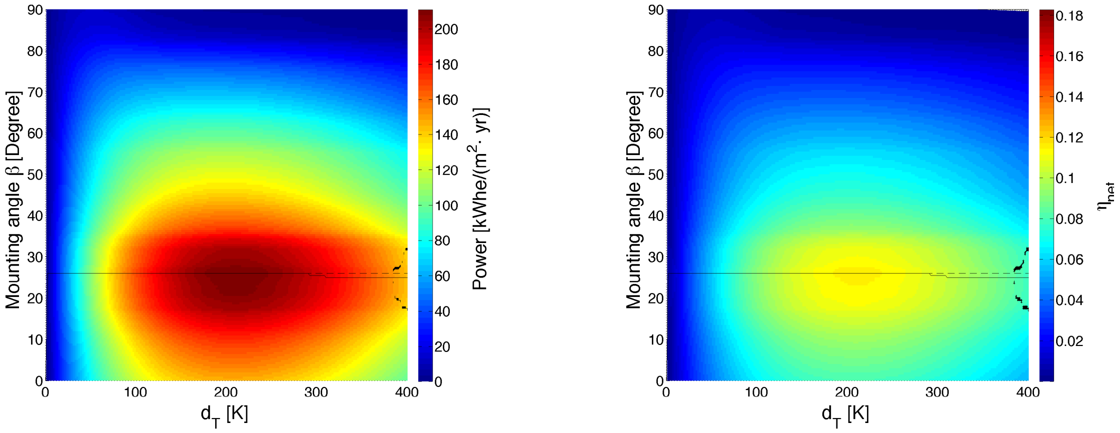

(c) E–W XCPC: annual energy yield per unit area.

(d) E–W XCPC: net efficency based on POAI maximum.

Figure 12.3: Constant temperature difference ORC results for Brownsville, TX (TMY2). Constant dashed line denotes β^* based on G_{eff}, Solid line denotes β^* based on E. If present, region enclosed in black perimeter denotes where the E–W XCPC design yields more energy than the N–S XCPC design.

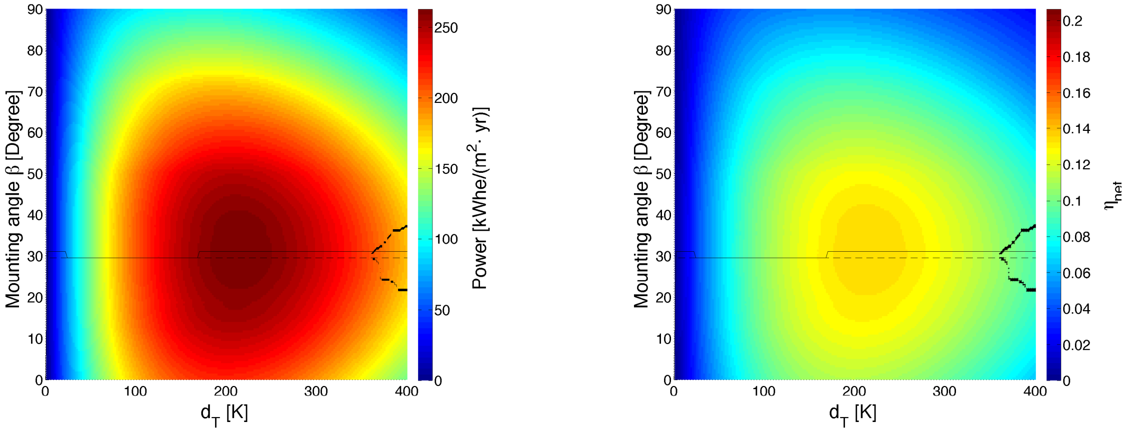

(a) N–S XCPC: annual energy yield per unit area.

(b) N–S XCPC: net efficency based on POAI maximum.

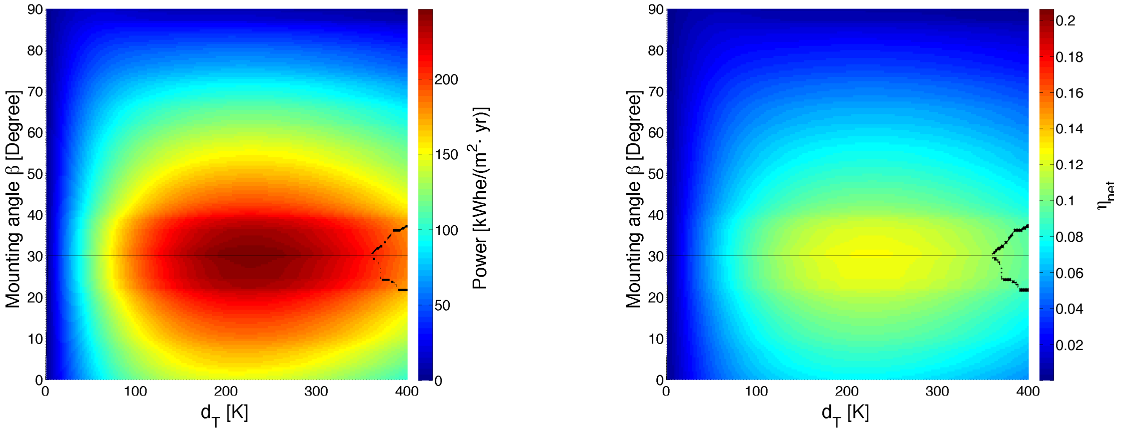

(c) E–W XCPC: annual energy yield per unit area.

(d) E–W XCPC: net efficency based on POAI maximum.

Figure 12.4: Constant temperature difference ORC results for Austin, TX (TMY2). Constant dashed line denotes β^* based on G_{eff}, Solid line denotes β^* based on E. If present, region enclosed in black perimeter denotes where the E–W XCPC design yields more energy than the N–S XCPC design.

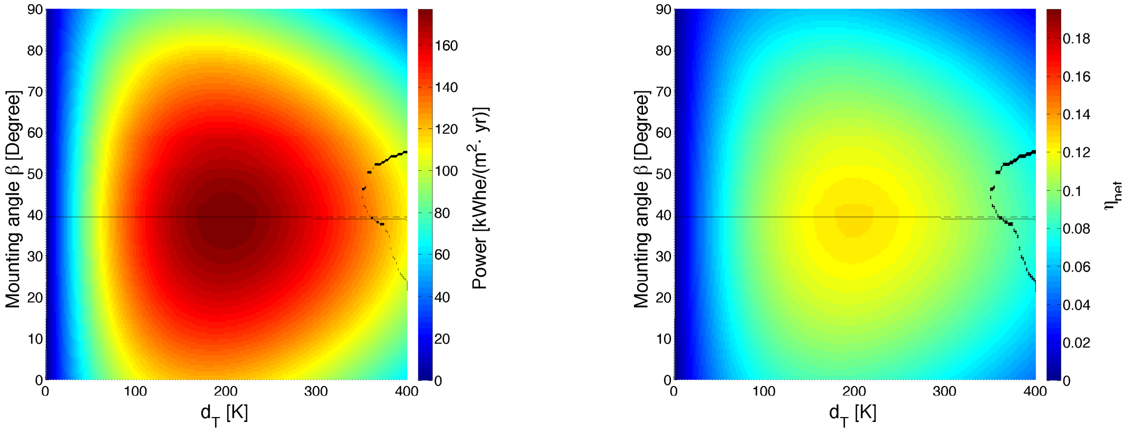

(a) N–S XCPC: annual energy yield per unit area.

(b) N–S XCPC: net efficency based on POAI maximum.

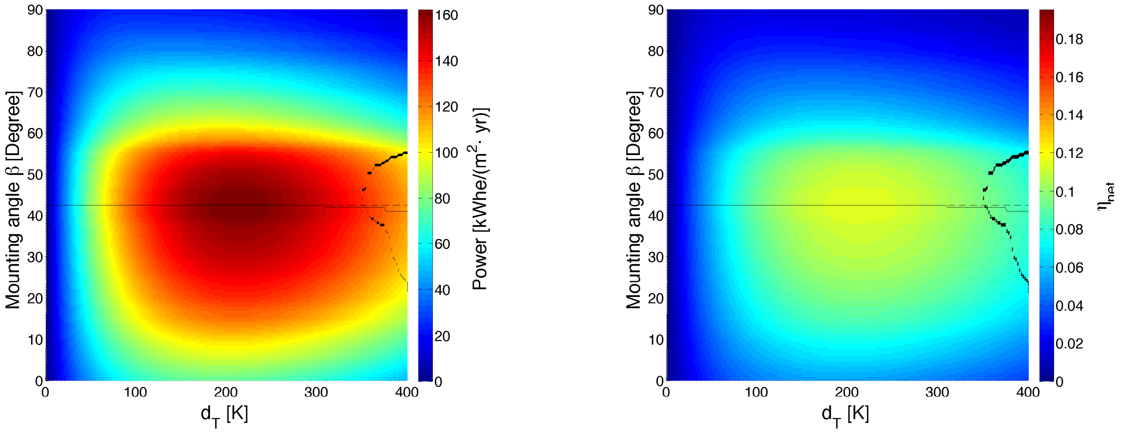

(c) E–W XCPC: annual energy yield per unit area.

(d) E–W XCPC: net efficency based on POAI maximum.

Figure 12.5: Constant temperature difference ORC results for Seattle, WA (TMY2). Constant dashed line denotes β^* based on G_{eff}, Solid line denotes β^* based on E. If present, region enclosed in black perimeter denotes where the E–W XCPC design yields more energy than the N–S XCPC design.

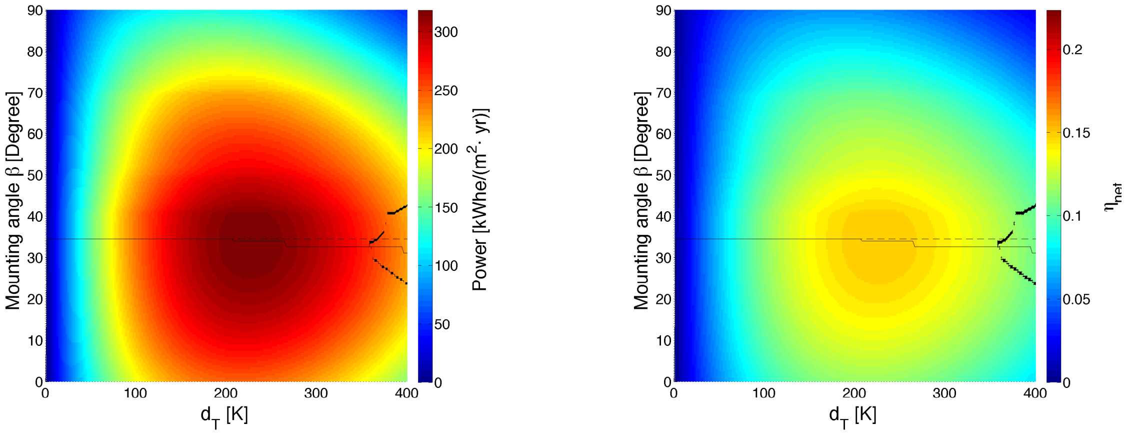

(a) N–S XCPC: annual energy yield per unit area.

(b) N–S XCPC: net efficency based on POAI maximum.

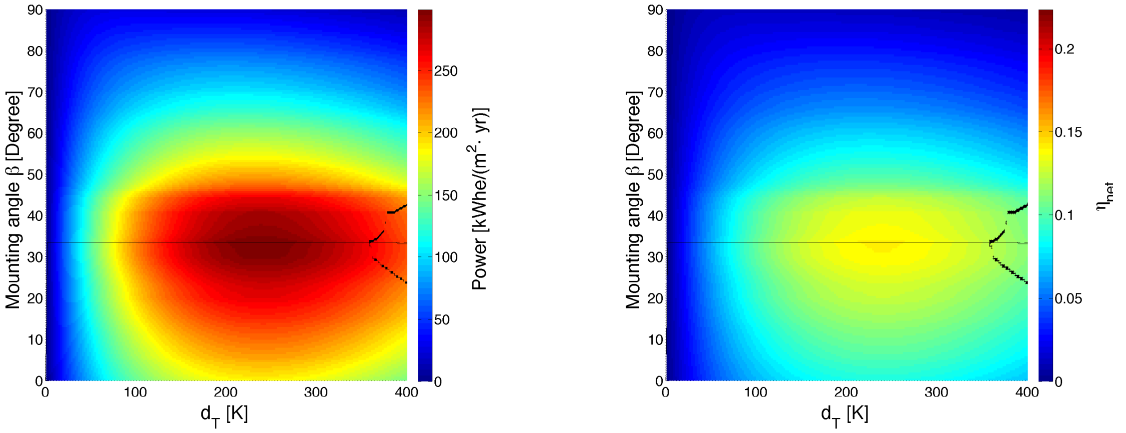

(c) E–W XCPC: annual energy yield per unit area.

(d) E–W XCPC: net efficency based on POAI maximum.

Figure 12.6: Constant temperature difference ORC results for Fresno, CA (TMY2). Constant dashed line denotes β^* based on G_{eff}, Solid line denotes β^* based on E. If present, region enclosed in black perimeter denotes where the E–W XCPC design yields more energy than the N–S XCPC design.

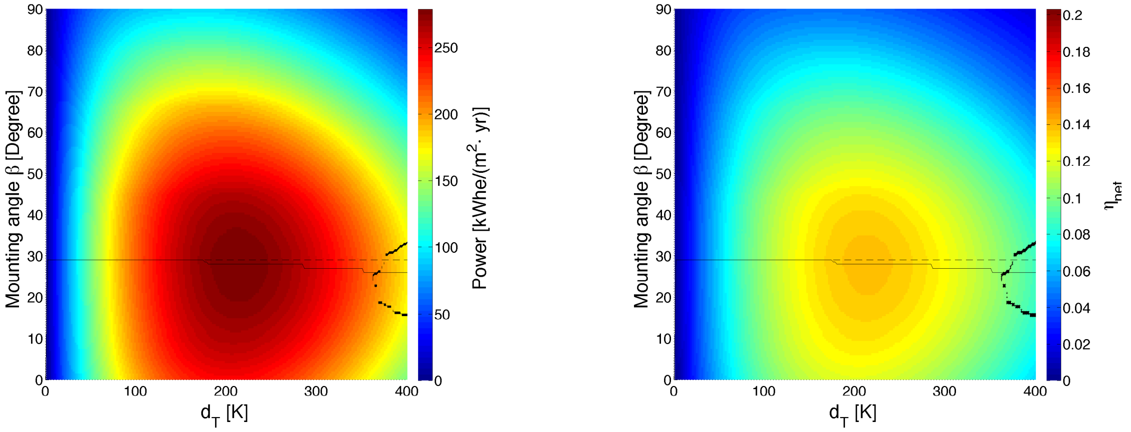

(a) N–S XCPC: annual energy yield per unit area.

(b) N–S XCPC: net efficency based on POAI maximum.

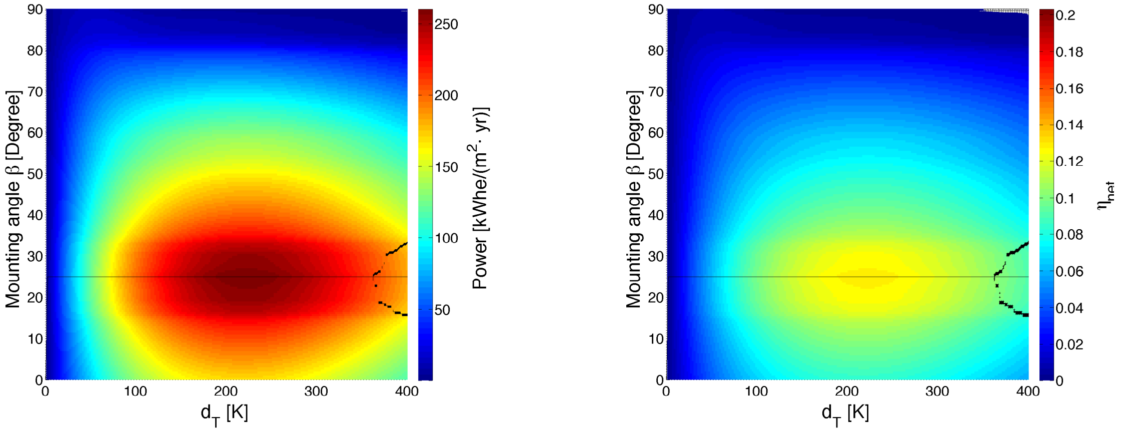

(c) E–W XCPC: annual energy yield per unit area.

(d) E–W XCPC: net efficency based on POAI maximum.

Figure 12.7: Constant temperature difference ORC results for Key West, FL in the TMY3 dataset. Constant dashed line denotes β^* based on G_{eff}, Solid line denotes β^* based on E. If present, region enclosed in black perimeter denotes where the E–W XCPC design yields more energy than the N–S XCPC design.

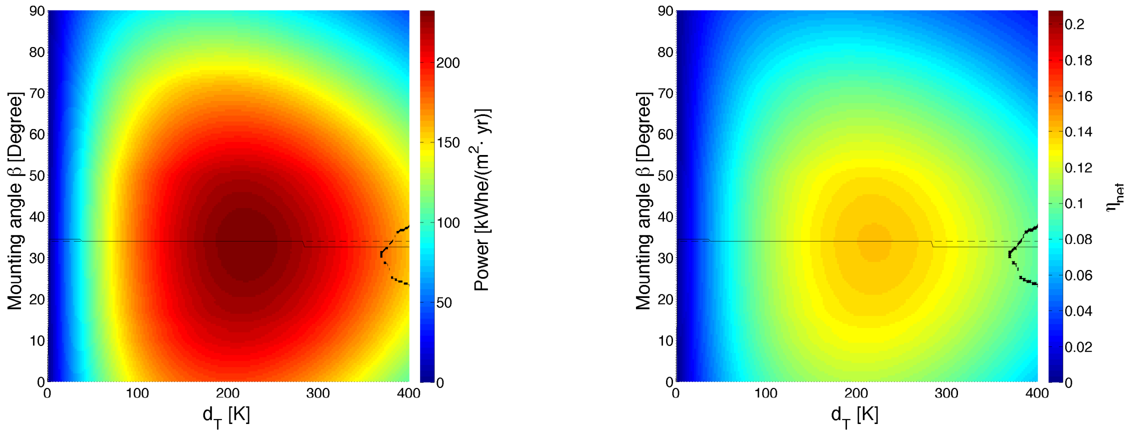

(a) N–S XCPC: annual energy yield per unit area.

(b) N–S XCPC: net efficency based on POAI maximum.

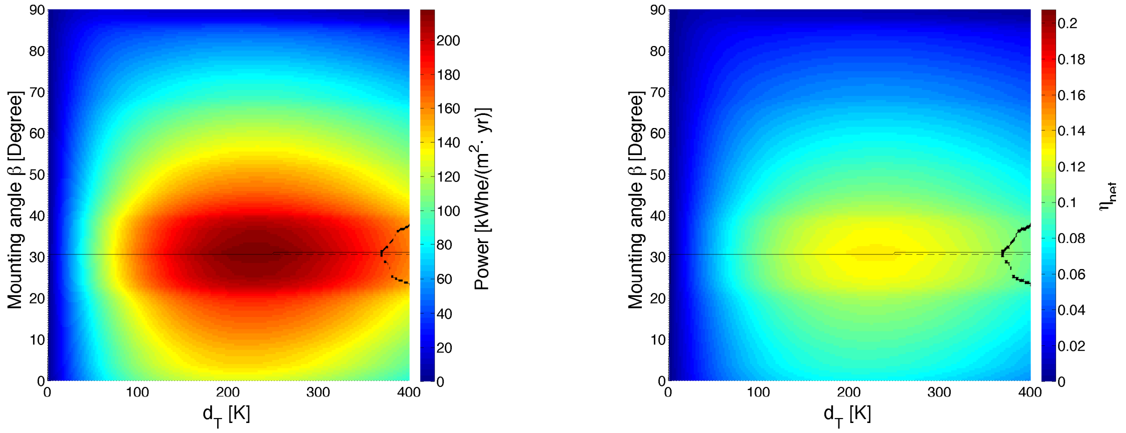

(c) E–W XCPC: annual energy yield per unit area.

(d) E–W XCPC: net efficency based on POAI maximum.

Figure 12.8: Constant temperature difference ORC results for College Station, TX (TMY3). Constant dashed line denotes β^* based on G_{eff}, Solid line denotes β^* based on E. If present, region enclosed in black perimeter denotes where the E–W XCPC design yields more energy than the N–S XCPC design.

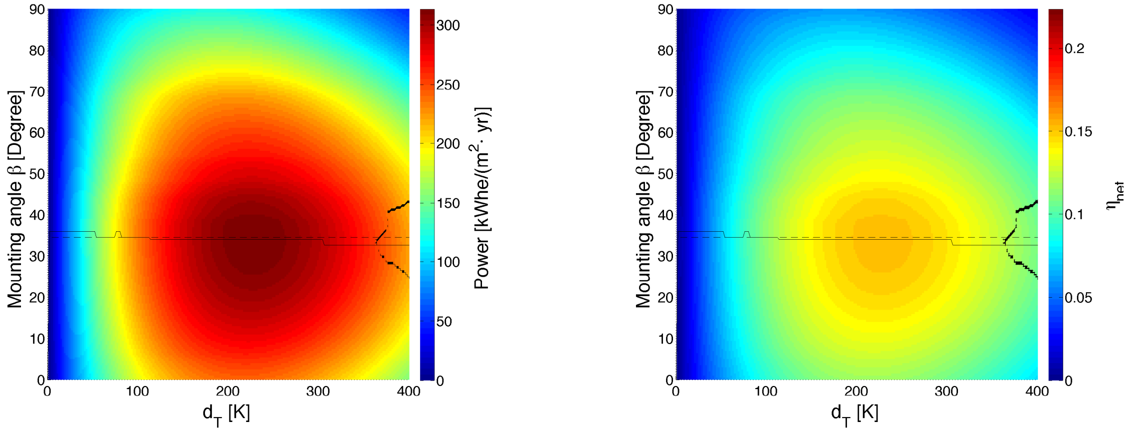

(a) N–S XCPC: annual energy yield per unit area.

(b) N–S XCPC: net efficency based on POAI maximum.

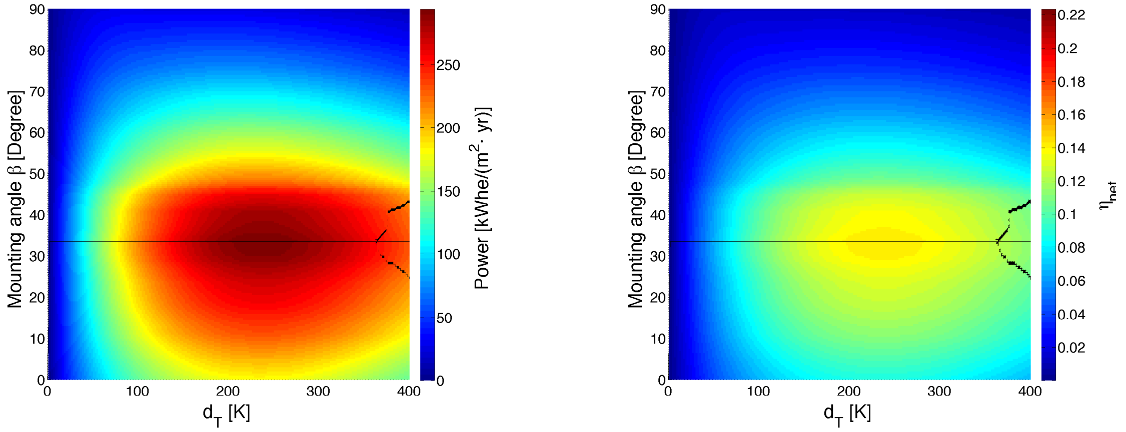

(c) E–W XCPC: annual energy yield per unit area.

(d) E–W XCPC: net efficency based on POAI maximum.

Figure 12.9: Constant temperature difference ORC results for Merced, CA (TMY3). Constant dashed line denotes β^* based on G_{eff}, Solid line denotes β^* based on E. If present, region enclosed in black perimeter denotes where the E–W XCPC design yields more energy than the N–S XCPC design.

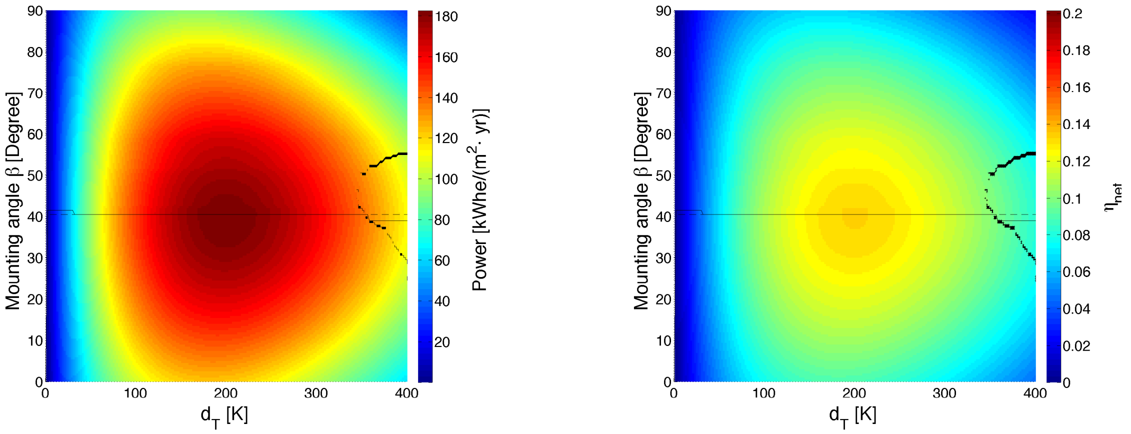

(a) N–S XCPC: annual energy yield per unit area.

(b) N–S XCPC: net efficency based on POAI maximum.

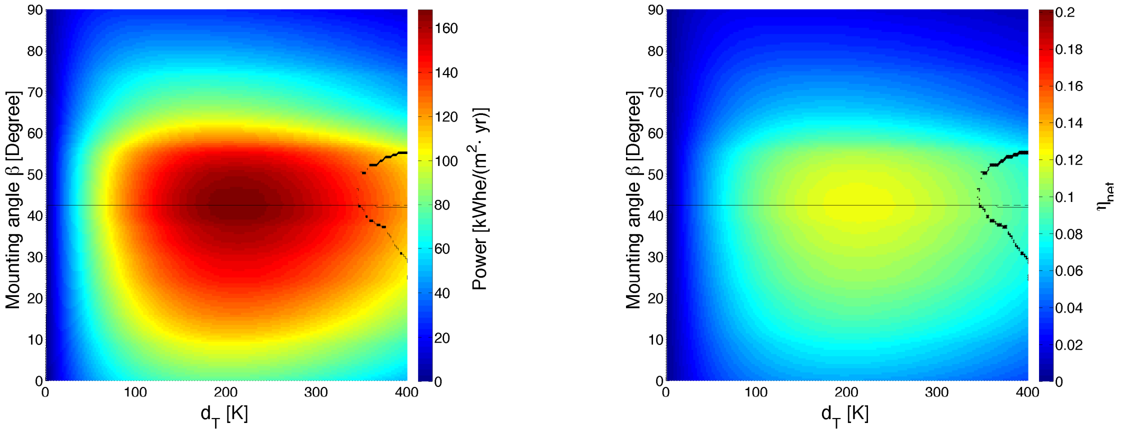

(c) E–W XCPC: annual energy yield per unit area.

(d) E–W XCPC: net efficency based on POAI maximum.

Figure 12.10: Constant temperature difference ORC results for Seattle, WA (TMY3). Constant dashed line denotes β^* based on G_{eff}, Solid line denotes β^* based on E. If present, region enclosed in black perimeter denotes where the E–W XCPC design yields more energy than the N–S XCPC design.

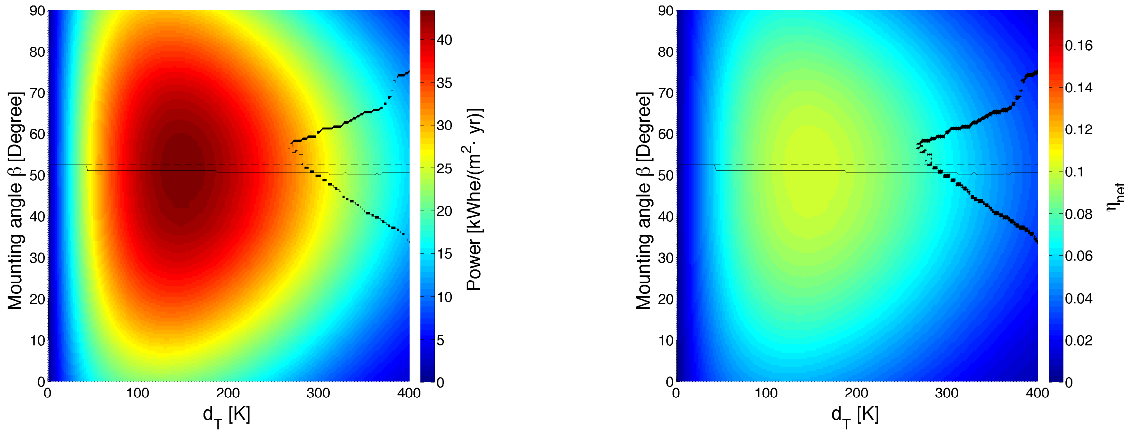

(a) N–S XCPC: annual energy yield per unit area.

(b) N–S XCPC: net efficency based on POAI maximum.

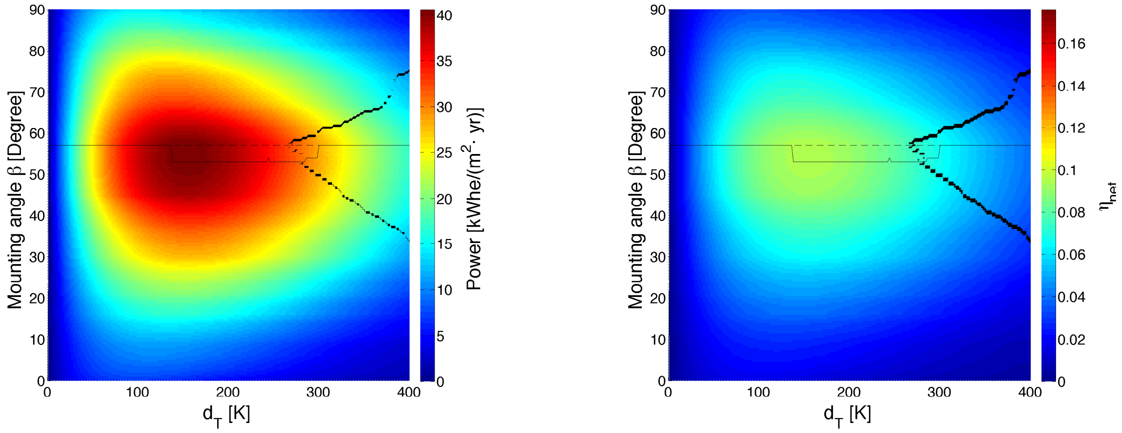

(c) E–W XCPC: annual energy yield per unit area.

(d) E–W XCPC: net efficency based on POAI maximum.

Figure 12.11: Constant temperature difference ORC results for Shemya, AK (TMY3). Constant dashed line denotes β^* based on G_{eff}, Solid line denotes β^* based on E. If present, region enclosed in black perimeter denotes where the E–W XCPC design yields more energy than the N–S XCPC design.

12.3 Results and discussion

12.3.1 Constant temperature difference

Constant temperature difference (ΔT) results for the selected five locations in the TMY2 dataset are shown in Figures 12.2–12.6. The results for the selected five locations in the TMY3 dataset are shown in Figures 12.7–12.11.

12.3.2 Variable temperature difference

The results for the selected five locations in the TMY2 dataset are shown in Figures 12.12–12.16. The results for the selected five locations in the TMY3 dataset are found in Figures 12.17–12.21.

12.3.3 Comparison and contrast variable vs. constant temperature options

The results are summarized in Table 12.1. From the results, the following characteristics are consistent with the previous optimal mounting angle results:

1. The optimal mounting angle deviated from latitude typically by no more than a few degrees.

2. Annual energy yield remained flat in the region near the optimum for the N–S XCPC and the peak became more pronounced for the E–W XCPC.

3. As expected, the addition of a heat engine substantially reduced the energy yield below that of the thermal results from the previous chapter.

4. Consistent with the results from the previous chapter, at optimum mounting angle for the effective irradiance, the N–S XCPC produced the most energy for each location.

5. Locations with better irradiance resources produced more energy.

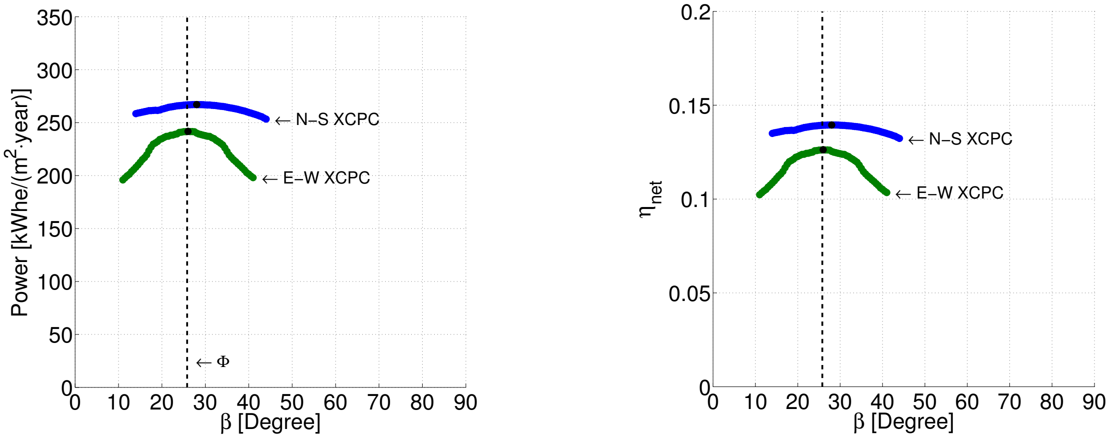

(a) Annual energy yield per unit area.

(b) Net efficency based on POAI maximum.

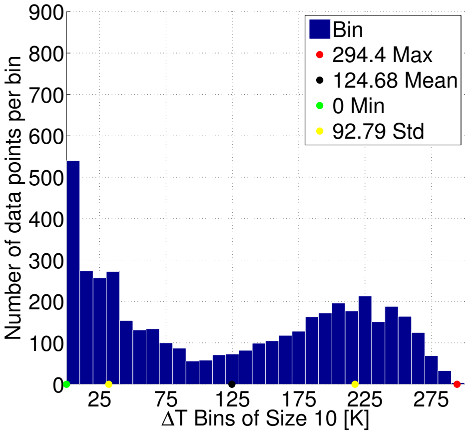

(c) Histogram of optimal temperature differences for the N–S XCPC.

Figure 12.12: Variable temperature difference ORC results for Miami, FL (TMY2).

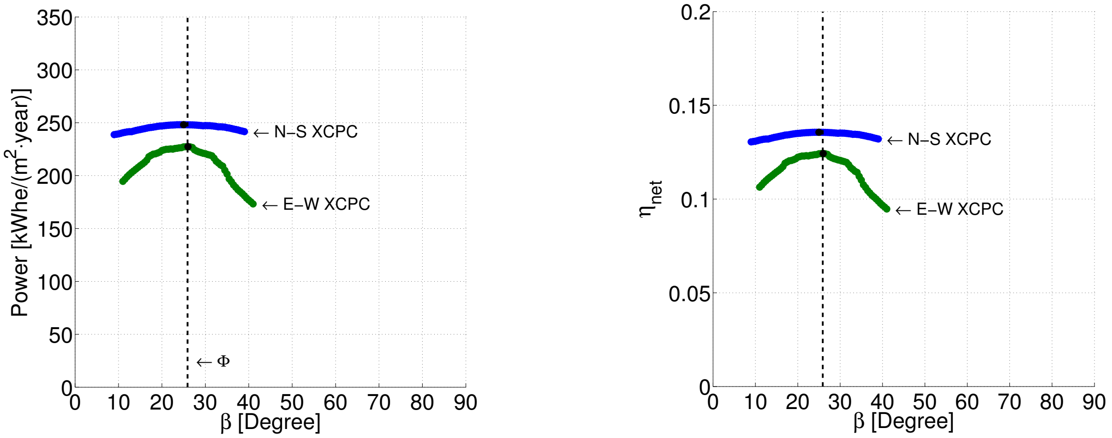

(a) Annual energy yield per unit area.

(b) Net efficency based on POAI maximum.

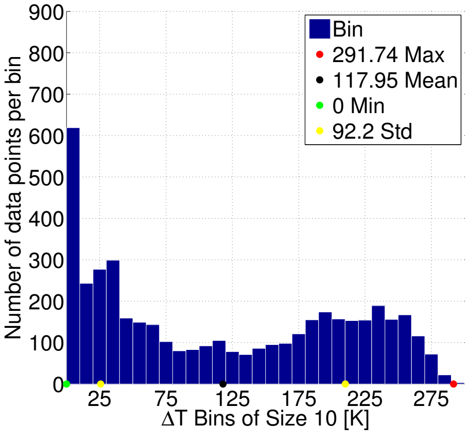

(c) Histogram of optimal temperature differences for the N–S XCPC.

Figure 12.13: Variable temperature difference ORC results for Brownsville, TX (TMY2).

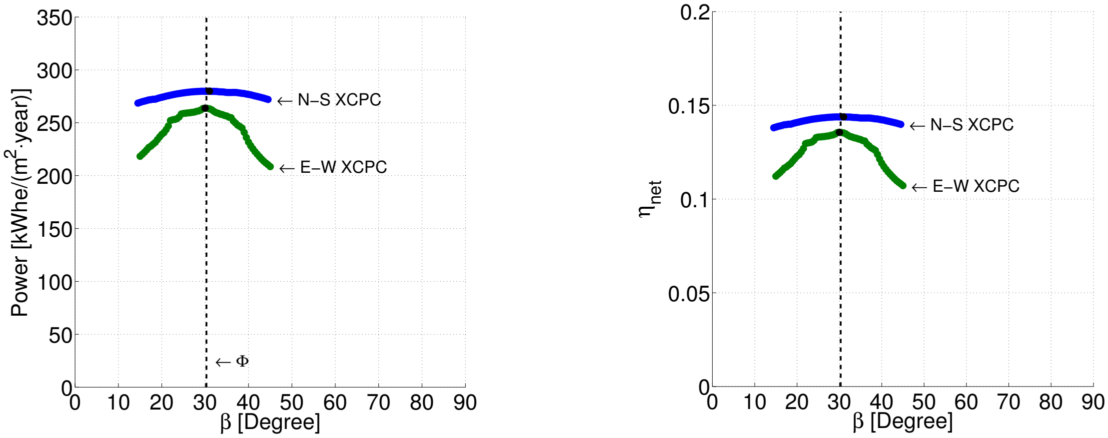

(a) Annual energy yield per unit area.

(b) Net efficency based on POAI maximum.

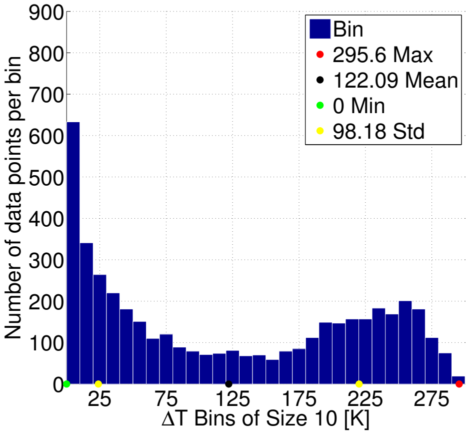

(c) Histogram of optimal temperature differences for the N–S XCPC.

Figure 12.14: Variable temperature difference ORC results for Austin, TX (TMY2).

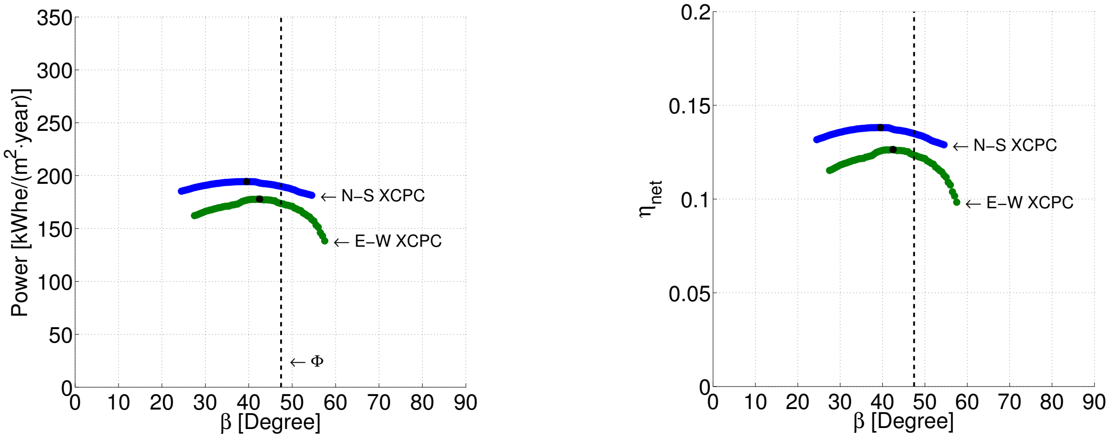

(a) Annual energy yield per unit area.

(b) Net efficency based on POAI maximum.

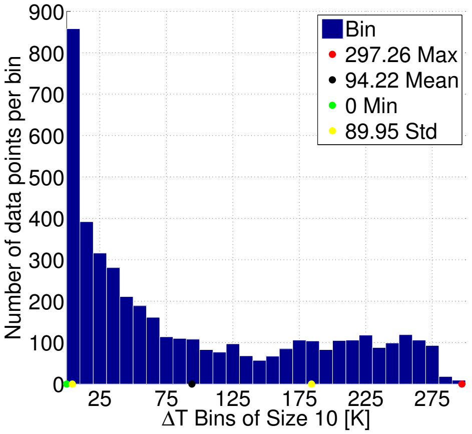

(c) Histogram of optimal temperature differences for the N–S XCPC.

Figure 12.15: Variable temperature difference ORC results for Seattle, WA (TMY2).

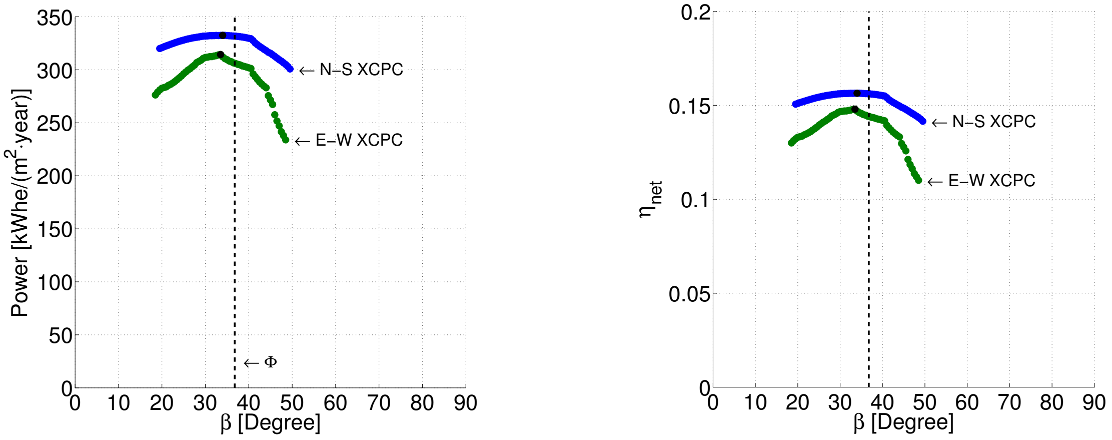

(a) Annual energy yield per unit area.

(b) Net efficency based on POAI maximum.

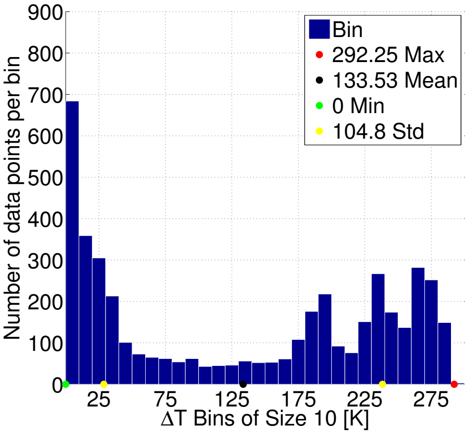

(c) Histogram of optimal temperature differences for the N–S XCPC.

Figure 12.16: Variable temperature difference ORC results for Fresno, CA (TMY2).

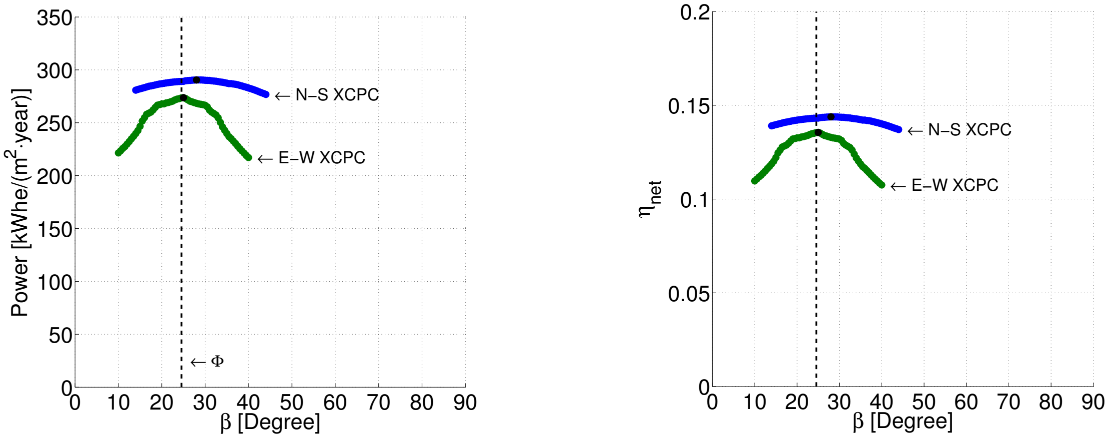

(a) Annual energy yield per unit area.

(b) Net efficency based on POAI maximum.

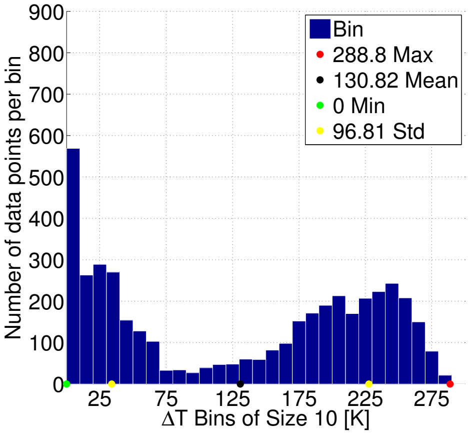

(c) Histogram of optimal temperature differences for the N–S XCPC.

Figure 12.17: Variable temperature difference ORC results for Key West, FL (TMY3).

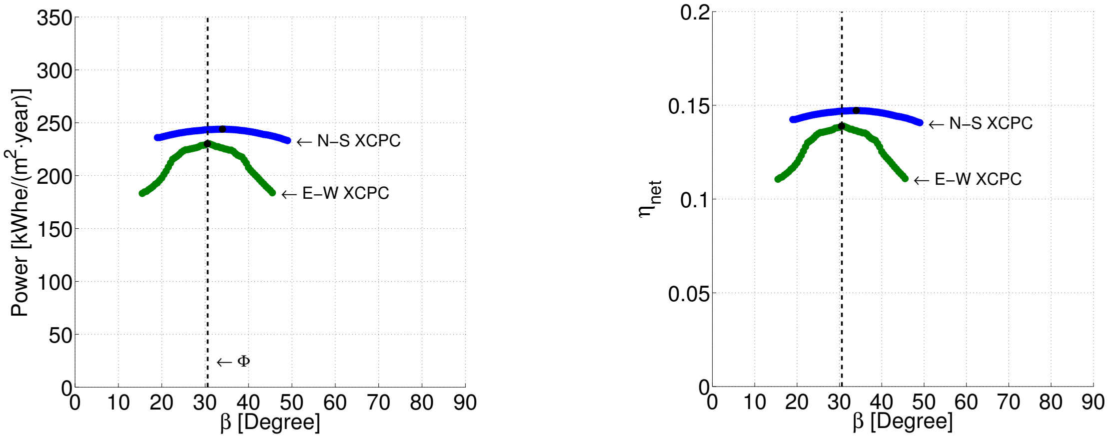

(a) Annual energy yield per unit area.

(b) Net efficency based on POAI maximum.

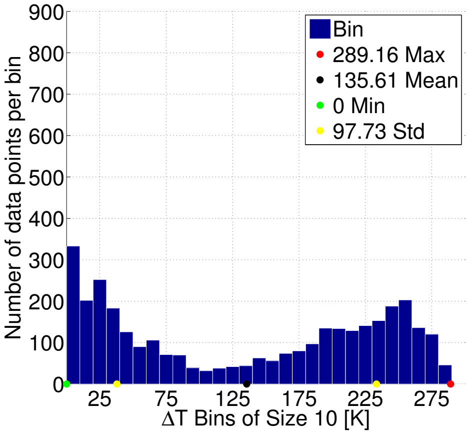

(c) Histogram of optimal temperature differences for the N–S XCPC.

Figure 12.18: Variable temperature difference ORC results for College Station, TX (TMY3).

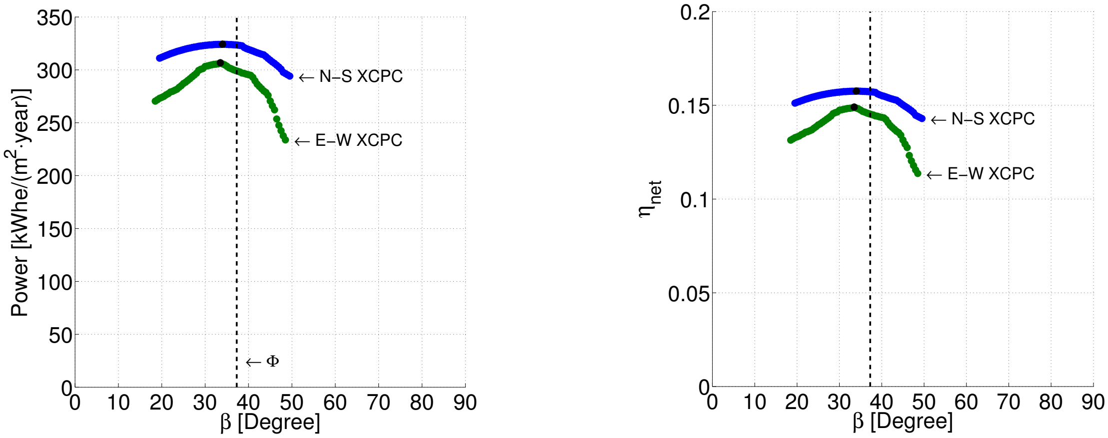

(a) Annual energy yield per unit area.

(b) Net efficency based on POAI maximum.

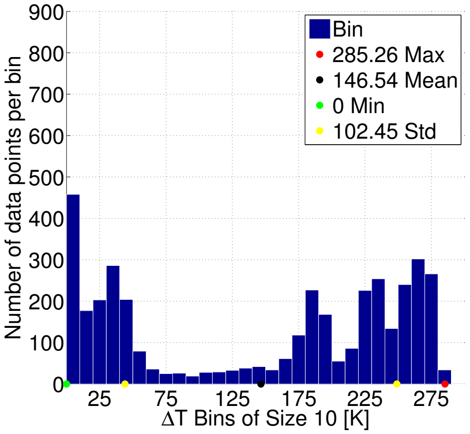

(c) Histogram of optimal temperature differences for the N–S XCPC.

Figure 12.19: Variable temperature difference ORC results for Merced, CA (TMY3).

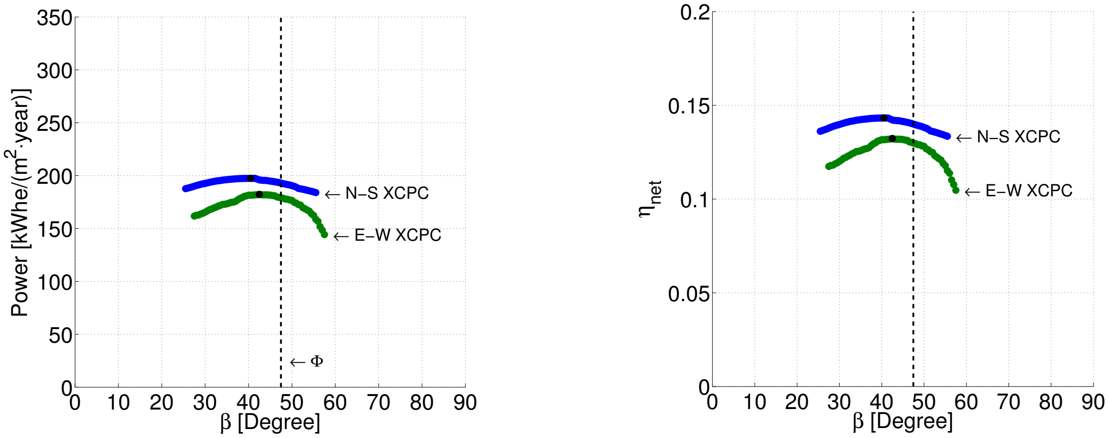

(a) Annual energy yield per unit area.

(b) Net efficency based on POAI maximum.

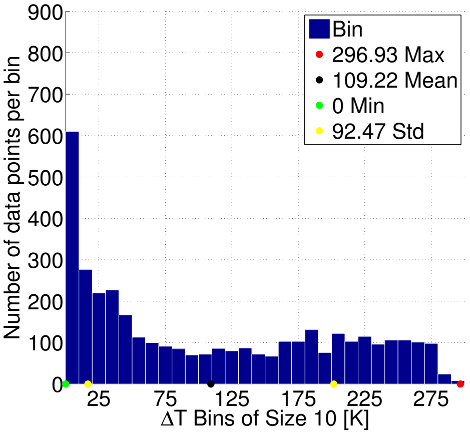

(c) Histogram of optimal temperature differences for the N–S XCPC.

Figure 12.20: Variable temperature difference ORC results for Seattle, WA (TMY3).

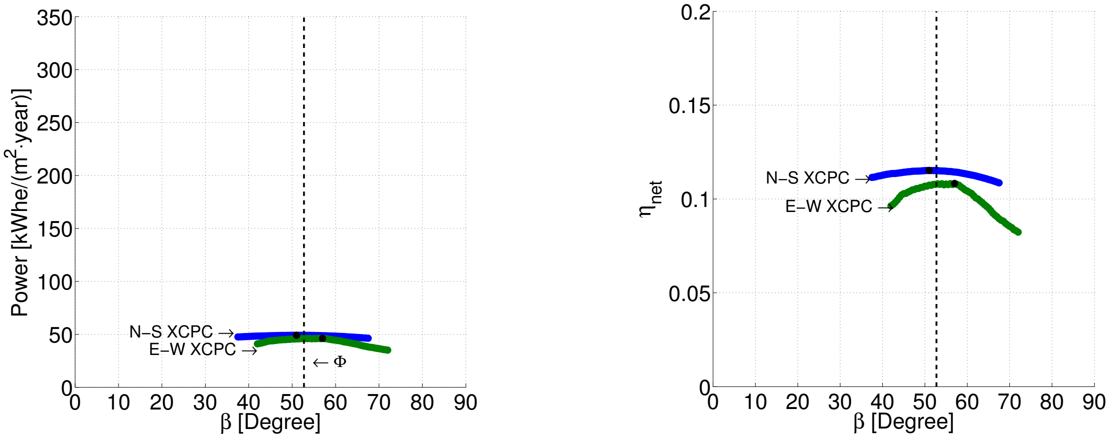

(a) Annual energy yield per unit area.

(b) Net efficency based on POAI maximum.

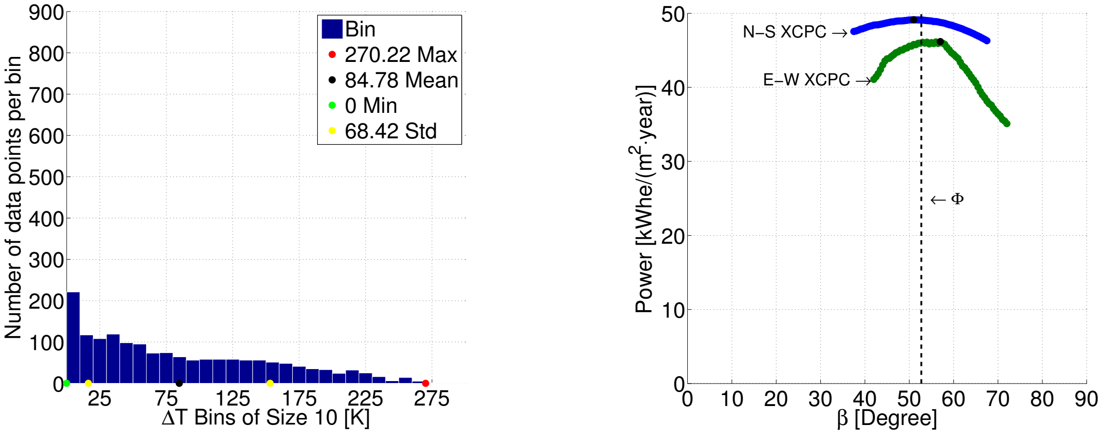

(c) Histogram of optimal temperature differences for the N–S XCPC.

(d) Annual energy yield per unit area (zoom).

Figure 12.21: Variable temperature difference ORC results for Shemya, AK (TMY3).

The following results are unique to the heat engine case:

1. The optimal constant temperature difference is consistent with the XCPC designs.
2. When compared against maximum POAI, the net efficiency, varies in the range 10–15%.
3. The optimal temperature differences correlate with the irradiance resource.
4. In the variable temperature difference case, the optimal temperature differences varied throughout the range of operating temperatures where the XCPC designs are expected to perform better than other types of collector designs.
5. Moving from the constant to variable case improves energy yield less than 10%, which is less than originally expected. The increased efficiency of the variable case may not warrant the increase in equipment complexity. Further and more detailed analysis are required.

12.4 Conclusions and summary

In this chapter, an oversimplified heat engine model was added to the solar thermal simulation developed in previous chapters. Although this new simulation does not exactly match a real thermodynamic cycle for a particular fluid, it approximates several characteristics of electricity production in a DSSTC system:

1. The N–S XCPC design is the clear choice to use for electricity generation applications.
2. The XCPC designs are well suited for the approximated optimal constant temperature differences (146–226 K) found using the 10 TMY locations.

Table 12.1: Optimal ORC performance: constant and variable temperature difference for selected sites in the TMY2 and TMY3 datasets

Name	ID	Constant ΔT				Variable ΔT						
		β^*	E^*	η^*_{net}	ΔT^*	β^*	E^*	η^*_{net}	ΔT^*			
									Mean	Std	Min	Max
		[°]	§	[%]	[K]	[°]	§	[%]	[K]	[K]	[K]	[K]
TMY2 Sites												
Miami, FL	12839	27.5	252	13.2	204	28	267	14.0	125	93	0	294
Brownsville, TX	12919	25.0	232	12.7	202	25.0	248	13.6	118	92	0	292
Austin, TX	13958	31.0	263	13.5	214	31.0	280	14.4	122	98	0	296
Seattle, WA	24233	39.5	177	12.6	198	39.5	194	13.8	94	90	0	297
Fresno, CA	93193	34	318	15.0	226	34.0	332	15.6	134	105	0	292
TMY3 Sites												
Key West Intl Arpt, FL	722010	28.0	279	13.8	212	28.0	290	14.4	131	97	0	289
College Station, TX	722445	34.0	232	14.0	218	34.0	244	14.7	136	98	0	289
Merced, CA	724815	34.0	313	15.2	226	34.0	324	15.8	147	102	0	285
Seattle-Tacoma Intl, WA	727930	40.5	183	13.3	198	40.5	197	14.3	109	92	0	297
Shemya AFB, AK	704140	51.0	43.4	10.2	146	51.0	49	11.5	85	68	0	270

§ E^* units [kWhe/(m^2·yr)]

3. The E–W XCPC annual energy yield sensitivity to mounting angle selection is more pronounced for electricity generation, otherwise optimal mounting angle results are quite similar to the previous works.
4. It is reasonable to expect system efficiency for constant temperature difference in the 10–15% range when normalized by maximum POAI for a location.
5. Variable temperature difference increase system efficiency by 0.6–1.2 percentage points above the constant case.
6. In the variable temperature difference case, temperature differences vary with irradiance in the range 0–300 K, which is well within the operating range of the designs.

The methods and findings of this chapter are the original work of this author.

12.5 Future work

There are two key ways to improve this work. First, one could run the simulation on all TMY2 and TMY3 locations for a more complete analysis of the climatic and latitude variability of the results. Second, one could use this simulation of real-world irradiance with the Roland Winston research group collector design methodology to explore the trade-off between a design more precisely tuned to a use and or location (greater energy yield and complexity) versus the current generalized design design method used by the group that considered only two types of hypothetical irradiance conditions (less complexity and energy yield).

PART IV. THERMOFLUID CONSIDERATIONS FOR HEAT ENGINES

13. THERMODYNAMIC CYCLE FOR HEAT ENGINES

> *"It is essential that a medium for mechanical refrigeration be stable and non-corrosive, and possess suitable vapor-pressure chracteristics. These may be called engineering properties. In addition, when certain special uses are contemplated, non-toxicity and non-inflammablitity become of equal importance, in order that serious health and fire hazards may be avoided in the event of accident." [160]*
>
> – Thomas Midgley, Jr., and Albert L. Henne, 1930

Given that there are additional health, safety, and environmental requirements, these words are even more true today. In this chapter, the fluid requirements are developed for DSSTC heat engines by adapting the refrigeration requirements.

13.1 Introduction/background

In Parts I–III, the need for improved modeling of DSSTC equipment was discussed, a new solar simulation was built, XCPC STC design was selected and simulated for annual irradiance, annual thermal energy, and annual electricity produced using an oversimplified heat engine model. In this part of the dissertation, the goal is to replace the oversimplified heat engine model with a more detailed thermodynamic cycle. To build a more detailed heat engine model, the thermodynamic cycle and fluid pair must be identified that will best suit the economic trade-offs of efficiency and machine size. In this chapter, the correct cycle definition and how that informs the needed fluid characteristics will be the focus of the work.

A holistic approach is taken by evaluating past work. In the history of thermodynamics, designers can either identify a fluid that will work best for a given cycle, or they can develop a cycle that works best with a given fluid for a particular application. For direct solar thermal power generation, a cycle will be selected and then a fluid will be sought for that cycle in the later chapters. The goal of this chapter is to identify the appropriate cycle by identifying requirements and then determine criteria for the fluid used in the cycle. To select a cycle, a review of a few cycles and fluids is required. From this review, it will become clear why certain cycle/fluid pairs work well with particular applications and inform the current design decisions.

Organic Rankine cycle (ORC) heat engines designed for waste heat recovery is the application nearest to the current design application. For use in waste heat recovery power generation equipement, ORC designers have a history of borrowing fluids from the refrigeration industry (HVAC-R), including air conditioning and heat pumps. These fluids are then evaluated and tested for suitability in ORC applications. The waste heat recovery industry typically focuses on using waste heat from large-scale processes with substantial temperature differences, for example, traditional power generation equipment using combustion. The ORC industry – a small sub-section of waste heat recovery industry – is quite small compared to both the traditional power generation and refrigeration industries. Refrigeration industries have a long history of searching for better working fluids [2, 160–163]. The modern search process has four steps: (1) Evaluate known fluids for a particular refrigeration application [164–168]; (2) Evaluate fluids using a thermodynamic cycle [169, 170]; (3) Compare known fluids against a theoretical thermodynamic space that describes what might be possible [170–172]; and (4) Predict fluid properties from molecular structure, which allows fluids to be evaluated using methods from Steps 1 and 2 [170–175]. Only recently have refrigerant manufactures recognized the ORC market by including ORC relevant criteria in the search process (e.g., R245fa). There is a small body of work that has focused on applying ORC knowledge to the solar power generation problem (e.g., [30–32, 176, 177]). At least one paper points out the limitations in simulating/modeling ORC performance [178]. Several review papers exist and provide evidence that the ORC field is diverse in size, applications, operating temperatures, and cycle/fluid choices, which cause many diverse results that appear to be contradictory on the surface [179, 180]. The reader is cautioned when applying knowledge gained for one application, size, and temperature difference to other ones, because it can be challenging to discern between domain-specific results and general results. Care must also be taken in equipment choices because of the varying operating conditions found throughout the literature.

One recent paper (Brown et al. 2015) explores a search for possible fluids for five ORC appliations including the indirect configuration for solar thermal power generation [177]. This recent paper simply assumes an operating temperature range for the solar thermal application and models a simple ORC heat engine with and without an internal heat exchanger (IHX). Brown et al. 2015 does not model the complete systems in which the heat engine is part. This over simplified method of modeling does not account for fluid-to-fluid heat transfer effects when moving heat into the heat engine. All five ORC applications considered by Brown et al. 2015 have the fluid-to-fluid heat transfer process. The current work is distinct and will show that the direct configuration does not have a fluid-to-fluid heat transfer process; rather, the heat is moved into the heat engine directly in the STC. The current work accounts for irradiance variability, ambient temperature, STC thermal performance, and heat engine performance. By completing a system-level model, the current work captures the interactions between the solar collector and the heat engine.

The refrigerant industry has gone through many transitions/generations (Table 13.1) because the design requirements have increased (Table 13.2). Some of these changes have been to improve machine performance and others have been to

Table 13.1: Calm 2012 refrigerant transistions [2]

Gen.	Description	Period
1	Whatever worked	1830s–1930s
2	Improved safety and durability	1930s–1990s
3	Stratospheric ozone protection	1990s–2010s
4	Global warming	2012–?
5	Efficiency and trade-offs	2020s–?

improve safety. Calm 2012 [2] provides an excellent summary. In the refrigeration industry, there are two figures of merrit for thermodynamic performance: 1) cycle efficiency (η_R) and 2) a measure of machine size called the *volumetric capacity* (Q_{vol}). Q_{vol} is defined by the ratio of heating (or cooling) versus volumetric flow at the inlet of the compressor ($\frac{\dot{Q}}{\dot{V}}$). In the case of air conditioning equipment, the cooling ($\dot{Q}$) is the amount of heat transfered to the working fluid in the evaporator, and the volumetric flow is determined at the exit of the evaporator/inlet of the compressor. The volumetric capacity for air conditioning equipment reduces to the enthalpy imparted to the fluid in the evaporator normalized by the specific volume (ν) of the inlet of the compressor (Equation 13.1). Q_{vol} is also known as *volumetric cooling capacity* (VCC) and *volumetric heating capacity* (VHC), terms commonly used in conjunction with cooling equipment and heat pumps, respectively. Because the concept can be used with both heat pumps and cooling equipment, many authors prefer the more generic term volumetric capacity. Q_{vol} and cycle efficiency (η_R) provide trade-offs where the designer cannot maximize both *engineering objectives* simultaneously [169]. One of the largest challenges in HVAC-R equipment design is to account for the design trade-offs of the engineering objectives Q_{vol} and η_R under the limitations of discrete fluid options that result from molecular chemistry.

Table 13.2: Key refrigeration industry fluid requirements

Gen.	Description
2+	Low toxicity
2+	Low flammability
2+	High molecular stability/low decomposition rate
3+	Low/no ozone depletion potential (ODP)
4+	Low global warming potential (GWP)
5+	Maximum thermodynamic cycle efficiency
5+	Minimum machine size/maximum volumetric capacity (Q_{vol})

$$Q_{vol} = \frac{\dot{Q}}{\dot{V}} = \frac{\dot{Q}}{\dot{m}\nu} = \frac{\frac{\dot{Q}}{\dot{m}}}{\nu} = \frac{\Delta h}{\nu} \tag{13.1}$$

As fluid requirements have become more stringent, search methods have become more sophisticated in response to increasing difficulty. Leveraging the search methods developed in the refrigeration industry, the goal of this part of the dissertation is to apply the search methods to the DSSTC design problem to identify a fluid and thermodynamic cycle that will perform best. The key is to identify the necessary adjustments to the fluid and cycle requirements and then follow the consequences of the updated requirements using refrigerant industry search methods.

13.2 Theory

The first step in the fluid search process for DSSTC is to recognize that many of the fluid requirements are the same or very similar to the refrigeration industry. The three requirements that must be adjusted are molecular stability, the measure of machine size, and thermodynamic cycle efficiency. Here, all three of these requirements will be explored in detail.

13.2.1 Molecular stability

In the refrigeration industry, the requirement for molecular stability has several issues all related to the question: Will the fluid decompose during machine operation? More detailed questions follow:

- Are the operating temperatures and thermal stability of the fluid compatible?
- Will leaks in the system allow air to infiltrate and cause adverse chemical reactions with the fluid?
- Does the fluid have adverse chemical reactions with the machine materials of construction including lubricants?

These issues remain largely unchanged because they are handled on an application/design basis. For solar applications, one must also be concerned with molecular stability under ultraviolet light (UV) exposure. This is an issue because some STC absorber tubes are made of glass that is transparent to UV light. More generally, one should ensure that no part of the solar spectrum will cause stability issues for the fluid or other materials of construction.

13.2.2 Volumetric power capacity (VPC), a measure of machine size

Here, the *volumetric power capacity* (VPC) is defined similarly to Q_{vol} for refrigeration equipment with the following two main differences:

- The specific volume is based on the outlet of the expander/inlet of the condenser.
- The enhalpy change is based on the work flow (power) out of the expander (Equation 13.2).

In the adjetive, "heating" is replaced with "power" because volumetric heating capacity (VHC) has several meanings in related fields, thus avoiding confusion and ambiguity. In the power generation field, the author could not find a corresponding concept in the literature and selected a unique name to avoid confusion. At least one research group has used the term *volumetric work output* to describe the same physical quanity [176, 177].

$$\psi = \frac{\frac{\dot{W}}{\dot{m}}}{\nu} = \Delta h \rho \tag{13.2}$$

where the specific volume ν and the density ρ are related by $\rho = \frac{1}{\nu}$.

13.2.3 Thermodynamic cycle

13.2.3.1 A brief review of thermodynamic cycles

A brief review of thermodynamic cycles is presented, which will help select the best cycle to maximize efficiency. Beginning with *Carnot efficiency* shown in Figure 13.1, one can simply derive Carnot's law, which states the theoretical maximum possible efficiency of the cycle is the ratio of the total energy to the maximum possible energy of the cycle (Equations 13.3).

$$\frac{\text{Maximum cycle energy}}{\text{Total energy}} = \frac{\Delta s(T_H - T_L)}{\Delta s(T_H - 0)} \tag{13.3a}$$

$$= \frac{\Delta s T_H \left(1 - \frac{T_L}{T_H}\right)}{\Delta s T_H} \tag{13.3b}$$

$$\eta_{\text{Carnot}} = \left(1 - \frac{T_L}{T_H}\right) \tag{13.3c}$$

The *second law efficiency* η_2 is introduced, and it is defined as the ratio of the efficiency of the thermodynamic cycle to the maximum possible efficiency (Equa-

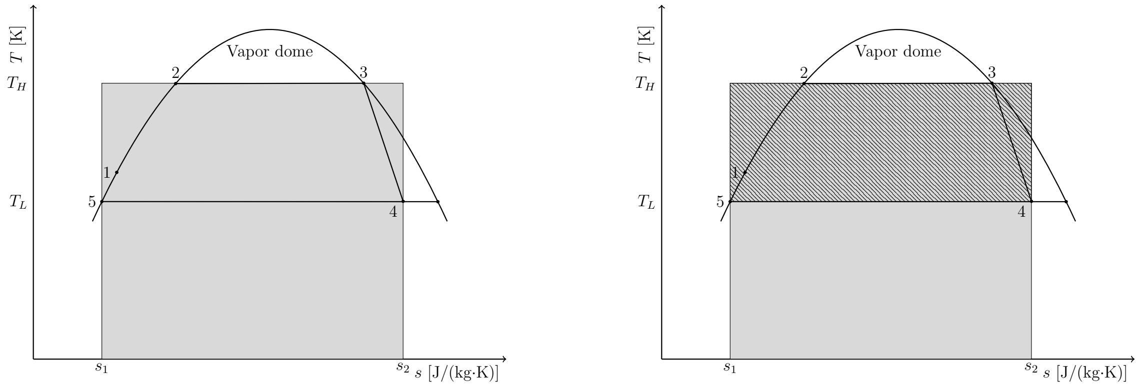

(a) Total energy possible (gray area).

(b) Maximum cycle energy (cross-hatched area).

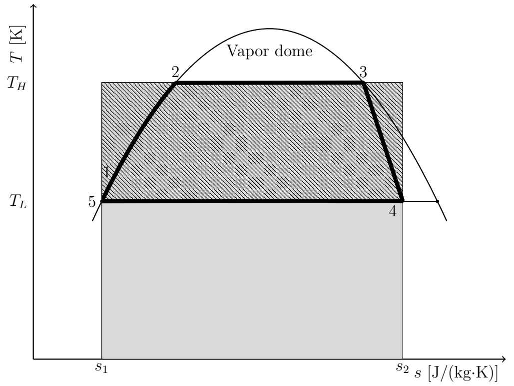

(c) Rankine cycle energy (enclosed in bold lines).

Figure 13.1: Graphical relationship of various energies in the Rankine cycle.

tion 13.4) [181],

$$\eta_2 = \frac{\eta_{\text{cycle}}}{\eta_{\text{Carnot}}} \tag{13.4}$$

Figure 13.1 shows the second law efficiency reduces to the ratio between the cross-hatched area and the area enclosed in bold lines. To approach the maximum theoretical efficiency for a given temperature difference, one must design a cycle that approaches Carnot within the process and component limits of finite time and size. An obvious question follows: Why not simply operate in a rectangle inside the vapor dome of Figure 13.2? There are several main challenges to this idea:

1. For many types of pumps, pumping a liquid-gas mixture can cause cavitation problems, which can cause poor efficiency and equipment damage.

2. Using conventional turbo machinery, expanding into the vapor dome forms droplets that can damage the blades. This issue can be overcome with other expander devices, e.g., gerotor, sliding vane, and twin screw designs.

3. When operating inside the vapor dome, the two most common measurement parameters (temperature and pressure) do not indicate the location along the constant temperature/pressure line. This issue is a control problem that makes it difficult to operate and maintain the equipment as intended. One potential reprieve to this control problem is to use a zeotropic mixture, which by definition has a temperature glide on a constant-pressure line moving from a saturated liquid to a saturated vapor.

Experimentation is required to show valid results that operate close to this cycle and will result in a practical design. This remains as future work.

There are two main approaches to the problem of maximizing efficiency of the heat engine:

1. Maximize the temperature difference to operate at higher absolute efficiency even if it must operate at a lower second law efficiency.

2. Given a constrained temperature difference, choose a cycle that maximizes the second law efficiency.

Much thermodynamic cycle work has focused correctly on finding ways to maximize the temperature difference, which will maximize the absolute efficiency of the cycle. A numerical example of the benefit is shown in Table 13.3. Traditional power generation

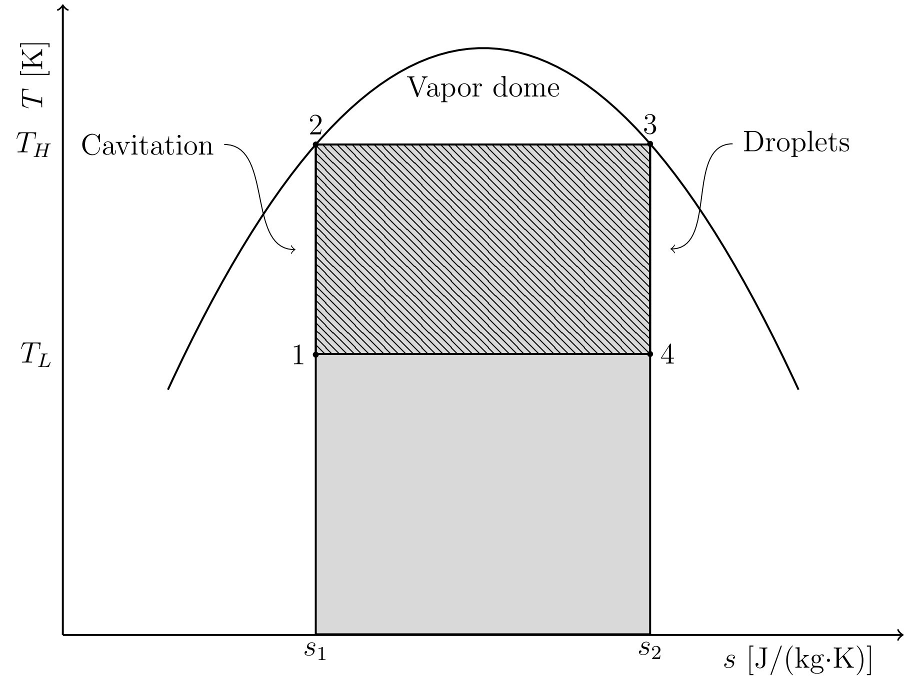

Figure 13.2: Carnot-like cycle that has not yet been achieved in pratice.

equipment uses fossil fuel combustion to produce high temperatures. It is natural to design cycles that benefit as much as possible in efficiency from high temperatures, even if second law efficiency is reduced. This principle is used in Brayton cycles (gas turbines), which use a high pressure ratio:

1. The high pressure ratio increases the temperature difference.
2. The high pressure ratio helps to increase the second law efficiency of the cycle within the limits of compressor and expander efficiency.

In this sense, the *T*-*s* diagram for a Brayton cycle is tall and attempts to approach a tall rectangular shape. For the Rankine cycle, the goal is to have superheating, which drastically improves cycle efficiency because of the enthalpy contours shown in Figure 13.3. This also helps to relieve problems with droplets that could dam-

Table 13.3: Example of efficiencies

η_2	η_{Carnot}	η_{cycle}
%	%	%
75	25	18.75
50	50	25

age the turbine by expanding into the vapor dome where the quality is less than 1.0. Avoiding superheating, the second law efficiency is naturally aided because the vapor dome of water has unusually wide specific entropy when compared to other fluids (Figure 13.4). This allows the inefficiency of the pump, constant-pressure contours, and expander to be normalized over greater width. Avoiding superheating and selecting a fluid with a wide vapor dome also allows the Rankine cycle to loosely resemble a rectangular shape that it is wider than it is tall.

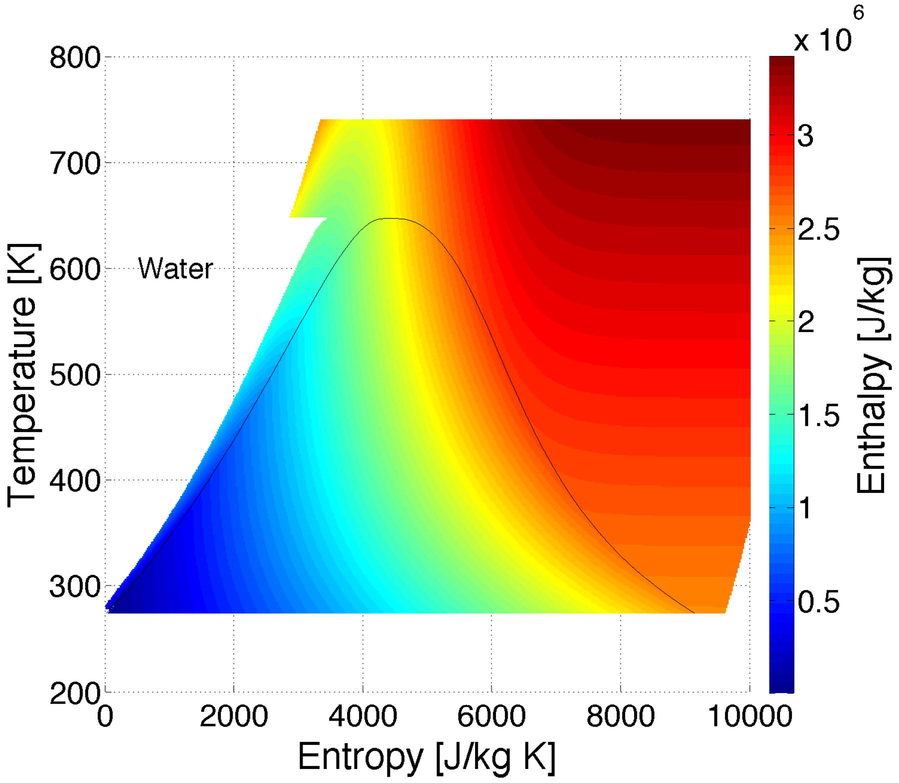

Figure 13.3: T-s diagram showing enthalpy values for water.

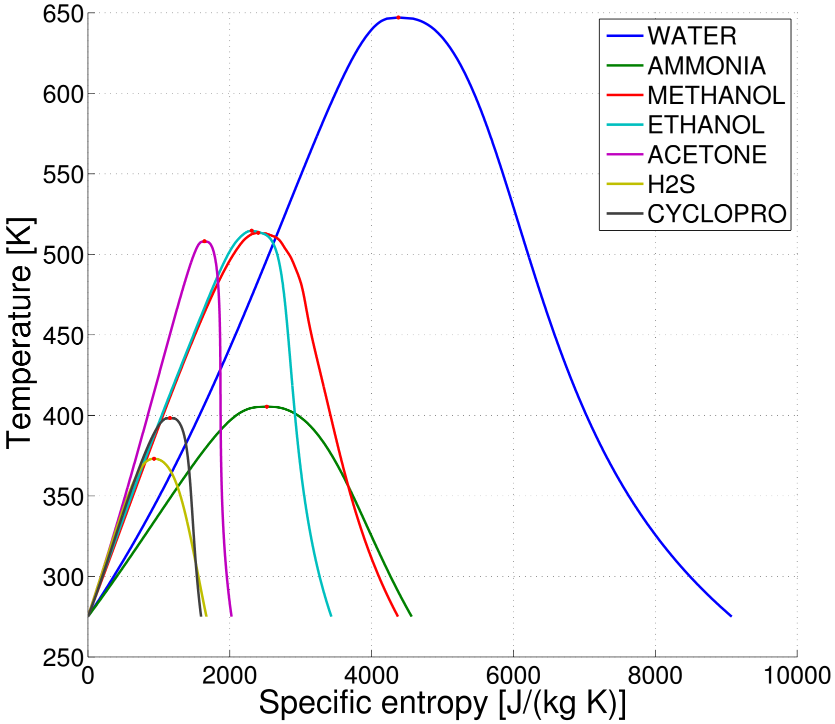

Figure 13.4: Seven pure fluids in REFPROP v9.1 with the widest vapor domes (measured at 275 K).

In a constrained temperature difference problem (e.g., waste-heat recovery or solar-thermal power generation), to increase efficiency, the designer cannot increase the cycle temperature difference beyond what is available. This means the single greatest thermodynamic tool to increase cycle efficiency is not available to the designer, which forces the designer to make choices that specifically increase second law efficiency.

This basic review of thermodynamic cycles is concluded. Next is to discuss advanced techniques used by designers when selecting some of the lesser-known cycles to achieve more ideal design trade-offs for a specific application.

13.2.3.2 Advanced review of thermodynamic cycles

In Chapter 4, the waste heat recovery application is discussed. ORC designers manage the trade-off between machine size and cycle efficiency by selecting refrigerants that provide small specific volume (large VPC) to keep machine size small. This means using fluids that tend to have higher molecular weight and a lower normal boiling point (T_{nbp}). One consequence of the higher-molecular-weight fluids is they tend to be "dry", meaning the vapor dome is tilted to the right in a T-s diagram [164]. There are two important consequences of this tilting:

1. The tilt allows the designer to select an ORC working fluid that best matches the heat transfer fluid in the pumping and heating regions (Figures 13.6–13.8). The goal is for the temperature difference to be as constant as possible between the heat transfer fluid and the ORC working fluid. The temperature difference is set by balancing entropy generation costs with heat exchanger costs because of size.

2. Notably, dry fluids present a problem because they are limited in the ability to use all the enthalpy above the condenser operating temperature because of the constant-pressure lines on the right side of the vapor dome. To counteract this, an *internal heat exchanger* (IHX) is installed (Figures 13.6–13.8). In the literature, IHX are also known as reheat heat exchangers or regenerators. The IHX adds machine complexity and because of the shape of the cycle, leads directly to low second law efficiency (typically about 50% or less for many cases).

ORC designers have put much effort into understanding these principles and balancing them. This has led directly to the configuration and fluid type choice that represents a local optimum for waste heat recovery and indirect configurations of solar-thermal equipment, namely an ORC with IHX and a dry fluid. Figure 13.5 shows the two canonical solar-thermal system configurations.

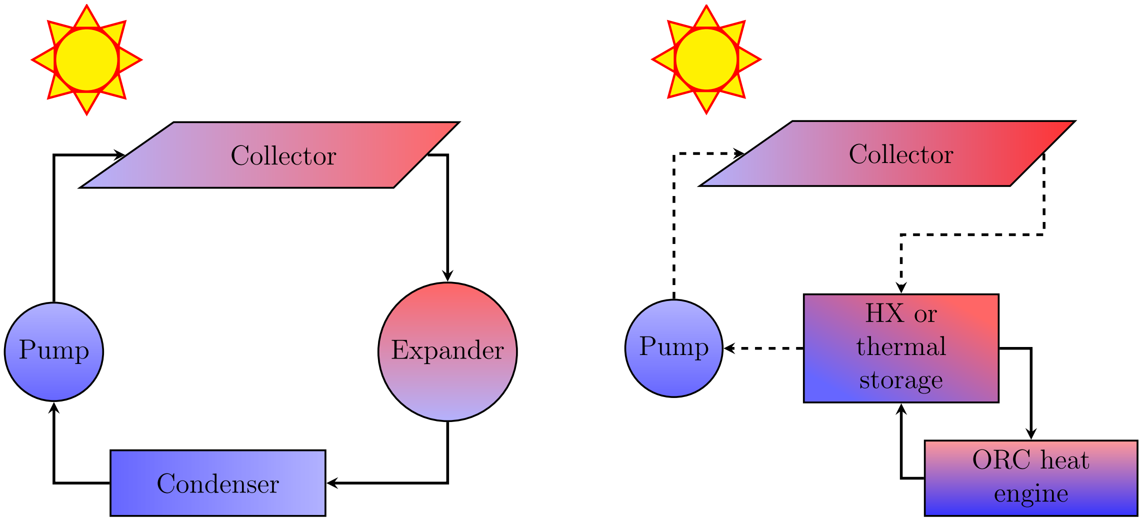

(a) Direct system. (b) Indirect system.

Figure 13.5: Two canonical solar-thermal system configurations.

The direct configuration for DSSTC does not have the fluid-to-fluid heat transfer constraint because there is only one working fluid in the system. This means the direct configuration for DSSTC may have a different local optimum (namely a different cycle and fluid). The thermodynamic state of the fluid in the STC can naturally vary based on the heat transfer physics of the radiation heat exchange process. Although both types of systems (direct and indirect) are constrained by temperature differences, for the direct system, the shape of the thermodynamic cycle is not limited by a heat transfer fluid circuit.

13.2.3.3 Thermodynamic cycle efficiency

The goal is to improve the cost-effective design of DSSTC. Chapter 3 discusses the long history of making solar-thermal power generation equipment; therefore,

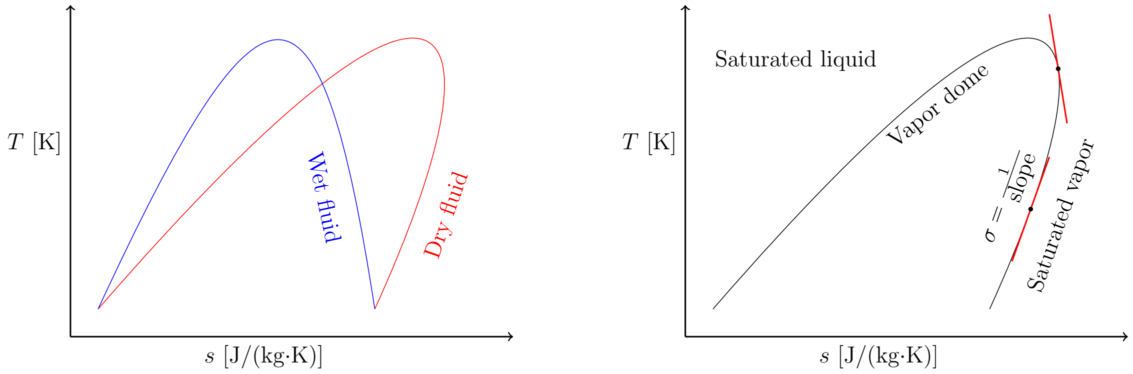

(a) Vapor dome for wet and dry fluids on the T-s diagram.

(b) σ of a dry fluid on the T-s diagram.

Figure 13.6: Fluid categorization method.

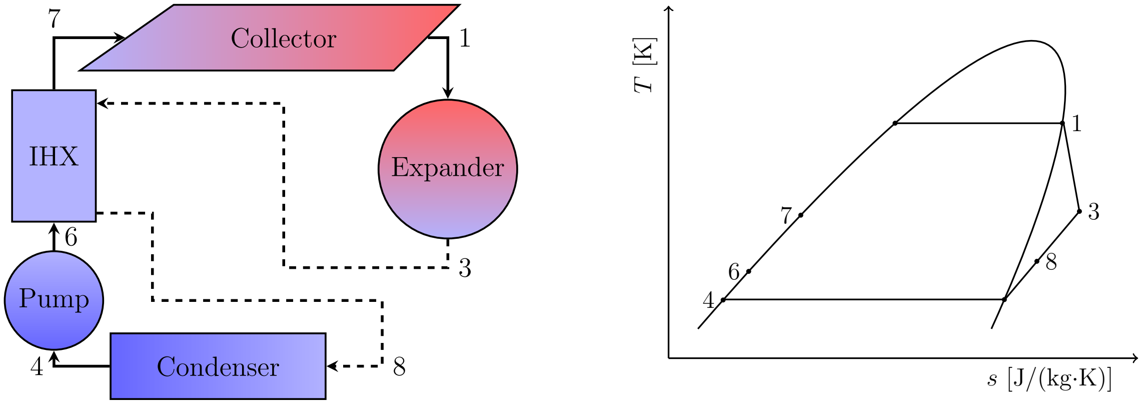

(a) Equipment configuration diagram.

(b) Thermodynamic cycle on the T-s diagram.

Figure 13.7: Direct system with regenerator.

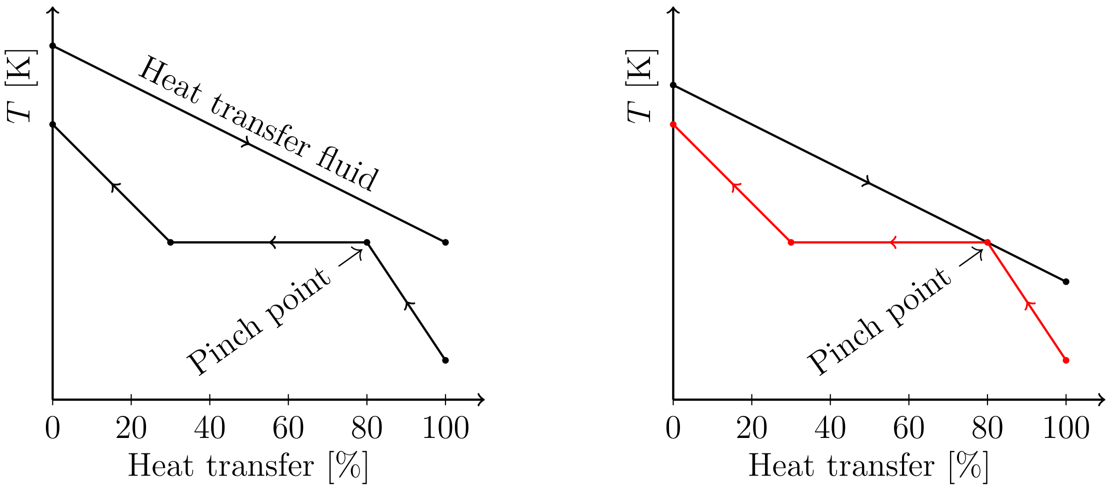

(a) Normal design must operate below heat transfer fluid.

(b) Design failure: the heat transfer fluid limits heat engine design options.

Figure 13.8: Heat transfer diagram between the heat transfer fluid and the working fluid of the heat engine.

there is no question if it is technically possible. Rather, can it be economically competitive with other forms of power generation? The lifecycle cost of energy (LCOE) is the relevant figure of merit (FOM). Given the box diagram of a DSSTC system (Figure 13.9) supplying a fixed annual load, one can readily see that increasing component efficiency reduces the size of all upstream components. As an example, the cost of increasing inverter efficiency can be borne by savings from reducing the size of all upstream components (Figure 13.10). This principle is especially true for renewable energy technologies that collect raw energy and convert it into a usable form because increases in efficiency reduce the size of collection equipment for a given amount of energy produced. In addition to this powerful principle, if one further assumes that changes in components do not materially change the underlying cost structure (i.e., the materials and manufacturing methods are not materially changed), adjusting the design to improve efficiency naturally reduces costs and lowers the LCOE while continuing to meet the required load. Additional exceptions are changes that increase machine size or complexity. In this case, a more detailed analysis would be required.

Considering the above economic thinking, the key question follows: Is it possible to find a thermodynamic cycle and fluid that maximize the efficiency without materially increasing machine size/machine complexity? This question can be further constrained: Given that a solar-driven heat engine is temperature constrained (discussed in Chapter 12), is it possible to find a thermodynamic cycle and fluid that maximize the second law efficiency in the range of expected operating temperatures without materially increasing machine size? From the above review of thermodynamics, a cycle that is wide and approaches the rectangular shape of the Carnot cycle is desired. To approach the rectangular shape, the cycle must operate well below the critical temperature. The vapor dome also must be favorably shaped where it is not substantially wet nor dry. This means that the fluid must be wide in entropy across the vapor dome, have a critical temperature (T_c) well above the operating temperature of the cycle, have a favorable enthalpy structure, and high heat capacity. In Chapter 12, it was estimated that the high temperature would be about 500–600 K or more depending on whether the design used a constant or variable temperature difference. This would include little to no superheating of the fluid. For a vapor dome to provide a wide rectangular shape for the cycle, the critical temperature must be much higher. To minimize machine size for the cycle, the fluid must have a favorable VPC. The single most important thermodynamic property that is correlated with machine size is the normal boiling point (T_{nbp}); the lower the normal boiling point the higher the working pressure. Note that this perspective neglects the effects of fluid heat capacity. Given that the machine must operate in

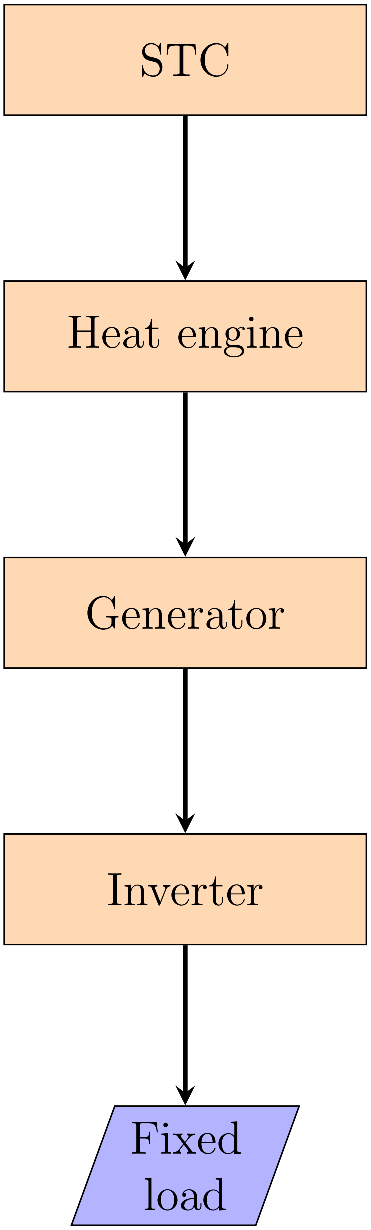

Figure 13.9: Simplifed diagram of a DSSTC system.

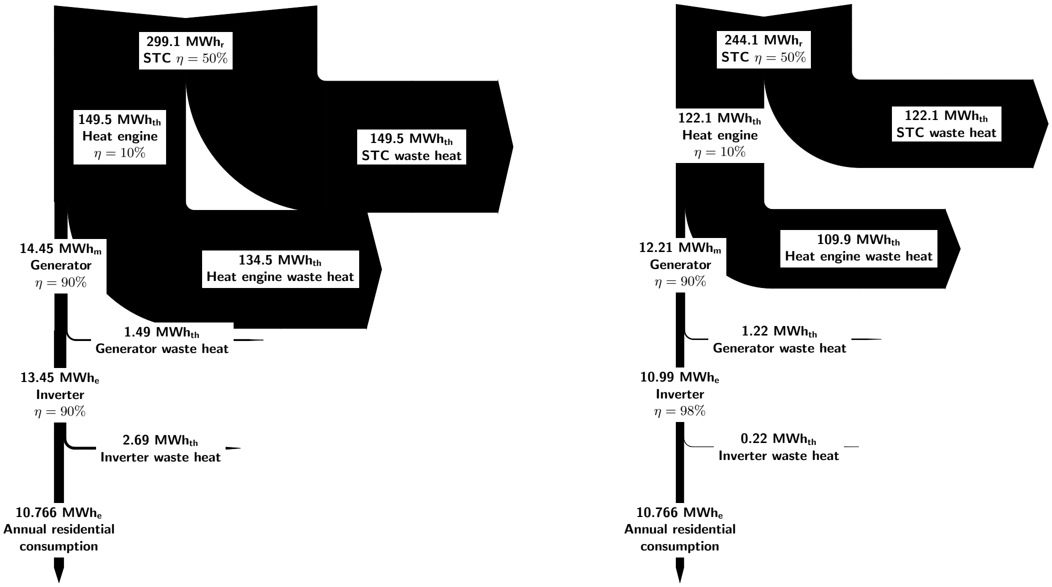

(a) Less efficient inverter.

(b) More efficient inverter.

Figure 13.10: Sankey-diagram of the energy flows in two similar DSSTC systems.

freezing temperatures (∼275 K), the lower the T_{nbp} the less likely air will infiltrate through a leak. The Rankine steam cycle has a large machine size primarily because water has a very high T_{nbp} (373 K). Most refrigerants have a substantially lower T_{nbp}. An initial search criteria can contain a subset of the general search criteria and use two simple thermodynamic values: (1) the critical temperature (T_c), and (2) the normal boiling point (T_{nbp}). More specifically, it is desired to have a high critical temperature ($T_c \geq 500$ K as a less restrictive limit) and a low normal boiling point ($T_{nbp} \leq 300$ K as a less restrictive limit). The T_{nbp} normalized by critical temperature (T_c) is known as the *reduced normal boiling point* (T_{rnbp}). A rule of thumb used in the refrigeration industry is that T_{rnbp} is roughly 0.6–0.7 for most refrigerants. For the Rankine power cycle, the sought fluid should have a reduced normal boiling point of 0.6 or less. This rule of thumb is a trend for refrigerants, which does not necessarily mean there is a true physical/chemical limit preventing a fluid from being found that has a substantially lower reduced normal boiling point. The central goal of finding a cycle/fluid pair that will maximize efficiency and minimize machine size has been reduced to finding a fluid that has a lower reduced normal boiling point. At the same time, the discussion has found that an ORC with little to no superheating would maximize second law efficiency, and therefore heat engine efficiency.

To test how much superheating is appropriate, an important challenge must be overcome. STC performance is based partly on the mean temperature of the collector. In Chapter 8, the collector testing standards are for liquid heating (sensible heat) and not fluid boiling (latent heat). The direct configuration requires boiling in the collector, which causes a non-linear temperature profile in the collector; therefore, a new method for determining the mean temperature is required. Normally, one would experimentally test the temperature profile in the collector and develop a generalized heat transfer correlation to describe it. To be useful, it must be general in collector design, fluid, and operating conditions. This is outside the scope of this research and remains as future work. To approximate the temperature profile in the T-s diagram of the thermodynamic cycle, the mean temperature will be calculated based on the temperature profile of the STC even though this method is not based on a physical length of absorber tube in the collector. The method provides an engineering approximation to a problem not yet solved (see Chapter 14 for more information).

13.3 Conclusions and summary

In this chapter, the idea of adapting search methods used by the refrigerant industry and applying them to ORC heat engine designs was introduced, discussed, and they are the original work of this author. The refrigeration industry fluid requirements were adapted:

1. Molecular stability must include stability when exposed to sunlight,

2. The measure of machine size was adapted and called *volumetric power capacity* (VPC),
3. The thermodynamic cycle for ORC applications was discussed and adapted.

The fluid/cycle requirements for typical ORC heat engines were reviewed. It was shown that the ORC fluid requirements are very similar for the indirect solar configuration and different for the direct configuration. The direct solar configuration allows for greater freedom in designing the cycle because of the lack of a fluid-to-fluid heat exchanger when inputting heat into the equipment. This results in the possibility of designing a cycle much closer to a Carnot cycle than previously found. To enable one to design a cycle approaching the Carnot cycle, the following fluid requirements were defined:

1. High efficiency (rectangular-shaped cycle)
    (a) Critical temperature must be well above the operating temperature of the cycle (less restrictively, $T_c \geq 500$ K).
    (b) Wide in entropy across the vapor dome.
    (c) Moderate fluid neither wet nor dry in vapor dome shape.
2. Small machine size (high VPC)
    (a) Low normal boiling point (less restrictively, $T_{nbp} \leq 300$ K).
    (b) Favorable enthalpy structure/high heat capacity.

These requirements can be reduced to searching for fluids based on critical temperature and normal boiling point because they are the most restrictive.

In Chapter 14, a test of the theory defining the ORC for the direct configuration will be devised and performed. Specifically, system efficiency will be determined for an effective irradiance level thus allowing one to evaluate the benefit, if any, of superheating. Chapter 15 will review several databases of fluid properties to search for a fluid that meets the reduced critical temperature and normal boiling point requirements.

14. TESTING THE THERMODYNAMIC CYCLE FOR HEAT ENGINES

14.1 Introduction/background

Chapter 13, applys similar fluid search methods used in the refrigeration industry to solar-thermal power generation. This method is specifically applied to the direct configuration DSSTC design problem. There were two key findings: (1) an ORC Rankine cycle without superheating was identified as the cycle with the greatest potential for efficiency, small machine size, and simple design; and (2) a set of working fluid requirements. Specifically, a fluid with a high critical temperature allows a wide rectangular-shaped *T*-*s* cycle to promote efficiency and low normal boiling point provides small machine size measured by the VPC. The goal of this chapter is to test these conclusions.

14.2 Methodology

Two fluids will be compared: water and R-11. Water meets the critical temperature requirement and R-11 meets the normal boiling point requirement. In Chapter 13, the requirements and conclusions were determined through simplified logic. Here, a collector/heat engine system simulation is developed to test the requirements in a holistic way.

14.2.1 Collector thermal model

The N–S XCPC solar collector model equation is used (see Chapters 8 and 9). The basic form with coefficients specific to the N–S XCPC (Equations 14.1) follows:

$$\eta_{\mathrm{col}} = \eta_0 - a_1 T_m^* - a_2 G_{eff} {T_m^*}^2 \tag{14.1a}$$

$$T_m^* = \frac{T_m - T_{amb}}{G_{eff}} \tag{14.1b}$$

where the effective irradiance (G_{eff}) is assumed to be 250, 500, 750, or 1000 W/m^2 in the current simulation. The reduced mean temperature (T_m^*) is typically based on liquid heating (sensible heating) in the collector where the mean temperature (T_m) is an average over the length of the absorber tube. When flowing liquid is heated in a tube using a uniform heat flux without phase change, T_m is simply the arithmetic average of the inlet and outlet temperatures, and this is the form that the STC testing standards have adopted. (Keep in mind that the heat flow into the compressed liquid is $q = \dot{m}C_p(T_H - T_L)$.) This perspective rests on the following assumptions: 1) steady-state conditions, 2) incompressible liquid, 3) negligible viscous dissipation, 4) constant fluid properties, and 5) fully developed flow. This allowed the enthalpy to be simplified ($h = C_pT$). For $T_m = \frac{T_H+T_L}{2}$ to be correct, one additional assumption must hold true. Uniform heat flux along the axial direction of the tube. There are several problems with making these assumptions:

- The net heat flux (per unit length of absorber) into the fluid is not constant even though the radiation incident on the surface of the tube is assumed to be uniform ($q''_{rad,net} = q''_{rad,in} - q''_{rad,out}$ where $q''_{rad,out} = \epsilon\sigma T_s^4$, ϵ is the emissivity of the absorber surface, σ is the Stefan-Boltzmann constant, and T_s is the absorber surface temperature). This means that generating moderate temperature differences from inlet to outlet violates the uniform heat flux assumption. Keep in mind that the uniform heat flux assumption applies reasonably well for pool and domestic hot water heating applications, just not for the medium-grade temperatures of interest here, or for the high temperatures of single- and dual-axis tracking systems.

- The constant fluid properties assumption is also violated when considering medium to large temperature changes ($C_p(T)$).
- Some STC have more complex absorber tube geometries, such as shell-in-tube configurations, that invalidate the simple heat transfer model used by the standard.

When a liquid is heated with a non-uniform heat flux and/or through a phase change, calculating T_m is much more complex and depends on the heat transfer physics (including geometry) and the fluid being heated. Most, if not all, of the above assumptions are violated when considering a general method to average the temperature over the length of the absorber tube. The general method must include sensible heating, latent heating (two-phase flow), vapor heating (superheating), and most importantly account for non-uniform heat flux. In a direct solar configuration, by definition a fluid is being boiled in the collector. This presents a significant problem because $T_m = \frac{T_H+T_L}{2}$ does not apply correctly to the XCPC under liquid heating or two-phase flow heat transfer conditions. Moving the research forward, two key assumptions are made:

1. It is assumed that two-phase flow heat transfer does not change the thermal performance equations (Equation 14.1);
2. It is further assumed that calculating T_m as the enthalpy-weighted average temperature will best approximate collector performance. This is discussed further in the next section.

Clearly, this engineering judgment is questionable, although it is required to move the work forward because the amount of experimentation required to create an engineering model (absorber surface temperature as a function of length) and validation is outside the scope of work and left as future work. Figure 14.1 shows that avearaging based on entropy or enthalpy are much better assumptions than averaging the inlet and outlet temperatures. There are a number of published papers that discuss systems with two-phase flow heat transfer and fail to discuss or address these issues [30, 33, 182–184]. A further complication is that the required engineering model is fluid, collector design, and collector orientation dependent. This means model coefficients for each fluid, collector, and orientation must be determined from experimentation. Even further complicating matters, the XCPC absorber tube is a shell-and-tube design, where the fluid makes two passes through the collector per tube (once through the inner tube and once through the outer shell). This results in a a non-linear relationship between the fluid temperature profile and the absorber surface temperature profile. No theory alone can properly account for these complications; therefore, performance models must be tuned to experimental data. Data that is not yet available. One of the key goals of this work is to estimate the performance of a direct configuration system because it has two notable benefits: 1) simple design (lower cost), and 2) higher efficiency (high benefit) when compared to the indirect system. This means that the direct configuration has a better chance of competing with PV for power production. Numerical modeling is one order of magnitude less expensive than experimentation. It makes good financial sense to first model DSSTC system performance using what is already known, then use the results to identify the 'best' direction forward.

14.2.2 Thermodynamic cycle

A thermodynamic state is defined by identifying the values of two state properties from which all other state property values are known. Keep in mind that T and P do not form a state pair inside the vapor dome. Outside the vapor dome, T and P do

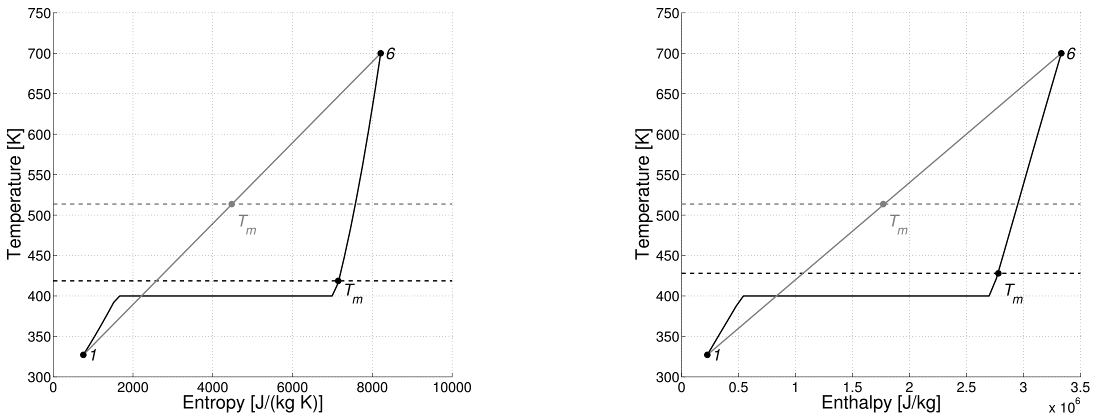

(a) Low pressure with superheating. Mean temperature based on Entropy.

(b) Low Pressure with superheating. Mean temperature based on Enthalpy.

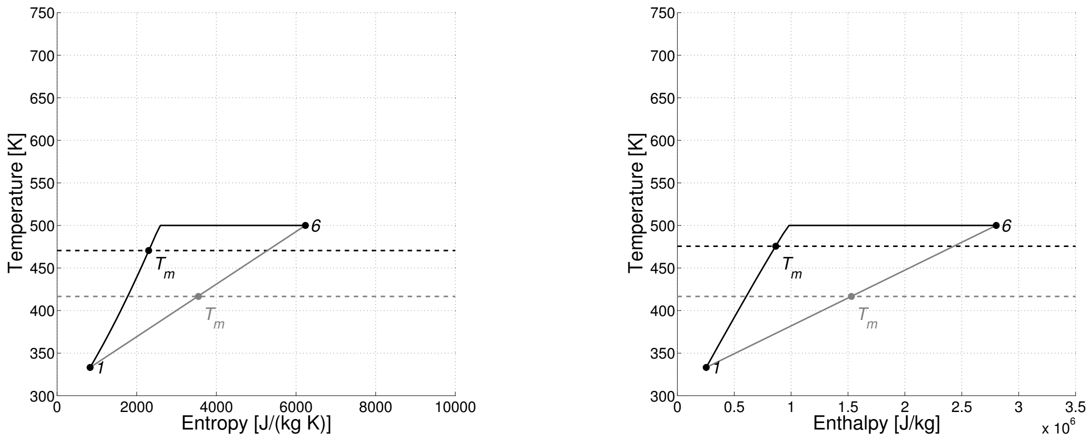

(c) High pressure without superheating. Mean temperature based on Entropy.

(d) High pressure without superheating. Mean temperature based on Enthalpy.

Figure 14.1: Mean temperature comparison of several calculation methods.

form a state pair. At the expander inlet (Figure 14.2, State 1), State 1 is specified by arbitrarily selecting temperature T and specific entropy s. Design-space exploration is performed by selecting State 1 from a domain of T and s values. At the pump inlet (Figure 14.2, State 4), State 4 is given by setting quality ($Q_4 = 0$) and temperature ($T_4 = 300$ K + 10 K). Furthermore, the expander efficiency η_t is assumed to be 0.85 and pump efficiency η_p is assumed to be $0.74375 = 0.875\eta_t$ because generally pumping is less efficient than expanding. Using the above givens, assumptions, and selections, the remaining thermodynamic states are calculated in Equations 14.2,

$$[P_1, h_1] = f(T_1, s_1) \tag{14.2a}$$

$$P_5 = P_6 = P_1 \tag{14.2b}$$

$$[P_4, h_4] = f(T_4, Q_4) \tag{14.2c}$$

$$P_3 = P_2 = P_4 \tag{14.2d}$$

$$s_2 = s_1 \tag{14.2e}$$

$$[h_2] = f(P_2, s_2) \tag{14.2f}$$

$$h_3 = h_1 - \eta_t(h_1 - h_2) \tag{14.2g}$$

$$\rho_3 = f(P_3, h_3) \tag{14.2h}$$

$$s_5 = s_4 \tag{14.2i}$$

$$[h_5] = f(P_5, s_5) \tag{14.2j}$$

$$h_6 = \frac{(h_5 - h_4)}{\eta_p} + h_4 \tag{14.2k}$$

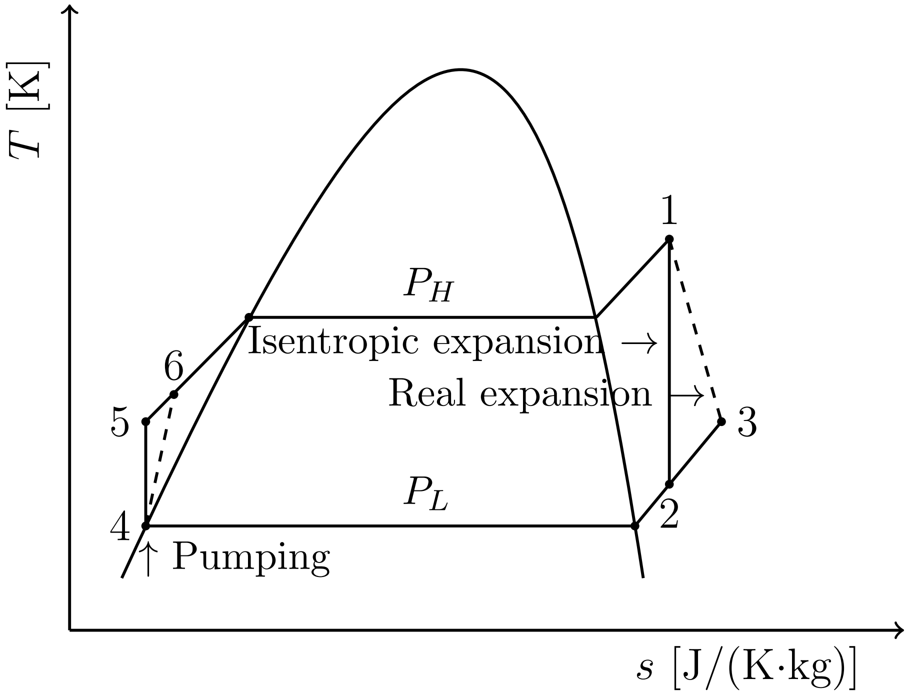

Figure 14.2: Rankine cycle as defined in the simulation.

where the fluid density is ρ. Using the state information, system efficiency and VPC are determined in Equations 14.3.

$$\eta_{\text{cycle}} = \frac{((h_1 - h_3) - (h_6 - h_4))}{(h_1 - h_6)} \tag{14.3a}$$

$$\eta_{\text{Carnot}} = 1 - \frac{T_4}{T_1} \tag{14.3b}$$

$$\eta_2 = \frac{\eta_{\text{cycle}}}{\eta_{\text{Carnot}}} \tag{14.3c}$$

$$\psi = (h_1 - h_3)\rho_3 \tag{14.3d}$$

In the direct configuration, the solar collector provides two functions: (1) solar radiance collection and (2) boiling the working fluid of the heat engine. The mean temperature of the collector T_m is meant to represent the average temperature over the fluid flow path in the absorber tube. Because this information has not yet be experimentally determined and depends on the fluid, the geometry and the heat transfer process, using current methods it is not possible to make this determination; therefore, T_m is approximated by numerically averaging over the specific enthalpy h (Equations 14.4),

$$dh = \frac{(h_1 - h_6)}{(n-1)} \tag{14.4a}$$

$$T_m = \frac{1}{n}\sum_{i=0}^{n-1} T(h_6 + idh) \tag{14.4b}$$

from State 6 to State 1 using 50 sample points (Figure 14.2). In thermodynamics the initial point (State 6) and the final point (State 1) are path independent meaning there are an infinity number of process paths between them. Conversely in heat transfer, the results are process path dependent. The difference is that the temperature profile as a function of absorber tube distance is unknown, and in place of this profile, the temperature along the constant pressure line as a function of entropy is used. This choice must induce some amount of unknown error, and at the same time, the choice is better than averaging the end point temperatures (Figure 14.1). The number of sample points $n = 50$ was chosen using convergence testing (see Figures 14.3 and 14.4) and the need to minimize computational cost because the T_m calculation is the most computationally expensive part of the algorithm.

14.2.3 System efficiency

The system efficiency is calculated as the product of the collector efficiency and heat engine efficiency shown in Equation 14.5.

$$\eta_{sys} = \eta_{\text{col}}\eta_{\text{cycle}} \tag{14.5}$$

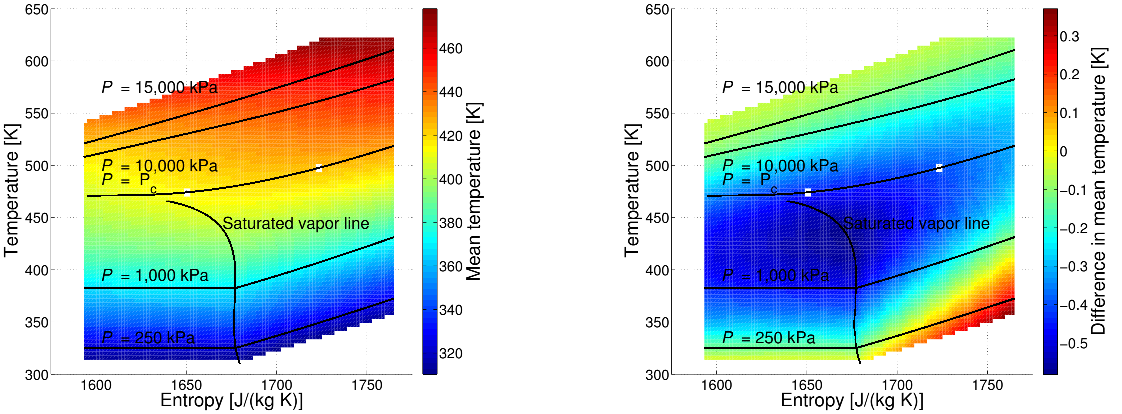

(a) T_m results based on enthalpy for $n = 50$.

(b) Difference in T_m results ($n = 50 - n = 2000$).

Figure 14.3: T_m based on enthalpy, results for R-11.

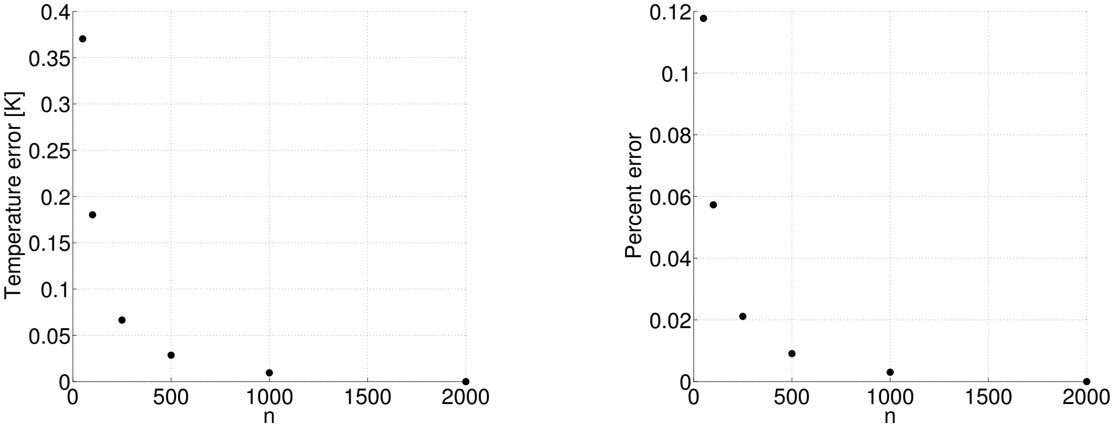

(a) Absolute error of point with maximum error.

(b) Percent error of point with maximum error.

Figure 14.4: Convergence plots for T_m calculation, results for R-11.

Design-space exploration is performed by selecting State 1 of the thermodynamic cycle model from a domain of T and s values. This design-space exploration is used to discover the topology of system efficiency, T_m, and VPC ψ. By comparing and constrasting results at the four irradiance values for water and R-11, the conclusions of T_c and T_{nbp} are tested.

14.3 Results and discussion

The results are presented in two main parts: 1) heat engine performance that is independent of irradiance and 2) system performance that is dependent on both heat engine performance and collector performance for a given irradiance level.

14.3.1 Heat engine performance results

Figures 14.5 and 14.6 show heat engine performance results. Water and R-11 have diverse results. Compared to R-11, Water has (1) greater cycle efficiency, (2) greater mean temperature, (3) smaller VPC, and (4) greater expansion ratios. The greater efficiency of the cycle is consistent with the greater critical temperature of water. The greater mean temperature of the cycle better matches the XCPC collector designs. The smaller VPC and greater expansion ratio are consistent with the higher normal boiling point of water. Next, overall system performance is reviewed.

14.3.2 System performance results

In this section, overall system performance is presented. Unlike the thermodynamic cycle results, system results depend on irradiance level. System efficiency is presented in Figures 14.7 and 14.8. At the system level, the figures show that water is the more efficient choice between the two fluids. R-11 also violates the cycle assumptions because at the higher irradiance levels, the most efficient cycle choices are outside the vapor dome. This is consistent with the lower critical temperature

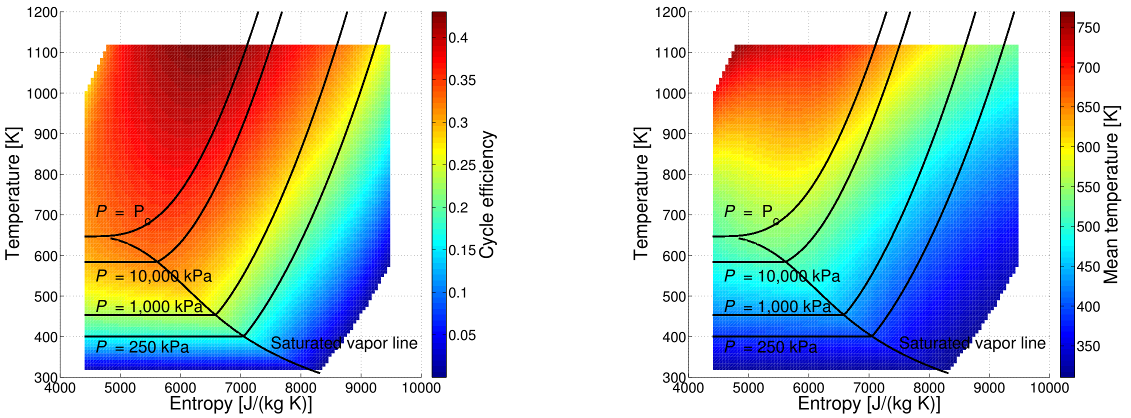

(a) Cycle efficiency.

(b) Mean temperature of the collector.

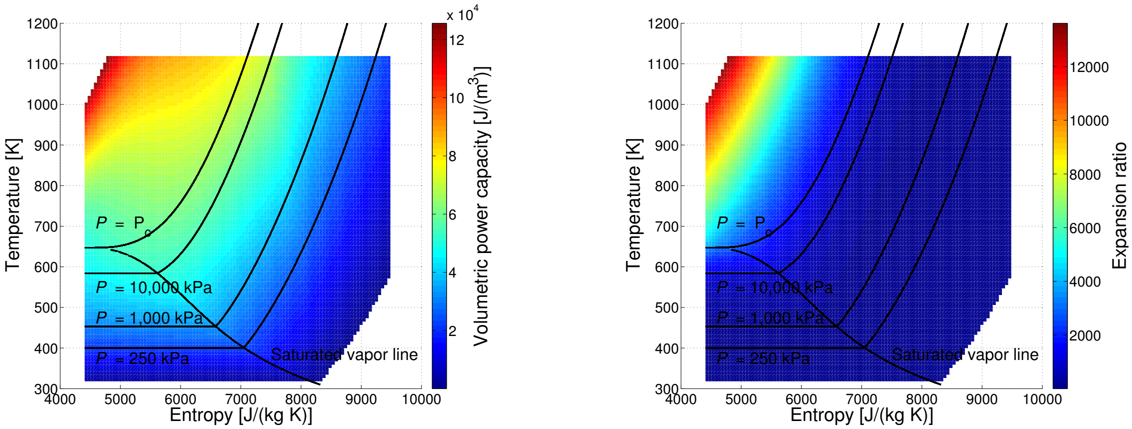

(c) Volumteric power capacity.

(d) Expansion ratio.

Figure 14.5: Thermodynamic cycle results for water.

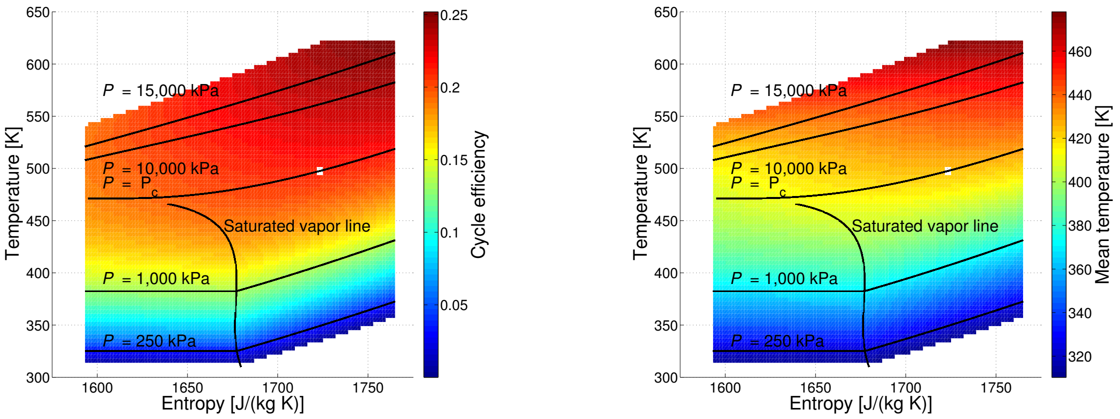

(a) Cycle efficiency. (b) Mean temperature of the collector.

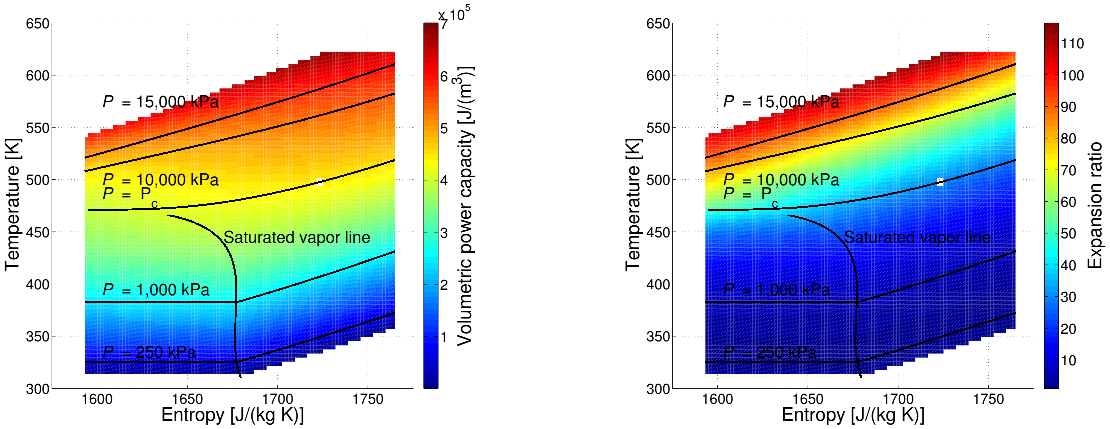

(c) Volumteric power capacity. (d) Expansion ratio.

Figure 14.6: Thermodynamic cycle results for R-11.

of R-11. A detailed view of various cycle attributes along the saturated vapor line and the maximum efficiency line for each irradiance level are presented. Figures 14.9 and 14.10 show system efficiency detail. The figures show that decreasing irradiance reduce efficiency, as expected. The figures also show that selecting water notably improves efficiency. When using R-11, superheating improves efficiency. In contrast, superheating water provides no notable increase in efficiency. This is consistent with the theory discussed in the previous chapter. Figures 14.11 and 14.12 show that water is the better match for the mean temperature of the collector requirement, which is consistent with the cycle results. Volumetric power capacity (VPC) also decreases with decreasing irradiance and water is one order of magnitude lower than R-11 (Figures 14.13 and 14.14); thus water requires a larger machine size. The expansion ratio also decreases and is an order of magnitude greater for water (Figure 14.15 and 14.16). These results are consistent with what was previously known about STC and heat engines. The new information presented here shows that selecting a transitional collector without tracking (XCPC design) is best matched to water when considering efficiency, but it has a machine size cost. During this work, the single most important discovery is that there are many possible choices for thermodynamic state at the expander inlet, which defines the cycle. Some of the design attributes are cycle efficiency, system efficiency, mean temperature, VPC, and expansion ratio. In many cases, these design attributes have competing performance. Maximizing efficiency may not minimize lifecycle cost of energy (LCOE).

14.4 Conclusions and summary

The results show that superheating is not required to define a thermodynamic cycle that maximizes efficiency when the critical temperature and entropy width requirements are met. However, when T_c is high enough, moderate superheating did

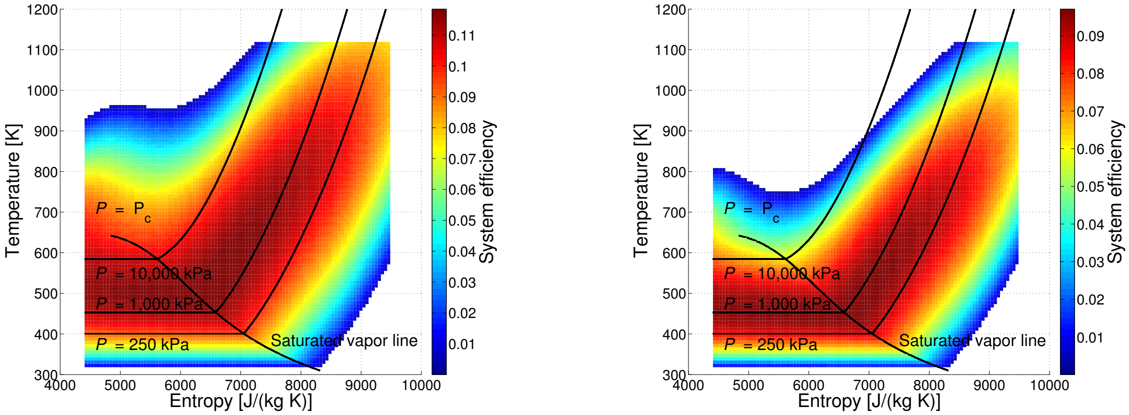

(a) Irradiance $G_{eff} = 1000$ W/m^2.

(b) Irradiance $G_{eff} = 750$ W/m^2.

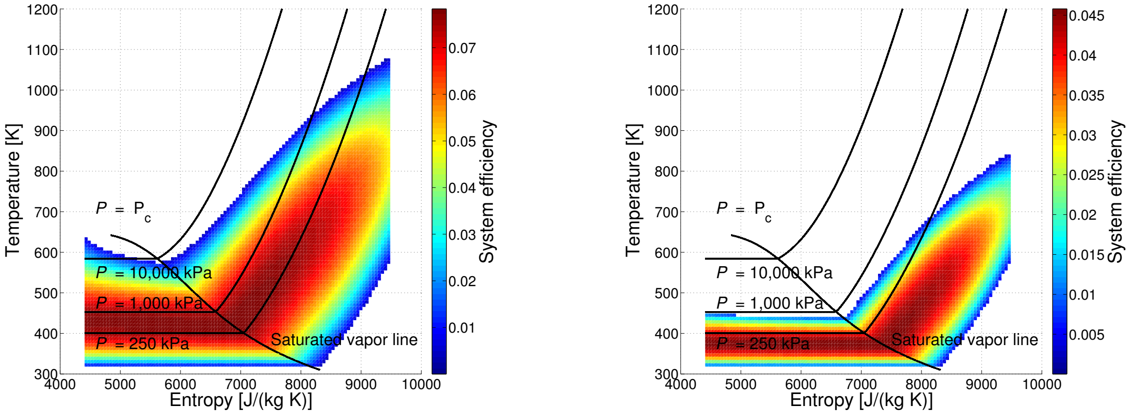

(c) Irradiance $G_{eff} = 500$ W/m^2.

(d) Irradiance $G_{eff} = 250$ W/m^2.

Figure 14.7: System efficiency at four irradiance levels using water as the working fluid.

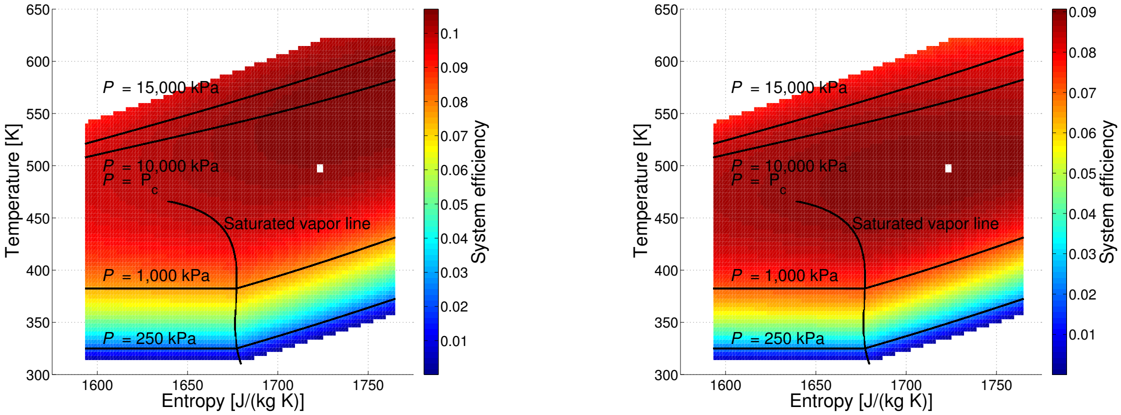

(a) Irradiance $G_{eff} = 1000$ W/m^2.

(b) Irradiance $G_{eff} = 750$ W/m^2.

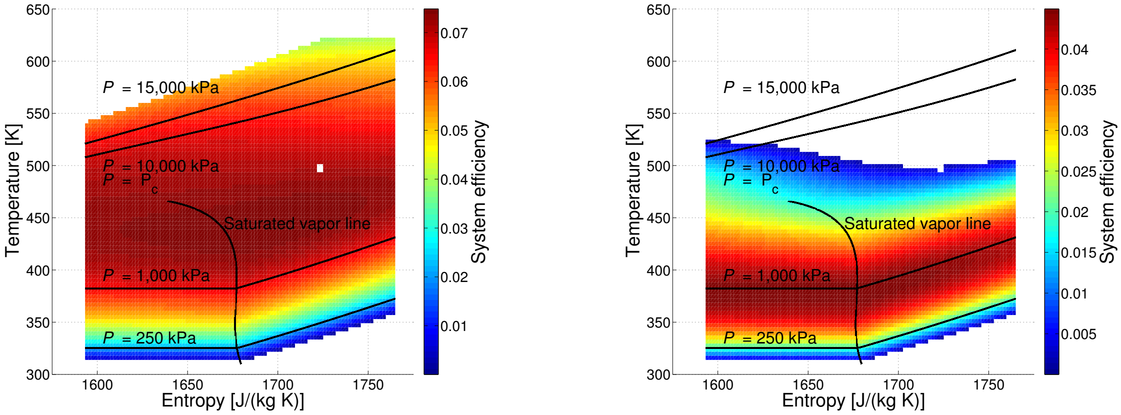

(c) Irradiance $G_{eff} = 500$ W/m^2.

(d) Irradiance $G_{eff} = 250$ W/m^2.

Figure 14.8: System efficiency at four irradiance levels using R-11 as the working fluid.

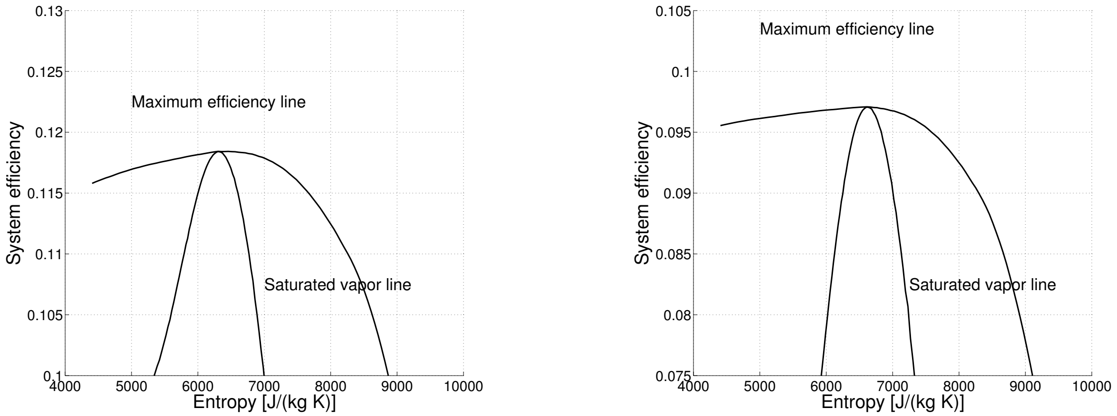

(a) Irradiance $G_{eff} = 1000$ W/m^2.

(b) Irradiance $G_{eff} = 750$ W/m^2.

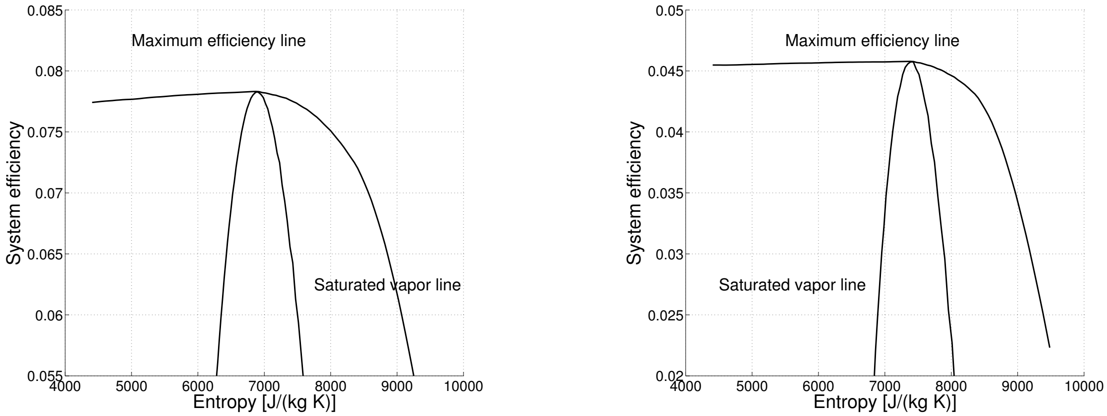

(c) Irradiance $G_{eff} = 500$ W/m^2.

(d) Irradiance $G_{eff} = 250$ W/m^2.

Figure 14.9: System efficiency detail at four irradiance levels using water as the working fluid.

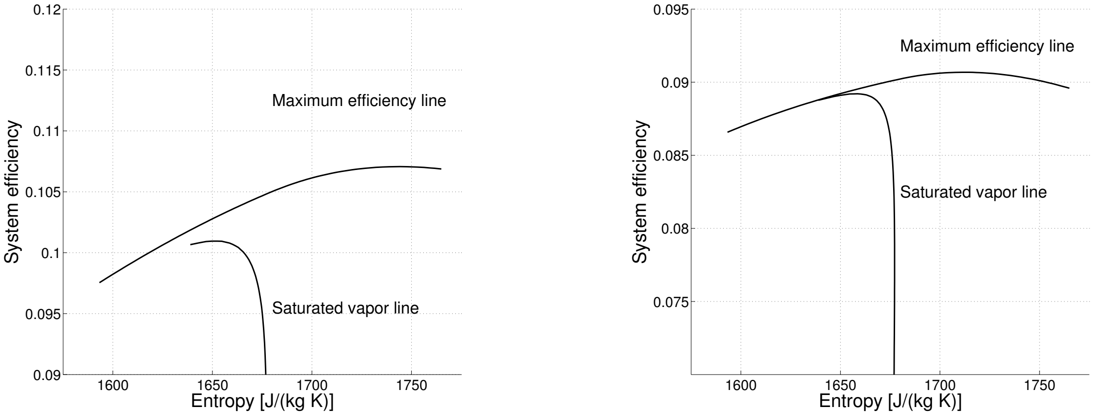

(a) Irradiance $G_{eff} = 1000$ W/m^2.

(b) Irradiance $G_{eff} = 750$ W/m^2.

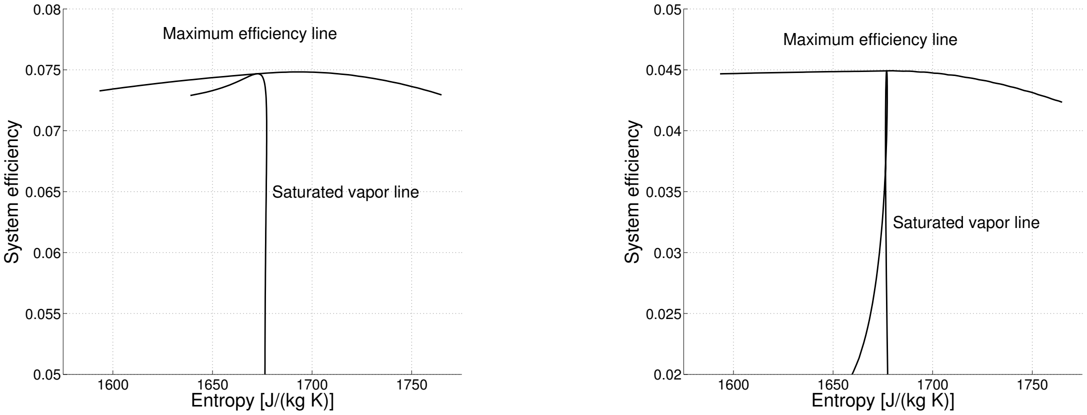

(c) Irradiance $G_{eff} = 500$ W/m^2.

(d) Irradiance $G_{eff} = 250$ W/m^2.

Figure 14.10: System efficiency detail at four irradiance levels using R-11 as the working fluid.

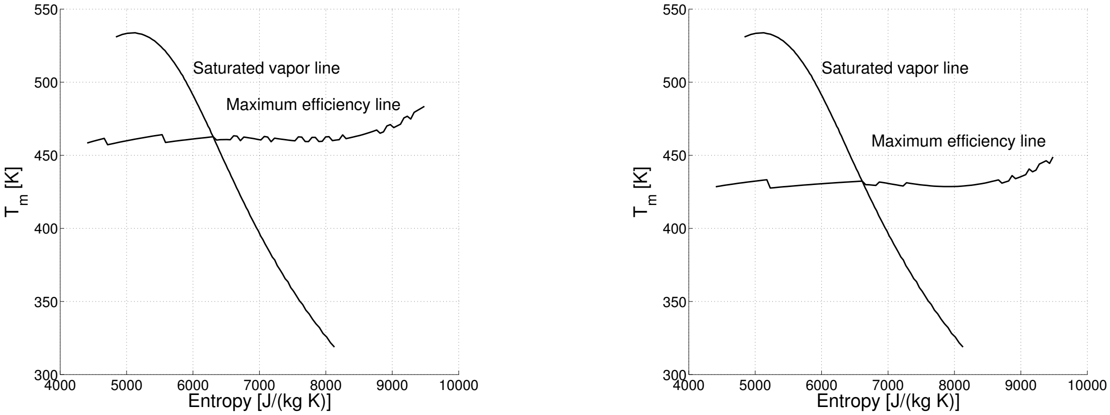

(a) Irradiance $G_{eff} = 1000$ W/m^2. (b) Irradiance $G_{eff} = 750$ W/m^2.

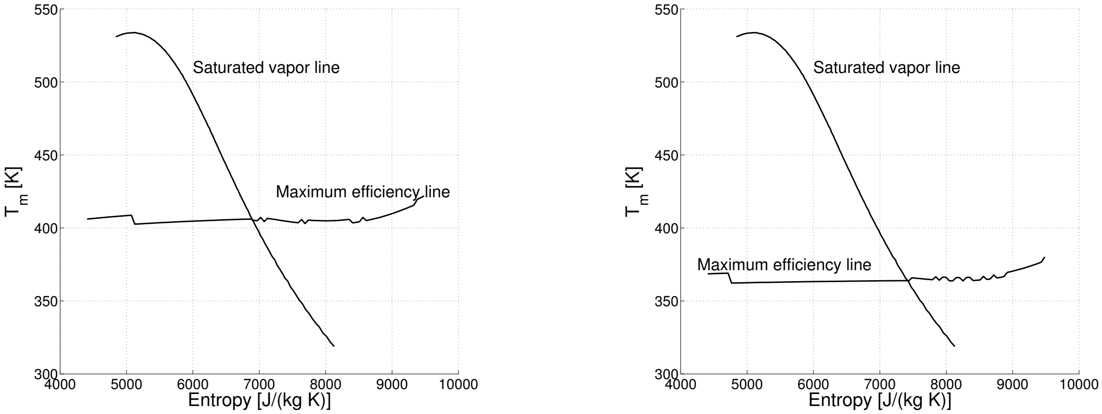

(c) Irradiance $G_{eff} = 500$ W/m^2. (d) Irradiance $G_{eff} = 250$ W/m^2.

Figure 14.11: Mean temperature of the collector detail at four irradiance levels using water as the working fluid.

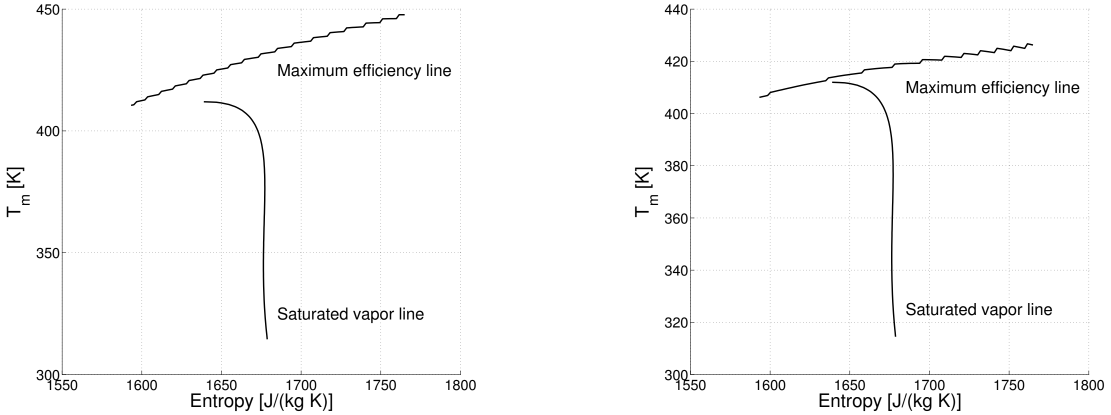

(a) Irradiance $G_{eff} = 1000$ W/m^2.

(b) Irradiance $G_{eff} = 750$ W/m^2.

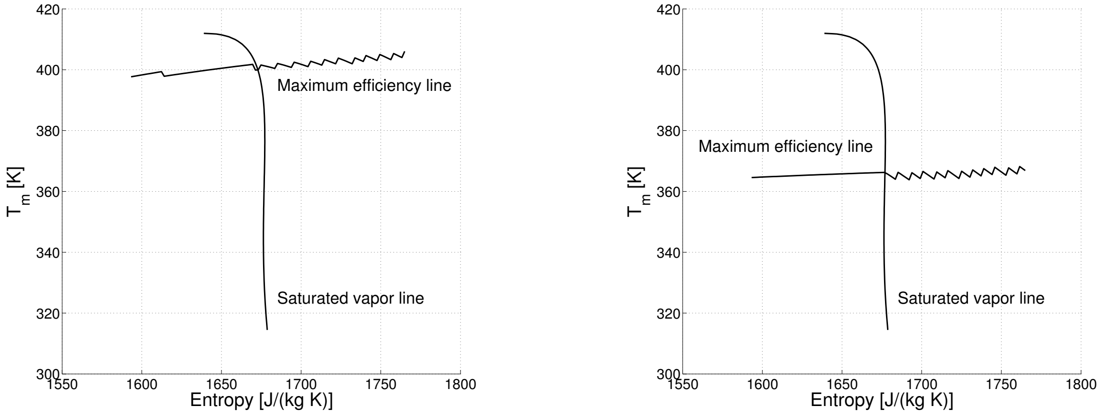

(c) Irradiance $G_{eff} = 500$ W/m^2.

(d) Irradiance $G_{eff} = 250$ W/m^2.

Figure 14.12: Mean temperature of the collector detail at four irradiance levels using R-11 as the working fluid.

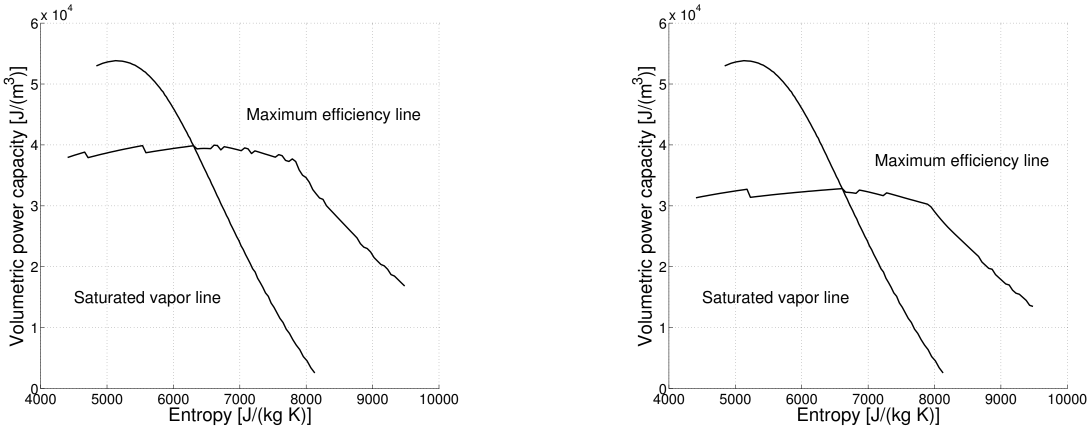

(a) Irradiance $G_{eff} = 1000$ W/m^2.

(b) Irradiance $G_{eff} = 750$ W/m^2.

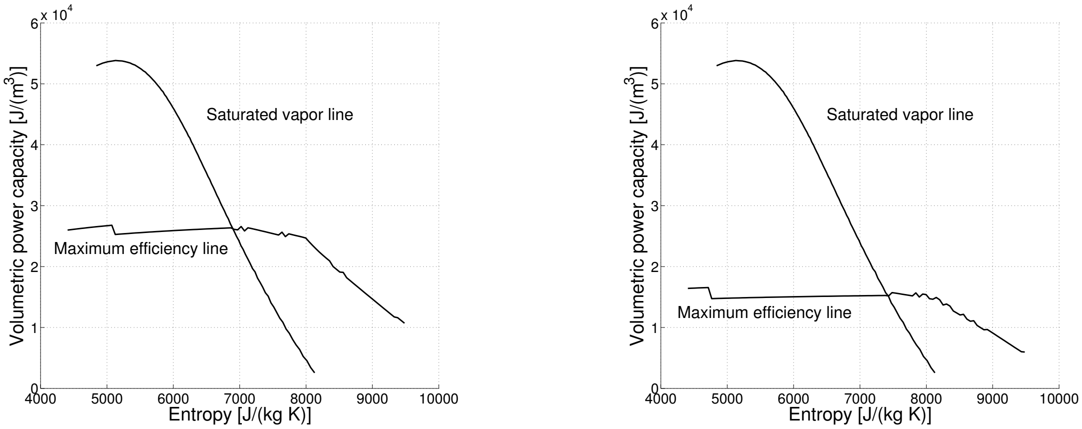

(c) Irradiance $G_{eff} = 500$ W/m^2.

(d) Irradiance $G_{eff} = 250$ W/m^2.

Figure 14.13: Volumetric power capacity detail at four irradiance levels using water as the working fluid.

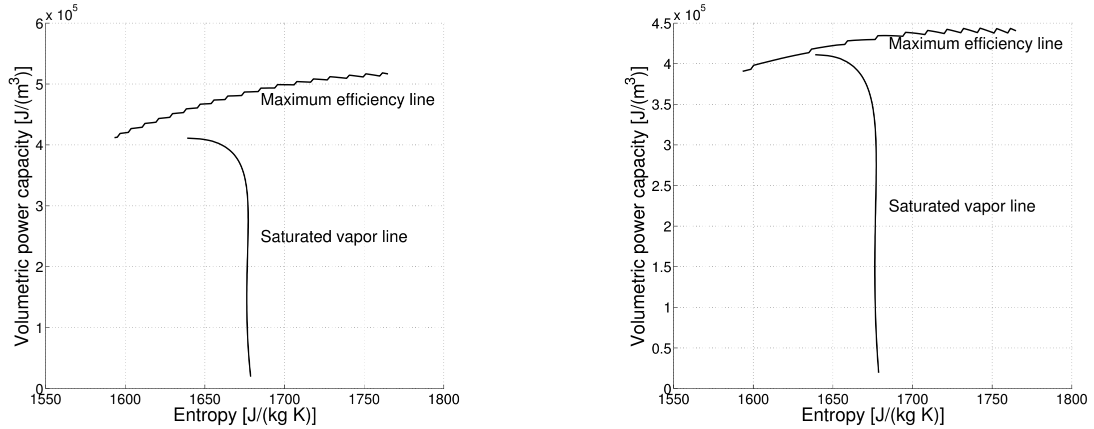

(a) Irradiance $G_{eff} = 1000$ W/m^2.

(b) Irradiance $G_{eff} = 750$ W/m^2.

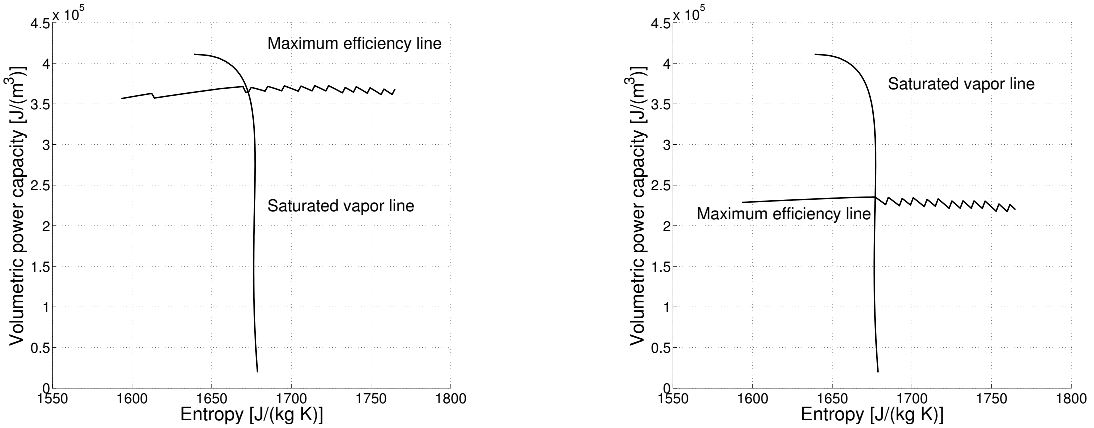

(c) Irradiance $G_{eff} = 500$ W/m^2.

(d) Irradiance $G_{eff} = 250$ W/m^2.

Figure 14.14: Volumetric power capacity detail at four irradiance levels using R-11 as the working fluid.

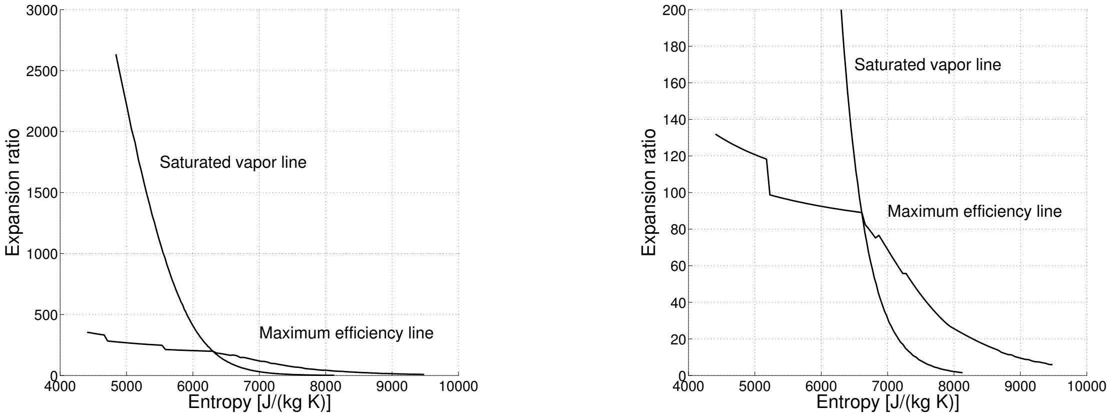

(a) Irradiance $G_{eff} = 1000$ W/m^2.

(b) Irradiance $G_{eff} = 750$ W/m^2.

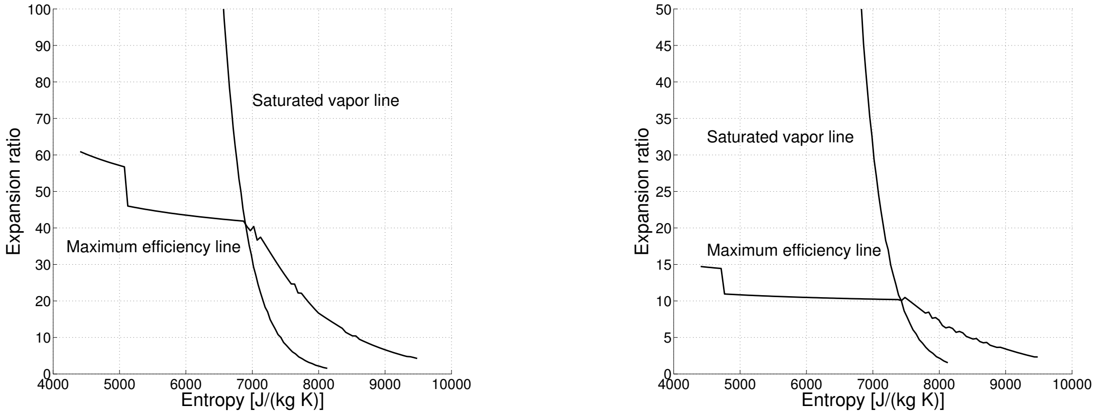

(c) Irradiance $G_{eff} = 500$ W/m^2.

(d) Irradiance $G_{eff} = 250$ W/m^2.

Figure 14.15: Expansion ratio detail at four irradiance levels using water as the working fluid.

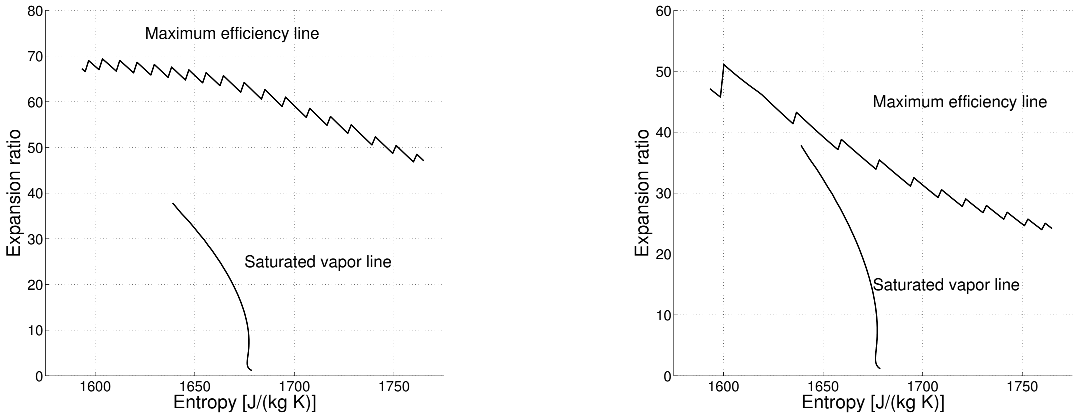

(a) Irradiance $G_{eff} = 1000$ W/m^2.

(b) Irradiance $G_{eff} = 750$ W/m^2.

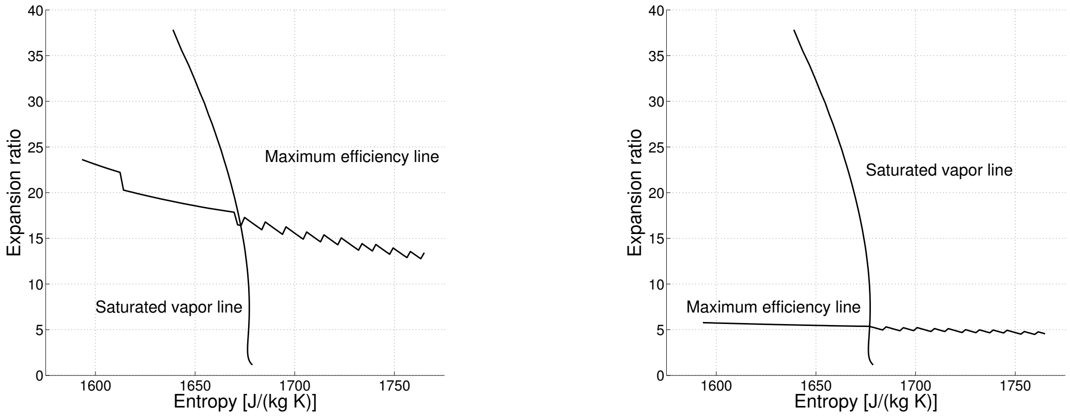

(c) Irradiance $G_{eff} = 500$ W/m^2.

(d) Irradiance $G_{eff} = 250$ W/m^2.

Figure 14.16: Expansion ratio detail at four irradiance levels using R-11 as the working fluid.

not adversely impact efficiency. When the T_c requirement was not met, superheating was required. Furthermore, the normal boiling point requirement corresponds to expansion ratio and VPC. In a simple system model, reviewing the performance of water and R-11 confirmed the theoretical results of the previous chapter and the T_m results were consistent with Chapter 12. Although reviewing two fluids is not proof that the guiding principles are absolutely correct, the results presented here fully support these principles. Chapter 17 models many fluids and reviews the two correlations in greater depth.

14.5 Future work

While preparing this chapter, the following future improvements were identified:

- Develop a regenerator cycle model that can accommodate superheating, which serves as a comparison.
- Include more sophisticated heat exchanger models that can predict pressure and temperature losses.
- Identify a method to select the best choice for the thermodynamic state at the expander inlet given that this work has shown competing benefits in the design attributes.
- Compare more fluids than two.

15. SEARCH OF KNOWN FLUIDS

15.1 Introduction/background

The HVAC-R industry has developed an advanced fluid search methodology, which is just beginning to be applied to organic Rankine cycles. It has not be applied to solar-driven organic Rankine cycle heat engines, which is a separate design problem than waste heat recovery organic Rankine cycle heat engines (Chapter 16). The first goal in the search methodology was accomplished in Chapter 13 where search criteria were adapted for the solar design problem, reduced criteria were identified (T_c and T_{nbp}), and less restrictive levels were set. In Chapter 14, the criteria were tested and confirmed. In this chapter, the second goal is accomplished: searching the known fluids based on the new criteria.

15.2 Methodology

This work explores existing fluids to determine which ones, if any, meet the less restrictive search criteria (critical temperature ($T_c \geq 500$ K) and normal boiling point ($T_{nbp} \leq 300$ K)). Chapter 13 showed that the selected normal boiling point and critical temperature requirements are outside of the acceptable value, which is an effort to be less restrictive. To design a rectangular shaped cycle inside a vapor dome, the critical temperature of the working fluid must be above the maximum temperature of the cycle. Chapter 12 found that a reasonable expectation is a high working temperature of $\sim$550 K. Chapter 13 discussed that to limit air infiltration, the working pressure in the condensor should be higher than ambient pressure. To achieve this, the normal boiling point temperature must be greater than the expected ambient temperatures. Because operation is difficult in the event of snow, the lower ambient temperature limit is selected as the freezing point of water 273.15 K. Additionally, the majority of TMY sites experience some number of daytime hours where the ambient temperature is 273.15 K or less. Because both efficiency and machine size/air infiltration are sliding scales, it is difficult to justify an exact cut off. For this reason, four regions of interest are created and outlined in Table 15.1. Given that the search is based on a limited set of the criteria, a fluid meeting the reduced criteria (Region 3) may not be acceptable (e.g., an extremely dry fluid). Also, a fluid not meeting the reduced criteria (Region 3) is highly likely to require superheating. Using the reduced criteria (Region 3) creates a test that may give a false positive and will not give a false negative in the search for a fluid that can provide a rectangular-shaped cycle and provide reduced machine size.

Three information sources are used: NIST database 23 REFPROP [185], DIPPR database [186], and NIST database 103b ThermoData Engine (TDE103b v9) [187]. REFPROP is not actually a database; rather, it is an algorithm used to accurately model thermal/transport properties of fluids commonly used in industry. DIPPR is a database of fluids with known physical measurements. In addition, some modeled properties are available. TDE103b is both a database and a property prediction algorithm. TDE103b contains all known fluids that have at least a single physical measurement from a published source. From the known structure and physical measurements, TDE103b then attempts to predict other physical properties with varying degrees of accuracy because of limited measurements and modeling methods.

Refrigerants are known to typically have a reduced normal boiling point of 0.6–0.7. This means that searching based on Region 3/Region 4 is expected to yield a smaller/larger list of fluids to evaluate, respectively. In this chapter, searches are conducted based on Region 3 criteria ($T_c \geq 500$ K and $T_{nbp} \leq 300$ K). Chapter 17 conducts a search based on Region 4 using REFPROP and then the fluids identi-

Table 15.1: Regions of interest and boundaries

Region	T_c [K]	T_{nbp} [K]	Description	Comments
Region 1	650	250	Most ideal region	Selected to ensure ideal rectangular shape
Region 2	550	275	Edge of ideal region	Selected to note the boundary where the ideal is likely to be achieved
Region 3	500	300	Less restrictive region	Selected to ensure any fluid that may work in the ideal is retained
Region 4	400	400	Least restrictive region	Selected to approximate the boundary of thermodynamically feasible fluids that would work using super heating

fied are further screened based on thermodynamic criteria and health, safety, and environmental criteria.

15.3 Results and discussion

15.3.1 REFPROP v9.1

REFPROP contains 121 pure fluids and 79 predefined mixtures. The fluids in REFPROP are plotted in Figure 15.2. Water is of interest because it has many favorable attributes, with the exception of the normal boiling point; its reduced normal boiling point is lower than most fluids. Water is considered an abnormal fluid because its properties are atypical resulting from the low atom count per molecule and its strong hydrogen bonds. Table 15.2 summarizes fluids in REFPROP with a reduce normal boiling point below 0.6 ($T_{rnbp} < 0.6$) and shows support for this perspective. Ammonia is another example. Figure 15.3 provides further details about the search area. R-11 and R-21 are two of the closest fluids to the search area. Unfortunately, both fluids are banned by the EPA for ozone depletion potential (ODP) (Table 15.3).

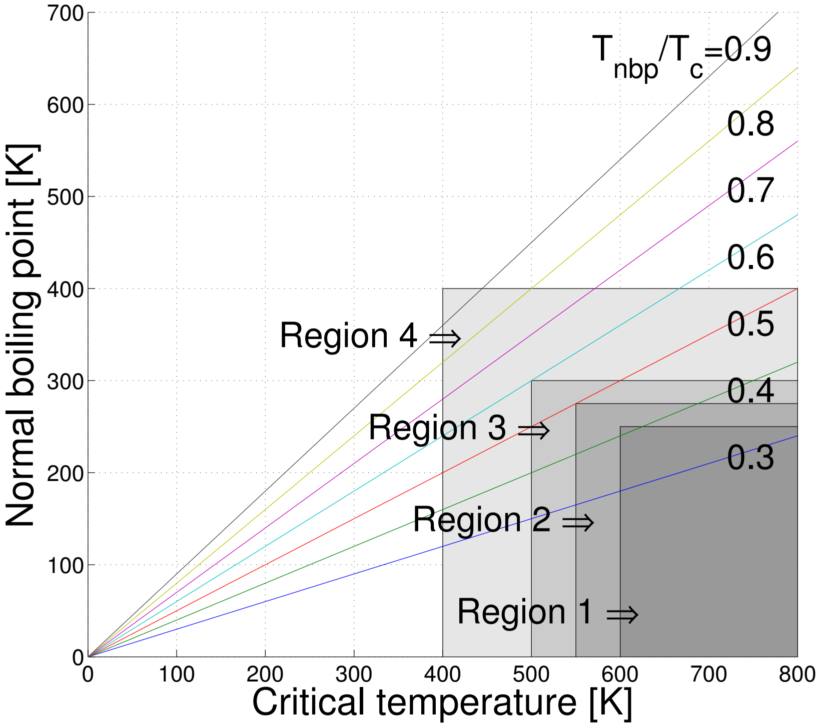

Figure 15.1: The four search regions. For example, Region 1 is a subset of all other regions.

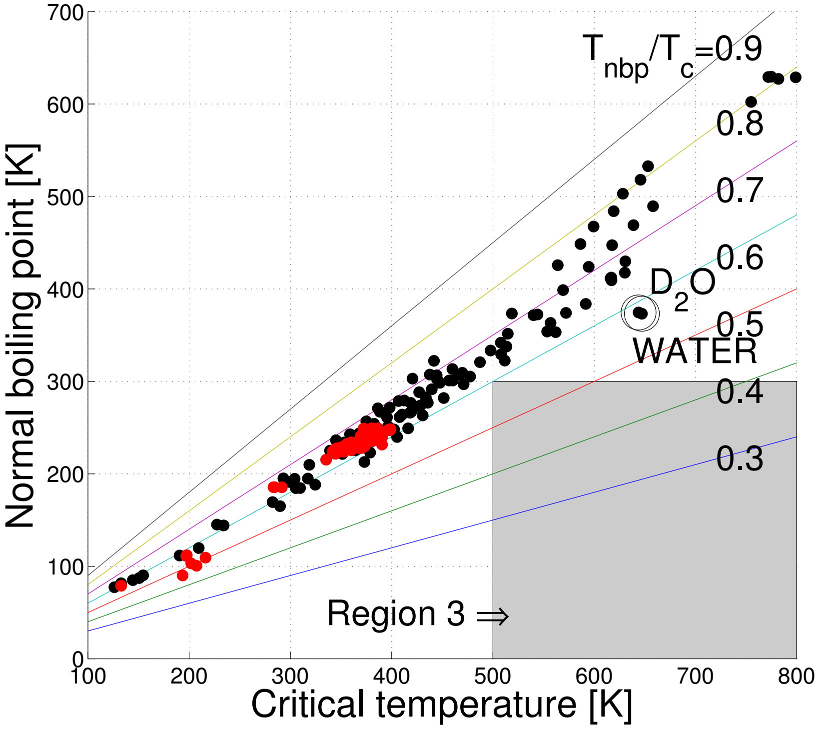

Figure 15.2: Normal boiling point vs. critical temperature: REFPROP v9.1. Target Region 3 in grey. Pure fluids in black. Predefined mixtures in red. Water and heavy water (D_2O) have the lowest reduced normal boiling point.

R-1233zd(E) and R-1336mzz(Z) are newer refrigerants specifically designed to be R-11 replacements. Note that both fluids are even further from the region of interest. No fluids in REFPROP were found in the region of interest. To further support the difference between waste heat recovery and direct solar ORC applications, Figure 15.4 shows a select set of fluids commonly considered for waste-heat-recovery ORC applications (Table 15.4).

15.3.2 DIPPR 2016

The DIPPR 2016 database contains 2130 substances of which 203 substances did not have either critical temperature or normal boiling point data; therefore, 1,927

Table 15.2: Fluids in REFPROP with reduced normal boiling point of 0.6 or less

Filename	Name	#†	CAS #	T_c[K]	T_{nbp}[K]	T_{rnbp}	Formula	#‡
ETHYLENE	Ethylene	R-1150	74-85-1	282.3	169.3	0.5999	$CH_2{=}CH_2$	6
R-40	Methyl Chloride	R-40	74-87-3	416.3	249.1	0.5985	CH_3Cl	5
N2O	Nitrous Oxide	R-744A	10024-97-2	309.5	184.6	0.5967	N_2O	3
AMMONIA	Ammonia	R-717	7664-41-7	405.4	239.8	0.5916	NH_3	4
FLUORINE	Fluorine		7782-41-4	144.4	085.0	0.5888	F_2	2
COS	Carbon Oxide Sulfide		463-58-1	378.7	222.9	0.5887	COS	3
METHANE	Methane	R-50	74-82-8	190.5	111.6	0.5860	CH_4	5
OXYGEN	Oxygen	R-732	7782-44-7	154.5	090.1	0.5834	O_2	2
D2O	Heavy Water		7789-20-0	643.8	374.5	0.5817	D_2O	3
HCL	Hydrogen Chloride		7647-01-0	324.5	188.1	0.5799	HCl	2
ARGON	Argon	R-740	7440-37-1	150.6	087.3	0.5794	Ar	1
WATER	Water	R-718	7732-18-5	647.0	373.1	0.5766	H_2O	3
KRYPTON	Krypton	R-784	7439-90-9	209.4	119.7	0.5716	Kr	1
H2S	Hydrogen Sulfide		7783-06-4	373.1	212.8	0.5705	H_2S	3
XENON	Xenon		7440-63-3	289.7	165.0	0.5697	Xe	1

†ASHRAE refrigerant number

‡Number of atoms per molecule

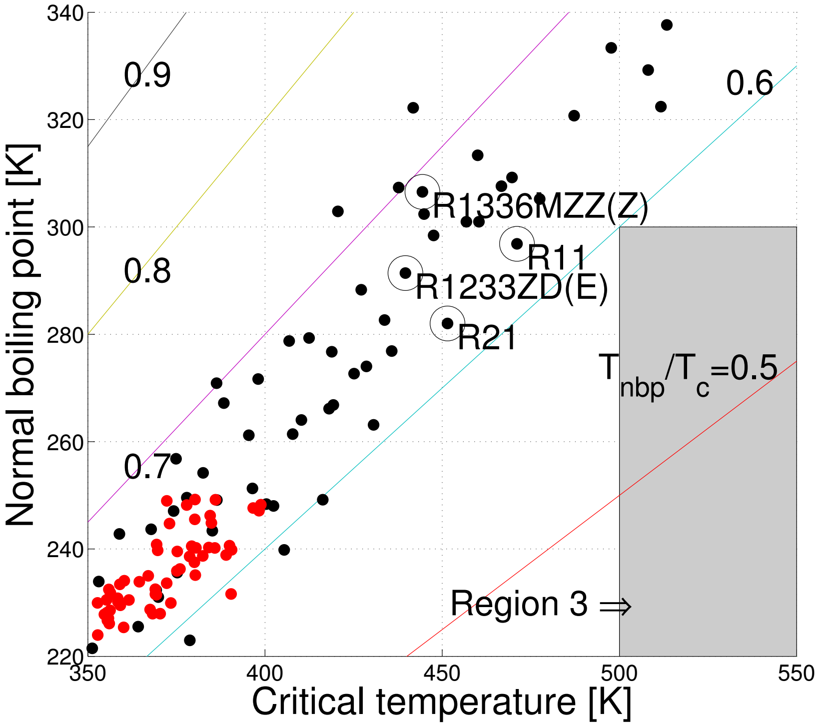

Figure 15.3: Normal boiling point vs. critical temperature: REFPROP v9.1 (zoom). Target Region 3 in grey. Pure fluids in black. Predefined mixtures in red. R-11 and R-21 are the closest, yet they are both banned by the EPA for ODP. R-1233zd(E) and R-1336mzz(Z) are R-11 replacements.

Table 15.3: Fluids in REFPROP closest to target Region 3

Filename	Name	#†	CAS #	T_c[K]	T_{nbp}[K]	T_{rnbp}	Formula	#‡
R-11	CFC-11	R-11	75-69-4	471.1	296.8	0.6301	CCl_3F	5
R-21	HCFC-21	R-21	75-43-4	451.4	282.0	0.6246	$CHCl_2F$	5

†ASHRAE refrigerant number

‡Number of atoms per molecule

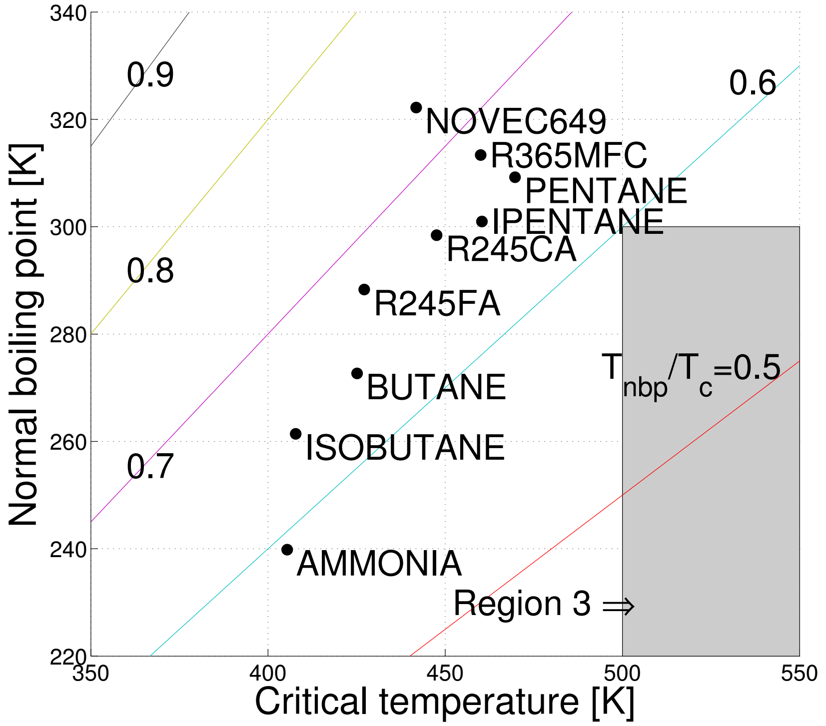

Figure 15.4: Normal boiling point vs. critical temperature: REFPROP v9.1 (Common ORC fluids). Target Region 3 in grey. Common fluids considered for ORC applications.

Table 15.4: Select pure fluids in REFPROP used in ORC waste heat recovery applications

Filename	Name	#†	CAS #	T_c[K]	T_{nbp}[K]	T_{rnbp}	Formula	#‡
AMMONIA	Ammonia	R-717	7664-41-7	405.4	239.8	0.5916	NH_3	4
BUTANE	Butane	R-600	106-97-8	425.1	272.6	0.6414	CH_3-2(CH_2)-CH_3	14
IPENTANE	Isopentane	R-601a	78-78-4	460.3	300.9	0.6538	$(CH_3)_2CHCH_2CH_3$	17
ISOBUTAN	Isobutane	R-600a	75-28-5	407.8	261.4	0.6410	$CH(CH_3)_3$	14
NOVEC649	Novec 649		756-13-8	441.8	322.2	0.7293	$CF_3CF_2C(=O)CF(CF_3)_2$	19
PENTANE	Pentane	R-601	109-66-0	469.7	309.2	0.6583	CH_3-3(CH_2)-CH_3	17
R-245CA	HFC-245ca	R-245ca	679-86-7	447.5	298.4	0.6667	$CHF_2CF_2CH_2F$	11
R-245FA	HFC-245fa	R-245fa	460-73-1	427.1	288.2	0.6749	$CF_3CH_2CHF_2$	11
R-365MFC	HFC-365mfc	R-365mfc	406-58-6	460.0	313.3	0.6812	$CF_3CH_2CF_2CH_3$	14

†ASHRAE refrigerant number

‡Number of atoms per molecule

substance were reviewed. The DIPPR database has one order of magnitude more fluids than REFPROP; however, the DIPPR database does not model fluid properties for a given thermodynamic state. The DIPPR database also covers a greater range of substances including those that are not typically considered fluids for HVAC-R applications (e.g., metals). Figure 15.5 shows the overall results. At first, this figure looks promising; however, a more detailed review shows no substances are in Region 3 (Figure 15.6). Surprisingly, liquid metals have an excellent reduced normal boiling point, although the boiling point is substantially greater than the required limit. This shows that it is possible for a molecule to have the correct reduced normal boiling point, however, none so far have the correct combination of critical temperature and normal boiling point. Although the underlying physics is not yet clear, it is becoming clear that there is a physical trade-off between normal boiling point and critical temperature; one cannot choose both. An informal review near Region 3 found fluids that were toxic, flammable, or unsuitable for another reason e.g., extreme vapor dome shape.

15.3.3 ThermoData Engine TDE103b v9

The ThermoData Engine has 27,680 substances of which 18,797 substances had measured or predicted critical temperature, normal boiling point, and critical pressure. The ThermoData Engine has one order of magnitude more fluids compared to DIPPR and two orders compared to REFPROP. Figure 15.5 shows the overall results, which also look promising. Surprisingly, a closer review shows that no fluids are in Region 3 (Figure 15.6). The results also show fluids very near Region 3 have an acceptable reduced normal boiling point, just the wrong combination of critical temperature and normal boiling point. This suggests it may be possible to find a fluid with the correct combination.

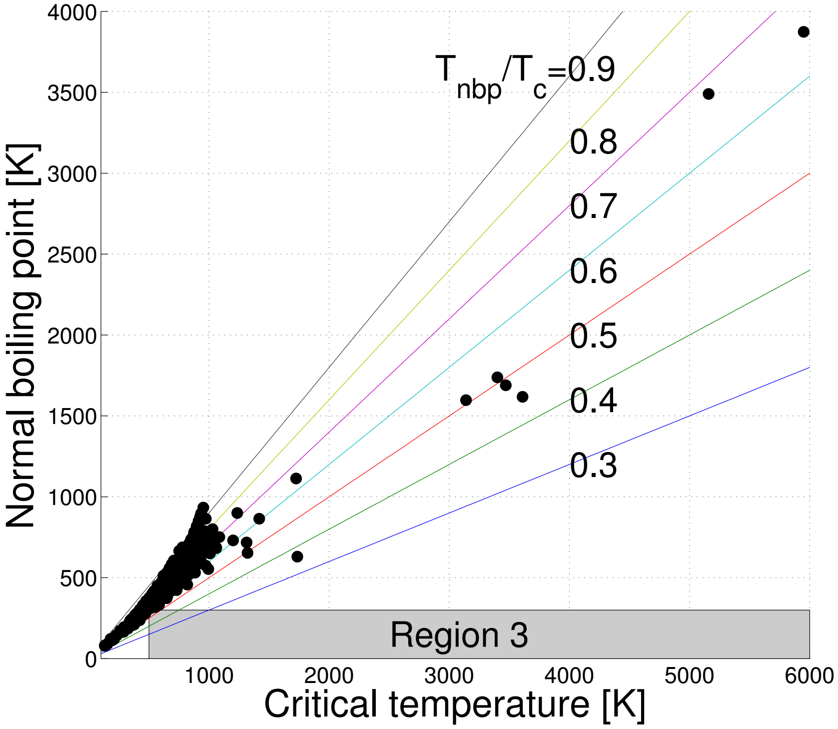

Figure 15.5: Normal boiling point vs. critical temperature: DIPPR 2016. Target Region 3 in grey.

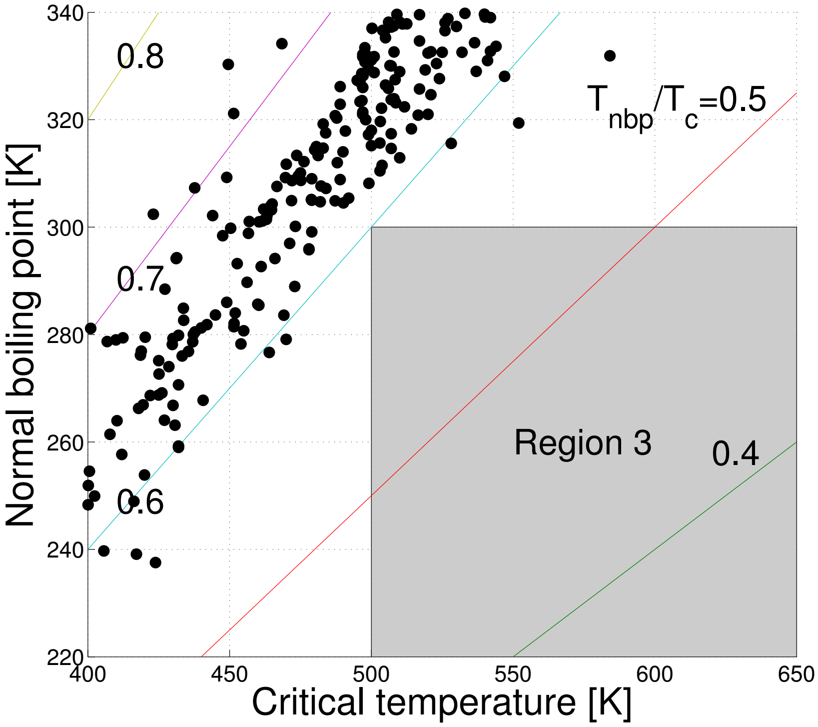

Figure 15.6: Normal boiling point vs. critical temperature: DIPPR 2016 detail. Target Region 3 in grey.

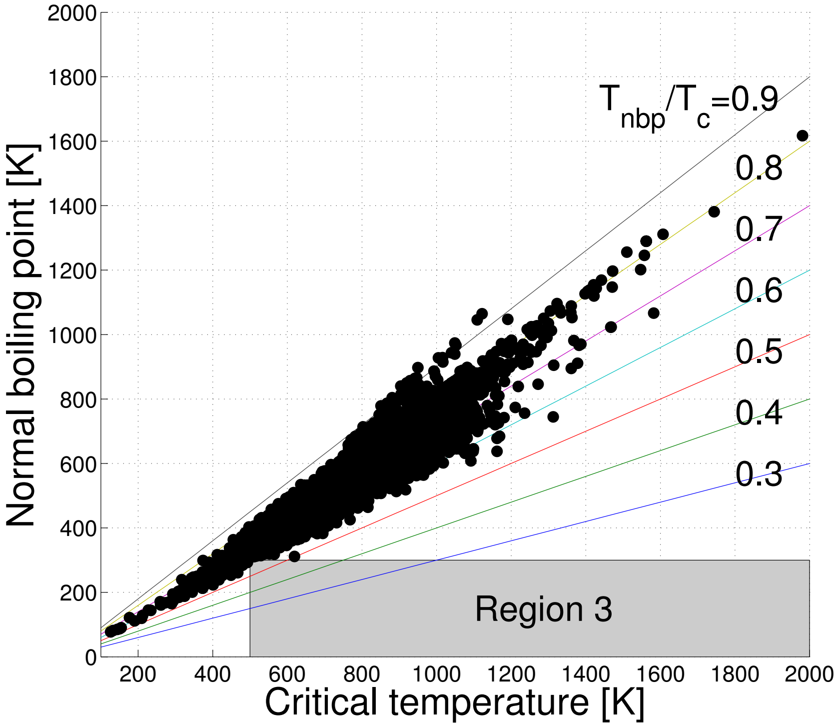

Figure 15.7: Normal boiling point vs. critical temperature: TDE 103b v9. Target Region 3 in grey.

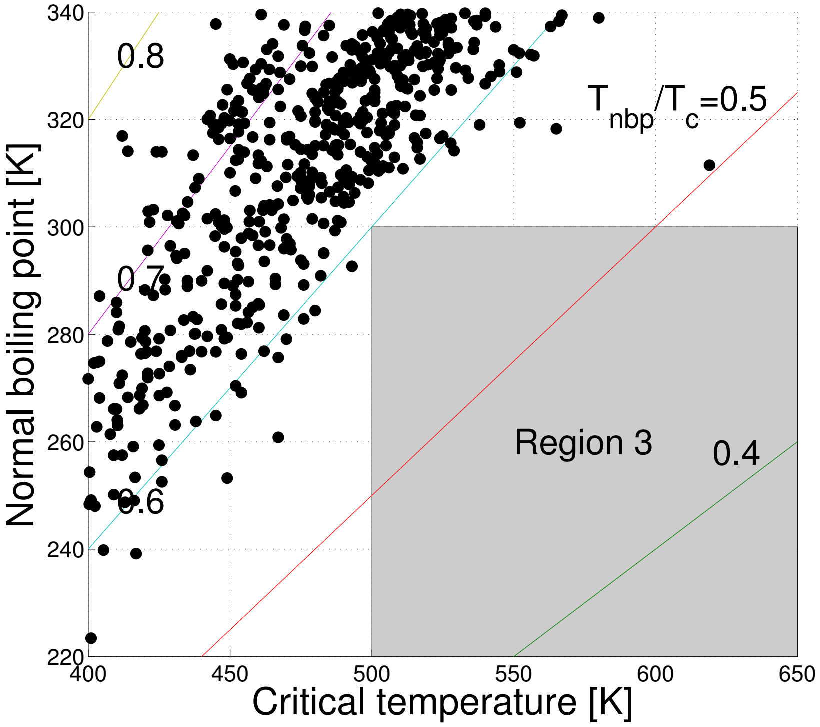

Figure 15.8: Normal boiling point vs. critical temperature: TDE 103b v9 detail. Target Region 3 in grey.

15.4 Conclusions and summary

The searches of all three data sources failed to find a fluid using the reduced criteria (T_c and T_{nbp}) of Region 3 ($T_c \geq 500$ K and $T_{nbp} \leq 300$ K). Although it was found that all three databases had several to many examples of fluids with a low reduced normal boiling point (T_{rnbp}), some of which were near the region of interest (Region 3). Searching the databases using the reduce criteria is original work by this author. This anecdotally shows support to continue the search with the next step, testing using Mark Mclinden's thermodynamic space [170–172]. The goal is to determine if it is possible for a fluid to exist with the desired thermodynamic properties. In particular, the trade-off between T_c and T_{nbp} — found in this work — will be explored. This is addressed in Chapter 16.

15.5 Future work

While completing this research, several future works were discovered:

- Upgrade the REFPROP results with the new beta version that was recently released.
- Update the ThermoData Engine results with the newest version that was recently released.
- Search for other sources of fluid data and include them.
- Perform cycle evaluations on the fluids in Region 4 for each data source.

16. THERMODYNAMIC SPACE OF FLUIDS FOR HEAT ENGINES

16.1 Introduction/background

In Chapter 15, a search of known fluids was completed and no fluids were found meeting the critical temperature (T_c) and normal boiling point (T_{nbp}) requirements of Region 3 (Figure 15.1). One perspective is that the HVAC-R fluid manufacturers have searched long and hard to find working fluids and have exhausted all possibilities including both HVAC-R and ORC applications. Another point of view is that the searches have been mainly focused on HVAC-R equipment and not on ORC equipment; therefore, it is possible that suitable ORC fluids have been missed. The following presentation is meant to help the reader resolve the two conflicting perspectives and provide a clear view of reality.

The following five key points motivate why a search for new ORC fluids should be completed:

- For HVAC-R applications, the critical temperature requirements are 320 K $\leq T_c \leq$ 420 K [188]. In contrast, for ORC applications, the general critical temperature requirements are 400 K $\leq T_c \leq$ 650 K. The ORC requirements are higher and include a different region of the search space. Depending on the ORC application, the search space may overlap with the search space for HVAC-R equipment (e.g., low-temperature ORC applications). This overlap may result in some confusion.
- Of the 100 million compounds in PubChem reported in 2014, 56,000 [170] are comprised of Midgley elements [161] (C, H, F, Cl, Br, O, N, or S) and have $\leq$ 15 atoms per molecule. Midgley elements are known to create molecules

that are volatile enough to serve as refrigrants. A second search of PubChem with ≤ 18 atoms per molecule found 184,000 compounds [188]. In 2013, NIST Database 103b [187] contained $\sim 27,000$ molecules (not necessarily all Midgley elements). Only 18,000 fluids in the database have measured T_c, P_c, and T_{nbp} or enough experimental data to predict the values. This means that there is only a small fraction of experimental data $\leq \frac{18{,}000}{1{,}000{,}000}$ on the known molecules. Although the research cited here has notably raised the difficulty in finding new refrigerants for HVAC-R applications, it will be many years before the engineering community can say with high confidence that all options have been tried. This is especially true of ORC applications because no major public search has been documented. The lack of a publicly documented search is enough to justify documenting such a search publicly.

- Chapter 15 showed that the location of Region 3 was in a gap in the scatter of the normal boiling point vs. critical temperature (Figure 15.8). What follows is a simple esitmate meant to begin to answer the question: What is the probablity that a new fluid would be found in Region 3 (Figure 15.1)? Of the 18,000 fluids in NIST db103b with experimental or estimated T_c, P_c, and T_{nbp} data, 115 have a $T_{rnbp} \leq 0.6$. Because NIST db103b spans a wide range of T_c, limiting the range to 250 K $\leq T_c \leq$ 650 K is reasonable. There is a population of 5,717 and 57 members with $T_{rnbp} \leq 0.6$, which is roughly 1% of the population. Assuming a uniform distribution of scatter in the given T_c range means that one can expect to find 1% of the population below the $T_{rnbp} \leq 0.6$ line. The first screening of PubChem found 600 compounds with estimated 450 K $\leq T_c \leq$ 550 K and GWP $\leq$ 200 [174]. Given that Region 3 covers half the area near $T_c = 500$ K below the $T_{rnbp} \leq 0.6$ line, one can expect to find about three fluids in Region 3 ($600 \times 0.01 \times 0.5 = 3$). It is likely that the scatter will be nonuniform, which reduces the certainty of this calculation. Even though this estimate is approximate, it suggests that thousands of fluids are not expected to be in Region 3; nonetheless, the possibility of finding a fluid in Region 3 is not vanishingly small.

- The more important message is that there are 600 fluids already identified that are highly likely to meet T_c and GWP requirements waiting to be modeled and further screened for ORC use. Even if completing the search process finds zero fluids in Region 3, it is expected that at least 60% of the fluids would fall within Region 4. Even if only 5% of the remaining fluids passed toxicity and stability preliminary screenings, this would mean that there were 18 candidates identified ($600 \times 0.6 \times 0.05 = 18$).
- The single most important reason to complete the search process for ORC applications is to show the most exhaustive search possible has been completed. There are no public literature records documenting such a search. Given, that the methods have already been developed and most of the computational machinery has been created, it is a relatively small matter to complete the search process and gain new knowledge. The benefit might be a notable cost shift in waste heat recovery ORC applications which could in turn enable more efficient energy consumption world-wide.

The above discussion does not address a key issue: does Mark Mclinden's thermodynamic space [169–172] allow a fluid to be in Region 3? Previous use of the McLinden space in HVAC-R screenings showed that it typically over estimates what is possible compared to quantitative structure–property relationship predictions made on the identifed molecules in PubChem [173–175]. In this chapter, Mark McLinden's thermodynamic space is used to explore the thermodynamic limits of fluid performance. This process requires writing REFPROP fluid files, which REFPROP uses as inputs to the algorithm (see [164–168] for details and past applications). The thermodynamic space relies on the Extended Corresponding States method (ECS) by Huber and Ely 1994 [189].

ECS is based on the idea that one can mathematically relate thermodynamic properties of two fluids; therefore, one can relate thermodynamic states of the two fluids. A known base fluid is used, and 10 parameters of the modeled fluid are required. Using ECS, one can model the thermodynamic states of a fluid without the expensive and time-consuming process of fluid fitting to match the fluid model to experimental fluid data. This allows a researcher with a limited amount of information to quickly model thermodynamic states of a fluid.

Mark McLinden's thermodynamic space is nine dimensional and is based on the minimum parameters required to define a fluid in REFPROP [185] using ECS (see Table 16.1). REFPROP also requires: (1) the critical density of the fluid, (2) upper density limit, and (3) a specific heat model, which are calculated from some of the nine thermodynamic space values by Equations 16.1

$$\rho_c = \frac{RT_c}{P_c}\rho_{c,\text{base fluid}} \tag{16.1a}$$

$$\rho_{max} = 4\rho_c \tag{16.1b}$$

$$C_p(T) = aT + b \tag{16.1c}$$

$$a = C_p^0\gamma \tag{16.1d}$$

$$b = C_p^0(1 - (300\text{ K})\gamma) \tag{16.1e}$$

where c notes critical properties, R is the universal ideal gas constant, and $C_p(T)$ is

Table 16.1: Thermodynamic space parameters

Parameter	Abreviation	Units
Critical temperature	T_c	K
Critical pressure	P_c	MPa
Acentric factor	ω	-
Fit	α_1	-
Fit	α_2	-
Fit	β_1	-
Fit	β_2	-
Ideal gas heat capacity	$C_p^0(300\text{ K})$	J/(mol·K)
Fit	γ	1/K

the constant-pressure specific heat as a function of temperature. The thermodynamic space combined with the ECS model allows researchers to explore the performance of a hypothetical fluid in a thermodynamic cycle. This methodology was used to explore the theoretical limits of fluid performance in several air conditioning and refrigeration applications.

In the context of the direct configuration for solar thermal power generation with non-tracking collectors, the thermodynamic space can be used to explore the theoretical possibility of a fluid existing that would meet the reduced criteria (Region 3: $T_c > 500$ K and $T_{nbp} < 300$ K) from Chapters 13 and 15.

16.2 Methodology

In this chapter, the thermodynamic space is used to explore the possible limit of fluid performance in the design trade-offs of the engineering objectives η_{sys} and VPC ψ. The thermodynamic space is reduced to eight dimensions by setting the critical temperature to a given value. Then, a genetic algorithm is used to minimize the normal boiling point for the given critical temperature. The minimization optimization problem is defined by Equations 16.2

$$T_{nbp}^{*} = \min_{\boldsymbol{x}} f(\boldsymbol{x}, T_c) \tag{16.2a}$$

subject to:

$$\boldsymbol{x} = [\boldsymbol{x_{lb}}, \boldsymbol{x_{ub}}] \tag{16.2b}$$

$$T_c = [305, 550] \tag{16.2c}$$

$$g_i(\boldsymbol{x}) \leq 0 \qquad i = 1, ..., 4 \tag{16.2d}$$

where:

$$g_1(\boldsymbol{x}) = |T_c - T_{c,actual}| - 4 \text{ K} \tag{16.2e}$$

$$g_2(\boldsymbol{x}) = \frac{|T_c - T_{c,actual}|}{T_c} - 0.01 \tag{16.2f}$$

$$g_3(\boldsymbol{x}) = \frac{|P_c - P_{c,actual}|}{P_c} - 150 \text{ MPa} \tag{16.2g}$$

$$g_4(\boldsymbol{x}) = \frac{|P_c - P_{c,actual}|}{P_c} - 0.08 \tag{16.2h}$$

$$x_1 = [2.0, 12.0] = P_c \tag{16.2i}$$

$$x_2 = [0.0, 0.6] = \omega \tag{16.2j}$$

$$x_3 = [-0.3, 0.3] = \alpha_1 \tag{16.2k}$$

$$x_4 = [-0.8, 0] = \alpha_2 \tag{16.2l}$$

$$x_5 = [-1.0, 1.0] = \beta_1 \tag{16.2m}$$

$$x_6 = [-0.8, 0.8] = \beta_2 \tag{16.2n}$$

$$x_7 = [20.8, 300] = C_p^0(300 \text{ K}) \tag{16.2o}$$

$$x_8 = [0.0, 0.0025] = \gamma \tag{16.2p}$$

The optimization problem is solved iteratively using T_c values in the given range at 5-K increments. A genetic algorithm is used to solve the minimization problem. The constraint function values for the actual critical point are determined where $\frac{dP}{d\rho} = 0$ and $\frac{d^2P}{d\rho^2} = 0$. This is accomplished by calling the REFPROP internal functions INFO and FNCRPT. INFO pulls information on the specified critical point directly from the fluid file, and FNCRPT determines the actual critical point from the derivatives. The constraint functions test how closely the actual critical point matches the specified critical point. These constraints are not part of the original thermodynamic space by McLinden. Instead, these constraints are original work, and are added to prevent the actual critical point from significantly deviating from the specified critical point. This means that portions of the thermodynamic space do not yield acceptable fluids. This is a direct result of bypassing the fluid-fitting process. Many of the aspects of fluid fitting have not yet been codified into mathematical equations or procedures that a computer can execute. Including this one constraint helps limit the space; however, there are other requirements that were not added to the current models.

16.3 Results and discussion

16.3.1 Initial unconstrained results and the need for constraints

Figure 16.2 shows unconstrained optimal results that are composed of extreme α and β parameters of the space (see Figure 16.3). It was found that these extreme results also corresponded to fluids with unrealistic vapor dome shape because of a discrepancy between the specified critical point and the actual critical point ($\frac{dP}{d\rho} = 0$ and $\frac{d^2P}{d\rho^2} = 0$).

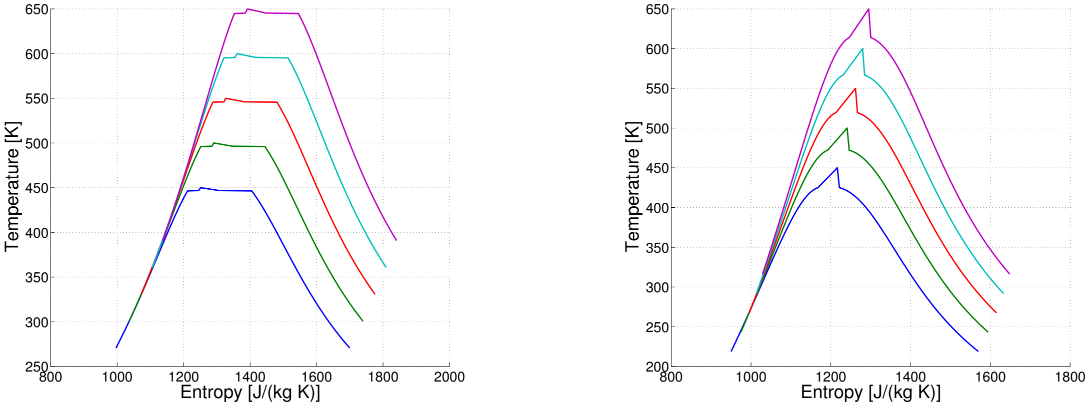

(a) Low α_1 case.

(b) High α_1 case.

Figure 16.1: Examples of unacceptable fluids in the thermodynamic space.

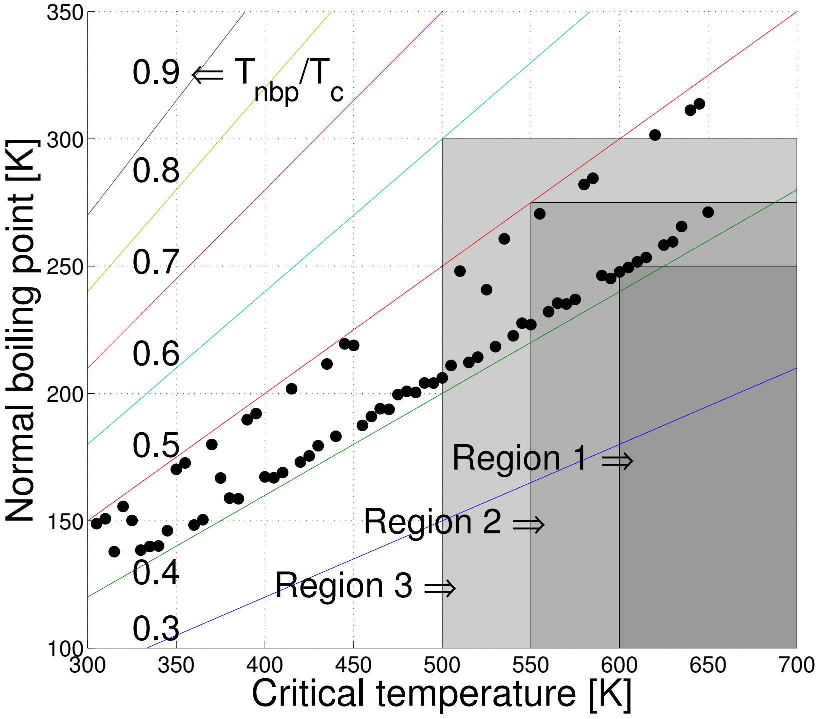

Figure 16.2: Normal boiling point vs. critical temperature using unconstrained optimization.

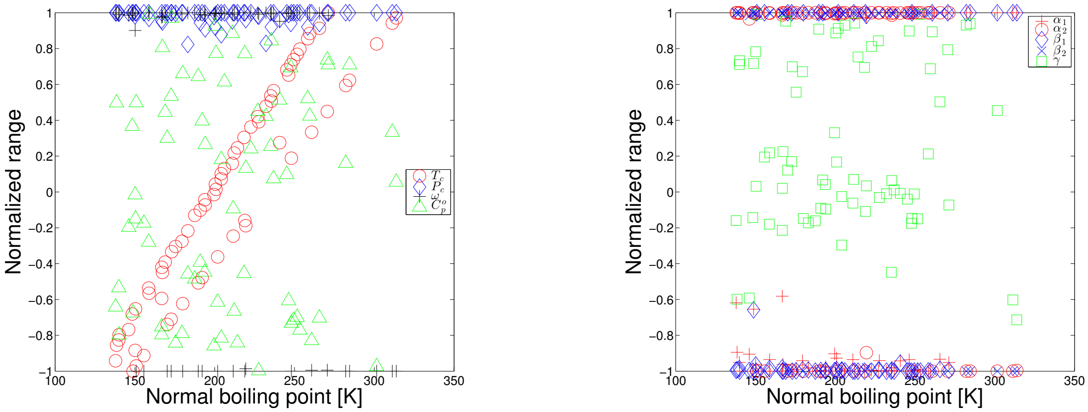

(a) Main fluid parameters.

(b) Secondary fluid parameters.

Figure 16.3: Optimal normalized fluid parameters using unconstrained optimization.

16.3.2 Results under constrained optimization

Figure 16.4 shows the results under constrained optimization. Even with the constraint, the results show that it is possible for a fluid to exist within the region of interest ($T_c \geq 500$ K and $T_{nbp} \leq 300$ K), although the possibilities are much more limited than the unconstrained results. Figure 16.5 shows the thermodynamic space parameters. The strong correlation in the α and β fitting parameters is broken by the constraint.

16.3.3 Pareto frontier

In Chapter 13, the idea of trade-offs between the engineering objectives (η_{sys} and ψ) was introduced. Here, to help explain the results, a brief introduction to some of the ideas of multi-objective design optimization are introduced. Because the thermodynamic cycle model for a direct solar-thermal heat engine only requires the inlet state of the expander to determine the cycle, the cycle attributes (VPC, efficiency, etc...) can be plotted on a T-s diagram at each possible expander inlet state. The

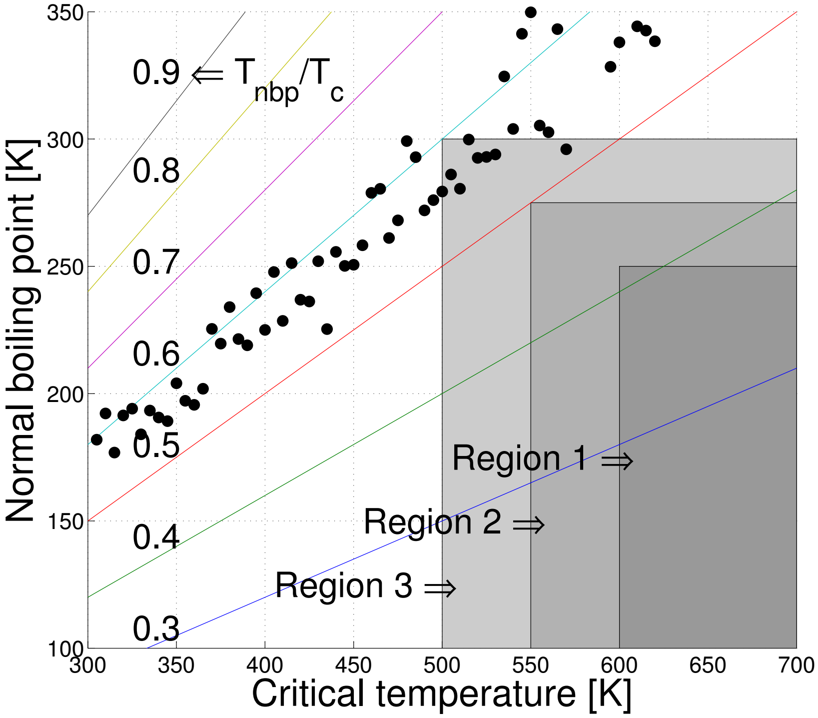

Figure 16.4: Normal boiling point vs. critical temperature using constrained optimization.

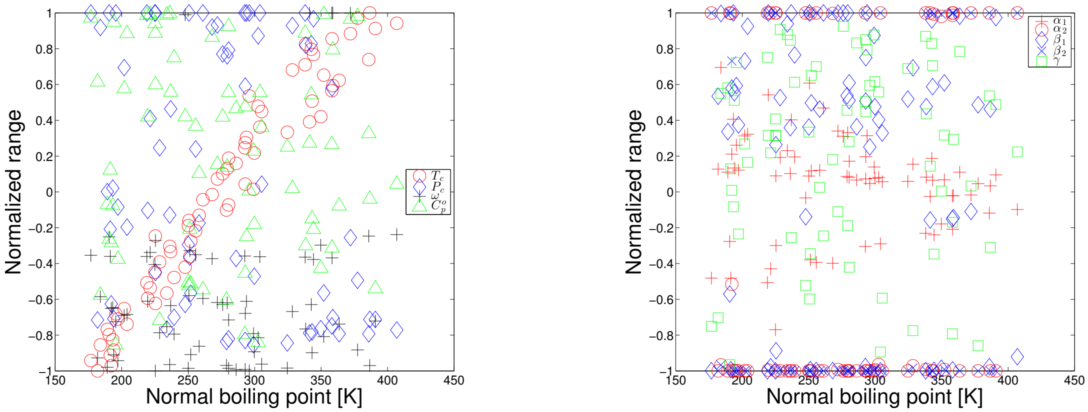

(a) Main fluid parameters.

(b) Secondary fluid parameters.

Figure 16.5: Optimal normalized fluid parameters using constrained optimization.

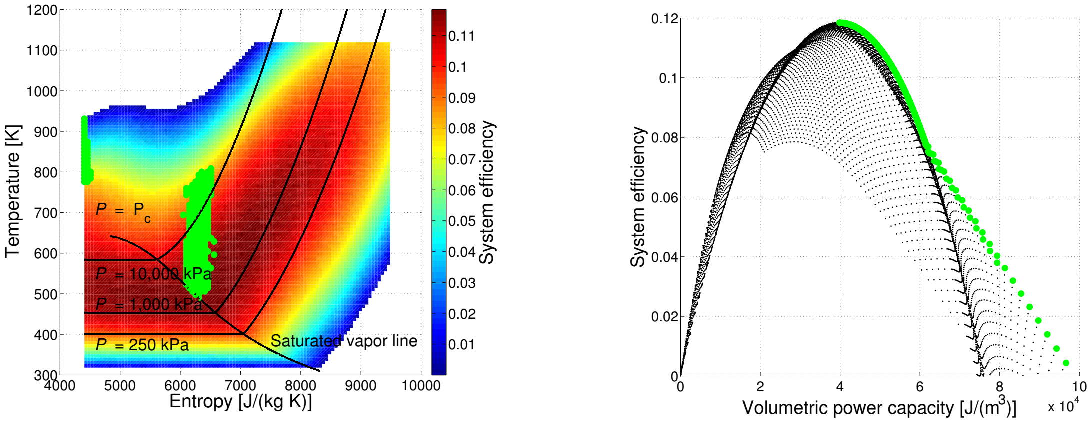

(a) Design variable space.

(b) Decision objective space with non-dominated set shown in green.

Figure 16.6: Multi-objective optimization spaces and Pareto frontier.

T-s diagram shown in Figure 16.6(a) is the *design variable space* with an overlay of η_{sys}. The design variables are the temperature and entropy at the inlet of the expander. Figure 16.6(b) shows the *decision objective space*. The engineering objectives are η_{sys} and ψ. In both spaces, each data point is an alternative. Alternative A is said to *Pareto dominate* Alternative B if it is as good or better than Alternative B in each objective, and better than Alternative B in at least one objective. The *non-dominated set* of data points form the *Pareto frontier* and are shown in green. Using system simulation results for water, R-11, and six hypothetical fluids at 1000 W/m^2 irradiance and 300 K ambient temperature, the relative trade-offs between the fluids can be explored.

Fluids were selected with low, medium, and high critical temperatures in the region of interest for both the unconstrained and constrained versions of the thermodynamic space. These six fluids were simulated using the same methodology found in Chapter 14 where water and R-11 were simulated. Of the six fluids, the three hypothetical fluids from the unconstrained thermodynamic space failed in many of the cycle calculations making the results unusable. For the constrained thermodynamic space, the low-critical-temperature fluid also has many failed cycle calculations. Figure 16.7 shows the constrained medium- and high-critical-temperature fluids; both have a banded region where failures happened. Water and R-11 are included for comparison.

Figure 16.8 shows the Pareto frontiers for each of the four fluids. Comparing the Pareto frontiers of water, R-11, and the two test fluids shows:

1. It may be possible to find a fluid that performs better than water or R-11 for both criteria (η_{sys} and ψ) i.e., thermodynamics allow for fluids in Region 3.
2. Using the reduced search criteria (T_c and T_{nbp} in place of η_{sys} and ψ) works well as an initial screening criteria.
3. Critical temperature is weakly correlated to cycle/system efficiency and normal boiling point is strongly correlated to VPC. The weak correlation between efficiency and T_c may result because both test fluids do not have high enough T_c to meet the cycle criteria of no superheating (see Figure 16.7). This confirms that the T_c lower limit of 500 K is less restrictive than the ideal.

16.4 Conclusions and summary

In this chapter, the thermodynamic space is used to explore the possibility of fluids existing that are in Region 3 for direct solar thermal power generation applications ($T_c \geq 500$ K and $T_{nbp} \leq 300$ K). Out of an abundance of caution, a constraint was added to limit the thermodynamic space. Using the McLinden thermodynamic space as part of an optimization to explore the relationship between T_c and T_{NBP} and the addition of the thermodyanmic space constraint are original work by this author. The results suggest a notable possibility of finding a fluid with the right

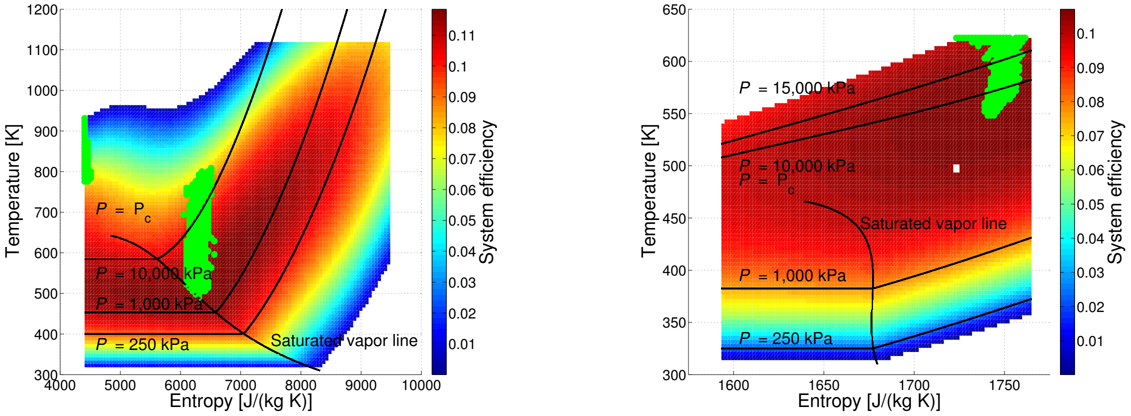

(a) Water.

(b) R-11.

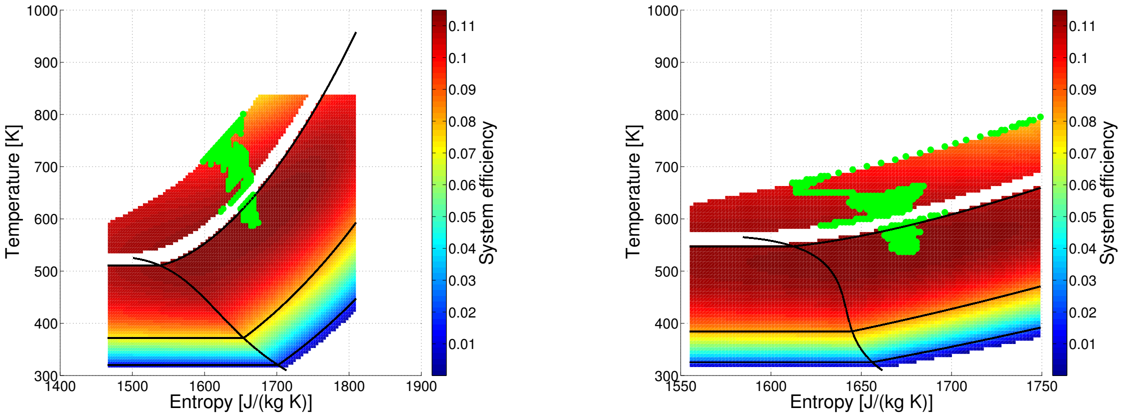

(c) Medium critical temperature hypothetical test fluid.

(d) High critical temperature hypothetical test fluid.

Figure 16.7: System efficiency plotted on the T-s diagram. Irradiance $G_{eff} = 1000$ W/m^2. Green dots denote points on the Pareto frontier. System efficiency is given as a ratio.

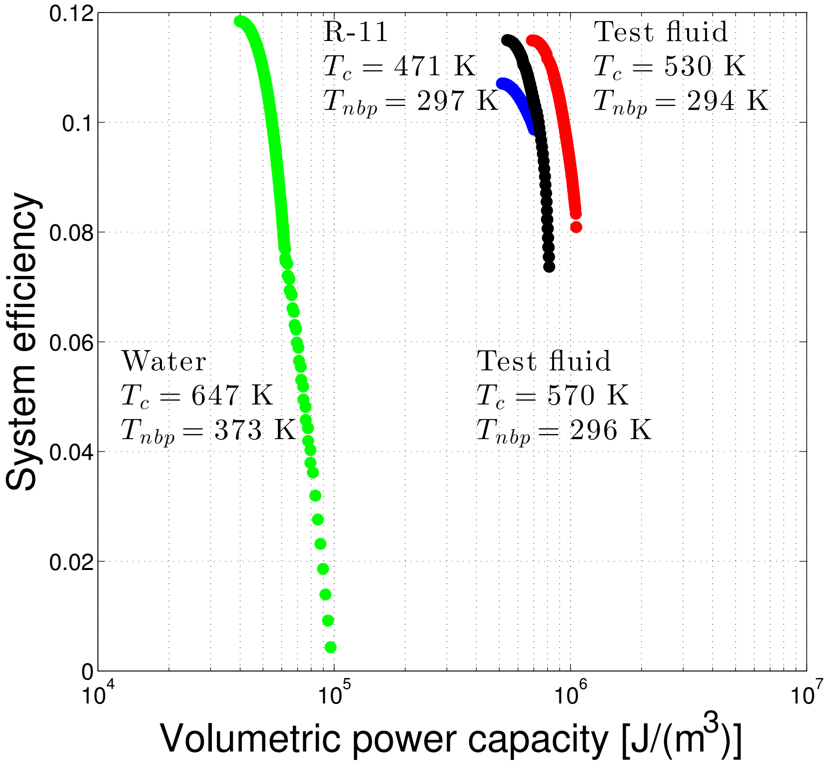

Figure 16.8: Pareto frontiers of four fluids: system efficiency versus volumetric power capacity. Irradiance $G_{eff} = 1000$ W/m^2 and ambient temperature $T_{amb} = 300$ K. System efficiency is given as a ratio.

set of thermodynamic properties for improvement in the performance of direct solar thermal power generation applications. The trade-off between efficiency and machine size is confirmed to exist in power generation cycles. During the exploration process, it was found that system efficiency (η_{sys}) is weakly correlated to critical temperature (T_c) and VPC (ψ) is strongly correlated to normal boiling point (T_{nbp}). This confirms T_c and T_{nbp} as good approximations and initial search criteria in place of the true design attributes of η_{sys} and ψ.

16.5 Future work

During the completion of this work, several future works were found. Most notable is the need to apply the Kazakov methods of using quantitative structure-property relationships (QSPR) to search the fluids listed in PubChem for the current application (see [170–175]). Specifically, Kazakov et al. 2012 has a list of PubChem fluids that were found to meet the their initial screening criteria [174]. More than half of the ~ 1200 fluids were in the range $450 \leq T_c \leq 550$. Here is a short list of potential future works:

- Apply these methods to waste-heat recovery applications.
- Apply these methods to indirect solar thermal configurations.
- Predict the necessary fluid properties and simulate the ~ 500 fluids of interest in the Kazakov et al. 2012 list.
- Complete a QSPR based search of PubChem fluids using the latest methods.
- Model fluid performance on a thermodynamic basis.
- Improve the thermodynamic space by including more constraints.

17. REDUCED CRITERIA FLUID SEARCH OF REFPROP

17.1 Introduction/background

In Chapter 13, the HVAC-R industry fluid search methods and criteria are adapted for the direct solar-thermal configuration. Waste heat recovery organic Rankine cycle is the closest thermodynamic application to the DSSTC direct configuration, yet the direct configuration was shown to be a unique design problem. The indirect and waste heat recovery problems are the same general design problem because both share a fluid-to-fluid heat transfer process to input heat to the engine. The direct solar-thermal configuration is a unique design problem because of the lack of an intermediate heat transfer fluid (i.e., only one fluid circuit). The ORC cycle without superheating is identified as the best candidate to maximize efficiency and testing found this to be correct using water; however, Chapter 14 showed that some fluids require superheating because of the lower critical temperature. Chapter 15 finds that no known fluids meet the Region 3 criteria ($T_c \geq 500$ K and $T_{nbp} \leq 300$). Chapter 16 notes that it may be possible to find one or more fluids in Region 3. It also shows that T_b is limited by T_c, which prevents finding a fluid that operates optimally at $T_H = 500$ K without superheating. Although it may be possible to find a fluid that would meet health, safety, and environmental requirements and perform better in efficiency and VPC than current fluids, fluid development is costly and time consuming. This means an existing industry must be a driver, not a potential new industry. The end result is a designer who wants to build a DSSTC system today must choose from currently available fluids, none of which fall within Region 3. This delima motivates the current effort to futher reduce the criteria (i.e., Region 4, $T_c \geq 400$ K and $T_{nbp} \leq 400$) and simulate using fluids identifed in REFPROP [185]. There are several benifits that will result from this less restrictive search: 1) REFPROP is a good first source for readily available fluids that have excellent thermo/transport information. 2) Identifying and simulating fluids near the region of interest will illustrate the trade-offs between system efficiency/volumetric power capacity (η_{sys}/ψ) and critical temperature/normal boiling point (T_c/T_{nbp}), respectively. 3) It will also show the lack of readily available fluids that clearly meet the health, safety, and environmental requirements and perform well (η_{sys} and ψ) or identify such fluids. Many of the fluids in DIPPR 2016 [186] and NIST DB 103b [187] cannot be readily modeled thermodynamically; therefore, thermodynamic model coefficients must be estimated from theory or experimental data for such fluids. This is outside the scope of work for this project and it is left as future work. The goal of the current work is to leverage the models and simulations developed in the previous chapters to 1) motivate the lack of good alternatives to using water as a working fluid; 2) develop results for many more real fluids than R-11 and water; 3) illustrate the challenging nature of health, safety and environmental requirements; and 4) use the results to further validate the screening criteria of T_c and T_{nbp}.

17.2 Methodology

There are two general evaluation steps for fluids: 1) thermodynamic performance and 2) health, safety, and environmental (HSE) concerns. Previously in this work, thermodynamic performance was the main focus because it tends to be more deterministic, especially when assuming fixed environmental conditions of irradiance and ambient temperature. HSE concerns are highly location dependent and therefore are much more challenging to address.

17.2.1 Thermodynamic performance

Of the 122 fluids in REFPROP, those in Region 4 ($T_c \geq 400$ K and $T_{nbp} \leq 400$) are identified and simulated. This new, less restrictive search will likely identify many fluids for simulation. The bulk of the methods used to simulate the fluids of interest are previously described in Chapter 14, namely the ORC simulation and related assumptions ($G_{eff} = 1000$ W/m^2, $T_{amb} = 300$ K, etc.). Because many fluids are dry (vapor dome tilted to the right), a second simulation is made by modifying the ORC simulation to include the internal heat exchanger (ORC + IHX) shown in Figure 17.1. The ORC + IHX model uses an assumed heat exchanger effectiveness (Equation 17.1) and limits results if basic thermodynamics are violated. It is important to note that this heat exchanger model does not properly address liquid/vapor mixtures, because the effectiveness equation is based on temperature rather than enthalpy of the the fluids. Both simulations use 10,000 data points in the T-s diagram because each cycle simulation can be defined by the temperature and specific entropy at the expander inlet. This allows cycle attributes to be plotted onto a T-s diagram. See Chapter 14 for further discussion.

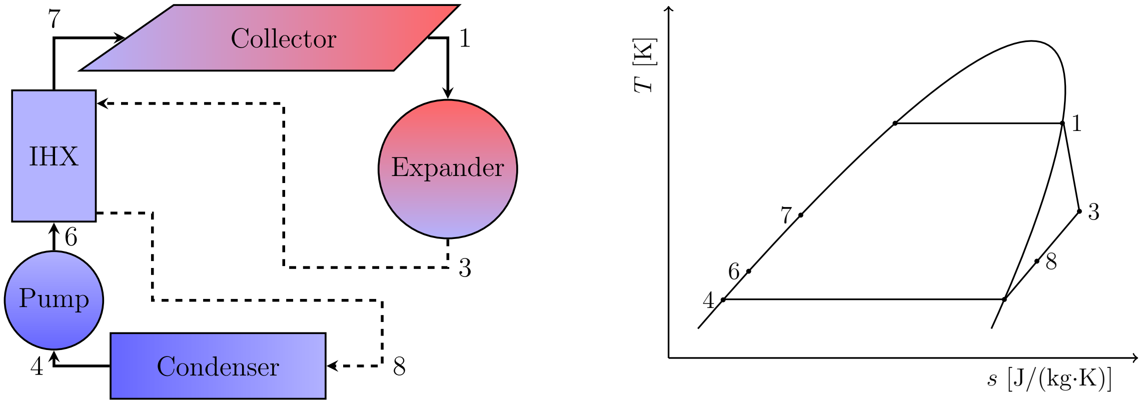

(a) Equipment configuration diagram.

(b) Thermodynamic cycle on the T-s diagram.

Figure 17.1: Direct system with IHX.

$$\eta_{\text{ihx}} = \frac{T_3 - T_8}{T_3 - T_6} = 0.55 \tag{17.1a}$$

$$T_8 = T_3 - \eta_{ihx}(T_3 - T_6) \tag{17.1b}$$

In Chapter 16, a Pareto frontier (η_{sys} versus ψ) for each fluid was introduced and several fluids were compared. To form this frontier for each fluid identified, the nondominated data points (η_{sys}, ψ) are determined from the 10,000 cycle simulations for each cycle type. Because each fluid typically has many nondominated data points, the nondominated data point with maximum efficiency is selected for further analysis.

17.2.2 Health, safety, and environmental concerns

HSE data can be challenging to gather and further challenging to process; as a result, no HSE analysis can be universally applied. Complicating matters further is that current laws and regulations are not targeted specifically to the solar-thermal application because such an industry does not yet exist. Even more challenging, because laws protecting the public vary from city to city, state to state, country to country, and region to region, an analysis performed for College Station, Texas is not necessarily valid in San Diego, California or Naples, Italy. Another complication is that the industry standards and laws are applied differently to different situations (e.g., the rules for HVAC-R fluids are less strict in an industrial plant than for a commercial or residential building). Institutions where persons are not necessarily able or free to move (e.g., hospitals, prisons, and mental health wards) have the most restrictive requirements. The possible permutations are endless.

All hope is not lost because there are a few key fluid ratings that can be used to gauge roughly if a fluid can be used. Although HSE requirements depend on application and location, one can get a general idea about the usability of a fluid from an HSE perspective. To this end, there are four key ratings that will be reviewed:

1) NFPA 704 [190], 2) ASHRAE 34 [191], 3) ODP, and 4) GWP, i.e., the National Fire Protection Association (NFPA) Standard 704, the American Society of Heating, Refrigeration, and Air conditioning Engineers (ASHRAE) Standard 34, Ozone Depletion Potential (ODP), and Global Warming Potential (GWP). The information is used to color code fluids based on concern of use: black for unusable, red for the highest concern, yellow for medium concern, and green for the lowest concern. Because this work seeks to treat the topic in a general way that is independent of any one location, no color coding system selected will be precise and the individual limits selected will be subjective. The reader is encouraged to make their own location- and application-specific evaluations using all relevant requirements and associated information.

17.2.2.1 NFPA Standard 704

NFPA Standard 704 is a standard in the United States that is used to determine how a material is labeled for shipping and storage. There are similar standards in most countries. These diamond-shaped labels aid personnel (e.g., fire fighters) to know how to deal with a substance during an emergency (e.g., a spill, traffic accident, or fire). The ratings have three main hazard categories and a fourth category for special notes. The three main hazard categories follow: 1) health (not necessarily toxicity), 2) flammability, and 3) instability. Each of the three categories are rated from 0 to 4, where the lower number is safer. NFPA 704 is used solely because not all fluids in REFPROP v9.1 have been classified under ASHRAE 34. In this work, the H-F-I triplets are used to code fluids by green, yellow, and red, where 3-2-0 or less for green, 4-4-2 or more for red, everything else yellow. This means that a fluid with a NFPA 704 rating of 2-0-0 would be yellow. Using the highest concern color rating for a fluid is applied across all characteristics considered. The NFPA

704 rating information is sourced from several locations such as the International Mechanical Code (IMC 2009 [192]), and from Material Safety Data Sheet (MSDS) from chemical supplier websites such as Airgas and Sigma-Aldrich. When more than one source was reviewed and a different rating was found, the highest hazard rating was selected.

17.2.2.2 ASHRAE Standard 34

ASHRAE Standard 34 covers the designation and safety classification of refrigerants, which is a companion to ASHRAE 15 the safety standard on refrigeration systems [193]. These two standards represent the closest match to a future solar-thermal power generation fluid standard. ASHRAE 15 does not apply to equipment installed outside a building 20 ft from a building opening with the excepting of a mechanical room door. The meaning of equipment does not include piping. It is important to note that ASHRAE 15 does not define a building opening; therefore, it is unclear if a building opening is simply a door, window, or HVAC-R fresh air intake. Possibly openings include sewer vents, attic soffit vents, etc. In general, maintaining a distance of 20 ft away from a building opening may be challenging to achieve. If one were to assume that a residential building has enough space to have collectors and heat engine meet the 20 feet exception, in theory, one could have equipment with any working fluid. Under the code, systems with 6.6 lbs or less are exempted. In theory, a system charged with 30 lb of R-40 (noted toxic) at high pressure and temperature could be 20 ft up wind of an open nursery window and still comply with the code. It is hard to imagine parents of young children would accept this hypothetical situation. As a result, this author assumes any selected ORC fluid must meet the ASHRAE 15 code, even though it is highly unlikely that a solar ORC system would be installed inside a build as HVAC-R equipment is. Only the

ASHRAE 15 Subcommittee can decide to extend coverage of the code to solar ORC applications. ASHRAE 34 provides a designation (e.g., R-11) and a safety classification. The classification has two parts: 1) toxicity and 2) flammability. Toxicity is rated two ways, with an 'A' or 'B'. Table 4-1 (pure fluids) and 4-2 (mixtures) in ASHRAE 34 also note if a fluid is toxic or highly toxic. The nomenclature section of ASHRAE 34 defines what is meant by toxic and highly toxic and they are based in even more standards. 'A' stands for lower toxicity and 'B' stands for elevated toxicity. Flammability is rated as 1, 2L, 2, and 3 where 1 is the lowest flammability and 3 is the highest. In this work, the ASHRAE 34 classification is used to code fluids by green, yellow, and red, where A2L or less for green, 3 for red, everything else yellow. This means that a fluid with an ASHRAE 34 classification of B2L would be yellow, and if it is noted toxic, it would be red. The ASHRAE 34 classification information was sourced directly from the standard.

17.2.2.3 ODP

Ozone Depletion Potential (ODP) is the ability of a substance to decompose ozone O_3 in the upper atmosphere. The abliblity of a substance to decompose the ozone depends upon two main factors: 1) The presents of atoms that decompose ozone, such as chlorine Cl or Bromine Br; and 2) the atmospheric lifetime of the substance. The Montreal Protocol is a set of international agreements to limit and phase out substances that deplete the stratospheric ozone layer. The US law empowering the Environmental Protection Agency (EPA) to regulate substances for ODP is 40 CFR Part 82, which lists specific regulated substances. As with any complex topic, a short description oversimplifies the topic and the reader is referred to the many sources of information on the subject, such as the US EPA website and 40 CFR Part 82 (Subpart A Appendix A and B for a list of regulated substances). In this work, fluids regulated by 40 CFR 82 Subpart A are coded black. ODP information was sourced from several locations: 1) 40 CFR 82 [194], 2) EPA website, and 3) known chemical structure-property relationships. For example, hydrofluoro olefins (HFOs) have zero ODP because the molecular structure of HFO molecules lack the required atoms to react with stratospheric ozone and decompose it, which is why HFOs were developed as working fluids for HVAC-R applications. R-1336mzz(Z) is an HFO for which the proceeding discussion is correct. R-1233zd(E) is also an HFO, with a chlorine atom. It has a non-zero yet very small ODP, an extremely short atmospheric lifetime, and is not regulated for ODP. Because of this, R-1233zd(E) is sometimes referred to by researchers as an hydrochlorfluoro olefin (HCFO).

17.2.2.4 GWP

The Paris Climate Accord is an international agreement that limits greenhouse gas emissions in an effort to slow or stop anthropogenic (human-caused) climate change. One aspect is to limit the manufacture of fluids that when released into the atmosphere contribute to climate change. Global Warming Potential (GWP) is the measure of how much energy 1 ton of gas will absorb over a given period of time normalized by the amount of energy 1 ton of CO_2 will absorb over the same time period. There are two key fluid characteristics: atmospheric lifetime and energy absorption rate. Here, the standard 100-year time period is used. The European Union has limited the use of refrigerants that have GWP > 200 and there is debate to change this limit to 150. Currently in the United States, efforts to regulate refrigerants based on GWP have failed. The HVAC-R industry has responded to these regulatory risks differently. Some refrigerant manufactures are strongly opposed to regulation, whereas others strongly support it; however, all manufactures are actively searching for alternative refrigerants with low GWP. GWP data was sourced from the IPCC [195]. In this work, fluids with GWP $\leq$ 200 are coded green, fluids with GWP $\geq$ 1000 are red, and everything else is yellow.

17.3 Results and discussion

17.3.1 Thermodynamic screening

Fluids in REFPROP were screened based on $T_c \geq 400$ K and $T_{nbp} \leq 400$ (Region 4) and 50 were identified. Heavy water (D_2O) cycle simulations failed. It is typically used as a compressed liquid in nuclear reactors (heavy water reactors) for moderation and cooling. It is believed that these calculations failed from the lack of a need to calculate superheated states and corresponding deficiencies in the EOS for heavy water. REFPROP v9.1 fluid file for heavy water uses an equation of state from 1982. REFPROP v10 uses an updated equation of state for heavy water. Heavy water is expensive to manufacture and has very similar thermodynamic properties as water; therefore, it was removed from the results (Table 17.1).

Each of the 49 fluids are simulated in 10,000 cycle simulations (Figures 17.2(a) and 17.2(b). Note the reduced area for ORC + IHX calculations. This is because the IHX requires certain conditions to be met before this cycle is possible (e.g., $T_3 - T_6 > 0$). Figure 17.2(c) shows the difference in system efficiency for the same expander inlet condition. Figure 17.2(d) shows the nondominated points of the Pareto frontier for each cycle using water. As expected, water has higher efficiency when used in an ORC. This is because water is a wet fluid (see discussions in Chapters 4 and 16 for more information). R-11 is a dry fluid and has the opposite result, where the ORC + IHX gives higher efficiency. Table 17.2 documents the full thermodynamic screening results.

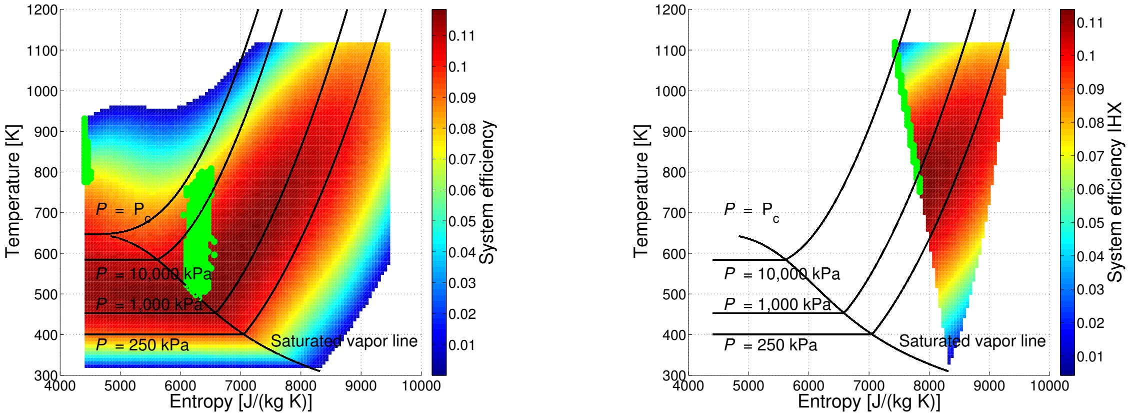

(a) ORC efficiency plotted on the temperature vs. specific entropy diagram. Green points denote the Pareto nondominated points.

(b) ORC + IHX efficiency plotted on the temperature vs. specific entropy diagram. Green points denote the Pareto nondominated points.

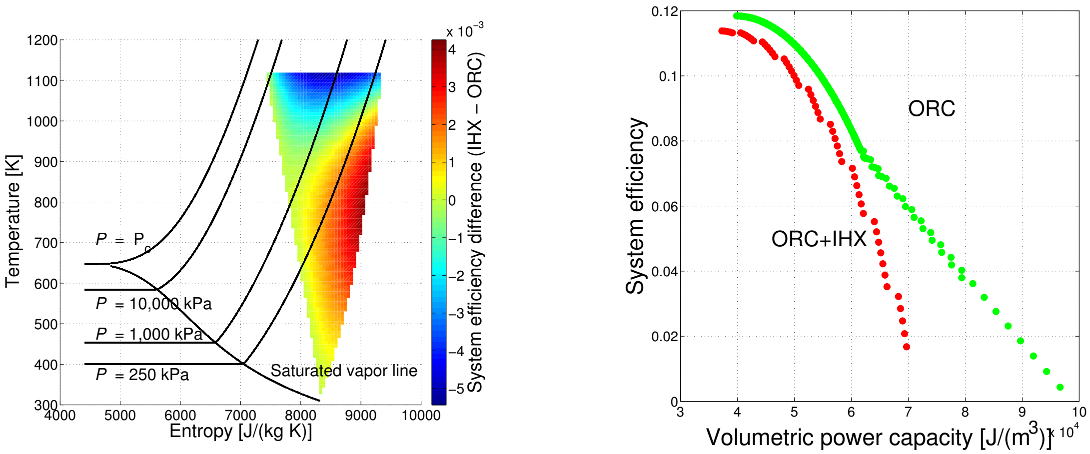

(c) Efficiency difference plotted on the temperature vs. specific entropy diagram.

(d) System efficiency vs. volumetric power capacity for the nondominated points of each cycle.

Figure 17.2: Comparison of the ORC and ORC + IHX using water.

Table 17.1: Fluids in REFPROP with $T_c \geq 400$ K and $T_{nbp} \leq 400$ K

	Filename	Name	#†	CAS #	Formula	#‡
1	1BUTENE	1-butene		106-98-9	CH_3-CH_2-CH=CH_2	12
2	ACETONE	Acetone		67-64-1	$(CH_3)_2CO$	10
3	AMMONIA	Ammonia	R-717	7664-41-7	NH_3	4
4	BENZENE	Benzene		71-43-2	C_6H_6	12
5	BUTANE	Butane	R-600	106-97-8	CH_3-2(CH_2)-CH_3	14
6	C1CC6	Methylcyclohexane		108-87-2	$C_6H_{11}(CH_3)$	21
7	C2BUTENE	Cis-butene		590-18-1	CH_3-CH=CH-CH_3	12
8	C5F12	Perfluoropentane		678-26-2	C_5F_{12}	17
9	CYCLOHEX	Cyclohexane		110-82-7	C_6H_{12}	18
10	CYCLOPEN	Cyclopentane		287-92-3	C_5H_{10}	15
11	DEE	Diethyl Ether		60-29-7	$C_4H_{10}O$	15
12	DMC	Dimethyl Carbonate		616-38-6	$C_3H_6O_3$	12
13	DME	Dimethylether	R-E170	115-10-6	$(CH_3)_2O$	9

†ASHRAE 34 refrigerant number

‡Number of atoms per molecule

Continuation of Table 17.1

	Filename	Name	#[†]	CAS #	Formula	#[‡]
14	ETHANOL	Ethanol		64-17-5	C_2H_6O	9
15	HEPTANE	Heptane		142-82-5	CH_3-5(CH_2)-CH_3	23
16	HEXANE	Hexane		110-54-3	CH_3-4(CH_2)-CH_3	20
17	IBUTENE	Isobutene		115-11-7	$CH_2{=}C(CH_3)_2$	12
18	IHEXANE	Isohexane		107-83-5	$(CH_3)_2CH(CH_2)_2CH_3$	20
19	IOCTANE	Isooctane		540-84-1	$(CH_3)_2CHCH_2C(CH_3)_3$	26
20	IPENTANE	Isopentane	R-601a	78-78-4	$(CH_3)_2CHCH_2CH_3$	17
21	ISOBUTAN	Isobutane	R-600a	75-28-5	$CH(CH_3)_3$	14
22	METHANOL	Methanol		67-56-1	CH_3OH	6
23	MM	Hexamethyldisiloxane		107-46-0	$2(CH_3)_3OSi_2$	27
24	NEOPENTN	Neopentane		463-82-1	$C(CH_3)_4$	17
25	NOVEC649	Novec 649		756-13-8	$CF_3CF_2C({=}O)CF(CF_3)_2$	19
26	OCTANE	Octane		111-65-9	CH_3-6(CH_2)-CH_3	26

[†] ASHRAE 34 refrigerant number

[‡] Number of atoms per molecule

Continuation of Table 17.1

	Filename	Name	#[†]	CAS #	Formula	#[‡]
27	PENTANE	Pentane	R-601	109-66-0	CH_3-3(CH_2)-CH_3	17
28	PROPYNE	Propyne		74-99-7	CH_3CCH	7
29	R11	CFC-11	R-11	75-69-4	CCl_3F	5
30	R113	CFC-113	R-113	76-13-1	CCl_2FCClF_2	8
31	R114	CFC-114	R-114	76-14-2	$CClF_2CClF_2$	8
32	R123	HCFC-123	R-123	306-83-2	$CHCl_2CF_3$	8
33	R1233ZDE	HFO-1233zd(E)	R-1233zd(E)	102687-65-0	$CF_3CH{=}CHCl$	9
34	R1336MZZ_Z	HFO-1336mzz(Z)	R-1336mzz(Z)	692-49-9	$C_4H_2F_6$	12
35	R141B	HCFC-141b	R-141b	1717-00-6	CCl_2FCH_3	8
36	R142B	HCFC-142b	R-142b	75-68-3	$CClF_2CH_3$	8
37	R21	HCFC-21	R-21	75-43-4	$CHCl_2F$	5
38	R236EA	HFC-236ea	R-236ea	431-63-0	$CF_3CHFCHF_2$	11
39	R245CA	HFC-245ca	R-245ca	679-86-7	$CHF_2CF_2CH_2F$	11

[†] ASHRAE 34 refrigerant number

[‡] Number of atoms per molecule

Continuation of Table 17.1

	Filename	Name	#†	CAS #	Formula	#‡
40	R245FA	HFC-245fa	R-245fa	460-73-1	$CF_3CH_2CHF_2$	11
41	R365MFC	HFC-365mfc	R-365mfc	406-58-6	$CF_3CH_2CF_2CH_3$	14
42	R40	Methyl Chloride	R-40	74-87-3	CH_3Cl	5
43	RE245CB2	HFE-245cb2	R-E245cb2	22410-44-2	$CF_3CF_2OCH_3$	12
44	RE245FA2	HFE-245fa2	R-E245fa2	1885-48-9	$CHF_2OCH_2CF_3$	12
45	RE347MCC	HFE-7000	R-E347mcc	375-03-1	$CF_3CF_2CF_2OCH_3$	15
46	SO2	Sulfur Dioxide	R-764	7446-09-5	SO_2	3
47	T2BUTENE	Trans-2-butene		624-64-6	$CH_3\text{-}CH{=}CH\text{-}CH_3$	12
48	TOLUENE	Toluene		108-88-3	$CH_3\text{-}C_6H_5$	15
49	WATER	Water	R-718	7732-18-5	H_2O	3

†ASHRAE 34 refrigerant number

‡Number of atoms per molecule

Table 17.2: Results for fluids in REFPROP with $T_c \geq 400$ K and $T_{nbp} \leq 400$ K

Row	Name			ORC		ORC+IHX	
		T_c	T_{nbp}	η_{sys}	ψ	η_{sys}	ψ
		[K]	[K]	%	$[\frac{\mathrm{J}}{\mathrm{m}^3}]$	%	$[\frac{\mathrm{J}}{\mathrm{m}^3}]$
1	1-butene	419.3	266.8	9.33	1.01e6	9.81	9.83e5
2	Acetone	508.1	329.2	11.21	2.02e5	11.52	1.94e5
3	Ammonia (R-717)	405.4	239.8	10.51	3.80e6	10.58	3.36e6
4	Benzene	562.0	353.2	11.24	9.19e4	11.57	8.94e4
5	Butane (R-600)	425.1	272.6	9.06	8.01e5	9.55	7.87e5
6	Methylcyclohexane	572.2	374.0	10.52	4.29e4	11.20	4.45e4
7	Cis-butene	435.8	276.8	9.91	8.47e5	10.40	8.12e5
8	Perfluoropentane	420.6	302.9	6.91	2.70e5	7.95	2.70e5
9	Cyclohexane	553.6	353.9	10.76	8.61e4	11.31	8.60e4
10	Cyclopentane	511.7	322.4	10.78	2.30e5	11.26	2.30e5
11	Diethyl Ether	466.7	307.6	9.71	3.21e5	10.26	3.17e5
12	Dimethyl Carbonate	557.0	363.2	11.19	6.23e4	11.54	6.05e4
13	Dimethylether (R-E170)	400.4	248.4	9.68	2.08e6	10.10	2.01e6
14	Ethanol	514.7	351.6	11.54	8.43e4	11.72	8.05e4
15	Heptane	540.1	371.5	10.07	4.23e4	10.92	4.48e4
16	Hexane	507.8	341.9	9.94	1.12e5	10.78	1.15e5
17	Isobutene	418.1	266.2	9.17	1.02e6	9.65	9.88e5
18	Isohexane	497.7	333.4	9.68	1.43e5	10.59	1.46e5
19	Isooctane	544.0	372.4	9.57	4.08e4	10.64	4.41e4
20	Isopentane (R-601a)	460.3	300.9	9.31	3.44e5	9.86	3.39e5

Continuation of Table 17.2							
Row	Name			ORC		ORC+IHX	
		T_c	T_{nbp}	η_{sys}	ψ	η_{sys}	ψ
		[K]	[K]	%	$[\frac{\text{J}}{\text{m}^3}]$	%	$[\frac{\text{J}}{\text{m}^3}]$
21	Isobutane (R-600a)	407.8	261.4	8.47	1.01e6	8.94	9.74e5
22	Methanol	512.6	337.6	11.62	1.66e5	11.69	1.49e5
23	Hexamethyldisiloxane	518.8	373.4	8.91	3.55e4	10.18	3.87e4
24	Neopentane	433.7	282.7	8.41	4.98e5	8.93	4.89e5
25	Novec 649	441.8	322.2	7.24	1.66e5	8.57	1.63e5
26	Octane	569.3	398.8	10.15	1.59e4	10.99	1.67e4
27	Pentane (R-601)	469.7	309.2	9.59	2.83e5	10.15	2.80e5
28	Propyne	402.4	248.0	9.49	1.66e6	9.83	1.58e6
29	CFC-11	471.1	296.8	10.71	5.13e5	11.14	4.99e5
30	CFC-113	487.2	320.7	10.11	2.23e5	10.65	2.21e5
31	CFC-114	418.8	276.7	8.57	6.88e5	9.06	6.75e5
32	HCFC-123	456.8	301.0	10.07	4.34e5	10.58	4.23e5
33	HFO-1233zd(E)	439.6	291.4	9.69	5.64e5	10.20	5.47e5
34	HFO-1336mzz(Z)	444.4	306.5	9.08	3.11e5	9.62	3.06e5
35	HCFC-141b	477.5	305.2	10.49	3.61e5	10.96	3.54e5
36	HCFC-142b	410.7	264.0	9.13	9.96e5	9.64	9.90e5
37	HCFC-21	451.4	282.0	10.15	6.73e5	10.27	6.42e5
38	HFC-236ea	412.4	279.3	7.83	5.44e5	8.31	5.43e5
39	HFC-245ca	447.5	298.4	9.19	3.84e5	9.75	3.85e5
40	HFC-245fa	427.1	288.2	8.76	4.98e5	9.29	4.97e5
41	HFC-365mfc	460.0	313.3	9.23	2.52e5	9.78	2.49e5

Continuation of Table 17.2							
Row	Name			ORC		ORC+IHX	
		T_c	T_{nbp}	η_{sys}	ψ	η_{sys}	ψ
		[K]	[K]	%	$[\frac{\mathrm{J}}{\mathrm{m}^3}]$	%	$[\frac{\mathrm{J}}{\mathrm{m}^3}]$
42	Methyl Chloride (R-40)	416.3	249.1	10.72	2.11e6	11.01	1.96e6
43	HFE-245cb2 (R-E245cb2)	406.8	278.8	7.87	6.17e5	8.34	6.04e5
44	HFE-245fa2 (R-E245fa2)	444.9	302.4	9.10	3.66e5	9.63	3.60e5
45	HFE-7000 (R-E347mcc)	437.7	307.4	8.12	2.59e5	8.83	2.55e5
46	Sulfur Dioxide (R-764)	430.6	263.1	10.55	1.63e6	10.52	1.49e6
47	Trans-2-butene	428.6	274.0	9.61	8.74e5	10.10	8.47e5
48	Toluene	591.8	383.8	11.11	3.33e4	11.57	3.23e4
49	Water (R-718)	647.0	373.1	11.84	3.99e4	11.38	3.73e4

Table 17.3: Health, Safety, and Environmental data for fluids in REFPROP with $T_c \geq 400$ K and $T_{nbp} \leq 400$ K

	Name	NFPA 704	ASHRAE	ODP[§]	GWP[$]	Comments
		H-F-I[†]	34[‡]			
1	1-butene	1-4-0				Red, flammability
2	Acetone	1-3-0			0.5	Yellow, flammability
3	Ammonia (R-717)	3-3-0	B2L			Yellow, flammability, toxicity
4	Benzene	2-3-0				Red, known carcinogen
5	Butane (R-600)	1-4-0	A3		4.0	Red, flammability
6	Methylcyclohexane	2-3-0				Yellow, flammability
7	Cis-butene	1-4-0				Red, flammability
8	Perfluoropentane	1-0-0			8550	Red, GWP, low efficiency
9	Cyclohexane	1-3-0				Yellow, flammability
10	Cyclopentane	2-3-0				Yellow, flammability
11	Diethyl Ether	0-4-0				Red, flammability
12	Dimethyl Carbonate	1-3-0				Yellow, flammability
13	Dimethylether (R-E170)	0-4-0	A3		1	Red, flammability
14	Ethanol	2-3-0			2.8	Yellow, flammability

Continuation of Table 17.3

Row	Name	NFPA 704	ASHRAE	ODP§	GWP$	Comments
		H-F-I†	34‡			
15	Heptane	1-3-0				Yellow, flammability
16	Hexane	1-3-0				Yellow, flammability
17	Isobutene	1-4-0				Red, flammability
18	Isohexane	2-3-0				Yellow, flammability
19	Isooctane	2-3-0				Yellow, flammability
20	Isopentane (R-601a)	1-4-0	A3			Red, flammability
21	Isobutane (R-600a)	1-4-0	A3			Red, flammability
22	Methanol	1-3-0				Yellow, flammability
23	Hexamethyldisiloxane	2-3-2				Red, instability
24	Neopentane	1-4-0				Red, flammability
25	Novec 649	3-0-1				Green
26	Octane	2-3-0				Yellow, flammability
27	Pentane (R-601)	1-4-0	A3			Red, flammability
28	Propyne	1-4-3				Red, flammability, Instability

Continuation of Table 17.3						
Row	Name	NFPA 704	ASHRAE	ODP[§]	GWP[$]	Comments
		H-F-I[†]	34[‡]			
29	CFC-11	2-0-0	A1	1.0	4,750	Black, ODP
30	CFC-113	2-0-0	A1	0.8	6,130	Black, ODP
31	CFC-114	2-0-0	A1	1.0	9,180	Black, ODP
32	HCFC-123	2-0-0	B1	0.02	77	Black, ODP
33	HFO-1233zd(E)	2-0-0	A1		1	Green
34	HFO-1336mzz(Z)	3-0-0	A1		2	Green
35	HCFC-141b	2-1-0		0.11	717	Black, ODP
36	HCFC-142b	0-4-0	A2	0.065	2,220	Black, ODP
37	HCFC-21	0-0-0	B1	0.04	151	Black, ODP, toxic[‡]
38	HFC-236ea	3-0-0		0	1,410	Red, GWP
39	HFC-245ca	3-4-0		0	726	Red, flammability
40	HFC-245fa	2-0-1	B1	0	1,050	Red, GWP
41	HFC-365mfc	0-4-1		0	842	Red, flammability
42	Methyl Chloride (R-40)	1-4-0	B2		13	Red, flammability, toxic[‡]

Continuation of Table 17.3

Row	Name	NFPA 704	ASHRAE	ODP§	GWP$	Comments
		H-F-I†	34‡			
43	HFE-245cb2 (R-E245cb2)	3-0-0		0	740	Yellow, GWP
44	HFE-245fa2 (R-E245fa2)	3-0-0		0	680	Yellow, GWP
45	HFE-7000 (R-E347mcc)	3-0-0		0	499	Yellow, GWP
46	Sulfur Dioxide (R-764)	3-0-0	B1			Yellow, toxicity
47	Trans-2-butene	1-4-0				Red, flammability
48	Toluene	2-3-0			2.7	Yellow, flammability
49	Water (R-718)	0-0-0	A1			Green, high efficiency low VPC

†NFPA 704 ratings for health, flammability, instability hazards; encoding or this work: 3-2-0 or less for green, 4-4-2 or more for red, everything else yellow

‡ASHRAE 34 safety classification of refrigerants; A/B for lower/higher toxicity and notes of toxic and highly toxic; 1, 2L, 2, 3 for low to high flammability; encoding A2L or lower for green, 3 for red, everything else yellow.

§Ozone depletion potential, > 0 prohibited by Montreal protocols, in the USA 40 CFR 82; > 0 encoded red

$ Global warming potential based on 100 year atmospheric lifetime; encoding ≤ 200 green, ≥ 1000 red

Figures 17.3(a) and 17.3(b) show the nondominated Pareto frontiers for each of the 49 fluids for both cycles. To obtain a better view of the results, the maximum efficiency point from the set of nondominated points of each fluid are shown in Figures 17.3(c) and 17.3(d), and each of these figures shows a nondominated Pareto set of fluids. Figures 17.4(a) and 17.4(b) show selected fluids. It is important to note that water and ammonia are well-known natural working fluids. Benzene performs well despite being a known carcinogen. R-11 and two R-11 replacement fluids are also shown. The manufacture or import of R-11 is banned by 40 CFR 82. R-1233zd(E) and R-1336mzz(Z) are substitues for R-11 in HVAC-R applications, both of which have reduced thermodynamic performance for the direct solar-thermal configuration. As expected, water has the highest efficiency and ammonia has the largest VPC (smallest machine size). There are several challenges to using water: 1) large machine size, 2) some states have adopted boiler and pressure vessel codes that require 24-hour licensed operators for steam systems, 3) low vapor pressure in the condenser causes air infiltration problems, and 4) need to accommodate fluid freezing. Any serious attempt to use water as a working fluid in an STC system must include an in-depth evaluation of all applicable boiler and pressure vessel codes. This research is left as future work. All these challenges lead to water being used as a power generation fluid at the very large scale to overcome the economic costs of these challenges. Ammonia has elevated toxicity and is typically limited to use in industrial settings. From this, it can be seen that a thermodynamic screening alone is not enough to complete the fluid selection process; HSE screening is also needed.

17.3.2 First HSE screening

Figures 17.5(a) and 17.5(b) show the color coding based on the HSE screening methodology described above. Table 17.3 documents the tabulated information and

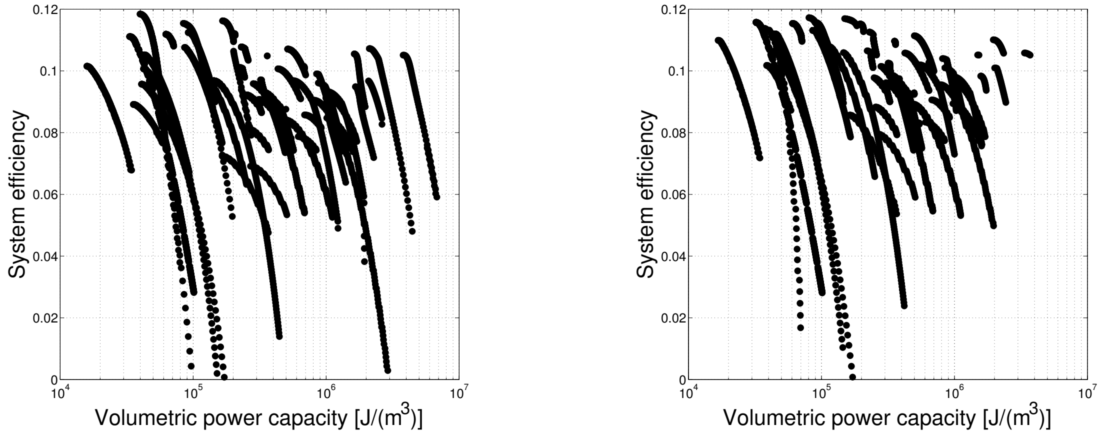

(a) Full Pareto frontiers for ORC.

(b) Full Pareto frontiers for ORC + IHX.

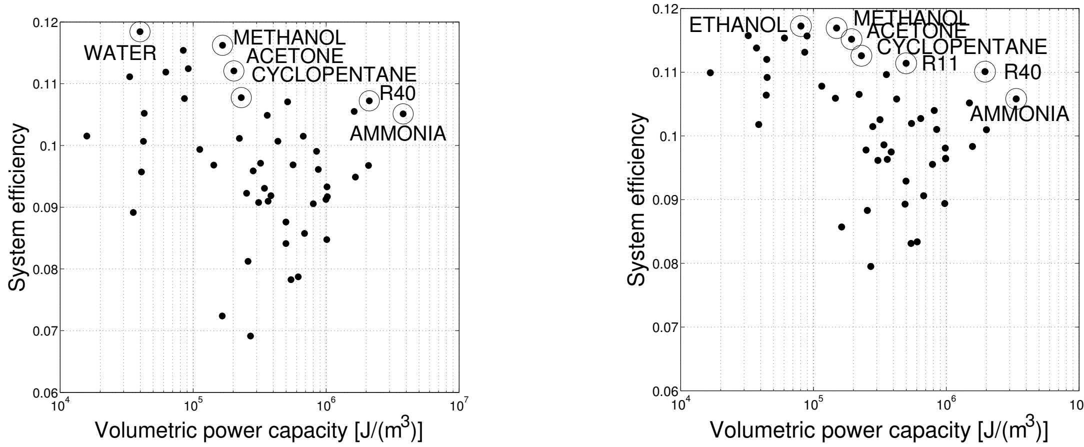

(c) Pareto frontier of maximum efficiency point of each fluid for ORC.

(d) Pareto frontier of maximum efficiency point of each fluid for ORC + IHX.

Figure 17.3: Introducing Pareto frontier data of 49 fluids in REFPROP with $T_c \geq$ 400 K and $T_{nbp} \leq 400$.

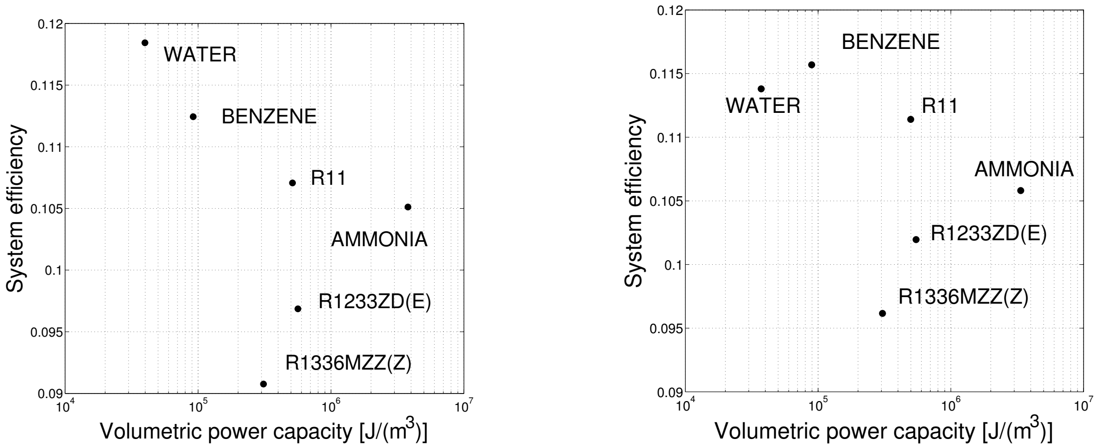

(a) ORC.

(b) ORC + IHX.

Figure 17.4: Maximum efficiency point of selected fluids.

the color coding. There are only four fluids: 1) water, 2) R-1233zd(E), R-1336mzz(Z), and 3) Novec 649 that are coded green (i.e., low concern). The challenges in using water at the distributed scale were discussed in the previous paragraph. R-1233zd(E) is a refrigerant sold by Honeywell. During a personal communication with Rajiv Singh of Honeywell, Rajiv noted that R-1233zd(E) has an upper temperature use limit of about ∼440 K (170°C) caused by trans-cis isomerization. After some time at ∼470 K (200°C), R-1233zd(E) is expected to shift to a mixture of R-1233zd(E)/1233zd(Z) (90/10). Stablity information is not yet complete and operation higher than ∼440 K (170°C) is not recommend. The stability information posses a problem for using R-1233zd(E) in a direct solar-thermal configuration because the predicted high operating temperatures are ∼ 500 K or more. Shutdowns during daylight hours for a stationary STC would achieve the stagnation temperature of the collector. For the N–S XCPC, stagnation temperature is ∼650 K. High stagnation temperature is a central challenge to the direct configuration with a stationary collector. Although R-1336mzz(Z) has been shown to be stable up to ∼520 K (250°C), it also has trans-cis isomerization concerns [196,197] and the thermodynamic performance is reduced. Novec 649 is used as a fire extinguishing agent for electronics and has low thermodynamic performance. Novec 649 has been previously considered for other ORC applications.

Discussing the remaining nondominated fluids for the ORC, R-40 is classified by ASHRAE 34 as toxic and use is highly cautioned. Methanol, acetone, and cyclopentane have elevated concern because of NFPA 704 rating of 3 for flammability. In the European Union HVAC-R working fluids with higher flammability are acceptable to use in very small quantities. The DSSTC application is anticipated to require larger quantities. In general, for HSE reasons, none of the nondominated fluids on the Pareto frontier are good candidates. In the case of water, there is excessive cost at smaller scale, because of large machine size and air infiltration. In special circumstances, it is possible to make limited cases for fluids that have been eliminated by the HSE screening. For example, in industrial applications, almost all health and safety concerns can be addressed through industrial hygiene and engineering safety measures. These measures may increase the LCOE for an installation. The use of benzene is a good example because it is used heavily in chemical manufacturing (e.g., plastics). Although this is true, it is balanced by the decreased use of benzene as a general industrial cleaning solvent after it was identified as a carcinogen. The above results and discussions clearly motivate why there is a need to search for new working fluids for the direct solar-thermal configuration, the indirect solar-thermal configuration, and medium-temperature waste heat recovery applications. Chapter 16 showed that it was possible to find a fluid that would have a better balance between system efficiency η_{sys} and VPC ψ. Using the ORC, Figure 17.6 shows the 'best' test fluid from Chapter 16 with the 49 fluids from REFPROP for comparison. It is likely that there would be one or more candidate fluids that would also have better HSE characteristics. Here, the importance of this new-not-yet identified fluid is highlighted. Reviewing Table 17.3, there are several fluids coded yellow based only on GWP. Because the ASHRAE 34 classification is not available for many fluids in REFPROP, the NFPA 704 rating is used as a substitute, which has several challenges. For example, R-40 is rated 1-4-0 and B2 toxic. The NFPA 704 health rating of 1 does not appear to account for toxicity. This perspective is further supported by the example of ammonia (3-3-0 and B2), which is rated 2 health hazard points higher than R-40 using the NFPA 704 standard, and ammonia is not label toxic in ASHRAE 34. Another challenge is that NFPA 704 information from multiple MSDS can sometimes appear to conflict each other. The challenge for any US system manufacturer is that any system that currently uses a fluid with elevated GWP is likely to face future restrictions domestically and current ones abroad in the European Union. This represents a notable concern when using such fluids in a product made by a start-up company attempting to foster a new industry. From this discussion, it is clear that more information is required to fully assess HSE restrictions for a particular location.

17.3.3 Second HSE screening

Reviewing the results of the first screening, several fluids were coded yellow based on GWP. In an effort to ensure reasonable working fluids were not eliminated, a second HSE review is conducted. Fluids with an NFPA 704 flammability hazard of 3 or 4 were always ASHRAE 34 Class 2 or 3 for flammability. Starting with all 49 fluids and removing fluids banned under 40 CFR 82, an NFPA 704 flammability rating of 3 or greater, and GWP $\geq$ 1000, the list is reduced to eight fluids. Removing sulfur dioxide because of toxicity in ASHRAE 34, seven fluids remain. Table 17.4 lists the remaining seven fluids and ammonia, which are also displayed in Figure 17.7. Novec

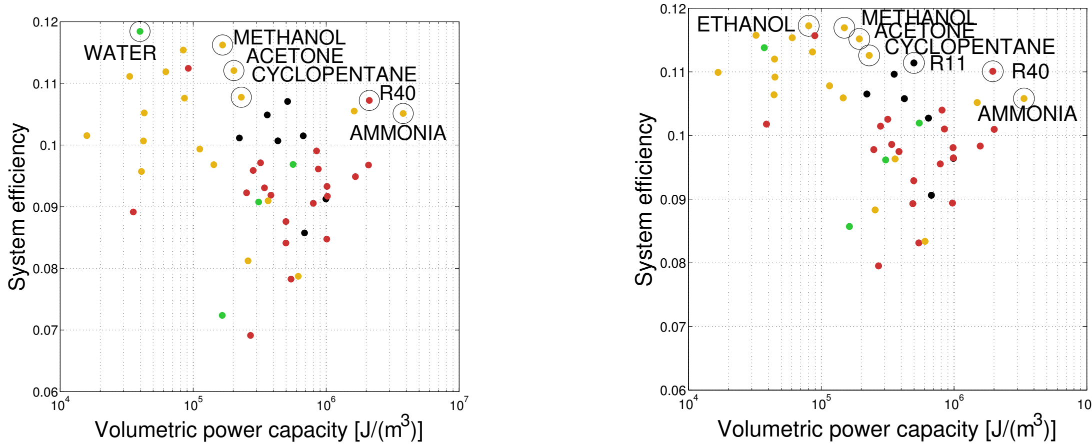

(a) ORC Pareto frontier results color coded by health, safety, and environmental concerns.

(b) ORC + IHX Pareto frontier results color coded by health, safety, and environmental concerns.

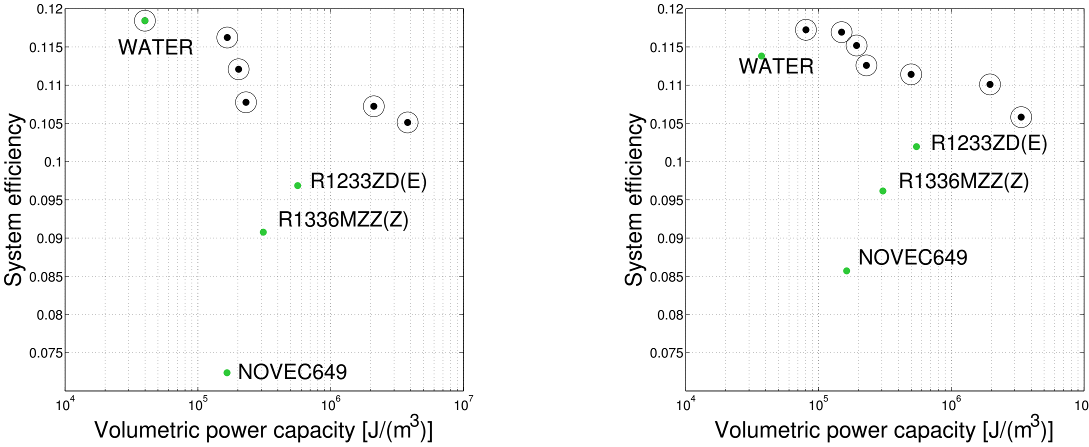

(c) ORC results for low concern fluids.

(d) ORC + IHX results for low concern fluids.

Figure 17.5: Health, safety, and environmental concerns for 49 fluids in REFPROP. Green, yellow, and red note low, medium, and higher concern respectively. Black notes fluids banned by 40 CFR 82.

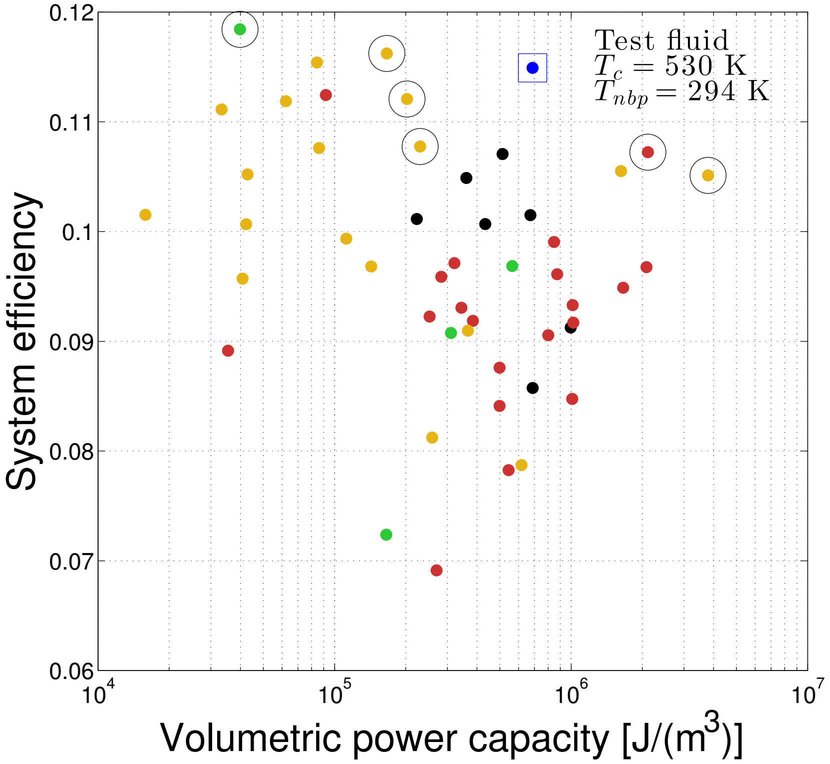

Figure 17.6: ORC results with test fluid for comparison.

649, HFE-245cb2, and HFE-7000 are removed for low system performance. HCFO-1233zd(E), HFO-1336mzz(Z), HFE-245fa2, and water remain. Ammonia is added back for comparison because it has the highest VPC of the 49 fluids, and it is a well-known natural refrigerant. HFE-245fa2 has elevated GWP and it is not acceptable for use in the European Union. Although HFE-245fa2 is not currently banned from use in the United States, the industry is moving away from working fluids with notable GWP. HCFO-1233zd(E) has an upper temperature limit of about $\sim$440 K. HFO-1336mzz(Z) is known to be stable up to 540 K [196, 197]. Both HCFO-1233zd(E) and HFO-1336mzz(Z) may not be able to withstand stagnation temperatures when the system is not in use and the stationary collectors are exposed to sunlight. Further investigation of stability is required and left as future work. HCFO-1233zd(E) has a $T_{nbp} = 291.4$ K, and HFO-1336mzz(Z) has a $T_{nbp} = 306.5$ K. This means both fluids are low-pressure refrigerants with internal condenser pressures below that of ambient for many operating conditions. The low pressure provides the possibility of 1) lower machine costs in terms of the thicknesses required to contain the fluid, 2) higher machine costs because of the larger machine size compared to ammonia, and 3) air infiltration and the associated costs required to mitigate and/or repair the resulting damage. Points 1 and 2 indicate a need to research the effect of T_{nbp} on machine costs; accounting for both effects and is left as future work. The second HSE screening illustrates the many and complex trade-offs that exist in the fluid options. The reader is again encouraged to use the methodologies demonstrated to perform a location/application-specific screening of fluids prior to selecting a fluid. Any serious attempt to build a non-tracking DSSTC system would likely have trouble using a fluid other than water because of the stagnation temperature issue. This means that an indirect system would be required to protect the ORC working fluid from stagnation temperatures in the collector. This shift would also result in lower system

Table 17.4: Results for fluids in REFPROP with $T_c \geq 400$ K and $T_{nbp} \leq 400$ K

Row	Name			ORC		ORC+IHX	
		T_c	T_{nbp}	η_{sys}	ψ	η_{sys}	ψ
		[K]	[K]	%	$\left[\frac{\mathrm{J}}{\mathrm{m}^3}\right]$	%	$\left[\frac{\mathrm{J}}{\mathrm{m}^3}\right]$
3	Ammonia (R-717)	405.4	239.8	10.51	3.80e6	10.58	3.36e6
25	Novec 649	441.8	322.2	7.24	1.66e5	8.57	1.63e5
33	HFO-1233zd(E)	439.6	291.4	9.69	5.64e5	10.20	5.47e5
34	HFO-1336mzz(Z)	444.4	306.5	9.08	3.11e5	9.62	3.06e5
43	HFE-245cb2 (RE-245cb2)	406.8	278.8	7.87	6.17e5	8.34	6.04e5
44	HFE-245fa2 (RE-245fa2)	444.9	302.4	9.10	3.66e5	9.63	3.60e5
45	HFE-7000 (RE-347mcc)	437.7	307.4	8.12	2.59e5	8.83	2.55e5
49	Water (R-718)	647.0	373.1	11.84	3.99e4	11.38	3.73e4

efficiency because of the heat exchange process between the two working fluid circuits in an indirect system. One possible alternative is to adjust the STC design with the goal to achieve a lower stagnation temperature without compromising efficiency at operational temperatures.

17.3.4 Testing critical temperature and normal boiling point temperature as reduced criteria

Figure 17.8 shows the correlation results and confirms that η_{sys} is correlated to T_c with some scatter and ψ is strongly correlated to T_{nbp}. The scatter is likely caused by influences from the specific heat, system effects, and vapor dome shape. These results also show that the Region 4 boundaries will not screen out relavent fluids for consideration. Comparing Figures 17.8(a) and 17.8(b) shows that using an IHX increases system efficiency in most cases. The LCOE analysis to decide whether or not to include an IHX is left as future work.

17.4 Conclusions and summary

Based on $T_c \geq 400$ K and $T_{nbp} \leq 400$ (Region 4), screening the fluids in REFPROP found 50 fluids. Simulating 49 fluids to determine η_{sys} and ψ showed there

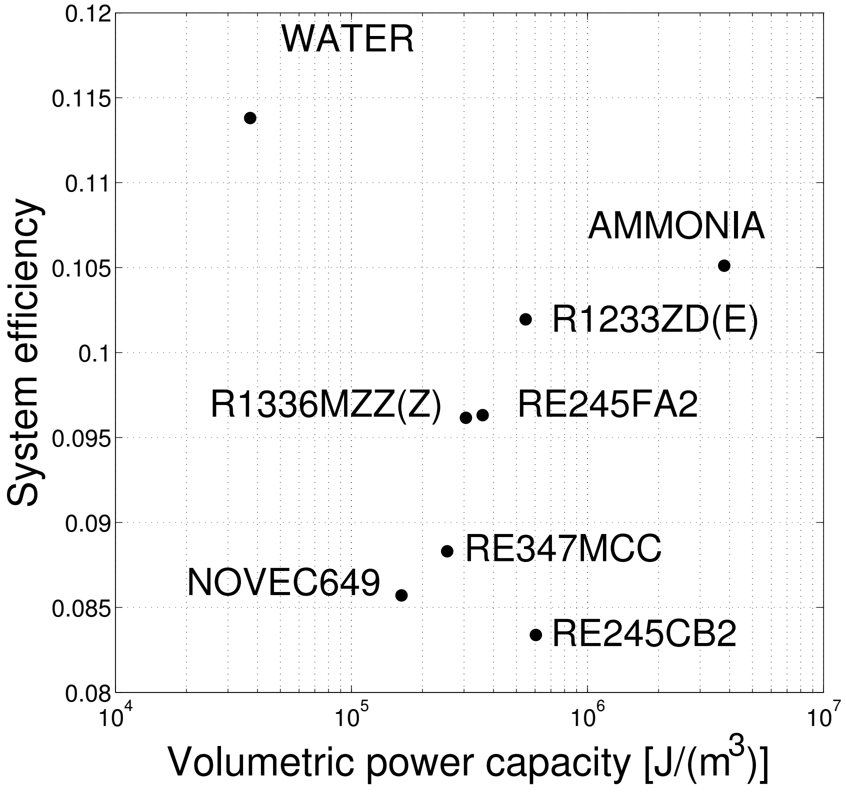

Figure 17.7: Second HSE screening. Ammonia and water use the ORC. The rest use ORC + IHX.

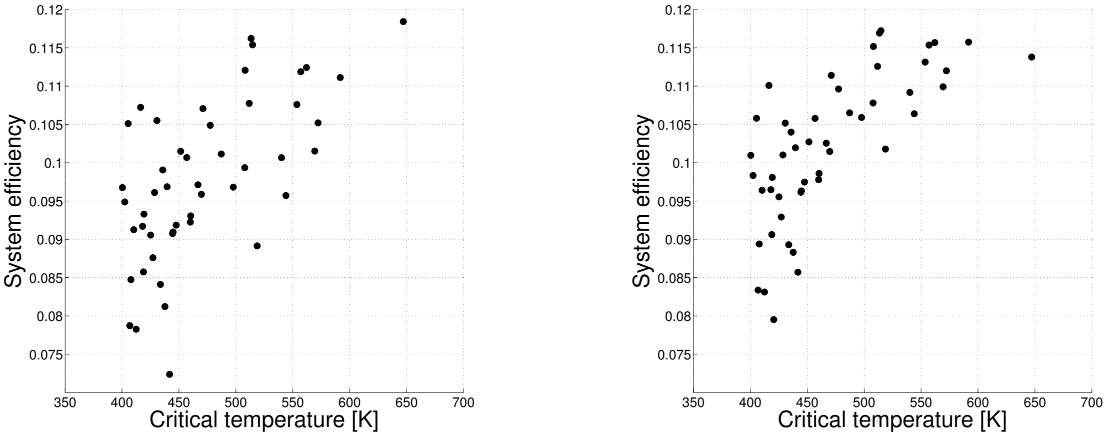

(a) System efficiency versus critical tempeature for ORC.

(b) System efficiency versus critical tempeature for ORC + IHX.

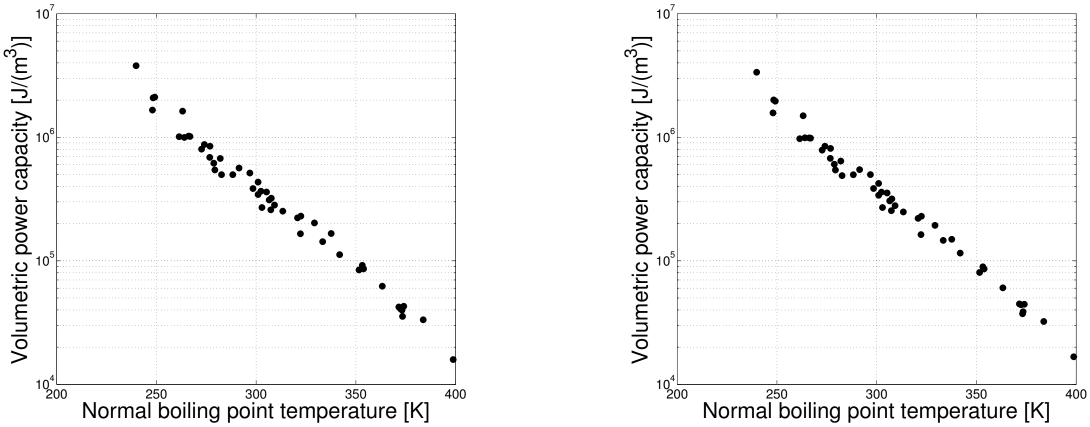

(c) Volumetric power capacity versus normal boiling point temperature for ORC.

(d) Volumetric power capacity versus normal boiling point temperature for ORC + IHX.

Figure 17.8: Reduced search criteria (T_c and T_{nbp}) correlations from 49 fluids in REFPROP.

are many options with various trade-offs between the two characteristics. The results confirmed that Region 4 is sufficiently less restrictive to ensure important fluids are not overlooked. Further screening based on health, safety, and environmental concerns left few, if any, good choices. R-1233zd(E) and R-1336mzz(Z) are identified as good options from a HSE standpoint despite a notable loss in efficiency compared to water. Upon further investigation, a stability problem with trans-cis isomerization was noted, with R-1336mzz(Z) stability being better documented. This leads to the need to evaluate stability of R-1233zd(Z) and R-1336mzz(Z) in the future. A second screening was performed identifying the same fluids as the best options. The second screening also identified a several of refrigerants with elevated GWP and therefore greater risk of use. Given the lack of highly stable alternatives, the stagnation issue will likely require the use of an indirect system to protect the the ORC working fluid. An alternative solution to the temperature issue is to redesign the STC to lower the stagnation temperature. This investigation highlights the need to seek out new fluids for DSSTC and waste heat recovery applications because no one fluid is 'best' in every category. T_c and T_{nbp} are confirmed good initial screening criteria to avoid the computationally expensive calculations needed to determine η_{sys} and ψ. While the original methods are adapted from the HVAC-R industry search for working fluids, adapting this search process to DSSTC and waste heat recovery applications is the original work of this author.

17.5 Future work

During the course of conducting this research, several additional routes of exploration were noted and left for future work:

- Model ORC and ORC + IHX performance for R-1233zd(Z) and further explore suitability.

- Upgrade IHX model to include enthalpy.
- Repeat this analysis for the fluids that only have a REFPROP v10 file format as REFPROP v9.1 was used in this work. This has two benefits: 1) additional fluids have been added and 2) the algorithms have been refined.
- Extend this analysis to the fluids in the DIPPR 2016 database by writing .fld files for them.
- Extend this analysis to the fluids in NIST DB 103b.
- Refine the HSE screening by including more screening characteristics such as refrigerant concentration limit (RCL), permissible exposure level (PEL), workplace environmental exposure limit (WEEL), etc.
- Repeat this analysis for indirect configurations and waste-heat-recovery applications.
- Upgrade analyses to include a lifecycle cost of energy (LCOE) estimation and minimization.
- Research boiler and pressure vessel code requirements to determine locations and impacts on design costs.
- Research fluid stability at stagnation temperatures.
- Research the effect of T_{nbp} on machine costs while accounting for both machine size and machine thicknesses.

18. PERFORMANCE ANALYSIS OF R-1233ZD(Z) IN A DIRECT SOLAR-THERMAL HEAT ENGINE

18.1 Introduction/background

Cis-1-chloro-3,3,3-trifluoropropene R-1233zd(Z) is a little-known compound that was explored for foam blowing applications. In recent years, trans-1-chloro-3,3,3-trifluoropropene R-1233zd(E) has been commericalized by Honeywell as a R-11 replacement and for ORC applications with a recommended operating temperature limit of ∼440 K (170°C) [198]. These two molecules form a trans-cis stereo isomer pair. Although there is a modest amount of research on the trans orientation of the molecule R-1233zd(E), only two papers were found on the cis orientation R-1233zd(Z) [199, 200]. For R-1233zd(E), Honeywell recommends a maximum operating temperature limit of ∼470 K (200°C) in the special case that a mixture of R-1233zd(E)/1233zd(Z) (90.0/10.0) is acceptable to form overtime. Percentages of refrigerant mixtures are based on molar mass throughout this work, although isomers provide a special case where the percentage based on mass is the same as that based on moles because the molar mass is the same. In Chapter 17, REFPROP v9.1 fluids were screened by T_c and T_{nbp}, then the remaining fluids were simulated for use in the direct solar-thermal configuration (Figure 18.1). The analysis found that R-1233zd(E) had favorable thermodynamic properties, whereas the information about chemical stability is limited, possibly unfavorable. The main challenge is to determine how the isomers will thermally react and change into the counterpart or decompose into something else (for chemical stablity background, see [26, 201]). At elevated temperatures, some isomers tend to shift from trans to cis, meaning the cis isomer is more stable e.g., R-1336mzz(Z); however, this is not necessarily always the case. Some trans-cis isomers can shift between the two configurations. The goal of this chapter is to study the thermodynamic performance of R-1233zd(Z) and explore the performance of various mixtures of both isomers. Because R-1233zd(Z) is under development, there is much to be learned about the isomerization process, including the thermal decomposition rate as a function of temperature, and isomerization conversion rates as a function of temperature. The thermodynamic and transport properties are not all well measured. The current study is asking and answering the question "Assuming the isomers R-1233zd(E) and R-1233zd(Z) can form a stable mixture, what would the thermodynamic performance be of a direct solar-thermal organic Rankine cycle with an internal heat exchanger ORC + IHX system (Figure 18.2)?" This information can be used to motivate further reseach into the isomerization and decomposition processes. Rajiv Singh of Honeywell has been kind enough to share a preliminary REFPROP v9.1 [185] fluid file for R-1233zd(Z) [198]. The equation of state (EOS) for R-1233zd(Z) is based on Extended Corresponding States (ECS) [189]. NIST has already measured and fit R-1233zd(E) for use in REFPROP [202]. Because fluid development is expensive and time consuming, it is important to check thermodynamic performance at multiple stages in the development process. Here, the goal is to perform a preliminary check of thermodynamic performance in a direct configuration solar-thermal organic Rankine cycle with an internal heat exchanger ORC + IHX system.

18.2 Methodology

Using the simulation methodology of Chapter 17, R-1233zd(Z) is simulated for use in a direct solar-thermal ORC + IHX heat engine. The simulation is performed at $T_{amb} = 300$ K and $G_{eff} = 1000$ W/m^2. The second portion of the simulation process is to analyze the special case where the two isomers approach a fixed ratio (assuming

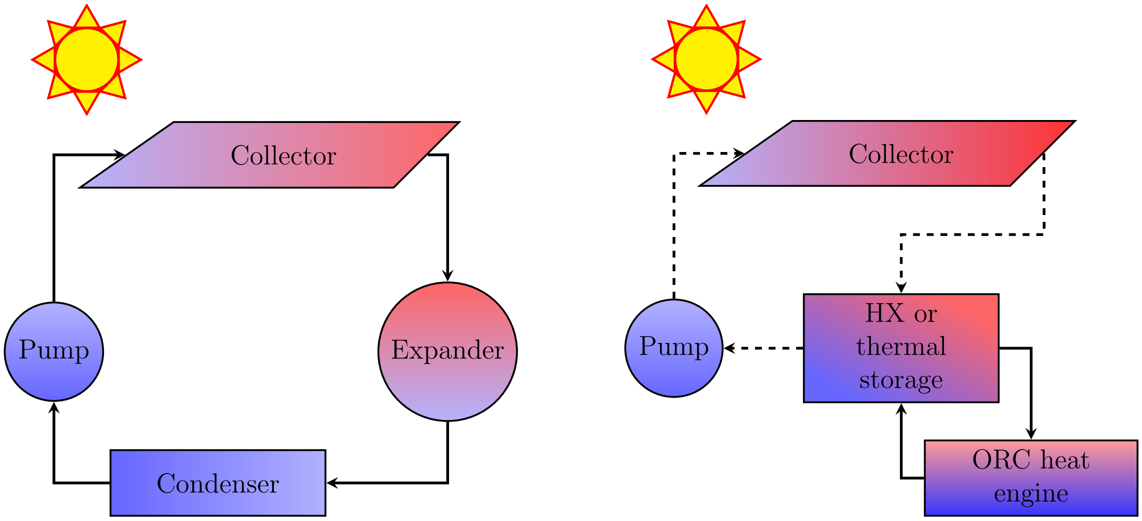

(a) Direct system.

(b) Indirect system.

Figure 18.1: Two canonical solar-thermal system configurations.

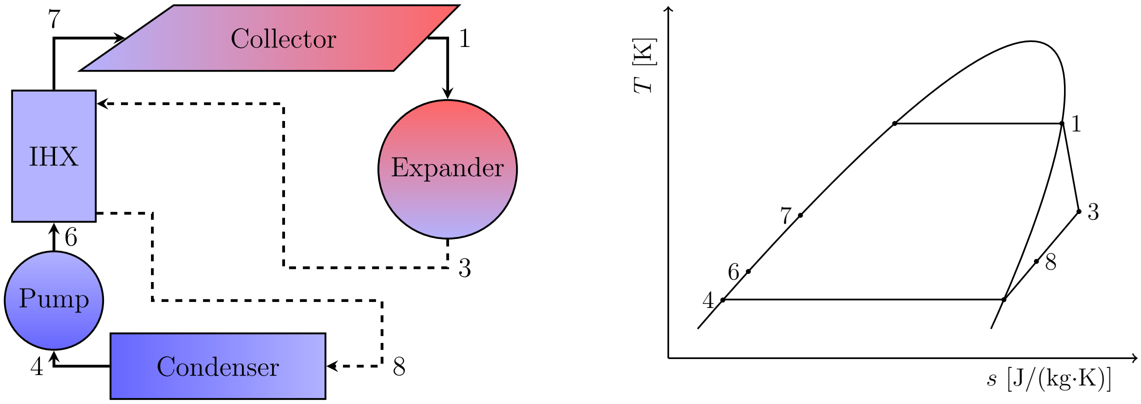

(a) Equipment configuration diagram.

(b) Thermodynamic cycle on the T-s diagram.

Figure 18.2: Direct configuration with internal heat exchanger (IHX).

that a specific ratio is achieved in the long run as a function of high operating temperature). Because it is not yet clear if this is possible or what the mixture ratio would be, nine mixture ratios are studied. The mixtures are uniformly distributed as follows: R-1233zd(E), R-1233zd(E)/1233zd(Z) (90.0/10.0),... ,R-1233zd(E)/1233zd(Z) (10.0/90.0), R-1233zd(Z). This leads to eleven results, one for each of the pure fluids, and nine results uniformly spanning the binary mixing possibilities. Operating a mixture is only possible if both isomers do not thermally decompose into products other than R-1233zd(E) or R-1233zd(Z). The thermal decomposition rate as a function of temperature of both isomers are not yet well studied.

18.3 Results and discussion

Because the thermodynamic cycle (ORC + IHX) can be defined by the location of the expander inlet in the T-s diagram (all other states are calculated from this and the assumptions, see Chapter 17 for more information), one can plot cycle and system performance attributes on a T-s diagram. Figure 18.3(a) shows the results for R-1233zd(E) based on the NIST-supplied fluid file. The green data points note the nondominated Pareto frontier in the system efficiency η_{sys} verses volumetric power capacity (VPC) ψ space for that fluid. Figure 18.3(d) shows the results for R-1233zd(Z) based on the Honeywell preliminary fluid file. There is an increase in area where calculations failed. These failures result from the T_m numerical averaging along/near the critical pressure line. See Chapter 14 and Equation 14.4 for more information. This is typical of fluids using preliminary fit coefficients for the EOS because the area around the critical point is the most difficult area to accurately model. Figures 18.3(b) and 18.3(c) show results for mixtures R-1233zd(E)/1233zd(Z) (70.0/30.0) and R-1233zd(E)/1233zd(Z) (30.0/70.0) respectively. Figure 18.4(a) shows preliminary results for R-1233zd(E)/1233zd(Z) (50.0/50.0). Note the area at the left where some results violate Carnot's law. Figure 18.4(b) shows the calculation domain shifted to avoid this problem. The most likely cause of the problem is the IHX heat exchanger model defined in Equations 17.1, because the IHX model assumes no phase change. Because the results of interest are not inside the vapor dome, the overall results are not affected. Although there are three noted issues with the performance of modeling R-1233zd(Z) in mixtures and as a pure fluid, these problems do not undermine the overall results.

The high operating temperatures 550 K or more of R-1233zd(E), R-1233zd(Z) and their binary mixtures in a direct solar-thermal ORC + IHX system create two similar concerns: 1) This is above the currently recommended maximum limit of ∼470 K (200°C) during operation, and 2) The direct configuration does not protect a fluid from the collector stagnation temperature which is estimated to be ∼650 K for the N–S XCPC (Chapter 9). There are three alternatives that may help to resolve this problem: 1) Use the fluid in an indirect configuration to protect the fluid from higher temperatures, which will also lower the system efficiency because of the entropy generation of the additional heat exchanger, 2) Explore the use of temperature-dependent coatings on the absorber area to increase heat rejection when the collector is above a predetermined temperature, and 3) Use noble metals or hastelloy materials of construction for all surfaces in fluid contact to increase chemical stablity of the fluid. The second option is currently being explored in STC to limit thermal stress thereby increasing longevity and lowering cost. A fourth alternative is to minimize the time the fluid is at high temperature [198]. This alternative is discounted because of the time it takes for the fluid to be heated in the collector and cooled in the expander is perceived to be a notable portion of the time it takes the fluid to complete one full cycle in the heat engine. A second issue exists with this fourth alternative. When the system is not operating while the sun is within

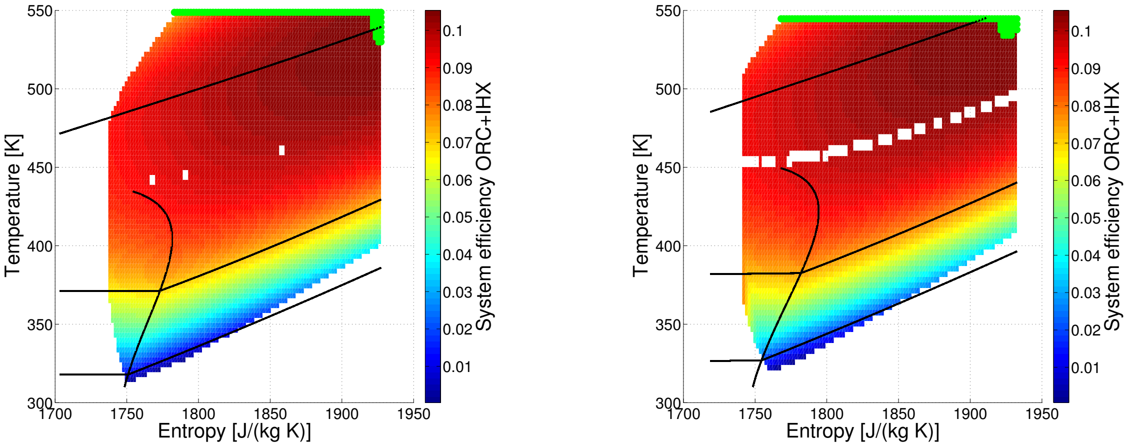

(a) R-1233zd(E).

(b) R-1233zd(E)/1233zd(Z) (70.0/30.0).

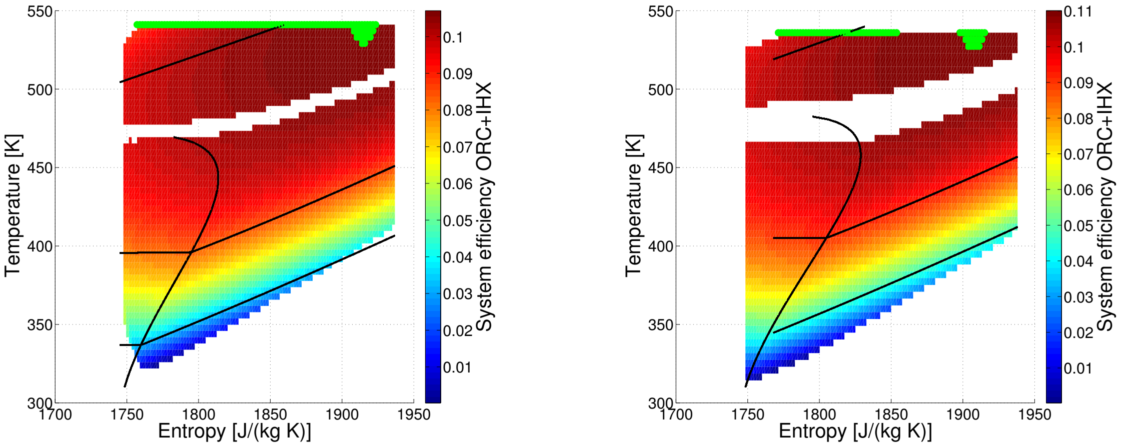

(c) R-1233zd(E)/1233zd(Z) (30.0/70.0).

(d) R-1233zd(Z).

Figure 18.3: Selected design exploration results.

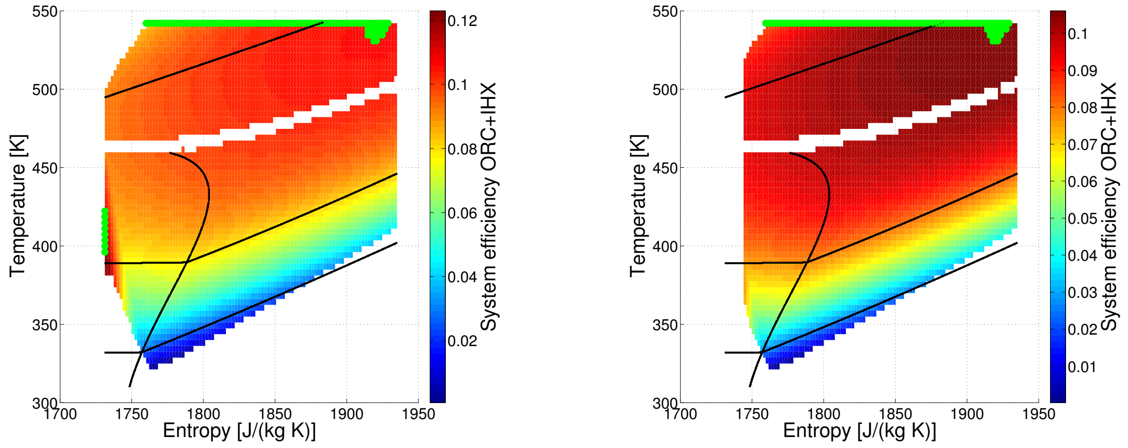

(a) Original results.

(b) Final results.

Figure 18.4: R-1233zd(E)/1233zd(Z) (50.0/50.0) showing problematic area of design exploration.

view of the solar collector, the fluid is exposed to stagnation temperatures of the collector until the equipment is returned to operation. The sun is typically within the collector view 8 to 16 hours per day, depending on the time of year and location.

The maximum efficiency point of each fluid is selected. These selected data points are used to represent each fluid in Figure 18.5, where R-1233zd(E) is green, R-1233zd(Z) blue, and the mixtures are uniformly shaded from green to blue. Water and ammonia use the ORC model whereas all other fluids use the ORC + IHX model. This result is quite powerful. It shows that a preliminary assessment of R-1233zd(E), R-1233zd(Z), and their mixtures perform notably better than R-1336mzz(Z) in efficiency and machine size for all but pure R-1233zd(Z), which has nearly the same machine size measure as R-1336mzz(Z). If both R-1233zd(E) and R-1233zd(Z) are chemically stable if they meet the following criteria: 1) A stable or constant mixture is possible based on high operating temperature, 2) Thermal decomposition rate is low (decomposition into something other than R-1233zd(E), and R-1233zd(Z) at the operating temperatures of the machine). If these criteria are met, then these results clearly show R-1233zd(E), R-1233zd(Z), and their mixtures are excellent candidates for ORC applications. This result is independent of the binary mixture ratio. The direct configuration for solar-thermal power generation has different thermodynamic performance than the indirect configuration or waste heat recovery ORC applications because of the lack of a second heat transfer fluid (Figure 18.1 and Chapter 13); therefore, the machine size and efficiency estimates here will not necessarily directly translate to the other applications. Further simulation using the indirect configuration for solar and waste heat recovery configurations are necessary for more specific analysis.

Chapter 17 found that health, safety, and environmental (HSE) requirements are far more restrictive than thermodynamic requirements. R-1233zd(E) has an ASHRAE 34 classification of A1. Ravij Singh of Honeywell shared that an engineering judgment (best guess) has been made that when R-1233zd(Z) is evaluated for classification, it will likely be class B1 with an occupational exposure limit OEL around 100 ppm [198]. For comparison, ammonia, R-1233zd(E), and R-1336mzz(Z) have OELs of 25 ppm, 800 ppm, and 500 ppm respectively. It is thought that R-1233zd(Z) may have similar toxicity to toluene, which is currently used in industrial ORC applications. This means that a mixture of R-1233zd(E) and R-1233zd(Z) may work to reduce the overall toxicity making R-1233zd(Z) more generally acceptable from an HSE perspective.

18.4 Conclusions and summary

Compared to R-1336mmz(Z), the thermodynamic performance of R-1233zd(Z) and the binary mixtures with R-1233zd(E) are excellent. The process of isomerization alone does not pose a market barrier to using a R-1233zd(E)/1233zd(Z) mixture in

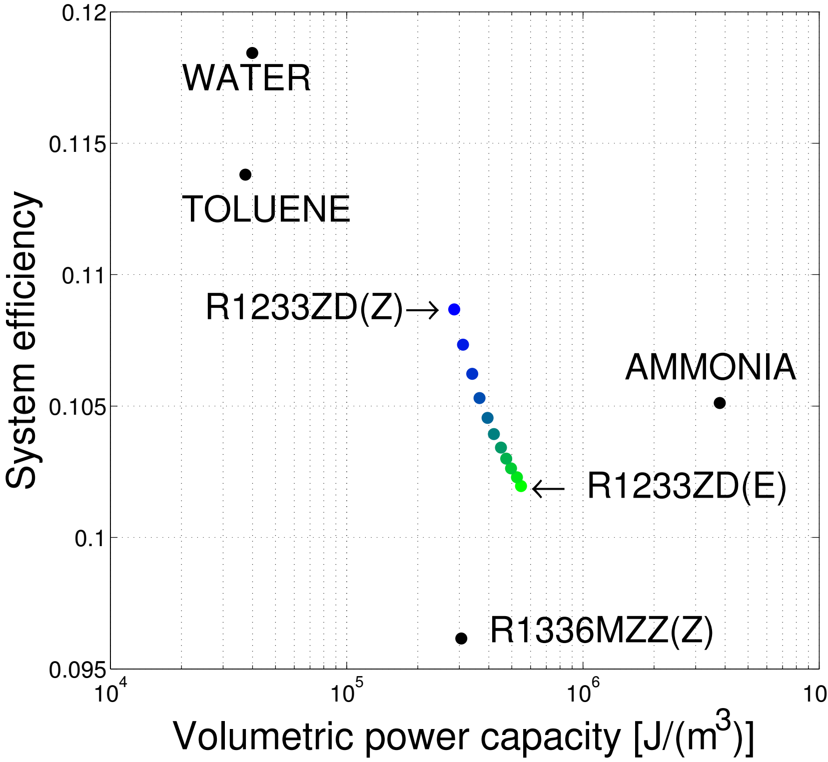

Figure 18.5: η_{sys} versus ψ. Mixtures shaded uniformly from green to blue. Water and ammonia use the ORC model. All other fluids use the ORC + IHX model.

medium- to high- temperature applications; however, thermal decomposition into byproducts other than R-1233zd(E) or R-1233zd(Z) may or may not pose a barrier. Using a mixture also allows for the possibility of reducing the overall toxicity of R-1233zd(Z). These results demonstrate the potential economic benefit of bringing R-1233zd(Z) to market for use as a pure fluid and in a mixture with R-1233zd(E). Using a R-1233zd(E)/1233zd(Z) mixture to lower the toxicity and avoid isomerization issues are the original work of this author. The results also motivate the value of performing further research. To accomplish this, further testing and evaluations are needed.

18.5 Future work

During the course of conducting this research, several opportunities for future work are noted:

- Research the trans-cis isomeration process and temperature dependence.
- Study the thermal decomposition rates of R-1233zd(E) and R-1233zd(Z).
- Refine the R-1233zd(Z) REFPROP fluid file.
- Determine more accurate mixing coefficients for R-1233zd(E) and R-1233zd(Z).
- Design exploration and simulation in additional ORC applications.

PART V. COMPONENT CONSIDERATIONS FOR HEAT ENGINES

19. SIMPLE SIMULATION OF A DSSTC SYSTEM

19.1 Introduction/background

The one main goal of the dissertation is to evaluate electricity generation performance of a DSSTC system. In Chapter 12, an oversimplified heat engine model was combined with the solar simulation created in Part II. In Part IV two basic Rankine cycle thermodynamic models of heat engine performance were created. The focus was to determine a fluid and cycle that resulted in the 'best' possible performance. Water/ammonia was determined to be the best fluid when considering system efficiency η_{sys}/volumetric power capacity ψ respectively. No known fluid performed 'best' when considering both η_{sys} and ψ as these two design attributes form a Pareto frontier. In Chapter 17, both a simple Rankine cycle with or without superheating (ORC) and a Rankine cycle with an internal-heat exchanger (ORC + IHX) were modeled for fixed irradiance and ambient temperature. Health, safety, and environmental (HSE) screening found that few if any fluids perform well in both thermodynamic and HSE requirements. R-1336mzz(Z) was identified as a potential working fluid and, R-1233zd(Z) was noted as a future possibility because it is not yet marketed. There are other thermodynamic cycle that might be considered such as using a combined cycle with a top and a bottom fluid to leverage the benefit of one fluid being high in critical temperature and the other low in normal boiling point. Additionally, one may consider a mixture of fluids as an alternative way of leveraging the benefits of individual components. In general, testing mixtures is difficult because for many fluids, especially organic fluids, mixtures with water require custom mixing coefficients to be experimentally determined. Some of these alternatives result in increasing machine complexity, therefore equipment cost. It was shown that efficiency is weakly correlated with critical temperature and VPC is strongly inversely correlated with normal boiling point. It was further shown that there is a relationship between critical temperature and normal boiling point, which prevents the fluid designer from independently selecting both fluid properties. The research showed that there is a possibility of finding a fluid that used the Rankine cycle with superheating to have a higher ψ than water and only a small reduction in η_{sys}. The results of Part IV show promise and fail to completely treat the subject. This leaves the search for what cycle and fluid pair are 'best' for the direct solar configuration furthered, yet incomplete.

In Chapter 4, The Twomey et al. 2013 [31] contribution was discussed. Twomey et al. 2013 considered solar and ambient temperature variability using a monthly value to update a sine function to model diurnal variability. The indirect configuration using thermal storage was considered in the Twomey et al. 2013 work. Here the direct configuration and variability are considered on an hourly basis using TMY data from NREL as discussed in Chapter 6. In Chapter 17, 49 fluids were considered and modeled using fixed irradiance and ambient temperature. The models used included part-load performance of the STC and fixed pump/expander efficiency. Two versions of the model were developed: 1) ORC and 2) ORC + IHX. The chapter included HSE evaluations of the fluids and left the reader with the challenging task of selecting a fluid and cycle for themselves because of the ambiguity of HSE and LCOE.

When accounting for the varying solar resource, it is natural to also account for machine size and part-load performance of equipment. At the same time, it is reasonable to consider equipment interfaces because the components are required to function in harmony over a wide range of operating conditions. In this part of the dissertation, the goal is to investigate how electricity generation of a DSSTC is impacted by considering the limits of components and interfaces between components.

The current chapter will address variability by simulating the previously made ORC and solar models on TMY data. The next chapter will focus on determining pump and expander performance as a function of first size and second part-load once the size has been fixed. Once the pump and expander models have been upgraded, the new heat engine model will be simulated on TMY data.

19.2 Methodology

In this chapter, water (ORC), ammonia (ORC), R1233zd(E) (ORC + IHX), and R1336mzz(Z) (ORC + IHX) are reviewed by simulating each of them on a standardized set of G_{eff} and T_{amb} pairs. Tabulated results will be presented for several locations. Graphical results will be presented for a single location. A second round of discussion will present the heat engine performance data for each fluid. The exact choice of fluid is somewhat unimportant as any fluid with a reasonable level of thermodynamic performance will allow the design methods and challenges to be demonstrated. The intent of this chapter is to demonstrate methods and principles which can be used to inform design. Accounting for the limits of components and the interfaces between them will be accomplished in several steps:

1. Graphically understand the variability of the solar resource and ambient temperature conditions.
2. Simulate the combined solar-heat engine system model on TMY data, using fixed expander/pump efficiency and part-load performance for only the STC.
3. Develop graphical methods to review results.

19.2.1 Resource variability, introducing the linearly normalized bivariate histogram

When using a solar collector to drive a heat engine there are two environmental parameters of note, irradiance and ambient temperature, because both of these

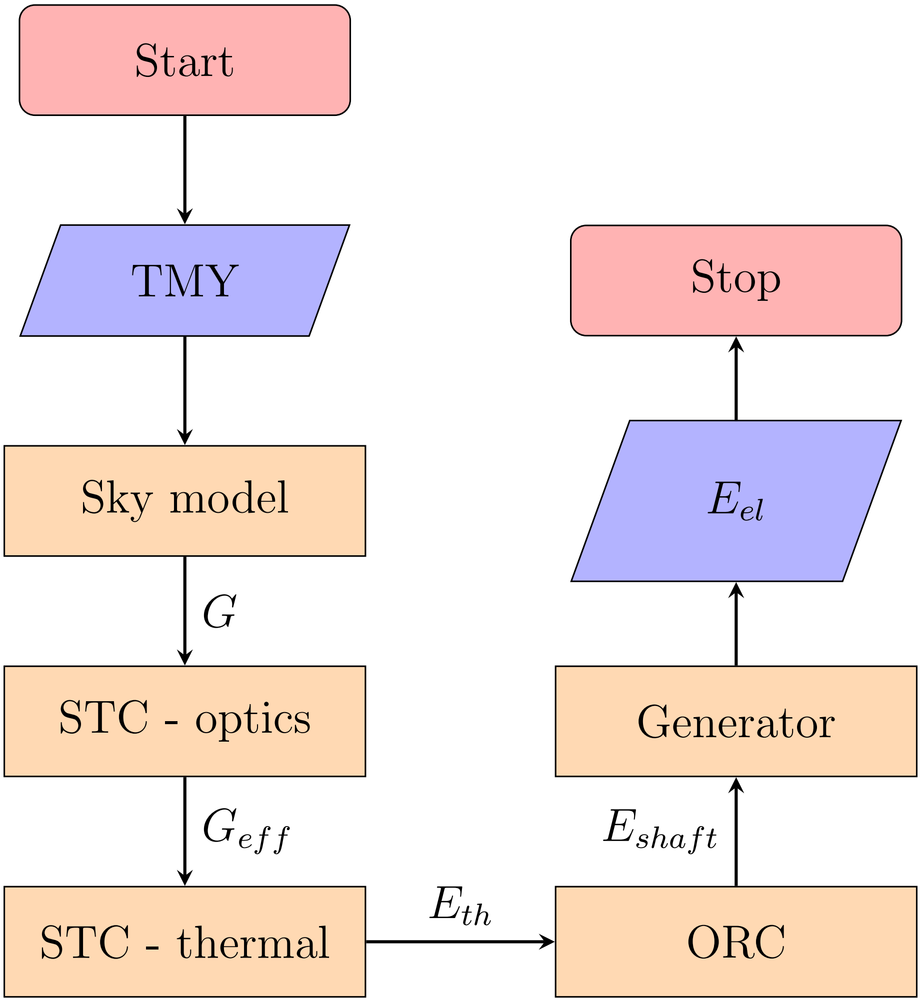

Figure 19.1: Overview of the model to be simulated on TMY data.

parameters effect equipment performance. Figure 19.2 shows histograms of each parameter for College Station, Texas. In the context of this discussion, the effective irradiance of the N–S XCPC is used because that particular collector was found to perform the best. Presenting the data in two separate histograms oversimplifies the design requirements because the relationship between irradiance and ambient temperature is neglected. To recover the lost information, one can plot the data on a bivariate histogram as shown in Figure 19.3. Bivariate histograms are typically used in statistics. The bivariate histogram is two variable binning and therefore an unobstructed top down view of the bin counts with color coding is used to display the data. There is a second problem with how the information is displayed, namely that bin counts of irradiance only communicates to a designer the number of hours (because the TMY data used is hourly) in a year a particular ambient condition exists. It does not tell the designer the energy yield potential of a particular bin. By converting the irradiance bin counts into a ratio (energy content of the bin normalized by the total annual energy content), the idea of a uniformly normalized histogram can be altered to display the linearly normalized histogram (linear in irradiance) (Equation 19.1). The converted bin counts show the distribution of energy over irradiance (Figure 19.4). This method can be used to create a new bivariate histogram that provides a designer with energy content information which is of great importance (Figure 19.5). The linearly normalized bivariate histogram can be used to better understand resource variability for a particular location, and it is original work by this author.

$$E_{\text{bin}} = (\text{Bin count}) * (\text{mean bin irradiance}) \tag{19.1a}$$

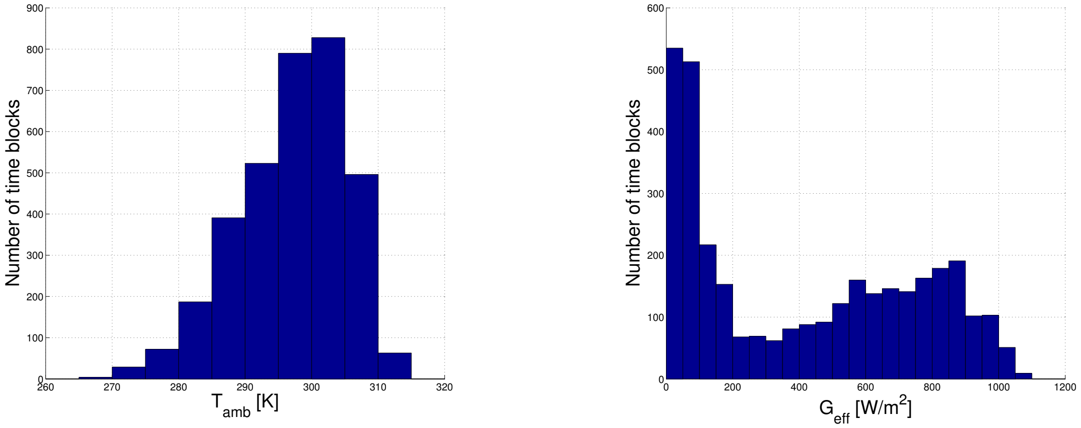

(a) Ambient temperature T_{amb}.

(b) Effective irradiance G_{eff} (N–S XCPC).

Figure 19.2: Histograms of T_{amb} and G_{eff}, results for College Station, TX (TMY3)

$$E_{\text{total}} = \sum_{\text{bins}} E_{\text{bin}} \tag{19.1b}$$

$$\text{ratio} = \frac{E_{\text{bin}}}{E_{\text{total}}} \tag{19.1c}$$

19.2.2 Simulation of the solar-heat engine system model

Figure 19.1 shows a simplified flow chart for the overall model being simulated. Part II discusses the irradiance and collector modeling which are based on the N–S XCPC design by Roland Winston [132], the AWM by Perez [126]. The solar model accounts for solar variablity and part-load thermal performance. Part IV discusses the ORC heat engine model which is based on fixed expander and pump efficiency. The generator model assumes a fixed 100% efficiency so the reader may add their own size appropriate assumption or stated anotherway, the discussion proceeds focusing on shaft power rather than electric power. The net result of efficiency assumptions are that the simulated model best matches the variable expansion/temperature difference case of Chapter 12, and the model best approximates being able to adjust

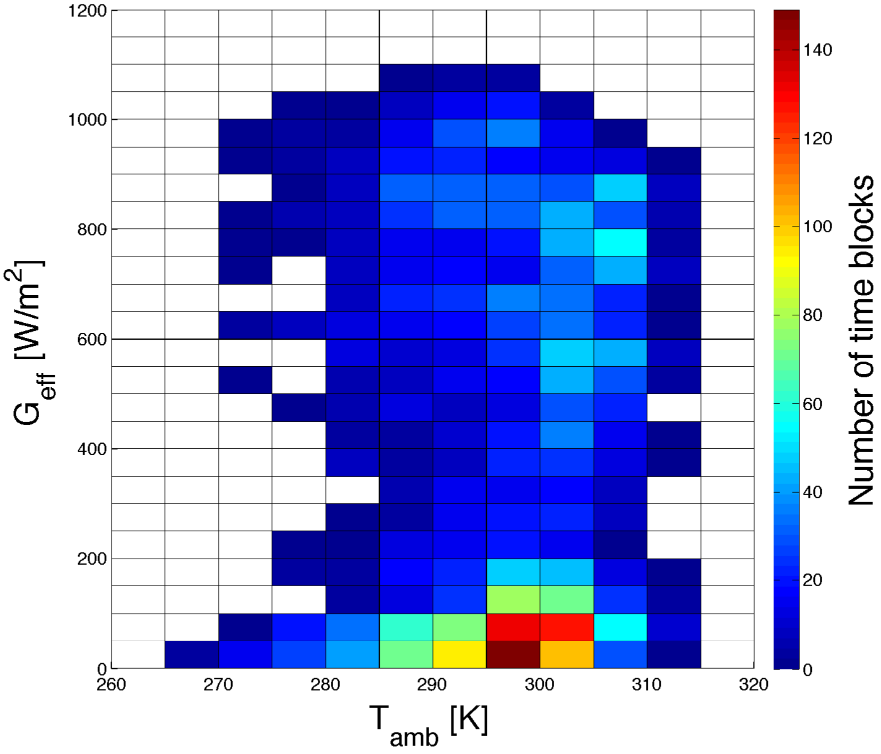

Figure 19.3: Bivariate histogram, results for College Station, TX (TMY3).

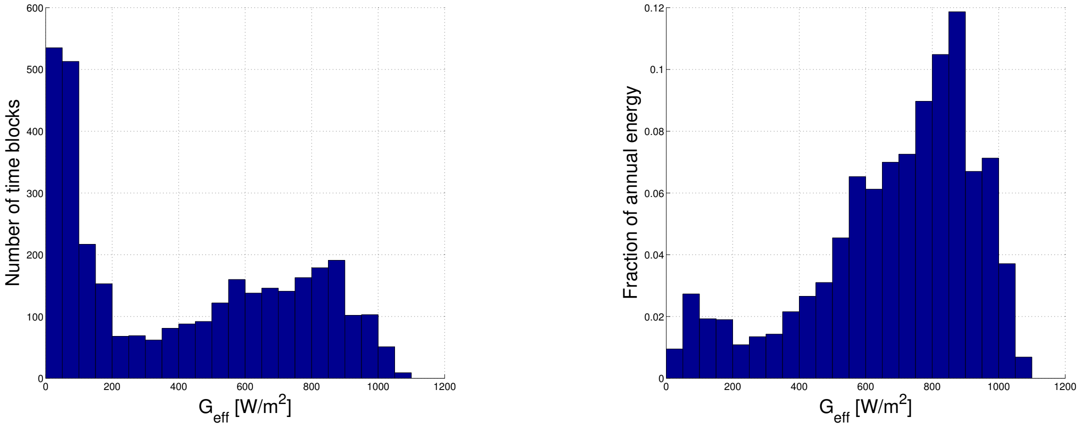

(a) Effective irradiance G_{eff} (N–S XCPC).

(b) Linearly normalized histogram of the effective irradiance G_{eff} (N–S XCPC).

Figure 19.4: Linearly normalized histogram of the effective irradiance, results for College Station, TX (TMY3).

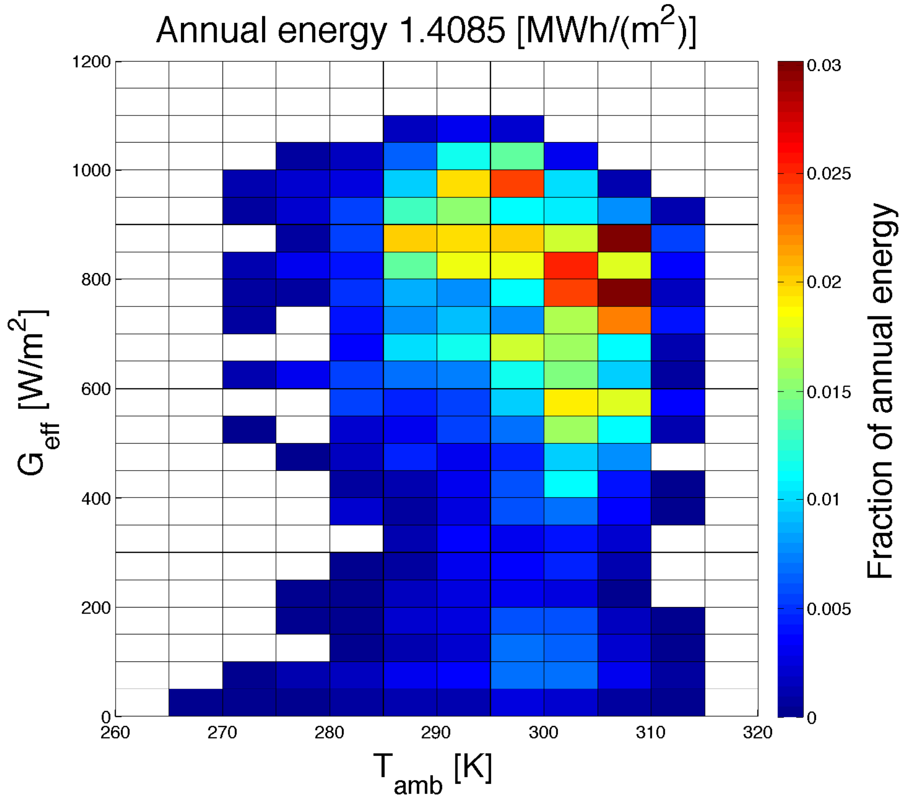

Figure 19.5: Linearly normalized bivariate histogram, results for College Station, TX (TMY3), based on G_{eff} for the N–S XCPC.

machine size each hour without the penalties for such advantages. While it is completely unrealistic to change machine size each hour, the results provide a base case to which the results of Chapter 12 can be compared. The simulation leverages the bivariate histogram for each location by modeling the 12 temperatures of each column of bins, because simulating heat engine performance is independent of irradiance. Then the simulation leverages the bivarate histogram again to multiply a vector of length 24 of collector performance by the array of heat engine performance. This process allows for $12 \times 24 = 288$ simulations be calculated efficiently and also avoid performing ~ 4300 simulation for each hour in the year with daylight. Even with these code improvements, calculating the necessary arrays for simulation took several hours for each fluid. The benefit is that the input performance arrays are calculated and saved, they can be called into memory and multiplied by the bivariate histogram bin counts for any of the TMY locations quite quickly. This means that the bivariate histogram and the linearly normalized bivariate histograms are highly useful in understanding the solar resource and in making efficient code. Using bivariate histograms to streamline simulation is original work by this author.

19.3 Results and discussion

19.3.1 Bivariate histograms

Figure 19.6 shows two bivariate histograms for irradiance at College Station, Texas. The plan of array irradiance POAI G provides a better basis for net energy calculation, and the G_{eff} N–S XCPC provides a better basis for energy modeling. These irradiance values are determined at the respective optimal mounting angle. Part II discusses irradiance basics and modeling methods in addition to the main topic of building a custom solar simulation. Part III discusses irradiance before and after optics at various latitudes and mounting angles.

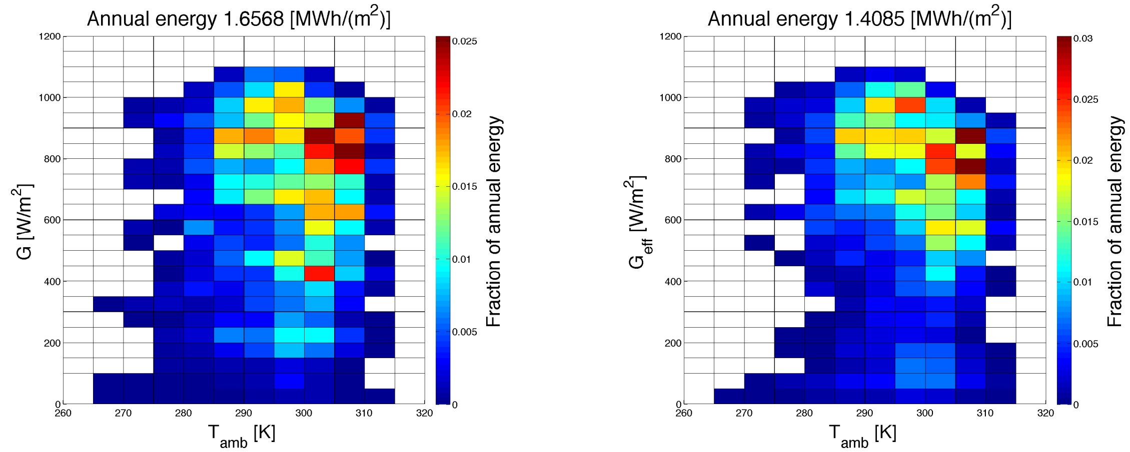
Annual energy 1.6568 [MWh/(m^2)]

Annual energy 1.4085 [MWh/(m^2)]

(a) G for POAI.

(b) G_{eff} for N–S XCPC.

Figure 19.6: Comparsion of two bivariate histograms: G for POAI and G_{eff}. Results for N–S XCPC at College Station, Texas using TMY3 data.

Table 19.1: Selected sites in the TMY3 dataset

Name	ID	Φ [°]	β^* [°]	$E^{*\S}$
Key West Intl Arpt, FL	722010	24.55	29.0	1.72
College Station, TX	722445	30.58	34.0	1.41
Merced, CA	724815	37.28	34.5	1.80
Seattle-Tacoma Intl, WA	727930	47.46	40.5	1.21
Shemya AFB, AK	704140	52.71	52.5	0.37

§ Annual energy based on G_{eff} (N–S XCPC) [MWh/(m^2·year)]

Table 19.1 is taken from Chapter 12 and provides the optimal mounting angle for each location being simulated. Figures 19.7 - 19.11 show the bivariate histogram results for the five TMY locations. Key West, Florida has good solar resource and a narrow range of ambient temperature compared to the other sites. Shema, Alaska has very poor solar resource. College Station, Texas has a marginally better solar resource than Seattle-Tacoma, Washington due to the humid haze during summer; where as, Seattle-Tacoma typically has cloudy/overcast conditions for a notable amount of the year. Merced, California has the best solar resource of the five because of the desert conditions there.

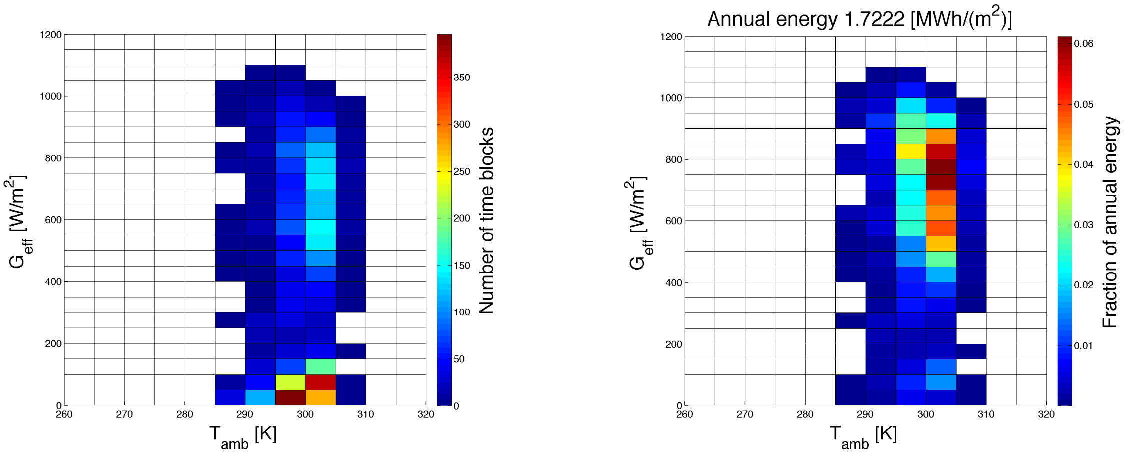

(a) Bivariate histogram.

(b) Linearly normalized bivariate histogram.

Figure 19.7: Key meteorological parameters for Key West, FL (TMY3). Annual energy based on G_{eff} for the N–S XCPC.

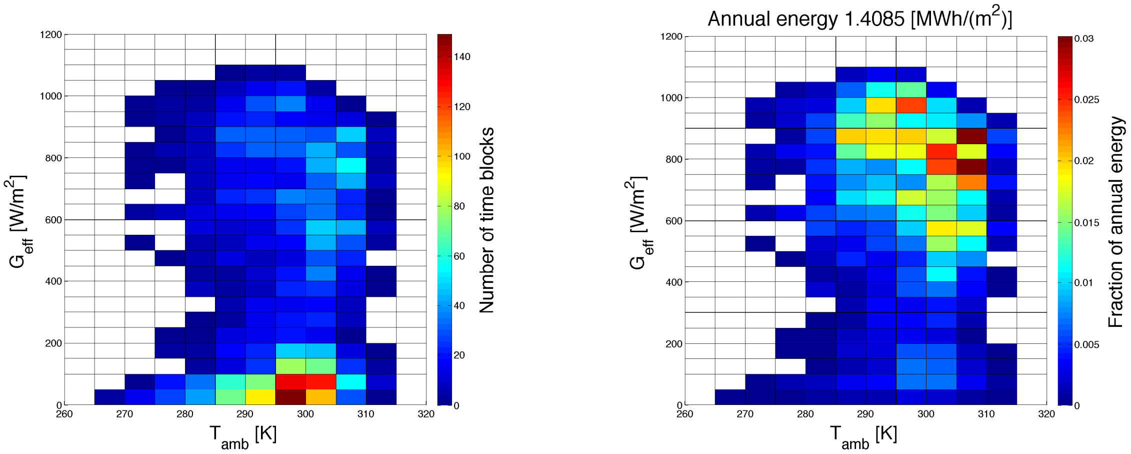

(a) Bivariate histogram.

(b) Linearly normalized bivariate histogram.

Figure 19.8: Key meteorological parameters for College Station, TX (TMY3). Annual energy based on G_{eff} for the N–S XCPC.

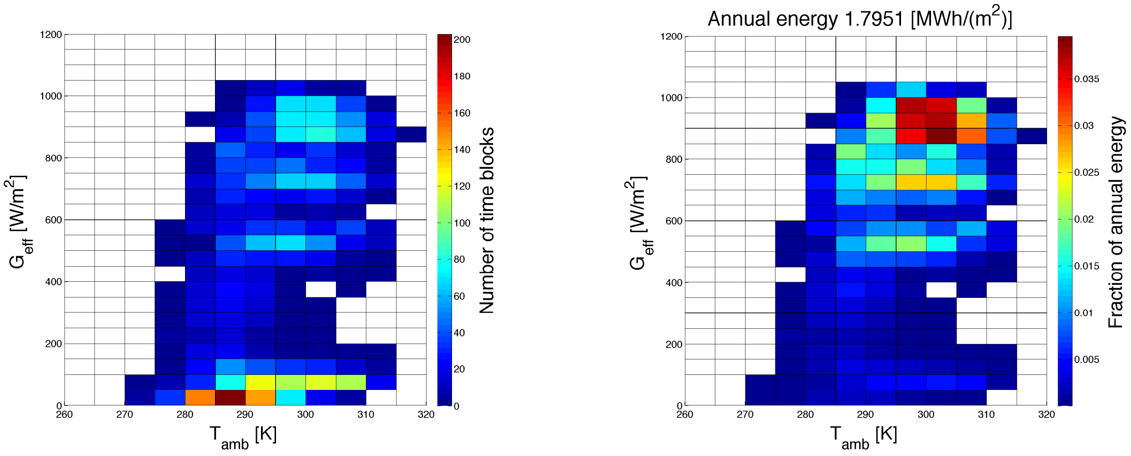

(a) Bivariate histogram.

(b) Linearly normalized bivariate histogram.

Figure 19.9: Key meteorological parameters for Merced, CA (TMY3). Annual energy based on G_{eff} for the N–S XCPC.

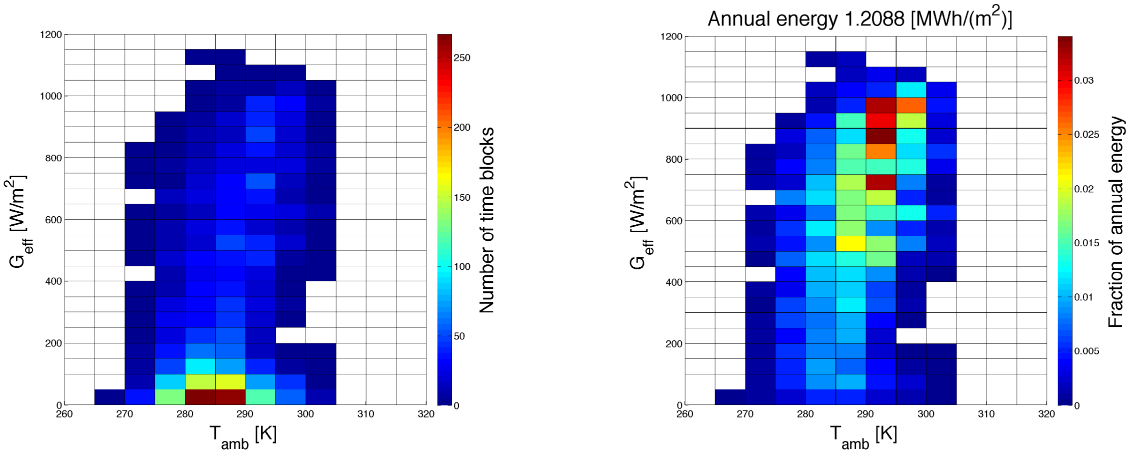

(a) Bivariate histogram.

(b) Linearly normalized bivariate histogram.

Figure 19.10: Key meteorological parameters for Seattle, WA (TMY3). Annual energy based on G_{eff} for the N–S XCPC.

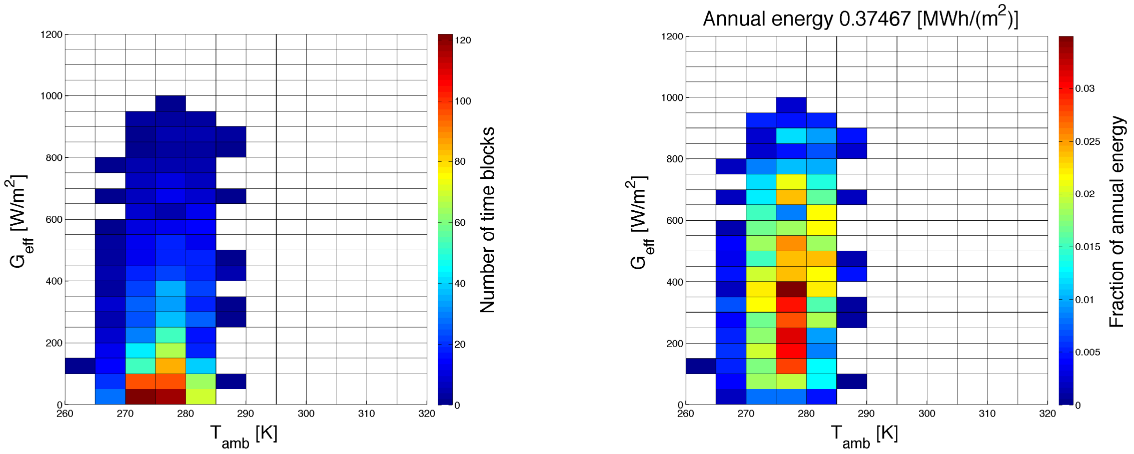

(a) Bivariate histogram.

(b) Linearly normalized bivariate histogram.

Figure 19.11: Key meteorological parameters for Shemya, AK (TMY3). Annual energy based on G_{eff} for the N–S XCPC.

19.3.2 Simulation simple - overall performance

Figure 19.12 shows the energy performance for four fluids using the N–S XCPC design with a simple heat engine simulation on TMY3 data for College Station, Texas. The relative energy distribution is nearly exactly the same for each fluid option. The total annual energy produced per square meter of collector area changes. Table 19.2 summarizes overall performance for the locations and fluid options. As expected, when ranking the fluids by the system efficiency, the same order is found as was indicated by the tests of Chapter 17 which used fixed ambient temperature and irradiance: 1) water, 2) ammonia, 3) R1233zd(E), and R1336mzz(Z). Water is problematic to use because of the high costs of: machine size, air infiltration, and regulation (Chapter 17). Ammonia is challenging to use in general because of the toxicity rating (ASHRAE 34 B2L), although it is more commonly used in industrial settings. One exception to this is the use of ammonia in hockey rink refrigeration systems. Both R1233zd(E) and R1336mzz(Z) have chemical stability concerns because of the heat engine high pressure side operating temperature. Chapter 18 showed that there was a possible way to use a mixture of R1233zd(E) and R1233zd(Z) to meet both health, safety, and environmental (HSE) requirements, chemical stability, and achieve a reasonable level of thermodynamic performance in both machine size (volumetric power capacity VPC or ψ) and system efficiency η_{sys}. R1336mzz(Z) has the lowest η_{sys} and smaller ψ than R1233zd(E). Each fluid has promise and problems. All four fluids will demonstrate the design principles and challenges.

Chapter 12 discussed an oversimplified heat engine performance model and simulated it using TMY data at several locations. There are two key results that can be compared to the current simple simulation of this chapter. First, the oversimplified model predicted the annual energy yield using variable temperature difference for College Station, Texas of 122 kWhe/(m^2·yr) assuming $\eta_2 = 0.5$, and the simplified model of this chapter predicted 118 kWhe/(m^2·yr) using R1233zd(E) as the working fluid. Second, the oversimplified model predicted a maximum ΔT of 275 K. This results in a mean temperature of 447.5 K assuming $T_L = 310$ K. Using the simplified model of this chapter predicted a maximum mean temperature of 430 K. These results are surprisingly close given the simple methods of the oversimplified model of Chapter 12, and show support that the oversimplified model can be used to gain performance knowledge prior to performing more in depth analysis that requires a notably larger amount of computational work. This shows that the oversimpified model can be used as a good screening tool for site locations.

19.3.3 Simulation simple - in-depth performance review

Heat engine performance depends on both the irradiance level G_{eff}, the ambient temperature T_{amb}, and the chosen working fluid. This means that heat engine performance modeling can be performed independent of location. Figure 19.13 shows the

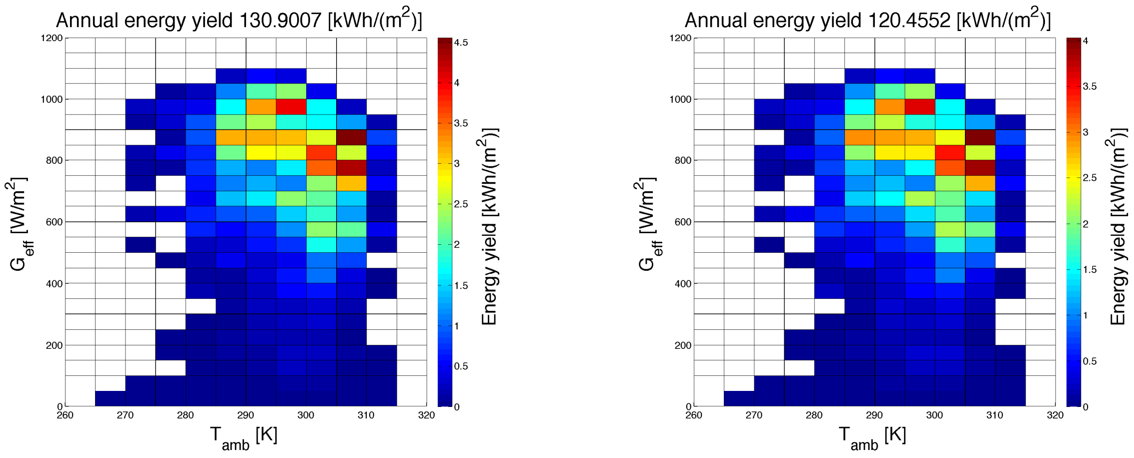
Annual energy yield 130.9007 [kWh/(m^2)]

Annual energy yield 120.4552 [kWh/(m^2)]

(a) Water.

(b) Ammonia.

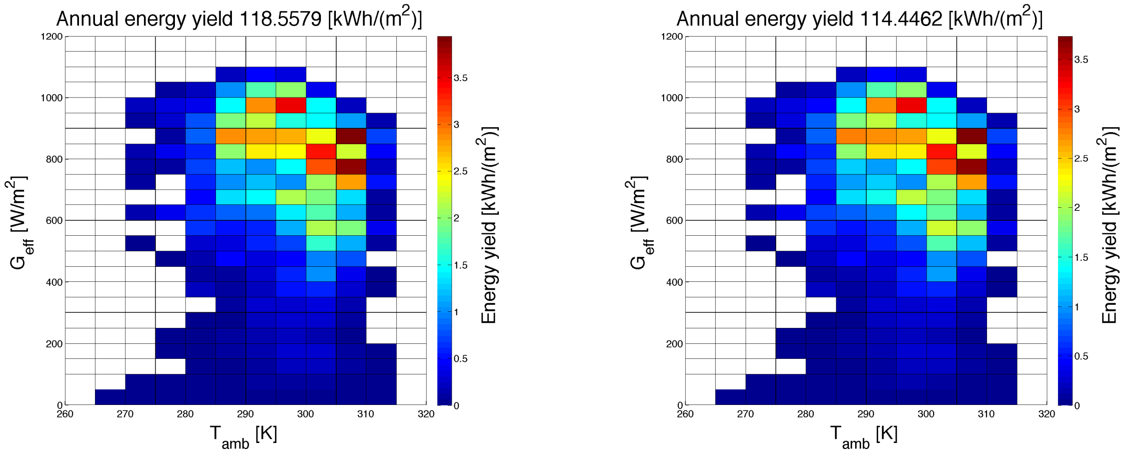
Annual energy yield 118.5579 [kWh/(m^2)]

Annual energy yield 114.4462 [kWh/(m^2)]

(c) R1233zd(E).

(d) R1336mzz(Z).

Figure 19.12: Shaft Energy E_{shaft} using four different fluids and the N–S XCPC at College Station, Texas

Table 19.2: Energy performance of several fluids at several locations in TMY3

Location	POAI	N–S XCPC	Water			Ammonia			R1233zd(E)			R1336mzz(Z)		
	$E^{\S}$	$E^{\dagger}$	$E^{\ddagger}$	$\eta^{\$}$	$\eta^{\pounds}$	$E^{\ddagger}$	$\eta^{\$}$	$\eta^{\pounds}$	$E^{\ddagger}$	$\eta^{\$}$	$\eta^{\pounds}$	$E^{\ddagger}$	$\eta^{\$}$	$\eta^{\pounds}$
Key West, FL	2.02	1.72	155.1	7.68	9.01	142.9	7.08	8.30	140.8	6.97	8.17	136.1	6.74	7.91
College Station, TX	1.66	1.41	130.9	7.90	9.29	120.5	7.27	8.55	118.6	7.16	8.42	114.4	6.91	8.13
Merced, CA	2.06	1.80	174.3	8.47	9.71	159.4	7.75	8.88	156.6	7.61	8.73	150.7	7.33	8.40
Seattle-Tacoma, WA	1.38	1.21	105.5	7.66	8.73	98.4	7.14	8.14	97.3	7.06	8.05	94.5	6.86	7.82
Shemya AFB, AK	0.43	0.37	25.6	6.00	6.83	24.5	5.73	6.53	24.5	5.74	6.54	24.5	5.74	6.54

§ Annual energy E^* based on G at POAI optimal slope [MWh/(m^2·year)]

†Annual energy E^* based on G_{eff} at N–S XCPC optimal slope [MWh/(m^2·year)]

‡Annual energy E_{shaft} [kWh/(m^2·year)]

\$ System efficiency η_{sys} based on G as a percentage

£ System efficiency η_{sys} based on G_{eff} as a percentage overall system efficiency based on G_{eff} for the four fluids of interest. Figure 19.14 shows four additional heat engine characteristics for R-1233zd(E). Figure 19.14(a) shows wide variance in expansion ratio. Figure 19.14(b) shows wide variance in volumetric power capacity ψ. The wide variance in expansion ratio and VPC pose significant challenges in designing a DSSTC system for use. While R-1233zd(E) results are discussed here, Figures 19.15–19.17 show similar results for each of the other three fluids. Chapter 14 discusses the challenge of identifying the 'best' thermodynamic state for the inlet of the expander and the need for future research into this problem. In the absence of a detailed analysis leading to a robust solution, the simple solution of selecting the state that maximizes system efficiency was chosen. Clearly, selecting the maximum system efficiency point results in heat engine design challenges because of the wide variability in expansion ratio and VPC found in the simulations here. It is not immediately clear what expander inlet state choice might reduce the variability in expansion ratio and VPC without comprising efficiency. More research on the methods for operating a DSSTC heat engine and selecting the expander inlet state are needed as one can not practically change heat engine designs each hour of operation to accommodate the changing expansion ratio.

19.4 Conclusions and summary

In this chapter, the use of bivariate histograms are developed and the linearly normalized bivariate histogram is introduced and are the original work of this author. A numerically efficient simulation of a simple DSSTC system is created. The simple simulation using fixed pump efficiency, fixed expander efficiency, and a part-load performance model of the N–S XCPC provides confirmation of the oversimplified model of Chapter 12. The detailed results in this chapter determine net system efficiency based on G for POAI in the range of 5–10% depending on fluid choice

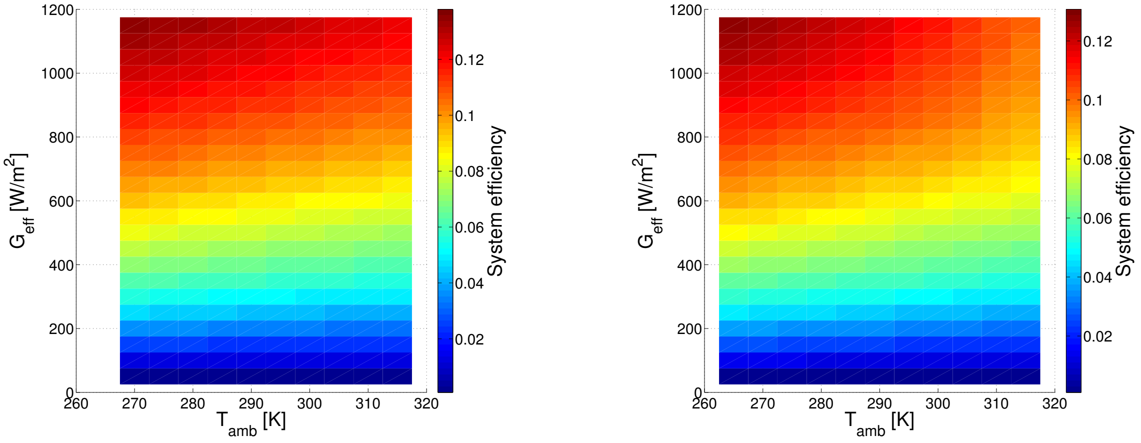

(a) Water. (b) Ammonia.

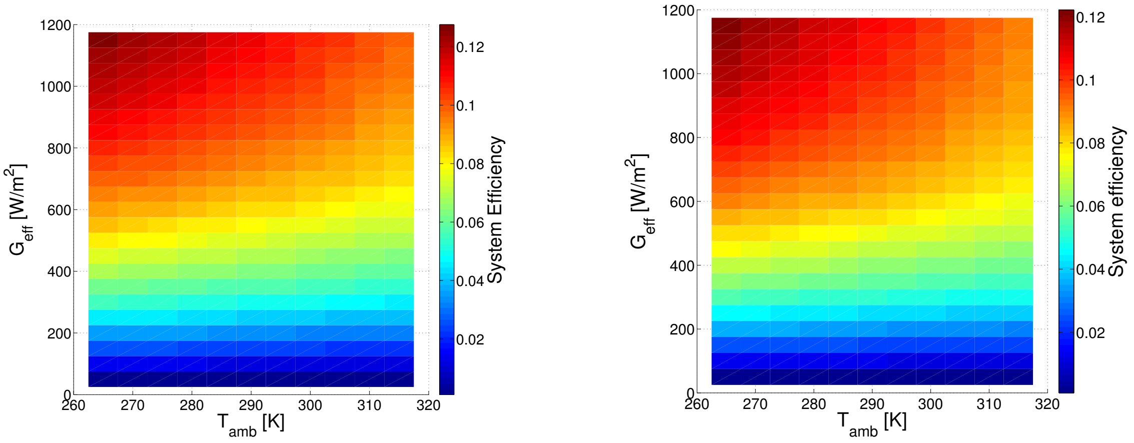

(c) R-1233zd(E). (d) R-1336mzz(Z).

Figure 19.13: System efficiency based on G_{eff} at College Station, Texas.

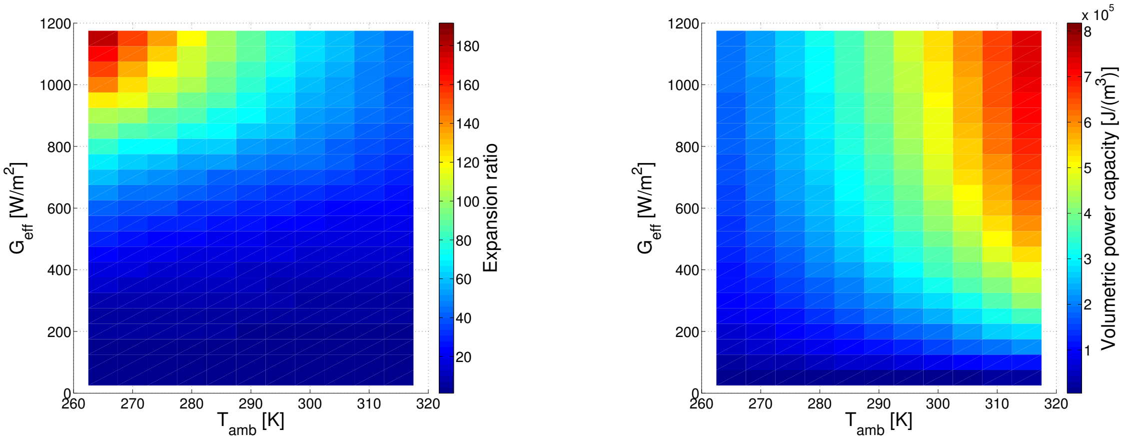

(a) Expansion ratio.

(b) Volumetric power capacity.

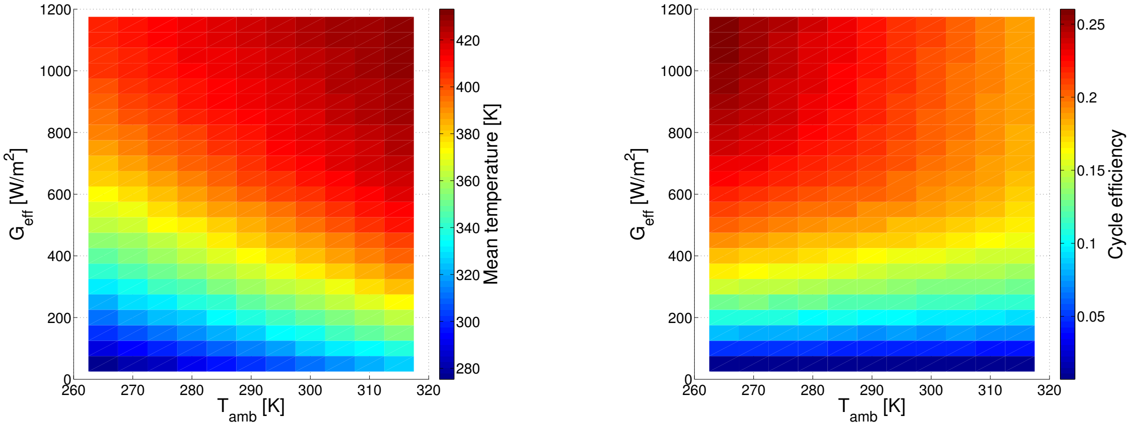

(c) Mean temperature.

(d) Cycle efficiency.

Figure 19.14: Various heat engine parameters for R1233zd(E).

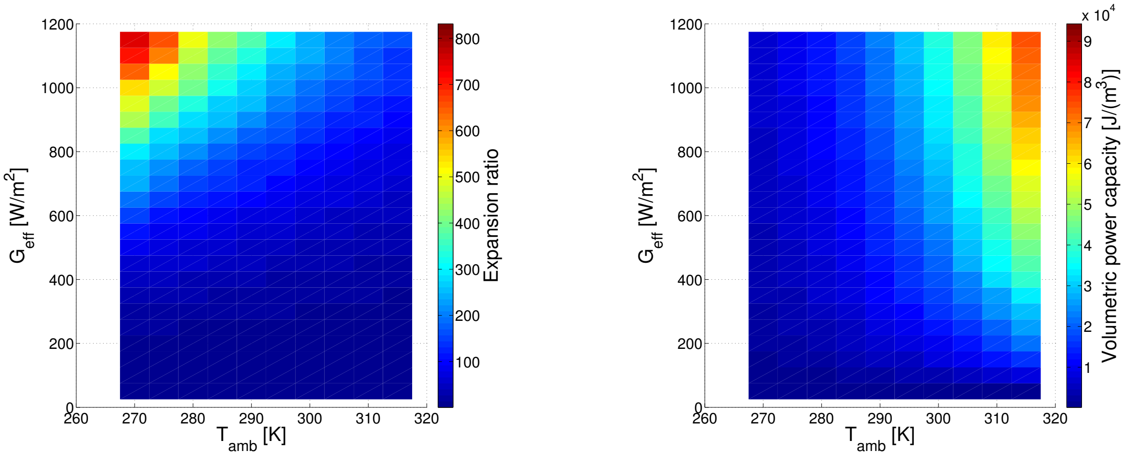

(a) Expansion ratio.

(b) Volumetric power capacity.

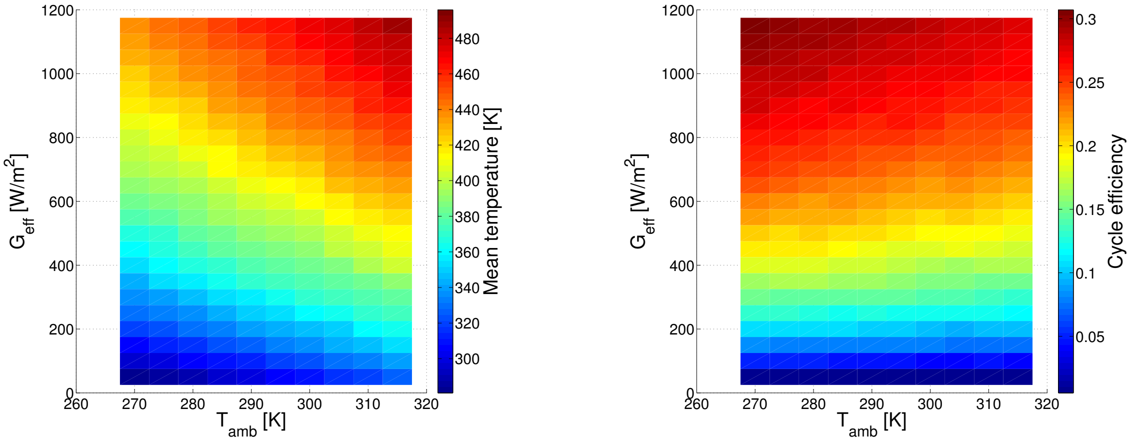

(c) Mean temperature.

(d) Cycle efficiency.

Figure 19.15: Various heat engine parameters for water.

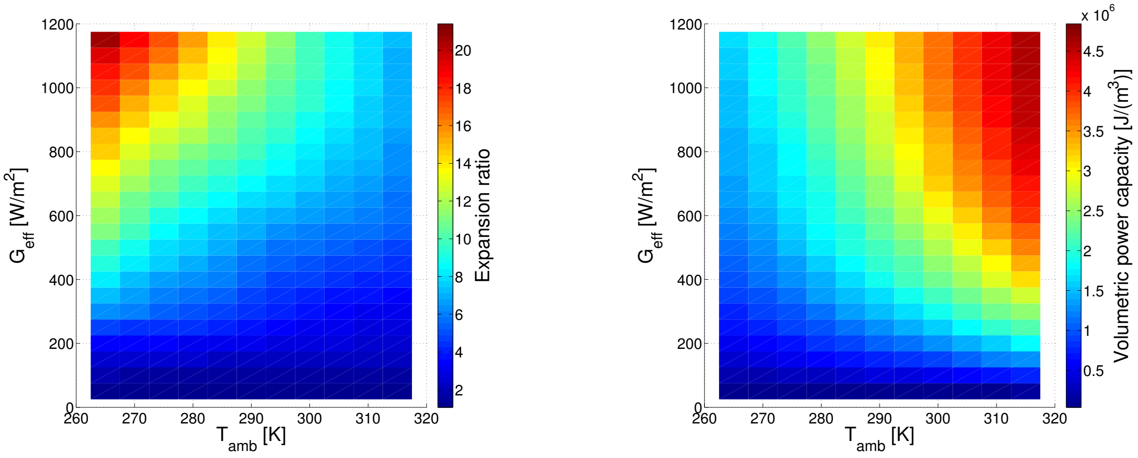

(a) Expansion ratio.

(b) Volumetric power capacity.

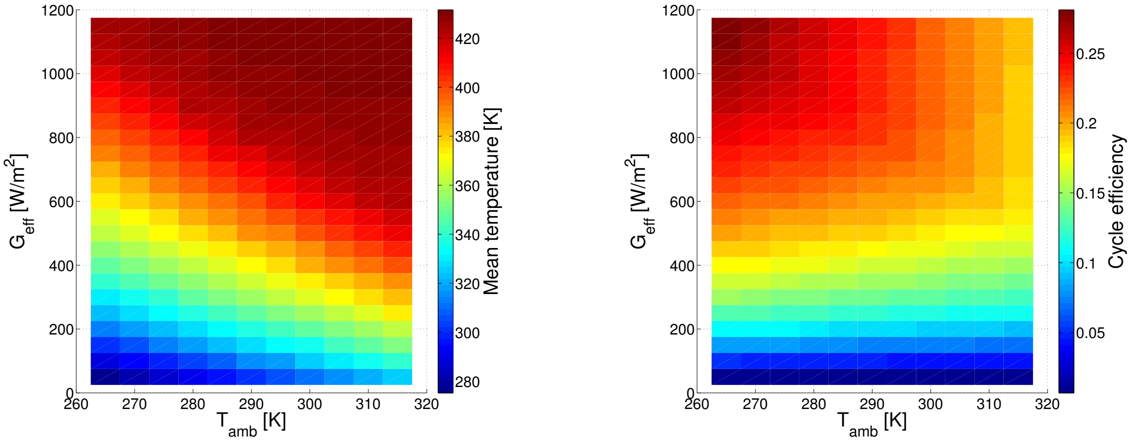

(c) Mean temperature.

(d) Cycle efficiency.

Figure 19.16: Various heat engine parameters for ammonia.

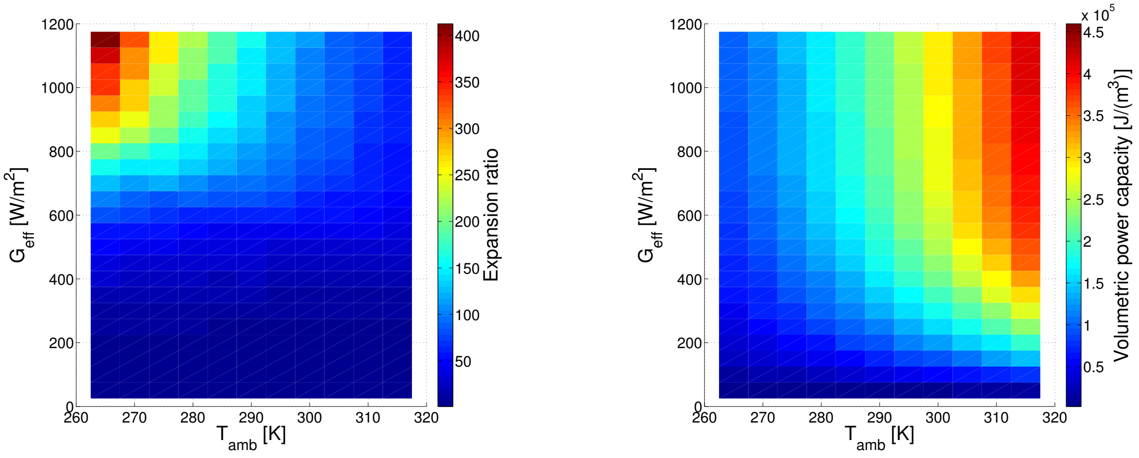

(a) Expansion ratio. (b) Volumetric power capacity.

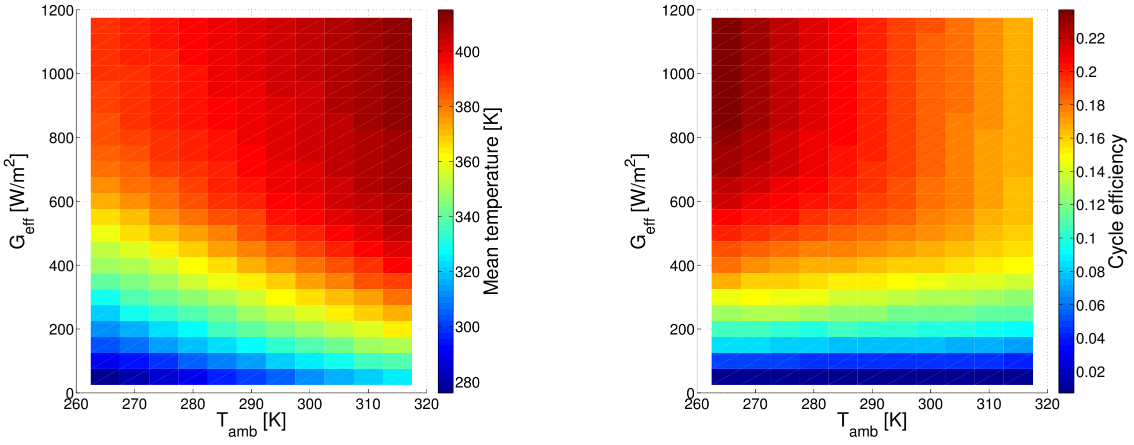

(c) Mean temperature. (d) Cycle efficiency.

Figure 19.17: Various heat engine parameters for R1336mzz(Z).

and solar resource. Four fluids were considered: water, ammonia, R1233zd(E), and R1336mzz(Z). While water is found to have the best efficiency, its use is challenged because of machine size and other related costs. R-1233zd(E) and R-1336mzz(Z) may not be chemically stable enough for use in a direct system. Ammonia may not be acceptable for use in residential applications because of elevated toxicity and flammability. The promise of smaller machine size, and good efficiency has proven challenging even for this unrealistic design method. Results confirm wide variance in expansion ratio and VPC resulting in design challenges that remain to be resolved. A compromise between the design attributes of system efficiency, machine size, expansion ratio is expected. It may be that an indirect system is required to lessen the variability by including storage which would lower performance predictions and increase system costs, yet the design might be more realistic. The simulation methods employed in this work and the results are the original contributions of this author. In Chapter 20, part-load performance of the pump and expander are included using the ORC model with superheating.

19.5 Future work

One future work is to simulate additional fluids and locations. A second future work is repeated from Chapter 14, "Identify a method to select the best choice for the thermodynamic state at the expander inlet given that this work has shown competing benefits in the design attributes." This second future work is of vital importance in the effort to create a design methodology based on system modeling that is consistent with real world performance. In Chapter 20, additional challenges will be identified that are required to be solved to enable realistic performance modeling.

20. PART-LOAD SIMULATION OF A DSSTC SYSTEM

20.1 Introduction/background

Chapter 14 covered building a organic Rankine cycle (ORC) heat engine model as shown in Figure 20.1. Model performance was calculated at $T_{amb} = 300$ K and $G_{eff} = 1000$ W/m^2. Chapter 19 used this model to simulate performance on typical meteorological year (TMY) data using part-load performance of the solar collector and fixed performance of the expander and pump on 288 unique weather conditions. Figure 20.2 shows the two canonical solar heat engine configurations. While the results of both chapters combined the 'best' irradiance modeling methods available, both fall short of realistically capturing the expected performance of a DSSTC direct configuration on real world weather data, because Chapter 19 showed the fixed pump and expander performance resulted in implicitly assuming variable machine size at each weather condition. This implicit assumption, commonly found in many solar heat engine modeling papers, severely limits the voracity of the results. In this chapter, size and technology appropriate part-load performance models of pump and exapnder are reviewed and the best available modeling is used to simulate realistic annual performance on TMY data by including part-load performance for a pump and expander.

20.1.1 The general search for the best technology

An informal review was conducting of all pumping and expanding technologies. There does not exist a single source or even several sources that discuss part-load performance of pumps or expanders that covers both scale of size and the wide range of flow conditions that are possible when an engineer is designing a process. This

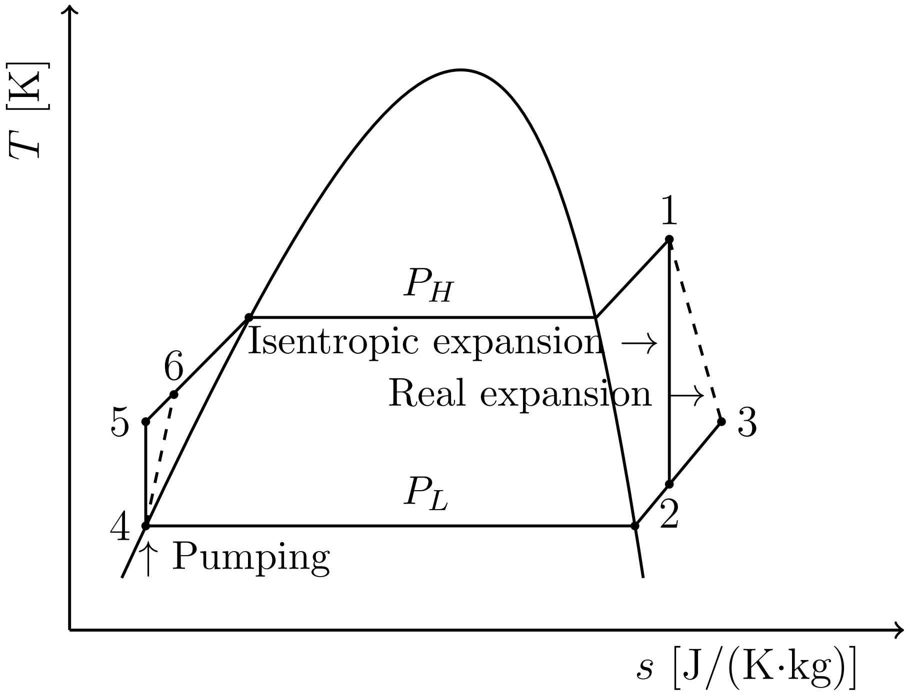

Figure 20.1: Rankine cycle as defined in the simulation.

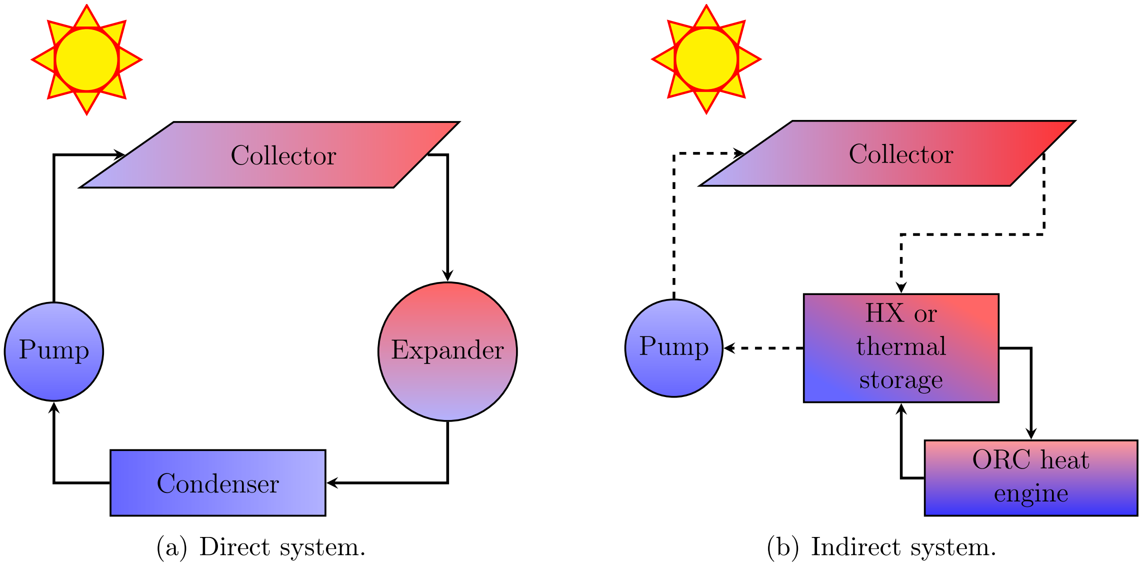

(a) Direct system.

(b) Indirect system.

Figure 20.2: Two canonical solar-thermal system configurations.

knowledge is domain specific such as in the oil and gas industry, manufacturing industry such as flow metering devices etc. There are an endless number of pumping devices (e.g., twin screw, sliding vane, piston, gear rotor, internal gear rotor, external gear rotor, axial turbine, radial turbine etc...). Also when considering compression devices, one can add many more design families to the list (e.g., scroll etc...). Almost all of the pumping compression devices can be redesigned to perform expansion. The physical basis upon which these devices are designed can be broken into two general categories: 1) positive displacement, and 2) velocity based (compression or expansion). Turbo-machinery can be a problematic term to use to delineate these two categories as turbo-machinery does not always provide velocity based expansion or compression. Devices that relying on velocity based compression/expansion typically do no perform well at small machine because the optimal rotational rate of the machine increases with decreasing size. As the machine becomes smaller the flow friction losses become greater. The result is that the best efficiency of the machine decreases with decreasing size. Because the size scale of a DSSTC system in this research is set to the residential scale (very small machine size), velocity based expansion devices are not the first choice. The remaining devices include, scroll, twin screw, sliding vane, gear rotors (both internal and external), and piston. Piston pumps are known to be less efficient than other options for most applications. Adding to the complexity, most equipment manufacturers do not give clear reliable efficiency data for equipment. Compounding this, even when efficiency information is given, it is typically for a single working fluid and a specific flow condition.

After an extensive research effort to identify technology for pumping and expanding that meet the modeling requirements, to be able to adjust scale, working fluid, and flow conditions only three technologies were found for pumping: Blackmer in Grand Rapids, Michigan; Smith Pumps in Newbury Park, California; and StarRotor in College Station, Texas. Blackmer is an industry leader in making many pumping technologies including sliding vane pumps and compressors. Unfortunately, at the time this research was completed in 2014, Blackmer only provided performance data using water as the working fluid. There was no clear way to create a reliable sliding vane model that would allow adjustment of the efficiency function based on fluid properties and flow conditions without substantial experimentation. This is well outside the scope of this research effort. Smith Pumps makes an external gear rotor pump that specializes in pumping liquid refrigeration products in transfer applications. This typically means low head pressure. Smith Pumps provides performance information based on viscosity of the working fluid. It was not readily clear how to adapt the Smith Pump performance curves for expansion without substantial experimental work. StarRotor is a start-up company that has designed a highly efficient gerotor (gerotor are also known as georotor and internal gear rotor and can be used in pumping, compression, and expansion applications). StarRotor uses patented technology to achieve extremely tight tolerances to maintain high volumetric efficiency (low leakage losses). StarRotor technology was selected because the technology can be used in pumping, compression, and expansion applications by adjusting the the design parameters. Performance curves provided by the CTO Dr. Mark Holtzapple show a comparison of StarRotor technology to traditional turbine where StarRotor is notably more efficient in the range of small to medium scale.

20.2 Methodology

Adapting the StarRotor models to make a thermodynamic model that consists of part-load performance of the solar thermal collector (STC), pump, and expander is outlined here. In addition to creating a thermodynamic model, the model is simluated on typical meteorological (TMY) data from the National Renewable Energy Lab

(NREL) (Chapter 6). To accomplish the simulation, a nested optimization structure is adopted where the inner optimization is determines the operating variables and the outer optimization determines the design variables.

20.2.1 StarRotor pump and expander models

StarRotor performance models are provided in two stages: 1) maximum efficiency vs. shaft power and efficiency vs. shaft speed for a specific size (Figure 20.3). Appendix N contains the details on how the data for the figures is determined. There are a few assumptions that were made to adapt the performance figures provided by StarRotor. It is common knowledge that pumping is generally less efficient than expansion processes. This is due to the fact that waste heat entering the fluid during pumping works to make the pumping process less efficient. Conversely, waste heat entering the fluid during expansion has the opposite effect. To account for this effect, the expansion performance curve is higher than the pumping curve. Secondly, the figures provided by StarRotor extrapolate to the stall shaft speed, meaning that the efficiency near the stall speed is not reliable. Figure 20.3(b) neglects this issue. There is a third issue with the figures provided by StarRotor, the performance data for expansion was for a fixed pressure ratio of 2. In this chapter, modeling performance is based on expansion ratio rather that pressure ratio to better account for performance. The leakage rate at a specific shaft speed is not properly accounted for as it is possible with different fluids to have the same expansion ratio and different pressure ratios. A fourth limitation is that the StarRotor models do not account for off design performance. Operating a StarRotor expander at expansion ratios other than the designed expansion ratio can not be accounted for. A fifth, limitation of the pump and expansion models is that the figures from StarRotor do not account for viscosity differences between fluids. The StarRotor data is based on the compression of air. The data from Smith Pumps has a clear advantage in this regard as the performance model is adjusted for viscosity. Figure 20.4 compares the viscosity of the fluids identified in Chapter 17 to air. Figure 20.4(b) shows that the viscosity of the fluids in the gas state are five times lower than that for air. The leakage is expected to be higher than the modeling methods used here predict and that over all efficiency is over predicted. Dr. Mark Holtzapple indicated that more detailed performance models existed internally and declined to share those models. In the provided figures from StarRotor, it was not immediately clear where the boundary between experimental data and theoretical prediction falls. Despite the limitation in the models and the information provided by StarRotor, StarRotor technology represents the best option to explore. In this work, the models are assumed engineering judgments. Should the research in this chapter show favorable results, the next step would be to experimentally verify the StarRotor technology and create accurate models that account for the problematic issues discussed. Consistent with the theme of the other chapters in this dissertation, inspiration is taken from the nearest related industry the heating ventilation air-conditioning and refrigeration (HVAC-R) industry [203–207]. AHRI Standard 540 accounts for off design compression ratio operation at full-load and requires separate performance equations for each specific design and fluid.

The lack of perfect part-load pump and expander models should not dissuade the research from progressing, because the simulation results can provide insights into the operation and performance over a wide range of operating conditions. This has never been done in the literature at any scale. For example, the Ivanpah solar thermal power plant north of Ivanpah, California across the state line from Primm, Nevada. The plant has three generating units and is designed to have a total annual production

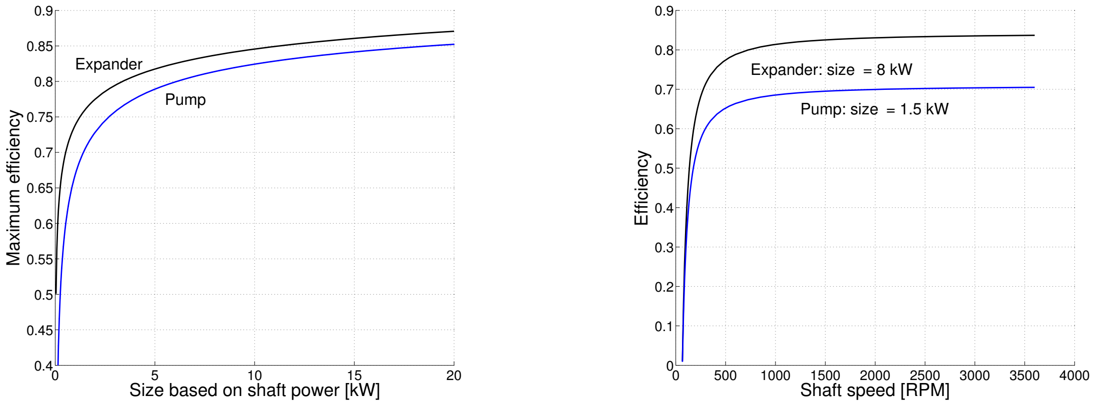

(a) Maximum efficiency vs. size.

(b) Efficiency vs. speed for a fixed size.

Figure 20.3: Pump and expander performance models.

of 940 GWh/year and it cost 2.2 billion dollars to build. Ivanpah has struggled with production problems since it was commissioned in 2014. These production problems are related in part to properly modeling and achieving part-load system performance. This highlights the importance of modeling part-load performance properly and in academia, the need to develop methods to do this properly. The design principles are the same in-depend of scale or technology.

20.2.2 Adapted heat engine models

The thermodynamic model is solved in a very similar way to the work in Chapter 14. The key difference is that the current model requires the mass flow rate to be taken into account. One must root find to determine the shaft speed of the pump. The shaft speed of the expander and the shaft speed of the pump are not necessarily the same. In this model, it is assumed that shaft energy can be transfered from expander to pump without loss. In practice this is not possible without direct shaft linkage. The second key difference is that the limitation of no being able to model off design performance requires the inlet and exit states of the expander be such that

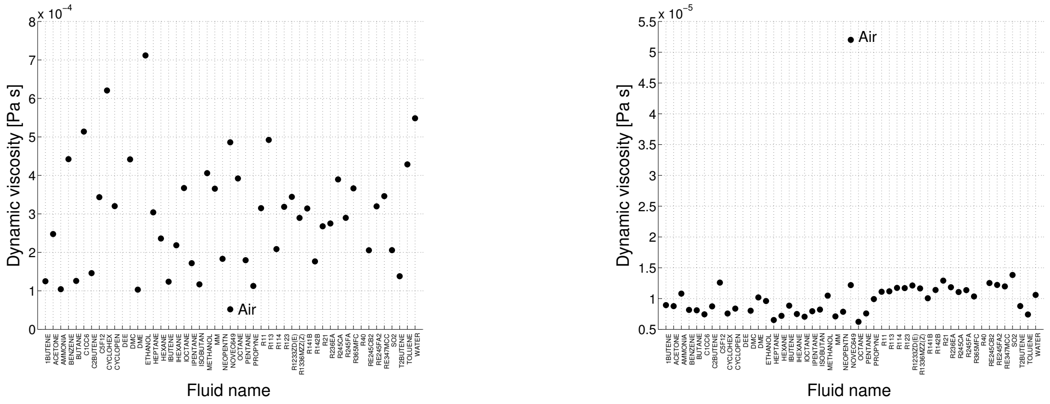

(a) Liquid.

(b) Gas.

Figure 20.4: Dynamic viscosity of 49 fluids compared to air.

the designed expansion ratio Υ is maintained. Both of these issues severely limit performance in practice. StarRotor has patented a variable expansion design; however, a prototype of the design has not been built or tested. This prevents modeling a variable expansion option. Appendix N contains the thermodynamic model code.

20.2.3 Optimization of operation variables

Of the 288 weather conditions defined in Chapter 19, optimization of the operating variables is carried out for each weather condition. The previous sentence is accompanied by one caveat, for a given location not all 288 operating conditions are represented; therefore, given a location, conditions with a zero bin count skip the optimization calculation for operating variables. This is done to increase computational efficiency. The optimization of operation variables for one weather condition is shown in Equation 20.1,

$$P_{shaft} = \max_{\boldsymbol{x}} f(\boldsymbol{x}, \boldsymbol{y}) \tag{20.1a}$$

subject to:

$$\boldsymbol{x} = [\boldsymbol{x_{lb}}, \boldsymbol{x_{ub}}] \tag{20.1b}$$

$$g_i(\boldsymbol{x}) \leq 0 \qquad i = 1, 2 \tag{20.1c}$$

where:

$$g_1(\boldsymbol{x}) = |P_4 - P_l| - 1 \tag{20.1d}$$

$$g_2(\boldsymbol{x}) = Q_{orc} - Q_{col} \tag{20.1e}$$

$$x_1 = [131, 3600] = \omega \tag{20.1f}$$

$$x_2 = [P_{lb}, P_{ub}] = P_1 \tag{20.1g}$$

$$x_3 = [S_{lb}, S_{ub}] = S_1 \tag{20.1h}$$

$$y_1 = V_{pump} \text{ (given)} \tag{20.1i}$$

$$y_2 = V_{expander} \text{ (given)} \tag{20.1j}$$

$$y_3 = \Upsilon \text{ (given)} \tag{20.1k}$$

$$P_{lb} = f_1(T = 260, Q = 1) \tag{20.1l}$$

$$P_{ub} = f_2(T = 675, S = f_1(T = 260, Q = 1)) \tag{20.1m}$$

$$S_{lb} = S_{right} - 0.5 * (S_{right} - S_{left}) \tag{20.1n}$$

$$S_{ub} = S_{right} + 3 * (S_{right} - S_{left}) \tag{20.1o}$$

$$S_{right} = f_1(T = 260, Q = 1) \tag{20.1p}$$

$$S_{left} = f_1(T = 260, Q = 0) \tag{20.1q}$$

where pressure is in Pa, temperature is in K, specific entropy is in J/(kg K), and power is in W. P_{shaft} is the shaft power output of the heat engine. The thermodynamic state properties are defined in Figure 20.1. P_l is the pressure at the exit of the expander which is calculated from expander performance. Because, $P_3 = P4$ and P_l may not match because of the choice of inlet expander state, this constraint forces the optimization algorithm to meet this physical requirement. Q_{orc} is the input heat required by the heat engine. Q_{col} is the heat produced by the collector. ω is the expander shaft speed given in RPM. V_{pump} is the inlet chamber volume of the pump given in m^3. $V_{expander}$ is the inlet chamber volume of the expander given in m^3. Υ is the expansion ratio. The bounds on P_1 and S_1 are chosen to allow the optimization great latitude in the choice of the inlet expander state, yet avoid, as much as possible, regions of the thermodynamic space were REFPROP will fail. The functions f_i denote using REFPROP to determine thermodynamic properties by giving two state properties from which all others can be calculated. The result of the optimization of operating conditions is to maximize the shaft power for each of the 288 weather conditions given a specific set of design variables. This is accomplished by finding the optimal expander shaft speed (therefore mass flow rate of the ORC heat engine) and the optimal expander inlet state in the T-s diagram for the thermodynamic cycle.

20.2.4 Optimization of design variables

For a given location, the optimization of the design variables is accomplished by aggregating the shaft power of the 288 individual weather conditions and the bin counts N. This method is shown in Equation 20.2,

$$E_{shaft} = \sum_{i=1}^{i=288} (P_{shaft})_i N_i \tag{20.2}$$

where E_{shaft} has units of Wh/year. This structure results in an outer optimization of design variables and optimization of operation variables (at most 288 times) at the inner level. The outer optimization is accomplished using a genetic algorithm with a population of 38. The optimization was completed on one node of Ada at the high performance computing research facility at Texas A&M University, which results in 19 cores for parallel processing. The optimization problem definition is shown in Equations 20.3,

$$E_{shaft} = \max_{\boldsymbol{y}} f(\boldsymbol{y}) \tag{20.3a}$$

subject to:

$$\boldsymbol{y} = [\boldsymbol{y_{lb}}, \boldsymbol{y_{ub}}] \tag{20.3b}$$

$$g_i(\boldsymbol{y}) \leq 0 \qquad i = 1, 2 \tag{20.3c}$$

where:

$$g_1(\boldsymbol{y}) = y_2 - 100 * y_1 \tag{20.3d}$$

$$g_2(\boldsymbol{y}) = y_1 - 10 * y_2 \tag{20.3e}$$

$$y_1 = [0, 1] = \qquad V_{pump} \tag{20.3f}$$

$$y_2 = [0, 10] = \qquad V_{expander} \tag{20.3g}$$

$$y_3 = [0, 40] = \qquad \Upsilon \tag{20.3h}$$

where constraint g_1 requires the inlet-chamber size of the expander $V_{expander}$ to be less than 100 times the inlet-chamber size of the pump V_{pump}, and constraint g_2 requires the inlet-chamber size of the pump V_{pump} to be less than 10 times the inlet-chamber size of the expander $V_{expander}$. While these are not physical constraints, conservation of the mass flow rate in both components must be matched by first calculating the mass flow rate of the expander and then the code attempts to determine the shaft speed of the pump. If the sizing is such that no shaft speed of the pump in the range of 131 - 3600 RPM can accomplish this the code will fail and return a not a number (NaN) value to the optimization algorithm. The constraints are meant to prevent calculating designs that are known to not work. During model testing it was determined that typical well functioning designs have a ratio $\frac{V_{expander}}{V_{pump}} \sim 10$. This simulation method is designed to work with any of the ten locations discussed in Chapter 11. The Merced, California location in the TMY3 dataset is selected, because it is the TMY location nearest the Roland Winston research group's testing facility where the XCPC designs were tested.

20.3 Results and discussion

The results and discussion are broken down into five parts:

1. Overall part-load simulation results
2. Part-load simulation results detail
3. Pump/expander shaft linkage issue
4. Electrical generation design issue
5. Flow conditions in the STC

20.3.1 Overall part-load simulation results

Figure 20.5 shows that the genetic algorithm moved toward convergence on a local optimal solution. This optimal solution is believed to be the global optimal solution for the given modeling methods. The optimal results are shown in Equation 20.4,

$$V^*_{pump} = 1.25\text{e}{-6}\ \text{m}^3 \tag{20.4a}$$

$$V^*_{expander} = 1\text{e}{-5}\ \text{m}^3 \tag{20.4b}$$

$$\Upsilon^* = 6.965 \tag{20.4c}$$

$$E^*_{shaft} = 31.72\ \text{MWh/year} \tag{20.4d}$$

where the $*$ denotes optimal results. At the optimum, the annual system efficiency η_{sys} is 7.85% based on G_{eff}. The net annual system efficiency is 6.85% based on G (plane of array irradiance (POAI)). Using the methods in Chapter 19 that assume fixed pump and expander efficiency resulted in annual system efficiency η_{sys} of 8.88% based on G_{eff} and net annual system efficiency of 7.75% based on G (plane of array irradiance (POAI)). This shows that the addition of practical requirements of mass flow rates, part-load performance of the pump and expander, and fixed expansion ratio result in lower performance. The optimum design for many locations in the TMY datasets should be similar to the optimum found for Merced, California, although it is left as future work to optimize designs for more locations and test the sensitivity the optimal result with location.

20.3.2 Part-load simulation results detail

Figure 20.6 shows the solar resource and ambient temperature conditions for Merced, California. Figures 20.7 - 20.12 show both the simple simulation results of Chapter 19 and the optimal part-load simulation results of this chapter for each heat engine characteristic of interest. The expansion ratio is not shown as the part-load simulation of this chapter fixes the expansion ratio $\Upsilon = 6.965$. The single largest change is that the part-load heat engine is not able to operate at all the solar conditions. This is due to having a fixed size and part-load efficiency. It is also due in part to having a fixed expansion ratio. However, note the modest reduction in overall efficiency.

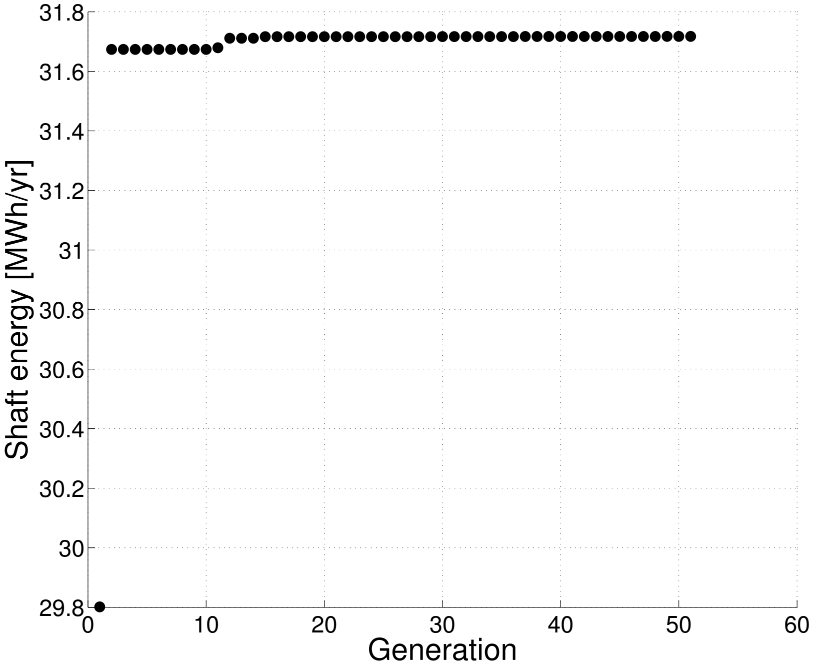

Figure 20.5: Convergence of the genetic optimization.

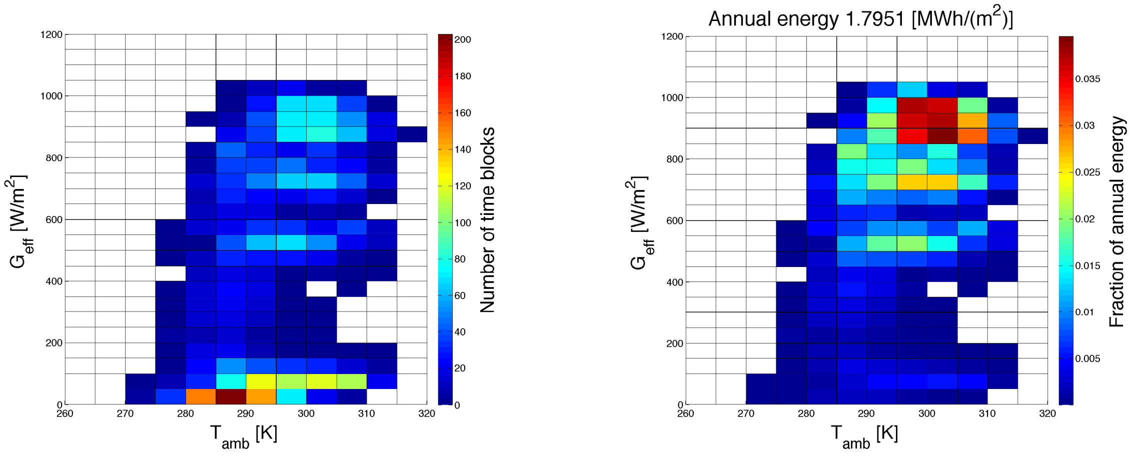

(a) Bivariate histogram.

(b) Linearly normalized bivariate histogram.

Figure 20.6: Key meteorological parameters for Merced, CA (TMY3). Annual energy based on G_{eff} for the N–S XCPC.

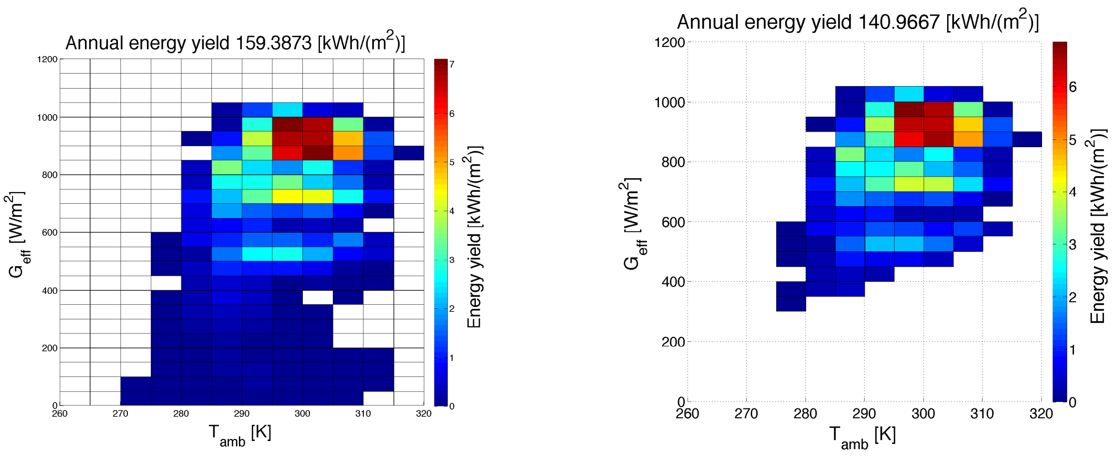

(a) Simple simulation.

(b) Part-load simulation.

Figure 20.7: Shaft Energy E_{shaft} per unit area using the N–S XCPC and ammonia at Merced, California.

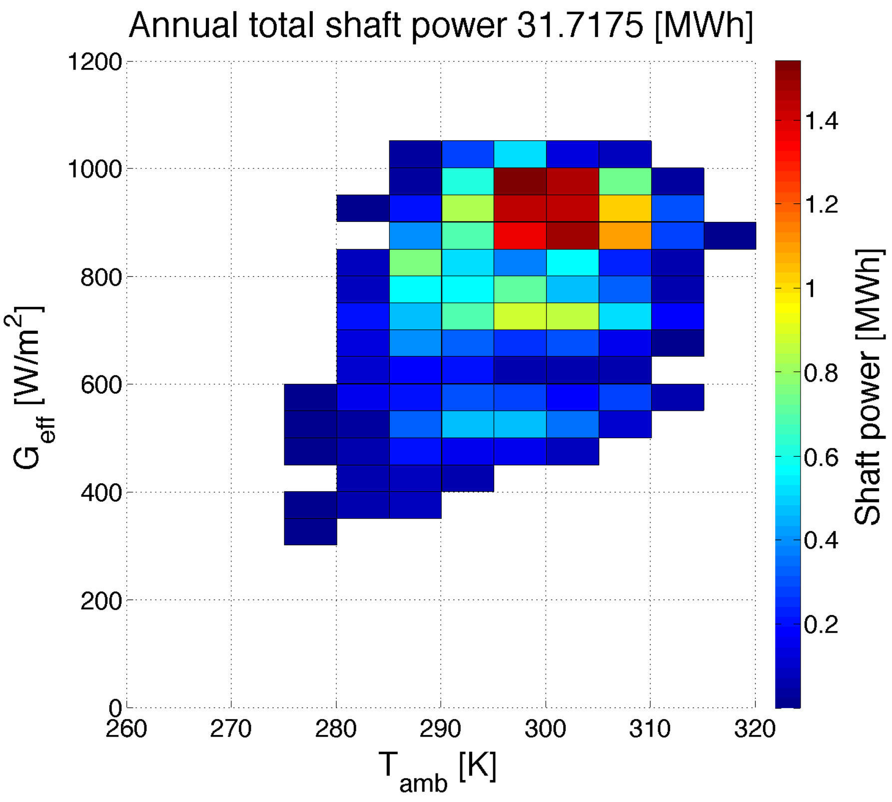

Figure 20.8: Part-load simulation: shaft energy E_{shaft} using the N–S XCPC and ammonia at Merced, California.

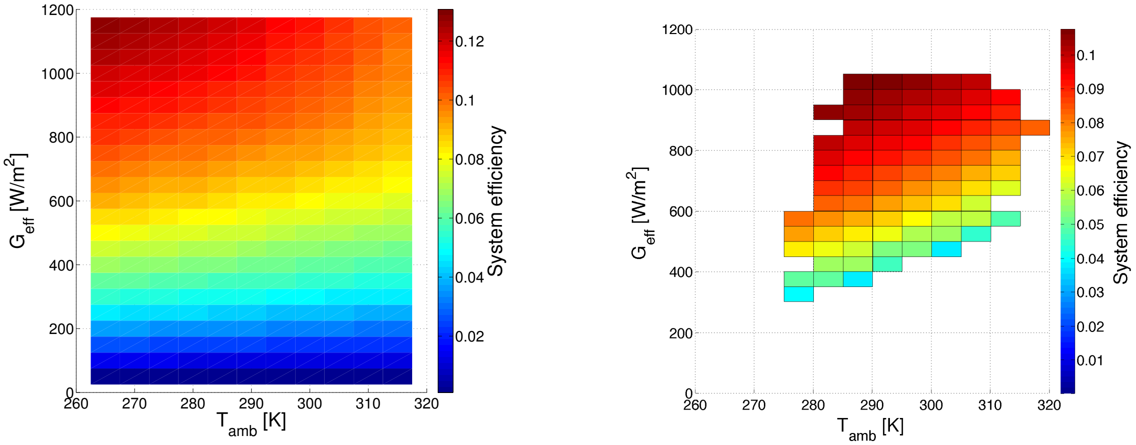

(a) Simple simulation.

(b) Part-load simulation.

Figure 20.9: System efficiency based on G_{eff} and ammonia at Merced, California.

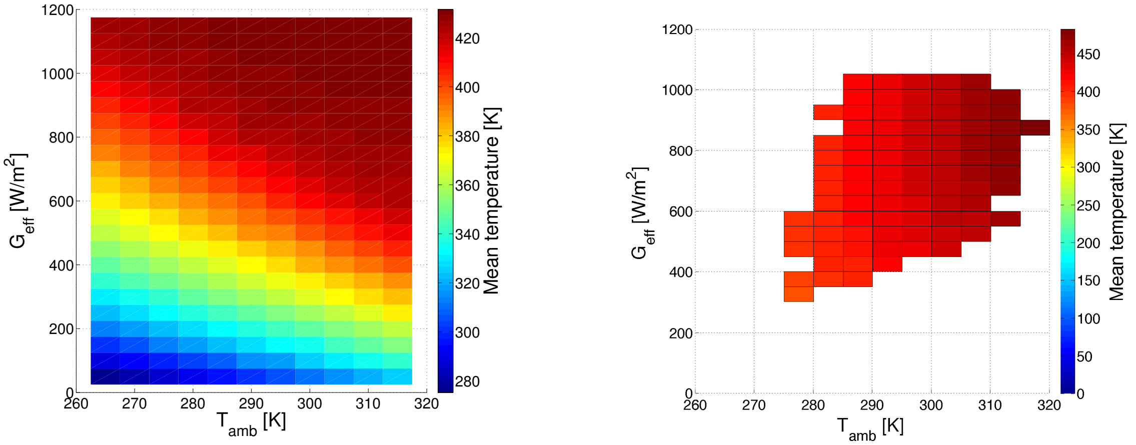

(a) Simple simulation.

(b) Part-load simulation.

Figure 20.10: Mean temperature based on G_{eff} and ammonia at Merced, California.

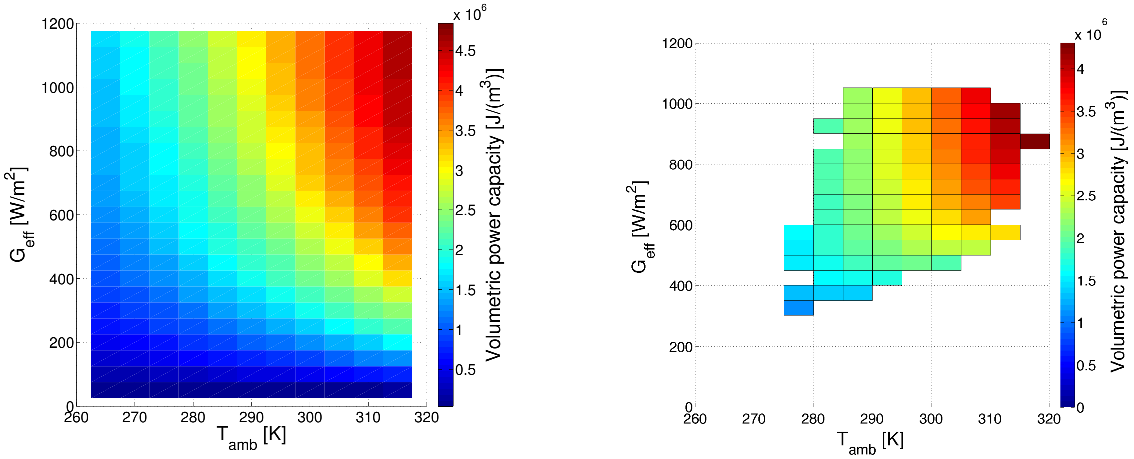

(a) Simple simulation.

(b) Part-load simulation.

Figure 20.11: Volumetric power capacity ratio based on G_{eff} and ammonia at Merced, California.

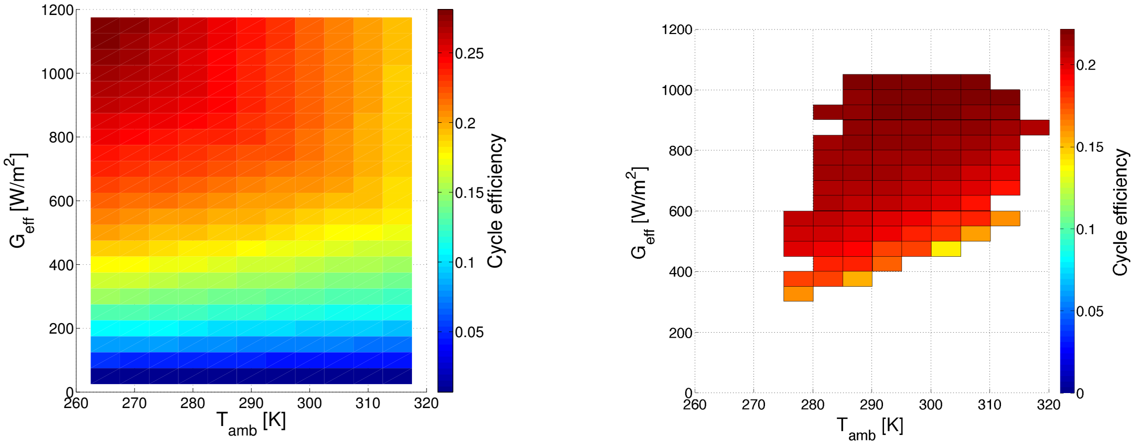

(a) Simple simulation.

(b) Part-load simulation.

Figure 20.12: Cycle efficiency based on G_{eff} and ammonia at Merced, California.

20.3.3 Pump/expander shaft linkage issue

As pointed out in the methodology section, the pump and expander do not necessarily have the same shaft speed. Figure 20.13 shows the shaft speeds of both components. Figure 20.14 shows the speed ratio of the two shafts. This problem represents a critical issue in the design of the heat engine that is left as future work. During the progress of completing this research, several options were briefly explored to resolve this issue. Including a continuously variable transmission (CVT) and/or a gear box results in additional losses in a system that is roughly only 6%–9% efficient (Figure 20.15). A CVT was identified in the correct size scale and is commonly used in ATV and golf cart vehicles. Nuvinci Technologies by Fallbrook Technologies makes the CVT. After contacting the company for further information found that the CVT is geometrically limited in the relative speed ratio of the two shafts by a factor of two. The variance of shafts speeds may limit what conditions it can operate at. A designer would have to accept the discrete gear ratios of a traditional gearbox and those losses are much greater for smaller transmissions than what are found in the automotive industry. The alternative is to accept losses from both technologies and have both a CVT and a traditional gearbox. A third option exists, which is to drive the pump using a separate electric motor/drive system and harvest shaft energy from the expander using a separate drive system (Figure 20.16). This also has problems with additional equipment and additional losses. Exploring solutions to these problems are left as future work.

20.3.4 Electrical generation design issue

Continuing the electrical discussion, many power applications have different shaft load profiles. For example, wind generation requires power produced reduces and stalls for high winds (high shaft speed). Power is not proportional with shaft speed

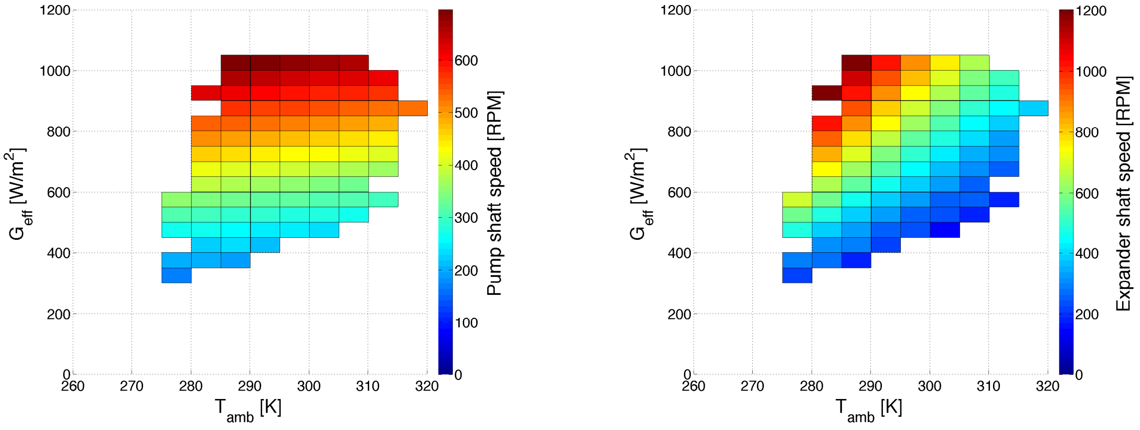

(a) Pump.

(b) Expander.

Figure 20.13: Shaft speed of the pump and expander over the operating conditions.

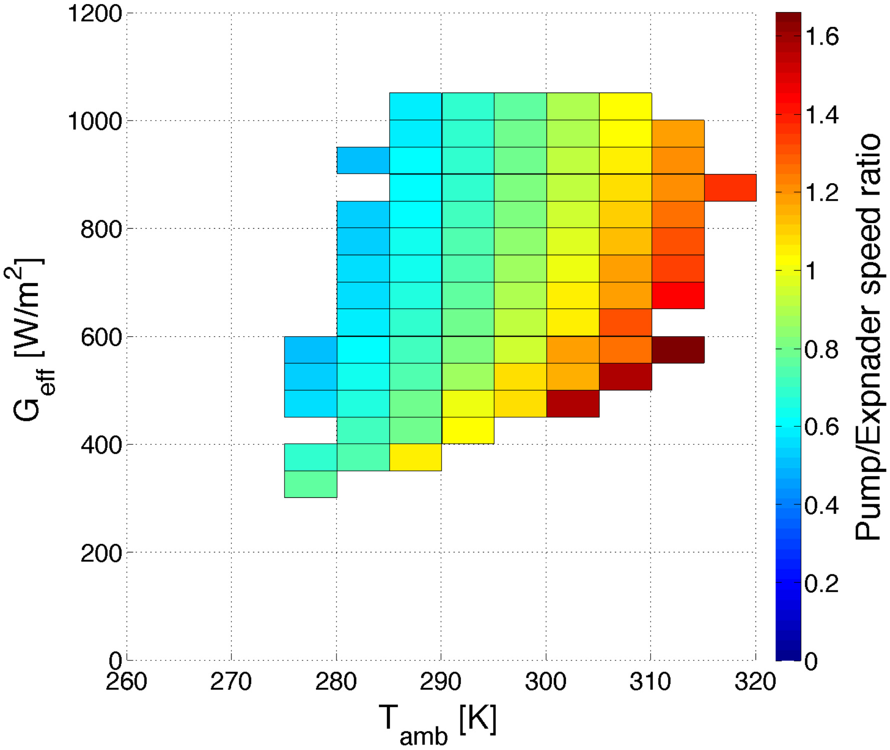

Figure 20.14: Speed ratio of pump to expander.

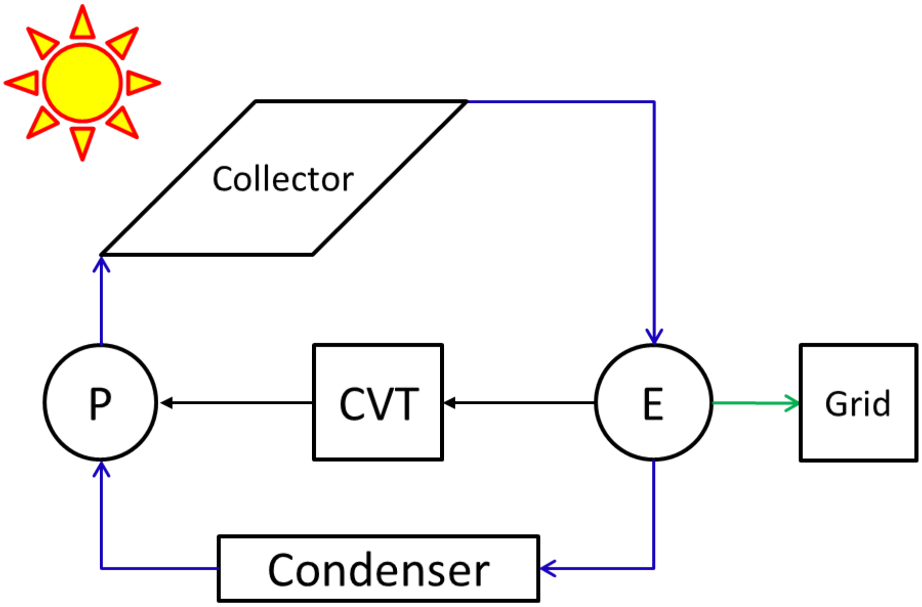

Figure 20.15: diagram of a direct configuration with CVT.

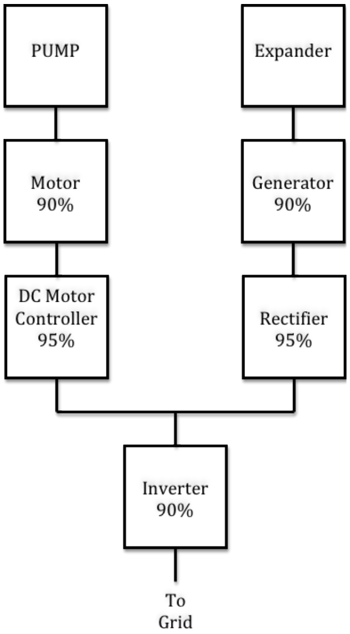

Figure 20.16: Electrical drive models with size appropreate performance assumptions.

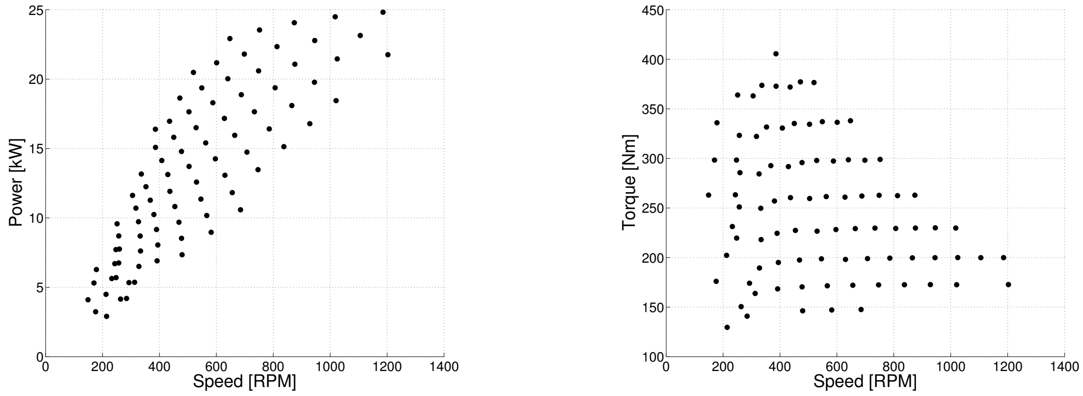

(a) Power vs. speed.

(b) Torque vs. speed.

Figure 20.17: Expander shaft: power, torque, and speed relationship.

over a wide range. Power generation in emergency vehicles requires maximum power at idle speeds while the vehicle is parked and low power production while at higher speeds corresponding to times when the vehicle is moving and there are no to little power power loads for emergency work. Raven Technologies makes such a product (http://raventechpower.com). AC synchronous power generation operates at a set shaft speed which is synchronized to the grid and is typically a fixed multiple of 60 Hz (in the USA). The ratio is fixed by the generator windings and the designed shaft speed of the generator. For AC synchronous generators, the torque on the shaft is varied to vary the power output while keeping a fixed shaft speed. Figure 20.17 shows that the part-load simulation results in a mixed case where both shaft speed and torque are varied.

20.3.5 Flow conditions in the STC

One of the simulation and model engineering judgments is to use the thermal performance equation of the STC determined using a heat transfer oil with alternate working fluids and flow conditions. In the models, the STC is used to heat a fluid from the liquid state, vaporize it under two-phase flow conditions, and finally superheat the fluid. These conditions are outside the scope of the testing that was performed to quantify the thermal performance. Using the simulation results of this chapter that include mass flow rate $\dot{m}$, allows for the evaluation of the engineering judgment.

To begin, and analysis of the flow conditions during performance testing is completed. Given variability of the dynamic viscosity μ, the hydraulic diameter D_h, and the cross-sectional area A, the Re number is bound, as shown in equation 20.5,

$$Re_d = \frac{\dot{m} D_h}{\mu A} \tag{20.5a}$$

$$0.56 \leq \mu \leq 71.57 \text{ cP at } 295^\circ\text{C and } 25\ ^\circ\text{C} \tag{20.5b}$$

where $\dot{m} = 0.08$ kg/s, D_h, and A vary between the inner tube and the outer annulus of the STC as shown in Figure 5 of Kim et al. 2013 [132]. See also Appendix N for additional details. Kim et al. 2013 Table 1 noted that the hydraulic diameter of the collector is $D_h = 3.5$ mm. Here, it is determined that there are two hydraulic diameters $D_h = 6$ mm and $D_h = 2.5$ mm for the inner tube and outer annulus respectively. It is not clear from Kim et al. 2013 or Balkoski 2011 [208] how the value of 3.5 was determined. The fluid property data for Duratherm 600 was obtained directly from https://durathermfluids.com. Figure 20.18 shows the results for the inner tube and outer annulus. Figure 20.18(a) shows that for many of the operating temperatures the collector is designed for, the flow is turbulent even though the heat transfer analysis performed by Balkoski 2011 assumed laminar flow. It is widely known in the turbulence field that once a flow trips turbulent it is difficult to return the flow to laminar conditions. Even though Figure 20.18(b) shows a much higher operating temperature before the flow trips turbulent, it is unlikely to be laminar, because the annular section is after the inner tube in the flow path. This is especially

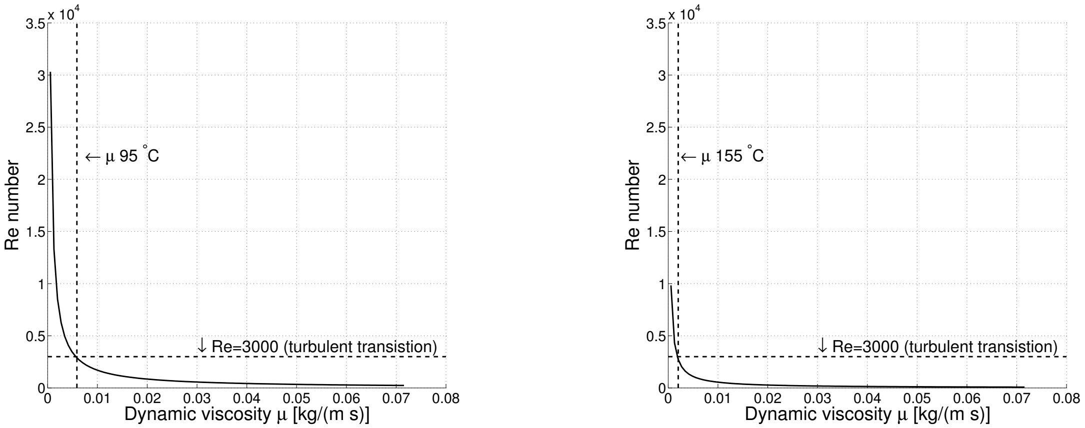

(a) Inner tube.

(b) Outer annulus.

Figure 20.18: Reynolds number of the flow using Duratherm 600.

true when considering the welds and piping to connect the inner tube to the outer annulus.

Figure 49 in Balkoski 2011 [208] shows that the temperature profile of the pipe surfaces are not constant. Figure 49 also shows that the heat flux is not uniform, because the temperature profile has curvature. If laminar flow is assumed, the Nusselt number should be between 3.66 and 4.36 for uniform temperature and uniform heat flux respectively, as shown in Equations 20.6,

$$
\begin{aligned}
Nu =& \frac{\bar{h}L}{k} && \text{(20.6a)}\\
\bar{h} =& \frac{kNu}{2L} \text{ W/(m}^2\text{ K)} && \text{(20.6b)}\\
3.66 \leq & Nu \leq 4.36 && \text{(20.6c)}\\
0.125 \leq & k \leq 0.140 \text{ W/(m K) at } 295^\circ\text{C and } 25\ ^\circ\text{C} && \text{(20.6d)}
\end{aligned}
$$

where Nu is the Nusselt number, k is the thermal conductivity, L is the length of the absorber tube, and h is the heat transfer coefficient. See also Appendix N for addi-

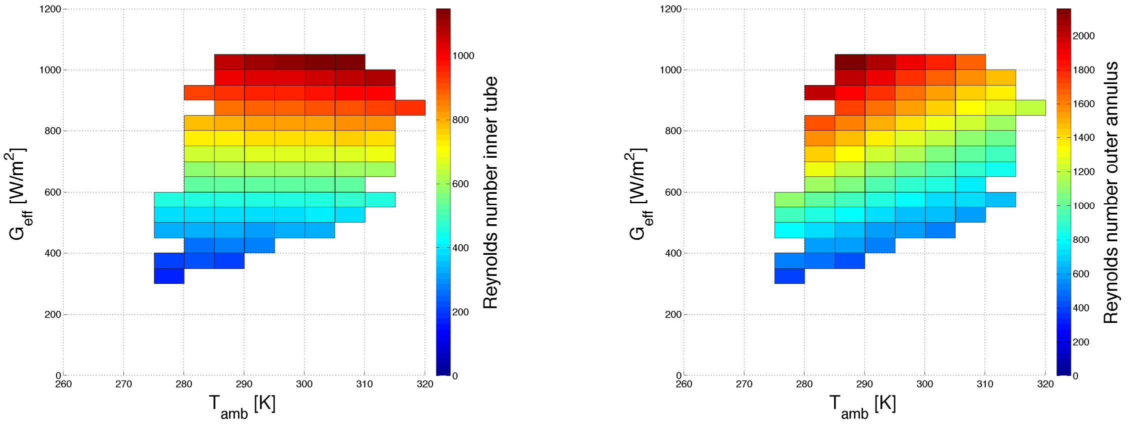

(a) STC inner tube.

(b) STC outer annulus.

Figure 20.19: Reynolods number Re for the operating conditions from the part-load simulation with ammonia as the working fluid.

tional details. Sampling in the ranges of Nu and k result in a minimum/maximum heat transfer coefficient $\bar{h}$ of 0.1395/0.1861 W/(m^2 K) respectively.

Performing a similar analysis on the simulation results using ammonia as the working fluid, Figure 20.19 shows that the flow is laminar for all conditions for both hydraulic diameters. In heat transfer it is common knowledge that turbulent flow promotes mixing; therefore, turbulent flow promotes heat transfer. While the laminar result, means that the theory applied by Balkoski 2011 is more fitting, it does not mean the resulting STC thermal performance equation is applicable to the ammonia case. A deeper look into the heat transfer coefficient is required.

The simulation results with ammonia can be divided into two categories: 1) $P_H > P_c$, and 2) $P_H < P_c$. The first category is a supercritical, cycle and the second category is a subcritical cycle. The first category does not have two-phase flow heat transfer or a clear division between liquid heating and vapor heating. The second category has clear boundaries between liquid heating, two-phase flow heating, and vapor heating. Because of the differences in the two categories, two distinct analyses will be completed.

First bounding the heat transfer coefficient for the supercritical category is completed by determining the enthalpy weighted average thermal conductivity along the constant pressure line from STC inlet to outlet. A greater accuracy is achieved, by determining the average conductivity using enthalpy weighting. Figure 20.20 shows density and thermal conductivity along a supercritical constant pressure line. Figure 20.21 shows the enthalpy weighted average thermal conductivity based on weather conditions. For supercritical cycles found in operating conditions, in a minimum/maximum heat transfer coefficient $\bar{h}$ of 0.1922/0.2752 $W/(m^2\ K)$ respectively. This bounding range is notably higher than the range previously found using the test conditions and Duratherm 600 as the working fluid. The conclusion is clear, supercritical cycles with ammonia have higher estimated heat transfer coefficients than liquid heating with Duratherm 600. Higher heat transfer coefficients result in lower temperature differences between the fluid and the absorber heat transfer fin, and higher thermal efficiency. For supercritical cycles with ammonia, using the thermal performance model equation unchanged results in a slight under estimate as the conductivity of the absorber fin and tubing walls are unchanged.

Second, bounding the heat transfer coefficient for the subcritical cycle category is completed by determining the ratio of heat transferred in the vapor phase to the heat transferred in the two-phase flow (Figure 20.22). Using liquid heat transfer as a base, a rule of thumb for: 1) vapor phase heat transfer is a factor of five lower heat transfer coefficient, and 2) two-phase flow heat transfer is a factor of five greater heat transfer coefficient. Reviewing the ratio of vapor phase heating to two-phase flow heating will indicate if the over all heat transfer coefficient is raised or lowered compared to the liquid heating phase. The results of this analysis determined only three operating conditions that have a ratio below 1. For the weather conditions using

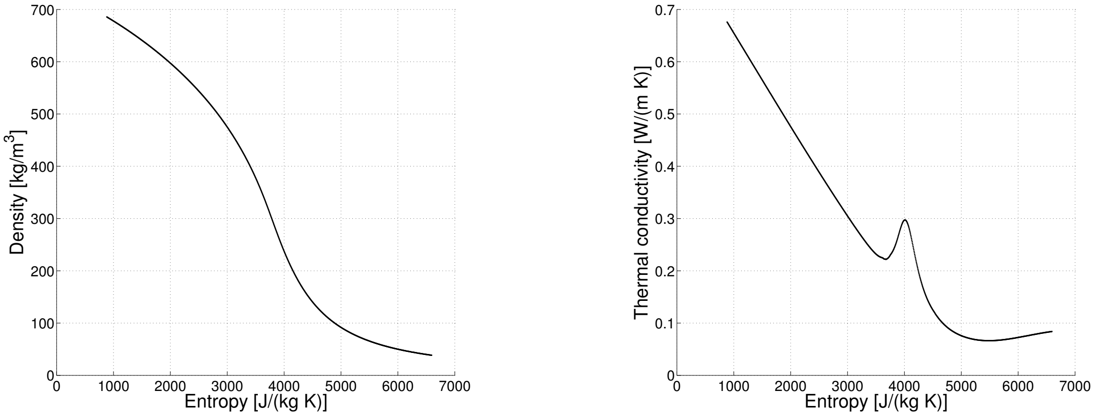

(a) Density.

(b) Thermal conductivity.

Figure 20.20: Properties along a supercritical constant pressure line for ammonia.

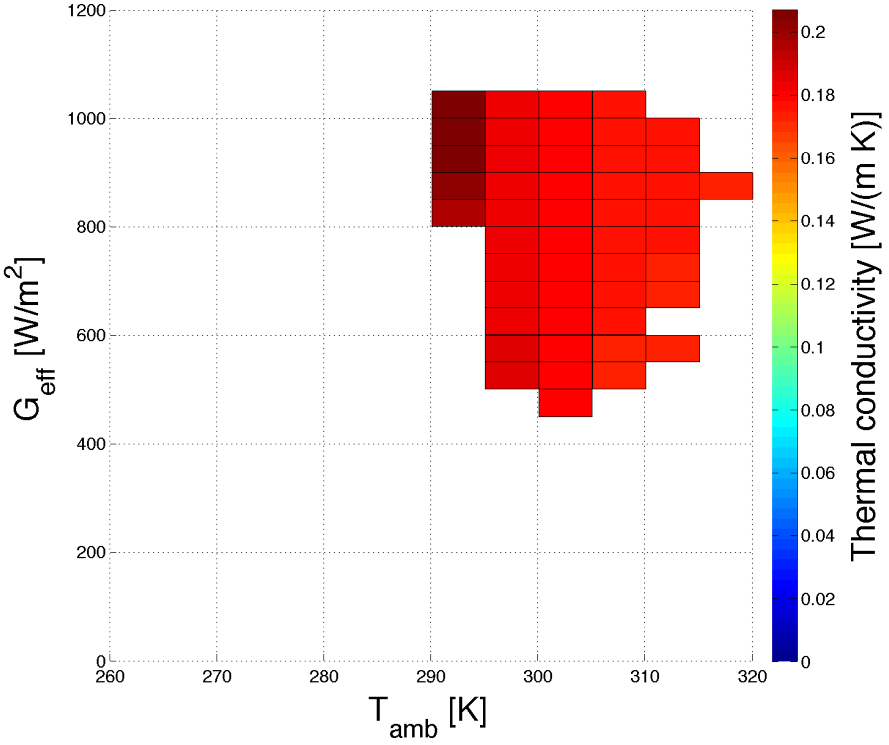

Figure 20.21: Enthalpy weighted average thermal conductivity. Results use ammonia as the working fluid.

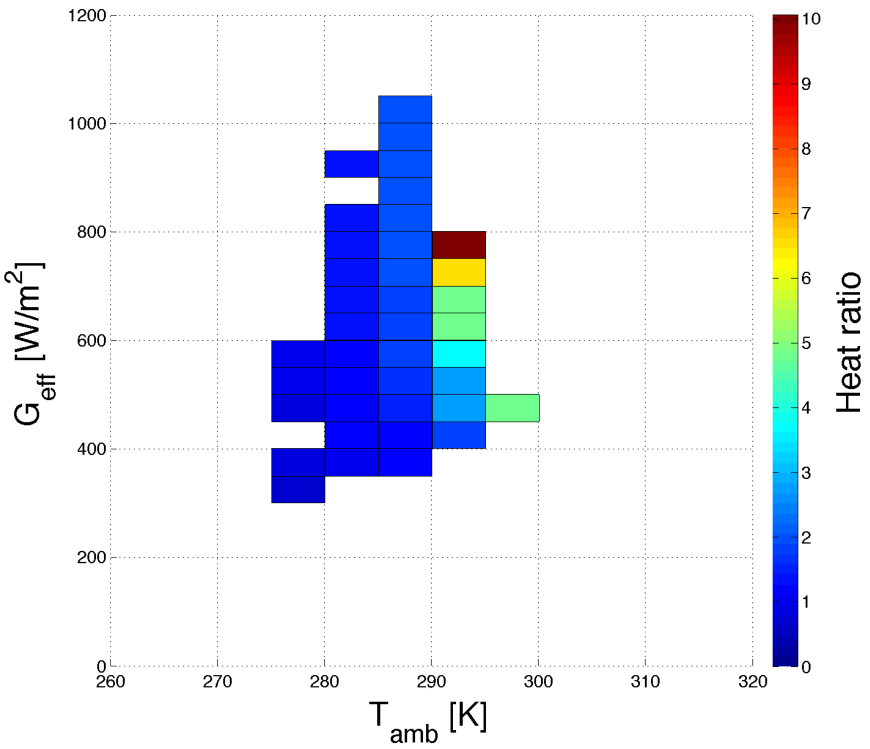

Figure 20.22: Vapor to two-phase heat ratio for subcritical cycles using ammonia.

a subcritical cycle, the net result is a lower heat transfer coefficient. This results in higher absorber surface temperatures which lead to lower collector thermal efficiency than is modeled. Because the convective heat transfer coefficient for the working fluid does not directly correlate to over all thermal efficiency, it is not possible to make any strong conclusions about the magnitude of the over or under prediction. Comparing Figures 20.8, 20.21, and 20.22 reveals that the weather conditions that correlate to subcritical cycles and lower than predicted efficiency are a smaller share of the annual energy than the weather conditions that correlate to supercritical cycles and higher than predicted efficiency. A reasonable engineering judgment is to conclude that there is a higher probability that the net annual energy yield is under predicted.

20.4 Conclusions and summary

The clearest and most powerful conclusion is that more research into part-load performance of the components of the system is needed. While this chapter is the most in depth system modeling ever completed for DSSTC in the public domain, it falls short of the originally desired accuracy because of limited performance information on the components. Despite these limitations, several design challenges have been identified: 1) The need to explore the benefit of adjustable expansion, 2) the need to address the pump/expander shaft linkage issue, 3) the need to create a collector thermal model that properly accounts for the operating conditions. Accounting for machine size, part-load, and component interfacing clearly results in lowered performance compared to Chapter 19. An in depth analysis of flow conditions in the STC shows that more research is required to achieve high accuracy modeling of thermal performance under a wide range of operating conditions and working fluids. The simulation methods employed and the results are the original contributions of this author.

20.5 Future work

During the research preparing this chapter, several future works were identified:

- Determine (experimentally and theoretically) heat transfer modeling to converge on a realistic model for collector thermal performance.
- Account for the effects of collector mounting angle in the heat transfer model.
- Redesign the absorber of the XCPC for accommodate two phase flow conditions.
- Create an exapnder performance testing standard.

- Investigate solutions to include variable expansion.
- Determine StarRotor expander performance including variable pressure and off design expansion ratio.
- Determine StarRotor pump performance for a wide range of operating conditions and working fluids.
- Explore electrical and mechanical solutions to the pump/expander shaft linkage issue.
- Identify electrical generation technologies to efficiently convert shaft energy to electrical energy for this application.
- Create a condenser model based on experimental results for a wide range of operating conditions and fluids.

PART VI. COMPARISON OF DSSTC TO PHOTOVOLTAIC SYSTEMS AND ROAD MAP

21. IN SUMMARY: A COMPARISON OF DSSTC TO PV

21.1 Introduction/background

The goal of the dissertation was to increase the depth and breadth in modeling solar thermal collector performance (STC). The work focused primarily on the performance prediction of combining an organic Rankine cycle heat engine (ORC) with STC in a direct configuration for electricity production (Figure 21.1). One key aspect of the work was to make size appropriate efficiency assumptions and to model part-load performance while simulating the system model on realistic weather data. These goals were achieved with mixed results. The direct system offers the simplest design and the potential for the highest electricity efficiency. This is true for standard peak solar conditions of 1000 W/m^2 irradiance and 300 K ambient temperature. Chapter 19 results show that assuming changing equipment size at each operating condition (fixed pump efficiency, fixed expander efficiency, and part-load performance for the STC) resulted in reduced performance from the standard peak solar conditions. Chapter 20 showed that the wide range in operating conditions found in the TMY datasets resulted in low electricity efficiency performance from the equipment when considering part-load performance of the STC, pump, and expander. The indirect system with thermal storage may have higher annual performance when simulating a STC + ORC model under part-load performance. Had the results been more favorable, this would have provided a new market for the XCPC designs. Throughout the research process many aspects of DSSTC performance modeling were advanced. Most of these contributions can be applied to the respective fields of study independent of the larger research outcome. Because the direct configuration at standard conditions offers the best efficiency and the lowest equipment costs, it can be compared to PV as a good benchmark. If PV is shown to perform better, then there is reduced expectation that the direct configuration can compete, because it will have both a cost and performance challenge to overcome. If the DSSTC system compares favorably over PV then there may be hope that a method will be found to increase performance under part-load conditions. To this end, a comparison of photovoltaic collector (PVC) and XCPC costs is undertaken. The goal of both PV and DSSTC is to be able to out compete the other in both electricity generation and thermal generation. When this is achieved, one set of collectors can be used to meet both electrical and thermal loads. When accounting for solar variability, electrical demand variability, and thermal demand variability thoughout the a typical year, there is greater freedom to balance production and demand with one set of collectors [34]. This characteristic provides additional economic value.

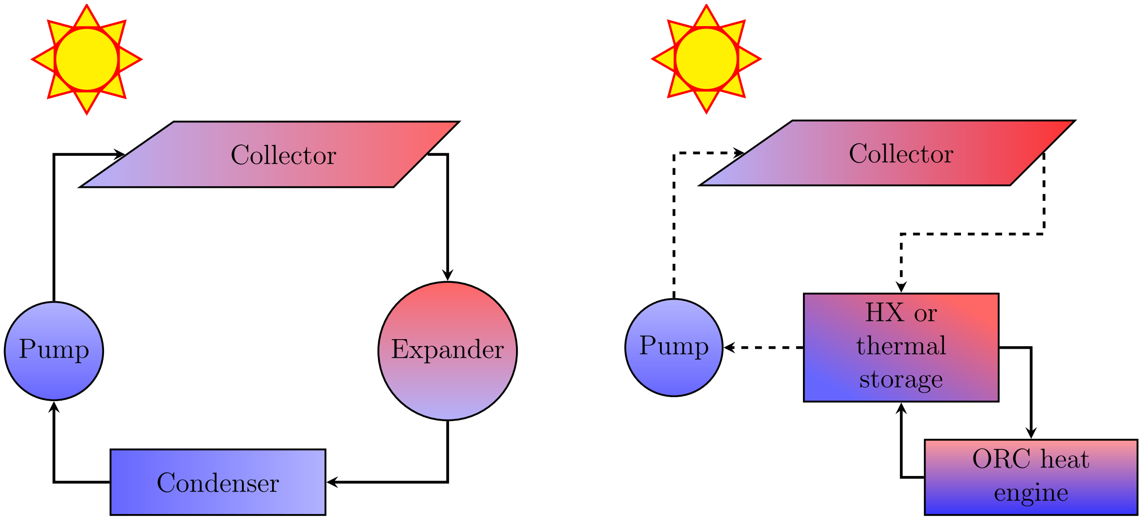

(a) Direct system.

(b) Indirect system.

Figure 21.1: Two canonical solar-thermal system configurations.

Table 21.1: Cost and production infromation for the Artic Solar XCPC

Year	Cost [\$/unit]	Cost† [\$/ft^2]	Production‡
2015	820–1200	31.64–46.30	0
2018	700–900	27.01–34.72	50

†Based on aperture area
‡January of the year

21.1.1 DSSTC data for direct configuration

At ideal conditions, Chapter 14 found that the direct configuration for DSSTC has second law efficiency of about 70% using water as the working fluid $(0.7 = 0.27/(1 - \frac{310}{500})$ at ideal conditions $T_{amb} = 300$ K and $G_{eff} = 1000$ W/m^2). Table 21.1 shows cost and production data provided by William Guiney CEO of Arctic solar [146,209]. Cost of the collector to an installer is the price the manufacturer has set and includes a profit margin for the manufacturer above the manufacturer's cost to make the collector. All values presented in this chapter are costs from the installers point of view. This is the cost to the installer to buy collectors on the whole sale market and does not include freight. The STC design has an aperture area of 25.92 ft^2 and a gross area of 29.05 ft^2. The design marketed by Arctic Solar is different than the design outlined in Kim 2013 [132] and modeled in this work. The Arctic Solar version maybe more efficient as it currently has an absorber tube design several generations more advanced. Arctic solar estimates a ballpark figure of \$1.50/W installed cost for the collectors depending on operating temperature and project conditions. There are currently orders for 1,000 units in the project pipeline. The Arctic Solar market is to supply industrial thermal energy loads, domestic and commercial hot water, space heating using heat pumps, and cooling using double effect absorption chillers. Double effect absorption chillers have a coefficient of performance (COP) of 1.4.

There is strong evidence that the solar heat for industrial processes (SHIP) industry is growing (https://www.solar-payback.com). Solar Payback is a three year initative to promote SHIP in four countries (South Africa, India, Mexico, and Brazil). To guesstimate market potential, a review of thermal uses in the United States is undertaken. Fox et al. 2011 [210], estimates the break down of US thermal energy use in the temperature range 0–260 °C. Using Fox et al. numbers for 2008 in the US about 8% of the total energy consumption is used thermally in the range of 100–260 °C across the residential, commercial, and industrial energy sectors. From the results of Chapter 11, one can approximate STC efficiency at 35% in this tempreature range. One can argue that this assumption is too low or high; however, this choice will illistrate the magnetude of the industry market potential. It is assumed that the XCPC design will only capture about 25% of the market. Using this information, the size of the US XCPC collector market can be estimated with data for annual energy consumption in the United States [211]. The resulting calculation is shown in Equation 21.1,

$$\text{370e6 collector} = \left[\frac{(0.25)(0.08)(97.399\frac{\text{Quad}}{\text{year}})(1.055\frac{\text{EJ}}{\text{Quad}})(2.778\text{e}11\frac{\text{kWh}}{\text{EJ}})}{(5\frac{\text{kWh}}{\text{m}^2\cdot\text{day}})(365\frac{\text{day}}{\text{year}})(0.35)(2.41\frac{\text{m}^2}{\text{collector}})}\right] \tag{21.1a}$$

21.1.2 PV data

To enable a comparison of PV and STC, PV data is gathered and presented in Table 21.2. In the last few years, domestic hot water heater manufacturers have brought heat pump based hot water heaters to market. Rather than using traditional electrical resistance heating elements that have a maximum efficiency of 1, the most efficient air sourced hot water heat pumps have a COP of 3. This means that for one unit of electricity the homeowner can receive 3 units of heat. This benefit is moderated by the additional cost of the unit and the potential for more expensive

Table 21.2: Costs and peak module efficiency for residential PV

Year[#]	Panel cost [$/$W_{dc}$][§]	System installed cost [$/$W_{dc}$][†]	Efficiency [%][‡]
2015	0.70	3.18	15.1
2016	0.64	2.98	15.6
2017	0.35	2.80	16.2

Report year, reported data typically from the prior year
§2015 report data from Figure 4 [212]
§2016 report data from Figure 13 [213]
§2017 report data from Figure 15 [214]
†In 2017 USD, from Figure 17 of [214]
‡Data from Figure 3 [214]

maintenance. These models are even available in common home improvement stores.

21.2 Methodology

To project XCPC manufacturing costs into the future, the data from Table 21.1 is used in a learning curve with learning rates of 5%, 10%, 15%, and 20%. Figure 21.2 shows that the STC system is similar to the PV system. The STC system has additional components, namely the heat engine components. Because the inverters are highly likely to be identical or have extremely similar costs, the STC must be less expensive than the PVC to compete in power production. The amount the STC is lower in cost than the PVC can be used to pay for the heat engine components. The goal is to compare current costs and performance of the two methods of producing electricity and evaluate *crossover* potential for DSSTC systems. Crossover is the ablity of a technology to meet both thermal and electrical demand. The future potential depends on the learning curve projections which can only be viewed as tentative estimates.

A second analysis is performed to evaluate the reverse question. What is the crossover potential of PV to compete in supplying thermal loads such as domestic hot water or heat pumps. To do this, the cost of PV is discounted by the COP of the

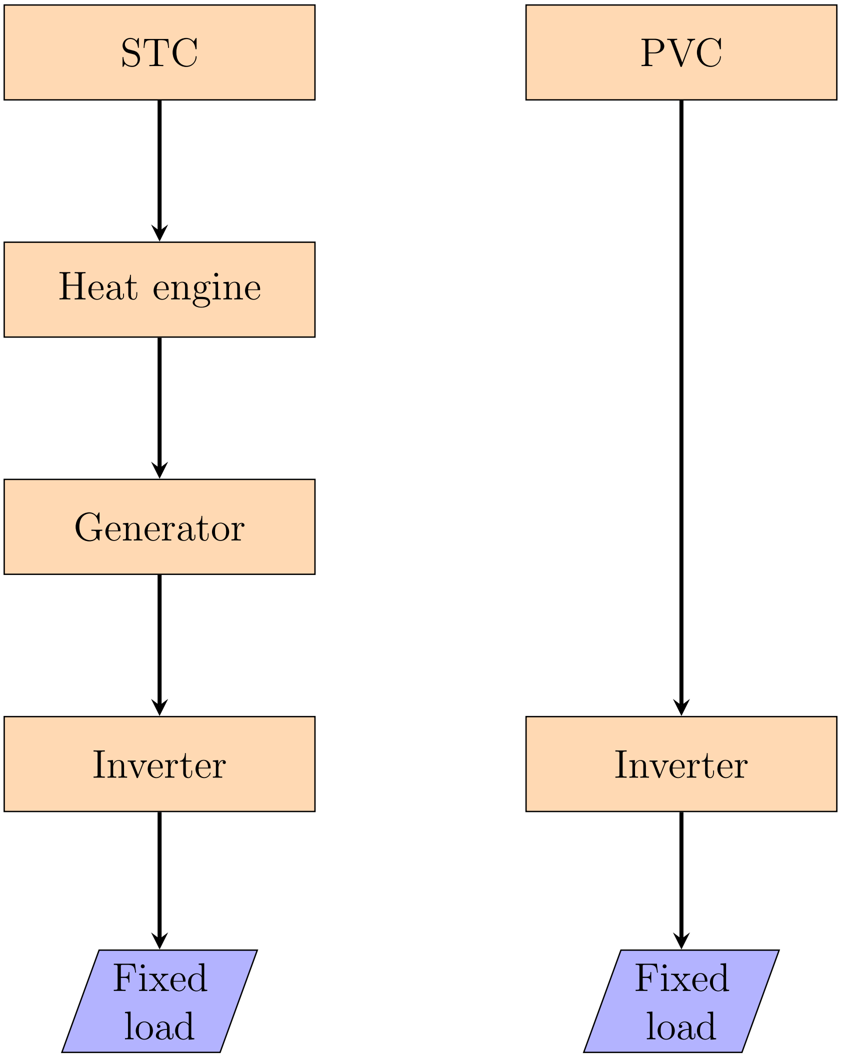

Figure 21.2: Box diagrams of DSSTC and PV systems.

heat process. In both analysis the system installed costs are neglected. This means that the results are for comparative purposes only as the collector costs are the only element of total system cost being compared. Installation costs for the remaining system components are neglected. Comparing the ability of DSSTC systems to compete is carried out for three cases: 1) 2015 data, 2) 2017 data for PV, 2018 data for the XCPC, and 3) 2017 data for PV, projected future cost data for the XCPC. The ability of PV systems to compete is carried out for the last case only: 2017 data for PV, projected future cost data for the XCPC.

21.3 Results and discussion

The first step is to project future XCPC cost using a learning curve (Figure 21.3). The results show that the large market potential provides a sizable opportunity for the XCPC cost to come down. Future cost from the learning curve, shows a range of values are possible from 100–400 \$/unit. The comparison results are presented in two parts: 1) comparison of collector costs for electricity production and 2) comparison of collector costs for thermal production. Appendix O contains the code used to perform the calculations and create the figures.

21.3.1 Comparison of collector costs for electricity production

Figure 21.4 shows that the XCPC collector was initially too expensive for a DSSTC system to out compete a PV system for electricity production. Figure 21.5 shows that the XCPC collector as part of a DSSTC will have only a small probability of being able to out compete PV for electricity generation. This is especially true when considering that PVC cost is not projected into the future. The limitation of this is lessened by the fact that PVC costs have dropped from \$7/W in 2006 to \$0.35/W in 2016. Figure 21.6 shows a sensitivity analysis for collector thermal performance using a future collector cost of \$250/unit. The results show that ±10%

changes in XCPC thermal performance do not materially change the conclusion that the XCPC design will most likely have trouble competing with PV in a electricity only application. From the analysis presented here, the limitations of DSSTC to compete against PV for electricity only production are a result of several conditions: 1) the low cost of PV panels on the whole sale market, 2) the efficiency of PV versus DSSTC to produce electricity (Carnot's law limitations of DSSTC), and 3) STC thermal losses as a function of temperature and irradiance.

The result that DSSTC has a low probability of competing with PV for electricity production does not mean that PV is always the best choice. For example, take an industrial manufacturer wants to do their part to help the environment by installing renewable energy production equipment to meet a large portion of their energy demand. The company is located in an area that has a colder more overcast weather pattern during the winter months which also matches the peak thermal loads and minimum electrical loads. The summer holds the opposite relationship. Having two sets of collectors to meet both electrical and thermal loads would mean both sets would have to be oversized to meet peak demand. This results in both sets of collectors being idle for part of the year which increases the levelized cost of energy (LCOE) and the payback period. The alternative is to undersize the systems and subsidize with energy from the natural gas and electricity grids. This lowers the size of the systems and reduces project cost effectiveness because of fixed project costs (e.g., permitting). Another alternative is to use a ORC heat engine to make electricity in the summer when thermal loads are low and electricity loads are high. The DSSTC system may not be cost effective in producing electricity, the additional cost of the ORC may be much less than the cost of the larger PV system and the cost of idle capital in the form of the thermal collectors not being fully used in summer. This example shows that there is a need to balance production and demand to max-

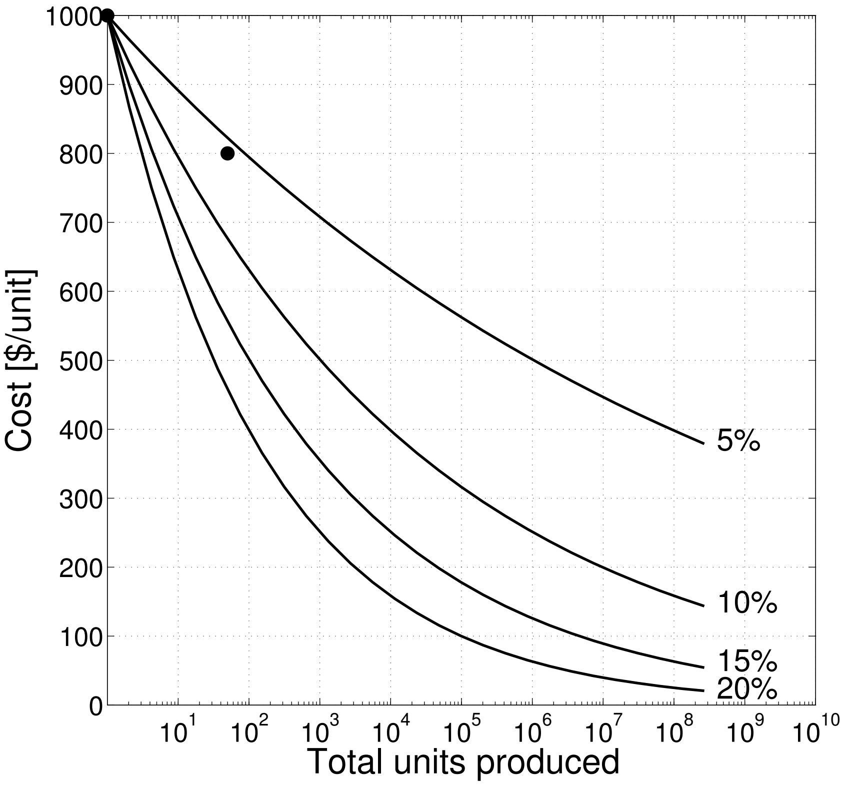

Figure 21.3: Learning curve for the XCPC. Results based on the mean reported cost.

imize capital effectiveness. Fully exploring the potential of DSSTC to accomplish this is left as future work. Another related future work is to explore how the reverse can be accomplished by using the PV system to supply thermal demand. A third future work is to compare PV and DSSTC options for several common installation applications.

21.3.2 Comparison of collector costs for thermal production

In this section, the reverse analysis is performed where an XCPC are used to produce heat and PVC are used to produce electricity for electric resistance heating (efficiency of 1 or COP of 1), absorption chillers, and heat pump applications. This is

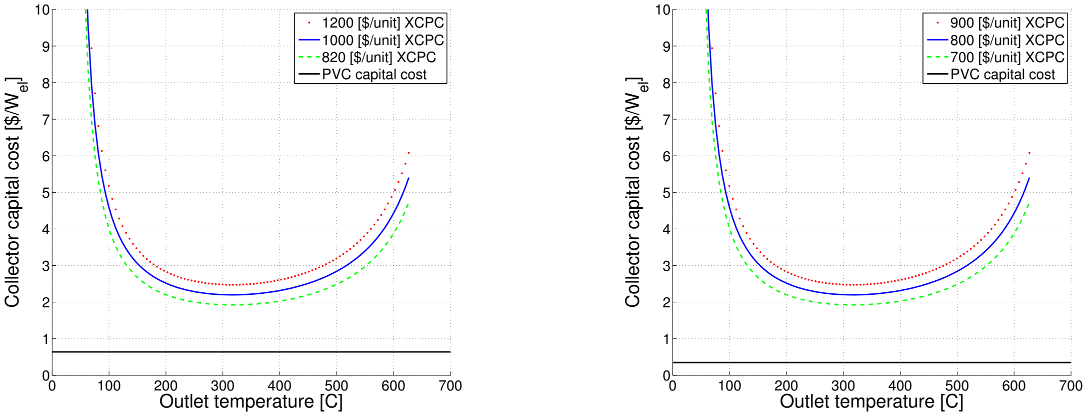

(a) 2015 data for both PVC and XCPC.

(b) 2017 data for PVC and 2018 data for XCPC.

Figure 21.4: Comparison of PV and DSSTC performance for electricity generation.

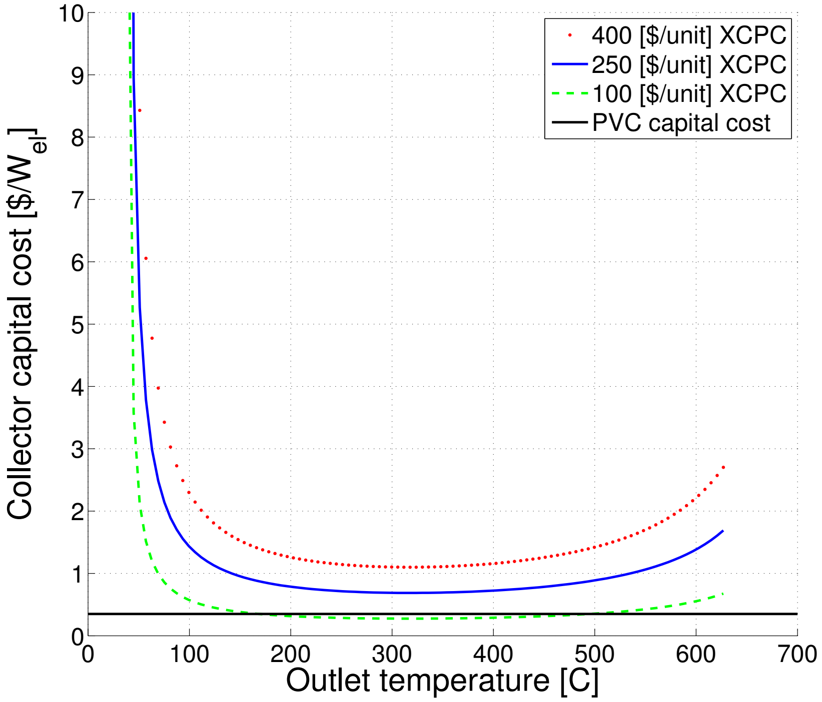

Figure 21.5: Comparison of PV and DSSTC performance for electricity generation using projected future XCPC cost.

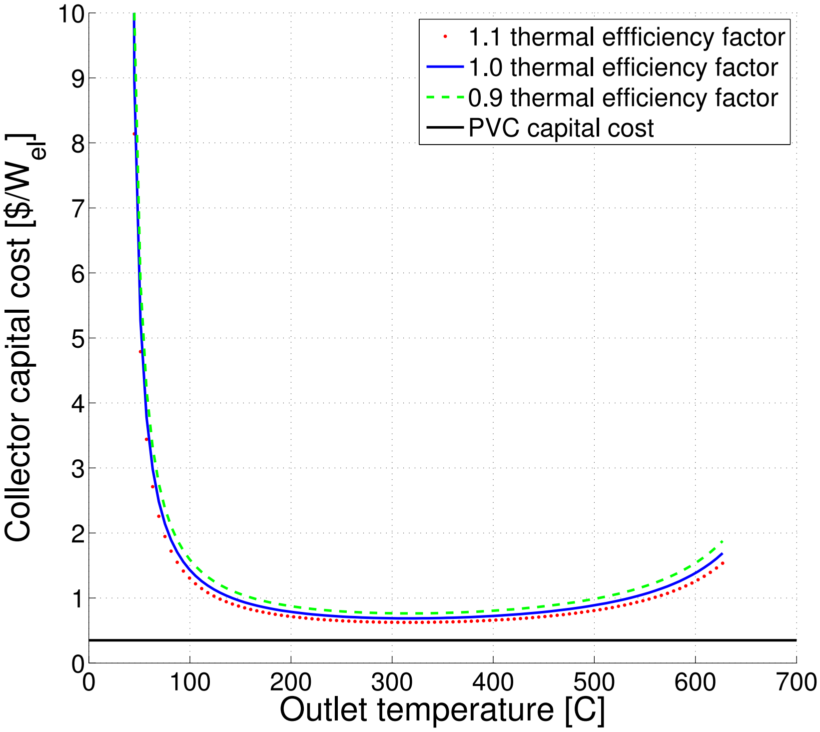

Figure 21.6: Comparison of PV and DSSTC performance for electricity generation using projected future XCPC cost of $250/unit and three collector thermal efficiency assumptions.

accomplished by plotting the XCPC cost in \$/W to the PVC cost in \$/W for several XCPC cost values from the learning curve and several COP (Figure 21.7). The XCPC design is meant to be competitive above 100 °C where most heat pumps are not efficient, because of larger temperature differnces. There are other STC designs that are more efficient below 100 °C (Chapter 8). This provides a clear market for PV systems to be combined with air source heat pumps to meet domestic hot water energy needs in residential, commercial, and industrial applications. Higher temperature hot water needs for hotels, hospitals and other applications are a likely market for the XCPC as the cost reduces through adoption and the technology moves down the learning curve. The figure also shows that electric resistance heating may have an advantage at high temperature differences over both the heat pumps and the XCPC. Because Fox et al. 2011 [210] showed that the majority of thermal demand in the United States was below 260 °C in 2008, the XCPC can meet the bulk of the thermal energy market, especially in industrial and commerical applications. Figure 21.6 show the cost performance of the XCPC at \$250/unit under three thermal efficiency assumptions. Adjustment of the thermal efficiency of the XCPC does not materially change the result.

21.4 Conclusions and summary

The direct DSSTC system was found to have a low probability of being able to compete against PV systems for electricity production even when considering future collector cost. Given solar resource and energy demand variability on an annual basis, further analysis is needed to determine whether or not direct or indirect configurations of DSSTC can compete in electricity production to increase thermal system utilization. Currently, neither PV or DSSTC systems are generally capable of wide application crossover. This tends to prevent one set of collector from being

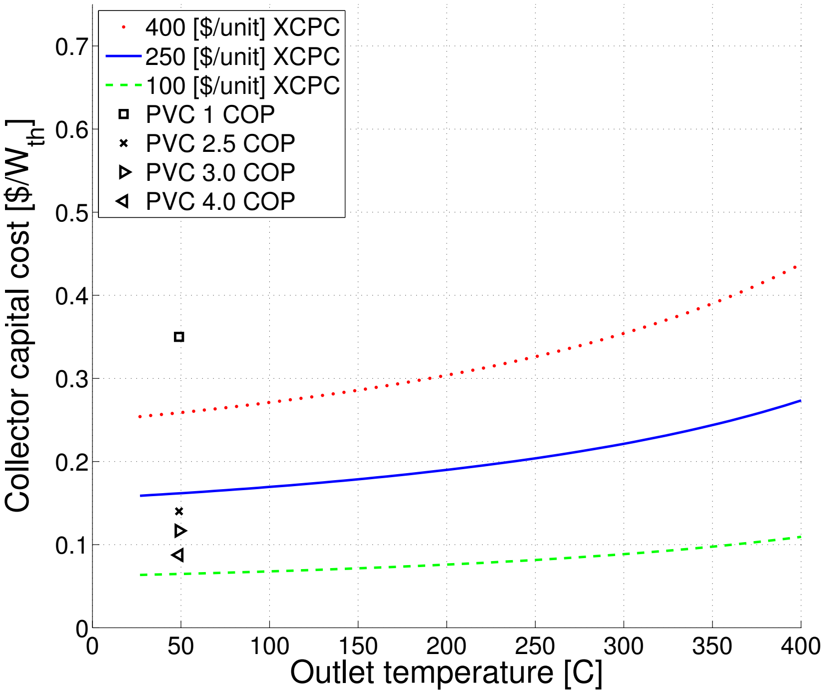

Figure 21.7: Comparison: PV and DSSTC using future cost for thermal production.

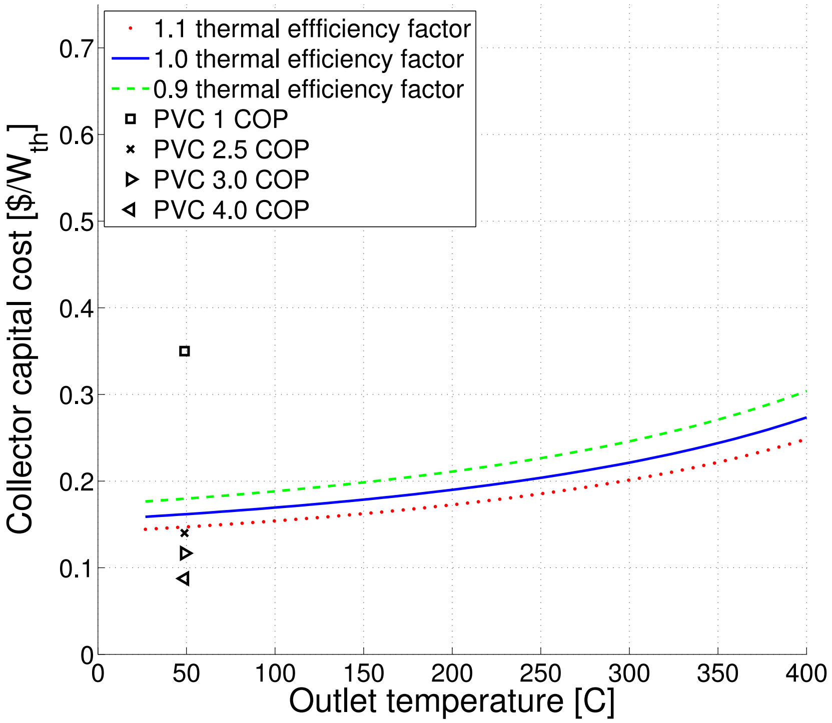

Figure 21.8: Comparison: PV and DSSTC using a future cost of \$250/unit for thermal production including three collector thermal efficiency assumptions.

installed to supply both electrical and thermal loads. One exception of this is to use PVC to supply energy to air source heat pump hot water heater for domestic hot water demand. This is particularly true in small scale installations such as residential, because the fixed project costs are eliminated for the STC system. In spite of these failures of the XCPC to compete against PV systems for electricity production and domestic hot water, there is a large US based market for the XCPC to supply thermal energy in the intended design range of 100–260 °C. This chapter is the original work of the author.

21.5 Future work

In this work, several future works were noted and are listed:

- Explore using DSSTC to improve collector utilization using both direct and indirect configurations.
- Research the extent that PV systems can be used to cost effectively supply energy to thermal demand with the use of heat pumps and other conversion equipment.
- Compare PV and DSSTC options for several common installation applications to explore crossover potential.

REFERENCES

[1] C. A. Gueymard. From global horizontal to global tilted irradiance: How accurate are solar energy engineering predictions in practice? In *Solar 2008 Conference*. American Solar Energy Society, 2008.

[2] James Calm. Refrigerant Transitions ... Again. In *Proceedings of the ASHRAE/NIST Conference*, Gaithersburg, MD, USA, October 2012.

[3] Charles Henry Pope. *Solar heat: Its practical applications*. C. H. Pope, Boston, 1903.

[4] Cliff I. Davidson, editor. *Clean hands: Clair Patterson's crusade against environmental lead contamination*. Nova Science, Commack, N.Y., 1999.

[5] Yale. F Herbert Bormann, helped discover acid rain, dies at 90. http://environment.yale.edu/news/article/f-herbert-bormann-helped-discover-acid-rain-dies-at-90/, June 2012. 2015-02-02.

[6] J. C. Farman, B. G. Gardiner, and J. D. Shanklin. Large losses of total ozone in Antarctica reveal seasonal ClOx/NOx interaction. *Nature*, 315(6016):207–210, May 1985.

[7] NSIDC. Quick Facts | Quick Facts on Ice Sheets | National Snow and Ice Data Center. https://nsidc.org/cryosphere/quickfacts/icesheets.html. 2016-04-07.

[8] Pieter Tans and Ralph Keeling. ESRL Global Monitoring Division - Global Greenhouse Gas Reference Network. http://www.esrl.noaa.gov/gmd/ccgg/trends/. 2015-02-02.

[9] Summary for policymakers. In T. F. Stocker, D. Qin, G.-K. Plattner, M. Tignor, S.K. Allen, J. Boschung, A. Nauels, Y. Xia, V. Bex, and P.M. Midgley, editors, *Climate Change 2013: The physical science basis. Contribution of Working Group I to the Fifth Assessment Report of the Intergovernmental Panel on Climate Change*. Cambridge University Press, Cambridge, United Kingdom and New York, NY, USA, 2013.

[10] S. Pacala and R. Socolow. Stabilization wedges: Solving the climate problem for the next 50 years with current technologies. *Science*, 305(5686):968–972, August 2004.

[11] C. G. Abbot. Harnessing the sun. In *The sun and the welfare of man. by Charles Greeley Abbot ...*, volume 2 of *Smithsonian scientific series*. Smithsonian institution series, inc., New York, N.Y., 4th edition, 1943.

[12] Zachary A. Smith and Katrina D. Taylor. *Renewable and alternative energy resources: A reference handbook*. Contemporary world issues. ABC-CLIO, Santa Barbara, CA, 2008.

[13] Charles Smith. Revisiting solar power's past. *Technology Review*, 98(5):38–47, 1995.

[14] Hoyt C. Hottel. Artificial converters of solar energy. *Sigma Xi Quarterly*, 29(1):49–80, 1941.

[15] C. G. Abbot. Harnessing the sun. In *The sun and the welfare of man. by Charles Greeley Abbot ...*, volume 2 of *Smithsonian scientific series*. Smithsonian institution series, inc., New York, N.Y., 3rd edition, 1934.

[16] C. G. Abbot. Utilizing solar energy. In *The sun. by Charles G. Abbot*. D. Appleton, New York and London, 1st edition, 1911.

[17] C. G. Abbot. Utilizing solar energy. In *The sun. by Charles G. Abbot*. D. Appleton and Co., New York and London, 3rd? edition, 1929.

[18] A. S. E. Ackermann. The utilisation of solar energy. *Journal of the Royal Society of Arts*, 63(3258):538–565, 1915.

[19] E.J. Burda, editor. *Applied solar energy research: A directory of world activity and bibliography of significant literature.* Standford Research Instititue, Standford, CA, 1955.

[20] Ken Butti and John Perlin. *A golden thread: 2500 years of solar architecture and technology.* Cheshire Books, Van Nostrand Reinhold Co., Palo Alto and New York, 1980.

[21] J. I. Yellott. Solar energy in ASME's first century. *Journal of Solar Energy Engineering*, 102(4):234–239, November 1980.

[22] L. C. Spencer. A comprehensive review of small solar-powered heat engines: Part I. A history of solar-powered devices up to 1950. *Solar Energy*, 43(4):191–196, 1989.

[23] L. C. Spencer. A comprehensive review of small solar-powered heat engines: Part II. Research since 1950-"conventional" engines up to 100 kW. *Solar Energy*, 43(4):197–210, 1989.

[24] L. C. Spencer. A comprehensive review of small solar-powered heat engines: Part III. Research since 1950-"unconventional" engines up to 100 kW. *Solar Energy*, 43(4):211–225, 1989.

[25] EIA. Monthly Energy Review - Energy Information Administration. http://www.eia.gov/totalenergy/data/monthly/#summary. 2015-06-17.

[26] David J. Schroeder and Neil Leslie. Organic Rankine cycle working fluid considerations for waste heat to power applications. *ASHRAE Transactions*, 116(1):525–533, 2010.

[27] James A. Mathias, Jon R. Johnston Jr., Jiming Cao, Douglas K. Priedeman, and Richard N. Christensen. Experimental resting of gerotor and scroll expanders used in, and energetic and exergetic modeling of, an organic Rankine cycle. *Journal of Energy Resources Technology*, 131(1):012201–012201, February 2009.

[28] Panpan Song, Mingshan Wei, Lei Shi, Syed Noman Danish, and Chaochen Ma. A review of scroll expanders for organic Rankine cycle systems. *Applied Thermal Engineering*, 75:54–64, January 2015.

[29] Neil P. Leslie, O. Zimron, R. S. Sweetser, and Therese K. Stovall. Recovered energy generation using an organic Rankine cycle system. *ASHRAE Transactions*, 115:220–230, 2009.

[30] Agustín M. Delgado-Torres and Lourdes García-Rodríguez. Analysis and optimization of the low-temperature solar organic Rankine cycle (ORC). *Energy Conversion and Management*, 51(12):2846–2856, December 2010.

[31] B. Twomey, P.A. Jacobs, and H. Gurgenci. Dynamic performance estimation of small-scale solar cogeneration with an organic Rankine cycle using a scroll expander. *Applied Thermal Engineering*, 51(1-2):1307–1316, March 2013.

[32] S. Quoilin, M. Orosz, H. Hemond, and V. Lemort. Performance and design optimization of a low-cost solar organic Rankine cycle for remote power generation. *Solar Energy*, 85(5):955–966, May 2011.

[33] Zachary Mills Norwood. *A better steam engine: Designing a distributed concentrating solar combined heat and power system.* Dissertation, University of California, Berkeley, Berkeley, CA, 2011.

[34] Zachary Mills Norwood, Nathan Kamphuis, and Dan Soltman. Distributed solar-thermal/electric generation. Unpublished report, University of California, Berkeley, Berkeley, CA, December 2006. Author Nathan Kamphuis maybe contacted at nkampy@gmail.com for a copy.

[35] Vincent Lemort, Sylvain Quoilin, Cristian Cuevas, and Jean Lebrun. Testing and modeling a scroll expander integrated into an organic Rankine cycle. *Applied Thermal Engineering*, 29(14-15):3094–3102, October 2009.

[36] Richard Perez, Pierre Ineichen, Robert Seals, Joseph Michalsky, and Ronald Stewart. Modeling daylight availability and irradiance components from direct and global irradiance. *Solar Energy*, 44(5):271–289, 1990.

[37] J. W. Spencer. Fourier series representation of the position of the sun. *Search*, 2(5):172, May 1971.

[38] Jean Meeus. *Astronomical algorithms.* Willmann-Bell, Richmond, VA, 2nd edition, December 1998.

[39] Ibrahim Reda and Afshin Andreas. Solar Position Algorithm for solar radiation applications. Technical Report NREL/TP-560-34302, NREL National Renew-

able Energy Labratory, 1617 Cole Boulevard, Golden, Colorado 80401-3393, January 2008.

[40] Christian A. Gueymard and Jose A. Ruiz-Arias. Extensive worldwide validation and climate sensitivity analysis of direct irradiance predictions from 1-min global irradiance. *Solar Energy*, 128:1–30, April 2016.

[41] ISO 9488 (1999). ISO 9488-1999 Solar energy - vocabulary. Standard ISO 9488-1999, International Organization for Standardization, Geneve, Switzerland, 1999.

[42] Nathan Robinson. *Solar radiation.* Elsevier Pub. Co., Amsterdam and New York, 1966.

[43] M. Sengupta, A. Habte, S. Kurtz, A. Dobos, S. Wilbert, E. Lorenz, Thomas Stoffel, D. Renne, Christian Gueymard, D. Myers, Stephen Wilcox, P. Blanc, and Richard Perez. Best practices handbook for the collection and use of solar resource data for solar energy applications. Technical Report NREL/TP-5D00-63112, National Renewable Energy Laboratory, Golden, CO, February 2015.

[44] Christian A. Gueymard and Daryl R. Myers. Evaluation of conventional and high-performance routine solar radiation measurements for improved solar resource, climatological trends, and radiative modeling. *Solar Energy*, 83(2):171–185, February 2009.

[45] Frank Vignola, Joseph Michalsky, and Thomas L. Stoffel. *Solar and infrared radiation measurements.* CRC Press, Boca Raton, FL, 2012.

[46] P. Blanc, B. Espinar, N. Geuder, C. Gueymard, R. Meyer, R. Pitz-Paal, B. Reinhardt, D. Renné, M. Sengupta, L. Wald, and S. Wilbert. Direct normal

irradiance related definitions and applications: The circumsolar issue. *Solar Energy*, 110:561–577, December 2014.

[47] NREL. NREL: Renewable Resource Data Center - Solar Resource Data. http://www.nrel.gov/rredc/solar_data.html. 2015-10-07.

[48] Stephen Wilcox and William Marion. Users manual for TMY3 data sets. Technical Report NREL/TP-581-43156, National Renewable Energy Laboratory, Golden, CO, May 2008.

[49] William Marion and Ken Urban. Users manual for TMY2s. Technical report, National Renewable Energy Laboratory (NREL), Golden, CO, June 1995.

[50] Manajit Sengupta, Andrew Weekley, Aron Habte, Anthony Lopez, and Christine Molling. Validation of the National Solar Radiation Database (NSRDB). In *EU PVSEC*, Hamburg, Germany, September 2015.

[51] Craig Christensen and Greg Barker. Effects of tilt and azimuth on annual incident solar radiation for United States locations. In *Solar Forum 2001*, pages 225–232, Washington, DC, April 2001. American Solar Energy Society.

[52] John A. Duffie and William A. Beckman. *Solar engineering of thermal processes*. John Wiley & Sons, Hoboken, NJ, 4th edition, April 2013.

[53] William B Stine and Michael Geyer. *Power from the sun*. Power from the sun.net, 2001.

[54] Ph. Blanc and L. Wald. The SG2 algorithm for a fast and accurate computation of the position of the Sun for multi-decadal time period. *Solar Energy*, 86(10):3072–3083, October 2012.

[55] U.S. Naval Observatory. The Astronomical Almanac Online-Delta T: Past, Present and Future. http://asa.usno.navy.mil/SecK/DeltaT.html. 2015-10-07.

[56] Philippe Blanc and Lucien Wald. On the effective solar zenith and azimuth angles to use with measurements of hourly irradiation. In *Advances in Science and Research*, volume 13, pages 1–6, Sofia, Bulgaria, 2016. Copernicus Pub.

[57] C. G. Abbot. The light of the sky. In *The sun. by Charles G. Abbot*, pages 299–307. D. Appleton, New York and London, 1st edition, 1911.

[58] T. Muneer, C. Gueymard, H. Kambezidis, and T. Muneer. *Solar radiation and daylight models*. Elsevier Butterworth Heinemann, Oxford ; Burlington, MA, 2004.

[59] Viorel Badescu, editor. *Modeling solar radiation at the earth's surface*. Springer, Berlin, 2008.

[60] D. T. Reindl, W. A. Beckman, and J. A. Duffie. Evaluation of hourly tilted surface radiation models. *Solar Energy*, 45(1):9–17, 1990.

[61] P. G. Loutzenhiser, H. Manz, C. Felsmann, P. A. Strachan, T. Frank, and G. M. Maxwell. Empirical validation of models to compute solar irradiance on inclined surfaces for building energy simulation. *Solar Energy*, 81(2):254–267, February 2007.

[62] V. Badescu. 3d isotropic approximation for solar diffuse irradiance on tilted surfaces. *Renewable Energy*, 26(2):221–233, June 2002.

[63] Tian Pau Chang. The Sun's apparent position and the optimal tilt angle of a solar collector in the northern hemisphere. *Solar Energy*, 83(8):1274–1284, August 2009.

[64] Wanxiang Yao, Zhengrong Li, Qun Zhao, Yuan Lu, and Ruiyang Lu. A new anisotropic diffuse radiation model. *Energy Conversion and Management*, 95:304–313, May 2015.

[65] Yu Xie and Manajit Sengupta. Diagnosing model errors in simulations of solar radiation on inclined surfaces. In *2016 IEEE 43rd Photovoltaic Specialists Conference (PVSC)*, Portland, Oregon, June 2016. IEEE.

[66] Johann Heinrich Lambert. *Photometry, or, On the measure and gradations of light, colors, and shade : translation from the Latin of Photometria, sive, De mensura et gradibus luminis, colorum et umbrae.* Illuminating Engineering Society of North America, New York, NY, 2001. Introductory monograph and notes by David L. DiLaura.

[67] David L. DiLaura. *A history of light and lighting: In celebration of the centenary of the illuminating engineering society of North America.* Illuminating Engineering Society of North America, New York, N.Y., 2006.

[68] Richard Kittler, Miroslav Kocifaj, and Stanislav Darula. Fundamental principles for daylight calculation methods. In *Daylight science and daylighting technology*, pages 187–208. Springer New York, New York, NY, 2011.

[69] C. G. Abbot and L. B. Aldrich. The silver disk pyrheliometer. *Smithsonian Misc. Collections*, 56(19):1–11, March 1911. Pub. No. 2008.

[70] C. G. Abbot and L. B. Aldrich. Smithsonian pyrheliometer revised. *Smithsonian Misc. Collections*, 60(18):1–7, February 1913. Pub. No. 2164.

[71] C. G. Abbot. *The sun and the welfare of man.*, volume 2 of *Smithsonian scientific series.* Smithsonian institution series, inc., New York, N.Y., 4th edition, 1943.

[72] C. G. Abbot and L. B. Aldrich. The pyranometer–an instrument for measuring sky radiation. *Smithsonian Misc. Collections*, 66(7):1–9, May 1916. Pub. No. 2417.

[73] C. G. Abbot and L. B. Aldrich. On the use of the pyranometer. *Smithsonian Misc. Collections*, 66(11):1–9, November 1916. Pub. No. 2427.

[74] C. G. Abbott and F. E. Fowle. Recent determination of the solar constant of radiation. *Terrestrial Magnetism and Atmospheric Electricity*, 13(2):79–82, June 1908.

[75] C. G. Abbot. Utilizing heat from the sun. *Electrical Engineering*, 58(7):294–298, July 1939.

[76] P. Moon and D. E. Spencer. Illumination from a non-uniform sky. *Illuminating Engineering*, 37:707–722, December 1942.

[77] Parry Hiram Moon. *The scientific basis of illuminating engineering.* Electrical engineering texts. McGraw-Hill, New York, London, 1st edition, 1936.

[78] P. Moon. Basic principles in illumination calculations. *Journal of the Optical Society of America*, 29:108–116, March 1939.

[79] Parry Moon. New methods of calculating illumination. *Journal of the Optical Society of America*, 33:115, 1943.

[80] Parry Hiram Moon. *The scientific basis of illuminating engineering.* Dover Publications, New York, rev. edition, 1961.

[81] Кирилл Яковлевич Кондратьев. *Transfer of long-wave radiation in the atmosphere (in Russian: Перенос длинноволнового излучения в атмосфере).* Госизд-во техн-теоретлит, Москва ; Ленинград, 1950.

[82] Hoyt Clarke Hottel. Harnessing the sun's energy. *Science Digest*, 7:85–90, May 1940.

[83] H. C. Hottel and B. B. Woertz. The performance of flat-plate solar-heat collectors. *Transactions of American Society of Mechanical Engineers*, 64:91–104, February 1942.

[84] Hoyt C. Hottel. The engineering utilization of solar energy. *Proceedings of the American Academy of Arts and Sciences*, 79(4):313, 1951.

[85] Hoyt C. Hottel and Adel F. Sarofim. *Radiative transfer.* McGraw-Hill series in mechanical engineering. McGraw-Hill, New York, 1967.

[86] Борис Абрамович Айзенштат. *Some features of the heat balance of the sandy desert (in Russian: Некоторые черты теплового баланса песчаной пустыни).* Главное управление гидрометеорологической службы при Совете Министров СССР. Труды Ташкентской геофизической обсерватории Вып. 6 (7). Гидрометеоиздат, Ленинград, 1952. pgs 3-55.

[87] Кирилл Яковлевич Кондратьев and Э. П. Подольская. Net radiation of slopes (in Russian: эффективное излучение склонов). *Известия Академии Наук СССР*, 4:370–375, 1953.

[88] Кирилл Яковлевич Кондратьев. *Radiant energy from the sun, (in Russian: Лучистая энергия Солнца).* Гидрометеоиздат, Ленинград, 1954.

[89] Кирилл Яковлевич Кондратьев. *Radiative heat exchange in the atmosphere (in Russian: Лучистый теплообмен в атмосфере).* Гидрометеоиздат, Ленинград, 1956.

[90] K. Ya. Kondratyev. *Radiative heat exchange in the atmosphere.* Pergamon Press, Oxford, New York, rev. and enl. edition, 1965.

[91] Кирилл Яковлевич Кондратьев and М. П. Манолова. Slopes radiation balance (in Russian: Радиационный баланс склонов). *вестник пенинградского университета*, 10:43–70, 1958.

[92] K. J. Kondratyev and M. P. Manolova. The radiation balance of slopes. *Solar Energy*, 4(1):14–19, January 1960.

[93] Benjamin Y. H. Liu and Richard C. Jordan. The interrelationship and characteristic distribution of direct, diffuse and total solar radiation. *Solar Energy*, 4(3):1–19, July 1960.

[94] B. Y. H. Liu and R. C. Jordan. Daily insolation on surfaces tilted toward the equator. *ASHRAE Journal*, 3:53–59, October 1961.

[95] Benjamin Y. H. Liu and Richard C. Jordan. The long-term average performance of flat-plate solar-energy collectors: With design data for the U.S., its outlying possessions and Canada. *Solar Energy*, 7(2):53–74, April 1963.

[96] Ralph C. Temps and K. L. Coulson. Solar radiation incident upon slopes of different orientations. *Solar Energy*, 19(2):179–184, 1977.

[97] J.E. Hay and J.A. Davies. Calculation of the solar radiation incidient on an inclined surface. In *First Canadian Solar Radiation Data Workshop*, Tronto, Ontario, Canada, April 1978.

[98] K. Ya. Kondratyev. *Radiation in the atmosphere*, volume 12 of *International geophysics series*. Academic Press, New York, 1969.

[99] Dazhi Yang. Solar radiation on inclined surfaces: Corrections and benchmarks. *Solar Energy*, 136:288–302, October 2016.

[100] Stefan Hess and Victor I. Hanby. Collector simulation model with dynamic incidence angle modifier for anisotropic diffuse irradiance. *Energy Procedia*, 48:87–96, 2014.

[101] O. W. Westbrook. A sky radiance-based approach to diffuse irradiance transposition. In *Photovoltaic Specialist Conference (PVSC), 2015 IEEE 42nd*, pages 1–5, June 2015.

[102] Christopher J. Smith, Piers M. Forster, and Rolf Crook. An all-sky radiative transfer method to predict optimal tilt and azimuth angle of a solar collector. *Solar Energy*, 123:88–101, January 2016.

[103] Гордов А.Н. Calculation of direct solar radiation on inclined surfaces differently oriented on the latitude 42° (in Russian: Расчет прямой солнечной радиации на различно ориентированные наклонные поверхности для широты 42°). In *Материалы по агроклиматическому районированию субтропиков СССР*, Ленинград, 1938. Гидрометеорологическое изд-во.

[104] Johann Heinrich Lambert. The natural history of twilight is related and defined. In *Photometry, or, On the measure and gradations of light, colors, and shade : translation from the Latin of Photometria, sive, De mensura et gradibus luminis, colorum et umbrae.*, page 352. Illuminating Engineering Society of North America, New York, NY, 2001.

[105] T. M. Klucher. Evaluation of models to predict insolation on tilted surfaces. *Solar Energy*, 23(2):111–114, 1979.

[106] Christian Gueymard. An anisotropic solar irradiance model for tilted surfaces and its comparison with selected engineering algorithms. *Solar Energy*, 38(5):367–386, 1987.

[107] C. A. Gueymard. Erratum to An anisotropic solar irradi- ance model for tilted surfaces and its comparison with selected engineering algorithms. *Solar Energy*, 40(2):175, January 1988.

[108] Christian A. Gueymard. On the correct use of the Gueymard diffuse radiation model for tilted surfaces. *Energy Conversion and Management*, 101:787–788, September 2015.

[109] R. Perez, R. Stewart, C. Arbogast, R. Seals, and J. Scott. An anisotropic hourly diffuse radiation model for sloping surfaces: Description, performance validation, site dependency evaluation. *Solar Energy*, 36(6):481–497, January 1986.

[110] Richard Perez, Robert Seals, Pierre Ineichen, Ronald Stewart, and David Menicucci. A new simplified version of the Perez Diffuse Irradiance Model for tilted surfaces. *Solar Energy*, 39(3):221–231, January 1987.

[111] R. Perez, R. Stewart, R. Seals, and T. Guertin. The development and verification of the Perez Diffuse Radiation Model. Technical Report SAND-88-7030, Sandia National Labs; Atmospheric Sciences Research Center at State Univ. of New York, Albany., Albuquerque, NM; Albany, NY, October 1988.

[112] Fritz Kasten. A new table and approximation formula for the relative optical air mass. Technical Report 136, U.S. Army Materiel Command, Cold Regions research and Engineering Labratory, Hanover, NH, November 1964.

[113] Fritz Kasten. A new table and approximation formula for the relative optical air mass. *Archiv für Meteorologie, Geophysik und Bioklimatologie*, 14:206–223, 1965.

[114] Christian A. Gueymard. Direct and indirect uncertainties in the prediction of tilted irradiance for solar engineering applications. *Solar Energy*, 83(3):432–444, March 2009.

[115] Colienne Demain, Michel Journée, and Cédric Bertrand. Evaluation of different models to estimate the global solar radiation on inclined surfaces. *Renewable Energy*, 50:710–721, February 2013.

[116] Frank P. Incropera, David P. Dewitt, Theodore L. Bergman, and Adrienne S. Lavine. *Fundamentals of heat and mass transfer*. John Wiley & Sons, Hoboken, NJ, 6th edition, 2007.

[117] R. Perez, J. Michalshy, and R. Seals. Modeling sky luminance angular distribution for real sky conditions: Experimental evaluation of existing algorithms. *Journal of the Illuminating Engineering Society*, 21(2):84–92, July 1992.

[118] F. C. Hooper and A. P. Brunger. A model for the angular distribution of sky radiance. *Journal of Solar Energy Engineering*, 102(3):196–202, 1980.

[119] A. P. Brunger. *The Magnitude, Variability, and Angular Characteristics of Shortwave Sky Radiance at Toronto*. Dissertation, University of Toronto, Canada, 1987.

[120] M. A. Rosen, F. C. Hooper, and A. P. Brunger. The characterization and modelling of the diffuse radiance distribution under partly cloudy skies. *Solar Energy*, 43(5):281–290, January 1989.

[121] Alfred P. Brunger and Frank C. Hooper. Anisotropic sky radiance model based on narrow field of view measurements of shortwave radiance. *Solar Energy*, 51(1):53–64, July 1993.

[122] Eero Vartiainen. A new approach to estimating the diffuse irradiance on inclined surfaces. *Renewable Energy*, 20(1):45–64, May 2000.

[123] Norio Igawa, Yasuko Koga, Tomoko Matsuzawa, and Hiroshi Nakamura. Models of sky radiance distribution and sky luminance distribution. *Solar Energy*, 77(2):137–157, 2004.

[124] A. Gracia, J. L. Torres, M. De Blas, A. García, and R. Perez. Comparison of four luminance and radiance angular distribution models for radiance estimation. *Solar Energy*, 85(9):2202–2216, September 2011.

[125] Norio Igawa. Improving the All Sky Model for the luminance and radiance distributions of the sky. *Solar Energy*, 105:354–372, July 2014.

[126] R. Perez, R. Seals, and J. Michalsky. All-weather model for sky luminance distribution-Preliminary configuration and validation. *Solar Energy*, 50(3):235–245, March 1993.

[127] Richard Perez, Robert Seals, and Joseph Michalsky. To all-weather model for sky luminance distribution-preliminary configuration and validation. *Solar Energy*, 51(5):423, 1993.

[128] Alfred P. Brunger. Erratum to Anisotropic sky radiance model based on narrow field of view measurements of shortwave radiance: by Alfred P. Brunger and Frank C. Hooper Solar Energy 51(1), 53-64 (1993). *Solar Energy*, 51(6):523, December 1993.

[129] Afshin Andreas and Thomas L. Stoffel. NREL Solar Radiation Research Laboratory (SRRL): Baseline Measurement System (BMS). Technical Report DA-5500-56488, National Renewable Energy Labratory, Golden, CO, 1981.

[130] Christian A. Gueymard and Daryl R. Myers. Validation and ranking methodologies for solar radiation models. In *Modeling solar radiation at the earth's surface : Recent advances. [edited by] Viorel Badescu*, pages 489–491. Springer, Berlin, 2008.

[131] Roland Winston, Bruce Johnston, Kevin Balkowski, David Hafemeister, Daniel Kammen, Barbara Goss Levi, and Peter Schwartz. Development of non-tracking solar thermal technology. In *AIP Conference Proceedings*, pages 406–412. AIP Publishing, 2011.

[132] Yong Sin Kim, Kevin Balkoski, Lun Jiang, and Roland Winston. Efficient stationary solar thermal collector systems operating at a medium-temperature range. *Applied Energy*, 111:1071–1079, November 2013.

[133] Lun Jiang and Roland Winston. Progress on integrated compound concentrator design. In *Energy Procedia*, volume 48 of *Proceedings of the 2nd International Conference on Solar Heating and Cooling for Buildings and Industry (SHC 2013)*, pages 114–122, 2014.

[134] Roland Winston, Lun Jiang, and Bennett Widyolar. Performance of a 23kw solar thermal cooling system employing a double effect absorption chiller

and thermodynamically efficient non-tracking concentrators. *Energy Procedia*, 48:1036–1046, 2014.

[135] Bennett Widyolar, Roland Winston, Lun Jiang, and Heather Poiry. Performance of the Merced demonstration XCPC collector and double effect chiller. *Journal of Solar Energy Engineering*, 136(4):041009–041009, June 2014.

[136] Yin Hang, Ming Qu, Roland Winston, Lun Jiang, Bennett Widyolar, and Heather Poiry. Experimental based energy performance analysis and life cycle assessment for solar absorption cooling system at University of California, Merced. *Energy and Buildings*, 82:746–757, October 2014.

[137] Nitin Karwa, Lun Jiang, Roland Winston, and Gary Rosengarten. Receiver shape optimization for maximizing medium temperature CPC collector efficiency. *Solar Energy*, 122:529–546, December 2015.

[138] Roland Winston and Lun Jiang. A new generation of medium temperature collector for solar cooling. *Journal of Solar Energy Engineering*, 137(5):051006–051006, July 2015.

[139] Boe Colabewala, Lun Jiang, and Roland Winston. String method of nonimaging optics from a radiation theory perspective. In *SPIE 9572*, volume 9572, pages 957202–1 – 957202–8. SPIE, August 2015.

[140] SRCC. Solar Rating & Certification Corporation Home Page. http://www.solar-rating.org/. 2015-10-07.

[141] Solar Keymark. Solar Keymark. www.solarkeymark.org. 2015-10-07.

[142] ISO 9806 (2013). ISO 9806-2013 Solar energy - Solar thermal collectors - Test methods. Standard ISO 9806-2013, European Committee for Standardization, November 2013.

[143] ENISO 12975-1 (2006)+A1 (2010). ENISO 12975-1-2006+A1-2010 Thermal solar systems and components - Solar collectors - Part 1: General requirements. Standard ENISO 12975-1-2006+A1-2010, European Committee for Standardization, 2010.

[144] ASHRAE 93 (2010). ASHRAE 93-2010 Methods of Testing to Determine the Thermal Performance of Solar Collectors. Standard ASHRAE 93-2010 (R2014), American Society of Heating, Refrigerating and Air-Conditioning Engineers, New York, NY, January 2014.

[145] ENISO 22975-3 (2014). ENISO 22975-3-2014 Solar energy - Collector components and materials - Part 3: Absorber surface durability. Standard ENISO 22975-3-2014, European Committee for Standardization, July 2014.

[146] William T. Guiney. Personal communication, June 2015.

[147] Chromasun. Chromasun. http://chromasun.com/MCT.html. 2015-11-02.

[148] simonsgreenenergy. soponova. http://www.simonsgreenenergy.com.au/pdf/-Data_Sheet_SopoNova_Web.pdf. 2015-11-03.

[149] P. H. Theunissen and W. A. Beckman. Solar transmittance characteristics of evacuated tubular collectors with diffuse back reflectors. *Solar Energy*, 35(4):311–320, 1985.

[150] Ehud Strobach, David Faiman, Samuel James Bader, and Samuel J. Hile. Effective incidence angles of sky-diffuse and ground-reflected irradiance for various incidence angle modifier types. *Solar Energy*, 89:81–88, March 2013.

[151] William R. McIntire. Factored approximations for biaxial incident angle modifiers. *Solar Energy*, 29(4):315–322, January 1982.

[152] W. R. McIntire and K. A. Reed. Orientational relationships for optically non-symmetric solar collectors. *Solar Energy*, 31(4):405–410, January 1983.

[153] Mats Rönnelid, Bengt Perers, and Björn Karlsson. On the factorisation of incidence angle modifiers for CPC collectors. *Solar Energy*, 59(4):281–286, April 1997.

[154] T. Tesfamichael and E. Wäckelgård. Angular solar absorptance and incident angle modifier of selective absorbers for solar thermal collectors. *Solar Energy*, 68(4):335–341, 2000.

[155] Christopher Pike and Katherine Harper Hall. A side by side outdoor performance analysis of three types of solar thermal collectors under varying ratios of direct and deffuse radiation. In *Proceedings of 42nd ASES Annual Conference*, Baltimore, Maryland, April 2013. American Solar Energy Society.

[156] Robert P. Spears and Vincent H. Waldin. ASHRAE 109 - a test standard for two-phase solar collectors. In *ASHRAE Transactions*, volume 90, pages 697–708. ASHRAE, 1984. 697.

[157] L. M. Murphy and E. Kenneth May. Steam generation in line-focus solar collectors- A comparative assessment of thermal performance, operating sta-

bility, and cost issues. Technical Report SERI/TR-632-1311, Solar Energy Research Institute, Golden, Colorado, April 1982.

[158] Richard Perez, Pierre Ineichen, Kathy Moore, Marek Kmiecik, Cyril Chain, Ray George, and Frank Vignola. A new operational model for satellite-derived irradiances: description and validation. *Solar Energy*, 73(5):307–317, November 2002.

[159] Aspects of solar power plant engineering. In C. J. Winter, Rudolf L. Sizmann, and Lorin L. Vant-Hull, editors, *Solar power plants*, pages 134–162. Springer Berlin Heidelberg, Berlin, 1991.

[160] Thomas Midgley Jr. and Albert L. Henne. Organic fluorides as refrigerants. *Industrial & Engineering Chemistry*, 22(5):542–545, 1930.

[161] Thomas Midgley. From the Periodic Table to production. *Industrial & Engineering Chemistry*, 29(2):241–244, February 1937.

[162] J. M. Calm and D. A. Didion. Trade-offs in refrigerant selections. In *Refrigerants for the 21st Century*, Gaithersburg, MD, USA, October 1997. ASHRAE.

[163] James M. Calm. The next generation of refrigerants - Historical review, considerations, and outlook. *International Journal of Refrigeration*, 31(7):1123–1133, 2008.

[164] J. Steven Brown. Preliminary selection of R-114 replacement refrigerants using fundamental thermodynamic parameters (RP-1308). *HVAC&R Research*, 13(5):697–709, 2007.

[165] J. Steven Brown. Predicting performance of refrigerants using the Peng–Robinson Equation of State. *International Journal of Refrigeration*, 30(8):1319–1328, December 2007.

[166] J. Steven Brown. Potential R-114 replacement refrigerants. *ASHRAE Transactions*, 114(2), 2008.

[167] J. Steven Brown. Methodology for estimating thermodynamic parameters and performance of alternative refrigerants. *ASHRAE Transactions*, 114(1), 2008.

[168] J. Steven Brown, Riccardo Brignoli, and Samantha Daubman. Methodology for estimating thermodynamic parameters and performance of working fluids for organic Rankine cycles. *Energy*, 73:818–828, August 2014.

[169] Piotr A. Domanski, J. Steven Brown, Jaehyeok Heo, Janusz Wojtusiak, and Mark O. McLinden. A thermodynamic analysis of refrigerants: Performance limits of the vapor compression cycle. *International Journal of Refrigeration*, 38:71–79, February 2014.

[170] Mark O. McLinden, Andrei F. Kazakov, J. Steven Brown, and Piotr A. Domanski. A thermodynamic analysis of refrigerants: Possibilities and tradeoffs for low-GWP refrigerants. *International Journal of Refrigeration*, 38:80–92, February 2014.

[171] Mark O. McLinden, Piotr A. Domanski, Andrei Kazakov, Jaehyeok Heo, and J. Steven Brown. Possibilities, limits, and tradeoffs for refrigerants in the vapor compression cycle. In *Conference Proceeding ASHRAE 2012*, Gaithersburg, MD, 2012.

[172] Mark O. McLinden, J. Steven Brown, Andrei F. Kazakov, and Piotr A. Domanski. Hitting the bounds of chemistry: limits and tradeoffs for low-GWP refrigerants. In *Proceedings of the 24th IIR International Congress of Refrigeration*, Yokohama, Japan, August 2015. International Institute of Refrigeration (IIR).

[173] Andrei Kazakov, Chris D. Muzny, Vladimir Diky, Robert D. Chirico, and Michael Frenkel. Predictive correlations based on large experimental datasets: Critical constants for pure compounds. *Fluid Phase Equilibria*, 298(1):131–142, November 2010.

[174] Andrei Kazakov, Mark O. McLinden, and Michael Frenkel. Computational design of new refrigerant fluids based on environmental, safety, and thermodynamic characteristics. *Industrial & Engineering Chemistry Research*, pages 12537–12548, September 2012.

[175] Wendy Hawley Carande, Andrei Kazakov, Chris Muzny, and Michael Frenkel. Quantitative structure–property relationship predictions of critical properties and acentric factors for pure compounds. *Journal of Chemical & Engineering Data*, 60(5):1377–1387, May 2015.

[176] Riccardo Brignoli and J. Steven Brown. Organic Rankine cycle model for well-described and not-so-well-described working fluids. *Energy*, 86:93–104, June 2015.

[177] J. Steven Brown, Riccardo Brignoli, and Timothy Quine. Parametric investigation of working fluids for organic Rankine cycle applications. *Applied Thermal Engineering*, 90(Supplement C):64–74, November 2015.

[178] Arnaud Landelle, Nicolas Tauveron, Philippe Haberschill, Rémi Revellin, and Stéphane Colasson. Organic Rankine cycle design and performance comparison based on experimental database. *Applied Energy*, April 2017.

[179] Junjiang Bao and Li Zhao. A review of working fluid and expander selections for organic Rankine cycle. *Renewable and Sustainable Energy Reviews*, 24:325–342, August 2013.

[180] Omar Aboelwafa, Seif-Eddeen K. Fateen, Ahmed Soliman, and Ibrahim M. Ismail. A review on solar Rankine cycles: Working fluids, applications, and cycle modifications. *Renewable and Sustainable Energy Reviews*, 82:868–885, February 2018.

[181] M. A. Paolino and M. D. Burghardt. Energy conservation and second law efficiency. *Journal of Engineering for Power*, 104(1):241–246, January 1982.

[182] Soteris A. Kalogirou. Solar thermal collectors and applications. *Progress in Energy and Combustion Science*, 30(3):231–295, January 2004.

[183] Agustín M. Delgado-Torres and Lourdes García-Rodríguez. Preliminary assessment of solar organic Rankine cycles for driving a desalination system. *Desalination*, 216(1-3):252–275, October 2007.

[184] Zack Norwood, Emil Nyholm, Todd Otanicar, and Filip Johnsson. A geospatial comparison of distributed solar heat and power in Europe and the US. *PLoS ONE*, 9(12):e112442, December 2014.

[185] Eric W. Lemmon, Marcia L. Huber, and Mark O. McLinden. NIST Standard Reference Database 23: Reference Fluid Thermodynamic and Transport Properties-REFPROP, 2013.

[186] Sponsored by AIChE Design Institute for Physical Properties. DIPPR Project 801 - Full Version. *Design Institute for Physical Property Research/AIChE.*, 2012.

[187] Vladimir Diky, Robert D. Chirico, Chris D. Muzny, Andrei F. Kazakov, Kenneth Kroenlein, Joseph W. Magee, Ilmutdin Abdulagatov, and Michael Frenkel. ThermoData Engine (TDE): Software implementation of the dynamic data evaluation concept. 9. Extensible thermodynamic constraints for pure compounds and new model developments. *Journal of Chemical Information and Modeling*, 53(12):3418–3430, December 2013.

[188] Mark O. McLinden, J. Steven Brown, Riccardo Brignoli, Andrei F. Kazakov, and Piotr A. Domanski. Limited options for low-global-warming-potential refrigerants. *Nature Communications*, 8:ncomms14476, February 2017.

[189] Marcia L Huber and James F Ely. A predictive extended corresponding states model for pure and mixed refrigerants including an equation of state for R134a. *International Journal of Refrigeration*, 17(1):18–31, January 1994.

[190] NFPA 704 (2017). NFPA 704-2017 Standard system for the identification of the hazards of materials for emergency response. Standard NFPA 704-2017, National Fire Protection Association, 2017.

[191] ASHRAE 34 (2010). ASHRAE 34-2010 Designation and safety classification of refrigerants. Standard ASHRAE 34-2010, American Society of Heating, Refrigerating and Air-Conditioning Engineers, 2004.

[192] IMC (2009). IMC 2009 International mechanical code. Standard IMC 2009, International Code Council, Country Club Hills, Ill., 1996.

[193] ASHRAE 15 (2016). ASHRAE 15-2016 Safety standard for refrigeration systems. Standard ASHRAE 15-2010, American Society of Heating, Refrigerating and Air-Conditioning Engineers, 2004.

[194] 40 CFR Part 82. *40 CFR Part 82 - Protection of stratospheric ozone.* U.S. Federal Regulation, July 1992.

[195] Gunnar Myhre, Drew Shindel, Francois-Marie Breon, William Collins, Jan Fuglestvedt, Jianping Huang, Dorothy Koch, Jean-Francois Lamarque, David S. Lee, Blanca Mendoza, Teruyuki Nakajima, Alan Robock, Graeme Stephens, Toshihiko Takemura, and Hua Zhang. Anthropogenic and natural radiative forcing. In *Climate Change 2013: The physical Science Basis. Contribution of Working Group I to the fifth Assessment Report of the Intergovernmental Panel on Climate Change*, pages 731–737. Cambridge University Press, Cambridge, United Kingdom and New York, NY, USA, 2013.

[196] Konstantinos Kontomaris. HFO-1336mzz-Z: High temperature chemical stability and use as a working fluid in organic Rankine cycles. In *15th International Refrigeration and Air Conditioning Conference*, Purdue, 2014. Purdue e-Pubs.

[197] Joaquín Navarro-Esbrí, Francisco Molés, Bernardo Peris, Adrián Mota-Babiloni, and Konstantinos Kontomaris. Experimental study of an organic Rankine cycle with HFO-1336mzz-Z as a low global warming potential working fluid for micro-scale low temperature applications. *Energy*, 133:79–89, August 2017.

[198] Rajiv R. Singh. Personal communication about R-1233zd(E), March 2018.

[199] Tomasz Gierczak, M. Baasandorj, and James B. Burkholder. OH + (E)- and (Z)-1-Chloro-3,3,3-trifluoropropene-1 ($CF_3CH{=}CHCl$) Reaction Rate Coefficients: Stereoisomer-Dependent Reactivity. *The Journal of Physical Chemistry A*, 118(46):11015–11025, November 2014.

[200] Yian Zhai, Andrew J. Poss, and Rajiv R. Singh. Stereoselective synthesis of cis-1-chloro-3,3,3-trifluoropropene. *Tetrahedron Letters*, 57(3):396–398, January 2016.

[201] Wendy C. Andersen and Thomas J. Bruno. Rapid screening of fluids for chemical stability in organic Rankine cycle applications. *Industrial & Engineering Chemistry Research*, 44(15):5560–5566, July 2005.

[202] María E. Mondejar, Mark O. McLinden, and Eric W. Lemmon. Thermodynamic properties of trans-1-chloro-3,3,3-trifluoropropene (R1233zd(E)): Vapor pressure, (p, ρ, T) behavior, and speed of sound measurements, and equation of state. *Journal of Chemical & Engineering Data*, 60(8):2477–2489, August 2015.

[203] AHRI 510 (2006). AHRI 510-2006 Performance rating of positive displacement ammonia compressors and compressor units. Standard AHRI 510-2006, Air-Conditioning, Heating, and Refrigeration Institute, Arlington, VA 22201, USA, 2006.

[204] ASHRAE 23.1 (2010). ASHRAE 23.1-2010 Methods of testing for rating the performance of positive displacement refrigerant compressors and condensing units that operate at subcritical temepratures of the refrigerant. Standard ASHRAE 23.1-2010, American Society of Heating, Refrigerating and Air-Conditioning Engineers, 2010.

[205] ASHRAE 23.2 (2014). ASHRAE 23.2-2014 Methods of test for rating the performance of positive displacement compressors that operate at supercritical pressures of the refrigerants. Standard ASHRAE 23.2-2014, American Society of Heating, Refrigerating and Air-Conditioning Engineers, 2014.

[206] AHRI 540 (2015). AHRI 540-2015 Performance rating of positive displacement refrigerant compressors and compressor units. Standard AHRI 540-2015, Air-Conditioning, Heating, and Refrigeration Institute, Arlington, VA 22201, USA, 2015.

[207] AHRI 545 (2017). AHRI 545-2017 Performance rating of modulating positive displacement refrigerant compressors. Standard AHRI 545-2017, Air-Conditioning, Heating, and Refrigeration Institute, Arlington, VA 22201, USA, 2017.

[208] Kevin Balkoski. Performance analysis of medium temperature non-tracking solar thermal concentrators. Master's thesis, University of California at Merced, December 2011.

[209] William T. Guiney. Personal communication, April 2018.

[210] Don B. Fox, Daniel Sutter, and Jefferson Tester. The thermal spectrum of low-temperature energy use in the United States. In *Thirth-Sixth Workshop on Geothermal Reservoir Engineering*, Standford, California, February 2011. Standford University.

[211] EIA. Annual Energy Outlook (2017). Government AEO2017, U.S. Energy Information Administration, January 2017.

[212] Donald Chung, Carolyn Davidson, Ran Fu, Kristen Ardani, and Robert Margolis. U.S. photovoltaic prices and cost breakdowns. Q1 2015 benchmarks for residential, commercial, and utility-scale systems. Technical Report NREL/TP–6A20-64746, 1225303, National Renewable Energy Laboratory, September 2015.

[213] Ran Fu, Donald Chung, Travis Lowder, David Feldman, Kristen Ardani, and Robert Margolis. U.S. solar photovoltaic system cost benchmark: Q1 2016. Technical Report NREL/TP-6A20-66532, National Renewable Energy Laboratory, September 2016.

[214] Ran Fu, David Feldman, Robert Margolis, Mike Woodhouse, and Kristen Ardani. U.S. Solar Photovoltaic System Cost Benchmark: Q1 2017. Technical Report NREL/TP-6A20-68925, National Renewable Energy Laboratory, September 2017.

[215] Fritz Kasten and Andrew T. Young. Revised optical air mass tables and approximation formula. *Applied Optics*, 28(22):4735, November 1989.

[216] Duane Shimogawa. Sopogy Inc., founded by Darren Kimura a decade ago, shuts down operations. http://www.bizjournals.com/pacific/news/2014/04/22/darren-kimuras-sopogy-inc-shuts-down-operations.html, April 2014. 2015-11-23.

APPENDIX A

CODES FOR THE USE OF THE SPA

This appendix includes the codes written to use the SPA by NREL. It does not contain the source code of the SPA, which can be obtained from the NREL website.

A.1 Shell script for downloading astronomical time data

```
# bash - /bin/bash
# ksh - /bin/ksh
# change shell: chsh -s SHELL Then logout and in.
EXECPATH=/usr/local/bin/
EXECPATH2=/usr/bin/
# c04 data IAU 2000 (Paris ut1-utc  data 1962 to present by month)
# with header
wget -N http://hpiers.obspm.fr/iers/eop/eopc04/eopc04_IAU2000.62-now
#
# USNO data delta_T = 32.184s + (TAI - UTC) - (UT1 - UTC)
# = TT - UT1 from maia.usno.navy.mil main page.
# USNO TAI - UTC = leapseconds NOTE: MJD = JD - 2400000.5
# from Astronomical Almanac 2016 page M4.
wget -N http://maia.usno.navy.mil/ser7/tai-utc.dat
# USNO 1600s to 1800's delta_T by 6month period
wget -N http://maia.usno.navy.mil/ser7/historic_deltat.data
# USNO deltat feb 1973 - present monthly period
wget -N http://maia.usno.navy.mil/ser7/deltat.data
```

```
# daily ut1-utc values can be downloaded at
# http://maia.usno.navy.mil/search/search.html
# from 1-2-1973 in 1 year chunks
#
cp eopc04_IAU2000.62-now DUT1.txt
# deleting 14 lines of header
sed '1,14d' DUT1.txt > DUT1_noheader.txt
cp deltat.data DT.txt
cp historic_deltat.data histDT.txt
sed '1,2d' histDT.txt > histDT_noheader.txt
cp tai-utc.dat leap_s.txt
```

A.2 Script for processing data

```
function [ leaps ] = leap( MJD, leap_s )
% Written by Nathan Kamphuis Mar 2017
% This code takes in leap second information
% and calculates the leap second
% for each day in the list MJD,
% where MJD is the Modified Juilean Date
% leap_s
%   1     2     3    4   5  6   7
% year, month, day, MJD, X, X1, X2
[ m, n ] = size(MJD);
leaps = NaN(m,n);
% base case Before First leap second in history
index = ( MJD < leap_s(1,4) );
```

```
leaps(index) = 0;
[ k, ~ ] = size(leap_s);
% main cases
for i=2:k,
    index = ( MJD >= leap_s(i-1,4) ) & ( MJD < leap_s(i,4) );
    leaps(index) = leap_s(i-1,5) +...
        ( MJD(index) - leap_s(i-1,6) )*leap_s(i-1,7);
end
% ending case Last known leap second and beyond
index = ( MJD >= leap_s(k,4) );
leaps(index) = leap_s(k,5) +...
    ( MJD(index) - leap_s(k,6) )*leap_s(k,7);
end %leap.m
```

```
clear all; clc, format long, format compact,
% Written by Nathan Kamphuis March 2017
% this code imports the data from the orginal sources
% less the headers and
% builds the needed array of Delta T and DUT1


%% loading DUT1 = UT1 - UTC data from Paris Observatory
% 1962 to present, daily resolution
load('DUT1_noheader.txt')
DUT1_noheader(:,[5,6,8:end]) = [];
%   1     2     3    4      5
% year, month, day, MJD, DUT1 in seconds
```

```
%% loading Delta T = TT - UT1 = 32.184 + (TAI - UTC) - (UT1 - UTC)
% TT = 32.184 + TAI
% TAI = Atomic time
% DT = 32.184 + leap seconds - DUT1
% Febuary 1, 1973 to present, monthly resolution
load('DT.txt')
% year, month, day, DT

%% loading historic DT data 1657 to 1984 semi-annual resolution
load('histDT_noheader.txt')
histDT_noheader(:,4:end) = []; % deleting LOD and error
% year, Delta T = TDT-UT1 in seconds, error in seconds

%% loading TAI - UTC = leap seconds, descrete jumps always just after
% on the start of the day.
fid = fopen('leap_s.txt','r');
%% Reading file data
A = textscan(fid,'%s','delimiter','\n'); % cell for each line
fclose(fid);

A = A{1,1}; % pulling out the cell
%% Setting up and reading in data
[j, ~]=size(A);
leap_s=NaN(j,7);
%   1     2     3    4   5  6   7
```

```
% year, month, day, MJD, X, X1, X2


for i=1:j,

    leap_s(i,1) = str2double(A{i,1}(1:4)); % Year

    DateVector = datevec(A{i,1}(6:8),'mmm');

    leap_s(i,2) = DateVector(1,2); % Month

    leap_s(i,3) = str2double(A{i,1}(11)); % Day


    leap_s(i,4) = str2double(A{i,1}(17:25)) - 2400000.5; % MJD

    leap_s(i,5) = str2double(A{i,1}(38:47)); % X in seconds

    leap_s(i,6) = str2double(A{i,1}(60:64)); % X1

    leap_s(i,7) = str2double(A{i,1}(70:77)); % X2

end


%% Determining leap years

% http://scienceworld.wolfram.com/astronomy/LeapYear.html

% http://scienceworld.wolfram.com/astronomy/GregorianCalendar.html

% 45:-3:9 BC leap years

% AD leap years 8:4:1580

% Oct 4 to Oct 15 in 1582 days 5-14 skipped switch to

% Gregorian calendar after 1582, years divisible by 100

% and not divisible by 400 are not leap years.

% 1584:4:present remove ( X/100 r=0 & X/400 r~=0)

% therefore 1700,1800,1900 are not leap years and 2000 is.
```

```
%% Determining days of the year by determining days in the month
% make a fist, start on the knuckle of either end, count months
% on the knuckles and grooves. Knuckles are 31, grooves are 30
% save Feb which is 28 or 29 depending on leap year.
Month = [31; 28; 31; 30; 31; 30; 31; 31; 30; 31; 30; 31];
num_days_1961 = sum(Month);

%% build array of dates in 1961
Year_1961 = NaN(num_days_1961,5);
%   1     2     3    4      5
% year, month, day, MJD, DUT1 in seconds
for i=1:12,
    for j=1:Month(i),
        index = sum(Month(1:i))- Month(i)+j;
        Year_1961(index,1:3) = [1961,i,j];
    end % j
end % i
% set MJD in Year_1961
Year_1961(:,4) = ( leap_s(1,4):1:(leap_s(3,4)-1) )';

%% cat on front of DUT1 and save as DUT1
DUT1 = cat(1,Year_1961,DUT1_noheader);

%% Memmory allocation for final results
[ m, n ] = size( DUT1 );
astro_data = NaN(m,n+1);
```

```
astro_data(:,[1:n-1,n+1]) = DUT1(:,1:n);
%   1     2     3    4    5   6
% year, month, day, MJD, DT, DUT1
% will use Dt (5) as temp storage for leap seconds

%% Calculate leap seconds
astro_data(:,5) = leap( astro_data(:,4), leap_s );

%% write code to back fill DUT1 data for 1961 from the other sources
% Note: Assume TDT = TT
DT_1961_1_1 = histDT_noheader(histDT_noheader==1961,2);
DT_1961_7_1 = histDT_noheader(histDT_noheader==1961.5,2);
% half day error
% Note: 365/2 = 182.5 and 7/1 is day 182
% calculate DT_1961_1_1 from known leap second and known DUT1 for
% continuity.
DT_1962_1_1 = 32.184 + astro_data(366,5) - astro_data(366,6);
% DT = TDT - UT1 = 32.184 (TAI - UTC) - (UT1 - UTC);
% DUT1 = (UT1 - UTC) = 32.184 + TAI-UTC - DT
% this allows one to back caluclate the DUT1 data for 1961
% which was not availible from Paris.

astro_data(1:182,6) =...
    linspace(DT_1961_1_1,DT_1961_7_1,182)';
```

```
temp = linspace( DT_1961_7_1,DT_1962_1_1,(37665 - 37480) )';
astro_data(183:365,6) = temp(2:end-1);
% DUT1 = (UT1 - UTC) = 32.184 + TAI-UTC - DT
astro_data(1:365,6) = 32.184 + astro_data(1:365,5) -...
astro_data(1:365,6);

%% overwriting leap seconds with DT
astro_data(:,5) = 32.184 + astro_data(:,5) - astro_data(:,6);

%% save leap_s and DUT1
save('astronomical_data','astro_data')

%%%%%% Now verification of the calculated data is needed. %%%%%%
%% Plotting error between DT and histDT_noheader: years 1974-1984
% annual resolution
year = histDT_noheader(635:2:655,1);
diff = DT(12:12:132,4) - histDT_noheader(635:2:655,2);

figure(1)
clf, hold on, grid on,
plot(year,diff,'.','MarkerSize',30)
set(gca,'FontSize',30) %,'XTick',0:10:90)%,'YTick',0:0.1:1)
% axis([0 90 0 1])
xlabel('Year','FontSize',30)
ylabel('DT_{USNO}-DT_{hist}','FontSize',30)
```

```
legend('Difference in years 1974 to 1984','Location','NorthEast')
hold off,

%% data testing for DT
dut1_max = max( abs( astro_data(:,6) ) );

%% plotting final data by MJD
index = ( astro_data(:,2)==1 | astro_data(:,2)==7 ) &...
    astro_data(:,3)==1;
astro_data_f_test = astro_data(index,:);
% reducing the years to match
astro_data_f_test(49:end, : ) = [];
histDT_test = histDT_noheader(609:end,:);

figure(2)
clf, hold on, grid on,
plot(astro_data(:,4)-37300,astro_data(:,5),'.',...
    astro_data_f_test(:,4)-37300,histDT_test(:,2),'.',...
    'MarkerSize',30)
set(gca,'FontSize',30) %,'XTick',0:10:90)%,'YTick',0:0.1:1)
% axis([0 90 0 1])
xlabel('MJD-37300','FontSize',30)
ylabel('DT_{calc}','FontSize',30)
% legend('Difference in years 1974 to 1984','Location','NorthEast')
hold off,
```

```
%% plotting difference
diff = astro_data_f_test(:,5) - histDT_test(:,2);
figure(3)
clf, hold on, grid on,
plot(astro_data_f_test(:,4)-37300,diff,'.',...
    'MarkerSize',30)
set(gca,'FontSize',30) %,'XTick',0:10:90)%,'YTick',0:0.1:1)
% axis([0 90 0 1])
xlabel('MJD-37300','FontSize',30)
ylabel('DT_{calc}-DT_{Hist.}','FontSize',30)
% legend('Difference in years 1974 to 1984','Location','NorthEast')
hold off,

%% Testing final data against USNO data for DT
% performed in the range provided in the DT data from USNO.
% this data is monthly and starts in feb of 1973.
% reducing astro_data_f which is daily to monthly
astro_data_f_test = astro_data(astro_data(:,3)==1,:);
% reducing the years to match
astro_data_f_test([1:145,674], : ) = [];

%% Plotting error between DT and astro_data_f_test for 1973 Feb
% to 2017 Jan, monthly resolution
diff = astro_data_f_test(:,5) - DT(:,4);
```

```
figure(4)
clf, hold on, grid on,
plot(diff,'.','MarkerSize',30)
set(gca,'FontSize',30) %,'XTick',0:10:90)%,'YTick',0:0.1:1)
% axis([0 90 0 1])
xlabel('month','FontSize',30)
ylabel('DT_{calc}-DT_{USNO}','FontSize',30)
% legend('Difference in years 1974 to 1984','Location','NorthEast')
hold off,
```

A.3 Script for calling the SPA C code in Matlab

```
#include "mex.h"
//#include <stdio.h>
#include "spa.h"
#include <matrix.h>

/*
 * spa_tmym.c - Nathan Kamphuis AUG 2013
 * This code allows MATLAB Calls to the SPA_Calculate by NREL
 * for calculating the position of the sun and related values
 */

/*
 * This Code is complied by MATLAB with the following command
 * mex -v spa_tmym.c spa.c
 * mex -v CFLAGS="\$CFLAGS -std=c99" spa_tmym.c spa.c for the SC EOS
```

```
 *
 * The following files are needed:
 * spa.c, spa.h and of course spa_tmym.c
 *
 * This code is called as follows:
 * []=spa_tmym(a,b)
 * where a is a double vector of [year; month; day; hour; minute;
 * second; DT; DUT1]
 * Its important to note that all these values need to convert to
 * int in C with (int)year type casting.
 * Except for second which can be an actual double
 * b is a double vector of [timezone; Lat; Lon; El; Pres.; Temp.;
 * Slope; Azm_Rot;]
 *
 * [incidence]=spa_tmym(a,b)
 * [incidence, zenith]=spa_tmym(a,b)
 * [incidence,zenith, azimuth_astro]=spa_tmym(a,b)
 *
 */

/* $Revision: 0.1 $ */

void mexFunction( int nlhs, mxArray *plhs[],
        int nrhs, const mxArray *prhs[] )
{
```

```
int spa_result;  // declare result
double *x,*x1,*y1,*y2,*y3,*y4,*y5,*y6;
// declare inputs and outputs
spa_data spa;       // declare the SPA structure
size_t mrows,ncols,mrows1,ncols1; // working vars

/* Check for proper number of arguments. */
if(nrhs!=2) {
    mexErrMsgIdAndTxt( "MATLAB:SPAm:invalidNumInputs",
            "two inputs required.");
} else if(nlhs>6) {
    mexErrMsgIdAndTxt( "MATLAB:SPAm:maxlhs",
            "Too many output arguments.");
}

/* The first input must be a noncomplex double 8x1 array.*/
mrows = mxGetM(prhs[0]);
ncols = mxGetN(prhs[0]);
if( !mxIsDouble(prhs[0]) || mxIsComplex(prhs[0]) ||
        !(mrows==8 && ncols==1) ) {
    mexErrMsgIdAndTxt( "MATLAB:SPAm:inputNotRealDouble6x1array",
       "The first input must be a noncomplex double 6x1 array.");
}

/* The second input must be a noncomplex double 8x1 array.*/
```

```
mrows1 = mxGetM(prhs[1]);
ncols1 = mxGetN(prhs[1]);
if( !mxIsDouble(prhs[1]) || mxIsComplex(prhs[1]) ||
       !(mrows1==8 && ncols1==1) ) {
    mexErrMsgIdAndTxt( "MATLAB:SPAm:inputNotRealarrayDouble",
   "The second input must be a 8x1 noncomplex array double.");
}

/* Create matrix for the return argument. */
plhs[0] = mxCreateDoubleMatrix(1, 1, mxREAL);
plhs[1] = mxCreateDoubleMatrix(1, 1, mxREAL);
plhs[2] = mxCreateDoubleMatrix(1, 1, mxREAL);
plhs[3] = mxCreateDoubleMatrix(1, 1, mxREAL);
plhs[4] = mxCreateDoubleMatrix(1, 1, mxREAL);
plhs[5] = mxCreateDoubleMatrix(1, 1, mxREAL);
/* Assign pointers to each input and output. */
x = mxGetPr(prhs[0]);
x1 = mxGetPr(prhs[1]);
y1 = mxGetPr(plhs[0]);
y2 = mxGetPr(plhs[1]);
y3 = mxGetPr(plhs[2]);
y4 = mxGetPr(plhs[3]);
y5 = mxGetPr(plhs[4]);
y6 = mxGetPr(plhs[5]);
```

```
/* Setting int values in spa input */
spa.year          = (int)x[0];
spa.month         = (int)x[1];
spa.day           = (int)x[2];
spa.hour          = (int)x[3];
spa.minute        = (int)x[4];
spa.second        = x[5];

/* setting double values in spa input */
spa.timezone      = x1[0];
spa.delta_ut1     = x[6]; /* Updated Mar 2017 for input value */
spa.delta_t       = x[7]; /* Updated Mar 2017 for input value*/
/* Updated Nov 2015 dt from 67 to 47  dut1 was zero */
spa.longitude     = x1[2]; /* To account for the reverse order*/
spa.latitude      = x1[1]; /* between tmy and SPA*/
spa.elevation     = x1[3];
spa.pressure      = x1[4];
spa.temperature   = x1[5];
spa.slope         = x1[6];
spa.azm_rotation  = x1[7];
spa.atmos_refract = 0.5667;

/* setting function type */
spa.function      = SPA_ALL;

/* Call the SPA subroutine. */
```

```
    spa_result = spa_calculate(&spa);
    if (spa_result == 0)  //check for SPA errors
    {
        /* set output array values */
        y1[0] = spa.incidence;   //surface incidence angle [degrees]
        y2[0] = spa.zenith;      //topocentric zenith angle [degrees]
        y3[0] = spa.azimuth_astro; //topocentric azimuth angle
        //(westward from south) [-180 to 180 degrees]
        y4[0] = spa.suntransit;
        y5[0] = spa.sunrise;
        y6[0] = spa.sunset;
    } else printf("SPA Error Code: %d\n", spa_result);
}
```

A.4 Wrapper script

```
function [ Theta, Zenith, Azimuth180 ] = spa_tmym_wrap(...
    tmytimept, tmyyrlydata, astro_data )
% Written by Nathan Kamphuis Nov 2016
% Wrapper for spa_tmym.m
% a=[Year Month Day Hour] Note Hour is at end of block
% SPA set to adjust to middle of 1 hour time block of data by
% subtracting an hour and adding 30 minutes.
% b=[timezone latitude longitude elevation avg pressure avg
% temperature,slope azm_rotation]
% astro_data(1) is DT in seconds
% astro_data(2) is DUT1 in seconds
```

```
% Adjust from the end of the hour time block to the middle of the
% block.
% Since the tmy data has hours from 1 to 24 this never causes an
% error even in locations like Alaska where the sun does not set
% for 7 days in the summer. The tmy hour is the hour at the end
% of the hour time block.
time=[tmytimept 30 0 astro_data(2), astro_data(1)]';
% must be 8x1 vector
time(4)=time(4)-1;
% the 30 and the hr - 1 find solar position in middle of
% data point that is a one hour block of time.
[Theta, Zenith, Azimuth180]=...
    spa_tmym(time,tmyyrlydata');
% f(a,b) Note the transpose
% surface incidence angle [degrees] Theta

end
```

A.5 Script for solar position calculation

```
function [ time, hrlydata ] =...
ZenithRemoval( time, hrlydata, yrlydata )
% Written by Nathan Kamphuis Feb 2017
% This function removes data points that have a solar zenith angle
% too high for use with the Perez 1990 and AWM models.
```

```
[m, ~]=size(hrlydata);
astro_data_vect = NaN(m,2);
%% Loading astronmical data and preparing DT and DUT1 data for tmy
load('astronomical_data.mat')
%% following 3.1.1 of the SPA user Manual for Julian Date Calc.
time_temp = time;
index = ( time_temp(:,2)==1 | time_temp(:,2)==2 );
time_temp(index,1)= time(index,1)-1;
time_temp(index,2) = time(index,2)+12;
mjd_tmy = floor( 365.25*(time_temp(:,1)+4716) ) +...
    floor( 30.6001*(time_temp(:,2)+1) ) + time_temp(:,3) +...
    2 - floor( time_temp(:,1)/100 ) +...
    floor( floor( time_temp(:,1)/100 )/4 ) -...
    1524.5; % note B for Gregorian Calendar
% IE OCT 15, 1582 and after.
mjd_tmy = mjd_tmy + (time_temp(:,4) - 0.5 - yrlydata(1,1))/24;
% shifting date by hour shift tocenter of hour time block / timezone
mjd_tmy = mjd_tmy - 2400000.5; % converting from JD to MJD.
mjd_tmy = floor( mjd_tmy );
% if shifts didn't cause MJD to change date then ignoring the change.
% This amounts to constant interpolation over one day for astro_data.
% using mjd to find indeies for astro data assignment
[ ~, tmy_mjd_i, astro_mjd_i ] =...
    intersect( mjd_tmy, astro_data(:,4),'stable' );
[ k, ~ ] = size( tmy_mjd_i );
% main cases
```

```
for i=1:k-1,
    tmy_index = ( tmy_mjd_i(i) ):1:( tmy_mjd_i(i+1) );
    astro_data_vect(tmy_index,1:2) =...
        ones(size(astro_data_vect(tmy_index,1)))*...
        astro_data(astro_mjd_i(i),5:6);
end
% end case
tmy_index = ( tmy_mjd_i(k) ):1:( m );
astro_data_vect(tmy_index,1:2) =...
    ones(size(astro_data_vect(tmy_index,1)))*...
    astro_data(astro_mjd_i(k),5:6);

%% Calculating Irradiance
for i=1:m,
    [~, hrlydata(i,12), hrlydata(i,13)]=...
        spa_tmym_wrap( time(i,:), yrlydata(1,:),...
        astro_data_vect(i,:) );
end

% removing data points where the Sun is too low for
% Perez and awm models
time(hrlydata(:,12)>90,:) = [];
hrlydata(hrlydata(:,12)>90,:) = [];
end %ZenithRemoval.m
```

APPENDIX B

DERIVATION OF THE ISOTROPIC SKY MODEL USING HOTTEL'S VIEW FACTOR RESULT

This appendix contains the simplest known method to derive the Isotropic Sky Model and uses a result from Hottel's 1967 book *Radiative Heat Transfer* [85]. It is unknown who originated this method of derivation, although it seems likely that it was Hottel himself. Chris Gueymard recommended this method in a helpful personal communication on the subject while preparing this manuscript. The diffuse irradiance DHI or $I_{d,h}$ are typically used interchangeably to mean the diffuse horizontal irradiance measured or modeled.

Hottel's Equation 2-17 on Page 37 of his book (Equation B.1), describes the area (A_2) and view factor (F_{12}) of an arbitrary surface subtending angles ψ_1 and ψ_2 viewed by an infinitesimally small Point 1. Hottel states that if the angles are on opposite sides of the normal of Surface 1 (that in the limit approaches a point) they must be of opposite sign.

$$F_{12} = \frac{\sin\psi_2 - \sin\psi_2}{2} \tag{B.1}$$

From basic heat transfer, one can write

$$\dot{Q}_{2\rightarrow 1} = I_2 A_2 F_{21} = I_2 A_1 F_{12} \tag{B.2}$$

$$\frac{\dot{Q}}{A_1} = I_2 F_{12} \tag{B.3}$$

For a horizontal Surface 1, F_{12} is 1 by Equation B.1; therefore, $I_2 = I_{d,h}$. Clearly

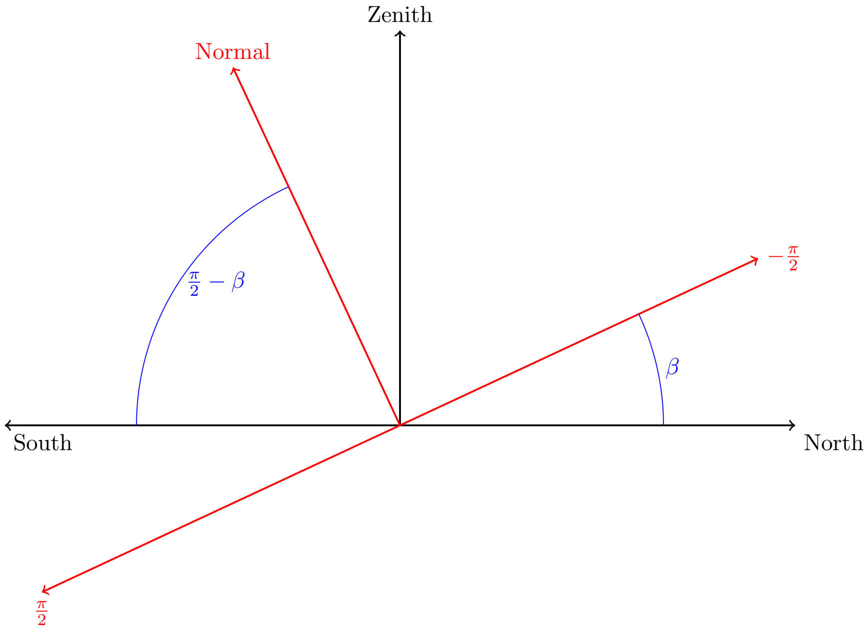

Figure B.1: Angles of interest.

$F_{12} = R_d$. Setting $\psi_2 = \frac{\pi}{2} - \beta$ and $\psi_1 = -\frac{\pi}{2}$ (see Figure B.1), the diffuse correction factor R_d is found for the ISM.

$$F_{12} = \frac{\sin(\frac{\pi}{2} - \beta) - \sin(-\frac{\pi}{2})}{2} \tag{B.4}$$

$$= \frac{1 + \cos\beta}{2}, \text{ by trig addition} \tag{B.5}$$

Using similar logic for the ground-reflected irradiance, taking $\psi_2 = \frac{\pi}{2}$ and $\psi_1 = \frac{\pi}{2} - \beta$, one can write

$$F_{12} = \frac{\sin(\frac{\pi}{2}) - \sin(\frac{\pi}{2} - \beta)}{2} \tag{B.6}$$

$$= \frac{1 - \cos\beta}{2} \tag{B.7}$$

APPENDIX C

2D DERIVATION OF THE ISOTROPIC SKY MODEL

This appendix contains a derivation of the Isotropic Sky Model by Badescu 2002 [62]. The model was (as far is known) originally derived by an alternate method by Moon and Spencer 1942 [76] and presented in Section 7.2.1. The diffuse horizontal irradiance DHI or $I_{d,h}$ are typically used interchangeably to mean the diffuse horizontal irradiance measured or modeled. In this appendix, $I_d(\theta)$ is the diffuse irradiance from the sky dome in a 1-radian field of view at the location (θ) on the dome using the zenith as reference normal $\vec{N}$.

C.1 Determination of the irradiance of a diffuse sky element

The irradiance of a diffuse sky element (I_d) is determined using the measured or modeled diffuse horizontal irradiance (DHI or $I_{d,h}$) to define the irradiance value I_d in Equation C.4, which is given by

$$I_{d,h} = \int_{-\frac{\pi}{2}}^{\frac{\pi}{2}} I_d(\theta) \cos\theta d\theta \tag{C.1}$$

$$= 2I_d \int_{0}^{\frac{\pi}{2}} \cos\theta d\theta \text{ by isotropic assumption and symmetry} \tag{C.2}$$

$$= 2I_d \tag{C.3}$$

$$I_d = \frac{I_{d,h}}{2} \tag{C.4}$$

C.2 Determination of the diffuse transposition factor for a tilted surface

The goal is to determine the diffuse contribution D_T and by inspection the diffuse transposition factor R_d. Here, the rotated panel normal $\vec{N}^*$ is not in the same direction as the zenith $\vec{N}$ (except for $\beta = 0$). By the isotropic assumption, $I(\theta)$ is simply I_d (a constant); therefore, θ does not need to be transformed. R_d is given in Equation C.11:

$$D_T = \int\limits_{-\frac{\pi}{2}}^{\frac{\pi}{2}-\beta} I_d(\theta)\cos\theta d\theta \tag{C.5}$$

$$= I_d \int\limits_{-\frac{\pi}{2}}^{\frac{\pi}{2}-\beta} \cos\theta d\theta \text{ by isotropic assumption} \tag{C.6}$$

$$= I_d[\sin(\frac{\pi}{2} - \beta) - \sin(-\frac{\pi}{2})] \tag{C.7}$$

$$\cos\beta = \sin(\frac{\pi}{2} - \beta) \tag{C.8}$$

$$D_T = I_d[\cos\beta + 1] \tag{C.9}$$

$$= I_{d,h}\left(\frac{1+\cos\beta}{2}\right) \tag{C.10}$$

$$R_d = \left(\frac{1+\cos\beta}{2}\right) \tag{C.11}$$

C.3 Determination of the irradiance of a ground reflected element

The irradiance of a ground-reflected element (I_r) is determined using the measured or modeled global horizontal irradiance (GHI or $I_{t,h}$) to define the irradiance value $I(\theta)$, which leads to Equation C.15 given by

$$\rho I_{t,h} = \int\limits_{-\frac{\pi}{2}}^{\frac{\pi}{2}} I_r(\theta)\cos\theta d\theta \tag{C.12}$$

$$= 2I_r \int_{0}^{\frac{\pi}{2}} \cos\theta d\theta \text{ by isotropic assumption and symmetry} \tag{C.13}$$

$$= 2I_r \tag{C.14}$$

$$I_r = \frac{\rho I_{t,h}}{2} \tag{C.15}$$

C.4 Determination of the reflected transposition factor for a tilted surface

Here, the goal is to determine the reflected contribution R_T and by inspection the reflected transposition factor R_r. Here, the rotated panel normal $\vec{N}^*$ is not in the same direction as the zenith $\vec{N}$ (except for $\beta = 0$). By the isotropic assumption, $I_r(\theta)$ is simply I_r (a constant); therefore, θ does not need to be transformed. R_r is given in Equation C.22:

$$R_T = \int_{\frac{\pi}{2}-\beta}^{\frac{\pi}{2}} I_r(\theta) \cos\theta d\theta \tag{C.16}$$

$$= I_r \int_{\frac{\pi}{2}-\beta}^{\frac{\pi}{2}} \cos\theta d\theta \text{ by isotropic assumption} \tag{C.17}$$

$$= I_r[\sin(\frac{\pi}{2}) - \sin(\frac{\pi}{2} - \beta)] \tag{C.18}$$

$$\cos\beta = \sin(\frac{\pi}{2} - \beta) \tag{C.19}$$

$$R_T = I_r[1 - \cos\beta] \tag{C.20}$$

$$= \rho I_{t,h} \left(\frac{1 - \cos\beta}{2} \right) \tag{C.21}$$

$$R_r = \left(\frac{1 - \cos\beta}{2} \right) \tag{C.22}$$

APPENDIX D

DERIVATION OF THE 3D ISOTROPIC SKY MODEL

This appendix contains a derivation of the 3D Isotropic Sky Model 2002 by Badescu [62]. The method assumes that the collector is a point receiver of irradiance, meaning that the collector area is much less than the distance squared between the source and receiver ($\frac{A_j}{r_j^2}$) [116]. The diffuse irradiance DHI or $I_{d,h}$ are typically used interchangeably to mean the diffuse horizontal irradiance measured or modeled. In this appendix, $I_d(\theta,\phi)$ is the diffuse irradiance from the sky dome in a 1-sr field of view at the location (θ,ϕ) on the dome using the zenith as reference normal $\vec{N}$.

D.1 Determination of the irradiance of a diffuse sky element

The irradiance of a diffuse sky element ($I_d(\theta,\phi)$) is determined using the measured or modeled diffuse horizontal irradiance (DHI or $I_{d,h}$) to define the irradiance value I_d in Equation D.7 given by

$$I_{d,h} = \int I_d(\theta,\phi)\cos\theta d\Omega \tag{D.1}$$

$$= \iint I_d(\theta,\phi)\cos\theta\sin\theta d\theta d\phi \tag{D.2}$$

$$= I_d \int_0^{2\pi} d\phi \int_0^{\frac{\pi}{2}} \cos\theta\sin\theta d\theta \tag{D.3}$$

$$\tfrac{d}{d\theta}\sin^2\theta = 2\sin\theta\cos\theta \tag{D.4}$$

$$= I_d\left(\phi\big|_0^{2\pi}\ \tfrac{1}{2}\left(sin^2\theta\right|_0^{\frac{\pi}{2}}\right. \tag{D.5}$$

$$I_{d,h} = \pi I_d \tag{D.6}$$

$$I_d = \frac{I_{d,h}}{\pi} \tag{D.7}$$

D.2 Determination of the diffuse transposition factor for a tilted surface

The goal is to determine the diffuse contribution D_T and by inspection the diffuse transposition factor R_d. Here, the rotated panel normal $\vec{N}^*$ is not in the same direction as the zenith $\vec{N}$ (except for $\beta = 0$). By the isotropic assumption, $I(\theta, \phi)$ is simply I_d (a constant); therefore, θ and ϕ do not need to be transformed. R_d is given in Equation D.15:

$$D_T = I_d \int_{-\frac{\pi}{2}}^{\frac{\pi}{2}} d\phi \int_{0}^{\frac{\pi}{2}-\beta} \cos\theta \sin\theta d\theta + \int_{\frac{\pi}{2}}^{\frac{3\pi}{2}} d\phi \int_{0}^{\frac{\pi}{2}} \cos\theta \sin\theta d\theta \tag{D.8}$$

$$= I_d \left[(\phi|_{-\frac{\pi}{2}}^{\frac{\pi}{2}} \tfrac{1}{2} \left(\sin^2\theta \right|_{0}^{\frac{\pi}{2}-\beta} + (\phi|_{\frac{\pi}{2}}^{\frac{3\pi}{2}} \tfrac{1}{2} \left(\sin^2\theta \right|_{0}^{\frac{\pi}{2}} \right] \tag{D.9}$$

$$= \frac{\pi I_d}{2} \left(\sin^2(\frac{\pi}{2} - \beta) + \sin^2(\frac{\pi}{2}) \right) \tag{D.10}$$

$$\cos\beta = \sin(\frac{\pi}{2} - \beta) \tag{D.11}$$

$$\cos^2\beta = \frac{1 + \cos 2\beta}{2} \tag{D.12}$$

$$D_T = \frac{\pi I_d}{2} \left(\frac{1 + \cos 2\beta}{2} + 1 \right) \tag{D.13}$$

$$= I_{d,h} \left(\frac{3 + \cos 2\beta}{4} \right) \tag{D.14}$$

$$R_d = \left(\frac{3 + \cos 2\beta}{4} \right) \tag{D.15}$$

D.3 Determination of the irradiance of a ground reflected element

The irradiance of a ground-reflected element ($I_r(\theta)$) is determined using the measured or modeled global horizontal irradiance (GHI or $I_{t,h}$) to define the irradiance value $I(\theta, \phi)$, which leads to Equation D.22 given by

$$\rho I_{t,h} = \int I_r(\theta, \phi) \cos\theta d\Omega \tag{D.16}$$

$$= \iint I_d(\theta, \phi) \cos\theta \sin\theta d\theta d\phi \tag{D.17}$$

$$= I_r \int_0^{2\pi} d\phi \int_0^{\frac{\pi}{2}} \cos\theta \sin\theta d\theta \tag{D.18}$$

$$\tfrac{d}{d\theta} \sin^2\theta = 2\sin\theta\cos\theta \tag{D.19}$$

$$\rho I_{t,h} = I_r \left(\phi\right|_0^{2\pi} \tfrac{1}{2} \left(sin^2\theta\right|_0^{\frac{\pi}{2}} \tag{D.20}$$

$$= \pi I_r \tag{D.21}$$

$$I_r = \frac{\rho I_{t,h}}{\pi} \tag{D.22}$$

D.4 Determination of the reflected transposition factor for a tilted surface

Here the goal is to determine the reflected contribution R_T and by inspection the reflected transposition factor R_r. Here, the rotated panel normal $\vec{N}^*$ is not in the same direction as the zenith $\vec{N}$ (except for $\beta = 0$). By the isotropic assumption, $I_r(\theta, \phi)$ is simply I_r (a constant); therefore, θ does not need to be transformed. R_r is given in Equation D.30:

$$R_T = I_r \int_{-\frac{\pi}{2}}^{\frac{\pi}{2}} d\phi \int_{\frac{\pi}{2}-\beta}^{\frac{\pi}{2}} \cos\theta \sin\theta d\theta \tag{D.23}$$

$$= I_r \left[\left(\phi\right|_{-\frac{\pi}{2}}^{\frac{\pi}{2}} \tfrac{1}{2} \left(\sin^2\theta\right|_{\frac{\pi}{2}-\beta}^{\frac{\pi}{2}} \right] \tag{D.24}$$

$$= \frac{\pi I_r}{2} \left(\sin^2(\frac{\pi}{2}) - \sin^2(\frac{\pi}{2} - \beta) \right) \tag{D.25}$$

$$\cos\beta = \sin(\frac{\pi}{2} - \beta) \tag{D.26}$$

$$\cos^2\beta = \frac{1 + \cos 2\beta}{2} \tag{D.27}$$

$$R_T = \frac{\pi I_r}{2} \left[1 - \left(\frac{1 + \cos 2\beta}{2} \right) \right] \tag{D.28}$$

$$= \rho I_{t,h} \left(\frac{1 - \cos 2\beta}{4} \right) \tag{D.29}$$

$$R_r = \left(\frac{1 - \cos 2\beta}{4}\right) \tag{D.30}$$

APPENDIX E

DERIVATION OF XIE AND SENGUPTA 2016 BOUNDARY CONDITION

This appendix contains a derivation of the Xie and Sengupta 2016 boundary condition for integrating the lune of a sphere. Use the notation in Xie and Sengupta 2016 [65] and begin by setting their Equation 4a to zero:

$$\cos\theta' = \cos\beta\cos\Theta_1 + \sin\beta\sin\Theta_1\cos\phi = 0 \tag{E.1}$$

$$\cos\beta\cos\Theta_1 = -\sin\beta\sin\Theta_1\cos\phi \tag{E.2}$$

$$\frac{1}{\tan\Theta_1} = -\tan\beta\cos\phi \tag{E.3}$$

$$\cot\Theta_1 = -\tan\beta\cos\phi \tag{E.4}$$

$$\cot u = \tan(\frac{\pi}{2} - u) \tag{E.5}$$

$$\tan(\frac{\pi}{2} - \Theta_1) = -\tan\beta\cos\phi \tag{E.6}$$

$$\frac{\pi}{2} - \Theta_1 = \arctan(-\tan\beta\cos\phi) \tag{E.7}$$

$$\Theta_1 = \frac{\pi}{2} - \arctan(-\tan\beta\cos\phi) \tag{E.8}$$

The lower part of their Equation 4b is recovered.

APPENDIX F

PEREZ MODEL 1990

Perez model is given in Equations F.1

$$\epsilon = \frac{\left[\frac{I_{d,h}+I_{b,n}}{I_{d,h}} + 1.041\zeta^3\right]}{\left[1 + 1.041\zeta^3\right]}, \text{ (Perez Sky Clearness Index)} \tag{F.1a}$$

$$\Delta = m\frac{I_{d,h}}{I_{b,n}^0}, \text{ (Perez Sky Brightness)} \tag{F.1b}$$

$$m = \left[\cos\zeta + 0.1500\left(90^\circ - \zeta + 3.885^\circ\right)^{-1.253}\right]^{-1},$$

$$\text{(Kasten 1965 Relative Optical Air Mass)} \tag{F.1c}$$

$$1.63860 = 93.885^\circ\frac{\pi}{180^\circ} \tag{F.1d}$$

$$0.0038399 = \left[0.1500^{\frac{1}{1.253}}\right]\left(\frac{\pi}{180^\circ}\right) \tag{F.1e}$$

$$m = \left[\cos\zeta + \left(\frac{0.00384}{1.63860 - \zeta}\right)^{1.253}\right]^{-1} \tag{F.1f}$$

$$R_d = (1 - F_1)\left(\frac{1 + \cos\beta}{2}\right) + \left(\frac{a}{b}\right)F_1 + F_2\sin\beta \tag{F.1g}$$

$$a = \max(0, \cos\theta_i) \tag{F.1h}$$

$$b = \max(0.087, \cos\zeta) \tag{F.1i}$$

$$F_1 = F_{11} + F_{12}\Delta + F_{13}\zeta, \text{ (Perez Circumsolar Brightening Coeff.)} \tag{F.1j}$$

$$F_2 = F_{21} + F_{22}\Delta + F_{23}\zeta, \text{ (Perez Horizon Brightening Coeff.)} \tag{F.1k}$$

Here, the solar zenith angle ζ is in radians and the relative optical air mass m function is converted from the original reference to take angles with radians rather than degrees. Collector mounting angle β is a given, the angle of incidence θ_i is calculated with the SPA, and F_{xx} are functions of ϵ, which are tabulated in Table F.1.

Table F.1: Perez 1990 model: irradiance coefficients (ϵ bins, where Bins 1 and 8 correspond to overcast and clear-sky conditions, respectively)

ϵ Bin	lower bound	upper bound	F_{11}	F_{12}	F_{13}	F_{21}	F_{22}	F_{23}
1	1	1.065	–0.008	0.588	–0.062	–0.060	0.072	–0.022
2	1.065	1.230	0.130	0.683	–0.151	–0.019	0.066	–0.029
3	1.230	1.500	0.330	0.487	–0.221	0.055	–0.064	–0.026
4	1.500	1.950	0.568	0.187	–0.295	0.109	–0.152	–0.014
5	1.950	2.800	0.873	–0.392	–0.362	0.226	–0.462	0.001
6	2.800	4.500	1.132	–1.237	–0.412	0.288	–0.823	0.056
7	4.500	6.200	1.060	–1.600	–0.359	0.264	–1.127	0.131
8	6.200	–	0.678	–0.327	–0.250	0.156	–1.377	0.251

It is interesting to note that Yang 2016 deviates from Perez et al. 1990 in formulation of the Perez 1990 model. The two differences are in choosing $\cos 85^\circ$ instead of 0.087 and the relative optical air mass correlation $m = [\cos(z)]^{-1}$ instead of the Kasten 1965 result. This brings up another interesting question: How would using the improved Kasten and Young 1989 [215] constants for m affect model performance? These questions could be answered through direct comparison or a sensitivity study.

After careful consideration of the Perez 1990 model, circumsolar brightening F_1 depends on the ratio of a/b and b is limited to values greater than 0.087, which, as far as circumsolar brightening is concerned, limits the solar position to values slightly less than 5° within the horizon and above. This value is used to limit the effect of the sun near the horizon as $\cos(90^\circ) = 0$ would result in $a/b = \infty$. There should be little consequence to this limit being 85°or slightly greater. This is especially true because Yang 2016 limits verification data to $\zeta < 85^\circ$.

The value of m determines where within the model a sky condition falls. It is known that $m = [\cos(z)]^{-1}$ approaches ∞ as ζ approaches 90°. For comparison, Kasten 1965 and Kasten and Young 1989 approach ∼36 and ∼38, respectively. Figure F.1 shows the differences in the three correlations in the range of values

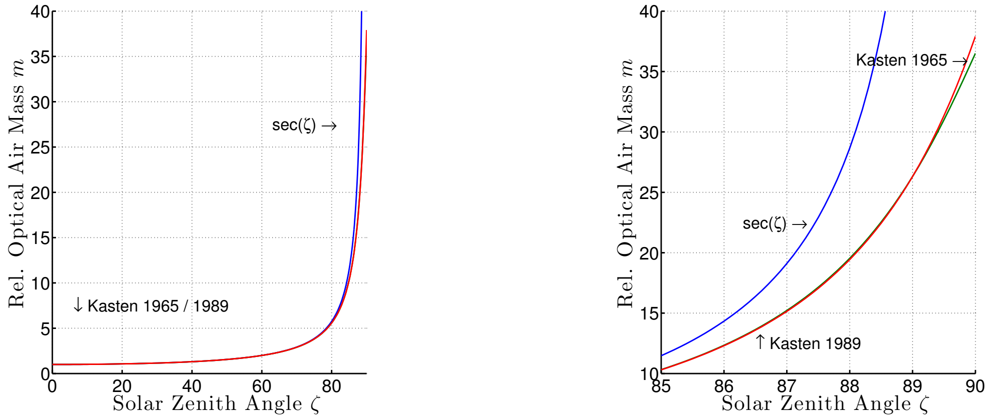

(a) Overall performance. (b) Performance detail near horizon.

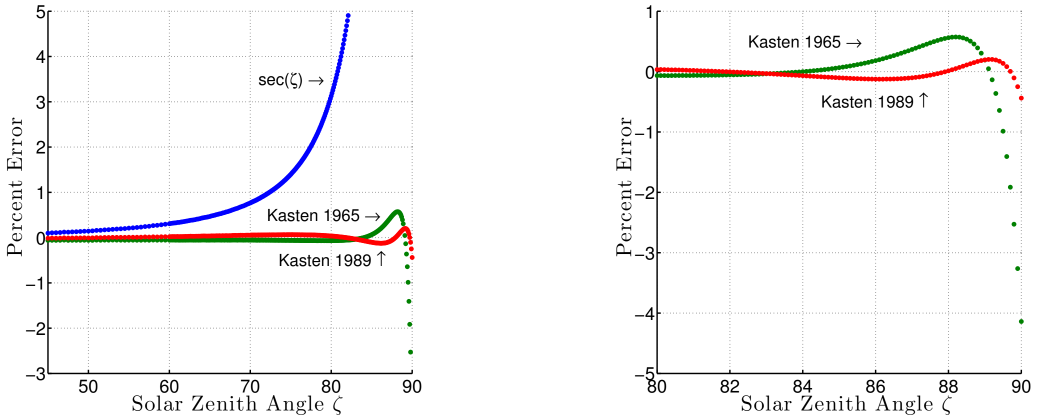

(c) Overall Error. (d) Error detail near horizon.

Figure F.1: Comparison of several relative optical air mass correlations: $\sec\zeta$, Kasten 1965, Kasten 1989.

used in the verification data. At the 85° limit, there is $\sim$11.2% error between the $m = [\cos(z)]^{-1}$ correlation and the data compiled by Kasten and Young 1989, which accounts for density changes, spherical geometry, and atmospheric refraction of a uniformly disperse atmosphere.

APPENDIX G

ALL-WEATHER MODEL BY PEREZ ET AL. 1993

G.1 Definition of the All-Weather Model

The All-Weather Model (AWM) is given in Equations G.1

$$\epsilon = \frac{\left[\frac{I_{d,h}+I_{b,n}}{I_{d,h}} + 1.041\zeta^3\right]}{\left[1+1.041\zeta^3\right]}, \text{ (Perez Sky Clearness Index)} \tag{G.1a}$$

$$\Delta = m\frac{I_{d,h}}{I_{b,n}^0}, \text{ (Perez Sky Brightness)} \tag{G.1b}$$

$$m = \left[\cos\zeta + 0.50572\left(90^\circ - \zeta + 6.07995^\circ\right)^{-1.6364}\right]^{-1}$$

$$\text{(Kasten 1989 Relative Optical Air Mass in degrees)} \tag{G.1c}$$

$$1.676911473 = 96.07995^\circ \frac{\pi}{180^\circ} \tag{G.1d}$$

$$0.0101291 = \left[0.50572^{\frac{1}{1.253}}\right]\left(\frac{\pi}{180^\circ}\right) \tag{G.1e}$$

$$m = \left[\cos\zeta + \left(\frac{0.0101291}{1.676911-\zeta}\right)^{1.253}\right]^{-1}$$

$$\text{(Kasten 1989 Relative Optical Air Mass in radians)} \tag{G.1f}$$

$$lv(\zeta_{se},\theta_{ses}) = \left[1 + a\cdot\exp\left(\frac{b}{\cos\zeta_{se}}\right)\right]\left[1 + c\cdot\exp(d\cdot\theta_{ses}) + e\cdot\cos^2\theta_{ses}\right] \tag{G.1g}$$

$$Lv = lv\frac{I_{d,h}}{\int_{\text{Sky Hemishpere }=2\pi\text{ sr.}}\left[lv(\zeta_{se},\theta_{ses})\cos\zeta_{se}\right]d\Omega} \tag{G.1h}$$

where lv is the relative radiance, Lv is the absolute radiance (which is the same as the previously introduced I_d), ζ_{se} is the zenith angle of the sky element (the same as the polar angle (θ) in the integration), θ_{ses} is the angle between the sky element and the sun, the coefficients a to e are least-squares fit from the experimental data and are given in Perez et al. 1993. Figure G.1 is a clear depiction of the relevant angles.

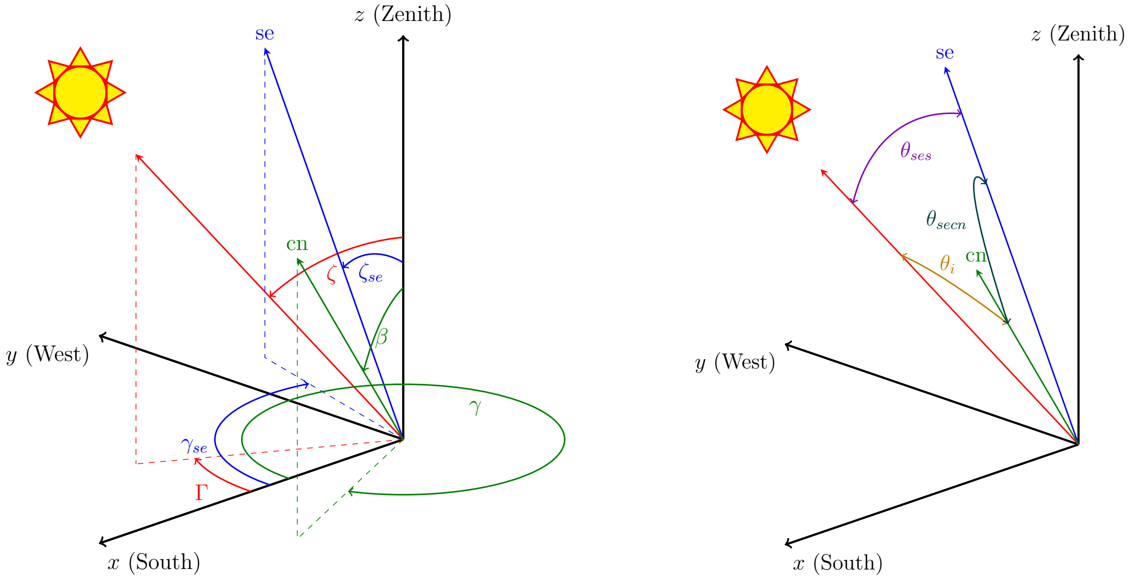

(a) Angles used to define the sun (s), the sky element (se) and the collector normal (cn).

(b) Angles between the sun (s), the sky element (se) and the collector normal (cn).

Figure G.1: Angles needed in calculation of sky models. Note the choice of coordinate system can vary from work to work.

The coefficients are discrete in the sky clearness index ϵ and continuous in the sky brightness index Δ and the solar zenith angle ζ.

G.2 AWM definition clarified

To use the AWM, one must perform some additional calculations given in Equations G.2.

$$\underbrace{I_{d,h}R_d}_{\text{Diffuse}} = \int_{\text{collector view of the sky}} [Lv\cos\theta_{secn}]d\Omega \tag{G.2a}$$

$$R_d = \left[\frac{\int_{\text{collector view of the sky}}[lv(\zeta_{se},\theta_{ses})\cos\theta_{secn}]d\Omega}{\int_{\text{Sky Hemishpere }=2\pi\text{ sr.}}[lv(\zeta_{se},\theta_{ses})\cos\zeta_{se}]d\Omega}\right] \tag{G.2b}$$

$$d\Omega = \sin\theta d\theta d\phi \tag{G.2c}$$

where θ_{secn} is the angle between the sky element and the collector normal (Figure 9.6). Although these additional equations are implied by experts in the field and are necessary to complete a numerical calculation, this author was not able to find any references for them and derived them here. It is also worth noting that the AWM does not depend directly on any coordinates other than the zenith direction because all angles are relative to the sun, the sky element, and the zenith. The coordinate system (unrotated (observer), double rotated (collector), or one defined by the solar direction) used to calculate those angles and integration are at the discretion of the researcher, so long as the notation is consistently applied (e.g., ϕ, $\phi^{'}$, $\phi^{''}$, $\phi_s^{''}$). Here, for consistency, those coordinates defined in the Solar Position Algorithm (SPA) and used previously are continued. This method is based on Perez et al. 1990 Equation 17, Garcia et al. 2011 Equation A18, and personal communication with Dr. Perez.

APPENDIX H

BRUNGER MODEL

The Brunger Model [121, 128] was created from the SKYSCAN '83/84 data set, which has approximately 90,000 measurements. The Brunger model is a three-dimensional model of the distribution of diffuse irradiance over the entire sky dome, and it is given by Equations H.1

$$\underbrace{I_{d,h}R_d}_{\text{Diffuse}} = \iint L(\theta,\phi)\cos\theta d\Omega = \iint L(\theta,\phi)\cos\theta\sin\theta d\theta d\phi \tag{H.1a}$$

$$L(\theta,\phi) = I_{d,h}\left[\frac{a_0 + a_1 cos\theta + a_2\exp(-a_3\Psi)}{\pi(a_0+2a_1/3)+2a_2 I(\theta_s,a_3)}\right] \tag{H.1b}$$

$$a_i = f_i(k,k_t) \text{ for } i=(0,3) \tag{H.1c}$$

$$k = \frac{I_{d,h}}{I_{t,h}} \tag{H.1d}$$

$$k_t = \frac{I_{t,h}}{I^0_{t,h}} \tag{H.1e}$$

$$\Psi = \arccos[\sin\theta\sin\theta_s\cos(\phi-\phi_s)+\cos\theta\cos\theta_s] \tag{H.1f}$$

$$I(\theta_s,a_3) = \frac{[1+\exp(-a_3\pi/2)]}{(a_3^2+4)} \left\{\pi - \left[1-\frac{2[1-\exp(-a_3\pi)]}{\pi a_3[1+\exp(-a_3\pi/2)]}\right][2\theta_s\sin\theta_s - 0.02\pi\sin(2\theta_s)]\right\} \tag{H.1g}$$

where (θ,ϕ) is the location of the 1 sr angle on the 3D sky dome (Figure 7.4), (θ_s,ϕ_s) is the location of the sun (Figure H.1), k is the cloud ratio [123], k_t is the Atmospheric Clearness Index, and $I^0_{t,h}$ is the extraterrestrial global horizontal irradiance. The coefficients a_i are fit from the 90,000 sky measurements and are tabulated in Brunger [121]. The Brunger Model has an accuracy of 11% for the diffuse compo-

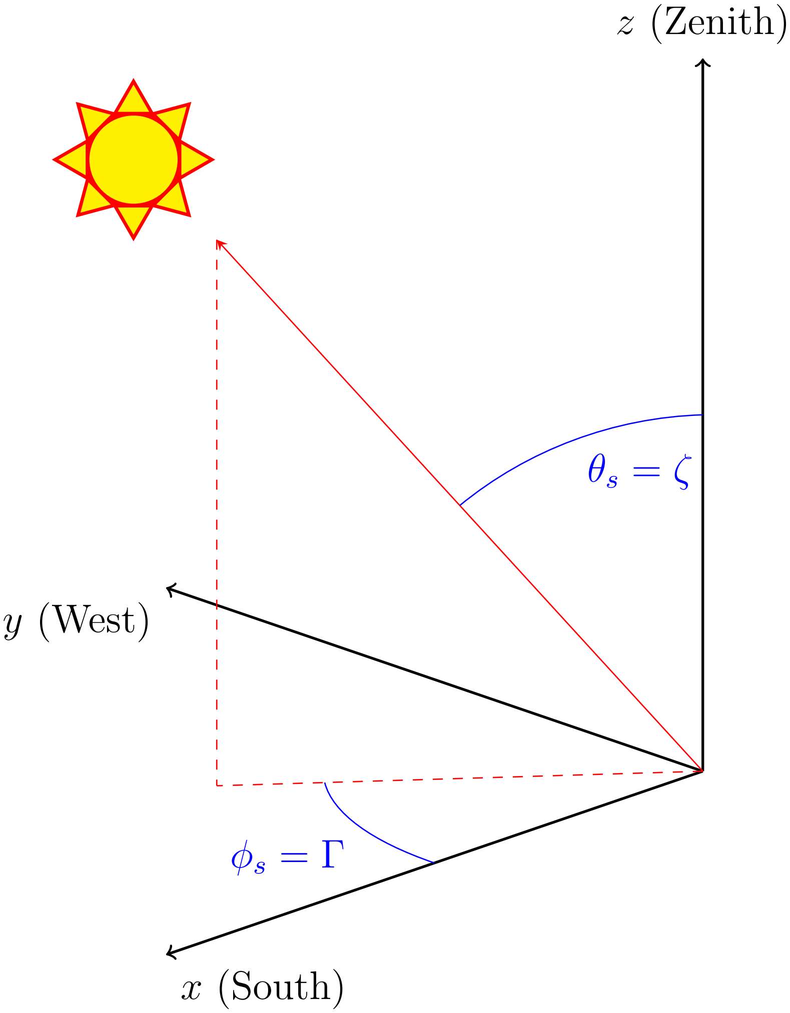

Figure H.1: Solar location (unrotated coordinates).

nent, although the isotropic model has an overall accuracy of 7.8% [1]. The Brunger Model is a *pre-integration method* because the sky conditions must be known prior to integrating the diffuse sky to determine the diffuse transposition factor R_d.

APPENDIX I

NUMERICAL INTEGRATION METHODS

I.1 AWM coordinate choice and method of integration

There is little published on the numerical methods used in sky radiance angular distribution modeling. To make a well-informed choice of coordinate system, one must consider several factors: (1) computational cost, (2) mesh consideration, (3) simplicity of code, and (4) numerical precision. Here computational cost and mesh considerations will be emphasized while keeping the other considerations in mind.

Given an arbitrary mounting, integrating the portion of the hemisphere of the sky within the field of view (FOV) of the collector requires two key tasks be accomplished: (1) meshing the hemisphere, and (2) limiting the results to the portion within the FOV. Given that the azimuth direction has 4 times the degrees as the polar direction, meshing the hemisphere was accomplished with a fixed ratio of 4 to 1. Once the calculations were prepared, a computer algorithm was created to vary the mesh size and determine convergence, from which a final mesh size was selected that balances computational cost and discretization error.

I.1.1 Elemental mesh of the surface of the hemisphere

Of paramount importance is to first realize that meshing the surface of a sphere with uniform grid points and uniform mesh size and shape is not possible. There are many sophisticated methods that do well attempting to approach uniformity and can be quite complex. Making the simplest assumption to parse the polar and azimuth angle ranges uniformly leads to the requirement that at high polar angles (where the elements are the largest), the element sizes must be small enough to avoid discretization error. If not managed well, this can lead to higher computational cost. Given that the azimuth direction has 4 times the degrees as the polar direction, meshing the hemisphere was accomplished with a fixed ratio of 4 to 1. This reduces the mesh degrees of freedom to 1.0 and convergence can be tested for by varying the mesh number. Should it be necessary one can shift to a more complex meshing of the surface to minimize costs while achieving the required accuracy.

I.1.2 Coordinate system choice

There are three obvious coordinate choices to consider:

1. Normal to the sun –The distribution of sky radiance is brightest in the circumsolar region and the size of the region changes with sky condition; therefore, this leads directly to the perspective of meshing the sky where the zero polar angle is in the direction of the normal to the sun.
2. Normal to the collector –Another perspective is to center the mesh on the normal of the collector given an arbitrary mounting (θ'',ϕ'').
3. Zenith –One could also simply center the mesh on the zenith direction.

Each of these three options has merit and challenges, including hemisphere vs sphere coverage and boundary conditions that limit the domain to the portions that correspond to the sky. The choice of boundary conditions must match the real sky within the view of the plane of array (POA). This importance is again highlighted by the Badescu 2002 paper and the original research by this author into the history of boundary condition choices found in Chapter 7.

Centering on the sun (Option 1) keeps the smallest mesh elements near the sun and minimizes the number of mesh points. For high solar zenith angles, this means the whole sphere must be meshed, not just the hemisphere of the sky or POA. It also requires the mesh location change for each data point in the the TMY data-set because the solar position is different at each data point.

Centering the mesh on the collector normal (Option 2) has a similar trade-off because contributions near the collector normal will have lower discretization error than other directions with higher angle of incidence. The collector view is at maximum 2π sr. The portion of the sky out of view of the collector does not need to be meshed and one can maintain a hemisphere coverage and simpler boundaries. The trade-off is between high-value grid points near the direction of the sun vs high grid point density near the zero polar angle of the coordinate system. For a fixed mounted collector, centering the mesh on the collector normal avoids changing mesh location.

Lastly, centering the mesh on the zenith (Option 3) loses the benefit of smaller elements being centered on high-value areas or areas of interest. Additionally, centering the mesh on the zenith also only requires a hemisphere coverage and simpler boundaries.

I.1.3 Coordinate system selection

After a simple thought experiment evaluating how the coordinate choices affect the difficultly of determining the required angles (i.e, ζ_{se}, θ_{ses}, θ_{secn} shown in Figure 9.6), it appears that each choice makes one of the angles a given and the other angles much more involved to calculate. Given the above cursory discussion on coordinate choice and the resulting impacts on the numerical analysis, centering on the sun (Option 1) appears likely to give the best results and require the most computations, centering on the collector (Option 2) appears to be much simpler given the fixed mounting and reduced mesh coverage, and centering on the zenith (Option 3) is conceptually the simplest yet does not first appear to provide a notable reduction in computation for the loss in benefit of being centered on the view of the collector.

For these reasons, centering the mesh on the collector (Option 2) is chosen. Future work may show a different choice is ‘best’ for a particular application, desired level of accuracy, or ability to pay the computational costs. This is especially true when one considers the ever-changing cost of high-performance computations.

APPENDIX J

METHODS USED FOR THE DETERMINATION OF STC PERFORMANCE COEFFICIENTS

This appendix discusses the methodology used and evaluates the coefficients that describe the steady-state thermal performance of the following collectors:

- HC.1
- Vitosol 300-T
- MCT
- XCPC
- SopoNova

J.1 Solar Keymark—Summary of Test Results

The Viessman Vitosol 300-T collector series (referenced in Delgado-Torres) has three evacuated tube models: SP3A, SP3B, and CD3V. The Viessman Vitosol 300-T and Tigi HC.1 are documented on the Solar Keymark website [141]. Figure J.1 displays the data from Solar Keymark and the extrapolated stagnation temperatures for each of the four collectors. Comparing the extrapolated and provided stagnation points reveals that Equation 8.1 is not valid between the two stagnation points and appears to be questionable between the last supplied data point and the supplied stagnation point. The full test report contains the data used to determine the model coefficients, which could be used to make a more informed engineering judgment. Unfortunately, the full report is confidential and is not available on the

Solar Keymark website. This presents a challenge to the designer desiring to model the annual energy yield of the collector for a given system design that may be outside the core intended use of the collector. As a best guess, one could fit the data including the provided stagnation point in an attempt to improve the calculations. For the comparisons in Figure 8.6, the coefficients provided by Solar Keymark were used. The SP3A version of the Vitosol 300-T was chosen because it provided the least discrepancy in stagnation point and the largest reported stagnation point.

J.2 Solar Rating and Certification Corporation (SRCC)

The Chormasun MCT collector was rated by the SRCC [140] under Standard 600 in 2011 and is posted online at the Chormasun website [147]. The following data were retrieved from the data sheet: the optical efficiency $F'(\tau\alpha)$ is η_0 from Equation 8.1, the heatloss coefficients c_1 and c_2 are also the same as a_1 and a_2, respectively, also from Equation 8.1. The certification data supplied on the form lacks a specified stagnation point; therefore, a self-consistency check—as was done with Solar Keymark data—was not possible. Figure J.2 displays the performance model.

J.3 Fitting a manufacturer supplied curve

The Sopogy SopoNova collector performance curve was found online [148]. Retrieving selected data points along the performance curve and fitting that data yielded the following:

- $\eta_0 = 0.6657$
- $a_1 = 0.1941$
- $a_2 = 0.001281$ (from $A_2 = 1.281 = a_2 G$, where G was assumed to be 1000 W/m^2)

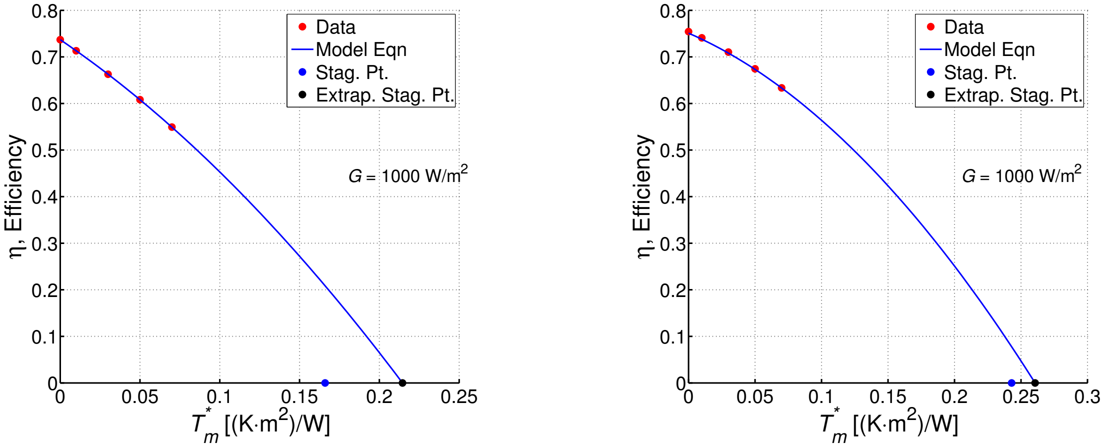

(a) HC.1.

(b) Visotol 300 T SP3A.

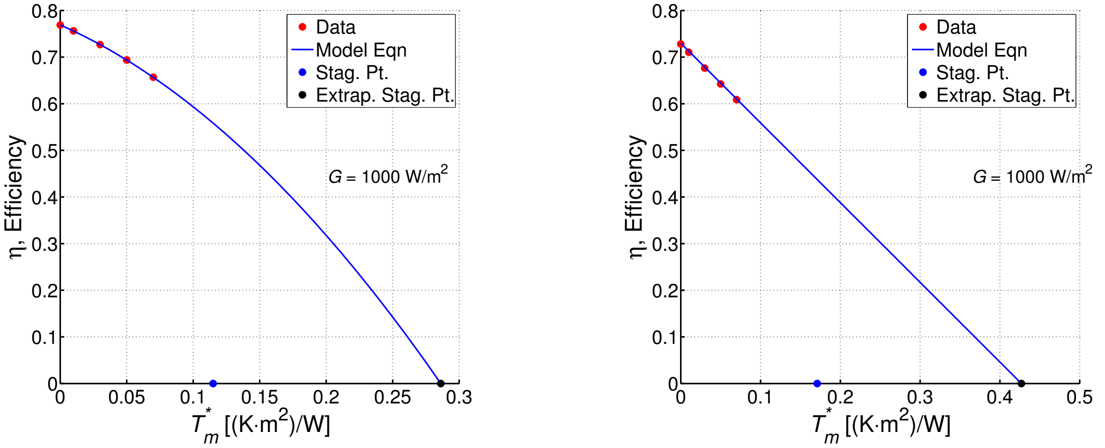

(c) Visotol 300 T SP3B.

(d) Visotol 300 T CD3V.

Figure J.1: Solar Keymark data on collector performance.

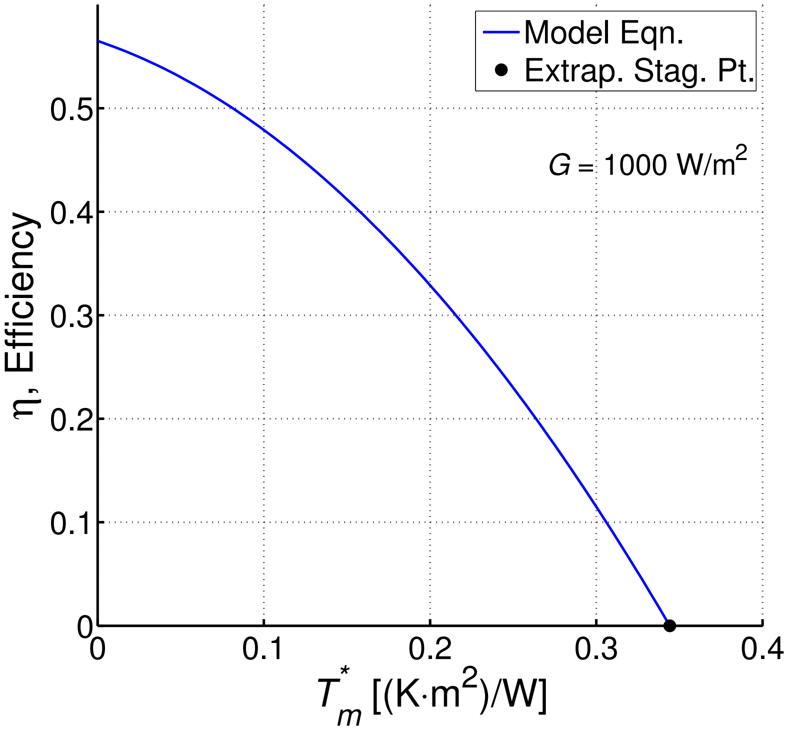

Figure J.2: Chromasun MCT performance data.

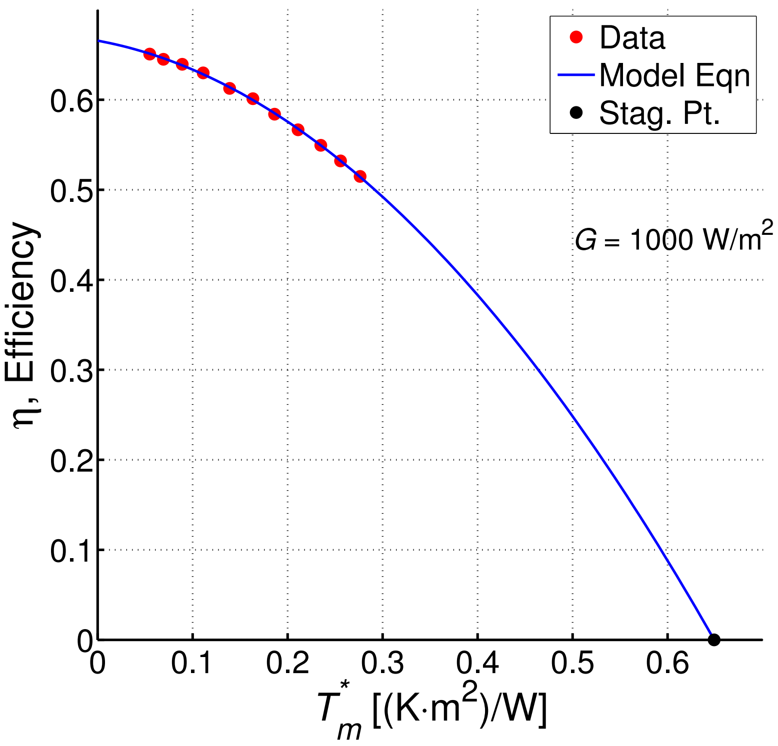

Figure J.3: Sopogy SopoNova performance data.

No certification data were found; therefore, a self-consistency check—as was done with Solar Keymark data—was not possible. Figure J.3 displays the performance model. Unfortunately, Sopogy closed for business in April, 2014 [216].

J.4 Custom fitting from Kim 2013 for the XCPC designs

The E–W XCPC collector performance curve was found in Kim [132]. Retrieving selected data points along the performance curve and fitting that data yielded the following:

- $\eta_0 = 0.6189$
- $a_1 = 0.8252$

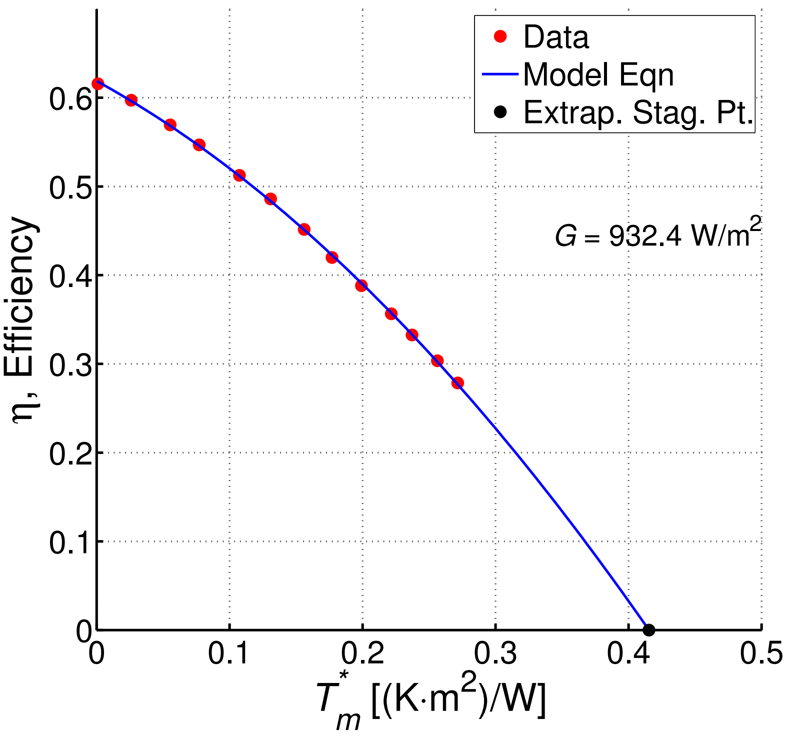

Figure J.4: E–W XCPC performance data.

- $a_2 = 0.00172$ (from $A_2 = 1.601 = a_2 G$, where $G = 932.41$ W/m^2)

And similarly for the N–S XCPC:

- $\eta_0 = 0.6589$
- $a_1 = 1.012$
- $a_2 = 0.0023251$

Here, the irradiance condition was atypical. Because of the slight concentration ratio of the collector, the net irradiance was determined in an alternate way, as seen in Equation 14 of Kim. Figure J.4 displays the performance model.

No certification data were found; therefore, a self-consistency check—as was done with Solar Keymark data—was not possible. Because the two XCPC counter-flow

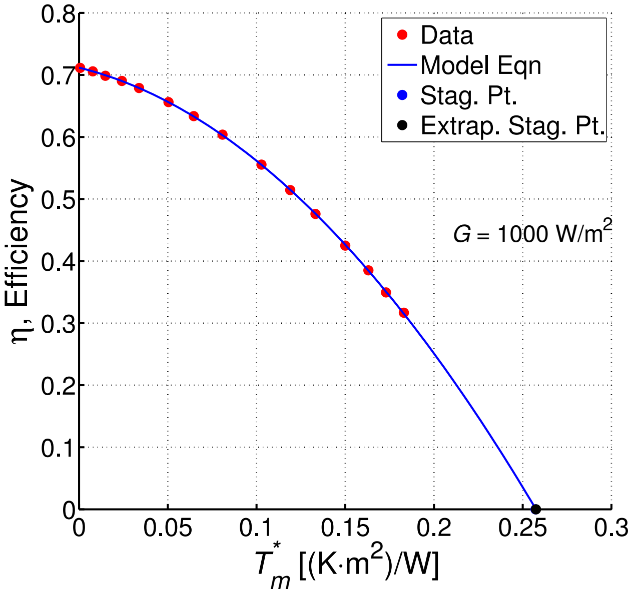

(a) U-tube.

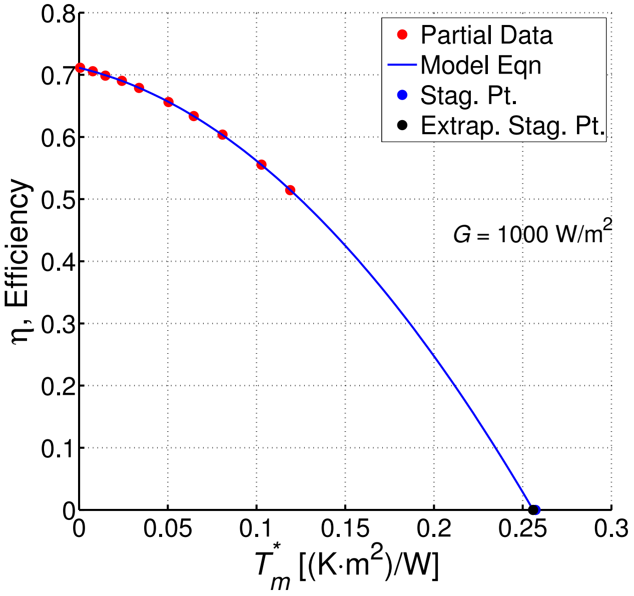

(b) U-tube partial data.

Figure J.5: XCPC U-tube performance data.

design was selected, an alternate test of self-consistency was sought. The previous version of the XCPC is the U-tube design [134], which has a stagnation point given along with a performance curve. Figure J.5(a) shows the extrapolated (0.2575,0) and provided (0.2573,0) stagnation point covering each other. Figure J.5(b) shows that when the data above $\frac{T^*_{m\,stag}}{2}$ are removed, the resulting curve fit coefficients extrapolate well. Clearly, the Winston research group provided a highly self-consistent fit for the U-tube design of the XCPC. Absent any information to the contrary, the extrapolation to stagnation for both of the Kim et al. 2013 XCPC designs is a valid and a reasonable engineering judgment.

APPENDIX K

MODIFIED 3D ISOTROPIC SKY MODEL DERIVATION

This appendix contains a derivation for the Modified 3D Isotropic Sky Model for use with collectors that can be modeled with an acceptance angle step function. This method is an adaption of the 3D Isotropic Sky Model by Badescu [62], derived in Appendix D. As noted in Chapter 7 this method is based on a wrong boundary condition; therefore, the M3DISM is not recommend for use.

K.1 M3DISM statement

The modified 3D Isotropic Sky Model is a compromise between using the numerical integration method of the Brunger Model and an oversimplified sky model with the concentration ratio correction. This model is developed by the author. The M3DISM applies to collectors that require a bi-directional IAM that can be modeled by a step IAM function. This method could also be extended to any IAM function that can be analytically integrated with $I(\theta, \phi)$. The M3DISM is based on repeating the integration (Equation 7.8) for the diffuse sky irradiance I_d with the product $I_d K$. Given that the XCPC has a sharp angle of acceptance function – similar to a step function – the product $I_d K$ reduces to I_d with the limits of integration adjusted by the angle of acceptance in each direction. Appendix K contains the derivation of the model and algorithm verification. M3DISM is given by equations found in Tables K.2 and K.3 for R_d and R_r respectively, where Table K.1 denotes the four cases. This method is also based on the same general Equations 9.9–9.12.

Table K.1: Cases of angle of acceptance limit

Case	Top/Bottom limit	Left/Right limit
I	$\beta \leq \alpha_{TB}$	$\beta \leq \alpha_{LR}$
II	$\beta \leq \alpha_{TB}$	$\beta > \alpha_{LR}$
III	$\beta > \alpha_{TB}$	$\beta \leq \alpha_{LR}$
IV	$\beta > \alpha_{TB}$	$\beta > \alpha_{LR}$
$0 \leq \beta \leq 90°$		

Table K.2: Diffuse transposition factor by case

Case	Top/Bottom limit	Left/Right limit	R_d
I	$\beta \leq \alpha_{TB}$	$\beta \leq \alpha_{LR}$	$\left(\frac{2+\cos(2\alpha_{TB})+\cos(2\alpha_{LR})}{4}\right)$
II	$\beta \leq \alpha_{TB}$	$\beta > \alpha_{LR}$	$\left(\frac{4+2\cos(2\alpha_{TB})+\cos(2\alpha_{LR})+\cos(2\beta)}{8}\right)$
III	$\beta > \alpha_{TB}$	$\beta \leq \alpha_{LR}$	$\left(\frac{4+\cos(2\alpha_{TB})+2\cos(2\alpha_{LR})+\cos(2\beta)}{8}\right)$
IV	$\beta > \alpha_{TB}$	$\beta > \alpha_{LR}$	$\left(\frac{4+\cos(2\alpha_{TB})+\cos(2\alpha_{LR})+2\cos(2\beta)}{8}\right)$

Table K.3: Reflected transposition factor by case

Case	Top/Bottom limit	Left/Right limit	R_r
I	$\beta \leq \alpha_{TB}$	$\beta \leq \alpha_{LR}$	0
II	$\beta \leq \alpha_{TB}$	$\beta > \alpha_{LR}$	$\left(\frac{\cos(2\alpha_{LR})-\cos(2\beta)}{8}\right)$
III	$\beta > \alpha_{TB}$	$\beta \leq \alpha_{LR}$	$\left(\frac{\cos(2\alpha_{TB})-\cos(2\beta)}{8}\right)$
IV	$\beta > \alpha_{TB}$	$\beta > \alpha_{LR}$	$\left(\frac{\cos(2\alpha_{TB})+\cos(2\alpha_{LR})-2\cos(2\beta)}{8}\right)$

K.2 General Setup

Starting with the general equation for irradiance, inserting the IAM for a given collector will determine the effective irradiance G_{eff}.

$$G = \int I(\theta, \phi) \cos\theta d\Omega \tag{K.1}$$

$$G = \int_0^{2\pi} \int_0^{\frac{\pi}{2}} I(\theta, \phi) \cos\theta \sin\theta d\theta d\phi \tag{K.2}$$

$$G_{eff} = \int_0^{2\pi} \int_0^{\frac{\pi}{2}} I(\theta, \phi) K(\theta_L, \theta_T) \cos\theta \sin\theta d\theta d\phi \tag{K.3}$$

This method of calculating the irradiance avoids the issue of determining an effective IAM for the diffuse and reflect components, although it requires determining $I(\theta, \phi)$ and then transforming it into the collector frame of reference. Most solar modeling does not use this method because it is more computationally expensive. Furthermore, it alters the meaning of efficiency from $(\frac{E_{\text{th}}}{G})$ to $(\frac{E_{\text{th}}}{G_{\text{eff}}})$. Effective irradiance is used here because it provides a more physically sound method for determining collector performance. The effective irradiance method can be greatly simplified when the IAM function K is close to a step function and can be approximated as a step function. This converts the limits of integration in Equation K.3 to account for limited field-of-view of the collector because of the acceptance angles. Changing the limits of integration to account for acceptance angles effectively breaks the integration into four parts. Including tilt of the collector breaks the integration parts into sub-parts. Accounting for angles of acceptance in a general way, various values for the longitudinal and transverse directions of the collector, results in the need to consider several cases. Table K.4 lists the cases considered, where α_{TB} and α_{LR} are the

Table K.4: Cases of angle of acceptance limit

Case	Top/Bottom limit	Left/Right limit
I	$\beta \leq \alpha_{TB}$	$\beta \leq \alpha_{LR}$
II	$\beta \leq \alpha_{TB}$	$\beta > \alpha_{LR}$
III	$\beta > \alpha_{TB}$	$\beta \leq \alpha_{LR}$
IV	$\beta > \alpha_{TB}$	$\beta > \alpha_{LR}$
$0 \leq \beta \leq 90^\circ$		

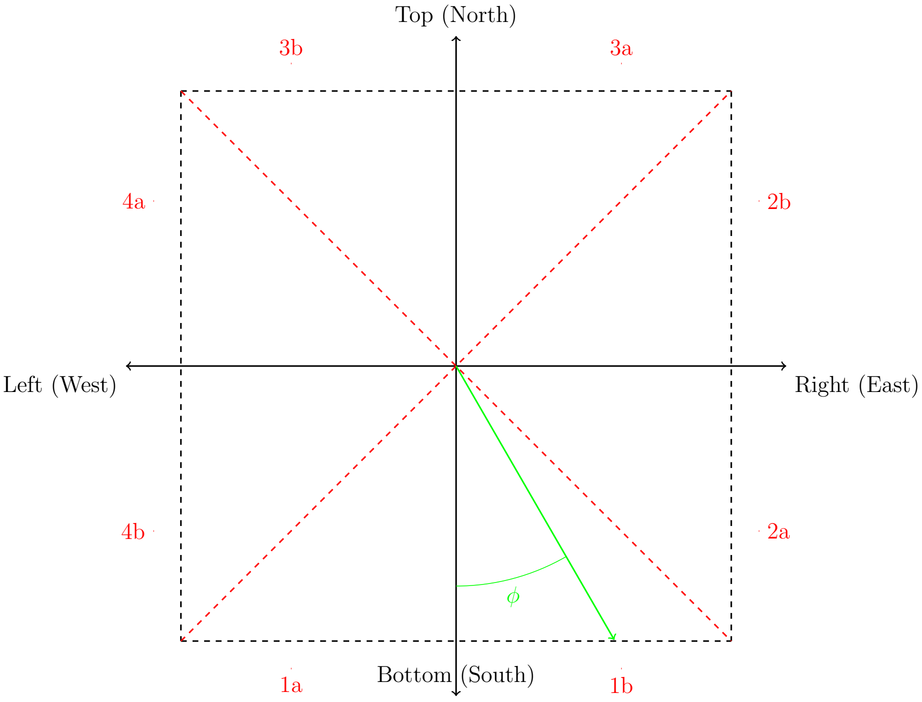

Figure K.1: Collector field-of-view regions.

half angle of acceptance in the top/bottom and left/right directions respectively. Figure K.1 shows the regions of interest, where $\theta = 0$ is out of the page and compass directions are in the original coordinates before tilt or azimuth rotations. Figure K.2 shows a side view of the collector under tilt rotation and includes several important angles.

This approach results in a large number of terms in many equations that are all similar and follow a pattern when calculating the diffuse and reflected transposition

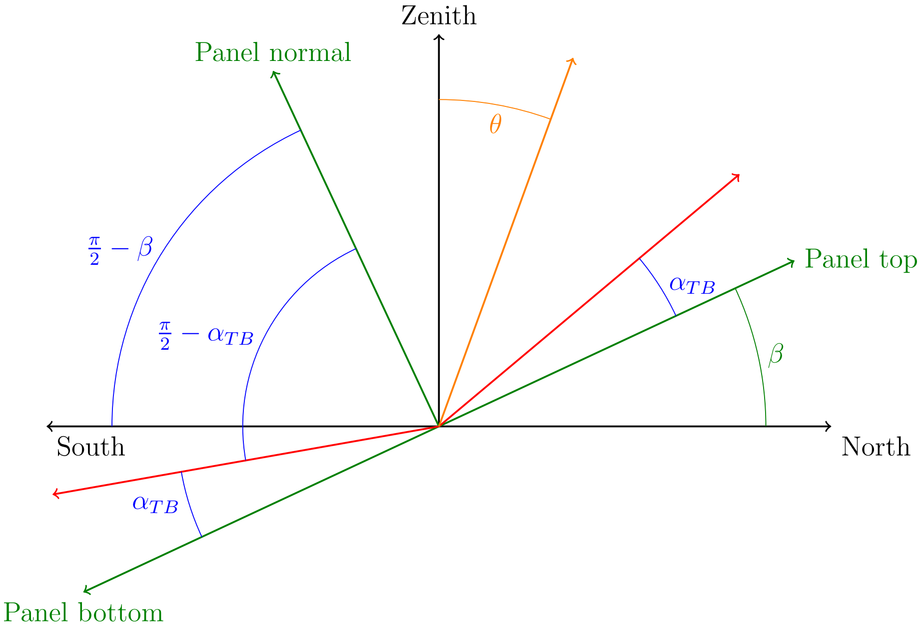

Figure K.2: Angles of interest in slope rotation.

factors. Equations K.4–K.6 note the pattern:

$$X = I_x \sum_i \left[\int_{a_i}^{b_i} d\phi \int_{c_i}^{d_i} \cos\theta \sin\theta d\theta \right] \tag{K.4}$$

$$= I_x \sum_i \left[\left(\phi\right|_{a_i}^{b_i} \tfrac{1}{2} \left(\sin^2\theta\right|_{c_i}^{d_i} \right] \tag{K.5}$$

$$= I_x \sum_i \left[(b_i - a_i)\tfrac{1}{2}(\sin^2 d_i - \sin^2 c_i) \right] \tag{K.6}$$

where i denotes the limits of integration for each region.

Some common simplifications to the existing pattern depend on the values of the limits of integration:

$$\left(\sin^2\theta\right|_0^{d_i} = \sin^2 d_i \tag{K.7}$$

$$\sin(\frac{\pi}{2} - x) = \cos x \tag{K.8}$$

Table K.5: Limits of integration for the diffuse transposition factor

Cases	Common			I	II	III	IV
Region	a	b	c	d			
1	$\frac{-\pi}{4}$	$\frac{\pi}{4}$	0	$\frac{\pi}{2}-\alpha_{TB}$	$\frac{\pi}{2}-\alpha_{TB}$	$\frac{\pi}{2}-\beta$	$\frac{\pi}{2}-\beta$
2a	$\frac{\pi}{4}$	$\frac{\pi}{2}$	0	$\frac{\pi}{2}-\alpha_{LR}$	$\frac{\pi}{2}-\beta$	$\frac{\pi}{2}-\alpha_{LR}$	$\frac{\pi}{2}-\beta$
2b	$\frac{\pi}{2}$	$\frac{3\pi}{4}$	0	$\frac{\pi}{2}-\alpha_{LR}$	$\frac{\pi}{2}-\alpha_{LR}$	$\frac{\pi}{2}-\alpha_{LR}$	$\frac{\pi}{2}-\alpha_{LR}$
3	$\frac{3\pi}{4}$	$\frac{5\pi}{4}$	0	$\frac{\pi}{2}-\alpha_{TB}$	$\frac{\pi}{2}-\alpha_{TB}$	$\frac{\pi}{2}-\alpha_{TB}$	$\frac{\pi}{2}-\alpha_{TB}$
4a	$\frac{5\pi}{4}$	$\frac{3\pi}{2}$	0	$\frac{\pi}{2}-\alpha_{LR}$	$\frac{\pi}{2}-\alpha_{LR}$	$\frac{\pi}{2}-\alpha_{LR}$	$\frac{\pi}{2}-\alpha_{LR}$
4b	$\frac{3\pi}{2}$	$\frac{7\pi}{4}$	0	$\frac{\pi}{2}-\alpha_{LR}$	$\frac{\pi}{2}-\beta$	$\frac{\pi}{2}-\alpha_{LR}$	$\frac{\pi}{2}-\beta$

$$\cos^2 x = \frac{1+cos2x}{2} \tag{K.9}$$

$$\tfrac{1}{2}\sin^2(\frac{\pi}{2}-x) = \frac{1+cos2x}{4} \tag{K.10}$$

Other related equations used to evaluate the general equation follow:

$$I_{d,h} = DHI = \pi I_d \tag{K.11}$$

$$\rho I_{t,h} = \rho(GHI) = \pi I_r \tag{K.12}$$

$$I_x = \text{Const.} \tag{K.13}$$

$$\tag{K.14}$$

K.3 Calculation of the diffuse transposition factor

Based on Figure K.1, Table K.4, Figure K.2, and the point-receiver assumption, Table K.5 lists the limits of integration used to determine the diffuse transposition factor R_d.

Table K.6: Diffuse transposition factor by case

Case	Top/Bottom limit	Left/Right limit	R_d
I	$\beta \leq \alpha_{TB}$	$\beta \leq \alpha_{LR}$	$\left(\frac{2+\cos(2\alpha_{TB})+\cos(2\alpha_{LR})}{4}\right)$
II	$\beta \leq \alpha_{TB}$	$\beta > \alpha_{LR}$	$\left(\frac{4+2\cos(2\alpha_{TB})+\cos(2\alpha_{LR})+\cos(2\beta)}{8}\right)$
III	$\beta > \alpha_{TB}$	$\beta \leq \alpha_{LR}$	$\left(\frac{4+\cos(2\alpha_{TB})+2\cos(2\alpha_{LR})+\cos(2\beta)}{8}\right)$
IV	$\beta > \alpha_{TB}$	$\beta > \alpha_{LR}$	$\left(\frac{4+\cos(2\alpha_{TB})+\cos(2\alpha_{LR})+2\cos(2\beta)}{8}\right)$

K.3.1 Example Simplification

The diffuse transposition factor for Case I ($\beta \leq \alpha_{TB}$ and $\beta \leq \alpha_{LR}$) is given by

$$D_T = I_d \left[\underbrace{\pi \left(\frac{1 + cos(2\alpha_{TB})}{4} \right)}_{1,3} + \underbrace{\pi \left(\frac{1 + cos(2\alpha_{LR})}{4} \right)}_{2,4} \right] \tag{K.15}$$

$$D_T = \frac{D_H}{4} \left[2 + \cos(2\alpha_{TB}) + \cos(2\alpha_{LR})\right] \tag{K.16}$$

$$R_d = \left(\frac{2 + \cos(2\alpha_{TB}) + \cos(2\alpha_{LR})}{4} \right) \tag{K.17}$$

K.3.2 Diffuse transposition factor results

Using the methods developed above for all four cases yeilds Table K.6.

K.3.3 Diffuse transposition factor verification

The simplest step is to check that for $\alpha_{TB} = 0$ and $\alpha_{LR} = 0$ that R_d reduces to the same values as 3DISM. Case I becomes $\beta = 0$ and $R_{d\text{M3DISM}} = R_{d\text{3DISM}} = 1$; therefore, Case I checks. Cases II and III do not apply. Case IV reduces to $(R_d)_{\text{M3DISM}} = (R_d)_{\text{3DISM}}$ exactly; therefore, it also checks. Now, for R_d, Figure K.3 shows that

1. M3DISM is equal to M3DISM for $\alpha_{TB} = \alpha_{LR} = 0$

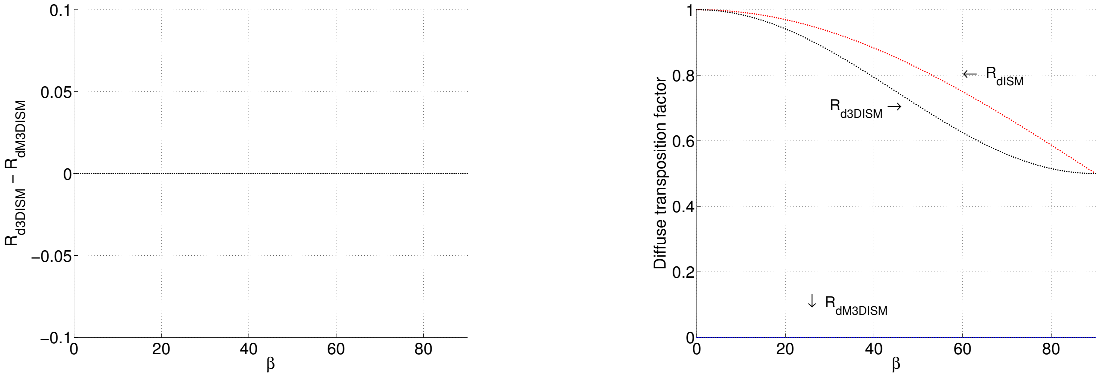

(a) Full view.

(b) No view.

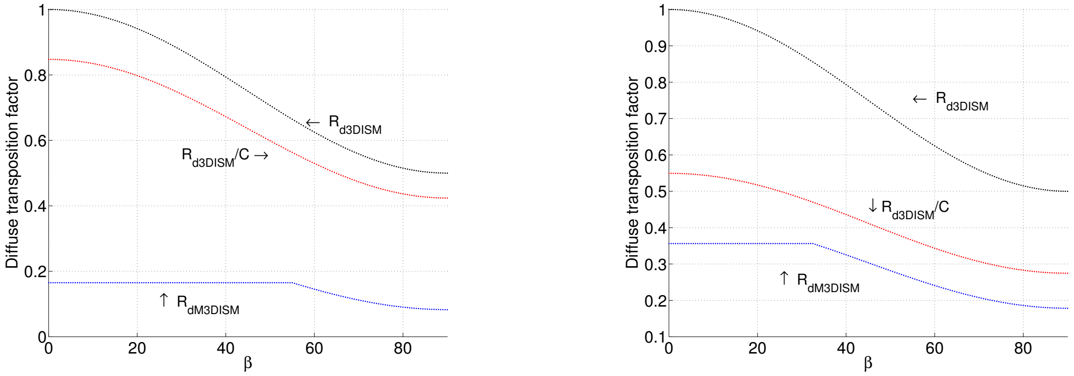

(c) N–S XCPC.

(d) E–W XCPC.

Figure K.3: Diffuse transposition factor verification.

2. M3DISM is zero with no view ($\alpha_{TB} = \alpha_{LR} = 90$

3. For intermediate values of α_{TB} and α_{LR} M3DISM is

   (a) continuous

   (b) has the correct form

   (c) is less than 3DISM

Table K.7: Limits of integration for the diffuse transposition factor

Cases	Common			I	II	III	IV
Region	a	b	c	d			
1	$\frac{-\pi}{4}$	$\frac{\pi}{4}$	$\frac{\pi}{2}-\beta$	N/A$^{*\&**}$	N/A*	$\frac{\pi}{2}-\alpha_{TB}$	$\frac{\pi}{2}-\alpha_{TB}$
2a	$\frac{\pi}{4}$	$\frac{\pi}{2}$	$\frac{\pi}{2}-\beta$	N/A$^{*\&**}$	$\frac{\pi}{2}-\alpha_{LR}$	N/A**	$\frac{\pi}{2}-\alpha_{LR}$
2b	No contribution, because $0 \leq \beta \leq 90°$						
3							
4a							
4b	$\frac{3\pi}{2}$	$\frac{7\pi}{4}$	$\frac{\pi}{2}-\beta$	N/A$^{*\&**}$	$\frac{\pi}{2}-\alpha_{LR}$	N/A**	$\frac{\pi}{2}-\alpha_{LR}$

* No contribution, because $\beta \leq \alpha_{TB}$

** No contribution, because $\beta \leq \alpha_{LR}$

Table K.8: Reflected transposition factor by case

Case	Top/Bottom limit	Left/Right limit	R_r
I	$\beta \leq \alpha_{TB}$	$\beta \leq \alpha_{LR}$	0
II	$\beta \leq \alpha_{TB}$	$\beta > \alpha_{LR}$	$\left(\frac{\cos(2\alpha_{LR})-\cos(2\beta)}{8}\right)$
III	$\beta > \alpha_{TB}$	$\beta \leq \alpha_{LR}$	$\left(\frac{\cos(2\alpha_{TB})-\cos(2\beta)}{8}\right)$
IV	$\beta > \alpha_{TB}$	$\beta > \alpha_{LR}$	$\left(\frac{\cos(2\alpha_{TB})+\cos(2\alpha_{LR})-2\cos(2\beta)}{8}\right)$

K.4 Calculation of the reflected transposition factor

Based on Figure K.1, Table K.4, Figure K.2, and the point-receiver assumption, Table K.7 lists the limits of integration used to determine the diffuse transposition factor R_r.

K.4.1 Reflected transposition factor results

Using the same method as before, Table K.8 is developed, which shows the results.

K.4.2 Reflected transposition factor verification

The simplest step is to check that for $\alpha_{TB} = 0$ and $\alpha_{LR} = 0$ that R_d reduces to the same values as 3DISM. Case I becomes $\beta = 0$ and $R_{r\text{M3DISM}} = R_{r\text{3DISM}} =$

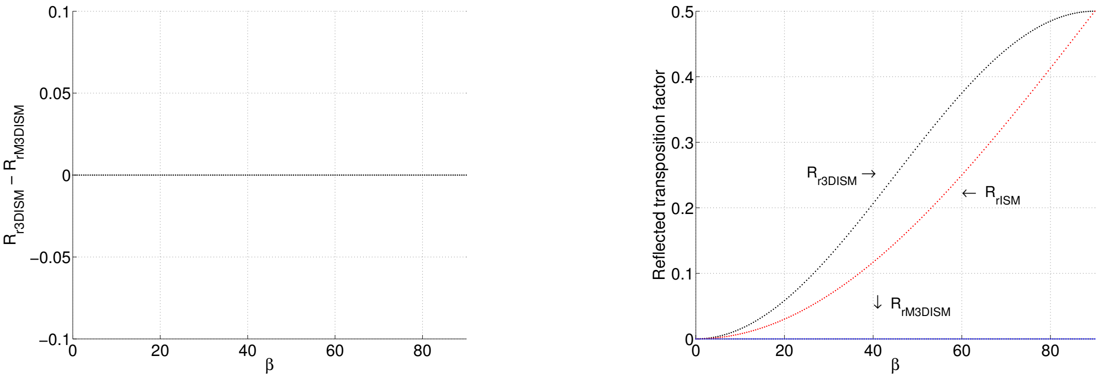

(a) Full view.

(b) No view.

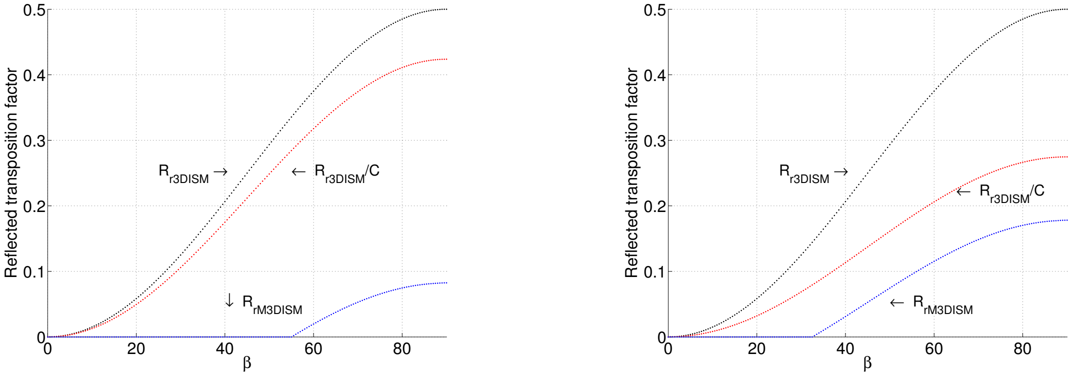

(c) N–S XCPC.

(d) E–W XCPC.

Figure K.4: Reflected transposition factor verification.

0; therefore, Case I checks. Cases II and III do not apply. Case IV reduces to $(R_r)_{\mathrm{M3DISM}} = (R_r)_{\mathrm{3DISM}}$ exactly; therefore, it also checks. Now, for R_r, Figure K.3 shows that

1. M3DISM is equal to M3DISM for $\alpha_{TB} = \alpha_{LR} = 0$
2. M3DISM is zero with no view ($\alpha_{TB} = \alpha_{LR} = 90$)
3. For intermediate values of α_{TB} and α_{LR} M3DISM is
   (a) continuous
   (b) has the correct form
   (c) is less than 3DISM

APPENDIX L

BRUNGER MODEL IMPLIMENTATION DETAILS

This appendix contains an explanation of the method and derivations of the tools used to implement the Brunger model. It must be clearly noted that this method uses the constant polar angle method from Badescu 2002, which is known to be wrong as discussed in Chapter 7.

L.1 Brunger method for the XCPC

The Brunger Model allows integration of the diffuse irradiance times the IAM K to give the proper calculation of the diffuse contribution to the effective irradiance. This method totally avoids the non-physical model of K_d and the issue of determining an effective angle of incidence. The Brunger model is also a validated anisotropic sky model. The Brunger model itself provides the diffuse transposition factor (R_d) based on sky conditions for each time block of data. Equations H.1 give the full model and can be shown in Equations L.1–L.6:

$$G_{eff} = \underbrace{K_{\theta b}(\theta_L, \theta_T) I_{b,n} \cos\theta_i}_{\text{Beam}} + \underbrace{I_{d,h} R_d}_{\text{Diffuse}} + \underbrace{\rho I_{t,h} R_r}_{\text{Reflected}} \tag{L.1}$$

$$K_{\theta b}(\theta_L, \theta_T) = \begin{cases} 1 & \text{if } |\theta_T| \leq 32.5^\circ \wedge |\theta_L| \leq 88^\circ \\ 0 & \text{otherwise} \end{cases} \tag{L.2}$$

$$R_d = \iint \frac{L(\theta(\theta'', \phi''), \phi(\theta'', \phi''))}{I_{d,h}} \cos\theta'' \sin\theta'' d\theta'' d\phi'' \tag{L.3}$$

$$R_r = \text{ undefined} \tag{L.4}$$

$$\eta = \eta_0 - a_1 T_m^* - a_2 G_{eff} {T_m^*}^2 \tag{L.5}$$

$$T_m^* = \frac{T_m - T_{amb}}{G_{eff}} \tag{L.6}$$

where the unprimed (unrotated) coordinate system describes the distribution of the diffuse light over the sky vault (dome) and the primed (rotated) coordinate system describes the mounting of the collector. For more information, see Appendix H. This model is specific to each data point (period of time) one wishes to calculate the irradiance on a sloped surface. For example, in the current discussion, the TMY3 data is used, which has hourly average data over a typical year for a given location. This means that the determined R_d value only applies to that specific data point whereas in the other models, the R_d value applies to all data points that are mounted at the same slope with the same collector.

To use the Brunger method, there are six considerations:

- Which reflected transposition factor to use?
- Do the coefficients tabulated by k and k_t span the range of values that will be encountered?
- How to properly interpolate given the a_i provided at each discrete (k, k_t) pair? (e.g., interpolate the integrated R_d and R_r values or the a_i coefficients)
- Is the computational cost affordable?
- Are the input irradiance values measured or modeled accurately enough to yield results outside the noise of those measurements? For example, will an accurate model with inaccurate inputs yield inaccurate results?
- Does the added complexity yield enough additional accuracy to outweigh the costs?

When considering these issues, TMY3 data are modeled (SUNY) from satellite measurements and known to be less accurate than the TMY2 data set. The computational cost to use the Brunger Model is also likely not affordable when using the simulation to study optimal mounting angle as a function of latitude, which is the scope of the next two chapters. At three locations that represent the diversity of sky conditions in the United States and a fourth of all TMY3 locations, Figure L.1 shows the coefficients (a_i) tabulated by k and k_t for the Brunger Model do not cover the range of values encountered. At best, extrapolation is a dangerous prospect because a_3 is non-linear. This results in the need for additional sky measurements that cover the range of values encountered. It is for these reasons that implementation of the Brunger Model cannot be used for later studies in this work.

L.2 Overview of calculations

Despite the limitations noted above, the Brunger Model can be used to compare and select from the other alternatives for calculating (R_d) using only irradiance data for which the Brunger Model has coefficients tabulated.

Here is a brief overview of the algorithm created to implement the Brunger Model:

1. Load TMY3 data and collector specifications.
2. Calculate k and k_t.
3. Remove TMY3 hourly values outside Brunger coeficients a_i for k and k_t.
4. Set a_i values for each data point (hourly data)
5. Call SPA to determine the solar location θ_s and ϕ_s
6. Loop over the collector field of view for each portion of that view.
    (a) Set limits of integration for this portion.

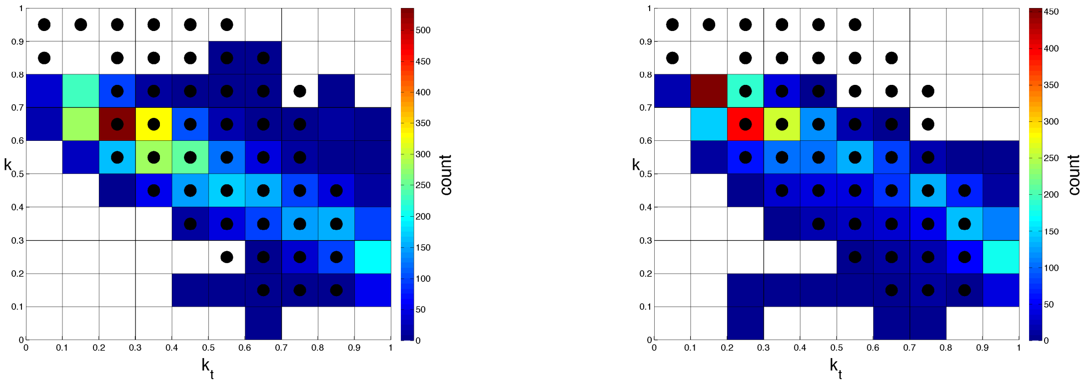

(a) Key West, Florida.

(b) College Station, Texas.

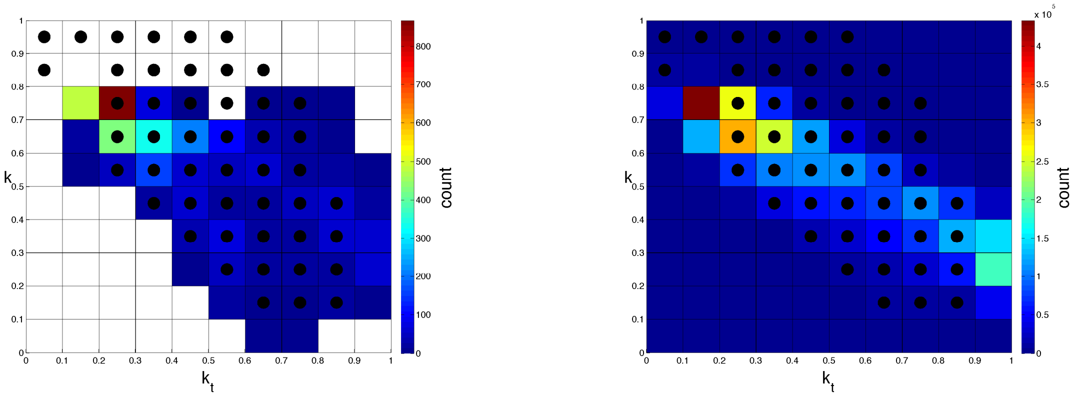

(c) Merced, California.

(d) All 1020 TMY3 locations.

Figure L.1: Brunger k and k_t data (black dots) compared with TMY3 values.

(b) Set arrays of θ'' and ϕ'' values that cover this portion.

(c) Calculate corrisponding $\theta(\theta'', \phi'')$ and $\phi(\theta'', \phi'')$ values.

(d) Calculate Ψ.

(e) Calculate I.

(f) Calculate $r_d = \frac{L}{I_{d,h}} sin\theta'' cos\theta'' d\theta'' d\phi''$.

(g) Calculate this portions contribution to R_d and aggregate.

There are several tasks that need to be accomplished to properly use the Brunger Model with the XCPC.

1. θ'' and ϕ'' limits of integration
2. $\theta(\theta'', \phi'')$ and $\phi(\theta'', \phi'')$

L.3 General Setup

Starting with the general equation for irradiance, inserting IAM for a given collector will determine the effective irradiance G_{eff}.

$$G = \int I(\theta(\theta'', \phi''), \phi(\theta'', \phi'')) \cos\theta'' d\Omega'' \tag{L.7}$$

$$G = \int_0^{2\pi} \int_0^{\frac{\pi}{2}} I(\theta(\theta'', \phi''), \phi(\theta'', \phi'')) \cos\theta'' \sin\theta'' d\theta'' d\phi'' \tag{L.8}$$

$$G_{eff} = \int_0^{2\pi} \int_0^{\frac{\pi}{2}} I(\theta(\theta'', \phi''), \phi(\theta'', \phi'')) K(\theta''_L, \theta''_T) \cos\theta'' \sin\theta'' d\theta'' d\phi'' \tag{L.9}$$

where I is the total irradiance (beam + diffuse) (not I from the Brunger Model in algorithm Step 6e above). In the case of determining the Brunger R_d transposition factor, $\frac{L}{I_{d,h}}$ will be used in place of the total irradiance I. This method for calculating

Table L.1: Cases of angle of acceptance limit

Case	Top/Bottom limit	Left/Right limit
I	$\beta \leq \alpha_{TB}$	$\beta \leq \alpha_{LR}$
II	$\beta \leq \alpha_{TB}$	$\beta > \alpha_{LR}$
III	$\beta > \alpha_{TB}$	$\beta \leq \alpha_{LR}$
IV	$\beta > \alpha_{TB}$	$\beta > \alpha_{LR}$
$0 \leq \beta \leq 90^\circ$		

the irradiance avoids the issue of determining an effective IAM for the diffuse and reflect components, although it requires determining the transformed contribution $I(\theta(\theta'', \phi''), \phi(\theta'', \phi''))$. Most solar modeling does not use this method because it is more computationally expensive. Furthermore, it alters the meaning of efficiency from $(\frac{E_{\text{th}}}{G})$ to $(\frac{E_{\text{th}}}{G_{\text{eff}}})$. Effective irradiance is used here, because it provides a more physically sound method for determining collector performance. The effective irradiance method can be greatly simplified when the IAM function K is close to a step function and can be approximated as a step function. This converts the limits of integration in Equation L.9 to account for limited field-of-view of the collector because of the acceptance angles. Changing the limits of integration to account for acceptance angles effectively breaks the integration into four parts. Including tilt of the collector breaks the integration parts into sub-parts. Accounting for angles of acceptance in a general way, various values for the longitudinal and transverse directions of the collector, results in the need to consider several cases. Table L.1 lists the cases considered, where α_{TB} and α_{LR} are the half angle of acceptance in the top/bottom and left/right directions respectively. Figure L.2 shows the regions of interest, where $\theta = 0$ is out of the page and compass directions are in the original coordinates before tilt or azimuth rotations. Figure K.2 shows a side view of the collector under tilt rotation and includes several important angles.

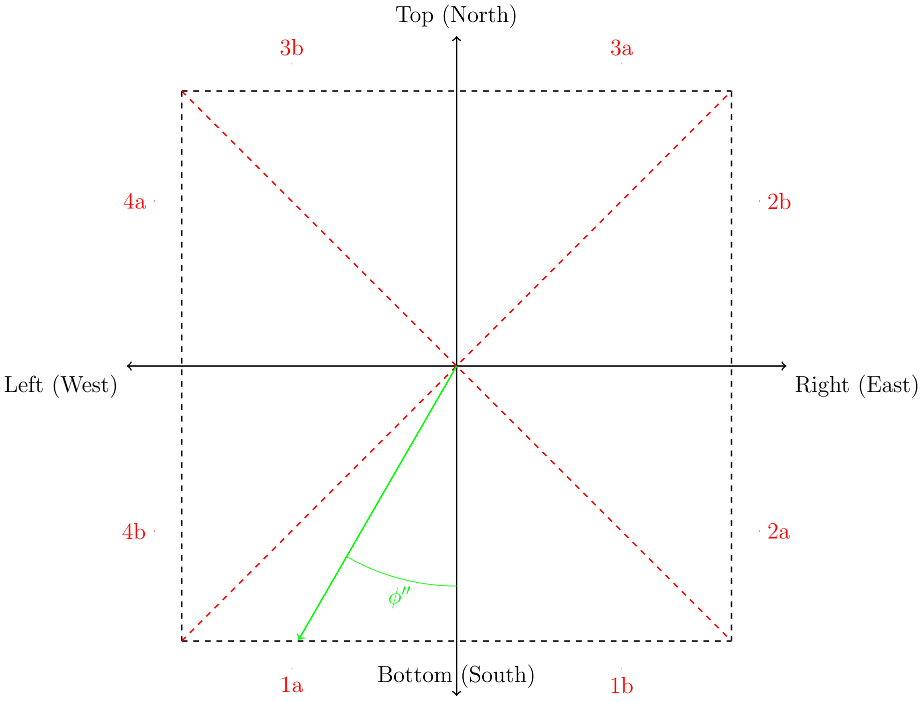

Figure L.2: Collector field-of-view regions.

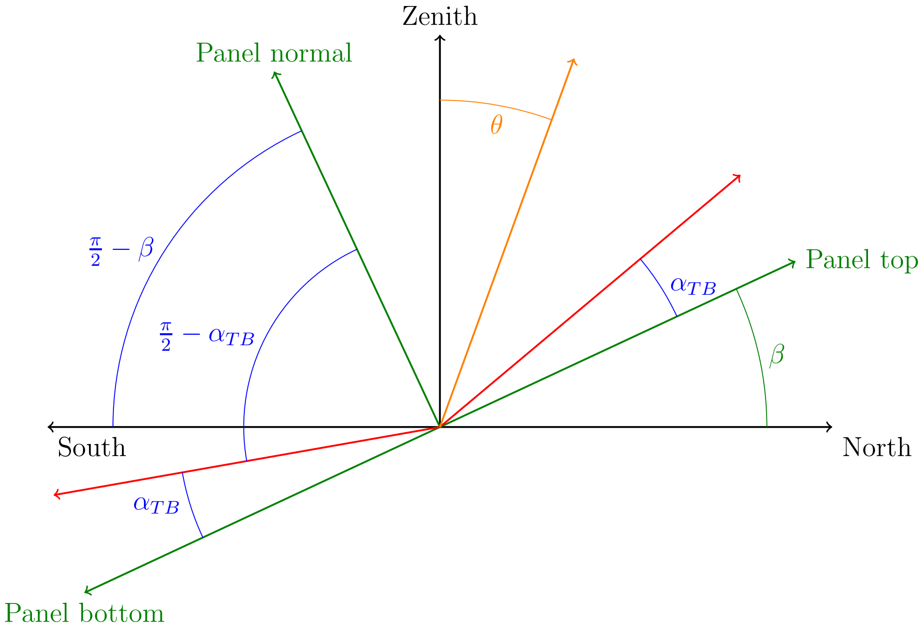

Figure L.3: Angles of interest in slope rotation.

Table L.2: Limits of integration for the diffuse transposition factor

Cases	Common			I	II	III	IV
Region	a	b	c	d			
1	$\frac{7\pi}{4}$	$\frac{9\pi}{4}$	0	$\frac{\pi}{2} - \alpha_{TB}$	$\frac{\pi}{2} - \alpha_{TB}$	$\frac{\pi}{2} - \beta$	$\frac{\pi}{2} - \beta$
2a	$\frac{3\pi}{2}$	$\frac{7\pi}{4}$	0	$\frac{\pi}{2} - \alpha_{LR}$	$\frac{\pi}{2} - \beta$	$\frac{\pi}{2} - \alpha_{LR}$	$\frac{\pi}{2} - \beta$
2b	$\frac{5\pi}{4}$	$\frac{3\pi}{2}$	0	$\frac{\pi}{2} - \alpha_{LR}$	$\frac{\pi}{2} - \alpha_{LR}$	$\frac{\pi}{2} - \alpha_{LR}$	$\frac{\pi}{2} - \alpha_{LR}$
3	$\frac{3\pi}{4}$	$\frac{5\pi}{4}$	0	$\frac{\pi}{2} - \alpha_{TB}$	$\frac{\pi}{2} - \alpha_{TB}$	$\frac{\pi}{2} - \alpha_{TB}$	$\frac{\pi}{2} - \alpha_{TB}$
4a	$\frac{\pi}{2}$	$\frac{3\pi}{4}$	0	$\frac{\pi}{2} - \alpha_{LR}$	$\frac{\pi}{2} - \alpha_{LR}$	$\frac{\pi}{2} - \alpha_{LR}$	$\frac{\pi}{2} - \alpha_{LR}$
4b	$\frac{\pi}{4}$	$\frac{\pi}{2}$	0	$\frac{\pi}{2} - \alpha_{LR}$	$\frac{\pi}{2} - \beta$	$\frac{\pi}{2} - \alpha_{LR}$	$\frac{\pi}{2} - \beta$

L.4 Limits of integration

Based on Figure L.2, Table L.1, Figure L.3, and the point-receiver assumption, Table L.2 lists the limits of integration used to determine the diffuse transposition factor R_d. Here a and b limits apply to ϕ''. Also the c and d values apply to the θ'' limits of integration.

L.5 Reverse coordinate rotations

Badescu [62] used the Brunger Model to verify the 3DISM derived in Appendix D. Badescu notes in his appendix that $\theta(\theta'', \phi'')$ and $\phi(\theta'', \phi'')$ and a transformation is required. The method he uses to determine θ and ϕ was based on a right-handed coordinate system whereas Brunger used a left-handed coordinate system. Badescu also did not present a method to determine ϕ in all four quadrants. As a result, a new method for determining θ and ϕ is presented here. Continuing the left-handed coordinate system work built in Appendix M, one can write:

$$\vec{x} = \boldsymbol{R}(-\gamma)\boldsymbol{R}(-\beta)\vec{x''} \tag{L.10}$$

$$\vec{x''} = \boldsymbol{R}(\beta)\boldsymbol{R}(\gamma)\vec{x} \tag{L.11}$$

$$\vec{x} = \boldsymbol{R}(-\gamma)\boldsymbol{R}(-\beta)\boldsymbol{R}(\beta)\boldsymbol{R}(\gamma)\vec{x} \tag{L.12}$$

$$\boldsymbol{I} = \boldsymbol{R}(-\beta)\boldsymbol{R}(\beta) \tag{L.13}$$

$$\boldsymbol{I} = \boldsymbol{R}(-\gamma)\boldsymbol{R}(\gamma) \tag{L.14}$$

$$\vec{x} = \vec{x} \tag{L.15}$$

For an arbitrary location of interest on the sky vault, $\vec{x''}$ is

$$x'' = \sin(\theta'')\cos(\phi'') \tag{L.16}$$

$$y'' = \sin(\theta'')\sin(\phi'') \tag{L.17}$$

$$z'' = \cos(\theta'') \tag{L.18}$$

$$\boldsymbol{R}(-\beta) = \begin{bmatrix} \cos(\beta) & 0 & \sin(\beta) \\ 0 & 1 & 0 \\ -\sin(\beta) & 0 & \cos(\beta) \end{bmatrix} \tag{L.19}$$

$$\boldsymbol{R}(-\gamma) = \begin{bmatrix} \cos(\gamma) & \sin(\gamma) & 0 \\ -\sin(\gamma) & \cos(\gamma) & 0 \\ 0 & 0 & 1 \end{bmatrix} \tag{L.20}$$

Using Equations L.10 and L.16-L.20 yields:

$$x = \cos\gamma\cos\beta\sin\theta''\cos\phi'' + \cos\gamma\sin\beta\cos\theta'' + \sin\gamma\sin\theta''\sin\phi'' \tag{L.21}$$

$$y = -\sin\gamma\cos\beta\sin\theta''\cos\phi'' - \sin\gamma\sin\beta\cos\theta'' + \cos\gamma\sin\theta''\sin\phi'' \tag{L.22}$$

$$z = \cos\beta\cos\theta'' - \sin\beta\sin\theta''\cos\phi'' \tag{L.23}$$

Now,

$$\theta = \arccos z \tag{L.24}$$

$$\phi = \arctan \frac{y}{x} \tag{L.25}$$

Lastly, a method for ensuring that the inverse trig-functions yield values in the correct quadrant is needed. Because the domain of θ'' is $(0, \frac{\pi}{2} - \beta)$, the domain of θ'' is contained in the range of θ and is always in the first quadrant; therefore, there is no issue of quadrants for θ. Now, determining the correct quadrant for ϕ is a more complicated process, although it is quite tractable. Obviously, one could easily derive a method to manually force ϕ to continuously move in the range $(0,\ 2\pi)$. Numerically, this would be less than desirable because it would require many conditional statements. Rather, using pre-compiled code is preferred; therefore, atan2 in MatLab is used in the following way:

1. Transform back to standard right-handed system then calculate ϕ

$$\phi = \text{atan2}(-x, -y) \tag{L.26}$$

2. Transform results to the defined left-handed system

$$\phi = (-\phi) - \frac{\pi}{2} \tag{L.27}$$

3. Force ϕ to be $[0,\ 2\pi]$ continuous

$$\phi(\phi < 0) = \phi(\phi < 0) + 2\pi \tag{L.28}$$

Now ϕ is continuous in the range $[0,\ 2\pi]$ for the left-handed coordinate system.

APPENDIX M

DERIVATION OF THE COMPONENT ANGLES COMPRISING THE ANGLE OF INCIDENCE.

This appendix contains the derivation of the method use to decompose the angle of incidence into its two components. This will be accomplished by transforming the solar direction from unrotated coordinates to the double-rotated coordinates of the mounting of a STC given by

$$\vec{x}'' = \boldsymbol{R}(\beta)\boldsymbol{R}(\gamma)\vec{x} \tag{M.1}$$

The derivation is organized as follows:

1. Coordinate system definition
2. Solar direction
3. Review of coordinate transformations
4. Azimuth rotation
5. Slope rotation
6. Determination of final results

M.1 Coordinate system definition

Based on the documentation by SPA by NREL, Figure M.1 defines the coordinate system. This is a left-handed system, so careful attention to angle definitions, rotations, and signs is required.

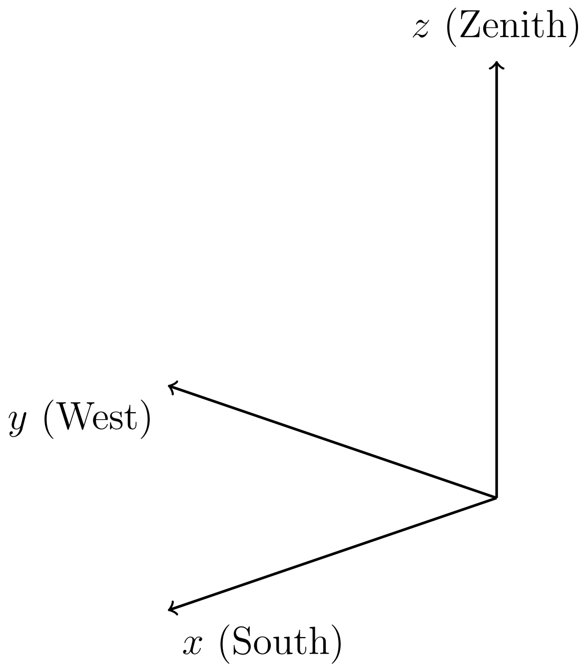

Figure M.1: Left-handed coordinate system.

M.2 Solar Direction

The SPA documentation defines the solar location as shown in Figure M.2. Based on the angle definitions,

$$z = \cos(\zeta) \tag{M.2}$$

$$y = \sin(\zeta)\sin(\Gamma) \tag{M.3}$$

$$x = \sin(\zeta)\cos(\Gamma) \tag{M.4}$$

where ζ and Γ are defined in Table 9.1. The reader should note that this definition is based on the left-handed coordinate system.

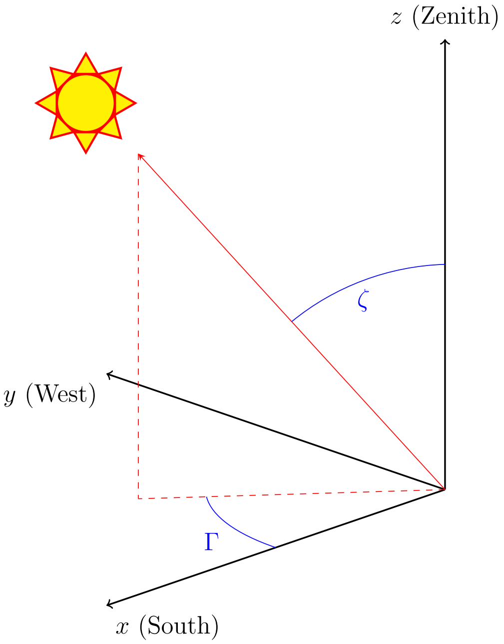

Figure M.2: Solar direction.

M.3 Review of coordinate rotations

A right-handed coordinate rotation is in general,

$$\boldsymbol{R}(\theta) = \begin{bmatrix} \cos(\theta) & \sin(\theta) & 0 \\ -\sin(\theta) & \cos(\theta) & 0 \\ 0 & 0 & 1 \end{bmatrix} \tag{M.5}$$

whereas a left-handed rotation matrix is defined as

$$\boldsymbol{R}(\theta) = \begin{bmatrix} \cos(\theta) & -\sin(\theta) & 0 \\ \sin(\theta) & \cos(\theta) & 0 \\ 0 & 0 & 1 \end{bmatrix} \tag{M.6}$$

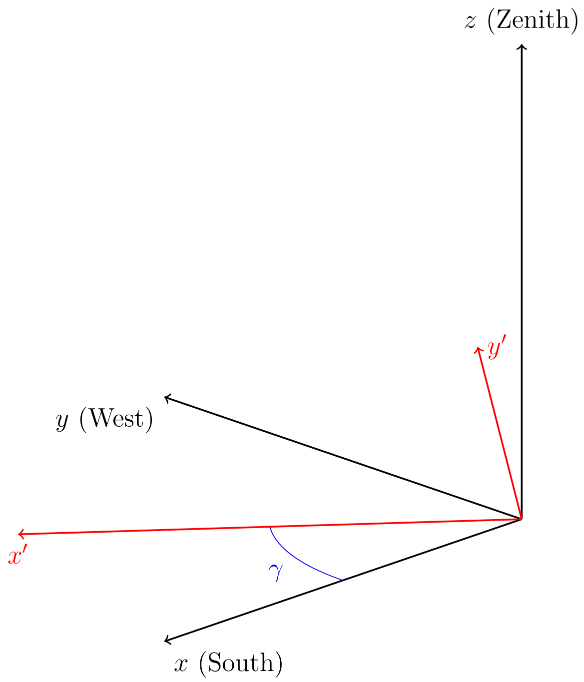

Figure M.3: Azimuth rotation.

M.4 Azimuth rotation

The azimuth rotation shown in Figure M.3 is given by

$$\boldsymbol{R}(\gamma) \implies \begin{bmatrix} x' \\ y' \\ z' \end{bmatrix} = \begin{bmatrix} \cos(\gamma) & -\sin(\gamma) & 0 \\ \sin(\gamma) & \cos(\gamma) & 0 \\ 0 & 0 & 1 \end{bmatrix} \begin{bmatrix} x \\ y \\ z \end{bmatrix} \tag{M.7}$$

Applying the rotation step $\boldsymbol{R}(\gamma)$ to the solar direction $\vec{x}$ yields:

$$x' = \sin(\zeta)[\cos(\gamma)\cos(\Gamma) + \sin(\gamma)\sin(\Gamma)] \tag{M.8}$$

$$\cos(\alpha \pm \beta) = \cos(\alpha)\cos(\beta) \mp \sin(\alpha)\sin(\beta) \tag{M.9}$$

$$x' = \sin(\zeta)\cos(\gamma - \Gamma), \text{ by M.9} \tag{M.10}$$

$$x' = \sin(\zeta)\cos(\Gamma - \gamma), \text{ by } \cos(-\theta) = \cos(\theta) \quad \text{(M.11)}$$

$$y' = \sin(\zeta)[-\sin(\gamma)\cos(\Gamma) + \cos(\gamma)\sin(\Gamma)] \quad \text{(M.12)}$$

$$z' = z = \cos(\zeta) \quad \text{(M.13)}$$

M.5 Slope or tilt rotation

The tilt rotation shown in Figure M.4 is given by

$$\boldsymbol{R}(\beta) \implies \begin{bmatrix} x'' \\ y'' \\ z'' \end{bmatrix} = \begin{bmatrix} \cos(\beta) & 0 & -\sin(\beta) \\ 0 & 1 & 0 \\ \sin(\beta) & 0 & \cos(\beta) \end{bmatrix} \begin{bmatrix} x' \\ y' \\ z' \end{bmatrix} \quad \text{(M.14)}$$

Applying the rotation step $\boldsymbol{R}(\beta)$ to the solar direction in the rotated coordinates $\vec{x'}$ yields:

$$x'' = \cos(\beta)\sin(\zeta)\cos(\Gamma - \gamma) - \sin(\beta)\cos(\zeta) \quad \text{(M.15)}$$

$$y'' = y' = \sin(\zeta)[-\sin(\gamma)\cos(\Gamma) + \cos(\gamma)\sin(\Gamma)] \quad \text{(M.16)}$$

$$z'' = \sin(\beta)\sin(\zeta)\cos(\Gamma - \gamma) + \cos(\beta)\cos(\zeta) \quad \text{(M.17)}$$

M.6 Determination of final results

The solar position in the double rotated panel coordinates is given by

$$\vec{x''} = \boldsymbol{R}(\beta)\boldsymbol{R}(\gamma)\vec{x} \quad \text{(M.18)}$$

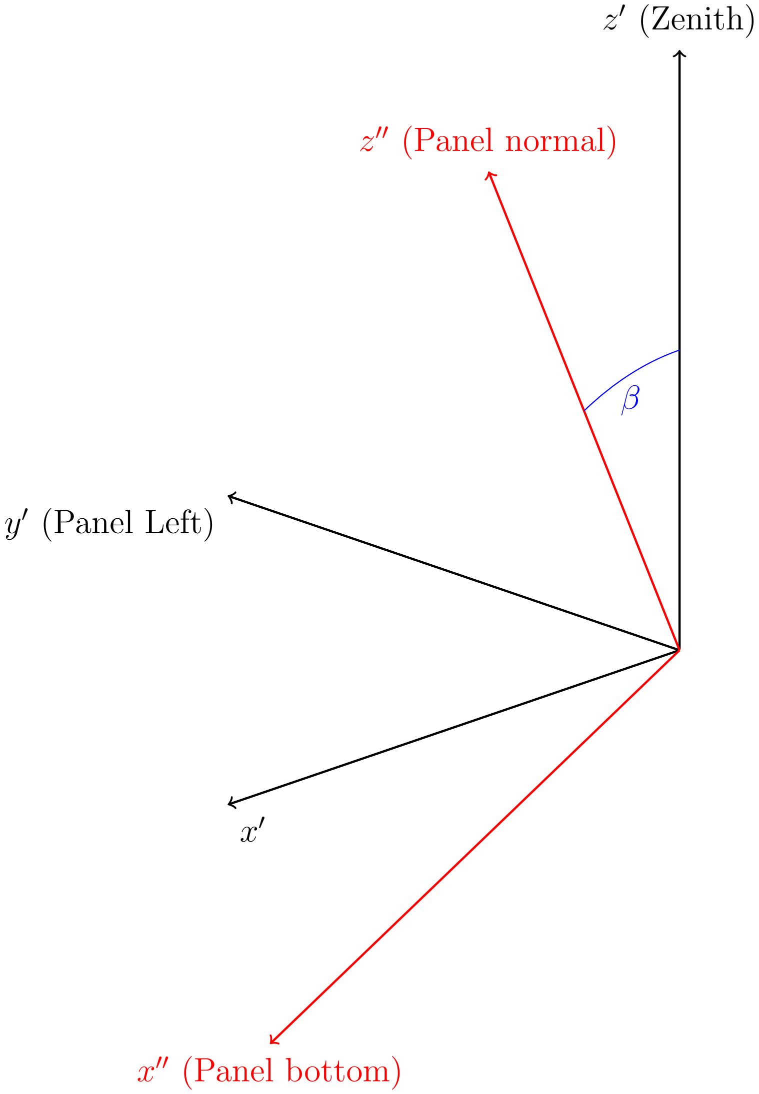

Figure M.4: Slope or tilt rotation.

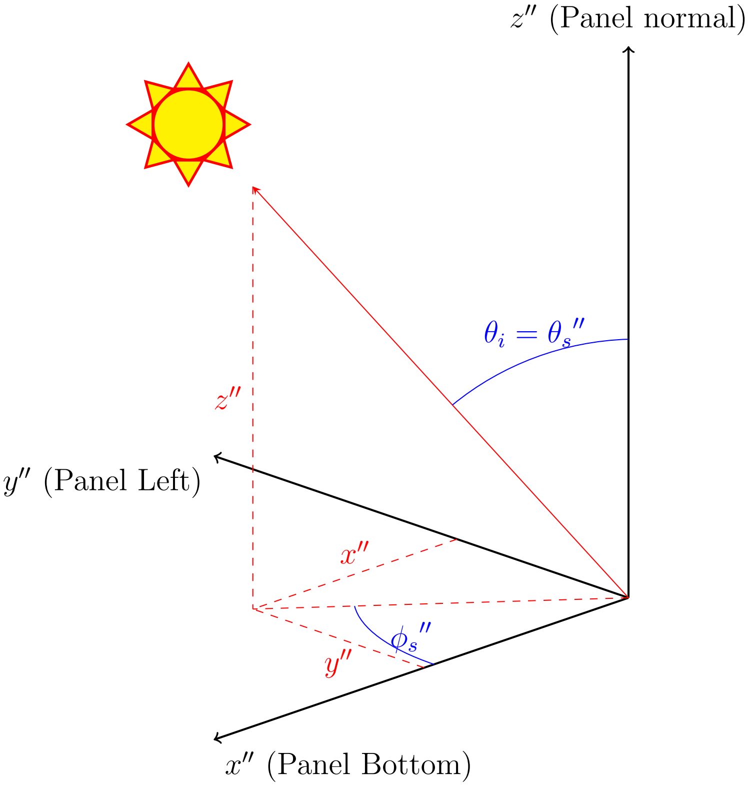

Figure M.5: The solar direction and the angle of incidence.

This information can be used to determine the three angles of interest (θ_i, θ_{LR}, and θ_{TB}). First, as depicted in Figure M.5

$$\theta_i = \arccos(z'') \tag{M.19}$$

This exactly matches Equation 47 of the SPA documentation and line 936 of SPA.c code where the SPA determines the angle of incidence.

Second as depicted in Figure M.6,

$$\theta_{LR} = \arctan(\frac{y''}{z''}) \tag{M.20}$$

$$\theta_{TB} = \arctan(\frac{x''}{z''}) \tag{M.21}$$

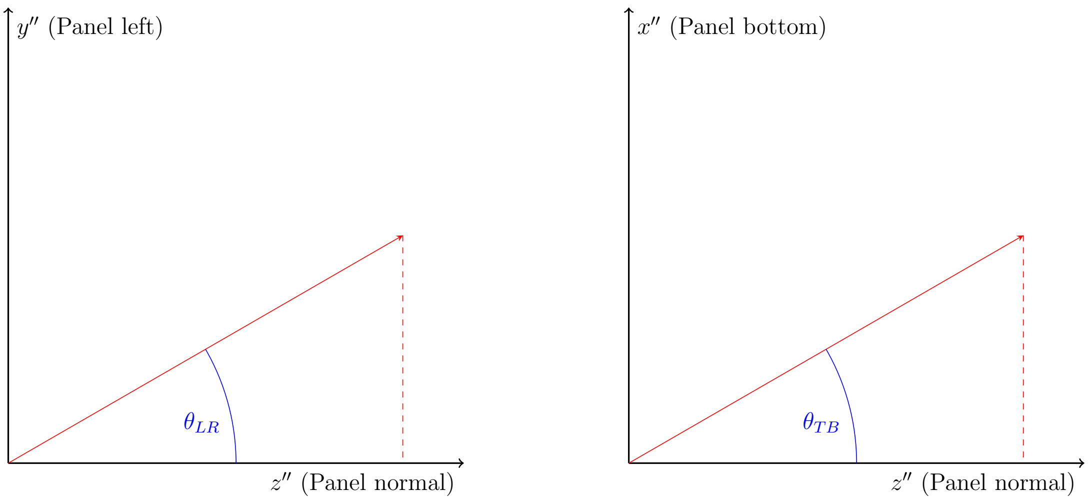

(a) Panel left-right angle of incidence.

(b) Panel top-bottom angle of incidence.

Figure M.6: Angle of incidence components.

where the arctan function is designed to correctly treat all four quadrants in two dimensions.

Now, dropping the double prime notation ($z'' \rightarrow z$), Equations 9.1–9.5 are recovered.

APPENDIX N

PART-LOAD MODEL CODE

N.1 Pump and expander models

```
function [x] = SizeAdj(kW_Size,n)
% Nathan Kamphuis July 2013
% Finds the Coefficients for use with thermalEff Local Function in
% Expander Model, The Coeff’s adjust the part load efficiency power
% law curve by the maxiumum efficiency at 3600 rpm by the efficiency
% as a function of size.
% n=1 for expander, n=2 for Compressor
if nargin == 1,
    n=1;
end
options = optimoptions(’fsolve’,’Display’,’off’);  % Turn off display
x=fsolve(@(x)Coeff(x,MaxEff(kW_Size,n)),[-150 -1 1],options);
end


function [F] = Coeff(x,Eff_Size)
% Nathan Kamphuis July 2013
% For use with Fsolve to root find the coefficients of the power law
% that fit the form of the efficiency curves
F=[x(1)*(66)^(x(2))+x(3);...
    x(1)*(1500)^(x(2))+x(3)-0.986174645356127*Eff_Size;...
```

```
    x(1)*(3600)^(x(2))+x(3)-Eff_Size];
end


function [y] = MaxEff(x,n)
% Nathan Kamphuis July 2013
% Taken From data on Star Rotor Estimation of max Efficiency by size
% and fit to the power law form
% x in units of kW
if n==1, % Expander Efficiency Curve
    y=-0.3379.*x.^(-0.1663)+1.076;
elseif n == 2, % Compressor Efficiency Curve
    y=-0.2927*x.^(-0.3311)+0.9609;
end
y(x<=0)=0;
y(y<0)=0;
end


function [y] = VolEff(x)
% Nathan Kamphuis July 2013
% Taken from Star Rotor Compressor Test at 1.9 pressure ratio on air
y=-65.98.*x.^(-1.002)+1.002;
y(x<=0|x>3600)=0;
y(y<0)=0;
end
```

```
function [H3 S3 RPM] = ExpanderModel(m_dot_act,s)
% Nathan Kamphuis Aug 2013
% Assumes the inlet state properties are known and the isentropic
% state has also been calculated
% This model Calculates the outlet state and returns the RPM

if m_dot_act-mdot(3600,s)>0,
    disp('ExpanderModel:Actual Mass flow is too large')
    H3=NaN; S3=NaN; RPM=NaN;
elseif m_dot_act-mdot(131,s)<0,
    disp('ExpanderModel:Actual Mass flow is too small')
    H3=NaN; S3=NaN; RPM=NaN;
else

    % Code to determine the RPM

    try
        RPM = fzero(@(x)(m_dot_act-mdot(x,s)),[131 3600]);
    catch err
        if strcmp(err.identifier,...
            'MATLAB:fzero:ValuesAtEndPtsSameSign')
            RPM=NaN;
            % This error happens when the mass flow is too high
        else
            rethrow(err);
        end
```

```
    end
    % Expansion for ORC diagram
    H3 = s.State(1).H-(s.State(1).H-s.State(2).H)...
        *ThermalEff(RPM,s.ExpanderModel.Coeffs);
    S3 = fzero(@(x)(H3-refpropm('H','D',s.State(2).D,'S',x,...
        s.Fluid.Name)),s.State(2).S); %Enthalpy(x,s)
end
end
```

N.2 Misc. models

```
function [mdot_act, mdot_act_NaN] = mdot(x,D1,s)
% Nathan Kamphuis July 2013
% for use with Expander Model
% x is rpm and s is a structure of the problem givens
% kg/s

% Change log:
% 9-9-14 NRK Reviewed to see if Volumetric Efficiency was handled
% properly. Since the expander flows from high pressure to low
% pressure the leakage adds to the flow rate and therefore VolEff
% should be divided by not multiplied.
% 4-2-18 NRK updated state notation to D1

mdot_act = D1.*s.ExpanderModel.NumberofChambers.*...
    s.ExpanderModel.InletChamberSize.*x./60./VolEff(x);
mdot_act_NaN=mdot_act;
```

```
mdot_act(isnan(mdot_act))=0;

end


function [y] = ThermalEff(RPM,x)

% Nathan Kamphuis July 2013

% Taken from Data Star Rotor Compressor Test at 1.9 Pressure Ratio

% on Air and fit to this form which can be adjusted by SizeAdj.m

% if nargin<2,x=[-153.7, -1.238, 0.8664];end,

y= x(1).*RPM.^(x(2))+x(3);

y(RPM<66|RPM>3600)=NaN;

% % ThermalEff not defined outside the operating range

% y(RPM<=131|RPM>3600)=0;

% y(RPM<=131|RPM>3600)=NaN;

% % ThermalEff not valid for negative numbers

% y(y<0)=0;

end


function [eta, RPM] = PumpModel_SR(m_dot_act,D4,s)

% Nathan Kamphuis January 2014

% Assumes the inlet state properties are known and the isentropic

% state has also been calculated

% This model Calculates the outlet state and returns the RPM


% Change Log:

% 4-2-18 NRK updated state notation to D4 for density at state 4
```

```
%% The If Block is for testing and code developement
if m_dot_act-mdotp(3600,D4,s)>0,
%     disp('PumpModel_SR:Actual Mass flow is too large')
    eta=NaN; RPM=NaN;
elseif m_dot_act-mdotp(131,D4,s)<0,
%     disp('PumpModel_SR:Actual Mass flow is too small')
    eta=NaN; RPM=NaN;
else

    % Code to determine the RPM
    % Is the Try Catch Block to protective given the if block
    % it is now part of the code? Which method is faster the if
    % block or the try block?

    try
        RPM = fzero(@(x)(m_dot_act-mdotp(x,D4,s)),[131 3600]);
        eta = ThermalEff(RPM,s.PumpModel.Coeffs); % Efficiency
    catch err
        if strcmp(err.identifier,...
            'MATLAB:fzero:ValuesAtEndPtsSameSign')
            RPM=NaN; eta=NaN;
            return
            % This error happens when the mass flow
            % is too high or to small
        else
            rethrow(err);
```

```
        end
    end
end
end
```

N.3 Thermodnamic cycle model

```
function [shaft_power] =...
    Superheat_Cycle_Partload(x,T_amb,G_eff,s)
%%%%%%%%%%%%%%%%%%%%%%%%%%%%%%%%%%%%%%%%%%%%%%%%%%%%%%%%%%%%%%%%%%%%
% Written by Nathan Kamphuis April 2018
%%%%%%%%%%%%%%%%%%%%%%%%%%%%%%%%%%%%%%%%%%%%%%%%%%%%%%%%%%%%%%%%%%%%
% This function was designed to calculate the partload cycle
% calculations
%%%%%%%%%%%%%%%%%%%%%%%%%%%%%%%%%%%%%%%%%%%%%%%%%%%%%%%%%%%%%%%%%%%%
% This code uses refpropm and is credited to many others see
% refpropm for further information on this and how to properly use
% it.
%ßßßßßßßßßßßßßßßßßßßßßßßßßßßßßßßßßßßßßßßßßßßßßßßßßßßßßßßßßßßßßßßßßßß
% refpropm Thermophysical properties of pure substances and mixtures.
%   Calling sequence for pure substances:
%      result=refpropm(prop_req, spec1, value1, spec2, value2,...
%      substance1)
%   and for mixtures
%      result=refpropm(prop_req, spec1, value1, spec2, value2,...
%                                    substance1, substance2, ..., x)
%
```

```
%   where
%       prop_req    is a character string showing what
%                   properties that are requested
%                   Each property is represented by one character:
%                           A   Speed of sound [m/s]
%                           B   Volumetric expansivity (beta) [1/K]
%                           C   Cp [J/(kg K)]
%                           D   Density [kg/m3]
%                           E   dP/dT (sat) [kPa/K]
%                           F   Fugacity [kPa] (returned as an array)
%                           G   Gross heating value [J/kg]
%                           H   Enthalpy [J/kg]
%                           I   Surface tension [N/m]
%                           J   Isenthalpic Joule-Thompson coeff.
%                                                            [K/kPa]
%                           K   Ratio of specific heats (Cp/Cv) [-]
%                           L   Thermal conductivity [W/(m K)]
%                           M   Molar mass [g/mol]
%                           N   Net heating value [J/kg]
%                           O   Cv [J/(kg K)]
%                           P   Pressure [kPa]
%                           Q   Quality (vapor fraction) (kg/kg)
%                           R   d(rho)/dP [kg/kPa]
%                           S   Entropy [J/(kg/K)]
%                           T   Temperature [K]
```

```
%                             U   Internal energy [J/kg]
%                             V   Dynamic viscosity [Pa*s]
%                             W   d(rho)/dT [kg/m^3-K]
%                             X   Liquid phase &
%                                      gas phase comp. (mass frac.)
%                             Z   Compressibility factor
%                             +   Liquid density of equilibrium phase
%                             -   Vapor density of equilibrium phase
%
%       spec1     is a character giving what we want to specify:
%                                             (T, P, H, D, C, or R)
%                 using the specifier C will return properties at:
%                                            The critical point
%                 using the specifier R will return properties at:
%                                            The triple point
%
%       value1    is the corresponding value
%
%       spec2     is a character giving the second specification:
%                                             (P, D, H, S, U or Q)
%
%       value2    is the value of the second specification
%
%       substance1
%       is the file name of the pure fluid (or the first
```

```
%                 component of the mixture), with the extension
%                 ".fld" excluded, that we are interested in.
%
%       substance2,substance3,...substanceN
%                 are the name of the other substances in the
%                 mixture. Up to 20 substances can be handled
%                 Valid substance names are equal to the file names
%                 in the C:\Program Files\REFPROP\fluids\' directory
%                 (with .FLD excluded).
%
%       x         is a vector with mass fractions of the substances
%                 in the mixture.
%
%   Examples:
%   1) P = refpropm('P','T',373.15,'Q',0,'water') gives
%         the vapor pressure of water at 373.15 K in [kPa]

%   2) [S Cp] = refpropm('SC','T',373.15,'Q',1,'water') gives
%         Entropy and Cp of saturated steam at 373.15 K

%   3) densmix =
%       refpropm('D','T',323.15,'P',1e2,'water','ammonia',[0.9 0.1])
%       gives the density of a 10% ammonia, water solution at:
%                                             100 kPa and 323.15 K.
%
```

```
%4) x = refpropm('X','P',5e2,'Q',0.4,'R134a','R32',[0.8, 0.2]) gives
%   temperature as well as gas and liquid compositions for a mixture
%   of two refrigerants at a certain pressure and quality.
%   Note that, when 'X' is requested, row 1 of the returned value is
%   the liquid phase composition and row 2 is the vapor phase
%   composition.
%
%5)T=refpropm('T','C',0,' ',0,'water') gives the critical temperature
%ßßßßßßßßßßßßßßßßßßßßßßßßßßßßßßßßßßßßßßßßßßßßßßßßßßßßßßßßßßßßßßßßßßßß
%%%%%%%%%%%%%%%%%%%%%%%%%%%%%%%%%%%%%%%%%%%%%%%%%%%%%%%%%%%%%%%%%%%%%
%% Setting Variable values
RPM_EXP = x(1);
P1 = x(2);
S1 = x(3);
try
    %% Calc State 4 (Pump Inlet)
    T4 = T_amb+s.Condenser.dT;
    [S4, P4, H4, D4] = refpropm('SPHD','T',T4,'Q',0,s.Fluid.Name);

    %% Calc State 1 (Expander Inlet)
    [T1, H1, D1] = refpropm('THD','P',P1,'S',S1,s.Fluid.Name);
    M_Dot = mdot(RPM_EXP,D1,s); % Requires D1 to be Calculated

    %% Calc State 2 (Isentropic Change Across Expander)
    % Density from Mass Conservation of positive displacment device
```

```
D2 = D1/s.ExpanderModel.VolumeRatio;
% Isentropic so S1 = S2 Now D2 and S2 known
[S2, H2] = refpropm('SH','D',D2,'S',S1,s.Fluid.Name);

%% Calc State 3 (Expander Outlet)
% First find the H and S at state 3 using the expander model
H3 = H1-(H1-H2)*ThermalEff(RPM_EXP,s.ExpanderModel.Coeffs);
S3 = fzero(@(x)(H3-refpropm('H','D',D2,'S',x,s.Fluid.Name)),S2);
% Enthalpy(x,s)
% Now that two state properties are known use
% them to define State 3 S=S3,
[P_l, H3, D3]=refpropm('PHD','D',D2,'S',S3,s.Fluid.Name);

%% Calc State 5 (Isentropic Change Across the Pump)
% s5=s4; p5=p1
[H5]=refpropm('H','P',P1,'S',S4,s.Fluid.Name);

%% Calc State 6 (Pump Outlet)
[eta_pump, RPM_Pump]=PumpModel_SR(M_Dot,D4,s);
% Find Enthalpy from efficiency
H6= H4 +(H5-H4)/eta_pump;
% %p5=p6
% [S6,T6,P6,D6,Q6]=refpropm('STPDQ','P',P5,'H',H6,s.Fluid.Name);

%% CVT Modeling
%{
```

```
try
    % power out of cvt
    Power_Pump_f=(H6-H4)*M_Dot;
    CF = (RPM_EXP*2*pi/60)*s.CVTModel.Max_Torque;
    Pin=fzero(@(y)(Power_Pump_f - y*...
        CVTModel_NV(RPM_Pump/RPM_EXP,y/CF)),...
        [0.2*CF CF]);
    CVT_Eff=CVTModel_NV(RPM_Pump/RPM_EXP,Pin/CF);
catch error
    CVT_Eff = NaN;
end
    %}
    CVT_Eff = 1;

    %%%%%%%%%%%%%%%%%%%%%%%%%%%%%%%%%%%%%%%%%%%%%%%%%%%%%%%%%%%%%%%%
    % % %% Remaining Calcs
    % % P_L = P4;
    % % P_H = P1;
    % % T_l = T4;
    % % dT = T1 - T4;

    %% Heat engine heat input
    Q_orc = (H1-H6)*M_Dot; % W_th

    %% Cycle Efficiency
    eta_R = ((H1-H3)-(H6-H4)/CVT_Eff)/(H1-H6);
```

```
% h1-h3 expander power, h6-h4 pump power, h1-h6 heat input

%% Carnot efficiency of cycle
eta_c = 1-T4/T1;

%% Second Law Efficiency
eta_2 = eta_R/eta_c;

% % %% VPC (delta h)rho
% % psi = (H1-H3)*D3;
% %
% % %% Expansion Ratio
% % exprat = D1/D3;

%% bad data removal and final calcs
if eta_R<0 || eta_c<0 || eta_2<0,
    eta_R=NaN;
    T_m=NaN;
    Q_orc=NaN;
else
    %% Mean Temperature in solar collector (Enthalpy section)
    n=50;
    T_m = 0;
    dH=(H1-H6)/(n-1);
    for i=1:n,
```

```
            T=refpropm(’T’,’P’,P1,’H’,(H6+(i-1)*dH),s.Fluid.Name);
            T_m=T_m+T; % sum Temperature values
        end
        T_m=T_m/n;
        % convert total temperature into average Temperature
    end

    %% Calculate collector efficinecy
    eta_col = s.CollectorModel.nsxcpc.eta((T_m-T_amb)/G_eff,G_eff);

    %% Calculate collector heat output
    Q_col = s.CollectorModel.nsxcpc.area*eta_col*G_eff; % W_th

    %% Calculate shaft power out
    if Q_col>=Q_orc,
        shaft_power = eta_R*Q_orc; % W
    else
        shaft_power = NaN;
    end
catch error
    shaft_power = NaN;
end
end %function Superheat_Cycle_Partload.m
```

N.4 STC flow analysis code

```
clear all; close all; clc; format long, format compact,
```

```
% Nathan Kamphuis April 2018
% This code analyizes the partload simulation results for STC flow
% conditions
%%%%%%%%%%%%%%%%%%%%%%%%%%%%%%%%%%%%%%%%%%%%%%%%%%%%%%%%%%%%%%%%%%%%
% This code uses refpropm and is credited to many others see
% refpropm for further information on this and how to properly use
% it.
%ßßßßßßßßßßßßßßßßßßßßßßßßßßßßßßßßßßßßßßßßßßßßßßßßßßßßßßßßßßßßßßßßßßß
% refpropm Thermophysical properties of pure substances and mixtures.
%   Calling sequence for pure substances:
%      result=refpropm(prop_req, spec1, value1, spec2, value2,...
%      substance1)
%   and for mixtures
%      result=refpropm(prop_req, spec1, value1, spec2, value2,...
%                                    substance1, substance2, ..., x)
%
%   where
%       prop_req    is a character string showing what
%                   properties that are requested
%                   Each property is represented by one character:
%                           A   Speed of sound [m/s]
%                           B   Volumetric expansivity (beta) [1/K]
%                           C   Cp [J/(kg K)]
%                           D   Density [kg/m3]
%                           E   dP/dT (sat) [kPa/K]
```

```
%                           F   Fugacity [kPa] (returned as an array)
%                           G   Gross heating value [J/kg]
%                           H   Enthalpy [J/kg]
%                           I   Surface tension [N/m]
%                           J   Isenthalpic Joule-Thompson coeff.
%                                                           [K/kPa]
%                           K   Ratio of specific heats (Cp/Cv) [-]
%                           L   Thermal conductivity [W/(m K)]
%                           M   Molar mass [g/mol]
%                           N   Net heating value [J/kg]
%                           O   Cv [J/(kg K)]
%                           P   Pressure [kPa]
%                           Q   Quality (vapor fraction) (kg/kg)
%                           R   d(rho)/dP [kg/kPa]
%                           S   Entropy [J/(kg/K)]
%                           T   Temperature [K]
%                           U   Internal energy [J/kg]
%                           V   Dynamic viscosity [Pa*s]
%                           W   d(rho)/dT [kg/m^3-K]
%                           X   Liquid phase &
%                                    gas phase comp. (mass frac.)
%                           Z   Compressibility factor
%                           +   Liquid density of equilibrium phase
%                           -   Vapor density of equilibrium phase
%
```

```
%       spec1     is a character giving what we want to specify:
%                                          (T, P, H, D, C, or R)
%                 using the specifier C will return properties at:
%                                         The critical point
%                 using the specifier R will return properties at:
%                                         The triple point
%
%       value1    is the corresponding value
%
%       spec2     is a character giving the second specification:
%                                          (P, D, H, S, U or Q)
%
%       value2    is the value of the second specification
%
%       substance1
%       is the file name of the pure fluid (or the first
%                 component of the mixture), with the extension
%                 ".fld" excluded, that we are interested in.
%
%       substance2,substance3,...substanceN
%                 are the name of the other substances in the
%                 mixture. Up to 20 substances can be handled
%                 Valid substance names are equal to the file names
%                 in the C:\Program Files\REFPROP\fluids\' directory
%                 (with .FLD excluded).
%
```

```
%       x         is a vector with mass fractions of the substances
%                 in the mixture.
%
%   Examples:
%   1) P = refpropm(’P’,’T’,373.15,’Q’,0,’water’) gives
%         the vapor pressure of water at 373.15 K in [kPa]

%   2) [S Cp] = refpropm(’SC’,’T’,373.15,’Q’,1,’water’) gives
%         Entropy and Cp of saturated steam at 373.15 K

%   3) densmix =
%       refpropm(’D’,’T’,323.15,’P’,1e2,’water’,’ammonia’,[0.9 0.1])
%       gives the density of a 10% ammonia, water solution at:
%                                             100 kPa and 323.15 K.
%
%4) x = refpropm(’X’,’P’,5e2,’Q’,0.4,’R134a’,’R32’,[0.8, 0.2]) gives
%   temperature as well as gas and liquid compositions for a mixture
%   of two refrigerants at a certain pressure and quality.
%   Note that, when ’X’ is requested, row 1 of the returned value is
%   the liquid phase composition and row 2 is the vapor phase
%   composition.
%
%5)T=refpropm(’T’,’C’,0,’ ’,0,’water’) gives the critical temperature
%ßßßßßßßßßßßßßßßßßßßßßßßßßßßßßßßßßßßßßßßßßßßßßßßßßßßßßßßßßßßßßßßßßßßß
%%%%%%%%%%%%%%%%%%%%%%%%%%%%%%%%%%%%%%%%%%%%%%%%%%%%%%%%%%%%%%%%%%%%%
```

```
%% loading results

cd ..

load('results_run_3/Sim_Partload_Calc_Test_fortesting_run_3_51.mat')

cd STC_flow_analysis


T_v=262.5:5:317.5; % Kelvin

I_v=25:50:1175; % W/m^2


%% calculation of DH and A from Fig 5 and Table 1 of Kim 2013

L = 1.640; % m Absorber tube length

% inlet

% DH = dI-tI = 8 mm - 2 mm

DH_inlet = 0.008 - 0.002; % m

A_inlet = pi*(0.006/2)^2; % m^2


% outlet

% DH = Dout -Din for annulus

% Dout = dO-to = 12 - 1.5 mm = 0.0105 m

% Din = dI = 8 mm = 0.008 m

DH_outlet = 0.0105 - 0.008; % m

% A = pi(dout/2)^2 - pi(dI/2)^2

A_outlet = pi*(0.0105/2)^2 - pi*(0.008/2)^2; % m^2


%% baseline from Kim 2013 paper which used duratherm 600

% Re number for internal flow 3000 is the transistion between

% laminar and turbulent flow
```

```
% Re = (rho Q DH)/(mu A)
% rho is density kg/m^3
% Q is volumetric flow rate m^3/s
% mdot = rho*Q kg/s
% mu is dynamic viscosity kg/(m s) = Pa s
% A is cross sectional area of the flow
% DH = 4A/P = Dout - Din for annulus m
% Kim 2013 Fig 19 two mass flow rates 80g/s and 40g/s
% mu in kg/(m s) is 1000 cP (centipoise (cP)) or 1 cP is 1 mPa S
% Duratherm 600 has mu = 71.57 cP @ 25 degree C
% mu = 0.56 cP @ 295 degree C
mu = linspace(71.57,0.56,100); % cP
mu = mu*1e-3; % cP to kg/(m s) or Pa s
% at 0.08 kg/s mass flow
% Re = mdot*DH/(mu A)
Re_inlet = 0.08*DH_inlet./mu/A_inlet;
Re_inlet_min = min(Re_inlet(:));
Re_inlet_max = max(Re_inlet(:));
Re_outlet = 0.08*DH_outlet./mu/A_outlet;
Re_outlet_min = min(Re_outlet(:));
Re_outlet_max = max(Re_outlet(:));

% h the heat transfer coefficient W/(m^2 k)
% Nu nesselt number
% Nu = hL/k = 4.36 for uniform heat flux and
```

```
% 3.66 for constant wall temp
% h = k*Nu/L
Nu = linspace(3.66,4.36,100);
% k is the fluid thermal conductivity W/(m K)
% for duratherm 600 k is 0.140 W/(m K) at 25 degree C
% k is 0.125 W/(m K) at 295 degree C
k = linspace(0.140,0.125,100);
[ k_m, Nu_m ] = meshgrid(k,Nu);
h = k_m.*Nu_m/(2*L); % W/(m^2 K)
h_min = min(h(:));
h_max = max(h(:));

%% per collector mass flow rate
STC_area = 29.05; % ft^2
STC_aperture_area = 25.92; % ft^2
STC_aperture_area = ft22m2(STC_aperture_area); % m^2
number_of_STC = s.CollectorModel.nsxcpc.area/STC_aperture_area;
M_Dot_stc = M_Dot./number_of_STC;
% kg/s of ammonia per collector

%% intialization of storage variables
mu_inlet = NaN(m,p);
cp_inlet = NaN(m,p);
k_inlet = NaN(m,p);
mu_outlet = NaN(m,p);
```

```
cp_outlet = NaN(m,p);

k_outlet = NaN(m,p);

H1 = NaN(m,p);

H_0 = NaN(m,p);

H_1 = NaN(m,p);

k_avg = NaN(m,p);


%% setting up vars for calc

P_c = refpropm('P','C',0,' ',0,s.Fluid.Name); % critical pressure


for i = 1:m,

    for j = 1:p,

        if ~isnan(P_H(i,j)*H6(i,j)*S1(i,j))

            % call state 6 for: mu, cp, k (Inlet of STC)

            [ mu_inlet(i,j), cp_inlet(i,j), k_inlet(i,j) ] =...

                refpropm('VCL','P',P_H(i,j),...

                'H',H6(i,j),s.Fluid.Name);

            % call state 1 for: mu,cp,k,h (enthalpy)(Outlet of STC)

            [ mu_outlet(i,j), cp_outlet(i,j),...

                k_outlet(i,j), H1(i,j) ] =...

                refpropm('VCLH','P',P_H(i,j),...

                'S',S1(i,j),s.Fluid.Name);

            try % average k based on enthalpy from inlet to outlet

                n=50;

                kavg = 0;
```

```
                dH=(H1(i,j)-H6(i,j))/(n-1);
                for k=1:n,
                    kkavg=refpropm(...
                        'L','P',P_H(i,j),'H',(H6(i,j)+(k-1)*dH),...
                        s.Fluid.Name);
                    kavg=kavg+kkavg; % sum
                end
                k_avg(i,j)=kavg/n;
            catch error
            end
            if P_H(i,j) < P_c
                % call H (enthalpy) for P_H Q=0 and Q=1,
                H_0(i,j) = refpropm('H','P',P_H(i,j),'Q',0,...
                s.Fluid.Name);
                H_1(i,j) = refpropm('H','P',P_H(i,j),'Q',1,...
                s.Fluid.Name);
            elseif P_H(i,j) > P_c
                % call H (enthalpy) for P_H liquid to gas transistion
            else
            end
        end
    end
end

%% STC inlet
% Re number for internal flow 3000 is the transistion between
```

```
% laminar andturbulent flow
% Re = (rho Q DH)/(mu A)
% rho is density kg/m^3
% Q is volumetric flow rate m^3/s
% mdot = rho*Q kg/s
% mu is dynamic viscosity kg/(m s) = Pa s
% A is cross sectional area of the flow
% DH = 4A/P = Dout - Din for annulus m
Re_inlet_ammonia = M_Dot_stc.*DH_inlet./mu_inlet./A_inlet;
Re_inlet_ammonia_min = min(Re_inlet_ammonia(:));
Re_inlet_ammonia_max = max(Re_inlet_ammonia(:));
% prandle number
% Pr = (cp mu)/k
% cp is specific heat at constant pressure J/(kg k)
% k is the fluid thermal conductivity W/(m K)
Pr_inlet_ammonia = cp_inlet.*mu_inlet./k_inlet;

% h the heat transfer coefficient W/(m^2 k)
% Nu nesselt number
% Nu = hL/k = 4.36 for uniform heat flux and
% 3.66 for constant wall temp
% h = k*Nu/L
h_basedon_k_avg_ammonia_436 = k_avg.*4.36./(2*L); % W/(m^2 K)
h_basedon_k_avg_ammonia_366 = k_avg.*3.66./(2*L); % W/(m^2 K)
h_k_avg_ammonia_min = min([min(h_basedon_k_avg_ammonia_436(:));...
```

```
    min(h_basedon_k_avg_ammonia_366(:))]);
h_k_avg_ammonia_max = max([max(h_basedon_k_avg_ammonia_436(:));...
    max(h_basedon_k_avg_ammonia_366(:))]);

%% STC outlet
% RE number
Re_outlet_ammonia = M_Dot_stc.*DH_outlet./mu_outlet./A_outlet;
Re_outlet_ammonia_min = min(Re_outlet_ammonia(:));
Re_outlet_ammonia_max = max(Re_outlet_ammonia(:));

% prandle number
Pr_outlet_ammonia = cp_outlet.*mu_outlet./k_outlet;

% h the heat transfer coefficient

%% determine the amount of heat in liquid phase
H_liq = H_0 - H6;

%% determine the amount of heat in two phase
H_2p = H_1 - H_0;

%% determine the amount of heat in gas phase
H_gas = H1-H_1;

%% Ratio of gas to two-phase flow heat transfered
```

```
heat_ratio = H_gas./H_2p;


%% Re number for duratherm 600 test
figure(1)
clf, hold on, grid on,
plot(mu,Re_inlet,'-k','LineWidth',2)
plot([0 0.08],[3000 3000],'--k','LineWidth',2)
plot([5.88*1e-3 5.88*1e-3],[0 3.5e4],'--k','LineWidth',2)
set(gca,'FontSize',20)
xlabel('Dynamic viscosity \mu [kg/(m s)]','Fontsize',26)
ylabel('Re number','Fontsize',26)
text('String','\downarrow Re=3000 (turbulent transistion)',...
'Position',...
    [0.03 4000],'FontSize',23)
text('String','\leftarrow \mu 95 ^{\circ}C','Position',...
    [0.0075 22500],'FontSize',23)
% axis([xl xh yl2 yh2])
hold off,


figure(2)
clf, hold on, grid on,
plot(mu,Re_outlet,'-k','LineWidth',2)
plot([0 0.08],[3000 3000],'--k','LineWidth',2)
plot([2.02*1e-3 2.02*1e-3],[0 3.5e4],'--k','LineWidth',2)
set(gca,'FontSize',20)
```

```
xlabel('Dynamic viscosity \mu [kg/(m s)]','Fontsize',26)
ylabel('Re number','Fontsize',26)
text('String','\downarrow Re=3000 (turbulent transistion)',...
'Position',...
    [0.03 4000],'FontSize',23)
text('String','\leftarrow \mu 155 ^{\circ}C','Position',...
    [0.0025 22500],'FontSize',23)
% axis([xl xh yl2 yh2])
hold off,


%% Re number for ammonia results
figure(3)
clf, hold on, grid on,
myhist3(X,{T_v I_v},Re_inlet_ammonia)
view(2),
set(gca,'FontSize',14)
xlabel('T_{amb} [K]','Fontsize',26);
ylabel('G_{eff} [W/m^2]','Fontsize',26);
% title(['Annual energy yield ', num2str(sum(energy_yield(:))),...
%     ' [kWh/(m^2)]'], 'fontsize',28);
set(gcf,'renderer','opengl');
set(get(gca,'child'),'FaceColor','interp','CDataMode','auto');
h6 = colorbar;
set(h6,'FontSize',14)
ylabel(h6,'Reynolds number inner tube','Fontsize',26)
hold off,
```

```
figure(4)
clf, hold on, grid on,
myhist3(X,{T_v I_v},Re_outlet_ammonia)
view(2),
set(gca,'FontSize',14)
xlabel('T_{amb} [K]','Fontsize',26);
ylabel('G_{eff} [W/m^2]','Fontsize',26);
% title(['Annual energy yield ', num2str(sum(energy_yield(:))),...
%     ' [kWh/(m^2)]'], 'fontsize',28);
set(gcf,'renderer','opengl');
set(get(gca,'child'),'FaceColor','interp','CDataMode','auto');
h6 = colorbar;
set(h6,'FontSize',14)
ylabel(h6,'Reynolds number outer annulus','Fontsize',26)
hold off,


%% Thermal Conductivity supercritical cycle
figure(5)
clf, hold on, grid on,
myhist3(X,{T_v I_v},k_avg)
view(2),
set(gca,'FontSize',14)
xlabel('T_{amb} [K]','Fontsize',26);
```

```
ylabel('G_{eff} [W/m^2]','Fontsize',26);
% title(['Annual energy yield ', num2str(sum(energy_yield(:))),...
%     ' [kWh/(m^2)]'], 'fontsize',28);
set(gcf,'renderer','opengl');
set(get(gca,'child'),'FaceColor','interp','CDataMode','auto');
h6 = colorbar;
set(h6,'FontSize',14)
ylabel(h6,'Thermal conductivity [W/(m K)]','Fontsize',26)
hold off,


%% heat transfer ratio subcritical cycle
figure(6)
clf, hold on, grid on,
myhist3(X,{T_v I_v},heat_ratio)
view(2),
set(gca,'FontSize',14)
xlabel('T_{amb} [K]','Fontsize',26);
ylabel('G_{eff} [W/m^2]','Fontsize',26);
% title(['Annual energy yield ', num2str(sum(energy_yield(:))),...
%     ' [kWh/(m^2)]'], 'fontsize',28);
set(gcf,'renderer','opengl');
set(get(gca,'child'),'FaceColor','interp','CDataMode','auto');
h6 = colorbar;
set(h6,'FontSize',14)
ylabel(h6,'Heat ratio','Fontsize',26)
hold off,
```

```
clear all; close all; clc; format long, format compact,
% Nathan Kamphuis April 2018
% refpropm test call for X
n=1000;
[P_c, S_c ] = refpropm('PS','C',0,' ',0,'ammonia');
S_l=refpropm('S','P',101.325,'Q',0,'ammonia');
S_r=refpropm('S','P',101.325,'Q',1,'ammonia');
S_test=linspace(S_l,S_r,n);
%% calls above P_c fail for quality Q
% H=refpropm('H','P',P_c+500,'Q',0,'ammonia')
% H=refpropm('H','P',P_c+500,'Q',1,'ammonia')
X = NaN(1,n);
D = NaN(1,n);
k = NaN(1,n);
for i=1:n,
    [ X(i) ] = refpropm('X','P',P_c+500,'S',S_test(i),'ammonia');
    [ D(i), k(i) ] =...
    refpropm('DL','P',P_c+500,'S',S_test(i),'ammonia');
end

%%
figure(1)
```

```
clf, hold on, grid on,

plot(S_test,D,'.k','LineWidth',2)

set(gca,'FontSize',20)

xlabel('Entropy [J/(kg K)]','Fontsize',26)

ylabel('Density [kg/m^3]','Fontsize',26)

% axis([xl xh yl2 yh2])

hold off,


figure(2)

clf, hold on, grid on,

plot(S_test,k,'.k','LineWidth',2)

set(gca,'FontSize',20)

xlabel('Entropy [J/(kg K)]','Fontsize',26)

ylabel('Thermal conductivity [W/(m K)]','Fontsize',26)

% axis([xl xh yl2 yh2])

hold off,
```

APPENDIX O

PV and DSSTC cost analysis code

O.1 Cost analysis

```
clear all; clc, format long, format compact,
% Written by Nathan Kamphuis September 2014
% for testing and debugging of Irradiance Calc

%% intializing Variables
a='/scratch/user/nathan.kamphuis/Matlab_Refprop/MainModel1/';
b='Functions/Specifications_Main';
run(strcat(a,b))
cd ..
cd xcpc_Cost_Comparison

Start_Time = tic;

%% 2017 reported data for PV future projection for XCPC
PV_Panel_Cost = 0.35; % $/W
STC_cost = [100; 250; 400;];
% in dollars 820-1200 for 2015. 700-900 for 2018



STC_area = 29.05; % ft^2
```

```
STC_aperture_area = 25.92; % ft^2

STC_cost = STC_cost/STC_aperture_area; % $ psf previous value was 15

total_collector_aperture_area = 1; % m^2



n=100;

G_EFF=1000; % W/M^2 Irradiance

Th=linspace(0,600,n); % Delta Temperature Kelivn Thigh-Tamb

dT=((Th+300)+(10+300)).*0.5-300;

% (Thigh+Tlow)/2-Tamb with Tlow being

X=dT./G_EFF;

% removing values that return negative efficiencies

X(X>s.CollectorModel.nsxcpc.X_Limit)=NaN;

q=G_EFF.*s.CollectorModel.nsxcpc.eta(X,G_EFF).*...

    total_collector_aperture_area; % [Wth]


eta_el = 0.7*(1-(300+10)./(Th+300));

Cap_Ex = NaN(3,n);

Cap_Ex_Power = NaN(3,n);

for i=1:3,

    Cap_Ex(i,:) = STC_cost(i).*...

    m22ft2(total_collector_aperture_area)./q;

    % $15psf to $ to $/Wth

    Cap_Ex_Power(i,:) = STC_cost(i)*...

        m22ft2(total_collector_aperture_area)./q./eta_el;
```

```
    % $15psf to $ to $/Wel
end
Cap_Ex_Power(Cap_Ex_Power<0) = NaN;

PV_cost_1=PV_Panel_Cost;
% $/w pannel cost divided by COP for ASHP SH
PV_cost_2=PV_Panel_Cost/2.5;
% $/w pannel cost divided by COP for ASHP SH
PV_cost_3=PV_Panel_Cost/2.75;
% $/w pannel cost divided by COP for ASHP DHW
PV_cost_4=PV_Panel_Cost/3;
% $/w pannel cost divided by COP for ASHP SH
PV_cost_5=PV_Panel_Cost/4;
% $/w pannel cost divided by COP for ASHP SH

Total_Time = toc(Start_Time);

% %%
% figure(1)
% clf, hold on, grid on,
% set(gca,'FontSize',20)
% plot(K2C(Th+300),q,'.k','MarkerSize',20,'LineWidth',2)
% xlabel('Outlet Temperature [C]','Fontsize',26)
% ylabel('Energy Flow [W_{th}]','Fontsize',26)

%%
```

```
% a=[0 350];
a=F2C(120);
b=F2C(120);
figure(1)
clf, hold on, grid on,
set(gca,'FontSize',20)
plot(K2C(Th+300),Cap_Ex(3,:),'.r',...
    K2C(Th+300),Cap_Ex(2,:),'-b',...
    K2C(Th+300),Cap_Ex(1,:),'--g','MarkerSize',8,'LineWidth',2)
plot(b,PV_cost_1,'sk',b,PV_cost_2,'xk',a,PV_cost_3,'+k',...
    b,PV_cost_4,'>k',b,PV_cost_5,'<k','MarkerSize',8,'LineWidth',2)
% [120 120],[0.2 0.44],
legend('400 [$/unit] XCPC','250 [$/unit] XCPC','100 [$/unit] XCPC',...
    'PVC 1 COP SH','PVC 2.5 COP SH',...
    'PVC 2.75 COP DHW','PVC 3.0 COP SH','PVC 4.0 COP SH',...
    'Location','NorthWest')
xlabel('Outlet temperature [C]','Fontsize',26)
ylabel('Collector capital cost [$/W_{th}]','Fontsize',26)
% axis([0 400 0.15 0.5])

%%
figure(2)
clf, hold on, grid on,
set(gca,'FontSize',20)
plot(K2C(Th+300),Cap_Ex(3,:),'.r',...
```

```
    K2C(Th+300),Cap_Ex(2,:),'-b',...
    K2C(Th+300),Cap_Ex(1,:),'--g','MarkerSize',8,'LineWidth',2)
plot(b,PV_cost_1,'sk',b,PV_cost_2,'xk',...
    b,PV_cost_4,'>k',b,PV_cost_5,'<k','MarkerSize',8,'LineWidth',2)
% [120 120],[0.2 0.44],
legend('400 [$/unit] XCPC','250 [$/unit] XCPC','100 [$/unit] XCPC',...
    'PVC 1 COP','PVC 2.5 COP',...
    'PVC 3.0 COP','PVC 4.0 COP','Location','NorthWest')
xlabel('Outlet temperature [C]','Fontsize',26)
ylabel('Collector capital cost [$/W_{th}]','Fontsize',26)
axis([0 400 0 0.75])

%%
% a=[0 350];
% a=F2C(120);
% b=F2C(120);
figure(3)
clf, hold on, grid on,
set(gca,'FontSize',20)
plot(K2C(Th+300),Cap_Ex_Power(3,:),'.r',...
    K2C(Th+300),Cap_Ex_Power(2,:),'-b',...
    K2C(Th+300),Cap_Ex_Power(1,:),'--g',...
    'MarkerSize', 8,'LineWidth',2)
plot([0 700],[PV_Panel_Cost PV_Panel_Cost],'-k','LineWidth',2) %
legend('400 [$/unit] XCPC','250 [$/unit] XCPC','100 [$/unit] XCPC',...
```

```
    'PVC capital cost','Location','NorthEast')
xlabel('Outlet temperature [C]','Fontsize',26)
ylabel('Collector capital cost [$/W_{el}]','Fontsize',26)
% text('String','{\it 6}','Position',...
%     [HH(end) T_h(end)],'FontSize',23)
axis([0 700 0 10])
```

O.2 STC sensitivity analysis

```
clear all; clc, format long, format compact,
% Written by Nathan Kamphuis September 2014
% for testing and debugging of Irradiance Calc

%% intializing Variables
a='/scratch/user/nathan.kamphuis/Matlab_Refprop/MainModel1/';
b='Functions/Specifications_Main';
run(strcat(a,b))
cd ..
cd xcpc_Cost_Comparison

Start_Time = tic;

%% 2017 reported data for PV future projection for XCPC
PV_Panel_Cost = 0.35; % $/W
STC_cost = [100; 250; 400;];
% in dollars 820-1200 for 2015. 700-900 for 2018
```

```
STC_area = 29.05; % ft^2

STC_aperture_area = 25.92; % ft^2

STC_cost = STC_cost/STC_aperture_area; % $ psf previous value was 15

total_collector_aperture_area = 1; % m^2



n=100;

G_EFF=1000; % W/M^2 Irradiance

Th=linspace(0,600,n); % Delta Temperature Kelivn Thigh-Tamb

dT=((Th+300)+(10+300)).*0.5-300;

% (Thigh+Tlow)/2-Tamb with Tlow being

X=dT./G_EFF;

% removing values that return negative efficiencies

X(X>s.CollectorModel.nsxcpc.X_Limit)=NaN;

q=G_EFF.*s.CollectorModel.nsxcpc.eta(X,G_EFF).*...

    total_collector_aperture_area; % [Wth]

q = [0.9; 1; 1.1]*q;

eta_el = 0.7*(1-(300+10)./(Th+300));

Cap_Ex = NaN(3,n);

Cap_Ex_Power = NaN(3,n);

for i=1:3,

    Cap_Ex(i,:) = STC_cost(2).*...

        m22ft2(total_collector_aperture_area)./q(i,:);
```

```
    % $15psf to $ to $/Wth
    Cap_Ex_Power(i,:) = STC_cost(2)*...
        m22ft2(total_collector_aperture_area)./q(i,:)./eta_el;
    % $15psf to $ to $/Wel
end
Cap_Ex_Power(Cap_Ex_Power<0) = NaN;

PV_cost_1=PV_Panel_Cost;
% $/w pannel cost divided by COP for ASHP SH
PV_cost_2=PV_Panel_Cost/2.5;
% $/w pannel cost divided by COP for ASHP SH
PV_cost_3=PV_Panel_Cost/2.75;
% $/w pannel cost divided by COP for ASHP DHW
PV_cost_4=PV_Panel_Cost/3;
% $/w pannel cost divided by COP for ASHP SH
PV_cost_5=PV_Panel_Cost/4;
% $/w pannel cost divided by COP for ASHP SH

Total_Time = toc(Start_Time);

% %%
% figure(1)
% clf, hold on, grid on,
% set(gca,'FontSize',20)
% plot(K2C(Th+300),q,'.k','MarkerSize',20,'LineWidth',2)
```

```
% xlabel('Outlet Temperature [C]','Fontsize',26)
% ylabel('Energy Flow [W_{th}]','Fontsize',26)


%%
% a=[0 350];
a=F2C(120);
b=F2C(120);
figure(1)
clf, hold on, grid on,
set(gca,'FontSize',20)
plot(K2C(Th+300),Cap_Ex(3,:),'.r',...
    K2C(Th+300),Cap_Ex(2,:),'-b',...
    K2C(Th+300),Cap_Ex(1,:),'--g','MarkerSize',8,'LineWidth',2)
plot(b,PV_cost_1,'sk',b,PV_cost_2,'xk',a,PV_cost_3,'+k',...
    b,PV_cost_4,'>k',b,PV_cost_5,'<k','MarkerSize',8,'LineWidth',2)
% [120 120],[0.2 0.44],
legend('1.1 thermal effficiency factor',...
    '1.0 thermal efficiency factor',...
    '0.9 thermal efficiency factor',...
    'PVC 1 COP SH','PVC 2.5 COP SH',...
    'PVC 2.75 COP DHW','PVC 3.0 COP SH','PVC 4.0 COP SH',...
    'Location','NorthWest')
xlabel('Outlet temperature [C]','Fontsize',26)
ylabel('Collector capital cost [$/W_{th}]','Fontsize',26)
% axis([0 400 0.15 0.5])
```

```
%%
figure(2)
clf, hold on, grid on,
set(gca,'FontSize',20)
plot(K2C(Th+300),Cap_Ex(3,:),'.r',...
    K2C(Th+300),Cap_Ex(2,:),'-b',...
    K2C(Th+300),Cap_Ex(1,:),'--g','MarkerSize',8,'LineWidth',2)
plot(b,PV_cost_1,'sk',b,PV_cost_2,'xk',...
    b,PV_cost_4,'>k',b,PV_cost_5,'<k','MarkerSize',8,'LineWidth',2)
% [120 120],[0.2 0.44],
legend('1.1 thermal effficiency factor',...
    '1.0 thermal efficiency factor',...
    '0.9 thermal efficiency factor',...
    'PVC 1 COP','PVC 2.5 COP',...
    'PVC 3.0 COP','PVC 4.0 COP','Location','NorthWest')
xlabel('Outlet temperature [C]','Fontsize',26)
ylabel('Collector capital cost [$/W_{th}]','Fontsize',26)
axis([0 400 0 0.75])

%%
% a=[0 350];
% a=F2C(120);
% b=F2C(120);
figure(3)
clf, hold on, grid on,
```

```
set(gca,'FontSize',20)
plot(K2C(Th+300),Cap_Ex_Power(3,:),'.r',...
    K2C(Th+300),Cap_Ex_Power(2,:),'-b',...
    K2C(Th+300),Cap_Ex_Power(1,:),'--g',...
    'MarkerSize', 8,'LineWidth',2)
plot([0 700],[PV_Panel_Cost PV_Panel_Cost],'-k','LineWidth',2) %
legend('1.1 thermal effficiency factor',...
    '1.0 thermal efficiency factor',...
    '0.9 thermal efficiency factor',...
    'PVC capital cost','Location','NorthEast')
xlabel('Outlet temperature [C]','Fontsize',26)
ylabel('Collector capital cost [$/W_{el}]','Fontsize',26)
% text('String','{\it 6}','Position',...
%      [HH(end) T_h(end)],'FontSize',23)
axis([0 700 0 10])
```